UAB
Universitat Autònoma de Barcelona

UNIVERSITAT AUTÒNOMA DE BARCELONA

DEPARTAMENT DE QUÍMICA

UNIVERSITÀ DEGLI STUDI DI TORINO

DIPARTIMENTO DI CHIMICA

Phenomena at Interstellar Core and Mantle Grains: a Quantum Mechanical Approach

---

DOCTORAL THESIS

Candidate:
Jessica PERRERO

Thesis Supervisors:
Prof. Albert RIMOLA
Prof. Piero UGLIENGO

September 2024

Memoria presentada per aspirar al Grau de Doctor per:

Jessica Perrero

Vist i plau,

Albert Rimola

Universitat Autònoma de Barcelona
Departament de Química

Piero Ugliengo

Università degli Studi di Torino
Dipartimento di Chimica

25 de Setembre de 2024

"We know accurately only when we know little; with knowledge doubt increases."

Johann Wolfgang von Goethe

Contents

Abstract

The evolution of an interstellar cloud into a planetary system is inextricably linked to the growth of chemical complexity. In the interstellar medium (ISM), chemical reactions occur either in the gas phase or on the surface of dust grains, which are refractory nanoparticles made of siliceous or carbonaceous material. In the coldest regions of space, these dust grains are coated with water-dominated ice mantles, and they play a crucial role in the growth of molecular complexity. This thesis aims to advance our comprehension of the physico-chemical processes that are regulated by dust grains through the use of computational chemistry techniques.

Particular emphasis is placed on the adsorption processes that influence the chemical composition of the gas phase, especially with respect to S-bearing species, whose main reservoirs during the early stages of planetary formation remain unidentified. Furthermore, a combined experimental and theoretical determination of the binding energies, which govern the adsorption and desorption processes, reveals the significance of employing both approaches to enhance the interpretation of experimental outcomes and to overcome their respective limitations.

Furthermore, the thesis investigates the role of chemical reactions on the surface of dust grains in the growth of chemical complexity in the ISM. The formation mechanisms of complex organic molecules, defined as species containing six or more atoms, including at least one carbon atom, are characterised. In particular, this research investigates the formation mechanisms of acetaldehyde, ethanol and urea, with a focus on reactions involving both closed-shell and radical species. The findings reveal that dust grains play a variety of roles in these processes, including supplying and concentrating reactants on their surface, acting as catalysts and, eventually, as third bodies that dissipate the energy released during exothermic reactions. This research provides new insights into the critical role of dust grains in the chemical evolution that precedes planetary system formation.

Preface

This thesis collects the results of a Ph.D. in computational chemistry undertaken at the Autonomous University of Barcelona (UAB), under the supervision of Prof. Albert Rimola, in cotutelle with the University of Turin (UniTo), under the supervision of Prof. Piero Ugliengo. During these four years I also had the opportunity to visit the LERMA laboratory of CY Cergy Paris University for one month, where I performed some experiments in an interstellar chamber. The subject of this thesis is astrochemistry, an intricate as well as fascinating topic. In particular, the research has been focused on the processes happening at the surface of dust grains, refractory nanoparticles found throughout the Universe, eventually covered in water ice.

Objectives of the thesis

The formation of Solar-type planetary systems from a primordial cloud involves five basic steps: prestellar, protostellar, protoplanetary disk, planetesimal, and planet formation phases. Observations show that the physical and chemical complexity grow together during the evolution of an interstellar cloud, where molecules react with each other, forming more complex species. The role of interstellar dust grains in the growth of chemical complexity is highly debated. There is enough consensus that dust grain surfaces provide the sites for heterogeneous catalysis leading to the formation of pivotal molecules (e.g., H_2, H_2O, and CH_3OH), but their role in the formation of more complex species, among which some with a strong prebiotic potential (e.g., CH_3CHO and $HCONH_2$), is a disputed argument in astrochemistry. Astronomical observations, astrochemical modelling and laboratory experiments are usually employed to provide physico-chemical data, but each technique suffers from some technical limitations. This is why theoretical quantum chemistry simulations can offer its contribution.

Three main fields can be investigated by computational chemistry:

i) development of realistic structural dust grain models;

ii) characterisation of the reaction mechanisms leading to the formation of molecules, from simple prestellar species to more complex organic protostellar molecules and biomolecules detected in comets and meteorites; evaluation of the role played by dust grains in such reactions;

iii) simulation of the adsorption and desorption processes, which determines the composition of the solid and the gaseous phase of the interstellar medium.

This thesis aimed at shedding some light onto each of the points listed above, focusing on the following topics:

i) characterisation of olivine nanoclusters representing the core of dust grains and construction of a periodic dirty ice model containing H_2O and CO, mimicking the icy mantles that are coating dust grains in the cold regions of the Universe;

ii) characterisation of the grain-surface reaction pathways of complex organic molecules (acetaldehyde, CH_3CHO, urea, NH_2CONH_2, and ethanol, CH_3CH_2OH) on the icy mantle of dust grains, and definition of the role of the surface in each process;

iii) simulation of the adsorption of sulphur bearing species on the mantle (water) and on the core (olivine) of dust grains, and characterisation of the adsorption and desorption processes of ethanol (CH_3CH_2OH) and ethylamine ($CH_3CH_2NH_2$) on pure water ice surfaces.

Structure of the thesis

This work is organized as a compendium of the research articles published during the four years of predoctoral work. Each article (or couple of articles, when suitable) is preceded by a short introductory chapter summarising the motivations and the main results of the research, followed by a perspective of the future investigations. The thesis is organised as follows.

Part I   The first part contains an extended introduction on astrochemistry (Chapter 1) and a chapter dedicated to the methodologies adopted in this work (Chapter 2).

Part II The second part is dedicated to the investigation of adsorption processes, which comprise: the study of the interaction between 23 S-bearing species with periodic models of crystalline and amorphous water ice (Chapter 3), the characterisation of the adsorption of 9 neutral and charged S-bearing species on olivine nanoparticles, representing the core of dust grains (Chapter 4), and the combined theoretical and experimental study of the binding energy of ethanol and ethylamine on water ice mantles (Chapter 5).

Part III The third part concerns reactivity, with the characterisation of urea and ethanol formation on small water ice clusters (Chapter 6) and of acetaldehyde formation on a periodic dirty ice surface model (Chapter 7).

Part IV Finally, the last part is dedicated to the main conclusions of this work (Chapter 8).

Part I

Introduction and Methodology

Chapter 1

Introduction

Abstract

The chemical processes occurring in the interstellar medium (ISM) present significant challenges to the astronomical and astrochemical communities. Here, the origin of the Universe and the fundamental steps in the formation of planetary systems are reviewed, followed by the characterisation of the ISM. Special attention is given to the chemistry at work in the coldest regions, the cradles of stellar birth. Dust grains, one of the two components of interstellar matter, are particularly relevant for the build-up of chemical complexity, which is closely linked to the evolution of the stellar system. The physical and chemical processes taking place at the surface of dust grains enrich the chemical network of the ISM, providing alternative and complementary pathways to gas-phase reactions. The two main topics of the thesis are then presented: i) the sulphur depletion problem, and ii) the formation of interstellar complex organic molecules. Finally, it is elucidated the role of quantum chemistry, on which the QUANTUMGRAIN project is based, in the interdisciplinary field of astrochemistry, emphasising the tight relationship between observations, modelling, and experiments, that underpin any progress in the field.

1.1 The Universe and the periodic table

It would be difficult to print a Ph.D. thesis on paper without chemical elements. There would be no paper, no ink, nor anything worth writing about. The existence of chemical elements is strictly related to the origin of the Universe, as summarised in the following paragraph.

1.1.1 The Big Bang and the nucleosynthesis of the elements

The 'Big Bang' theory seems to be the most plausible explanation for the origin of the Universe (Weinberg, 1993). In 1949, F. Hoyle, a supporter of the steady state Universe, invented this expression to mock the theory proposed by A. Friedmann, G. Lemaitre and G. Gamow, who at the time lacked experimental evidence to support their argument. The 1948 paper by R.A. Alpher, H. Bethe and G. Gamow, entitled 'The Origin of Chemical Elements' actually provided support for the Big Bang model, in addition to the 1929 discovery by E. Hubble that distant galaxies are redshifted in proportion to their distance from us. Further research on the subject led R.A. Alpher and R. Herman to predict the presence of an isotropic cosmic microwave background radiation (CMBR) as a residue of the initial Big Bang. However, their prediction was ignored until 1964, when P.J.E. Peebles and R.H. Dicke predicted the presence of the CMBR, measured by A. Penzias and R.W. Wilson.

The Big Bang theory postulates that the Universe we inhabit can be traced back in time to a singularity, with the most significant milestones summarised in Table 1.1. The Big Bang consisted in the expansion of this singularity and marked the beginning of space

Time	Temperature	Events
10^{-43}s	10^{32} K	Gravity is now distinct from the three other forces: strong, weak nuclear and electromagnetic.
10^{-35}s	10^{27} K	Inflation of the Universe. The strong force separates.
10^{-12}s	10^{15} K	Weak and electromagnetic forces separate. Neutrons and protons are formed by photon-photon collisions.
10^{-2}s	10^{11} K	Electrons and positrons are formed through collisions of photons.
1 s	10^{10} K	The Universe becomes transparent to neutrinos.
180 s	10^{9} K	Nucleosynthesis: hydrogen, deuterium, helium, and some lithium.
10^{5} s	3000 K	Light element atoms form, and the Universe is now transparent to radiation: CMBR is emitted.
10^{9} yr	20 K	Galaxies form.
Present	2.725 K	Scientists investigating the origin of the Universe.

Table 1.1: The history of the Universe according to the Big Bang theory. Adapted from Table 1.1 of Shaw, 2007.

and time. In a brief period of time, the Universe underwent a rapid expansion, during which its dimensions grew exponentially. This was followed by a rapid decrease in temperature and density, which fundamentally determined the composition and the shape of the current Universe (Weinberg, 1993).

The first three minutes were pivotal in the differentiation of the four fundamental forces and in the formation of the elemental reservoir of which all existing objects are composed. The first particles to be formed were neutrons and protons, following the separation of weak and electromagnetic forces. Subsequently, when the temperature reduced by four orders of magnitude, electrons and positrons were also formed. Finally, at a temperature of 10^{9} K, the aforementioned ingredients were able to mix to produce atomic nuclei, namely hydrogen (H), deuterium (D), helium (He) and a small amount of lithium (Li). For the further 10^{6} s these light atoms continued to form, marking a period in which matter was created by Big Bang nucleosynthesis. As the temperature decreased to 3000 K, the Universe became transparent to radiation, allowing the CMBR to be emitted. The first stars appeared after about 400 Myr, and the first galaxies after 1 Gyr. The Universe is currently believed to be almost 14 Gyr old, calculated by inverting the Hubble constant. The age of the Earth is established by radioisotope dating at 4.55 Gyr (Shaw, 2007).

In the present era, the chemical elements that were generated in the Big Bang represent 98% of ordinary matter in mass, with the remaining 2% accounting for heavier elements. The latter have been synthesised as a result of the nuclear reactions occurring in the cores of the stars and some additional reactions occurring upon their death. Furthermore, it has been observed that the chemical composition of distant galaxies tends to be more scarce in heavy elements. This implies that the percentage of heavy elements increases with time (Kwok, 2013). Stellar nucleosynthesis is the only source of heavier nuclei and hence the large majority of the periodic table. The thermonuclear reactions responsible for the variety of chemical elements were elucidated by F. Hoyle, W. Fowler, and M. and G. Burbidge (Burbidge et al., 1957). During the same period, also A.G.W. Cameron was investigating the nucleosynthesis of elements in stars, and in 1957 both groups published their findings (Cameron, 1957). The star interior acts as a nuclear furnace at tens of millions of degrees.

As the star ages, its interior temperature increases, allowing heavier elements to be synthesised. Nuclear reactions also provide the star with energy, as the mass defect of the nuclei formed in its interior is converted into energy through the equation $E = mc^2$. This energy counterbalances the gravitational force that would otherwise cause the star to collapse.

The first generation of stars was formed from a cloud of hydrogen, helium, and lithium. The initial stage of nuclear fusion consists of converting hydrogen nuclei into helium nuclei, in a process known as the *proton-proton cycle*. Once all the hydrogen has been converted to helium, the core of the star contracts, causing the internal temperature to rise, and triggering the *triple-alpha process*. The conversion of helium nuclei into carbon nuclei dictates the end of the life of low-mass stars. In these bodies, the core never reignites, and the outer layers are expelled to such an extent that gravity is insufficient to maintain the integrity of the star. The remnants of the star consist of a white dwarf, which will eventually cool down and become a black dwarf, composed of carbon and oxygen, and surrounded by a 'planetary' nebula formed from the expelled material.

In contrast, massive stars are capable of producing heavier elements through the *alpha capture process*. The formation of ^{16}O, ^{20}Ne, ^{24}Mg, ^{28}Si, and ^{32}S occurs in sequence once ^{12}C is available, concomitantly with the production of less stable nuclei, such as ^{13}C, ^{13}N, ^{14}N, and ^{15}O, resulting from the *carbon-nitrogen-oxygen cycle*. A stratified structure, centred at the core of the star, is built up through successive burning layers of lighter elements. The nuclear fusion process is exothermic up to the production of ^{56}Fe nuclei, after which thermonuclear reactions become endothermic. The lack of energy produced by nuclear reactions causes the core to collapse, and the increase in density results in protons and electrons reacting, forming neutrons and neutrinos. The neutrons halt the collapse of the core, however, the collision of the outer layers of material against the neutron core causes such an energetic rebound that the subsequent shock waves rip apart the star and spread its mass over large distances, resulting in a supernova event. This violent explosion propagates through space, perturbing the interstellar clouds and possibly triggering their collapse and the subsequent birth of new stars.

The death of massive stars is accompanied by the formation of elements heavier than iron, through two principal processes. The *s-process* is a slow neutron capture occurring during the collapse of the core of the star. In contrast, the *r-process* is a rapid neutron capture that takes place during the supernova event and is responsible for the formation of the majority of the heavier nuclei.

The wealth of elements constituting the periodic table in Figure 1.1 is the result of the processing of the elemental budget made available by the Big Bang. Lighter elements remain the most abundant fraction and constitute also the pivotal molecules of life, while heavier nuclei become progressively more rare and, occasionally, unstable. Considering the elemental composition and the age of planet Earth, it is plausible that the Sun belongs to a second generation of stars formed subsequent to the Big Bang, from a cloud of material enriched in heavier elements by previous supernova events.

1.1.2 Planetary systems formation

Once formed and ejected from the stars, the chemical elements proceeded to combine with one another, thereby yielding a variety of chemical species. The increase in the chemical complexity of stellar environments is strictly intertwined with the stages that characterise the formation of a planetary system (Ehrenfreund et al., 2000; Kwok, 2016). Molecules formed during the initial stages of planetary formation are thought to be inherited by
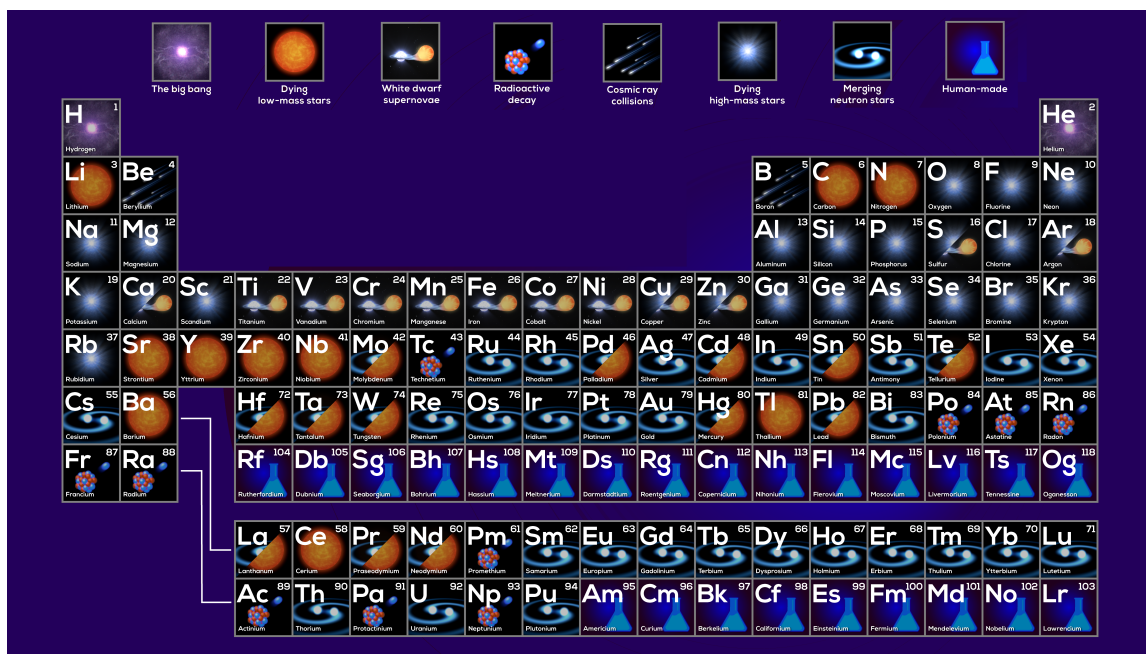
Figure 1.1: The periodic table of the elements has been colour-coded to indicate the probable origins of the elements. Adapted from https://svs.gsfc.nasa.gov/13873.

the small bodies constituted from the remnants of the planet growth process. The evolution of a primordial interstellar cloud (constituted of dust grains and gas-phase atoms and molecules), which ultimately yields a Solar-like planetary system, is supposed to go through five major phases, sketched in Figure 1.2 (Caselli et al., 2012).

1. **Pre-stellar cores.** Diffuse clouds characterised by T = 50–100 K and density ρ = 10–10^2 cm^{-3} start contracting. The matter gradually accumulates towards the centre of the nebula, resulting in a dense cloud with T = 5–10 K and ρ = 10^3–10^4 cm^{-3}. Gas-phase atoms and molecules freeze-out onto the cold surfaces of the sub-micron dust grains, forming icy mantles coating the cores of the grains. In the densest pre-stellar cores, more than 99% of all the species heavier than He reside in thick icy mantles (Caselli et al., 2022). Due to the high abundance of H atoms, hydrogenation reactions dominate the prestellar grain surface chemistry, forming molecules such as water (H_2O, Dishoeck et al., 2013), formaldehyde (H_2CO), methanol (CH_3OH, Hama et al., 2013) and other hydrogenated species.

2. **Protostellar envelopes.** The collapse of the cloud proceeds, with gravitational energy being converted into radiation, and gives rise to a 'hot core' with T = 100–300 K. As the temperature increases, the molecules frozen in grain mantles acquire mobility and eventually sublimate, returning to the gas phase. During this phase, many common organic compounds are formed. The central protostar continues to accrete mass from the surrounding cloud core. To preserve the angular momentum some of the accreting material spreads out into a disk. Concomitantly with the collapse, a fraction of the matter is violently ejected outward, forming collimated jets and molecular outflows. When the ejected material encounters the quiescent gas of the envelope and of the molecular cloud, it creates shocks, where the grain mantles and refractory grains are (partially) sputtered and vaporised. Some observations suggest that the process of planet formation might already start in this phase (Harsono et al., 2018).
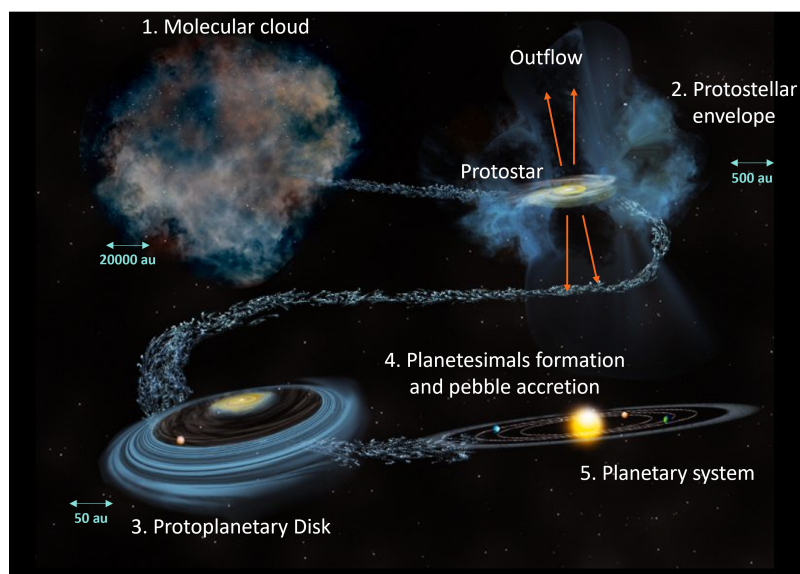
Figure 1.2: Stages of planetary system formation. The figure focuses on the first three stages, while the final two stages are presented in a unified manner. Credit: Bill Saxton/NSF/AUI/NRAO.

3. **Protoplanetary disks.** From the original envelope, only a protoplanetary disk remains. In regions close to the central object, new complex molecules are synthesised by reactions between the species formed in the previous phase. In the cold regions of the disk, where the vast majority of matter resides, the less volatile molecules freeze-out again onto the dust grain, where they are believed to engage in reactions similarly to those taking place in the dense molecular clouds. The transition zone of a species from the gas phase to the solid phase is identified by the snow-line and determines the future planet composition, influencing the formation of gaseous and rocky planets (Öberg et al., 2021).

4. **Planetesimals formation.** Sub-micron dust grains coagulate into larger rocks, termed planetesimals, which constitute the building blocks of the future planets, comets and asteroids. A fraction of the icy mantles are likely preserved during the collision of dust grains (Mumma et al., 2011). However, they can undergo alteration processes, such as hydrothermal alteration, leading to an additional increase in molecular complexity (Trigo-Rodríguez et al., 2019).

5. **Planets formation.** Collisions of planetesimals and pebbles accretion results in the formation of planets and moons. The prevailing hypotheses regarding the formation of planetary bodies suggest that accreting pebbles would result in a faster planet growth, compared with collisions between larger bodies (Johansen et al., 2017). The leftover material, constituted by comets and asteroids, eventually falls on the primitive planets, providing a constant input of external material that could have a biological potential for the development of life. A notable example is glycine, which has been identified in 81P/Wild (Sandford et al., 2006; Elsila et al., 2009) and 67P/C-G (Altwegg et al., 2016) comets. Indeed, comets are composed of silicates, ices and a refractory organic fraction (Mumma et al., 2011; Calmonte et al., 2016; Altwegg et al., 2022), which could be of prebiotic interest and have implications in the exogenous delivery theories.

1.1.3   The interstellar medium

The interstellar medium (ISM) is defined as the matter and radiation that exist in the space between the star systems in a galaxy. The existence of the ISM was initially inferred on the basis of the observations of a few dark patches in the Milky Way, which resulted from starlight being blocked by intervening interstellar dust absorption. The ISM is the consequence of the mixing of ejected material from different generations of stars (during distinct phases of their evolution), as well as shaping and processing of such material by radiative and mechanical events. In the Milky Way, the star-formation rate is 5 $M_\odot$ (solar masses) per year, and the supernova rate is 0.03 events per year. Therefore, every 10^9 years, all interstellar matter is processed in the interior of the stars (Krugel, 2007).

The interaction between radiation and matter in the ISM is fundamental to understand its physical conditions. The heating and cooling mechanisms are based on the absorption and emission of light. For example, ultraviolet (UV) light ionises H and He in the surroundings of hot stars, and the ejection of electrons heats the interstellar gas. In diffuse and dense clouds, dust grain temperatures can increase due to starlight absorption and can decrease due to self-radiation in the middle and far infrared (IR). Cosmic rays and UV photons interacting with atoms and molecules trigger radiochemistry and photochemistry, respectively. Ultimately, absorption and emission of specific wavelengths are crucial for astronomers to be able to detect species in the ISM (Kwok, 2007).

The ISM can be classified into different phases, depending on the state of gaseous hydrogen. A schematic view of the various phases is shown in Figure 1.3.

- **Ionic state (H II).** H^+ is mainly found in two environments. The **coronal gas** is low density gas shock-heated by blastwaves racing outward from supernova explosions, able to ionise the gas until forming ions such as O^{5+}. It cools down on Myr time scales and it is often referred to as 'hot ionised medium' (HIM). Alternatively, **H II gas** corresponds to gaseous hydrogen that is photo-ionised by UV photons from hot stars. It can also be found in planetary nebulae created by the rapid mass loss happening at the late stage of Sun-like stars evolution.

- **Atomic state (H I).** Depending on the temperature and the pressure of the environment, it can be classified under **warm H I** regions, that consists mainly in atomic gas heated to T = $10^{3.7}$ K, with densities around n_H = 0.6 cm^{-3}, and also called 'warm neutral medium' (WNM). Atomic hydrogen is also found in **cold H I** regions, that are mainly atomic gas at T $\sim$ 100 K and densities around n_H = 30 cm^{-3}, constituting 1% of the volume of the ISM. These regions are also called 'cold neutral medium' (CNM).

- **Molecular state (H$_2$).** As the density of the environment increases, atomic hydrogen coexists with molecular hydrogen, from which the name 'molecular clouds' (MCs) was derived. **Diffuse MCs** are similar to CNM regions, but dense enough to allow the formation of H$_2$ in the cloud interior. **Dense MCs** are gravitationally bound clouds with a density greater than 10^3 cm^{-3} and a visual extinction $A_V > 3$ mag. As the cloud evolves, H$_2$ becomes more abundant than H.

Additionally, there are environments in which ionic, atomic, and molecular hydrogen coexist. Their relative abundances depend on the physical characteristics of each specific region.

- **Photon dominated regions (PDRs).** They constitute the interface between ionised and molecular gas. In these regions, UV and far-UV photons are responsible for
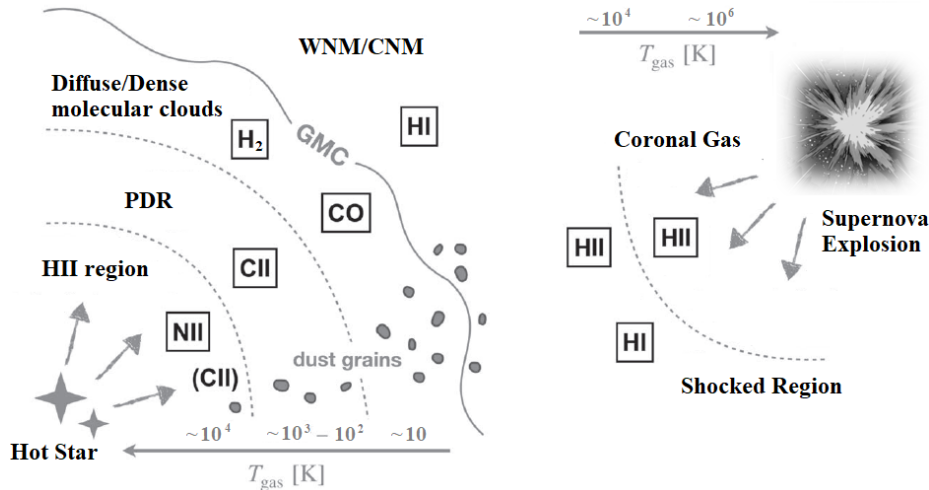
Figure 1.3: Schematic representation of ISM phases. Adapted from (Sun et al., 2019). GMC indicates a giant molecular cloud.

the photodissociation of molecules, causing the matter to be atomic and partially ionised.

- **Shock regions.** They are environments characterised by a sudden change in the physical conditions of the gas, tipically caused by high-velocity impacts, such as collisions between clouds. Stellar winds, shock waves generated by supernovae explosions, and jets through which newborn stars balance the angular momentum acquired by the collapse of a dense cloud, are also responsible for shocks. In these environments, ice mantles are sputtered and grain cores are shattered, making SiO a unique tracer of these regions. The velocity of the gas in the shock determines whether the hydrogen is molecular, atomic or ionised.

The application of spectroscopy to astronomy represented the beginning of astrophysics. Optical astronomy was the first technique used to investigate the ISM. In fact, the first lines to be detected in emission were originating by electronic transitions of highly excited atoms and ions in high temperature environments (e.g., Harrington et al., 1981). The Copernicus satellite and the Voyager mission provide two examples of spectroscopic observations in the far UV (Rogerson et al., 1973; Kohlhase et al., 1977).

Successively, the analysis of absorption features, measured against a stellar background, corresponding to transitions between different electronic states allowed the detection of the first molecules. This phenomenon concerns the UV/vis and the IR regions of the electromagnetic spectrum (e.g., Bakker et al., 1996). The first molecules to be detected were CH, CN and CH$^+$ (Swings et al., 1937; McKellar, 1940; Douglas et al., 1942).

Finally, the development of radioastronomy in the 1950s brought to the discovery of the wide presence of atomic hydrogen in our galaxy and in the Universe thanks to its 21 cm hyperfine transition (Altschuler et al., 1986). In general, the detection of neutral heavy atoms in low temperature environments is more difficult because the low-lying energy states that are likely to become excited have small energy separations and their transitions lay in the far-IR or sub-millimeter part of the spectrum (which are not affected by dust extinction).

However, in the following years, an increasing number of molecules started to be detected owing to their rotational transitions, measured in absorption against the stellar background. Further enhancements in the field were made when the placement of telescopes in Earth-orbiting spacecraft became possible, overcoming the limit of the Earth

opaque atmosphere. The number of documented species is on the rise, in line with the ongoing advancements in technology and the increasing resolution of the instruments.

More than 300 gas-phase species have been detected in the ISM[1], including a number of exotic species that are unlikely to survive for long in the physical conditions of the Earth (Müller et al., 2005; McGuire, 2022). Furthermore, the presence of organic molecules has prompted several questions about the degree of chemical complexity that can be reached in an interstellar environment and how this is linked with the origin of life.

1.1.4   The Origin, the chemical composition and the role of dust grains

Gas-phase ions, atoms, and molecules contributes to 99% of the mass of interstellar clouds, while the remaining 1% is constituted by dust grains (Williams et al., 2002). As an example, in the Milky Way, the mass of gaseous material is 5×10^9 M$_\odot$, whereas dust mass is 3×10^7 M$_\odot$ (Krugel, 2007). Noted for the first time in 1784 by William Herschel as a region of apparently lacking of stars, the presence of interstellar dust has been confirmed by multiple lines of evidence.

First, the phenomenon of interstellar reddening, whereby stars appear redder than expected based on their spectral type (thus, on their temperature), suggests the existence of a material capable of absorbing specific radiation wavelengths. In a second instance, the observation that starlight is usually a few percent linearly polarised led to the conclusion that non-spherical and aligned grains are present in the diffuse interstellar medium, probably as a consequence of an interstellar magnetic field. Moreover, the gas-phase depletion of heavy elements, such as iron, silicon, calcium, and titanium, suggests that these elements may reside in a different state of matter. The correlation of the gas-phase abundances with the condensation temperature of different atoms provides insight into which elements are most likely to form part of the solid phase and which reside preferentially in the gas phase. Indeed, it has been estimated that two-thirds of carbon and the majority of silicon and iron are in the solid form (Kwok, 2007). Additionally, 1% of the silicon budget is estimated to be trapped in nanosilicates, irregular sub-nanometer particles likely to be responsible for the Anomalous Microvawe Emission (a foreground feature which extends over the 10–60 GHz range and peaks at 20–30 GHz) observed in many astrophysical environments including the diffuse ISM and galactic clouds, and spatially correlated with regions of dust IR emission (see Macià Escatllar et al., 2019; Macià Escatllar et al., 2020, and references therein).

Thanks to the development of infrared spectroscopic techniques, it became possible to detect the continuous emission from interstellar dust grains, as described by Planck's black body radiation formula. The temperature of these grains was inferred from the peak radiation wavelength using Wien's law, which states that the wavelength at which the maximum radiation flux occurs is characteristic of the temperature of the black body. The temperature of dust is determined by the ratio between its emission and absorption efficiency. The size of the grains influences the type of starlight they interact with, resulting in smaller grains being warmer than larger ones. Typical dust sizes range from tenths of nanometer to tenths of micrometer, and grains up to ~ 1 μm have been observed previous to the protostellar phase. Dust emission, consequent to starlight absorption, is the primary mechanism for grains to cool down, and accordingly is the most efficient cooling mechanism in giant clouds, where collisions between gas-phase and solid-phase matter are ineffective due to the extremely low densities. Because the radiative processes involving gas and dust differ, their temperatures are usually decoupled, with the only exception

---

[1]https://cdms.astro.uni-koeln.de/classic/molecules

being dark clouds (Krugel, 2007).

Dust formation and growth are poorly understood. Dust grains are likely formed by stochastic growth processes, either by particle-particle addition or by cluster addition, leading to irregularly shaped grains. The formation of an icy mantle due to the freeze-out of the gas-phase material in MCs could also be considered as grain growth, although this part of the process is successive to the formation of the grain core and is governed by condensation and sublimation cycles dependent on the temperature of the environment.

The origin of grain cores is debated, with predominant theories suggesting that their formation occurs within environments associated with dying stars (Zhukovska et al., 2014). Dust grains are believed to nucleate from gas-phase species under high-temperature conditions. This process occurs primarily in asymptotic giant branch (AGB) stars, where convective motes bring up C and O from the interior of the star, through H and He layers, and in type II supernovae, that eject up to 10 $M_\odot$ of material, of which 3 $M_\odot$ are heavy elements. Another hypothesis is that the formation of silicates could occur within cold and dense MCs due to the freeze-out of Si atoms or SiO molecules (Krasnokutski et al., 2014; Ferrara et al., 2016; Ginolfi et al., 2017). However, it is unclear to what extent these processes contribute to the formation of dust grains. Although some sources claim that AGB stars produce up to three times more dust than supernova explosions, others suggest that the latter are the main contributors to dust production (Krugel, 2007; Ceccarelli et al., 2018).

Unlike its formation, dust destruction is better understood. The processes that occur are evaporation caused by radiative heating, sputtering due to energetic particles (ions) in the gas phase, and chemical sputtering resulting from exothermic reactions. Furthermore, collisions between grains can lead to the evaporation of the mantle and the shattering of the core, while photodesorption occurs when the atoms of the grain are ejected as a consequence of photon absorption. These destruction processes occur primarily due to passages through supernovae shocks, where more than 50% of the iron and silicon cosmic abundances can be found in the gas phase, compared to the usual 1% found in other environments.

The core of interstellar dust grains consists mainly of silicates and carbonaceous materials. Their composition depends on the carbon-to-oxygen ratio in the region where they formed. In environments characterised by C/O < 1, carbon is trapped in CO, and grains are primarily formed by silicates, such as olivines and pyroxenes. Their general formulas are $Mg_{2x}Fe_{2-2x}SiO_4$ and $Mg_xFe_{1-x}SiO_3$ (with x = 0−1), respectively. In regions with C/O > 1, the major dust constituents would be graphite, polycyclic aromatic hydrocarbons (PAHs), non-hydrogenated and hydrogenated amorphous carbon, silicon carbides, or mixtures of hydrocarbon-based disordered structures (Tielens, 2008; Molpeceres et al., 2017). In these environments, oxygen is mostly found in metallic oxides such as MgO, FeO, Fe_3O_4, and Al_2O_3.

Although the precise nature of carbonaceous materials has yet to be determined, silicates have been clearly observed and identified as a major component of interstellar dust (Henning, 2010; Boogert et al., 2015; McClure et al., 2023). The broad IR bands at 9.7 μm ($\simeq$ 1000 cm^{-1}) and 18 μm ($\simeq$ 550 cm^{-1}), corresponding to the Si-O stretching and O-Si-O bending modes, are indicative of the amorphous nature of silicates, characterised by a distribution of bond lengths and angles. Their band profiles are altered in accordance with a number of factors, including the nature of the background, the optical thickness of the foreground, the temperature of the environment, and the degree of crystallinity of the grains. For instance, forsterite (Mg_2SiO_4) and enstatite ($MgSiO_3$) have been observed in their crystalline forms. Warm environments or cosmic ray irradiation provide enough
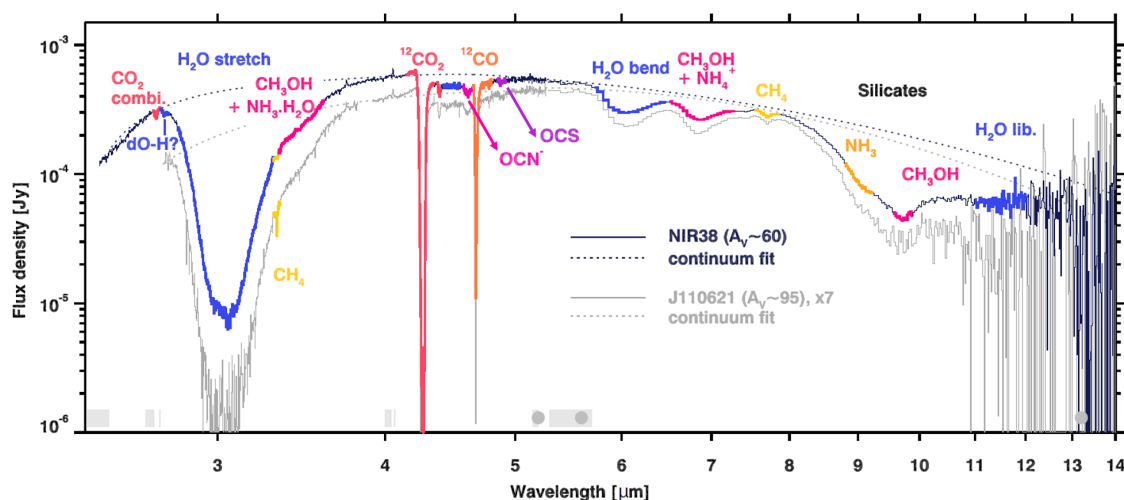
Figure 1.4: Near- and mid-IR spectrum of pristine cloud ices against the background stars NIR38 (solid navy line) and J110621 (solid light gray line), with associated continuum fits (dotted lines). The light gray bars and dark gray filled circles at the bottom of the spectrum indicates the regions used to fit the continuum star emission in the near- and mid-IR, respectively. Image from McClure et al., 2023.

energy for the reorganization and crystallization of the amorphous material.

In the coldest regions of the ISM, where clouds are shielded from UV radiation and molecular species are allowed to form, dust grains are coated in thick icy mantles resulting from the freeze-out of gas-phase species on the surface of grain cores and *in situ* chemical reactions. Ice mantles have been characterised by IR spectroscopy (Boogert et al., 2015; McClure et al., 2023; Rocha et al., 2024), with water emerging as the dominant component through the O-H stretching 3 μm ($\simeq 3300$ cm^{-1}) band. Furthermore, small amounts of other volatile species such as CO, CO_2, CH_4, NH_3, anions, and complex organic molecules (COMs, described in Section 1.2.2) are also present, as illustrated in Figures 1.4 and 1.5. For this reason, interstellar ice mantles are usually referred to as 'dirty ices'. The prevalence of hydrogenated species is attributed to hydrogenation reactions, which constitute the majority of the reactive processes occurring on the surface of grains, owing to the abundance of atomic hydrogen.

In Figure 1.6, the physico-chemical processes occurring on the icy mantles of dust grains are depicted. Adsorption, desorption, and diffusion of species on the surface of the grain are influenced not only by thermal effects, such as cooling and heating of the cloud, but can also be induced by the impact of cosmic rays and UV photons. Additionally, exothermic reactions can lead to the chemical desorption of the products formed.

The importance of dust grains stems from the fact that ice mantles are believed to facilitate the reactions occurring at their surfaces (Watanabe et al., 2008; Hama et al., 2013). They serve four primary functions: (i) pre-concentrators of chemical species, which are particularly significant in rarefied MCs, where the rate of collision between gas-phase species is extremely low, (ii) reactant suppliers, as species belonging to the ice mantle can participate in chemical reactions (Rimola et al., 2018), (iii) chemical catalysts, which offer alternative reaction pathways with low activation energies, thus surmountable under interstellar conditions (Potapov et al., 2021), and (iv) third bodies, by absorbing the large energy excess released by exothermic reactions, without undermining the stability of the newly formed products (Pantaleone et al., 2020; Pantaleone et al., 2021).
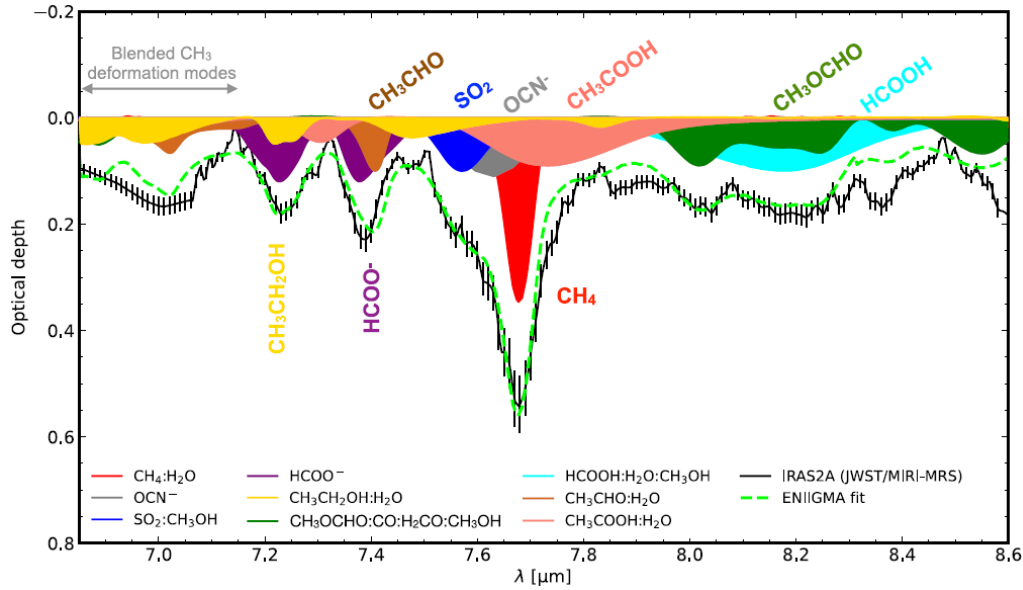
Figure 1.5: Fitted IR spectrum of IRAS 2A. Several ice mixtures were used in the fits, and the main chemical species names are shown close to the bands. This spectrum represents the first evidence for the presence of COMs and anions in interstellar ices. Image adapted from Rocha et al., 2024.

Grains can also be positively or negatively charged, which influences their reactivity. The absorption of UV photons causes the excitation of electrons that diffuse through the grain and eventually leave the surface. Additionally, grains can capture free electrons from the gas phase. In WNM, grains of all sizes are positively charged, while in CNM both positively and negatively charged dust grains coexist. In contrast, dust grains present in MCs are thought to be negatively charged or neutral (Ibáñez-Mejía et al., 2019). Photoemission, primarily caused by the interaction with the UV field, plays a pivotal role in determining the grains charge. In regions where there is no photoemission, grains are expected to be negatively charged, as electrons move faster than cations, making their impact more probable. Conversely, where photoemission is at work, the grains are positively charged and capable of bearing several charges (Krugel, 2007).

1.2 The main topics of the thesis

At first glance, the chemistry of the ISM may seem simpler than terrestrial chemistry, due to the limited factors influencing it: low temperatures, low pressures, absence of a liquid phase, and energy inputs coming mainly from radiation or environmental warming. However, understanding the processes that occur in such a distant environment poses several challenges, and its chemical complexity suggests the presence of much more intricate processes. Among the many questions arising from this field, this thesis focuses on two specific topics: i) the sulphur depletion problem and ii) the formation of interstellar complex organic molecules in the coldest regions of the ISM.

1.2.1 The sulphur depletion problem

Sulphur is the tenth most abundant element in the Sun photosphere (Asplund et al., 2009), with a cosmic abundance of $[S]/[H] = 1.73 \times 10^{-5}$ (Lodders, 2003) and of $[S^+]/[H] = 1.66 \times 10^{-5}$ for its ionized form (Esteban et al., 2004). Sulphur holds significant importance for
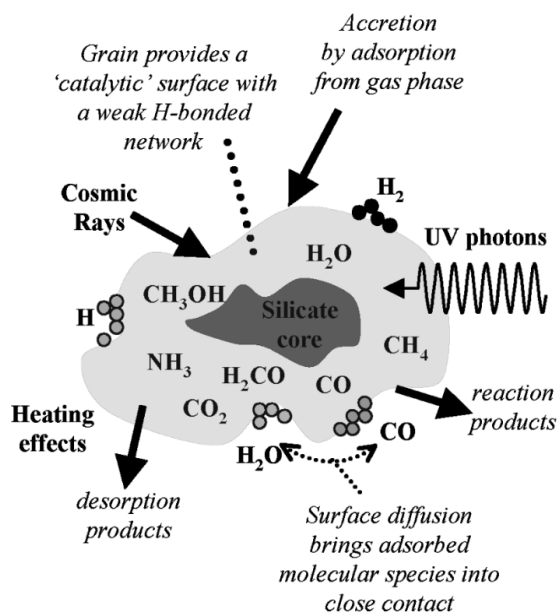
Figure 1.6: Typical energetic processes to which a dust grain is exposed in the ISM. Image from Fraser et al., 2002.

2 atoms	3 atoms	4 atoms	5 atoms	6 atoms	9 atoms
NS	C_2S	C_3S	HC_3S^+	CH_3SH	CH_3CH_2SH
SO	HCS^+	HNCS	H_2C_2S	C_5S	
SO^+	H_2S	H_2CS	C_4S	H_2C_3S	
CS	OCS	HSCN	HCOSH	HC_3HS	
SiS	SO_2	$HCCS^+$	HCSCN	HC_4S	
SH^+	HS_2	HCCS	HC_3S	NCHCCS	
SH	HCS	HCNS			
NS^+	HSC	$HOCS^+$			
NaS	NCS	HNSO			
MgS	HSO	NC_3S			

Table 1.2: S-bearing species detected at present day (September 25th, 2024).

terrestrial life and possibly played a crucial role in its emergence (e.g., Shalayel et al., 2020). It is an essential component of our bodies, as it is found in cysteine and methionine amino acids, in coenzyme A, in vitamin B1 and biotin, in antioxidants as glutathione, and in other molecules. Nevertheless, sulphur played an important role long before life appeared on Earth, and its chemistry in the ISM is currently a challenge for the astronomical and the astrochemical community. Presently, 43 S-bearing species have been detected in the ISM, as listed in Table 1.2.

In diffuse clouds, the sulphur abundance is consistent with the cosmic value and mostly resides in its ionised form S^+. In dense molecular clouds, it is more than a factor 100 less abundant, in accordance with the freeze-out of this element on dust grains, which should become part of the icy mantles coating the grains (e.g., Phuong et al., 2018; Vastel et al., 2018; van 't Hoff et al., 2020). However, the depletion persists also in warm objects, such as hot cores and hot corinos, where the dust icy mantles sublimate, but the abundances of all detected gaseous S-bearing species only reaches $\sim 1-10\%$ of the initial budget (Codella et al., 2021). Thus, it seems that sulphur progressively depletes as the cloud evolves (Hily-Blant et al., 2022). Even in shock regions, where icy mantles are sputtered and grain cores
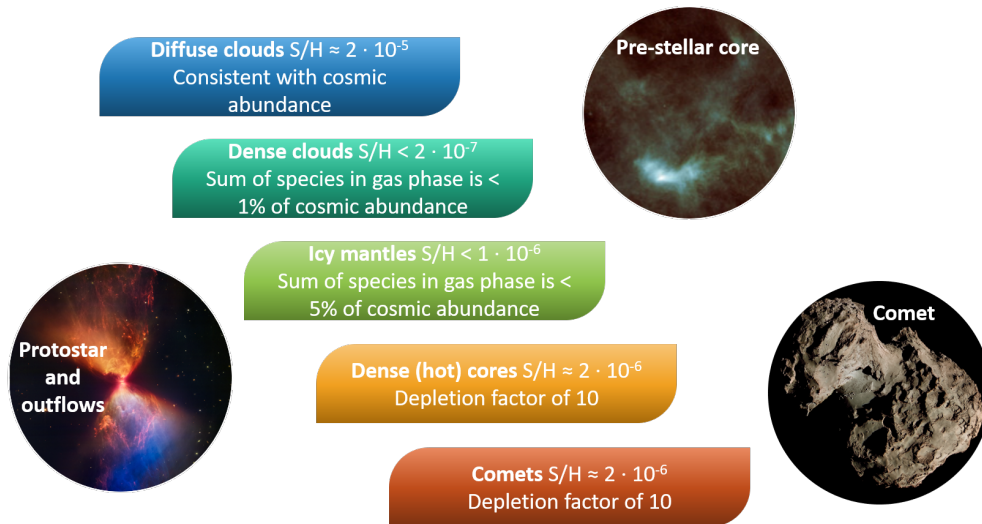
Figure 1.7: Summary of the sulphur to hydrogen abundance ratios measured in different phases of a planetary system formation.

are shattered, sulphur bearing species, such as C_2S, H_2CS, OCS, SO, and SO_2, only account for 10% of the elemental budget (Holdship et al., 2019).

However, in successive phases of the formation of a planetary system, S depletion in protoplanetary disks and later stages can be explained by the presence of refractory minerals, such as troilite (FeS) and other sulphides, in dust grains (Keller et al., 2002; Kama et al., 2019), that later become part of cometary dust and meteoritic rocks (Trigo-Rodríguez, 2012). Moreover, numerous sulphur-bearing species (S_2, S_3 and S_4, CH_3SH, C_2H_6SH, together with the most common H_2S, OCS, SO, S_2, SO_2, and CS_2) are detected in comets, such as 67P/Churyumov-Gerasimenko (Calmonte et al., 2016), whose composition seems to be inherited from the prestellar and protostellar evolutionary phases (Drozdovskaya et al., 2019; Altwegg et al., 2020). In 67P/C-G, H_2S is the most abundant S-bearing species ($\sim$ 57%) followed by atomic sulphur ($\sim$ 27%), and very recent observations found NH_4SH, a semi-refractory species, to be the most abundant salt (Altwegg et al., 2022). Other comets, such as 46P/Wirtanen, show a similar behavior, even though there is a relatively large variability on the abundance of H_2S with respect to other S-bearing species (Biver et al., 2021). Clearly, there is a missing piece of the puzzle regarding under which form is stored sulphur in the first stages of stellar evolution.

In dense clouds, H_2S was expected to be the main sulphur sink of dust grains (Garrod et al., 2007; Jiménez-Escobar et al., 2011), but astronomical observations, including those by JWST, have failed to detect frozen H_2S at a level at least 10 times lower than the predicted one (Boogert et al., 2015; McClure et al., 2023). The only species detected in the icy mantles are OCS and SO_2 (McClure et al., 2023; Rocha et al., 2024). However, their low abundance cannot account for the totality of sulphur (Sturm et al., 2023). Computational studies suggest that H_2S is likely to desorb from dust grains mantles because its binding energy is not large enough to keep the species bound to the ice once it has been formed by hydrogenation of atomic S, even in the hypothesis that 90% of its formation energy is dissipated by the water ice mantle (Bariosco et al., 2024). If this was the case, gas-phase chemistry could be a major contributor in sulphur astrochemistry (Mifsud et al., 2021).

Accordingly, the most important S-carriers are still unknown. At present day, there are few hypothesis regarding which species may act as sulphur reservoirs. The candidates are organo-sulphur compounds (Laas et al., 2019), polysulphanes (H_2S_n, with n $\geq$ 2, Druard

et al., 2012), sulphur allotropes (S_n, with $2 \leq n \leq 8$, Wakelam et al., 2004), and salts such as NH_4SH. These are refractory species that, once trapped on the mantles or in the core of the grains, rarely desorb and are therefore hardly detectable (Woods et al., 2015). Another hypothesis is that sulphur is contained in semi-refractory or volatile species that are undetectable when they are in the gas-phase.

The formation of organo-sulphur molecules was observed for the first time in an experimental work where a 2:1:1 mixture of H_2O:CH_3OH:NH_3 ice was bombarded with S^{7+} ions, although showing a possible source of compounds relative to more evolved environments, like icy moons, Kuiper belt objects, comets and their building blocks (Ruf et al., 2019). A recent review of the laboratory experiments performed on the chemistry of sulphur in the condensed phase highlighted that the formation of SO_2, SO_3, hydrates of H_2SO_4 and related species is the consequence of photolysis, proton-irradiation and radiolysis of mixed ices (Mifsud et al., 2021). Moreover, Boogert et al. (2022) argued that SO_2, instead of CS, is likely to be the precursor of solid OCS. In contrast, CS chemistry is thought to proceed in a similar fashion to that of CO, yielding H_2CS and CH_3SH after subsequent hydrogenation steps (Lamberts, 2018).

Ultimately, sulphur is known to exist in distinct molecular allotropes, forming chains and rings of up to 20 atoms, as it easily tends to react with itself even in a diluted medium. Several experiments have documented the production of S_n species, together with H_2S_n (with $n \geq 2$), consequent to the photoprocessing of H_2S-containing ices (e.g., Ferrante et al., 2008; Jiménez-Escobar et al., 2011; Jiménez-Escobar et al., 2014; Cazaux et al., 2022). When including *ad hoc* reaction pathways, astrochemical models also predict their formation (Laas et al., 2019). In particular, if cosmic-ray-driven radiation chemistry and fast non-diffusive reactions for bulk radicals are considered, pure sulphur allotropes are among the main products (Shingledecker et al., 2020). Although extensive spectroscopic characterisation of the most common gaseous and crystalline sulphur allotropes exists (Eckert et al., 2003), so far the only species characterised by a $S-S$ bond has been gaseous S_2H. This radical was detected in the Horsehead nebula, a moderately UV-irradiated environment (Fuente et al., 2017).

The interplay between astronomical observations, chemical modelling, laboratory experiments, and theoretical simulations is vital to add more pieces to the sulphur depletion puzzle and finally understand the sulphur chemistry in star-formation environments. This thesis explores the interaction of several S-bearing species with the core of dust grains, represented by the olivine family, and with the icy mantles coating their cores in more evolved clouds. Furthermore, the spectroscopic features of sulphur allotropes adsorbed onto icy mantles are characterised.

1.2.2 Interstellar complex organic molecules

Interstellar Complex Organic Molecules (COMs or iCOMs), defined as molecules with six or more atoms that contain at least one carbon atom (Herbst et al., 2009; Herbst, 2017; Ceccarelli et al., 2017), have been observed in a variety of interstellar environments, such as star formation regions (e.g., Rubin et al., 1971; McGuire et al., 2018), the circumstellar envelopes of AGB stars (e.g., Cernicharo et al., 2000), shocked regions (e.g., Arce et al., 2008; Codella et al., 2020), and external galaxies (e.g., Muller et al., 2011). They constitute around 40% of the molecules detected in the ISM.

COMs tend to be terrestrial-like in nature, whereas another class of molecules, known as 'carbon chains', is quite exotic (Herbst et al., 2022). Carbon chains are linear and unsaturated molecules consisting mainly of carbon atoms, including anions and cations, as well as radicals, such as C_nH (n = 2−8) and the cyanopolyynes $HC_{2n}CN$ (n = 1−5). Polycarbon
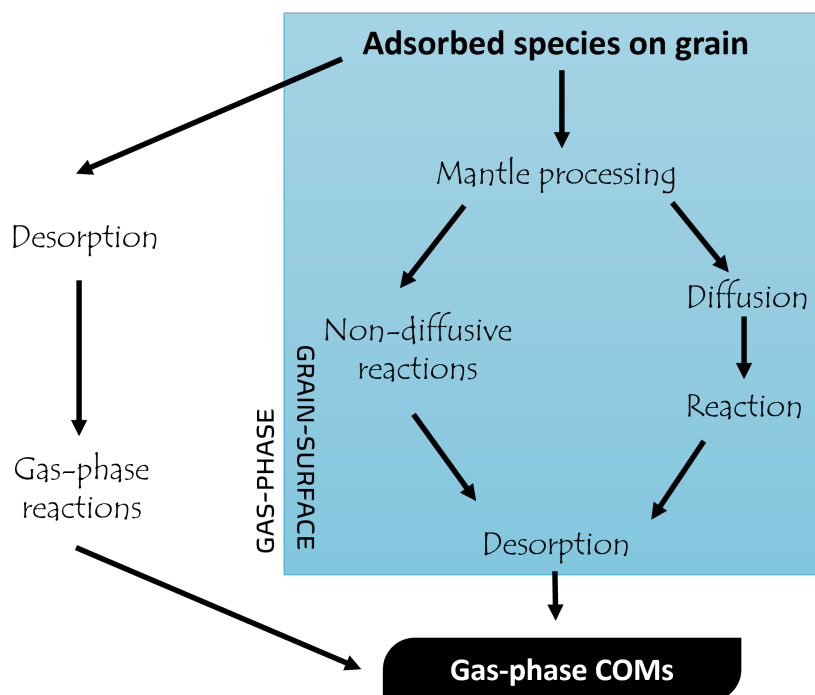
Figure 1.8: Sketch of gas-grain and grain-surface COMs formation paradigms.

sulphides are another class of carbon chains including neutral and charged H_xC_nS species (x = 0−2 and n = 1−5), whose number of detections has been increasing in recent years (McGuire, 2022). This thesis is focused on the terrestrial-like class of COMs, since there is evidence that a fraction of these species, that formed in the ISM, were inherited by the small objects of the Solar System (Caselli et al., 2012; Ligterink et al., 2018; Drozdovskaya et al., 2019). After thermal and hydrothermal alterations, COMs can be converted into more complex organic molecules (Yabuta et al., 2007; Callahan et al., 2011; Rotelli et al., 2016), therefore potentially paving the way to the emergence of life on Earth.

The presence of COMs in warm environments was surprising, but plausible due to the temperature of these environments. However, their detection in cold regions such as prestellar cores, where the low temperatures (T ≤ 10K) and the absence of any heating source or outflow exclude any efficient warm gas-phase or warm dust chemistry, implies that non-thermal desorption processes are at work (Bacmann et al., 2012).

The reaction pathways that lead to COMs are still a matter of debate, as both gas-phase and grain-surface chemistry are invoked to play a crucial role in their synthesis (Ceccarelli et al., 2023). Several paradigms for the formation of COMs have been proposed in the literature, the most popular being schemes based on (i) gas-phase reactions (e.g., Charnley et al., 1992; Charnley et al., 1997; Balucani et al., 2015; Taquet et al., 2016; Skouteris et al., 2018; Vazart et al., 2020) and (ii) networks of radical-radical couplings occurring on the surface of grains (e.g., Garrod et al., 2006; Garrod et al., 2008). Both paradigms share a common initial step that consists in the formation of hydrogenated species on the surface of grains that either sublimate in a warmer environment ((i), in favour of the gas-phase scheme) or from which radicals that react directly on the icy mantle can be obtained ((ii), in favour of the grain-surface chemistry). The latter scheme requires temperatures of around 30 K to ensure that the radicals present in the lukewarm ice mantle have sufficient mobility to recombine and form COMs (see Figure 1.8). Other paradigms include a mechanism based

on the condensation of atomic C (Ruaud et al., 2015; Krasnokutski et al., 2020), the insertion of excited O-atoms (Bergner et al., 2017; Bergner et al., 2019), and the formation of HCO radicals on ice surfaces as the parent precursors of other COMs (Fedoseev et al., 2017; Simons et al., 2020). Furthermore, nondiffusive three-body processes, which involve the formation of radicals in close proximity to another reactant through reaction or photodissociation, represent a promising mechanism due to their significantly faster kinetics than those observed for normal diffusion of reactants (Jin et al., 2020). Indeed, the photolysis of CH_3OH (in argon matrix) demonstrated the formation of several COMs, up to methoxymethanol (CH_3OCH_2OH, Gutiérrez-Quintanilla et al., 2021).

Although the formation routes of COMs are a matter of debate, their destruction pathways are more constrained. The main agents responsible for the destruction of COMs are H_3^+ and atomic C (Agúndez et al., 2023). The reaction with H_3^+ produces a protonated form of COMs, which, after electronic dissociative recombination, results in a small percentage of the original COM being reformed. An illustrative example is the reaction between ethanol and H_3^+, which forms $C_2H_5OH_2^+$ and produces less than 7% of ethanol (Hamberg et al., 2010). The destruction caused by atomic C is another efficient mechanism, as this reaction is usually barrierless (Shannon et al., 2014; Hickson et al., 2021). Other relevant destruction pathways include reactions with C^+, H^+, S^+, and He^+ (Agúndez et al., 2023).

In this thesis, the formation of ethanol (CH_3CH_2OH), acetaldehyde (CH_3CHO), and urea (NH_2CONH_2) were investigated. Additionally, the binding energies of ethanol and ethylamine ($CH_3CH_2NH_2$) were determined both computationally and experimentally. Ethanol and acetaldehyde have been observed in several environments. On the contrary, urea and ethylamine have been detected only in a few sources and urea was found in the Murchison meteorite. Investigating the grain-surface formation pathways of these species has a twofold purpose: firstly, to ascertain whether the formation of a species is feasible through grain-surface reactions; and secondly, to provide insights into its abundance, which may justify its ubiquitous presence or absence in the ISM. Finally, the determination of the binding energies is related to the thermal desorption mechanisms responsible for the sublimation in the gas phase of species formed on the surface of grains. Indeed, the non-detection of a species in the gas phase could be due to spectroscopic issues such as noise or line saturation, to its segregation in the condensed phase, or to its actual absence.

1.3   The role of computational chemistry in astrochemistry

Astrochemistry is an interdisciplinary subject that progresses thanks to the joint effort of scientists from different fields (Fortenberry et al., 2022).

Astronomers conduct observations via ground- and space-based telescopes, in order to gather information about the physics and chemistry of each environment that comprises the Universe. Experimental chemists reproduce at their best the conditions of the ISM with special chambers that recreate the temperature range of the ISM, but struggle to achieve the proper density. This is due to the limitations of vacuum pumps, which can reach densities around 10^7 particles cm^{-3}, whereas diffuse clouds have a density of 10^2 particles cm^{-3}. Although radiation fluxes and timescales cannot be directly compared with those of the Universe, laboratory experiments are still useful to obtain the chemical properties of its molecules. Consequently, astrophysical chemists build and run their models using the data obtained from the experiments, simulating the evolution of stellar systems and their relative chemistry, with the aim of reproducing what is observed by astronomers. In this

strict collaboration, computational chemistry has something to offer to each field.

Computational simulations produce spectroscopic data of unstable chemical species that cannot be handled and analysed in a laboratory, providing the astronomers with the information required to identify such species in the ISM. A theoretical approach is suitable for investigating the atomistic details or the reactions performed in laboratory experiments, offering an interpretation of the most elusive details. Furthermore, they can provide the parameters required by astrochemical models, in case they cannot be measured experimentally due to technical limitations. It is important to note that computational chemistry, like all scientific disciplines, is subjected to certain limitations. These include: i) the morphology and size of the systems are sometimes unknown or the models are too small to accurately represent the reality; ii) the short timescales of the simulations are not representative of the vast timescales of the Universe; iii) the choice of a suitable methodology to characterise a system, which would benefit from an experimental reference, is not straightforward.

However, there are some unquestionable major advantages: i) the simulation of isolated systems, effectively being at zero Kelvin and zero pressure, is particularly suitable for the cold, low densities of the ISM more than any other analytical techniques, and no other method can provide such detailed insights, staying within a chemical accuracy of 1 kcal mol^{-1}; ii) any kind of system, included highly unstable ones, can be modelled, provided to find a methodology appropriate for its description; iii) quantum chemistry adopts a bottom-up approach, computing the properties of the examined molecules. In contrast, experiments investigate which are the molecules responsible for the observed phenomenon, adopting therefore a top-down perspective (Fortenberry, 2024).

In summary, each branch of this discipline is strictly codependent on the others, as it provides and requires given data for and from the other fields.

1.3.1 Astrochemical models

The chemical evolution of pre-stellar cores is simulated through astrochemical models. Their objective is to reproduce the chemical evolution of gas and dust mixtures during the formation of stars and planetary systems. Initially, models accounted for gas-phase reactions (e.g., Herbst et al., 1973), to which grain-surface chemistry was subsequently implemented (Hasegawa et al., 1993). Finally, three-phase models, which distinguish between the bulk of the ice mantles, the surface of the ices, and the gas-phase processes, became the standard choice (Vasyunin et al., 2013; Garrod, 2013).

Astrochemical models compute the abundances of species by solving time-dependent equations that account for the formation and destruction rates of each species. These processes include gas-phase and grain-surface reactions, radiochemistry, photochemistry, etc.

Alternatively, stochastic approaches, such as micro and Monte Carlo methods, are employed for the modelling of smaller but more accurate reaction networks, which are particularly suited to the description of surface processes and in cases of extremely low abundances (Green et al., 2001; Cuppen et al., 2013).

Both models rely on a number of parameters, such as reaction rate coefficients, collision rates, binding energies, desorption efficiencies, photochemical data, and so forth, which are not always available. These data can be obtained from laboratory experiments or computational calculations, although quite often they are extrapolated from similar processes using chemical intuition (Linnartz et al., 2015; Cuppen et al., 2017). The quantity of data stored in databases is growing exponentially (Müller et al., 2005; Wakelam et al., 2015),

yet a significant proportion of the necessary information remains unavailable. Computational chemistry represents a valuable resource for filling this gap, particularly for those processes that are challenging to replicate in terrestrial laboratories.

Thermal desorption rates rely on the binding energy (BE, e.g., Penteado et al., 2017):

$$k_{des} \propto \exp\left(-\frac{BE}{k_B T}\right) \tag{1.1}$$

The rate of diffusion of an adsorbate on the surface of dust grains is also dependent on the BE. Given the paucity of data on diffusion barriers, they are typically assumed to be a fraction of the BE values.

$$k_{diff} \propto \exp\left(\frac{f \cdot BE}{k_B T}\right) \tag{1.2}$$

In the literature, it is usually found that $f = 0.3-0.8$ (Ruffle et al., 2000; Mispelaer et al., 2013; Cuppen et al., 2017; Maté et al., 2020; Kouchi et al., 2020). The diffusion process of only a few species has been accurately characterised from a theoretical and an experimental point of view. Species such as CO and CO_2 are properly described with a theoretical $f = 0.3-0.4$ (Karssemeijer et al., 2014), while experiments have determined $f = 0.55$ for the N and O atoms (Minissale et al., 2016) and $f = 0.3-0.6$ for O_2, N_2, CH_4, and Ar in ASW (He et al., 2018), where the lower values are associated with sub-monolayer surface coverages.

Conversely, the branching ratios and reaction rates depend on the reaction barriers and the presence of competitive processes that impede the reaction of interest. A successful grain-surface reaction occurring through the Langmuir-Hinshelwood (LH) mechanism, depends on the probability that the adsorbed reactants meet and react. This is in contrast with the Eley-Rideal (ER) mechanism, in which species from the gas-phase directly react with surface molecules, avoiding diffusion, provided reactions do not possess an activation energy. Therefore, the efficiency of a LH reaction (ε_{LH}) should consider the diffusion and desorption rates (k_{diff} and k_{des}) of the reactants i and j, and the rate constant related to the activation energy (k_{aeb}) of their reaction. Theoretically, each rate constant can be derived using the Eyring's transition state theory equation, upon calculation of the reaction energy barrier (more details in Section 2.5.3).

$$\varepsilon_{LH} = \frac{k_{LH}}{k_{LH} + k_{diff,i} + k_{diff,j} + k_{des,i} + k_{des,j}} \tag{1.3}$$

Consequently, it is necessary to provide each species with specific parameters in order to describe its physico-chemical behaviour in the ISM. It is clear that astrochemical models consider a wider range of processes than those listed here (such as chemical desorption, radiochemistry, photochemistry), each of which requiring a specific set of parameters. Nevertheless, the goal of this thesis was to determine binding energies, in particular of S-bearing molecules, and reaction barriers relative to the formation of a few COMs on the surface of dust grains.

1.3.2 The importance of the binding energies

Binding energies delineate the strength of the interaction between a volatile species and a surface. In the previous paragraph, it has been demonstrated that BEs play a pivotal role in governing the freeze-out of gas-phase species onto dust grain surfaces, in addition to their diffusion and desorption. Furthermore, the mobility of a species on the surface of a grain can significantly influence its reactivity, notably in mechanisms such as LH, where

previously adsorbed species migrate on the surface in order to meet and react. Consequently, BEs serve as crucial parameters in shaping the ISM chemistry and its resulting composition, particularly in low-temperature environments (Penteado et al., 2017; Heyl et al., 2022).

The determination of BEs poses a considerable challenge. Experimentally, desorption energies (E_{des}) are often obtained through temperature programmed desorption (TPD) experiments. Volatile species are deposited on a surface allowing them to adsorb, then throughout the heating process, the species progressively sublimate and desorb at a temperature that depends on their nature and on the BE with each site offered by the surface. The result is a TPD spectrum where the abundance of each atomic mass unit is monitored against its thermal desorption temperature. However, despite its utility, this technique exhibits some limitations, the most critical of which is the dependency of E_{des} on the substrate morphology, composition, and coverage (e.g., Noble et al., 2012; Chaabouni et al., 2018). Furthermore, E_{des}, which is derived from experimental desorption rates via the Polanyi-Wigner equation, align closely with the computed BEs only under specific conditions, that is, the absence of other activated processes, such as ice restructuring. The latter is usually assumed to be negligible (He et al., 2016), however, this process is favoured by the energy provided to the system during the experiment. A notable example is the crystallisation of amorphous water during desorption. Only a limited set of stable closed-shell species has been considered in these experiments, due to the impracticality of handling reactive species and radicals, which have a short life span (e.g., Collings et al., 2004; Noble et al., 2012; Dulieu et al., 2013; Fayolle et al., 2016; He et al., 2016; Smith et al., 2016). In addition, constant thermal energy is provided to the molecules, which is used to diffuse and move toward stronger binding sites, where the system is more stable, rendering the TPD more sensitive to the highest values of adsorption energies, and thus providing higher limits to the realistic BE values. Finally, co-desorption of adsorbed species together with the substrate causes the determination of the desorption energy of the species under investigation unfeasible (Minissale et al., 2022).

A complementary approach to TPD is the adoption of state-of-the-art computational chemistry. By allowing control over surface morphology and composition, as well as adsorbate coverage, *ab initio* calculations can bridge data gaps in astrochemical models, particularly when referred to unstable species. However, the main limitation of this approach is the trade-off between the system size and the accuracy of the calculation. Consequently, high theory levels are often only applicable to small systems due to the availability of computational resources. Several theoretical studies have reported the BEs of important astrochemical species such as H, H_2, N, O, HF, CO, and CO_2 on icy surfaces modelled through both periodic and cluster approach, using crystalline (CI) and amorphous (ASW) systems (e.g., Al-Halabi et al., 2007; Karssemeijer et al., 2014; Zamirri et al., 2017; Shimonishi et al., 2018; Bovolenta et al., 2020; Ferrero et al., 2020; Duflot et al., 2021).

Focusing on the ASW ice, recent advances have been made in the development of their models and the computations of BEs. For instance, while some studies propose periodic slab models with specific surface features (Ferrero et al., 2020), others employ cluster models with sophisticated computational methods, e.g., ONIOM QMHigh/QMLow, to achieve high accuracy in BEs determination (Duflot et al., 2021). The use of multiple small clusters was also proposed in order to reproduce the structural variability of a large realistic ice mantle (Shimonishi et al., 2018) and this approach was further developed with the creation of tools such as the Binding Energy Evaluation Platform (BEEP) facilitating automated BE determination for molecules adsorbed on randomly amorphised ASW clusters (Bovolenta et al., 2022).

An alternative approach to obtain a broad spectrum of BEs suitable to define a statistical distribution involves an unbiased search towards all the binding sites offered by the icy mantle model developed with the ACO-FROST scheme (Germain et al., 2022; Tinacci et al., 2022). The code allows to grow icy clusters by random step-by-step addition of water molecules up to the desired size. Attempts to obtain an extended BE catalogue for small molecules on water ice have been limited to density functional theory (DFT) simulations on small water clusters (from one to six molecules), which often lack statistical significance and fail to consider the cooperative effects established by the H-bonding network within the ice structure, particularly important when working with soft matter (Wakelam et al., 2017; Das et al., 2018). It should be noted that the size of the crystal and the choice of the functional are crucial to surely assess an accurate BE value.

Despite these advancements, many astrochemical models still resort to simplistic approaches like the linear addition method, particularly for newly detected species that lack experimental or theoretical characterisation (Garrod et al., 2006; Shingledecker et al., 2020; Cazaux et al., 2022). With this method, the BE of a molecule is determined by splitting its components into atoms and molecular fragments whose BEs are known and subsequently adding them together (Allen et al., 1977). Although this method is relatively inexpensive, it does not account for the electronic effects specific to the species and for the type of surface onto which the species are adsorbed.

Considerable efforts have been made in recent years to enhance our understanding of binding energies. However, three key areas still necessitate thorough investigation: (i) the composition and morphology of ice models; (ii) the development of a reliable methodology for conducting extensive statistical studies, applicable even to exotic species with charges, unpaired electrons, or uncommon structures; (iii) and the incorporation of BEs distributions into astrochemical models.

Exploring the construction of 'dirty' ice models, incorporating species commonly detected in ice mantles such as CO, CH_4, NH_3, CO_2, and (to a lesser extent) CH_3OH, and characterizing BEs on the multiple sites offered by such models, constitutes an intriguing avenue. It is known that BEs depend not only on the volatiles but also on the grain surface composition. From an experimental standpoint, deriving specific binding energies for molecules in mixed ices is generally challenging due to concurrent diffusion, segregation, and crystallization processes (Martín-Doménech et al., 2014). However, algorithms like ACO-FROST could prove suitable, as they allow for the addition of various molecules alongside water during the built-up of the ice clusters (Germain et al., 2022).

Addressing methodological challenges remains a hurdle, particularly in finding a unified level of theory suitable for treating a multitude of systems exhibiting diverse electronic density behaviors. ONIOM (such as QM/MM and QMHigh/QMLow) methodologies are promising candidates, enabling the treatment of specific areas of a system with high-level theory methods, e.g., post-Hartree-Fock (Duflot et al., 2021). Achieving uniformity in theoretical descriptions would facilitate better comparisons of BEs obtained for different species and ice surfaces. Alternatively, machine learning (ML) has become one of the most prominent scientific tools of the 21st century. While supervised learning algorithms show promise in predicting BEs, they are limited by their reliance on training data and may struggle with novel species (Villadsen et al., 2022). ML interatomic potentials offer a low-cost alternative to *ab initio* calculations for investigating molecular reactivity, adsorption, and diffusion on dust grains (Mazo-Sevillano et al., 2021; Molpeceres et al., 2021; Zaverkin et al., 2022). Yet, the construction of a ML potential requires accurate data from

DFT or post-Hartree-Fock calculations, slightly limiting the power of such methodology, especially when considering exotic astrochemical species.

The last aspect involves the integration of BEs into astrochemical models, where single binding energy frameworks are typically adopted. Despite the potential benefits of incorporating BE distributions, their inclusion has been explored in only a few cases due to its computational costs, necessitating additional efforts to simplify their numerical implementations (Grassi et al., 2020).

1.4 The QUANTUMGRAIN project

The ERC awarded project 'Quantum Chemistry on Interstellar Grains' (QUANTUMGRAIN, Grant agreement number 865657) has the aim to investigate in details the chemistry happening on the surface of interstellar dust grains, providing structures, energetics and dynamics of the phenomena and processes occurring on them.

To achieve this objective, the project has been organised in three work-packages: i) the construction of structural models of silicaceous grain cores and icy mantles to characterise their morphological, energetic and spectroscopic features, ii) the simulation of grain-surface reactions (formation of simple molecules, COMs, and biomolecules) to disentangle the most favourable mechanisms, and iii) the assessment of the role of dust grain cores and mantles in each reaction (e.g., catalyst, concentrator, third body) to know whether and why their presence is fundamental for the development of chemical complexity in the ISM.

Previous (Joan Enrique-Romero, Stefano Ferrero, Jesús Luque-Urrutia, and Eloy Peña-Asensio) and current (Niccolò Bancone, Vittorio Bariosco, Alicja Bulik, Andreha Gelli, Leana Jubert, Harjasnoor Kakkar, Eric Mates-Torres, Berta Martínez-Bachs, Gerard Pareras, and myself) members of the team are lead by the principal investigator, Prof. Albert Rimola. The present thesis is fully involved in this project, by tackling the adsorption and the surface reactivity occurring on the icy mantles of dust grains in the ISM. Complete information about the project can be found at cordis.europa.eu and on our website www.quantumgrain.eu.

References

Agúndez, M. et al. (2023). "Detection of ethanol, acetone, and propanal in TMC-1. New O-bearing complex organics in cold sources". *Astron. Astrophys.* **673**, A34. DOI: 10.1051/0004-6361/202346076.

Allen, M. et al. (1977). "The molecular composition of dense interstellar clouds". *Astrophys. J.* **212**, 396. DOI: 10.1086/155059.

Altschuler, D. R. et al. (1986). "Detection of atomic hydrogen in the young planetary nebula IC 4997". *Astrophys. J. Lett.* **305**, L85. DOI: 10.1086/184690.

Altwegg, K. et al. (2016). "Prebiotic chemicals-amino acid and phosphorus-in the coma of comet 67P/Churyumov-Gerasimenko". *Sci. Adv.* **2**, e1600285. DOI: 10.1126/sciadv.1600285.

Altwegg, K. et al. (2020). "Evidence of ammonium salts in comet 67P as explanation for the nitrogen depletion in cometary comae". *Nat. Astron.* **4**, 533. DOI: 10.1038/s41550-019-0991-9.

Altwegg, K. et al. (2022). "Abundant ammonium hydrosulphide embedded in cometary dust grains". *Mon. Not. R. Astron. Soc.* **516**, 3900. DOI: 10.1093/mnras/stac2440.

Arce, H. G. et al. (2008). "Complex molecules in the L1157 molecular outflow". *Astrophys. J.* **681**, L21. DOI: 10.1086/590110.

Asplund, M. et al. (2009). "The chemical composition of the Sun". *Annu. Rev. Astron. Astrophys.* **47**, 481. DOI: `10.1146/annurev.astro.46.060407.145222`.

Bacmann, A. et al. (2012). "Detection of complex organic molecules in a prestellar core: a new challenge for astrochemical models". *Astron. Astrophys.* **541**, L12. DOI: `10.1051/0004-6361/201219207`.

Bakker, E. J. et al. (1996). "Detection of C_2, CN, and NaID absorption in the AGB remnant of HD 56126". *Astron. Astrophys.* **310**, 893. DOI: `10.48550/arXiv.astro-ph/9510122`.

Balucani, N. et al. (2015). "Formation of complex organic molecules in cold objects: the role of gas-phase reactions." *Mon. Not. R. Astron. Soc.* **449**, L16. DOI: `10.1093/mnrasl/slv009`.

Bariosco, V. et al. (2024). "The binding energy distribution of H_2S: why it is not the major sulphur reservoir of the interstellar ices". *Mon. Not. R. Astron. Soc.* **531**, 1371. DOI: `10.1093/mnras/stae1210`.

Bergner, J. B. et al. (2017). "Methanol formation via oxygen insertion chemistry in ices". *Astrophys. J.* **845**, 29. DOI: `10.3847/1538-4357/aa7d09`.

Bergner, J. B. et al. (2019). "Oxygen atom reactions with C_2H_6, C_2H_4, and C_2H_2 in ices". *Astrophys. J.* **874**, 115. DOI: `10.3847/1538-4357/ab07b2`.

Biver, N. et al. (2021). "Molecular composition of comet 46P/Wirtanen from millimetre-wave spectroscopy". *Astron. Astrophys.* **648**, A49. DOI: `10.1051/0004-6361/202040125`.

Boogert, A. et al. (2015). "Observations of the icy universe". *Annu. Rev. Astron. Astrophys.* **53**, 541. DOI: `10.1146/annurev-astro-082214-122348`.

Boogert, A. et al. (2022). "Survey of ices toward massive young stellar objects. I. OCS, CO, OCN^-, and CH_3OH". *Astrophys. J. Lett.* **941**, 32. DOI: `10.3847/1538-4357/ac9b4a`.

Bovolenta, G. M. et al. (2020). "High level ab initio binding energy distribution of molecules on interstellar ices: hydrogen fluoride". *Mol. Astrophys.* **21**, 100095. DOI: `10.1016/j.molap.2020.100095`.

Bovolenta, G. M. et al. (2022). "Binding Energy Evaluation Platform: a database of quantum chemical binding energy distributions for the astrochemical community". *Astrophys. J. Suppl. Ser.* **262**, 17. DOI: `10.3847/1538-4365/ac7f31`.

Burbidge, E. M. et al. (1957). "Synthesis of the elements in stars". *Rev. Mod. Phys.* **29**, 547.

Callahan, M. P. et al. (2011). "Carbonaceous meteorites contain a wide range of extraterrestrial nucleobases". *Proc. Natl. Acad. Sci.* **108**, 13995. DOI: `10.1073/pnas.1106493108`.

Calmonte, U. et al. (2016). "Sulphur-bearing species in the coma of comet 67P/Churyumov-Gerasimenko". *Mon. Not. R. Astron. Soc.* **462**, S253. DOI: `10.1093/mnras/stw2601`.

Cameron, A. (1957). "Stellar evoution, nuclear astrophysics, and nucleogenesis". *Chalk River Report CRL-41*.

Caselli, P. et al. (2012). "Our astrochemical heritage". *Astron. Astrophys. Rev.* **20**, 56. DOI: `10.1007/s00159-012-0056-x`.

Caselli, P. et al. (2022). "The central 1000 au of a prestellar core revealed with ALMA. II. Almost complete freeze-out". *Astrophys. J.* **929**. DOI: `10.3847/1538-4357/ac5913`.

Cazaux, S. et al. (2022). "Photoprocessing of H_2S on dust grains. Building S chains in translucent clouds and comets". *Astron. Astrophys.* **657**, A100. DOI: `10.1051/0004-6361/202141861`.

Ceccarelli, C. et al. (2017). "Seeds Of Life In Space (SOLIS): the organic composition diversity at 300–1000 au scale in solar-type star-forming regions". *Astrophys. J.* **850**, 176. DOI: `10.3847/1538-4357/aa961d`.

Ceccarelli, C. et al. (2018). "The evolution of grain mantles and silicate dust growth at high redshift". *Mon. Not. R. Astron. Soc.* **476**, 1371. DOI: `10.1093/mnras/sty313`.

Ceccarelli, C. et al. (2023). "Organic chemistry in the first phases of solar-type protostars". *Protostars and Planets VII*. Ed. by S. Inutsuka et al. Vol. 534. Astronomical Society of the Pacific Conference Series, 379.

Cernicharo, J. et al. (2000). "A λ2 mm molecular line survey of the C-star envelope IRC+10216". *Astron. Astrophys. Suppl. Ser.* **142**, 181. DOI: `10.1051/aas:2000147`.

Chaabouni, H. et al. (2018). "Thermal desorption of formamide and methylamine from graphite and amorphous water ice surfaces". *Astron. Astrophys.* **612**, A47. DOI: `10.1051/0004-6361/201731006`.

Charnley, S. B. et al. (1992). "On the molecular complexity of the hot cores in Orion A: grain surface chemistry as 'The last refuge of the scoundrel'". *Astrophys. J.* **399**, L71. DOI: `10.1086/186609`.

Charnley, S. B. et al. (1997). "Deuterated methanol in the Orion compact ridge". *Astrophys. J.* **482**, L203. DOI: `10.1086/310697`.

Codella, C. et al. (2020). "Seeds of Life in Space (SOLIS) - V. Methanol and acetaldehyde in the protostellar jet-driven shocks L1157-B0 and B1". *Astron. Astrophys.* **635**, A17. DOI: `10.1051/0004-6361/201936725`.

Codella, C. et al. (2021). "SOLIS - XII. SVS13-A Class I chemical complexity as revealed by S-bearing species". *Astron. Astrophys.* **654**, A52. DOI: `10.1051/0004-6361/202141485`.

Collings, M. P. et al. (2004). "A laboratory survey of the thermal desorption of astrophysically relevant molecules". *Mon. Not. R. Astron. Soc.* **354**, 1133. DOI: `10.1111/j.1365-2966.2004.08272.x`.

Cuppen, H. M. et al. (2013). "The Kinetic Monte Carlo method as a way to solve the master equation for interstellar grain chemistry". *Chem. Rev.* **113**, 8840. DOI: `10.1021/cr400234a`.

Cuppen, H. M. et al. (2017). "Grain surface models and data for astrochemistry". *Space Sci. Rev.* **212**, 1. DOI: `10.1007/s11214-016-0319-3`.

Das, A. et al. (2018). "An approach to estimate the binding energy of interstellar species". *Astrophys. J. Suppl. Ser.* **237**, 9. DOI: `10.3847/1538-4365/aac886`.

Dishoeck, E. F. van et al. (2013). "Interstellar water chemistry: from laboratory to observations". *Chem. Rev.* **113**, 9043. DOI: `10.1021/cr4003177`.

Douglas, A. E. et al. (1942). "Band spectrum and structure of the CH^+ molecule; identification of three interstellar lines". *Can. J. Res.* **20a**, 71. DOI: `10.1139/cjr42a-008`.

Drozdovskaya, M. N. et al. (2019). "Ingredients for solar-like systems: protostar IRAS 16293-2422 B versus comet 67P/Churyumov-Gerasimenko". *Mon. Not. R. Astron. Soc.* **490**, 50. DOI: `10.1093/mnras/stz2430`.

Druard, C. et al. (2012). "Polysulphanes on interstellar grains as a possible reservoir of interstellar sulphur". *Mon. Not. R. Astron. Soc.* **426**, 354.

Duflot, D. et al. (2021). "Theoretical determination of binding energies of small molecules on interstellar ice surfaces". *Front. Astron. Space Sci.* **8**. DOI: `10.3389/fspas.2021.645243`.

Dulieu, F. et al. (2013). "How micron-sized dust particles determine the chemistry of our Universe". *Sci. Rep.* **3**. DOI: `10.1038/srep01338`.

Eckert, B. et al. (2003). "Molecular spectra of sulfur molecules and solid sulfur allotropes". In: *Elemental Sulfur und Sulfur-Rich Compounds II*. Ed. by R. Steudel. Berlin, Heidelberg: Springer Berlin Heidelberg, 31. DOI: `10.1007/b13181`.

Ehrenfreund, P. et al. (2000). "Organic molecules in the interstellar medium, comets, and meteorites: a voyage from dark clouds to the early earth". *Annu. Rev. Astron. Astrophys.* **38**, 427. DOI: `10.1146/annurev.astro.38.1.427`.

Elsila, J. E. et al. (2009). "Cometary glycine detected in samples returned by Stardust". *Meteorit. Planet. Sci.* **44**, 1323. DOI: `10.1111/j.1945-5100.2009.tb01224.x`.

Esteban, C. et al. (2004). "A reappraisal of the chemical composition of the Orion nebula based on Very Large Telescope echelle spectrophotometry". *Mon. Not. R. Astron. Soc.* **355**, 229. DOI: `10.1111/j.1365-2966.2004.08313.x`.

Fayolle, E. et al. (2016). "N$_2$ and CO desorption energies from water ice". *Astrophys. J.* **816**, L28. DOI: `10.3847/2041-8205/816/2/l28`.

Fedoseev, G. et al. (2017). "Formation of glycerol through hydrogenation of CO ice under prestellar core conditions". *Astrophys. J.* **842**, 52. DOI: `10.3847/1538-4357/aa74dc`.

Ferrante, R. F. et al. (2008). "Formation of interstellar OCS: radiation chemistry and IR spectra of precursor ices". *Astrophys. J.* **684**, 1210. DOI: `10.1086/590362`.

Ferrara, A. et al. (2016). "The problematic growth of dust in high-redshift galaxies". *Mon. Not. R. Astron. Soc. Lett.* **463**, L112. DOI: `10.1093/mnrasl/slw165`.

Ferrero, S. et al. (2020). "Binding energies of interstellar molecules on crystalline and amorphous models of water ice by ab initio calculations". *Astrophys. J.* **904**, 11. DOI: `10.3847/1538-4357/abb953`.

Fortenberry, R. C. et al. (2022). "10 years of the ACS Phys Astrochemistry Subdivision". *J. Phys. Chem. A* **126**, 6571. DOI: `10.1021/acs.jpca.2c06091`.

Fortenberry, R. C. (2024). "Quantum chemistry and astrochemistry: a match made in the heavens". *J. Phys. Chem. A* **128**, 1555. DOI: `10.1021/acs.jpca.3c07601`.

Fraser, H. J. et al. (2002). "Laboratory surface astrophysics experiment". *Rev. Sci. Instrum.* **73**, 2161. DOI: `10.1063/1.1470232`.

Fuente, A. et al. (2017). "First Detection of Interstellar S$_2$H". *Astrophys. J. Lett.* **851**, L49. DOI: `10.3847/2041-8213/aaa01b`.

Garrod, R. T. et al. (2006). "Formation of methyl formate and other organic species in the warm-up phase of hot molecular cores". *Astron. Astrophys.* **457**, 927. DOI: `10.1051/0004-6361:20065560`.

Garrod, R. T. et al. (2007). "Non-thermal desorption from interstellar dust grains via exothermic surface reactions". *Astron. Astrophys.* **467**, 1103. DOI: `10.1051/0004-6361:20066704`.

Garrod, R. T. et al. (2008). "Complex chemistry in star-forming regions: an expanded gas-grain warm-up chemical model". *Astrophys. J.* **682**, 283. DOI: `10.1086/588035`.

Garrod, R. T. (2013). "A three-phase chemical model of hot cores: the formation of glycine". *Astrophys. J.* **765**, 60. DOI: `10.1088/0004-637X/765/1/60`.

Germain, A. et al. (2022). "Computer generated realistic interstellar icy grain models: physicochemical properties and interaction with NH$_3$". *ACS Earth Space Chem.* **6**, 1286. DOI: `10.1021/acsearthspacechem.2c00004`.

Ginolfi, M. et al. (2017). "Where does galactic dust come from?" *Mon. Not. R. Astron. Soc.* **473**, 4538. DOI: `10.1093/mnras/stx2572`.

Grassi, T. et al. (2020). "A novel framework for studying the impact of binding energy distributions on the chemistry of dust grains". *Astron. Astrophys.* **643**, A155. DOI: `10.1051/0004-6361/202039087`.

Green, N. J. B. et al. (2001). "A stochastic approach to grain surface chemical kinetics". *Astron. Astrophys.* **375**, 1111. DOI: `10.1051/0004-6361:20010961`.

Gutiérrez-Quintanilla, A. et al. (2021). "iCOM formation from radical chemistry: a mechanistic study from cryogenic matrix coupled with IR and EPR spectroscopies". *Mon. Not. R. Astron. Soc.* **506**, 3734. DOI: `10.1093/mnras/stab1850`.

Al-Halabi, A. et al. (2007). "Hydrogen adsorption and diffusion on amorphous solid water ice". *Mon. Not. R. Astron. Soc.* **382**, 1648. DOI: `10.1111/j.1365-2966.2007.12415.x`.

Hama, T. et al. (2013). "Surface processes on interstellar amorphous solid water: adsorption, diffusion, tunneling reactions, and nuclear-spin conversion". *Chem. Rev.* **113**, 8783. DOI: `10.1021/cr4000978`.

Hamberg, M. et al. (2010). "Experimental studies of the dissociative recombination of CD$_3$CDOD$^+$ and CH$_3$CH$_2$OH$_2^+$". *Astron. Astrophys.* **522**, A90. DOI: `10.1051/0004-6361/201014774`.

Harrington, J. et al. (1981). "Ultraviolet spectra of planetary nebulae. IV-The $C_{III\lambda}$ 2297 dielectronic recombination line and dust absorption in the $C_{IV\lambda}$ 1549 resonance doublet". *Mon. Not. R. Astron. Soc.* **195**, 21P. DOI: `10.1093/mnras/195.1.21P`.

Harsono, D. et al. (2018). "Evidence for the start of planet formation in a young circumstellar disk". *Nat. Astron.* **2**, 646. DOI: `10.1038/s41550-018-0497-x`.

Hasegawa, T. I. et al. (1993). "New gas-grain chemical models of quiscent dense interstellar clouds: the effects of H_2 tunnelling reactions and cosmic ray induced desorption." *Mon. Not. R. Astron. Soc.* **261**, 83. DOI: `10.1093/mnras/261.1.83`.

He, J. et al. (2016). "Binding energy of molecules on water ice: laboratory mesurements and modeling". *Astrophys. J.* **825**, 89. DOI: `10.3847/0004-637x/825/2/89`.

He, J. et al. (2018). "Measurements of diffusion of volatiles in amorphous solid water: application to interstellar medium environments". *Astrophys. J.* **863**, 156. DOI: `10.3847/1538-4357/aad227`.

Henning, T. (2010). "Cosmic silicates". *Annu. Rev. Astron. Astrophys.* **48**, 21. DOI: `10.1146/annurev-astro-081309-130815`.

Herbst, E. et al. (1973). "The formation and depletion of molecules in dense interstellar clouds". *Astrophys. J.* **185**, 505. DOI: `10.1086/152436`.

Herbst, E. et al. (2009). "Complex organic interstellar molecules". *Annu. Rev. Astron. Astrophys.* **47**, 427. DOI: `10.1146/annurev-astro-082708-101654`.

Herbst, E. (2017). "The synthesis of large interstellar molecules". *Int. Rev. Phys. Chem.* **36**, 287. DOI: `10.1080/0144235X.2017.1293974`.

Herbst, E. et al. (2022). "Synthetic approaches to complex organic molecules in the cold interstellar medium". *Front. Astron. Space Sci.* **8**, 789428. DOI: `10.3389/fspas.2021.789428`.

Heyl, J. et al. (2022). "Using statistical emulation and knowledge of grain-surface diffusion for bayesian inference of reaction rate parameters: an application to a glycine network". *Astrophys. J.* **931**, 26. DOI: `10.3847/1538-4357/ac6606`.

Hickson, K. M. et al. (2021). "Kinetic study of the gas-phase $C(^3P) + CH_3CN$ reaction at low temperatures: rate constants, H-atom product yields, and astrochemical implications". *ACS Earth Space Chem.* **5**, 824. DOI: `10.1021/acsearthspacechem.0c00347`.

Hily-Blant, P. et al. (2022). "Sulfur gas-phase abundance in dense cores". *Astron. Astrophys.* **658**, A168. DOI: `10.1051/0004-6361/201936498`.

Holdship, J. et al. (2019). "Sulfur Chemistry in L1157-B1". *Astrophys. J. Lett.* **878**, 64. DOI: `10.3847/1538-4357/ab1cb5`.

Ibáñez-Mejía, J. C. et al. (2019). "Dust charge distribution in the interstellar medium". *Mon. Not. R. Astron. Soc.* **485**, 1220. DOI: `10.1093/mnras/stz207`.

Jiménez-Escobar, A. et al. (2011). "Sulfur depletion in dense clouds and circumstellar regions - I. H_2S ice abundance and UV-photochemical reactions in the H_2O-matrix". *Astron. Astrophys.* **536**, A91. DOI: `10.1051/0004-6361/201014821`.

Jiménez-Escobar, A. et al. (2014). "Sulphur depletion in dense clouds and circumstellar regions. Organic products made from UV photoprocessing of realistic ice analogs containing H_2S". *Mon. Not. R. Astron. Soc.* **443**, 343. DOI: `10.1093/mnras/stu1100`.

Jin, M. et al. (2020). "Formation of complex organic molecules in cold interstellar environments through nondiffusive grain-surface and ice-mantle chemistry". *Astrophys. J. Supp. Ser.* **249**, 26. DOI: `10.3847/1538-4365/ab9ec8`.

Johansen, A. et al. (2017). "Forming planets via pebble accretion". *Annu. Rev. Earth Planet. Sci.* **45**, 359. DOI: `10.1146/annurev-earth-063016-020226`.

Kama, M. et al. (2019). "Abundant refractory sulfur in protoplanetary disks". *Astrophys. J.* **885**, 114. DOI: `10.3847/1538-4357/ab45f8`.

Karssemeijer, L. J. et al. (2014). "Diffusion-desorption ratio of adsorbed CO and CO_2 on water ice". *Astron. Astrophys.* **569**, A107. DOI: `10.1051/0004-6361/201424792`.

Keller, L. P. et al. (2002). "Identification of iron sulphide grains in protoplanetary disks". *Nature* **417**, 148.

Kohlhase, C. E. et al. (1977). "Voyager mission description". *Space Sci. Rev.* **21**, 77. DOI: 10.1007/BF00200846.

Kouchi, A. et al. (2020). "Direct measurements of activation energies for surface diffusion of CO and CO_2 on amorphous solid water using in situ transmission electron microscopy". *Astrophys. J. Lett.* **891**, L22. DOI: 10.3847/2041-8213/ab78a2.

Krasnokutski, S. A. et al. (2014). "Formation of silicone oxide grains at low temperature". *Astrophys. J.* **782**, 15. DOI: 10.1088/0004-637X/782/1/15.

Krasnokutski, S. A. et al. (2020). "Condensation of atomic carbon: possible routes toward glycine". *Astrophys. J.* **889**, 67. DOI: 10.3847/1538-4357/ab60a1.

Krugel, E. (2007). *An introduction to the physics of interstellar dust*. Taylor & Francis.

Kwok, S. (2007). *Physics and chemistry of the interstellar medium*. University Science Books.

Kwok, S. (2013). *Stardust: the cosmic seeds of life*. Springer Science & Business Media.

Kwok, S. (2016). "Complex organics in space from Solar System to distant galaxies". *The Astronomy and Astrophysics Review* **24**, 8. DOI: 10.1007/s00159-016-0093-y.

Laas, J. et al. (2019). "Modeling sulfur depletion in interstellar clouds". *Astronomy and Astrophysics* **624**, A108. DOI: 10.1051/0004-6361/201834446.

Lamberts, T. (2018). "From interstellar carbon monosulfide to methyl mercaptan: paths of least resistance". *Astron. Astrophys.* **615**, L2. DOI: 10.1051/0004-6361/201832830.

Ligterink, N. F. W. et al. (2018). "The ALMA-PILS survey: stringent limits on small amines and nitrogen-oxides towards IRAS 16293-2422B". *Astron. Astrophys.* **619**, A28. DOI: 10.1051/0004-6361/201731980.

Linnartz, H. et al. (2015). "Atom addition reactions in interstellar ice analogues". *Int. Rev. Phys. Chem.* **34**, 205. DOI: 10.1080/0144235X.2015.1046679.

Lodders, K. (2003). "Solar System abundances and condensation temperatures of the elements". *Astrophys. J.* **591**, 1220. DOI: 10.1086/375492.

Macià Escatllar, A. et al. (2019). "Structure and properties of nanosilicates with olivine $(Mg_2SiO_4)_N$ and pyroxene $(MgSiO_3)_N$ compositions". *ACS Earth Space Chem.* **3**, 2390. DOI: 10.1021/acsearthspacechem.9b00139.

Macià Escatllar, A. et al. (2020). "Assessing the viability of silicate nanoclusters as carriers of the anomalous microwave emission: a quantum mechanical study". *Astron. Astrophys.* **634**, A77. DOI: 10.1051/0004-6361/201936419.

Martín-Doménech, R. et al. (2014). "Thermal desorption of circumstellar and cometary ice analogs". *Astron. Astrophys.* **564**, A8. DOI: 10.1051/0004-6361/201322824.

Maté, B. et al. (2020). "Diffusion of CH_4 in amorphous solid water". *Astron. Astrophys.* **643**, A163. DOI: 10.1051/0004-6361/202038705.

Mazo-Sevillano, P. del et al. (2021). "Neural network potential energy surface for the low temperature ring polymer molecular dynamics of the $H_2CO + OH$ reaction". *J. Chem. Phys.* **154**, 094305. DOI: 10.1063/5.0044009.

McClure, M. K. et al. (2023). "An Ice Age JWST inventory of dense molecular cloud ices". *Nat. Astron.* **7**, 431. DOI: 10.1038/s41550-022-01875-w.

McGuire, B. A. et al. (2018). "Detection of the aromatic molecule benzonitrile (c-C_6H_5CN) in the interstellar medium". *Science* **359**, 202. DOI: 10.1126/science.aao4890.

McGuire, B. A. (2022). "2021 census of interstellar, circumstellar, extragalactic, protoplanetary disk, and exoplanetary molecules". *Astrophys. J. Suppl. Ser.* **259**, 30. DOI: 10.3847/1538-4365/ac2a48.

McKellar, A. (1940). "Evidence for the molecular origin of some hitherto unidentified interstellar lines". *Publ. Astron. Soc. Pac.* **52**, 187. DOI: 10.1086/125159.

Mifsud, D. V. et al. (2021). "Sulfur ice astrochemistry: a review of laboratory studies". *Space Sci. Rev.* **217**, 14. DOI: 10.1007/s11214-021-00792-0.

Minissale, M. et al. (2016). "Direct measurement of desorption and diffusion energies of O and N atoms physisorbed on amorphous surfaces". *Astron. Astrophys.* **585**, A146. DOI: 10.1051/0004-6361/201526702.

Minissale, M. et al. (2022). "Thermal desorption of interstellar ices: a review on the controlling parameters and their implications from snowlines to chemical complexity". *ACS Earth Space Chem.* **6**, 597. DOI: 10.1021/acsearthspacechem.1c00357.

Mispelaer, F. et al. (2013). "Diffusion measurements of CO, HNCO, H_2CO, and NH_3 in amorphous water ice". *Astron. Astrophys.* **555**, A13. DOI: 10.1051/0004-6361/201220691.

Molpeceres, G. et al. (2021). "Binding energies and sticking coefficients of H_2 on crystalline and amorphous CO ice". *Astron. Astrophys.* **648**, A84. DOI: 10.1051/0004-6361/202040023.

Molpeceres, G. et al. (2017). "Structure and infrared spectra of hydrocarbon interstellar dust analogs". *Phys. Chem. Chem. Phys.* **19** (2), 1352. DOI: 10.1039/C6CP06043A.

Muller, S. et al. (2011). "Molecules at z = 0.89 - A 4-mm-rest-frame absorption-line survey toward PKS 1830-211". *Astron. Astrophys.* **535**, A103. DOI: 10.1051/0004-6361/201117096.

Müller, H. S. P. et al. (2005). "The Cologne Database for Molecular Spectroscopy, CDMS: a useful tool for astronomers and spectroscopists". *J. Mol. Struct.* **742**, 215. DOI: 10.1016/J.MOLSTRUC.2005.01.027.

Mumma, M. J. et al. (2011). "The chemical composition of comets-emerging taxonomies and natal heritage". *Annu. Rev. Astron. Astrophys.* **49**, 471. DOI: 10.1146/annurev-astro-081309-130811.

Noble, J. et al. (2012). "The desorption of H_2CO from interstellar grains analogues". *Astron. Astrophys.* **543**, A5. DOI: 10.1051/0004-6361/201219437.

Öberg, K. I. et al. (2021). "Astrochemistry and compositions of planetary systems". *Phys. Rep.* **893**, 1. DOI: 10.1016/j.physrep.2020.09.004.

Pantaleone, S. et al. (2020). "Chemical desorption versus energy dissipation: insights from ab initio molecular dynamics of HCO· formation". *Astrophys. J.* **897**, 56. DOI: 10.3847/1538-4357/ab8a4b.

Pantaleone, S. et al. (2021). "H_2 Formation on Interstellar Grains and the Fate of Reaction Energy". *Astrophys. J.* **917**, 49. DOI: 10.3847/1538-4357/ac0142.

Penteado, E. M. et al. (2017). "Sensitivity analysis of grain surface chemistry to binding energies of ice species". *Astrophys. J.* **844**, 71. DOI: 10.3847/1538-4357/aa78f9.

Phuong, N. et al. (2018). "First detection of H_2S in a protoplanetary disk. The dense GG Tauri A ring". *Astron. Astrophys.* **616**, L5. DOI: 10.1051/0004-6361/201833766.

Potapov, A. et al. (2021). "Physics and chemistry on the surface of cosmic dust grains: a laboratory view". *Int. Rev. Phys. Chem.* **40**, 299. DOI: 10.1080/0144235X.2021.1918498.

Rimola, A. et al. (2018). "Can formamide be formed on interstellar ice? An atomistic perspective". *ACS Earth Space Chem.* **2**, 720. DOI: 10.1021/acsearthspacechem.7b00156.

Rocha, W. et al. (2024). "JWST Observations of Young protoStars (JOYS+): Detecting icy complex organic molecules and ions - I. CH_4, SO_2, $HCOO^-$, OCN^-, H_2CO, HCOOH, CH_3CH_2OH, CH_3CHO, CH_3OCHO, and CH_3COOH". *Astron. Astrophys.* **683**, A124. DOI: 10.1051/0004-6361/202348427.

Rogerson, J. B. et al. (1973). "Spectrophotometric results from the Copernicus satellite. I. Instrumentation and performance". *Astrophys. J. Lett.* **181**, L97. DOI: 10.1086/181194.

Rotelli, L. et al. (2016). "The key role of meteorites in the formation of relevant prebiotic molecules in a formamide/water environment". *Sci. Rep.* **6**, 38888. DOI: 10.1038/srep38888.

Ruaud, M. et al. (2015). "Modelling complex organic molecules in dense regions: Eley-Rideal and complex induced reaction". *Mon. Not. R. Astron. Soc.* **447**, 4004. DOI: 10.1093/mnras/stu2709.

Rubin, R. H. et al. (1971). "Microwave detection of interstellar formamide". *Astrophys. J. Lett.* **169**, L39. DOI: 10.1086/180810.

Ruf, A. et al. (2019). "Organosulfur Compounds Formed by Sulfur Ion Bombardment of Astrophysical Ice Analogs: Implications for Moons, Comets, and Kuiper Belt Objects". *Astrophys. J. Lett.* **885**, L40. DOI: 10.3847/2041-8213/ab4e9f.

Ruffle, D. P. et al. (2000). "New models of interstellar gas-grain chemistry - I. Surface diffusion rates". *Mon. Not. R. Astron. Soc.* **319**, 837. DOI: 10.1046/j.1365-8711.2000.03911.x.

Sandford, S. A. et al. (2006). "Organics captured from comet 81P/Wild 2 by the Stardust spacecraft". *Science* **314**, 1720. DOI: 10.1126/science.1135841.

Shalayel, I. et al. (2020). "Cysteine chemistry in connection with abiogenesis". *Eur. J. Org. Chem.* **2020**, 3019. DOI: 10.1002/ejoc.202000089.

Shannon, R. J. et al. (2014). "The fast $C(^3P)$ + CH_3OH reaction as an efficient loss process for gas-phase interstellar methanol". *RSC Adv.* **4**, 26342. DOI: 10.1039/C4RA03036B.

Shaw, A. M. (2007). *Astrochemistry: From astronomy to astrobiology*. John Wiley & Sons.

Shimonishi, T. et al. (2018). "Adsorption energies of carbon, nitrogen, and oxygen atoms on the low-temperature amorphous water ice: a systematic estimation from quantum chemistry calculations". *Astrophys. J.* **855**, 27. DOI: 10.3847/1538-4357/aaaa6a.

Shingledecker, C. et al. (2020). "Isomers in interstellar environments. I. The case of Z- and E-cyanomethanimine". *Astrophys. J.* **897**, 158. DOI: 10.3847/1538-4357/ab94b5.

Simons, M. A. J. et al. (2020). "Formation of COMs through CO hydrogenation on interstellar grains". *Astron. Astrophys.* **634**, A52. DOI: 10.1051/0004-6361/201936522.

Skouteris, D. et al. (2018). "The genealogical tree of ethanol: gas-phase formation of glycolaldehyde, acetic acid, and formic acid". *Astrophys. J.* **854**, 135. DOI: 10.3847/1538-4357/aaa41e.

Smith, R. et al. (2016). "Desorption kinetics of Ar, Kr, Xe, N_2, O_2, CO, methane, ethane, and propane from graphene and amorphous solid water surfaces". *J. Phys. Chem. B* **120**, 1979. DOI: 10.1021/acs.jpcb.5b10033.

Sturm, J. A. et al. (2023). "A JWST inventory of protoplanetary disk ices - The edge-on protoplanetary disk HH 48 NE, seen with the Ice Age ERS program". *Astron. Astrophys.* **679**, A138. DOI: 10.1051/0004-6361/202347512.

Sun, G. et al. (2019). "A Self-consistent framework for multiline modeling in line intensity mapping experiments". *Astrophys. J.* **887**, 142. DOI: 10.3847/1538-4357/ab55df.

Swings, P. et al. (1937). "Considerations regarding interstellar molecules". *Astrophys. J.* **86**, 483. DOI: 10.1086/143880.

Taquet, V. et al. (2016). "Formation and recondensation of complex organic molecules during protostellar luminosity outbursts". *Astrophys. J.* **821**, 46. DOI: 10.3847/0004-637X/821/1/46.

Tielens, A. G. G. M. (2008). "Interstellar polycyclic aromatic hydrocarbon molecules". *Annu. Rev. Astron. Astrophys.* **46**, 289. DOI: 10.1146/annurev.astro.46.060407.145211.

Tinacci, L. et al. (2022). "Theoretical distribution of the ammonia binding energy at interstellar icy grains: a new computational framework". *ACS Earth Space Chem.* **6**, 1514. DOI: 10.1021/acsearthspacechem.2c00040.

Trigo-Rodríguez, J. M. et al. (2019). "Accretion of water in carbonaceous chondrites: current evidence and implications for the delivery of water to early Earth". *Space Sci. Rev.* **215**, 1. DOI: 10.1007/s11214-019-0583-0.

Trigo-Rodríguez, J. M. (2012). *Meteoritos, Colección ¿Qué sabemos de?* Editorial Catarata-CSIC, Madrid.

van 't Hoff, M. L. et al. (2020). "Temperature profiles of young disk-like structures. The case of IRAS 16293A". *Astron. Astrophys.* **633**, A7. DOI: 10.1051/0004-6361/201936839.

Vastel, C. et al. (2018). "Sulphur chemistry in the L1544 pre-stellar core". *Mon. Not. R. Astron. Soc.* **478**, 5514. DOI: `10.1093/mnras/sty1336`.

Vasyunin, A. I. et al. (2013). "Reactive desorption and radiative association as possible drivers of complex molecule formation in the cold interstellar medium". *Astrophys. J.* **769**, 34. DOI: `10.1088/0004-637X/769/1/34`.

Vazart, F. et al. (2020). "Gas-phase formation of acetaldehyde: review and new theoretical computations". *Mon. Not. R. Astron. Soc.* **499**, 5547. DOI: `10.1093/mnras/staa3060`.

Villadsen, T. et al. (2022). "Predicting binding energies of astrochemically relevant molecules via machine learning". *Astron. Astrophys.* **666**, A45. DOI: `10.1051/0004-6361/202244091`.

Wakelam, V. et al. (2004). "Sulphur-bearing species in the star forming region L1689N". *Astron. Astrophys.* **413**, 609. DOI: `10.1051/0004-6361:20031572`.

Wakelam, V. et al. (2015). "The 2014 KIDA network for interstellar chemistry". *Astrophys. J. Suppl. Ser.* **217**, 20. DOI: `10.1088/0067-0049/217/2/20`.

Wakelam, V. et al. (2017). "Binding energies: new values and impact on the efficiency of chemical desorption". *Mol. Astrophys.* **6**, 22. DOI: `10.1016/j.molap.2017.01.002`.

Watanabe, N. et al. (2008). "Ice surface reactions: a key to chemical evolution in space". *Progress in Surface Science* **83**, 439. DOI: `10.1016/j.progsurf.2008.10.001`.

Weinberg, S. (1993). *The first three minutes : a modern view of the origin of the universe*. Basic Books.

Williams, D. A. et al. (2002). "It's a dusty Universe: surface science in space". *Surf. Sci.* **500**, 823. DOI: `10.1016/S0039-6028(01)01538-2`.

Woods, P. M. et al. (2015). "A new study of an old sink of sulphur in hot molecular cores: the sulphur residue". *Mon. Not. R. Astron. Soc.* **450**, 1256.

Yabuta, H. et al. (2007). "The insoluble carbonaceous material of CM chondrites: a possible source of discrete organic compounds under hydrothermal conditions". *Meteorit. Planet. Sci.* **42**, 37. DOI: `10.1111/j.1945-5100.2007.tb00216.x`.

Zamirri, L. et al. (2017). "Forsterite surfaces as models of interstellar core dust grains: computational study of carbon monoxide adsorption". *ACS Earth Space Chem.* **1**, 384. DOI: `10.1021/acsearthspacechem.7b00041`.

Zaverkin, V. et al. (2022). "Neural-network assisted study of nitrogen atom dynamics on amorphous solid water - II. Diffusion". *Mon. Not. R. Astron. Soc.* **510**, 3063. DOI: `10.1093/mnras/stab3631`.

Zhukovska, S. et al. (2014). "Life cycle of dust in the Magellanic Clouds and the Milky Way". *PoS Proc. Sci.* **207**, 016. DOI: `10.22323/1.207.0016`.

Chapter 2

Methodology

Abstract

This chapter provides an overview of the theoretical framework on which quantum chemistry is based. Starting with the Schrödinger equation, the development of quantum mechanical methods from Hartree-Fock to post-Hartree-Fock, Density Functional Theory, and semiempirical approaches is traced. The characteristics and classification of the basis sets used to describe atoms in quantum mechanical methods are discussed. In addition, the chapter introduces molecular mechanics as an alternative approach to quantum chemistry. The concept of potential energy surface, a hyperspace that relates the energy of a chemical system to its atomistic structure, is explored. Then, the chapter looks at the computational modelling of solid state systems, introducing the two main approaches and providing guidelines for the simulation of surface models and surface chemistry. Finally, the structure of interstellar chambers and the theory onto which the experimental determination of binding energies is based are presented.

2.1 The birth of computational chemistry

'Computers do not solve problems, people do.'[1] Computers simply generate numbers. The real strength of computational chemistry is the ability to generate data from which a scientist may gain insights, thereby rationalizing the behaviour of a chemical system. In the field of astrochemistry, computational chemistry provides essential reference data for both astronomical observations and modelling. Molecules can be seen as collections of charged particles (positive nuclei and negative electrons), whose interaction is determined by the rules of quantum mechanics. Given a molecule, several properties can be calculated, e.g., the nuclei geometrical arrangements, energies, spectroscopic response (like IR emission and NMR coupling constants), etc. All these features are needed to advance the knowledge of how chemistry works in the field of astrochemistry. This chapter is primarily based on the Jensen (2017) and Lewars (2016) textbooks.

2.1.1 The Schrödinger equation

A molecule can be considered as a group of electrons surrounding a set of positively charged nuclei, hold together by Coulombic attraction. This interaction potential is one of the ingredients needed to describe the system, the other being an equation defining how the system evolves in time. In classical mechanics, such requirement would be satisfied by the second law of Newton, $F = ma$. However, matter at the nanoscale level should be described by quantum mechanics (QM). A chemical system is therefore defined by the non-relativistic time-dependent Schrödinger equation (Schrödinger, 1926).

---

[1]Jensen, F. (1999). *Introduction to computational chemistry, 1st Edition*. John Wiley & Sons, Ltd.

$$i\hbar\frac{\partial}{\partial t}\psi(\mathbf{R},\mathbf{r},t) = \hat{\mathcal{H}}\psi(\mathbf{R},\mathbf{r},t) \tag{2.1}$$

where $i = \sqrt{-1}$ is the imaginary unit and $\hbar$ is the reduced Planck constant. $\psi(\mathbf{R},\mathbf{r},t)$ is the wave function, an object that completely describes the state of the system, and depends on the time (t), on the coordinates of the nuclei ($\mathbf{R}$), and on those of the electrons ($\mathbf{r}$). $\hat{\mathcal{H}}$ is the Hamiltonian operator, representing the total energy of the system, given by the sum of kinetic ($\hat{\mathcal{T}}$) and potential ($\hat{\mathcal{V}}$) energy operators.

$$\hat{\mathcal{H}} = \hat{\mathcal{T}} + \hat{\mathcal{V}} = \sum_i \frac{\hat{\mathbf{p}}_i^2}{2m_i} + \hat{\mathcal{V}} \tag{2.2}$$

In equation 2.2, m_i is the mass of the particle i and $\hat{\mathbf{p}}_i$ is the quantum mechanical momentum operator.

$$\hat{\mathbf{p}}_i = -i\hbar\nabla_i = -i\hbar\left(\frac{\partial}{\partial x_i} + \frac{\partial}{\partial y_i} + \frac{\partial}{\partial z_i}\right) \tag{2.3}$$

If the Hamiltonian $\hat{\mathcal{H}}$ is time-independent, the wave function can be rewritten as a product of two factors, the first depending on the coordinates of the electrons and the nuclei, and the second describing the time evolution as a phase factor.

$$\psi(\mathbf{R},\mathbf{r},t) = \psi(\mathbf{R},\mathbf{r})e^{-iEt/\hbar} \tag{2.4}$$

By doing so, equation 2.1 becomes the time-independent Schrödinger equation:

$$\hat{\mathcal{H}}\psi_n(\mathbf{R},\mathbf{r}) = E_n\psi_n(\mathbf{R},\mathbf{r}) \tag{2.5}$$

The solution of equation 2.5 returns a number of *eigenvectors* $\psi_n(\mathbf{R},\mathbf{r})$ associated with E_n *eigenvalues*, which represent the stationary states of the system, i.e., the states in which the gradient on the forces acting on all the nuclei of the system is zero and that are invariant with time.

2.1.2 The Born-Oppenheimer approximation

The Schrödinger equation can be solved analytically only for one-electron systems, regardless of their number of nuclei, such as the hydrogen atom, He$^+$, H$_2^+$, etc. In general, to treat systems that contain M nuclei and N electrons, the Born-Oppenheimer (BO) approximation is required (Born et al., 1927). This approximation assumes that heavy nuclei and light electrons have distinct velocities due to their different masses (the proton is 1840 times heavier than the electron); hence, the electrons relax instantaneously for each configuration adopted by the nuclei and their motion can be treated separately. Thanks to this approximation, the Hamiltonian can be written in terms of kinetic and potential energy of electrons and nuclei and, in atomic units ($\hbar = m_e = |e| = 4\pi\varepsilon_0 = 1$), it takes the form:

$$\begin{aligned}
\hat{\mathcal{H}} = \hat{\mathcal{T}}_N + \hat{\mathcal{T}}_e + \hat{\mathcal{V}}_{NN} + \hat{\mathcal{V}}_{ee} + \hat{\mathcal{V}}_{Ne} = \\
-\frac{1}{2}\sum_A^M \frac{\nabla_A^2}{M_A} - \frac{1}{2}\sum_i^N \nabla_i^2 + \frac{1}{2}\sum_{A,B}^M \frac{Z_A Z_B}{|\mathbf{R}_{AB}|} + \frac{1}{2}\sum_{i,j}^N \frac{1}{|\mathbf{r}_{ij}|} - \sum_A^M\sum_i^N \frac{Z_A}{|\mathbf{R}_A - \mathbf{r}_i|}
\end{aligned} \tag{2.6}$$

where $\hat{\mathcal{T}}_N$ and $\hat{\mathcal{T}}_e$ are the kinetic energy terms for the nuclei and the electrons, respectively, and $\hat{\mathcal{V}}_{NN}$, $\hat{\mathcal{V}}_{ee}$, and $\hat{\mathcal{V}}_{Ne}$ are the electron-electron, nucleus-nucleus and nucleus-electron potential energy terms. Therefore, the Schrödinger equation can be separated in

two parts: one describing the electronic wave function for a fixed nuclear geometry; the other concerning the nuclear wave function, where the electronic energy plays the role of potential energy. Under this assumption, the electronic hamiltonian (in which $\hat{\mathcal{T}}_N$ is neglected) can be defined as:

$$\hat{\mathcal{H}}_{el} = \hat{\mathcal{T}}_e + \hat{\mathcal{V}}_{NN} + \hat{\mathcal{V}}_{ee} + \hat{\mathcal{V}}_{Ne} \tag{2.7}$$

where $\hat{\mathcal{V}}_{NN}$ is constant because of the fixed nuclei positions. The prior approximation causes the spatial wave function $\psi(\mathbf{R}, \mathbf{r})$ to be factorized in the product of a nuclear and an electronic term, which depends on the nuclei position.

$$\psi(\mathbf{R}, \mathbf{r}) = \psi_{nucl}(\mathbf{R})\psi_{el}(\mathbf{r}; \mathbf{R}) \tag{2.8}$$

Equation 2.5 can thus be rewritten considering only the electronic part.

$$\hat{\mathcal{H}}_{el}\psi_{el}(\mathbf{r}; \mathbf{R}) = E_{el}(\mathbf{R})\psi_{el}(\mathbf{r}; \mathbf{R}) \tag{2.9}$$

From its solution, we obtain the potential energy surface constituted by the collection of each electronic energy of the system $E_{el}(\mathbf{R})$, a term that depends on the spatial configuration of the nuclei. The BO approximation usually yields a good performance, however, it fails when two or more solutions of equation 2.9 are close in energy. An example is the homolitic cleavage of LiF bond in the gas phase, which at short distances is instead better described by an ionic (Li^+F^-) wave function. However, for the majority of the systems, the BO approximation introduces only very small errors and it can be applied without altering the outcome of the calculation.

2.1.3 The variational principle

Considering that the exact wave function of the system is unknown, the variational principle is needed to solve equation 2.9. Given a normalized wave function ψ_{trial}, which depends on one or more parameters, the variational principle states that the expectation value of the energy E_{trial}, is an upper bound to the ground state energy E_0, and the best trial function is obtained by minimizing the energy as a function of those parameters. For a normalized wave function, for which $\langle\psi_{trial}|\psi_{trial}\rangle$=1, this can be expressed through the Dirac notation (Dirac, 1939).

$$E_{trial} = \langle\psi_{trial}|\hat{\mathcal{H}}_{el}|\psi_{trial}\rangle \tag{2.10}$$

The energy is a functional of the wave function, whose minimisation is required to obtain E_0.

$$E_0 = \min_{\psi \to N} E[\psi] = \min_{\psi \to N} \langle\psi_{trial}|\hat{\mathcal{H}}_{el}|\psi_{trial}\rangle \tag{2.11}$$

The notation $\psi \to N$ indicates that the search is conducted over N-electron wave functions ψ_{trial}, which must be normalized and antisymmetric. The antisymmetry condition dictates that the wave function changes sign upon the exchange of any two electrons, resulting in the Pauli exclusion principle.

2.2 Wave Function-based Methods

The Schrödinger equation can be solved only for systems with no interacting electrons. For atoms with many electrons, the V_{ee} term becomes very challenging to handle. This

difficulty arises from the mutual interaction of each electron with all other electrons in the system. Consequently, this introduces a non-linearity and a many-body problem, as the energy depends on the relative and instantaneous positions of all electrons. To properly account for electron-electron interactions, it is essential to consider electron correlation, which refers to the adjustments in the motion of each electron due to the presence of the others.

Unfortunately, a rigorous solution to this problem remains unknown. To overcome such limitation, many good approximations were developed, giving rise to several methods and theories, defining the electronic structure methods. Among them, the most employed are those based on the wave function and the Density Functional Theory (DFT). Hartree-Fock (HF) and post-Hartree-Fock (post-HF) belong to the wave function-based methods, since their theoretical framework is based on building the wave function that better suits the system. Such approximated (numerical) ways to solve equation 2.9 are referred to as *ab initio*, since no reference to experimental data is made to solve the equation.

In HF, post-HF and DFT theories, relativistic effects, which are normally negligible for the first three periods of the periodic table ($Z < 36$, although they start to become relevant for heavier nuclei), are neglected. To compensate for their absence, spin terms are introduced as *ad hoc* quantum effects in equation 2.9.

Each electron has a spin quantum number of ½, which in presence of an external magnetic field can assume two states: α for parallel and β for anti-parallel orientation with respect to the magnetic field. Due to this characteristic, electrons are fermionic particles and their wave function must be antisymmetric with respect to the exchange of two particles. An antisymmetric wave function takes the form of a Slater determinant (Φ_{SD}), where the columns represent the N one-electron wave functions (orbitals), the rows represent the N electron coordinates, and $1/\sqrt{N!}$ is the normalisation factor (Slater, 1930).

$$\Phi_{SD} = \frac{1}{\sqrt{N!}} \begin{vmatrix} \phi_1(1) & \phi_2(1) & \dots & \phi_N(1) \\ \phi_1(2) & \phi_2(2) & \dots & \phi_N(2) \\ \dots & \dots & \dots & \dots \\ \phi_1(N) & \phi_2(N) & \dots & \phi_N(N) \end{vmatrix} \tag{2.12}$$

2.2.1 The Hartree-Fock method

The first approximation that allows to solve the electronic Schrödinger equation was formulated by D. Hartree and V. Fock (Hartree, 1928a; Hartree, 1928b; Hartree, 1928c; Hartree, 1929; Fock, 1930). An antisymmetric trial wave function ψ_{trial} can be built from a Slater determinant as that in expression 2.12. Each one-electron wave function is a molecular orbital (MO, also called spin orbital, denoted $\phi(\mathbf{x})$) given by the product of a spatial function $\chi(\mathbf{r})$ and a spin function $\sigma(s)$, which can assume the value α or β, and is usually orthonormal, $\langle \phi_i | \phi_j \rangle = \delta_{ij}$.

$$\phi(\mathbf{x}) = \chi(\mathbf{r})\sigma(s) \tag{2.13}$$

The spatial functions $\chi(\mathbf{r})$ are usually expanded as a linear combination of atomic orbitals (LCAO), which are atomic functions centred on the nuclei ($f(\mathbf{r} - \mathbf{r}_A)$) and constitute the X functions of the 'basis set', one of the key ingredients of a calculation.

$$\chi_j(\mathbf{r}) = \sum_{i=1}^{X} c_{ij} f_i(\mathbf{r} - \mathbf{r}_A) \tag{2.14}$$

The Hartree-Fock approximation treats electrons as independent particles, considering the ground state many-electron wave function as a single Slater determinant built with

MOs functions. The HF energy (E_{HF}) is given by the expectation value of the electronic hamiltonian acting on the Slater determinant.

$$E_{HF} = \langle \Psi_{SD} | \hat{\mathcal{H}}_{el} | \Phi_{SD} \rangle \tag{2.15}$$

The minimisation of the energy functional yields *N* pseudo-*eigenvalue* equations resulting from the Fock operator acting on each spin orbital (Szabo et al., 1996).

$$\hat{F}(i) | \phi_\mu(i) \rangle = \left[\hat{h}_i + \sum_{\nu=1}^{N} \left(\hat{J}_\nu(i) - \hat{K}_\nu(i) \right) \right] | \phi_\mu(i) \rangle = \epsilon_\mu | \phi_\mu(i) \rangle \tag{2.16}$$

where $\hat{h}_i$ is the mono-electronic Hamiltonian, $\hat{J}_\nu(i)$ is the Coulomb operator and $\hat{K}_\nu(i)$ is the exchange operator arising from the antisymmetry of the wave function.

In a calculation, the spin orbitals arise from the expansion of the basis set. This process transforms the HF theory into a linear problem, which can be expressed by the Roothaan-Hall equations and can be represented in matrix formulation as:

$$\mathbf{FC} = \mathbf{SCE} \tag{2.17}$$

Here, **F** is the Fock matrix containing the elements $F_{ij} = \langle \phi_i | \hat{F} | \phi_j \rangle$, **C** is the matrix of the coefficients of the LCAO expansion of the basis set, **S** is the overlap matrix given by the elements $S_{ij} = \langle \phi_i | \phi_j \rangle$ and **E** is a diagonal matrix collecting the *eigenvalues*, $E_{ii} = \epsilon_i$ (Roothaan, 1951; Hall et al., 1951). Exploiting the LCAO approach causes the highly non-linear problem of equation 2.11 to become linear and solvable with a constrained minimisation over the MOs, in which the orbitals are required to be orthonormal. The aim is to find the most suitable combination of MOs that minimizes the energy of the system. This procedure is called self-consistent field (SCF) and consists of three main steps: (i) building an initial guess of the wave function based on the chosen basis set, thus selecting the coefficients c_{ij}; (ii) computing the expectation value of the energy; (iii) minimizing the energy functional providing that the energy is stationary with respect to a change in the coefficients c_{ij}.

$$\delta E[\psi] = \frac{\partial E[\psi]}{\partial c_{ij}} = 0 \quad with \quad i,j = 1, ..., N \tag{2.18}$$

At every SCF step, the c_{ij} coefficients are updated and the process is repeated in an iterative way, until the energy variation between two successive steps falls below a given threshold. In a few words, the HF method transforms a *N* body problem into *N* single-particle problems, where every electron is subjected to the interaction with the mean-field generated by the other electrons of the system. For this reason, the HF approach is usually referred to as mean-field approximation. Nonetheless, the HF theory has an important limitation: the bi-electronic operator $\hat{K}_\nu$, which accounts for Pauli exclusion principle, only considers the Fermi correlation, that is the correlation between electrons with the same spin state ($\alpha\alpha$ and $\beta\beta$). Consequently, the case involving opposite spin states ($\alpha\beta$) is only considered in an average way, thereby losing the instantaneous electron-electron (Coulomb) correlation.

2.2.2 The basis set

One of the approximations introduced by *ab initio* methodologies is the use of basis sets. In principle, expanding the wave function in a set of known functions (the basis set) is not an approximation, provided that the set is complete. This implies using an infinite number of functions, which is not feasible in a real calculation. Knowing that *ab initio* methods scale formally as at least M^4, where *M* is the number of functions, it is of primary

importance to choose a basis set as small as possible without compromising the accuracy of the calculation.

Atomic orbitals are typically represented by mathematical functions that fall into two main categories. A Slater-type orbital (STO) is an exponential function describing the cusp condition near the nucleus and the decay at large distances, taking the form:

$$f_{\zeta,n,m,l}(\mathbf{r},\theta,\phi) = N Y_{l,m}(\theta,\phi) r^{n-1} e^{-\zeta r} \tag{2.19}$$

However, it is not convenient to adopt this type of functions, since they require the calculation of three- and four-centres two-electron integrals that cannot be performed analytically. In contrast, Gaussian functions are more suitable to compute analytically bielectronic integrals. The Gaussian-type orbitals (GTOs) are defined as:

$$f_{\zeta,n,m,l}(\mathbf{r},\theta,\phi) = N Y_{l,m}(\theta,\phi) r^{2n-2-l} e^{-\zeta r^2} \tag{2.20}$$

The disadvantage of GTOs lies in their inability to properly describe the form of the function at the nucleus, where there should be a cusp, and to faithfully reproduce the long-range behaviour, due to their exceedingly rapid decay when moving away from the nucleus (Boys et al., 1950). This issue can be addressed by using linear combinations of GTOs with different ζ, thereby adjusting their width. Although this approach implies a larger number of calculations, it remains computationally more efficient compared to using STOs. In summary, using a combination of GTOs is more convenient than adopting a single STO to describe a specific orbital, especially when dealing with large systems that require the computation of numerous integrals. A large variety of basis sets exists nowadays, each suitable for specific classes of chemical systems.

Classification of basis set functions

Several characteristics have to be considered in the construction and in the choice of a basis set. The simplest and smallest basis sets, such as STO-*n*G (Hehre et al., 1969) and MINI-1 (Tatewaki et al., 1980), contain the minimal number of functions needed to describe the electronic configuration of the atom. Essentially, they consist of a function for each occupied orbital.

The first improvement resides in enlarging the number of functions adopted to describe each orbital, resulting in NZ quality basis sets, where each orbital is defined by N = D, T, Q, 5, etc. contracted Gaussian functions (CGTOs). The latter can be defined as linear combinations of primitive Gaussian functions (PGTOs) sharing the same exponents, but different weights. This method simplifies the basis set optimisation procedure, addressing the disproportionate effort previously devoted to optimising basis functions for core electrons. While core electrons make up over 50% of the total functions and play a crucial role in energy definition, they are chemically unimportant compared to the valence region. The most common contraction method involves incorporating all PGTOs into the linear combination of each CGTO and determining suitable coefficients for this combination. This method is referred to as 'general contraction'.

To save computational time, split-valence NZV basis sets (with N = D, T, Q, 5, etc.) were proposed. Here, orbitals of the valence shell are described by two or more contracted Gaussian functions, while inner shells are represented by a single function, in that their are energetically, but not chemically, important (Ditchfield et al., 1971).

Polarisation functions are higher angular momentum functions added to describe the deformation of the electron density, for example when bond formation occurs (Frisch et al., 1984). The first set of polarisation functions plays a crucial role in describing charge polarisation effects when single determinant wave functions are used. Their inclusion into

the basis set becomes essential when methods incorporate the description of electron correlation effects. Higher angular momentum functions are needed to account for angular correlation, while radial correlation is better described by increasing the ζ quality of the basis set.

Finally, diffuse functions are small exponent (broad) Gaussian functions particularly useful when describing properties that depend on the wave function tail, as for example the polarisability or the presence of loosely bound electrons. Thus, they are indicated to describe excited states and anions.

Contracted basis sets

One of the most remarkable scientific groups in basis sets development was lead by J.A. Pople. Many basis sets families where developed in his group, starting from STO-nG, which are Slater type orbitals consisting of n PGTOs (Hehre et al., 1969). This is a small basis set where the exponents of the PGTOs are determined by fitting them against an STO, instead of using the classical variational optimisation procedure. The most common is the STO-3G basis set.

*k-nlm*G basis sets are probably the most widespread family and are split valence basis sets (e.g., Hehre et al., 1972; Krishnan et al., 1980). *k* indicates the number of PGTOs used for the core orbitals, while *n*, *l*, and *m* are the numbers of PGTOs used in the contraction of valence orbitals, beside suggesting whether the basis set is split valence (*nl*) or triple split valence (*nlm*). An example of such notation is given by the 6-31G and 6-311G basis sets, respectively. Polarisation and diffuse functions can be added to these basis set, so that 6-311++G(d,p) represents a triple split valence basis sets with two sets of diffuse functions, a *d*-type polarisation function on heavy atoms (all except H) and a *p*-type polarisation function on hydrogen (Frisch et al., 1984).

Dunning-Huzinaga basis sets results from the application of several contraction schemes that allowed varying the exponents of the PGTOs (Huzinaga, 1965; Dunning, 1971). Despite resulting in the definition of basis sets composed by a large number of basis functions, their accuracy was not satisfying.

Karlsruhe-Type Basis Sets have been developed in the group of R. Ahlrichs and are contracted basis sets that span from the DZ, TZ, and QZ, to the corresponding split valence SVP, TZV, and QZV. The latter group has been updated, resulting in the 'def2' family of basis sets (Weigend et al., 2005) that has been applied several times in this thesis. They are computationally quite efficient and available for a large fraction of atoms in the periodic table, up to radon. Furthermore, two slightly different sets of polarization functions are available for some atoms, depending on whether the basis set is combined with HF/DFT or with electron correlation methods. The 'def2' basis sets family is also available in a minimally augmented version, which consists of an extension in which a minimal set of diffuse functions is added to a subset of chemical elements. Diffuse functions are not quite as important for def2 basis sets as would be for the Pople basis sets, but they improve the quality of the results obtained on barrier heights and electron affinities (Zheng et al., 2011).

Atomic natural orbitals (ANOs) are derived using a general contraction scheme applied to a large number of PGTOs in order to obtain a small number of CGTOs. Natural orbitals, which are used to guide the contraction of PGTOs into CGTOs, derive from a correlated calculation on free atoms, typically run at CISD level (described later), and tend to provide a more compact and accurate description of the electron distribution. (Almlöf

et al., 1990; Almlöf et al., 1991). The natural orbitals are obtained from the diagonalisation of the density matrix and the corresponding *eigenvalues* define the orbital occupation number, that is allowed to vary from 0 (empty orbital) to 2 (full orbital). The advantage of ANOs is that their contraction generates balanced basis sets, where the number of functions of a certain type decrease when their angular momentum increases.

Correlation consistent (cc) basis sets have been developed with the twofold aim of enabling the conduction of calculations with improving basis set quality and of allowing for the extrapolation of desired quantities to the limit of an infinite basis set, known as the complete basis set (CBS) approximation. These basis sets overcome the limitation of ANOs basis sets, that is the large number of PGTOs required to converge to the CBS limit. Despite the smaller number of PGTOs, they yield results comparable to those of ANOs. Furthermore, they recover the correlation energy of valence electrons (Dunning, 1989). Several different sizes of correlation consistent basis sets are available in terms of final number of contracted functions (X). Moreover, they can be augmented by addition of diffuse functions for non-hydrogen atoms, resulting in the aug-cc-pVXZ family of basis sets. The main advantage of ANOs and cc basis sets is the ability to generate a sequence of basis sets that converges toward the CBS limit. Correlation consistent basis sets have been at the centre of the development of procedures to extrapolate a given property to the CBS limit, such as R12 and F12 methodologies.

Finally, tailored basis sets optimised specifically to be used in conjunction with a specific HF- or DFT-based method exist, e.g., HF-3c (Sure et al., 2013), B97-3c (Brandenburg et al., 2018), and r^{2}SCAN-3c (Grimme et al., 2021). The principal objective of these methodologies is to reduce the cost of the calculation without compromising the accuracy of the results. Furthermore, they address the primary issue associated with the use of a limited number of functions in the basis set, namely the basis set superposition error (BSSE).

Basis Set Superposition Error

The BSSE arises from using a finite basis set of localized functions to describe a chemical system. It becomes particularly evident when computing the interaction energy of an $A+B$ complex made by the fragments A and B (Paizs et al., 1998). The variational theorem ensures that the total energy of any system will be lowered if a larger number of basis set functions is chosen to describe its electron density. When calculating the interaction energy (ΔE) of the $A+B$ complex, expected to be negative in case of a favourable interaction between A and B, the number of basis set functions used is inevitably different from the one of A and B alone.

$$\Delta E = E_{A+B} - E_A - E_B \tag{2.21}$$

Therefore, an artificial lowering of the energy of the $A+B$ complex is expected due to the larger set of basis functions with respect to the separate constituents A and B.

$$\Delta E = \Delta E^C - E_{BSSE} \tag{2.22}$$

where E_{BSSE} represents the artificial lowering in energy and ΔE^C is defined as the *BSSE-*corrected interaction energy. The latter term can be obtained through the counterpoise method proposed by Boys et al. (1970). The total energies of the $A+B$ complex and of the separate A and B fragments are calculated with the same number of basis functions of the

complex *A+B*. This can be achieved by adding *ghost* functions to the basis sets of *A* and *B*.

$$\Delta E^C = E_{A+B} - E_{A(B)} - E_{(A)B} \qquad (2.23)$$

From these equations, the energy terms contributing to the E_{BSSE} can be worked out.

$$E_{BSSE} = \delta_A + \delta_B = E_A - E_{A(B)} + E_B - E_{(A)B} \qquad (2.24)$$

Both δ_A and δ_B are positive according to the variational theorem. Thus, the E_{BSSE} is a positive quantity and $\Delta E^C > \Delta E$. However, it should be noted that E_{BSSE} may be slightly overestimated, as the added ghost functions are not populated, at variance with what happens for the complex *A+B*. Computing $E_{A(B)}$ and $E_{(A)B}$ requires the use of a large number of basis set functions, which increases the cost of the calculation.

An alternative strategy to correct for the BSSE consists in the geometrical counterpoise (gCP, Kruse et al., 2012), which depends only on the coordinates of the atoms in the structure, and thus it can be applied to larger structures with thousands of atoms. The gCP consists of an atomic correction (parametrised against the counterpoise correction of Boys-Bernardi), in which each atom is characterised by four parameters specific to a particular combination of method and basis set. This correction scheme addresses both inter- and intra-molecular BSSE and provides BSSE-corrected gradients, thus acting not only on the energies but also on the geometries. The gCP scheme has been adopted in the development of the '3c' methods, such as HF-3c (Sure et al., 2013), PBEh-3c (Grimme et al., 2015), and r^{2}SCAN-3c (Grimme et al., 2021), developed in the last decade with the goal of providing high-quality results in a reduced computational time.

Alternatives to localized basis sets

When dealing with heavier atoms, particularly those from the fourth period onwards, the number of core electrons notably increases. Consequently, a significant fraction of the basis functions must be allocated to describe the core electrons, leaving only a limited number of functions available for the description of valence electrons. Furthermore, as one moves to the lower half of the periodic table, relativistic effects become increasingly important in the description of atoms and traditional basis sets become inadequate for accurately capturing these effects. The introduction of effective core potentials (ECPs, or pseudopotentials) offers a solution to both challenges. The ECPs, often tabulated, replace the core electrons, allowing for the explicit treatment of valence electrons only. This guarantees to partly accounting for relativistic effects without resorting to fully relativistic calculations, but also significantly reduces the number of integrals to be computed, thereby enhancing computational efficiency (Cundari et al., 1996).

When performing periodic calculations, it is possible to describe atoms using both atom-centred GTOs and plane waves (PWs). While GTOs require adaptation to Gaussian-type Bloch functions in order to adhere to the periodicity of the chemical system, PWs are combinations of sine and cosine functions that naturally and uniformly fill the space of a given cell. The number of PWs to be used depends on the size of the cell rather than on the number of the atoms it contains, intrinsically leading to 3D-periodic calculations, even for systems with lower periodicity such as surfaces, polymers, and molecules. These systems are usually treated by defining a 3D cell in which a sufficiently large spacing is left between the non-periodic directions of the model, to mitigate the inevitable interactions between the replicas of the unit cell. One of the primary advantages of PWs is that they constitute a universal basis set, since they do not depend on atoms types and positions. The total number of plane waves, which is determined by an energy cutoff, is the only

parameter that determines how accurately the system is described. Additionally, PWs are BSSE-free because they fill in the whole space of the unit cell avoiding the biasing of localized functions.

Nevertheless, incorporating the exact HF exchange into a calculation with PWs can be computationally expensive, making calculations with hybrid DFT functionals extremely demanding. Furthermore, PWs do not adequately describe highly localized core electrons, although this issue can be mitigated by using pseudopotentials to represent core electrons and treat only valence electrons with PWs (Kresse et al., 1996; Bylaska, 2017).

2.2.3   Post-Hartree-Fock methods

Due to the mean-field approximation, the HF approach lacks a fraction of the exact energy (E_{exact}). This quantity, defined as correlation energy (E_{corr}) arises from the instantaneous correlation of electron motion (Shavitt, 1977) and translates to:

$$E_{exact} = E_{corr} + E_{HF} \tag{2.25}$$

Usually, the correlation energy is a small fraction of the exact energy (around 2%) but represents a determining quantity when it comes to describing the cleavage and the formation of chemical bonds, as well as intra- and inter-molecular interactions.

Electronic correlation is usually classified as radial/angular or static/dynamic correlation. These definitions are linked, but they address different aspects of electronic correlation. Radial correlation concerns a situation in which one electron is close to the nucleus and the other is far, while angular correlation refers to a situation in which two electrons are in opposite sides of the nucleus. In contrast, considering that each electron is interacting with the mean-field generated by other electrons, rather than individually interacting with every other electron introduces dynamic correlation. Finally, static correlation is caused by a single Slater determinant being insufficient to describe degenerate electronic configurations, for which multiple determinants would be more appropriate.

In order to account for the electronic correlation, a number of approaches have been developed under the designation of post-HF methods, since they are designed to go beyond the capabilities of the mean-field approximation. The most common are the many body perturbation theory (MBPT), the configuration interaction (CI) method and the coupled cluster (CC) method.

Many Body Perturbation Theory

In the MBPT methods, the correlation energy is recovered by treating the electronic correlation as a perturbation of the system. Therefore, the unperturbed hamiltonian $\hat{\mathcal{H}}_0$ is summed to a perturbation $\hat{\mathcal{H}}'$, whose strength is regulated by a parameter, λ.

$$\hat{\mathcal{H}} = \hat{\mathcal{H}}_0 + \lambda\hat{\mathcal{H}}' \tag{2.26}$$

The energy and the wave function corrections are expanded as a Taylor series of powers of λ, where the zeroth-order represents the unperturbed system, namely the HF Hamiltonian. From the second order, virtual orbitals are needed to compute the energy terms and cause the computational cost of the calculation to increase by a significant amount with respect to HF. When the unperturbed Hamiltonian is chosen to be a sum over Fock operators, it leads to Møller-Plesset (MP) perturbation theory (Møller et al., 1934). Depending on how many orders are included in the expansion, MP2, MP3, etc. methods arise. Nevertheless, their main drawback is that they are not based on the variational

principle, therefore they could return energy values that are lower than E_{exact} due to a slow convergence of the expansion.

Configuration Interaction

The CI method is based on the variational principle and its trial wave function is defined as a linear combination of several Slater determinants, each one weighted by an expansion coefficient a_i, determined by requiring the corresponding energy to be a minimum (Sherrill et al., 1999).

$$\Psi_{CI} = a_0 \Phi_{HF} + \sum_{i=1} a_i \Phi_i \tag{2.27}$$

The added determinants are defined as 'excited', because they are generated by assuming that one or more electrons are occupying virtual orbitals in reason of their excitation. The determinants are classified as singly (S), doubly (D), etc. excited, depending on how many electrons are promoted to higher energy orbitals in the added determinants. The exact wave function can be obtained by including all the determinants that can be created in equation 2.27, leading to the full CI wave function. However, the computational cost of such a calculation becomes unfeasible as soon as few electrons are present in the system, dictating the need for truncated methods (e.g., CISD, CISDT) that take into account only a fraction of the possible excited Slater determinants. Nevertheless, truncated CI methods are not size extensive.

Coupled Cluster

The CC methods add all types of corrections (S, D, T, etc.) to the HF wave function at a given order (2, 3, 4, etc.). In this case, the excited Slater determinants derive from the application of the cluster operator $\hat{\mathcal{T}}$ to the HF wave function (Bartlett et al., 2007).

$$\Psi_{CC} = e^{\hat{\mathcal{T}}} \Phi_{HF} \tag{2.28}$$

The cluster operator is expanded in $\hat{\mathcal{T}} = \sum_{i=1}^{N} \hat{\mathcal{T}}_i$ where each $\hat{\mathcal{T}}_i$ moves i electrons in higher energy orbitals. If all cluster operators are considered, the coupled cluster treatment becomes equivalent to a full CI. However, the exponential operator can be expanded in a Taylor series, enabling truncation to a desired order and rendering the calculation feasible. The most common truncation is the CCSD(T), where single and double excitations are computed with CC theory and triple excitations are treated as a perturbation to the system. A major advantage of truncated CC methods is their size extensivity.

2.2.4 Extrapolation to the CBS limit

The wave functions of CI, CC, and MP theory are based on the expansion of the N-electron wave function in terms of Slater determinants. Such expansions, usually with very slow convergence, are unable to satisfy the electronic cusp condition, rendering extremely difficult (basically impossible, except with very large one-electron basis sets) to accurately describe the Coulomb holes in the wave function. As a result, the convergence of the CI, CC, and MP2 energies toward their respective basis set limit is extremely slow.

Furthermore, GTO basis set quality also deeply affects the accuracy of the final energy of the system. To overcome such limitations, correlation consistent basis sets have been developed, enabling calculations to be conducted with improving basis set quality and allowing for the extrapolation of desired quantities to the limit of an infinite basis set, known as the CBS approximation. However, this procedure demands significant computational

resources, and calculations using QZ or 5Z quality basis sets are often prohibitively expensive. To address this challenge, several techniques have been developed in order to extrapolate results to the CBS limit (Dunning, 1989).

In the following, the three CBS extrapolation methodologies applied in this work are outlined: i) extrapolation of the desired energy based on fitting the energies computed with basis sets of increasing ζ quality; ii) application of an empirical equation based on DZ and TZ quality results; iii) calculations at the CCSD(T)-F12 level of theory.

Extrapolation with correlation consistent basis sets

Given the dependency of CCSD(T) results on the size of the basis set, Dunning correlation consistent *aug-cc-pVXZ* basis sets (where X = 2, 3, 4, 5, ... corresponds to ζ = D, T, Q, 5, ...) are employed to compute the desired property. Thus, the obtained data are plotted against $a = 1/X^3$ and the CBS limit is obtained for $a = 0$, corresponding to $X = \infty$.

This method has been applied to improve the accuracy of DFT level results in an additive ONIOM2 scheme (described in Section 2.6.4) for the computation of binding energies (Perrero et al., 2022a).

Okoshi empirical equation

A similar way to extrapolate a specific property at the CBS limit is to apply the OAN(C) extrapolation scheme (Okoshi et al., 2015). This empirical approach is based on CCSD(T)/aug-cc-pVXZ (with X = D,T) data, which makes it more competitive than the previous extrapolation scheme (where at least QZ quality data were required).

$$E_{CBS}^{OAN(C)} = \frac{3^3 E(T) - s^3 E(D)}{3^3 - s^3} \tag{2.29}$$

In this equation, the scaling factor s depends on the chosen combination of method (MP2, CCSD, or CCSD(T)) and basis set (cc-pVXZ or aug-cc-pVXZ), while E(D) and E(T) are the energies computed with the DZ and TZ quality basis sets, respectively. The accuracy of this model is comparable to those obtained with the original CBS model of Helgaker, Klopper, Koch, and Noga (HKKN), which was based on calculations performed with higher ζ quality basis sets, and failed to yield accurate results when including DZ quality data (Helgaker et al., 1997).

In this thesis, the OAN(C) equation has been integrated in an ONIOM2 scheme to improve the accuracy of DFT reaction energies (Perrero et al., 2023a). The comparison of the two outlined methodologies (extrapolation and OAN(C) scheme) revealed a comparable performance, at least for the chemical systems treated in this study. However, the advantage of the OAN(C) empirical equation lies in the requirement of only DZ and TZ quality data to determine the CBS energy. In contrast, the fitting procedure for extrapolation, which involves plotting the desired property against $1/X^3$, requires the inclusion of QZ quality data and benefits from the inclusion of the extremely expensive 5Z quality data. Therefore, it is more convenient to apply the procedure proposed by Okoshi et al. (2015), especially when dealing with extended *model* systems.

R12 and F12 methodologies

The adoption of explicitly correlated wave functions represents a significant advancement beyond the conventional approach of expanding the wave function as a linear combination of one-electron Slater determinants. The main objective is to overcome the difficulties in representing the wave function in those regions where the inter-electronic distance r_{ij}

approaches zero. This technique allows for the computation of electronic correlation energies of molecular ground and excited states close to the limit of a CBS at high levels of theory, as exemplified by the CC theory (Hättig et al., 2012). The seeds of the present-day R12 and F12 methodologies, developed at this scope, can be traced back to the development of the HF theory.

In 1929, an explicitly correlated wave function was used for the first time to compute the energy of the He atom, including the dependency on the distance between the two electrons r_{12} in the wave function (Hylleraas, 1929). A few years later, Hartree and Ingman argued that a better description of the Coulomb correlation hole could be obtained if the wave function depends on both r_{12} and r_{12}^2 (Hartree et al., 1933). The proposal of Hylleraas (1929) is at the foundation of R12 methods (Kutzelnigg, 1985), while the work of Hartree et al. (1933) contributed to the development of F12 methods (Werner et al., 2007). A key step in the growth of application of these methods has been the introduction of a complementary auxiliary basis set (CABS), which is used in the factorisation of the many-electron integrals that results from the use of explicitly correlated wave functions. This enabled the use of medium-sized standard basis sets for R12 and F12 methods without compromising the quality of the results (Valeev, 2004; Klopper et al., 2002).

In order to perform CCSD(T)-F12 calculations on both closed-shell and open-shell large systems, its linear scaling variant named domain-based local pair natural orbital (DLPNO) method is needed (Guo et al., 2018; Kumar et al., 2020). This approximation reduces the cost of electronic structure calculations by taking advantage of the locality of electronic interactions within a molecular system. The DLPNO scheme partitions the molecular system into smaller and non-overlapping domains and approximates the electronic structure of each domain using local pair natural orbitals (PNO). The PNOs are optimised to reproduce the electronic structure of the full system, while minimizing the size of the variables required for an accurate description, therefore reducing the cost of the calculation (Meyer, 1973; Ahlrichs et al., 1975). In this way, CBS limit quality energies are directly obtained without the need of further extrapolation schemes.

In this thesis, CCSD(T)-F12 and DLPNO-CCSD(T)-F12 have been employed as reference methodologies in the characterisation of processes occurring on water and olivine clusters (Perrero et al., 2023b; Perrero et al., 2024b), improving the accuracy guaranteed by the well known 'gold standard' CCSD(T)/aug-cc-pVTZ level of theory.

2.3 Density Functional Theory

In the theories explored so far, the wave function has been the pivotal element for deriving all the properties of the system under investigation. However, these methods often entail considerable computational demands due to the complexity of the wave function, which relies on $3N$ spatial variables + N spin variables, where N represents the number of electrons within the system. In pursuit of mitigating the computational costs, a distinct class of methods was developed.

2.3.1 Formalism

The following approach diverges significantly from wave function-based methods, and it relies on the electron density $\rho(r)$ as the primary quantity for deriving the properties of the system (Koch et al., 2015).

$$\rho(r) = N \int \dots \int |\psi(\mathbf{x}_1, \dots, \mathbf{x}_N)|^2 ds_1 d\mathbf{x}_2 \dots d\mathbf{x}_N \tag{2.30}$$

The electron density, consisting of the square of the wave function integrated over *N-1* electron coordinates, simply depends on three coordinates, irrespective of the number of electrons. Furthermore, $\rho(r)$ represents the probability density of locating any of the *N* electrons within the volume element dr_1, given the positions and the spins of the remaining *N-1* electrons. Notably, $\rho(r)$ is a positive definite function, encapsulating three pivotal characteristics:

1. when integrated over the entire volume, $\rho(r)$ gives the number of electrons in the system;

2. $\rho(r)$ has a cusp in correspondence of every nucleus present in the system;

3. the height of the cusp defines the nuclear charge.

The foundations of the density functional theory (DFT) were established by E. Fermi and P. Dirac three decades before the actual development of modern DFT theory. The 1927 Thomas-Fermi model was an early attempt to describe the distribution of electrons in an atom using statistical methods rather than solving the Schrödinger equation for each electron. This model approximated the many-electron problem by considering a statistical distribution of electrons (Fermi, 1927). A significant advancement in addressing the many-electron problem, arising from the electron-electron interaction term, came from the idea that the electron exchange energy for a uniform electron gas could be estimated as a function of the electron density (Dirac, 1930). These statements contributed to shifting the focus from the wave function to the electron density, which became a fundamental variable for describing the system and simplified the description of the interactions occurring in many-electron systems.

Modern DFT was formulated for the first time in 1964 by P. Hohemberg and W. Kohn and was based on two fundamental theorems, called Hohemberg-Kohn (HK) theorems (Hohenberg et al., 1964). The first HK theorem states that: *'The external potential V_{ext} is a unique functional of $\rho(r)$ and, given that V_{ext} specifies a Hamiltonian, it follows that the ground state wave function is a unique functional of $\rho(r)$.'*

In the DFT formalism, the electron-nucleus attraction term V_{Ne} of equation 2.6 is defined as external potential V_{ext}. This classification stems from the fact that it represents an interaction that does not originate directly from the electron density. Consequently, in accordance with the first theorem, it becomes evident that the energy of the system can be expressed as a functional of the electron density, denoted $E[\rho]$. The second HK theorem establishes a variational principle in the context of DFT and states that: *'Given an external potential, the ground state energy E_0 can be found by minimizing the functional $E[\rho]$ with possible trial densities that satisfy the boundary conditions and that the electron density that minimizes the functional is the ground state electron density $\rho_0(r)$'.*

As a direct consequence of these theorems, it follows naturally that every energetic term within the Hamiltonian can be expressed as a functional of the electron density.

$$E_0 = \min_{\rho \to N, V_{ext}} E[\rho] \tag{2.31}$$

where $E[\rho] = V_{ext}[\rho] + T_e[\rho] + V_{ee}[\rho]$. The sum $T_e[\rho] + V_{ee}[\rho]$ constitutes $F_{HK}[\rho]$, which is the universal Hohemberg-Kohn functional, whereas the $V_{ext}[\rho]$ term depends on the system under study and can be written as:

$$V_{ext}[\rho] = \int \rho(\mathbf{r}) V_{ext}(\mathbf{r}) dr \tag{2.32}$$

In principle, knowing the explicit expression for every term of the energy functional would solve exactly the electronic Schrödinger equation 2.9. However, the exact form of $F_{HK}[\rho]$ is unknown, and the elusive part can be isolated from the rest of the terms. The $V_{ee}[\rho]$ can be split in a classical electrostatic term $J[\rho]$ and a non-classical term $E_{ncl}[\rho]$, which contains all the unknown operators.

$$V_{ee}[\rho] = J[\rho] + E_{ncl}[\rho] = \int \frac{\rho(\mathbf{r}_1)\rho(\mathbf{r}_2)}{|\mathbf{r}_{12}|} d\mathbf{r}_1 d\mathbf{r}_2 + E_{ncl}[\rho] \tag{2.33}$$

Ultimately, the energy functional can be rewritten as:

$$E[\rho] = \int \rho(\mathbf{r}) V_{ext}(\mathbf{r}) dr + \int \frac{\rho(\mathbf{r}_1)\rho(\mathbf{r}_2)}{|\mathbf{r}_{12}|} d\mathbf{r}_1 d\mathbf{r}_2 + E_{ncl}[\rho] + T_e[\rho] \tag{2.34}$$

A substantial advance in the resolution of the hitherto unresolved issue of the unknown functional was achieved in 1965 with the work of W. Kohn and L.J. Sham, which provided the foundation for the implementation of DFT (Kohn et al., 1965).

The Kohn-Sham (KS) formalism is based on a non-interacting reference system of electrons similarly to the HF method. In this framework, a single Slater determinant is constructed using the Kohn-Sham MOs, denoted ϕ^{KS}, which closely resembles the conventional MOs, but possesses the additional characteristic of being subjected to an external potential (V_{ext}). This potential is built such that the ground state electron density matches that of the interacting system. This assumption is of particular significance as it allows for the explicit expression of the quantum kinetic energy functional ($T_e[\rho]$) as the sum of the exact kinetic energy of the non-interacting reference system ($T_S[\rho]$) plus an unknown term ($\Delta T_e[\rho]$). The latter quantity accounts for the difference between the kinetic energy of the real interacting system and that of the non-interacting one.

$$T_e[\rho] = T_S[\rho] + \Delta T_e[\rho] = -\frac{1}{2}\sum_{i=1}^{N}\int \phi_i^{KS}(\mathbf{r})\nabla^2\phi_i^{KS}(\mathbf{r})d\mathbf{r} + \Delta T_e[\rho] \tag{2.35}$$

A further step consisted in grouping the terms $\Delta T_e[\rho]$ and $E_{ncl}[\rho]$ as the exchange correlation (XC) functional $E_{XC}[\rho]$. However, the mathematical expression of this functional remains unknown. Consequently, the development of DFT methods is devoted to identifying the most suitable form of this functional, through various approximations. In principle, as for the HF method, the Kohn-Sham MOs can be introduced in equation 2.31 and the minimisation of the functional yields the KS equations, which are pseudo-*eigenvalue* equations containing the KS operator, $\hat{f}^{KS}$.

$$\hat{f}^{KS}\phi_i^{KS} = \epsilon_i\phi_i^{KS} \tag{2.36}$$

When the LCAO approximation is introduced, this problem can be transformed into a linear one, in the same manner as for the HF theory.

$$\mathbf{fC} = \mathbf{SCE} \tag{2.37}$$

Where $\mathbf{f} = f_{ij} = \langle\phi_i^{KS}|\hat{f}^{KS}|\phi_j^{KS}\rangle$ are the KS matrix elements. The HF and DFT methods have similar SCF procedures and, as a result, comparable computational costs. However, the primary distinction between them resides in their underlying principles. The HF theory employs the exact Hamiltonian operator and approximates the wave function. In contrast, the DFT is an exact reformulation of the quantum mechanics based on the electronic density, in which the approximation arises from the mathematical form of the XC

functional. It follows that it is much more straightforward to improve the description of the wave function than to rectify the inaccuracies of the Hamiltonian.

In light of these considerations, may DFT be defined as an *ab initio* theory? If one considers the theoretical background, the answer is affirmative. Nevertheless, some approximations of the XC functional include parameters that have been estimated by fitting against experimental data. It can thus be concluded that not all DFT functionals are truly *ab initio*.

2.3.2   Classification of DFT functionals

The approximations of the XC functional developed over the years have led to the creation of numerous distinct functionals. For the sake of simplicity, all the functionals are categorized into different families based on the approximations underlying their forms. J. Perdew introduced such a classification, defining the 'Jacob's ladder' of DFT methods (Perdew et al., 2001; Perdew et al., 2005). This metaphorical progression, ranging from the 'Hell' of the Hartree-Fock (HF) theory to the 'Heaven' of the exact solution of the Schrödinger equation, encompasses five distinct rungs, each gathering DFT functionals according to their level of approximation. As one ascends the ladder, both the accuracy and computational cost of the functionals tend to increase.

- I rung. **Local Density Approximation (LDA)**. This approximation originates from the Thomas-Fermi model. It is based on the assumption that electrons behave like a homogeneous electron gas and therefore the electron density is a slowly varying function. LDA functionals can be employed to treat metal systems, but they are not suitable to describe other chemical systems.

- II and III rung. **Generalized Gradient Approximation (GGA) and meta-GGA**. These two families of functionals account for the non-homogeneity of the electron density, introducing a dependency of the energy from the gradient of the density $\nabla\rho$ (GGA) or $\nabla^2\rho$ (meta-GGA). For this reason, these methods are also called semi-local functionals. They yield good geometries and acceptable frequencies for the majority of the systems.

- IV rung. **Hybrid Methods (hyper-GGA)**. These functionals incorporate a portion of exact exchange (computed via HF or derivatives), depending on their mathematical formulation. Global hybrids maintain a constant amount of exact exchange across all positions **r**; local hybrids incorporate a position dependent exact exchange; range-separated hybrids separate the electron-electron repulsion operator $1/\mathbf{r}_{12}$ in a short-range and a long-range term, to which distinct exact exchange contributions are assigned. These functionals are probably the best compromise between cost and accuracy for small- to medium-sized systems.

- V rung. **Double-Hybrid Methods (DH)**. In addition to the exact exchange, a treatment of non-local orbital correlation energy at MP2 level of theory is also included. Double-hybrids functionals are fully non-local due to the contributions from HF theory. Their performance is very close to that of couple cluster theory, but at a feasible computational cost. Recently, the development of a DLPNO-MP2 scheme has significantly enhanced their computational efficiency, enabling their use with both small and medium-sized systems (Neugebauer et al., 2023).

The main limitation of DFT methods is that although a progression of functionals going from LDA, to GGA and hyper-GGA provides successively lower errors for a specific reference dataset, this trend may not transfer universally to other properties or systems.

Consequently, the reliability of the results can only be determined by comparison with experimental data or high quality wave function-based results.

In order to facilitate the selection of the most appropriate methodology for a given chemical system, reviews such as those by Mardirossian et al. (2017) and Bursch et al. (2022) offer valuable guidance to the readers.

2.3.3 Challenging cases for DFT

DFT methods are widely adopted because of their outstanding cost/accuracy ratio. They provide high quality geometries and vibrational frequencies, good dipole moments, thermochemistry and reaction barriers, and they introduce electron correlation effects (improving the description of intermolecular interactions such as the hydrogen bond) at a cheaper cost than wave function-based methods. However, DFT methods show some difficulties in describing properly phenomena such as charge transfer processes, open-shell systems, and weak interactions.

The strength of charge transfer interactions is usually overestimated by DFT methods. Conversely, HF underestimates this type of interaction, reason why the inclusion of a fraction of exact exchange in the functional mitigates the problem, although it does not solve it. A more detailed discussion is dedicated to weak interactions and open-shell systems, which are largely present in this work.

Open-shell systems and the broken (spin) symmetry approach

Radicals, also defined as open-shell systems, are chemical species with one or more unpaired electrons, each with an electronic spin quantum number $S = 1/2$. The electronic spin multiplicity is defined as *2S + 1* and systems with a multiplicity equal to 1, 2, 3, etc., are defined as singlet, doublet, triplet, etc., respectively. Tipically, open-shell systems have a multi-reference character which is not well represented by the single determinant DFT approach, which additionally suffers from an incomplete cancellation of the self-interaction term.

Consequently, radicals are treated with an unrestricted formalism, that consists in using different molecular orbitals for the α and β electrons, in contrast to what is done in the restricted open-shell formalism (Pople et al., 1954). This approach is still based on a single determinant. Furthermore, the wave function resulting from the unrestricted formalism is not an *eigenvector* of the total spin operator $\hat{S}^2$, because it does not describe pure electronic spin states. Such characteristics introduce spin contamination of the ground state by higher (excited) electronic spin states. The *eigenvalue* $< \hat{S}^2 >$ is used as a quality indicator of the unrestricted approach, in that when a little deviation from the theoretical value is observed, the formalism appears suitable to describe open-shell systems. In contrast, a large deviation indicates that single-reference methods are not appropriate to treat the radicals.

A particular case of open-shell systems in which a specific approach has been developed to perform calculations are diradicals. As the name suggests, diradicals are species in which there are two unpaired electrons occupying different spin orbitals. Depending on their spin, $\alpha\alpha$ or $\alpha\beta$, their multiplicity can be triplet or open-shell singlet, respectively. An example of the latter are systems in which two doublets closely interact. Furthermore, the unpaired electrons often occupy two spin-orbitals close in energy, therefore a single Slater determinant is not suitable to treat them. Multi-reference methods like MRCI and MCSCF would be the proper choice to describe these systems and recover the static correlation; however, they are often not computationally feasible.

A cost effective strategy, based on a single Slater determinant, offers a solution to such limitation. The broken (spin) symmetry (BS) approach is based on mixing up localized spin orbitals, resulting from the linear combination of the single occupied molecular orbitals, in order to recover a CI-like behaviour from a single determinant wave function (Noodleman, 1981; Neese, 2004; Neese, 2009). The resulting guess wave function possesses the correct shape but an incorrect spin distribution, which is equal to zero due to the sum of a positive and a negative region, instead of being zero in every point of the space.

The expression of the BS wave function includes contributions from the triplet spin state alongside ionic and neutral components originating from the closed-shell singlet solution. The relative weights of the ionic and triplet components are determined by applying the variational principle to the guess wave function, while the contribution of the neutral component remains fixed, constituting the major difference from a CI-like approach. The use of the broken symmetry approach enables the precise characterisation of open-shell singlet states under the DFT and HF frameworks, thus allowing the modelling of these complex systems at a reasonable computational cost.

Description of dispersion interactions

Dispersion interactions are non-covalent interactions which are usually weaker than electrostatic and hydrogen bond interactions. However, since they are very common in chemical systems and their strength grows with the system size, they play a crucial role in the structure, the stability, and the properties of the materials (Stöhr et al., 2019). These interactions have a quantum mechanical origin, residing in the interaction between induced multipole moments on different atoms. The probability of an atom forming or inducing a multipole moment depends on its polarisability. Unfortunately, DFT lacks a proper description of such interactions, because dispersion forces are accounted for by the long-range electronic correlation energy of a system, which is usually included in post-HF methods. Different strategies have been developed over the years in order to recover their description, among which the most popular ones are presented.

Atom pair-wise additive schemes. Common approaches use atom pair-wise additive schemes, such as the dispersion correction models proposed by Grimme (from D to D4, Grimme, 2004; Grimme, 2006; Grimme et al., 2010; Grimme et al., 2011; Caldeweyher et al., 2019). They are *a posteriori* corrections consisting of a semi-empirical term (E_{disp}) added to the DFT energy.

$$E = E_{DFT} + E_{disp} \tag{2.38}$$

Here, E_{disp} is composed of a two-body and a three-body interaction terms.

$$E_{disp} = -\sum_{AB}\sum_{n=6,8} s_n \frac{C_n^{AB}}{R^n} f_{damp}(R_{AB}) + \sum_{ABC} E^{ABC} f_{damp}(R_{ABC}) \tag{2.39}$$

In equation 2.39, C_n^{AB} is an averaged isotropic dispersion coefficient of order n for the atom pair AB, which depends on atomic polarisabilities, s_n is a functional dependent scaling factor, and f_{damp} is a damping function used to determine where to apply dispersion corrections in order to avoid near singularity errors at short internuclear distances R_{AB}. The three-body term E^{ABC} (in equation 2.40) includes the so called triple-dipole or Axilord-Teller-Muto (ATM) term, where θ_a, θ_b, and θ_c are the internal angles of the triangle formed by R_{AB}, R_{BC}, and R_{CA}, respectively, and C_9^{ABC} is the triple-dipole constant, approximated

as $C_9^{ABC} \simeq -\sqrt{C_6^{AB} C_6^{AC} C_6^{BC}}$. Finally, R_{ABC} is the geometrical average of the distances between the three atoms A, B, and C.

$$E_{ABC} = \frac{C_9^{ABC}(3\cos\theta_a \cos\theta_b \cos\theta_c + 1)}{(R_{AB} R_{BC} R_{CA})^3} \tag{2.40}$$

In the latest D4 dispersion scheme, a dependency upon atomic partial charges calculated on the fly has been introduced in order to scale the polarisabilities for the effect of the atomic environment (Caldeweyher et al., 2019). Thanks to such implementation, E_{disp} comes practically at no cost and for this reason, this kind of dispersion is widely employed in QM calculations. However, atom pair-wise additive schemes suffer from the limitation of not being self-consistent, and thus are unable to correct the MOs or any computed property besides the energies.

van der Waals Density Functional methods. An alternative approach to include the description of dispersion interactions is through the van der Waals Density Functional (vdW-DF) method, which employs the same electron density to incorporate dispersion effects (Lee et al., 2010). The Vydrov-Van Voohris (VV) correlation functional (Vydrov et al., 2009; Vydrov et al., 2012) appears to be one of the most promising candidates for a general and accurate electronic structure method. This kind of approach adds a non-local, electron density-dependent functional term $E_C^{VV10}[\rho]$ to the DFT exchange and correlation functionals selected to treat the system.

$$E_{XC}[\rho] = E_X[\rho] + E_C[\rho] + E_C^{VV10}[\rho] \tag{2.41}$$

Here, the dispersion correlation functional is calculated self-consistently, at a higher cost than atom pair-wise approaches, and has to be preferred when dealing with metallic systems or chemical processes in which the basic electronic structure changes significantly (e.g., oxidations and ionisations).

Many body dispersion correction. Finally, the many body dispersion (MBD) correction builds upon the Tkatchenko-Scheffler dispersion correction energy (Tkatchenko et al., 2009), by approximating the dynamic response of a system by that of a dipole-coupled quantum harmonic oscillator, each of which representing a fragment of the system under study (Tkatchenko et al., 2012). This approach offers a more rigorous and less empirical treatment of dispersion effects, albeit at a higher computational cost compared to the methods previously outlined. Nevertheless, the MBD correction has not been applied in the present work.

2.4   Molecular Mechanics and QM/MM approaches

A much faster strategy for computing the energy and the geometry of a chemical system, with a substantially reduced computational cost, is through molecular mechanics (MM) methods. Unlike traditional methods that solve the Schrödinger equation, MM methods simplify molecules as assemblies of atoms held together by bonds (Dinur et al., 1991).

In MM, each atom is represented as an 'atom type', analogous to the concept of 'functional group' used in organic chemistry, which identifies structurally similar portions of different molecules. Basis sets are thereby replaced by atom types, which are defined by the atomic number and the type of chemical bond they participate in. Consequently, the total energy of the system is computed as a sum of terms, each describing the energy required to distort a molecule in a specific manner.

$$E_{MM} = E_{str} + E_{bend} + E_{tors} + E_{vdw} + E_{el} + E_{cross} \qquad (2.42)$$

The first three terms describe covalent interactions: E_{str} is the energy function for stretching a bond between two atoms, E_{bend} represents the energy required for bending two adjacent bonds, and E_{tors} is the energy needed for rotating around a bond. The non covalent interaction terms include the van der Waals E_{vdw} and the electrostatic interactions E_{el}, while E_{cross} accounts for the coupling between the first three terms. The expression is a parametric function of the coordinates of the nuclei. Thus, different sets of parameters define distinct force fields (FFs), that are parameterized against datasets obtained from experiments or high-level *ab initio* theory calculations.

FFs can be tailored to describe specific classes of molecules, e.g., GAFF for organic compounds (Wang et al., 2004) and AMBER for biomolecular systems (Salomon-Ferrer et al., 2013), or designed for universal use, such as UFF (Rappe et al., 1992). In the last years, a new universal force field, representing a great improvement over UFF, was developed. The performance of GFN-FF stands out for the modelling and design of materials, organometallic, and biochemical systems (Spicher et al., 2020). Additionally, its application was also extended to periodic systems (Gale et al., 2021).

The primary advantage of these methods is their capability to simulate systems with thousands of atoms using modest computational resources. They are particularly useful for predicting geometries and relative energies of structures, as well as for studying structural changes such as interconversion barriers between different conformers.

However, these methods are not suitable for simulating reactivity, as they do not explicitly consider electrons. To address this limitation, techniques have been developed to model transition states, such as *ad hoc* modifications of the force field to represent the transition state as a minimum energy structure (Eksterowicz et al., 1993) or based on the intersection of reactant and product potential energy surfaces (Jensen, 1994). More recently, several reactive force fields (ReaxFF) have been developed to address the reactivity of various chemical systems and processes, such as combustion and solvation. The first ReaxFF to be developed was specific for hydrocarbons reactions (van Duin et al., 2001).

Nevertheless, FFs have an intrinsic limitation in treating processes dominated by extensive electrons rearrangement. A gentle solution to overcome this problem without overlooking on the advantages offered by FFs is to adopt an hybrid QM/MM approach, in which the system is divided in two regions, one accurately described at a QM theory level and the other treated at an MM theory level, resulting in the total energy of the system being a combination of both parts. Field et al. (1990) were the first proposing a combined QM and MM potential for the study of reactions in the condensed phase. Successively, Maseras et al. (1995) developed the IMOMM scheme, an integrated '*ab initio* + molecular mechanics' geometry optimisation scheme, that led to the development of the ONIOM approach, whose acronym stands for 'Our own N-layered Integrated molecular Orbital and Molecular mechanics'. This scheme enables the definition of multiple layers in the chemical system, each treated at a different level of theory (Svensson et al., 1996).

2.5 The potential energy surface

Solving equation 2.9 yields the potential energy surface (PES), a hyperspace of *3N* dimensions, where *N* represents the number of degrees of freedom within the system (see Figure 2.1). The PES establishes a relation between the energy of the system and its corresponding geometry, given by the atomic coordinates. Within this surface, stationary points, namely,
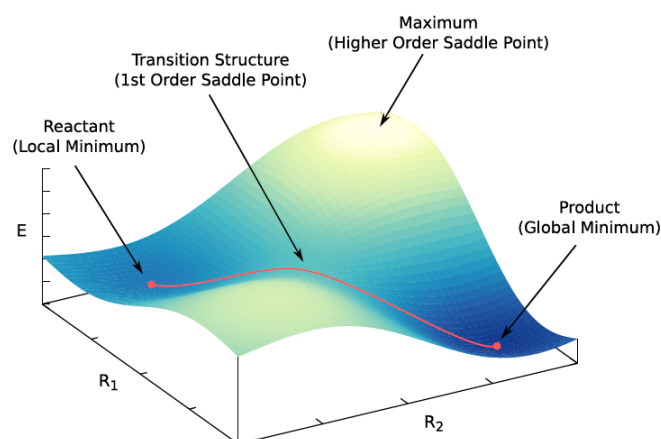
Figure 2.1: Example of a potential energy surface (PES) for a hypothetical system, defined by two coordinates, R_1 and R_2. The minima of the PES represent stable states of the system, such as reactants or products. The latter are connected by paths (in red) along which reactions occur. The maximum along such a path is referred to as a transition state structure. Figure from Keith et al. (2021).

points that are invariant with time, are special positions where the first derivative of the energy with respect to the atomic coordinates equals zero. Such points can be identified by performing geometry optimisation calculations, choosing one of the many algorithms available nowadays, grouped in three main categories.

2.5.1 Characterisation of stationary points

The steepest descent (SD) method is the simplest approach for optimising the geometry of a chemical system. The energy of the system is lowered by performing a step in the opposite direction to that of the largest gradient, $\mathbf{d} = -\mathbf{g}$. This method consistently decreases the energy function value and ensures progression toward a minimum. However, each step is taken perpendicularly to the previous one, causing the algorithm to oscillate around the minimum without actually reaching it. SD is typically used in initial optimisation stages or when other algorithms fail to converge to a minimum.

The conjugate gradient (CG) method represents an enhancement of the SD. Unlike SD, CG takes steps on the potential energy surface (PES) in the direction determined by a combination of the current negative gradient and all the previous search directions. Consequently, the first optimisation step is an SD step. CG methods are generally more robust than SD and require slightly more memory. Both SD and CG methods are limited to locating minima on the PES.

In contrast, Newton-Raphson (NR) methods adopt a different approach to handle the PES, enabling them to locate both the minima and the saddle points. NR methods are based on a second order Taylor expansion around a specific point $\mathbf{x}_0$.

$$E(\mathbf{x}) = E(\mathbf{x}_0) + \mathbf{g}^t(\mathbf{x} - \mathbf{x}_0) + \frac{1}{2}(\mathbf{x} - \mathbf{x}_0)^t \mathbf{H}(\mathbf{x}_0)(\mathbf{x} - \mathbf{x}_0) \tag{2.43}$$

Where $\mathbf{g}$ is the gradient and $\mathbf{H}$ is the Hessian matrix. Requiring the gradient to be zero in equation 2.43, the step to be performed on the PES can be calculated as:

$$(\mathbf{x} - \mathbf{x}_0) = -\mathbf{H}^{-1}\mathbf{g} \qquad (2.44)$$

In proximity of a minimum, all the *eigenvalues* of the Hessian matrix are positive by definition, and the step is taken in the direction opposite to the gradient. However, if one *eigenvalue* is negative, the step will be taken in the direction of the gradient. This potentially increases the energy and leads the system to a first-order saddle point, where all the Hessian *eigenvalues* are positive, except for the first. Overall, Newton-Raphson convergence occurs toward the nearest stationary point, whether it is a minimum or a first-order saddle point. Therefore, providing an accurate initial geometry guess is crucial for effective convergence.

NR methods offer numerous advantages but also come with some drawbacks. Issues may arise in flat regions of the PES where the Hessian *eigenvalues* are close to zero. In such cases, the step size tends toward infinity due to the inversion of the Hessian matrix. To address this problem, a step control procedure is employed, limiting the step to the trust radius, which is the region where the Taylor expansion remains valid. This limitation is achieved through a shift parameter, denoted as λ, which can also be utilized to determine whether the algorithm should seek a minimum or a first-order saddle point. These modified methods are commonly referred to as level-shifted Newton-Raphson algorithms.

The second problem within NR methods is that they require the calculation of the entire Hessian matrix at every step, which poses a significant computational burden. However, an initial guess can be made by assuming the Hessian matrix to be a unit matrix in the first step, and updating it at each subsequent step using the information gathered from the calculation of the gradients. An example of such an updating scheme is the Broyden-Fletcher-Goldfarb-Shanno (BFGS) algorithm, which is also available in a low-memory version known as L-BFGS. In this variant, only the last n gradients are considered to update the Hessian matrix. When these updating schemes are used, the methods are referred to as pseudo-Newton-Raphson or variable metric. Although they may require more steps to converge to a stationary point, the computational speed-up gained from not having to calculate the entire Hessian matrix compensates for this drawback.

The final issue pertains to the diagonalisation of the Hessian matrix, which is even more computationally demanding than the calculation of the matrix itself. In large systems, many off-diagonal elements are nearly zero, resulting in the Hessian matrix being a *sparse matrix*. Newton-Raphson (NR) methods can exploit this characteristic by neglecting off-diagonal blocks. For instance, a 300x300 matrix can be reduced to a hundred 3x3 matrices, significantly reducing the cost of inversion. These methods are known as truncated Newton-Raphson methods.

The methods outlined above are effective in locating stationary points on the PES, that are typically local minima located in the surroundings of the initial geometry. However, as the number of variables increases, the proliferation of local minima poses a challenge, making the task of finding a global minimum a combinatorial explosion problem. To address this issue, various conformational sampling techniques are employed, including Monte Carlo methods, molecular dynamics, and meta-dynamics. Often, these calculations require the use of MM or semi-empirical methods due to their computational burden.

Meta-dynamics emerged as a promising tool for exploring the PES. By adding a history-dependent bias potential to the original potential energy landscape of the system, meta-dynamics counteract free energy barriers, allowing the system to escape local minima and

explore new regions of the PES, thereby identifying additional stationary points. One notable advancement in this field is the developement of the Conformer-Rotamer Ensemble Sampling Tool (CREST), a meta-dynamics-driven search algorithm (Pracht et al., 2020). CREST facilitates the exploration of the molecular conformational space and supports tasks such as structure prediction, ligand-binding studies, and reaction pathway exploration in computational chemistry.

When a stationary point is identified on the PES, its internal energy is given by the electronic energy computed through a geometry optimisation, to which the zero-point energy (ZPE) is added. The latter term acknowledges the residual vibrational kinetic energy retained by atoms and molecules even at absolute zero temperature, treated with the harmonic oscillator approximation. The mass-weighted Hessian matrix is diagonalized to determine its *eigenvalues*, which correspond to harmonic vibrational frequencies, and its *eigenvectors*, representing vibrational modes.

In a system consisting of M nuclei, there are a total of $3M$ degrees of freedom. Among these, three coordinates describe the translation of the molecule, and three (two for a linear molecule) account for the rotation along the x, y, and z axes. Consequently, $3M - 6(5)$ coordinates remain to describe the internal motion of the nuclei, resulting in their vibrational modes. The ZPE is given by the sum of the energies of each fundamental vibrational mode of the chemical system, according to the equation:

$$ZPE = \frac{1}{2}h\left(\sum_i^{3M-6(5)} \nu_i\right) \tag{2.45}$$

where ν_i is the fundamental vibrational frequency at which the system oscillates.

2.5.2 Characterisation of transition states

First-order saddle points generally correspond to transient structures between two minima. In the context of chemical reactivity, the two minima represent the reactant and the product, while the saddle point is defined as the transition state (TS). There is no universal method guaranteed to locate a TS (e.g., Henkelman et al., 2002). Rather, two main strategies are commonly employed.

The first strategy consists in the distinguished reaction coordinate (DRC) procedure, which involves performing a scan calculation along the internal coordinate that governs the reaction. The highest energy structure obtained from the DRC pseudo-PES is successively optimised to localize the actual TS structure (Rothman et al., 1980). This strategy is effective for investigating simple reaction profiles and conformational barriers, especially when the internal coordinate along which the scan is performed can be manually defined. The DRC method was largely used for transition-state structure searching in periodic calculations when alternative techniques were not providing satisfying results. However, not every system was well behaved when undergoing such calculations (Williams et al., 1982).

However, the characterisation of complex reaction steps requires alternative strategies. These include: i) methods that propagate the geometry of a unique structure by using the information regarding the wave function and its derivatives at the specific point that it occupies on the PES. This approach does not require prior knowledge of reactants and products and is suitable for an unbiased exploration of the PES. However, these methods are often computationally expensive (e.g., Henkelman et al., 2001); ii) algorithms that search for the minimum energy path (MEP) connecting a reactant and a product. Several methods based on the interpolation between reactant and product geometries exist. Their objective is not to find the exact TS, but rather to locate a region around it. The TS structure

can be successively identified with a dedicated optimisation (Jónsson et al., 1998).

In this work, the Nudged Elastic Band (NEB) method, which pertains to the second group, was employed. The NEB algorithm searches for the MEP connecting given reactant and product minima on the PES, with the aim of locating the highest energy region, in which a first-order saddle point may be present. Initially, a path is generated, represented by a discrete set of configurations of the atoms, known as images of the system. The number of images is specified by the user and must be sufficiently large to ensure an adequate resolution of the path (Jónsson et al., 1998). Rigorous convergence to a first-order saddle point can be obtained with the climbing image NEB (CI-NEB), where the highest energy image is pushed uphill in energy along the tangent to the path while relaxing downhill in orthogonal directions (Henkelman et al., 2000).

An effective strategy for the identification of first-order saddle points consists in the NEB-TS, which performs a CI-NEB calculation with a loose tolerance on the optimisation thresholds, and successively conducts a TS optimisation adopting the highest energy image as initial guess structure (Ásgeirsson et al., 2021). This combined approach is particularly suitable for complex reactions where it would be impractical to manually define the reaction coordinate and where 2D relaxed surface scans are required to obtain an accurate initial guess structure for the TS.

Once a TS has been located, it is essential to verify whether it is a true first-order saddle point, connecting the desired minima. To this purpose, the mass-weighted second derivatives of the energy with respect to the degrees of freedom of the system have to be computed, obtaining the vibrational modes of the system under exam. The transition state is characterized by one imaginary mode, which represents the motion of atoms involved in the chemical process. Although this calculation confirms that the structure is a TS, it does not guarantee that it is precisely the one sought after. This uncertainty is solved by the Intrinsic Reaction Coordinate (IRC). It is a particular form of MEP located in the mass-weighted coordinates space, able to connect a TS to the respective reactants and products (Ishida et al., 1977). The IRC path is defined by a differential equation.

$$\frac{d\mathbf{x}(s)}{ds} = -\frac{\mathbf{g}}{|\mathbf{g}|} = \mathbf{t} \tag{2.46}$$

Where $\mathbf{x}(s)$ are the mass-weighted coordinates, s is the path length and $\mathbf{t}$ is the tangent to the reaction path, defined by the normalized gradient. Determining the IRC requires solving equation 2.46 starting from a geometry slightly displaced from that of the TS along the normal coordinate for the imaginary vibrational mode. Once it has been identified the reaction coordinate, which is the *eigenvector* corresponding to the imaginary mode of the TS, two geometry optimisations are performed, one increasing and the other decreasing the reaction coordinate. These two calculations return the geometries of the reactant and the product connected by the TS under investigation.

2.5.3   Rate constant calculation

The rate constant of a reaction is a macroscopic property that can be extracted from a microscopic system such as those simulated with computational chemistry. The link between the microscopic and the macroscopic worlds is represented by partition functions, which form the foundation of statistical mechanics. The partition function for a single species is denoted q and is defined as a sum over all possible ε_i energy states that a system can

assume.

$$q = \sum_i e^{\varepsilon_i/k_B T} \tag{2.47}$$

For a system composed of N molecules, the partition function becomes $Q = q^N$. Once the partition function of a system is known, thermodynamic functions such as the internal energy U, the enthalpy H, and the entropy S can be defined. A function of particular interest is the Gibbs energy, G:

$$G = H - TS = k_B T V \left(\frac{\partial lnQ}{\partial V}\right)_T - k_B T lnQ \tag{2.48}$$

where k_B is the Boltzmann constant and V is the volume. The Gibbs energy enters in the Eyring equation, which is used to compute the rate constant of a unimolecular chemical reaction.

$$k(T) = \kappa \frac{k_B T}{h} e^{\frac{-\Delta G^\ddagger}{RT}} \tag{2.49}$$

In this equation, κ is the transmission coefficient (which is equal to 1 when tunnelling effects are not operative), T is the temperature, h is the Planck constant, $\Delta G^\ddagger$ is the Gibbs energy barrier between the TS and the reactant (computed at a given temperature) and R is the gas constant. This equation is valid only for unimolecular reactions and assumes that all the molecules crossing the barrier proceed directly to the product, without the possibility of returning to the reactant.

This equation is derived from the transition state theory (TST), which postulates that a reaction progresses from one energy minimum to another by passing through a saddle point on the PES, corresponding to the TS (Eyring, 1935). The TST assumes an equilibrium energy distribution among the possible quantum states of the system along the reaction coordinate. This means that the probability of finding a system in a given quantum state is determined by the Boltzmann distribution.

Once the unimolecular rate constant is obtained, the half-life time of the reactant can be computed with the equation $t_{1/2}(T) = ln(2)/k(T)$. The $t_{1/2}$ is the time required for the reactant to be half-consumed and provides insights on the timescales of the reaction. In astrochemistry, this is crucial for determining the feasibility of a process during the distinct evolutionary phases of the formation of a planetary system.

A microcanonical TST formulated in terms of total energy is known as the RRKM theory, named after Rice, Ramsperger, Kassel and Marcus (Rice et al., 1927; Kassel, 1928; Marcus, 1952). It has been developed for unimolecular reactions, holding onto the same premises as the Eyring's TST, assuming additionally that the energy within a molecule is distributed among its various vibrational and rotational modes according to the principles of statistical mechanics. The reaction rate is determined by the probability that a species with a given amount of energy will overcome the activation barrier and form a product, so that an energy dependent reaction rate, $k(E)$, is obtained.

$$k(E) = \frac{N_{TS}(E - E_0)}{h\rho(E)} \tag{2.50}$$

The rate constant is derived from the density of states of the reactant $\rho(E)$ and the transition state $N_{TS}(E - E_0)$, where E_0 represents the energy barrier. The latter term can be expressed as an integral of the density of states over the translational energy of the reaction coordinate. It is also possible to include tunnelling effects by introducing the energy dependent transmission probability in the formulation of $k(E)$. Finally, the conversion of

the energy-dependent rate constant $k(E)$ into a temperature-dependent rate constant $k(T)$ involves a convolution, that is the integration of $k(E)$ over the energy, weighted by the Boltzmann distribution $P(E)$.

$$k(T) = \int_{E_0}^{\infty} k(E) \times P(E) dE \tag{2.51}$$

where $P(E) = g(E) \exp(-E/k_B T)/Q(T)$, with $g(E)$ being the degeneracy of each energy level and $Q(T)$ the partition function.

2.6 Solid state systems modelling

Solid systems exist in either amorphous or crystalline forms. Both can be modelled using either a cluster or a periodic approach (Rimola et al., 2021), although it is often more convenient to use the cluster approach to model amorphous systems and the periodic approach to simulate crystalline structures.

2.6.1 Cluster approach

A straightforward method for modelling a crystal structure is to extract a small portion from its periodic structure, thereby ensuring that the resulting cluster retains the properties of the entire crystal. The properties of the system should converge toward those of the crystal as the size of the cluster increases. Another approach involves building the cluster through the addition of single molecules, which is more suitable for modelling amorphous materials or molecular crystals (e.g., Sauer et al., 1994; Germain et al., 2022).

An undeniable advantage of the cluster approach is its compatibility with any molecular code, which enables the performance of calculations at high theoretical levels. However, this approach has also a few drawbacks, including the limited size of the models, the high surface-to-volume ratio, and the undesired edge effects, which can lead to excessively flexible systems. One partial solution is to increase the cluster size at the expenses of the computational cost. Alternatively, the coordinates of the atoms located at the edges can be fixed during geometry optimisations in order to reproduce the crystal rigidity. Furthermore, the ONIOM approach is particularly suitable for treating large clusters at different theory levels, allowing for the description of a specific region at a high computational level, such as post-HF methods that require a significant amount of computing power (Svensson et al., 1996).

In this work, the molecular codes ORCA 5.0.3 (Neese, 2022) and GAUSSIAN16 (Frisch et al., 2016) were adopted to simulate adsorption and reactivity on water (Perrero et al., 2022b; Perrero et al., 2024b) and olivine clusters (Perrero et al., 2023b). The two codes offer the flexibility to perform calculations ranging from MM to DFT and post-HF. The major difference between the two codes lies in their scalability. Gaussian is distributed under a payment fee license and scales well over a few dozen CPUs but does not support multinode configurations, whereas ORCA, as an open source software, supports multi-node configurations, scaling effectively over several dozen CPUs.

The cluster models adopted in this thesis include two clusters of 18 and 33 water molecules (see top panel of Figure 2.2), which simulate the amorphous solid water (ASW) ice coating interstellar grains. The 18-H_2O cluster represents a compact, flat water ice surface, while the 33-H_2O cluster features a cavity structure of approximately 6 Å in diameter. Additionally, a set of olivine clusters of composition $Mg_{(4-x)}Fe_xSi_2O_8$ (with x = 0−1)

W18 W33

Cluster O Cluster A Cluster B Cluster C
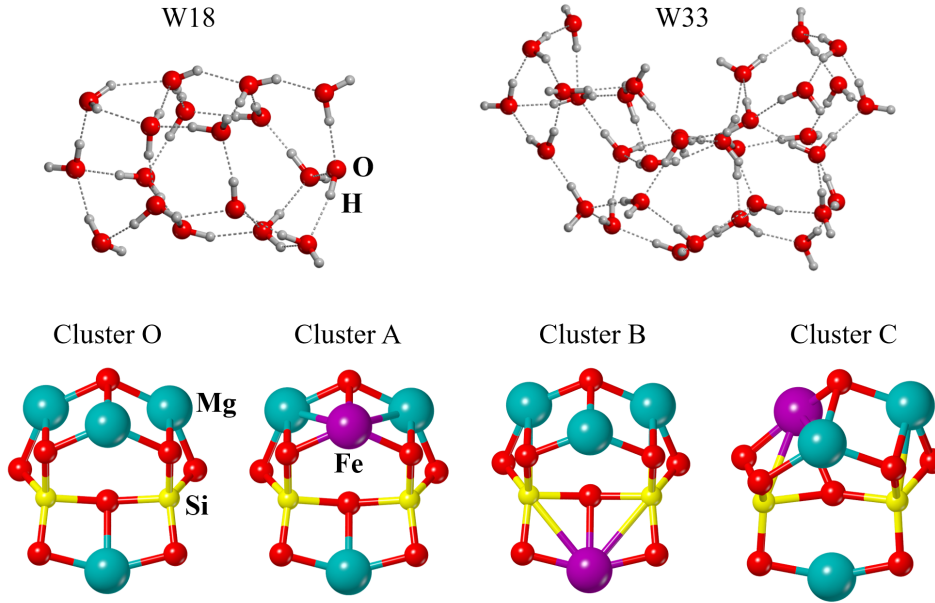
Figure 2.2: Cluster models adopted in this thesis. The top panel showcases the 18 and 33 water molecules clusters, respectively, W18 and W33. The bottom panel displays the four olivine clusters in which Fe is either absent (cluster O) or present (clusters A, B and C).

is considered, with the Fe atom occupying different positions, when present (see bottom panel of Figure 2.2).

2.6.2 Periodic approach

The previous approach cannot account for the long-range order, nor the periodicity inherent to a crystalline structure, often resulting in an inadequate description of the macroscopic properties of a crystal. In contrast, the periodic approach requires a relatively small number of atoms to do so, by exploiting the repetition of the unit cell in each periodic direction, due to the application of the Born-von Karman periodic boundary conditions (PBCs). Moreover, the presence of symmetry within the system can be exploited by the programs, dramatically reducing the calculation requirements in terms of both time and memory. The asymmetric unit is the smallest portion of a crystal structure to which symmetry operations can be applied to generate the complete unit cell.

It is evident that the periodic approach is particularly advantageous when dealing with symmetric structures. However, even amorphous-like systems can be modelled using a periodic model, provided that the unit cell is sufficiently large to ensure local disorder (Buch et al., 2008). Since structural atomistic details cannot be obtained directly from the experiments, a common method to generate an amorphous material involves performing a melt and quench process onto a crystalline bulk using molecular dynamics simulations at high temperatures to induce local disorder in the unit cell (Suter et al., 2006).

A periodic system is fully defined when the type and positions of the nuclei within the unit cell are specified, along with the lattice vectors that define the periodicity (Bravais lattices). The three-dimensional unit cell is defined by the direct lattice vector $\mathbf{T}$ as:

$$\mathbf{T} = n_1 \mathbf{a}_1 + n_2 \mathbf{a}_2 + n_3 \mathbf{a}_3 \tag{2.52}$$

where n_i are integers and the $\mathbf{a}_i$ vectors are known as the lattice parameters. From this definition, it is possible to build a vector $\mathbf{G}$ in the reciprocal space, also defined as $\mathbf{k}$-space, where the $\mathbf{b}_i$ vectors define the reciprocal cell unit parameters.

$$\mathbf{G} = m_1\mathbf{b}_1 + m_2\mathbf{b}_2 + m_3\mathbf{b}_3 \tag{2.53}$$

For all the couples of direct ($\mathbf{T}$) and reciprocal ($\mathbf{G}$) vectors, $\exp(i\mathbf{G} \cdot \mathbf{T}) = 1$. Furthermore, every couple of $\mathbf{k}$-points p and q, for which $p = q + \mathbf{G}$, returns the same value of the exponential function, therefore p and q are equivalent. Consenquently, the $\mathbf{k}$-points needed to describe the entire lattice are those, among all the infinite equivalent points, located closer to the origin of the reciprocal lattice. The region delimited by such $\mathbf{k}$-points is defined as the first Brillouin zone (BZ), whose volume is inversely proportional to the volume of the direct lattice cell.

The application of PBCs to a system is reflected also on its wave function and on the Hamiltonian. The latter, as well as the potential $V(\mathbf{r})$, is periodic over the translation of the primitive unit cells and can also be expressed as a Fourier series:

$$V(\mathbf{r}) = V(\mathbf{r} + \mathbf{T}) = \sum_{\mathbf{G}} C_{\mathbf{G}} \exp^{i\mathbf{G} \cdot \mathbf{r}} \tag{2.54}$$

where $C_{\mathbf{G}}$ represents the expansion coefficient. From the periodicity of the potential, it follows that $\mathbf{G} \cdot \mathbf{T} = 2\pi n$, with n being an integer, from which the orthogonality rule arises: $\mathbf{a}_i \cdot \mathbf{b}_j = 2\pi\delta_{ij}$.

The Bloch theorem defines the form of the *eigenvectors* of the Schrödinger equation subjected to a periodic potential and states that: '*Any physically acceptable solution of the Schrödinger equation in a periodic potential takes the form of a traveling plane wave modulated on the microscopic scale by an appropriate function with the lattice periodicity*' (Bloch, 1929). A Bloch function takes the form:

$$\Phi^{\mathbf{k}}(\mathbf{r}) = e^{i\mathbf{k} \cdot \mathbf{r}} u(\mathbf{r}) \tag{2.55}$$

where a plane wave $e^{i\mathbf{k} \cdot \mathbf{r}}$ is multiplied by a function that contains the periodicity of the lattice, $u(\mathbf{r})$. Bloch functions can be compared to atomic orbitals and they can be employed in linear combinations to give a crystalline orbital, i.e., the equivalent of a molecular orbital but for periodic systems (Zicovich-Wilson et al., 1998a; Zicovich-Wilson et al., 1998b).

$$\Psi_n^{\mathbf{k}}(\mathbf{r}) = \sum_{\mu} c_{\mu n}^{\mathbf{k}} \Phi_{\mu}^{\mathbf{k}}(\mathbf{r}) \tag{2.56}$$

where $\Phi_{\mu}^{\mathbf{k}}(\mathbf{r})$ represents the Bloch functions and $c_{\mu n}^{\mathbf{k}}$ their coefficients. Indeed, following the procedure described for the Roothaan-Hall equations, $c_{\mu n}^{\mathbf{k}}$ are determined variationally after self-consistently solving the matrix equation:

$$f^{\mathbf{k}} C^{\mathbf{k}} = S^{\mathbf{k}} C^{\mathbf{k}} E^{\mathbf{k}} \tag{2.57}$$

where $f^{\mathbf{k}}$ is the Fock matrix, $E^{\mathbf{k}}$ contains the eigenvalues $\varepsilon_n^{\mathbf{k}}$, $S^{\mathbf{k}}$ is the overlap matrix, and $C^{\mathbf{k}}$ is the coefficients matrix. This calculation is restricted to the unit cell and its solutions are dependent on $\mathbf{k}$.

Therefore, the $\mathbf{k}$-point sampling is a crucial step to obtain convergence in solid-state calculations and must be calibrated accordingly with the characteristics of the system under study. From the PBCs, it follows that there are as many $\mathbf{k}$-points as the number of cells considered, so that in the limit of an infinite crystal, the number of $\mathbf{k}$-points tends to infinity. For each $\mathbf{k}$-point, there is one solution to the Schrodinger equation, so that the total

energy of an infinite crystal is obtained by integrating over all **k**-points in the reciprocal space.

Since the energy associated with each **k**-point usually changes in a gradual way, without discontinuities, for the majority of the systems (except metals), a sum over a discrete set of **k**-points until the desired property reaches convergence is often sufficient to obtain the total energy of the system. The most used methodology for **k**-points sampling was developed by Monkhorst and Pack (Monkhorst et al., 1976). In this method, the **k**-points grid used for evaluating integrals is constructed within the first BZ. Depending on the symmetry of a periodic system, **k**-points in special positions emerge, representing regions of high symmetry in the reciprocal space (Dal Corso, 1996). Among those, the most widely known is the Γ-point, at the origin of the reciprocal lattice. The number of **k**-points required for sampling is typically small for large direct lattice primitive cells, resulting in a very small first BZ in the reciprocal space.

In this thesis, periodic calculations were performed with CRYSTAL17 code, capable of simulating systems ranging from zero to three periodic dimensions, i.e., molecules, polymers, surfaces and bulks. Unlike common periodic codes employing plane waves, CRYSTAL describes atoms through GTOs. This enables the creation of true one-dimensional and two-dimentional models, to which PBCs are applied only along the periodic directions, resulting in a finite thickness along the non-periodic directions (Dovesi et al., 2018).

2.6.3 Surface modelling

The most common method to model a surface through the periodic approach is the 'slab model'. It consists of cutting the bulk structure in order to extract a layer of finite thickness exposing two (top and bottom) surfaces. Conventionally, each surface is indicated by three integers, known as Miller indices (hkl), which identify the family of crystallographic planes to which the surface belongs. Cutting the crystal along a plane usually causes a number of chemical bonds to be cut at the surface. Depending on the chemical nature of the material (ionic, metallic, molecular, or covalent) different strategies can be adopted to cope with the unfilled valencies resulting by the slab being cut, requiring to add extra atoms in order to obtain electroneutral and stoichiometric surfaces.

As a rule of thumb, the most stable surfaces are those defined by the lowest Miller indices, thus characterized by the highest atomic density. The stability of a surface is quantified by its surface energy, E_S (in J m^{-2}), which is the energy required to cut the slab out of the bulk.

$$E_S = \frac{E_{slab} - N \cdot E_{bulk}}{2A} \tag{2.58}$$

where E_{slab} is the energy of the surface, E_{bulk} is the energy of the bulk, $N = z_{slab}/z_{bulk}$ with z being the number of molecules contained in the unit cells of the surface and the bulk, respectively, and A is the area of the surface. The factor 2 accounts for the existence of two equivalent surfaces at the top and bottom of the slab. The most stable surfaces are those with the lowest E_S, a value that converges to a constant value when increasing the thickness of the slab. Therefore, it is essential to balance the accuracy of the converged E_S, which improves as the slab thickness increases, and the computational cost of the calculation, which rises when enlarging the model.

Additionally, the cohesive energy, E_C (in kJ mol^{-1}), of a surface describes the energy required to break the physical interactions holding the molecules together and is given by the equation:

(010) Crystalline H$_2$O ice

(010) Amorphous H$_2$O ice

(001) H$_2$O:CO dirty ice

(010) H$_2$O:CO dirty ice

(100) H$_2$O:CO dirty ice

(100) Crystalline CH$_3$CH$_2$NH$_2$ ice

(010) Crystalline CH$_3$CH$_2$OH ice
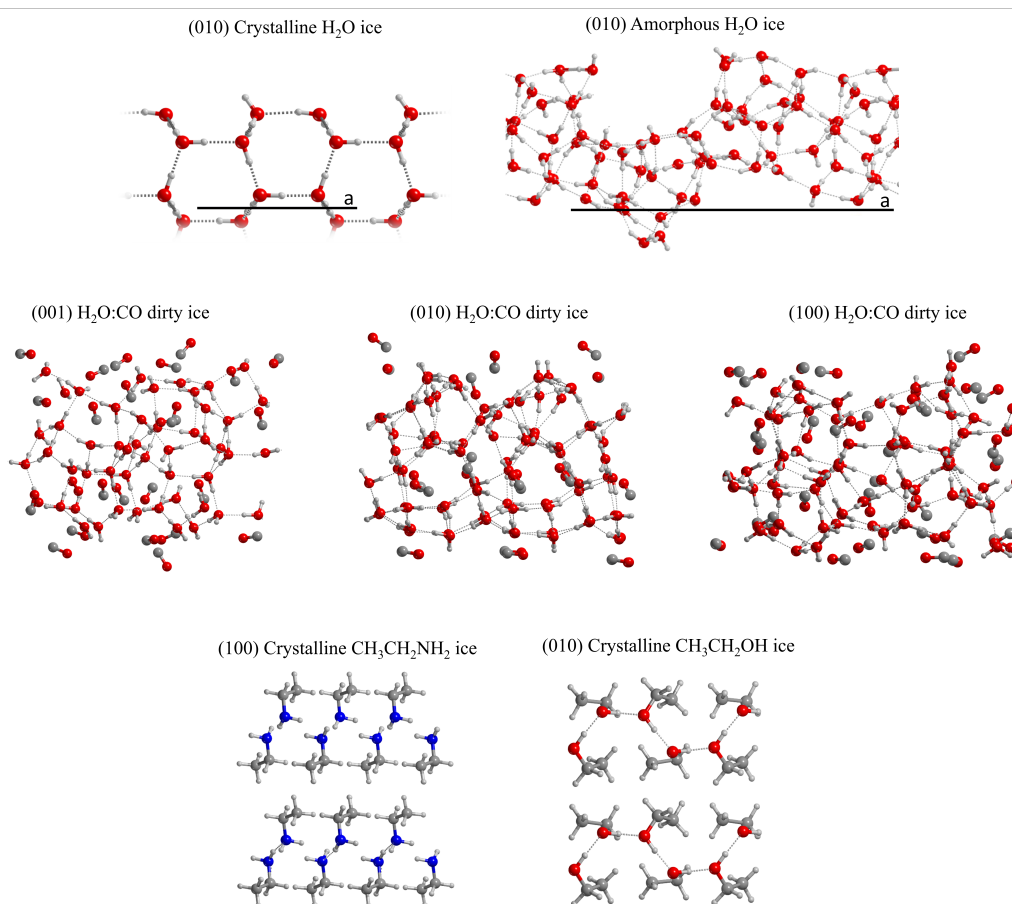
Figure 2.3: Periodic models adopted in this thesis. The top panel shows the crystalline (010) slab and the amorphous-like surfaces adopted in the binding energy calculation investigations. In the middle panel, the amorphous-like (001), (010), and (100) surfaces, developed for the study of acetaldehyde formation, are depicted. Finally, the most stable slabs of crystalline ethylamine (100) and ethanol (010), modelled to explore the relation between experiments and calculations, are represented in the bottom panel.

$$E_C = \frac{E_{slab}}{z} - E_{mol} \qquad (2.59)$$

where E_{mol} is the energy of the isolated molecule in the gas phase. This information is somehow complementary to the surface energy, in that both describe the stability of a slab. Indeed, the most stable surface of a crystal is characterised by the lowest E_S, and the highest E_C.

The periodic surfaces adopted in this thesis are collected in Figure 2.3. The crystalline and amorphous water surface models used to compute the binding energies of S-bearing species and COMs (Perrero et al., 2022a; Perrero et al., 2024a; Perrero et al., 2024c) were characterised in previous works. The crystalline model consists of a 2 × 1 supercell (010) slab model cut from the bulk of a proton ordered crystalline ice (Casassa et al., 1997), whose unit cell is characterised by cell parameters $|a|$ = 9.065 Å and $|b|$ = 7.153 Å and consists of twelve atomic layers. The amorphous ice is represented by an amorphous-like periodic structure with cell parameters $|a|$ = 20.355 Å, $|b|$ = 10.028 Å, and $|\gamma|$ = 103.0°, containing 60 disordered water molecules per unit cell. Such model was obtained by joining three amorphous water clusters and applying PBC to the structure in two directions to

yield a periodic surface (Ferrero et al., 2020).

The H$_2$O:CO dirty ice model was obtained from the bulk model of the pure H$_2$O crystalline P-ice described above, in which one every four water molecules was replaced by CO. Three surfaces were cut along the (001), (010), and (100) planes, then fully relaxed, causing a heavy reorganisation in their internal structure. While the external layers of each surface are characterised by the presence of faintly interacting CO molecules, the inner CO species broke the symmetric structure of the initial bulk structure, creating clathrate-like cages in which one or more CO molecules are surrounded by a H-bonded network of H$_2$O molecules (Perrero et al., 2023a).

Finally, a variety of surfaces were modelled from the crystalline bulk structures of ethanol and ethylamine, originally determined by X-ray diffraction. Through the calculation of E_S and E_C, the unit cell structures and the order of stability of the most frequently occurring surfaces of ethanol and ethylamine were determined (Perrero et al., 2024c). The most stable surface obtained from each bulk structure is represented in Figure 2.3.

2.6.4 Binding energy calculations

Many physical and chemical phenomena occur at the interface between a solid material and the environment, thus, at its surface. As mentioned in the Introduction, one of the fundamental processes taking place at the surface is the adsorption of chemical species.

The BE is defined as the opposite of the interaction energy $\Delta E = E_{complex} - E_{adsorbate} - E_{surface}$ corrected for the BSSE, arising due to the use of a finite basis set of localized GTOs to describe the system (see Section 2.2.2 for a detailed explanation).

$$BE = -(\Delta E - BSSE) \tag{2.60}$$

The interaction energy is given by a sum of terms that provide additional insights into the adsorption process, according to the equation:

$$\Delta E = \Delta E^* + \delta E_S + \delta E_\mu + E_L \tag{2.61}$$

where ΔE is given by the sum of the deformation-free interaction energy (ΔE^*), the deformation energy of the slab (δE_S) and of the adsorbate (δE_μ), and the lateral interaction (E_L). The latter term measures the interaction between adsorbed species in different replicas of the cell, allowing the estimation of the effect of surface coverage. As an example, when simulating single adsorption processes, the E_L value should be minimised, often requiring the enlargement of the unit cell to achieve $E_L \approx 0$.

It is useful to define the adsorption enthalpy, $-\Delta H_{ads}$, also found as BE(0):

$$BE(0) = BE - \Delta ZPE \tag{2.62}$$

It consists of the BE corrected for the $\Delta ZPE = ZPE_{complex} - ZPE_{ice} - ZPE_{species}$. Due to its definition, ΔZPE is a positive quantity, thus the BE(0) is always lower than the BE. Conventionally, the BE(0) is used to compare computational simulations with experimental results. In the framework of astrochemistry, especially in the ISM, where the temperature and the pressure are close to zero, the enthalpy of a chemical system, $H = U - PV$, is approximated with its internal energy $U = E + ZPE$. The internal energy is given by the addition of the ZPE to the electronic energy E, analogous to the definition of the BE(0).

ONIOM2 scheme

As mentioned in Section 2.4, the ONIOM approach grants the definition of multiple layers in a chemical system, each treated at a different level of theory (Svensson et al., 1996). It is

particulary useful when dealing with large models in which the chemical phenomenon of interest occurs only in a small portion. This approach can also be used when a refinement of a certain property at a higher level of theory is required. An example is given by the evaluation of the accuracy of the BEs computed on the (010) surface of water ice. In this case, a periodic system has been treated with a software that does not support calculations at CCSD(T) level of theory.

The ONIOM2 additive scheme implies dividing the system in two parts (*model* and *real*), which are described by two different levels of theory (*high* and *low*). The *model* system (the fragment of interest) is described by both the *high* and the *low* level of theory. The *real* system (that is, the whole system) is described by the *low* level of theory (Dapprich et al., 1999). In our case, the *high* level of theory is defined by CBS extrapolated CCSD(T) energies, while the *low* level corresponds to DFT energies.

Such scheme allows extracting a fragment from the periodic system and treating it as a molecular system, onto which post-HF calculations can be performed. In the computation of BEs, the *model* system carved out of the *real* adsorption complex is constituted by the adsorbate and the two closest water molecules of the (010) crystalline surface. The final energy of the system results from adding a correction term, given by the difference between the *high* and *low* level energies of the *model* system, to the energy of the *real* system.

$$E(ONIOM2) = E(DFT; real) + E(CCSD(T)/CBS; model) - E(DFT; model) \qquad (2.63)$$

This approach has also been applied to correct reaction barriers in the formation of the acetyl radical on dirty H_2O:CO ice surfaces. In that case, the *model* system corresponds to the $CH_3 + CO_{ice}$ fragment, whereas the *real* system is the whole periodic structure.

2.7 Experimental determination of binding energies

The experimental determination of the binding energies of astrochemically relevant species is conducted in a special apparatus (represented in Figure 2.4), aimed at reproducing the conditions of the ISM. There, the species are deposited onto a substrate, and their desorption is monitored via temperature programmed desorption (TPD). Interstellar chambers, such as ISAC, FORMOLISM, and VENUS, consist of an ultra-high vacuum stainless steel chamber, where experiments are conducted on a gold-coated copper sample holder. The latter is attached to the cold head of a closed-cycle He cryostat, that allows to vary its temperature via a computer-controlled resistive heater. The chamber is equipped with an infrared spectrometer that allows monitoring the species present on the sample holder *in situ* and a quadrupole mass spectrometer (QMS) placed in front to monitor the species leaving the surface (Amiaud et al., 2006; Muñoz Caro et al., 2010; Congiu et al., 2020).

The first phase of the experiment consists in the deposition of the species of interest, eventually followed by specific treatments provided for in the experiment. Later, during the TPD analysis, the temperature of the substrate increases, resulting in the progressive sublimation and desorption of the various chemical species present on the surface. This process is dependent on a number of factors, including the binding energy of the species with the surface, the surface coverage, and the heating ramp adopted in the experiment. Sublimating species are identified through the use of a QMS, which employs electrons produced by a heated filament to induce the fragmentation of molecules into several ions. The TPD spectrum consists of the abundance of each atomic mass unit against its desorption temperature.
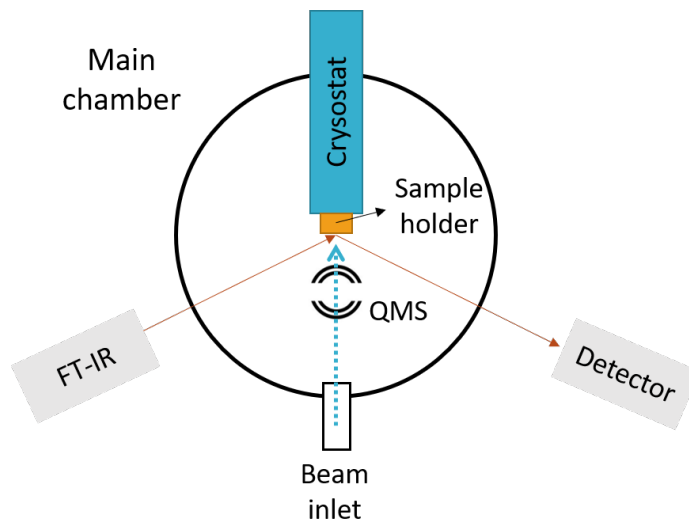
Figure 2.4: Schematic representation of an interstellar chamber. The main chamber, where experiments are performed, consists of a cryostat on which is mounted the sample holder. There, incoming species from the beam inlet are deposited and analysed through IR spectroscopy and mass spectrometry.

The thermal desorption of a species bound to a substrate can be approximately described by the Polanyi-Wigner equation (Kolasinski, 2012):

$$k(T) = -\frac{\mathrm{d}N}{\mathrm{d}t} = \nu_n \theta^n e^{-\frac{E_{\mathrm{des}}}{RT}} \tag{2.64}$$

where the desorption rate $k(T)$ depends on the number density of molecules adsorbed on the surface θ (molecules cm^{-2}), the desorption energy of a molecule on the surface E_{des} (J mol^{-1}), and the temperature of the surface T(K). In equation 2.64, ν_n is the preexponential factor (molecules^{1-n} s^{-1}), R is the ideal gas constant (J mol^{-1} K^{-1}), and n is the order of the desorption process. For a zeroth order desorption, corresponding to a multilayer coverage, E_{des} is independent from θ. However, for a first order desorption, accounting for a submonolayer coverage, both ν and E_{des} are in principle coverage-dependent.

Therefore, the desorption parameters that have to be determined are n, ν and E_{des}. The latter can be obtained from the Redhead equation, which is a simplified approach derived from the Polanyi-Wigner equation valid only under the assumption of a first-order desorption profile and a constant heating rate (Redhead, 1962; King, 1975):

$$E_{\mathrm{des}} = T_{peak} \cdot \left(ln\left(\frac{\nu \cdot T_{peak}}{\beta}\right) - 3.64 \right) \tag{2.65}$$

This equation takes the peak of the desorption trace (T_{peak}, K) in combination with the heating rate (β, K s^{-1}) and a pre-exponential factor (ν, s^{-1}) to determine E_{des} in K energy unit. Occasionally, in astrochemical models, the pre-exponential factor ν is calculated with the harmonic oscillator reaction (Hasegawa et al., 1992):

$$\nu = \sqrt{\frac{2N_s E_{\mathrm{des}}}{\pi^2 m_X}} \tag{2.66}$$

where N_s is the number of sites per surface area and m_X is the mass of species X. For typical values of E_{des} in case of physisorption, this formula leads to prefactor values of about 10^{12}

to 10^{13} s^{-1}. This approach works to evaluate the pre-exponential factor of atoms or small molecules such as Ar or N_2 (Minissale et al., 2022). However, larger molecules may exhibit prefactor values several orders of magnitude higher than what is predicted by the previous formula (e.g., Doronin et al., 2015). This discrepancy originates from the fact that equation 2.66 neglects the rotational partition function of the desorbing molecules. Indeed, the pre-exponential factor reflects the entropic effect associated with the desorption kinetics. A more accurate estimation implies adopting the formalism established by Tait et al. (2005), based on an equation derived from the TST:

$$\nu_{TST} = \frac{k_B T_{peak}}{h} \cdot q_{tr,2D}^{\ddagger} \cdot q_{rot,3D}^{\ddagger} = \frac{k_B\, T}{h} \frac{A}{\Lambda^2} \frac{\sqrt{\pi}}{\sigma\, h^3} (8\pi^2\, k_B\, T_{peak})^{3/2} \sqrt{I_x\, I_y\, I_z} \qquad (2.67)$$

In this equation, k_B is the Boltzmann constant, h is the Planck constant, and A is the surface area per adsorbed molecule, i.e., the inverse of the number of surface sites per unit area, fixed at 10^{-19} m^2. The thermal wavelength of a molecule (Λ, defined in equation 2.68) depends on its atomic mass (m_{mol}), and on the temperature of the maximum of the desorption T_{peak}.

$$\Lambda = \frac{h}{\sqrt{2\pi m_{mol} k_B T_{peak}}} \qquad (2.68)$$

The symmetry factor σ is the number of different but indistinguishable rotational configurations of the species. The principal moments of inertia I_x, I_y, and I_z, of the molecules are collected in databases, such as the CCCBDB[2]; alternatively, they can be easily computed. In the factor $k_B T/h$, the temperature T is taken to be equal to T_{peak}, approximating the temperature dependence of ν_{TST} with a constant value calculated at T_{peak}. The TST method can provide a reliable estimate of the pre-exponential factor; however, it may overestimate its value due to the assumption that adsorbates are immobile, whereas the possibility of migration represents a degree of freedom for the adsorbed species. Equation 2.68 also neglects quantum effects and is not suitable for the description of the behaviour of large species, containing more than twenty atoms.

Nevertheless, a more rigorous approach for the determination of E_{des} involves fitting the TPD profile obtained in the experiment with equation 2.64, provided the prefactor ν has been determined. This procedure can be adopted only in the case that the T_{peak} of the adsorbate is lower than that of the surface.

Conversely, the co-desorption of the surface molecules and the adsorbates precludes the possibility of distinguishing the two processes and calculating the E_{des} of the adsorbates, since the desorption energy of the surface is the parameter that determines whether the adsorbate resides in the condensed or in the gas phase (Minissale et al., 2022). In the case of a water ice surface, this phenomenon occurs with species whose interaction energy with water molecules is larger than the binding energy of water with itself (for a classification of desorption behaviours, see Collings et al., 2004; Burke et al., 2015). In such circumstances, a computational approach is particularly useful to provide the missing data, since simulations allow to determine the desorption energy of the adsorbate while leaving the water surface unaltered during the desorption process.

---

[2]NIST Computational Chemistry Comparison and Benchmark Database, NIST Standard Reference Database Number 101 Release 22, May 2022, Editor: Russell D. Johnson III. http://cccbdb.nist.gov/

References

Ahlrichs, R. et al. (1975). "PNO–CI (pair natural orbital configuration interaction) and CEPA–PNO (coupled electron pair approximation with pair natural orbitals) calculations of molecular systems. I. Outline of the method for closed-shell states". *J. Chem. Phys.* **62**, 1225. DOI: `10.1063/1.430637`.

Almlöf, J. et al. (1990). "General contraction of Gaussian basis sets. II. Atomic natural orbitals and the calculation of atomic and molecular properties". *J. Chem. Phys.* **92**, 551. DOI: `10.1063/1.458458`.

Almlöf, J. et al. (1991). "Atomic Natural Orbital (ANO) basis sets for quantum chemical calculations". *Adv. Quantum Chem.* **22**, 301. DOI: `10.1016/S0065-3276(08)60366-4`.

Amiaud, L. et al. (2006). "Interaction of D_2 with H_2O amorphous ice studied by temperature-programed desorption experiments". *J. Chem. Phys.* **124**, 094702. DOI: `10.1063/1.2168446`.

Ásgeirsson, V. et al. (2021). "Nudged elastic band method for molecular reactions using energy-weighted springs combined with eigenvector following". *J. Chem. Theory Comput.* **17**, 4929. DOI: `10.1021/acs.jctc.1c00462`.

Bartlett, R. J. et al. (2007). "Coupled-cluster theory in quantum chemistry". *Rev. Mod. Phys.* **79**, 291. DOI: `10.1103/RevModPhys.79.291`.

Bloch, F. (1929). "Über die quantenmechanik der elektronen in kristallgittern". *Zeitschrift für physik* **52**, 555. DOI: `10.1007/BF01339455`.

Born, M. et al. (1927). "Zur Quantentheorie der Molekeln". *Annalen der Physik* **389**, 457. DOI: `10.1002/andp.19273892002`.

Boys, S. F. et al. (1950). "Electronic wave functions - I. A general method of calculation for the stationary states of any molecular system". *Proc. R. Soc. Lond. A* **200**, 542. DOI: `10.1098/rspa.1950.0036`.

Boys, S. F. et al. (1970). "The calculation of small molecular interactions by the differences of separate total energies. Some procedures with reduced errors". *Mol. Phys.* **19**, 553. DOI: `10.1080/00268977000101561`.

Brandenburg, J. G. et al. (2018). "B97-3c: a revised low-cost variant of the B97-D density functional method". *J. Chem. Phys.* **148**, 064104. DOI: `10.1063/1.5012601`.

Buch, V. et al. (2008). "Proton order in the ice crystal surface". *Proc. Natl. Acad. Sci.* **105**, 5969. DOI: `10.1073/pnas.0710129105`.

Burke, D. J. et al. (2015). "Trapping and desorption of complex organic molecules in water at 20 K". *J. Chem. Phys.* **143**, 164704. DOI: `10.1063/1.4934264`.

Bursch, M. et al. (2022). "Best-practice DFT protocols for basic molecular computational chemistry". *Angew. Chem. Int. Ed.* **61**, e202205735. DOI: `10.1002/ange.202205735`.

Bylaska, E. J. (2017). "Chapter Five - plane-wave DFT methods for chemistry". *Annu. Rep. Comput. Chem.* **13**, 185. DOI: `10.1016/bs.arcc.2017.06.006`.

Caldeweyher, E. et al. (2019). "A generally applicable atomic-charge dependent London dispersion correction". *J. Chem. Phys.* **150**, 154122. DOI: `10.1063/1.5090222`.

Casassa, S. et al. (1997). "Proton-ordered models of ordinary ice for quantum-mechanical studies". *J. Chem. Phys.* **106**, 8030.

Collings, M. P. et al. (2004). "A laboratory survey of the thermal desorption of astrophysically relevant molecules". *Mon. Not. R. Astron. Soc.* **354**, 1133. DOI: `10.1111/j.1365-2966.2004.08272.x`.

Congiu, E. et al. (2020). "A new multi-beam apparatus for the study of surface chemistry routes to formation of complex organic molecules in space". *Rev. Sci. Instrum.* **91** (12), 124504. DOI: `10.1063/5.0018926`.

Cundari, T. R. et al. (1996). "Effective core potential approaches to the chemistry of the heavier elements". In: *Rev. Comput. Chem.* John Wiley & Sons, Ltd, 145. DOI: `10.1002/9780470125854.ch3`.

Dal Corso, A. (1996). "Reciprocal space integration and special-point techniques". In: *Quantum-Mechanical Ab-initio Calculation of the Properties of Crystalline Materials*. Ed. by C. Pisani. Berlin, Heidelberg: Springer Berlin Heidelberg, 77. DOI: `10.1007/978-3-642-61478-1_4`.

Dapprich, S. et al. (1999). "A new ONIOM implementation in Gaussian98. Part I. The calculation of energies, gradients, vibrational frequencies and electric field derivatives". *Comput. Theor. Chem.* **461-462**, 1. DOI: `10.1016/S0166-1280(98)00475-8`.

Dinur, U. et al. (1991). "New approaches to empirical force fields". In: *Rev. Comput. Chem.* John Wiley & Sons, Ltd, 99. DOI: `10.1002/9780470125793.ch4`.

Dirac, P. (1930). "Note on exchange phenomena in the Thomas atom". *Mathematical proceedings of the Cambridge philosophical society*. Vol. 26. Cambridge University Press, 376.

Dirac, P. (1939). "A new notation for quantum mechanics". *Math. Proc. Camb. Philos. Soc.* **35**, 416. DOI: `10.1017/S0305004100021162`.

Ditchfield, R. et al. (1971). "Self-Consistent Molecular-Orbital Methods. IX. An Extended Gaussian-Type Basis for Molecular-Orbital Studies of Organic Molecules". *J. Chem. Phys.* **54**, 724. DOI: `10.1063/1.1674902`.

Doronin, M. et al. (2015). "Adsorption energies and prefactor determination for CH_3OH adsorption on graphite". *J. Chem. Phys.* **143**, 084703. DOI: `10.1063/1.4929376`.

Dovesi, R. et al. (2018). "Quantum-mechanical condensed matter simulations with CRYSTAL". *Wiley Interdiscip. Rev. Comput. Mol. Sci.* **8**, e1360. DOI: `10.1002/wcms.1360`.

Dunning, T. H. (1971). "Gaussian basis functions for use in molecular calculations. III. Contraction of (10s6p) atomic aasis sets for the first-row atoms". *J. Chem. Phys.* **55**, 716. DOI: `10.1063/1.1676139`.

Dunning, T. H. (1989). "Gaussian basis sets for use in correlated molecular calculations. I. The atoms boron through neon and hydrogen". *J. Chem. Phys.* **90**, 1007. DOI: `10.1063/1.456153`.

Eksterowicz, J. E. et al. (1993). "Transition-state modeling with empirical force fields". *Chem. Rev.* **93**, 2439. DOI: `10.1021/cr00023a006`.

Eyring, H. (1935). "The activated complex in chemical reactions". *J. Chem. Phys.* **3**, 107. DOI: `10.1063/1.1749604`.

Fermi, E. (1927). "Un metodo statistico per la determinazione di alcune prioprietà dell'atomo". *Rend. Accad. Naz. Lincei* **6**, 602.

Ferrero, S. et al. (2020). "Binding energies of interstellar molecules on crystalline and amorphous models of water ice by ab initio calculations". *Astrophys. J.* **904**, 11. DOI: `10.3847/1538-4357/abb953`.

Field, M. J. et al. (1990). "A combined quantum mechanical and molecular mechanical potential for molecular dynamics simulations". *J. Comput. Chem.* **11**, 700. DOI: `10.1002/jcc.540110605`.

Fock, V. (1930). "Näherungsmethode zur Lösung des quantenmechanischen Mehrkörperproblems". *Zeitschrift für Physik* **61**, 126. DOI: `10.1103/PhysRev.97.1490`.

Frisch, M. J. et al. (1984). "Self-consistent molecular orbital methods 25. Supplementary functions for Gaussian basis sets". *J. Chem. Phys.* **80**, 3265. DOI: `10.1063/1.447079`.

Frisch, M. J. et al. (2016). *Gaussian16 Revision C.01*. Gaussian Inc. Wallingford CT.

Gale, J. D. et al. (2021). "A universal force field for materials, periodic GFN-FF: implementation and examination". *J. Chem. Theory Comput.* **17**, 7827. DOI: `10.1021/acs.jctc.1c00832`.

Germain, A. et al. (2022). "Computer generated realistic interstellar icy grain models: physicochemical properties and interaction with NH_3". *ACS Earth Space Chem.* **6**, 1286. DOI: 10.1021/acsearthspacechem.2c00004.

Grimme, S. (2004). "Accurate description of van der Waals complexes by density functional theory including empirical corrections". *J. Comput. Chem.* **25**, 1463. DOI: 10.1002/jcc.20078.

Grimme, S. (2006). "Semiempirical GGA-type density functional constructed with a long-range dispersion correction". *J. Comput. Chem.* **27**, 1787. DOI: 10.1002/jcc.20495.

Grimme, S. et al. (2010). "A consistent and accurate ab initio parametrization of density functional dispersion correction (DFT-D) for the 94 elements H-Pu". *J. Chem. Phys.* **132**, 154104. DOI: 10.1063/1.3382344.

Grimme, S. et al. (2011). "Effect of the damping function in dispersion corrected density functional theory". *J. Comput. Chem.* **32**, 1456. DOI: 10.1002/jcc.21759.

Grimme, S. et al. (2015). "Consistent structures and interactions by density functional theory with small atomic orbital basis sets". *J. Chem. Phys.* **143**, 054107. DOI: 10.1063/1.4927476.

Grimme, S. et al. (2021). "r^{2}SCAN-3c: a 'Swiss army knife' composite electronic-structure method". *J. Chem. Phys.* **154**, 064103. DOI: 10.1063/5.0040021.

Guo, Y. et al. (2018). "Communication: an improved linear scaling perturbative triples correction for the domain based local pair-natural orbital based singles and doubles coupled cluster method [DLPNO-CCSD(T)]". *J. Chem. Phys.* **148**, 011101. DOI: 10.1063/1.5011798.

Hall, G. G. et al. (1951). "The molecular orbital theory of chemical valency VIII. A method of calculating ionization potentials". *Proc. R. Soc. Lond. A* **205**, 541. DOI: 10.1098/rspa.1951.0048.

Hartree, D. R. (1928a). "The wave mechanics of an atom with a non-coulomb central field. Part I. Theory and methods". *Math. Proc. Camb. Philos. Soc.* **24**, 89. DOI: 10.1017/S0305004100011919.

Hartree, D. R. (1928b). "The wave mechanics of an atom with a non-coulomb central field. Part II. Some results and discussion". *Math. Proc. Camb. Philos. Soc.* **24**, 111. DOI: 10.1017/S0305004100011920.

Hartree, D. R. (1928c). "The wave mechanics of an atom with a non-coulomb central field. Part III. Term values and intensities in series in optical spectra". *Math. Proc. Camb. Philos. Soc.* **24**, 426. DOI: 10.1017/S0305004100015954.

Hartree, D. R. (1929). "The wave mechanics of an atom with a non-coulomb central field. Part IV. Further results relating to terms of the optical spectrum". *Math. Proc. Camb. Philos. Soc.* **25**, 310. DOI: 10.1017/S0305004100014031.

Hartree, D. R. et al. (1933). *Mem. Proc. Manchester Lit. Philos. Soc.* **77**, 69.

Hasegawa, T. I. et al. (1992). "Models of gas-grain chemistry in dense interstellar clouds with complex organic molecules". *Astrophys. J. Suppl. Ser.* **82**, 167. DOI: 10.1086/191713.

Hättig, C. et al. (2012). "Explicitly correlated electrons in molecules". *Chem. Rev.* **112**, 4. DOI: 10.1021/cr200168z.

Hehre, W. J. et al. (1969). "Self-consistent molecular-orbital methods. I. Use of Gaussian expansions of Slater-type atomic orbitals". *J. Chem. Phys.* **51**, 2657. DOI: 10.1063/1.1672392.

Hehre, W. J. et al. (1972). "Self-consistent molecular-orbital methods. XII. Further extensions of Gaussian-type basis sets for use in molecular orbital studies of organic molecules". *J. Chem. Phys.* **56**, 2257. DOI: 10.1063/1.1677527.

Helgaker, T. et al. (1997). "Basis-set convergence of correlated calculations on water". *J. Chem. Phys.* **106**, 9639. DOI: 10.1063/1.473863.

Henkelman, G. et al. (2000). "A climbing image nudged elastic band method for finding saddle points and minimum energy paths". *J. Chem. Phys.* **113**, 9901. DOI: 10.1063/1.1329672.

Henkelman, G. et al. (2001). "Long time scale kinetic Monte Carlo simulations without lattice approximation and predefined event table". *J. Chem. Phys.* **115**, 9657. DOI: 10.1063/1.1415500.

Henkelman, G. et al. (2002). "Methods for finding saddle points and minimum energy paths". In: *Theoretical Methods in Condensed Phase Chemistry*. Ed. by S. D. Schwartz. Dordrecht: Springer Netherlands, 269. DOI: 10.1007/0-306-46949-9_10.

Hohenberg, P. et al. (1964). "Inhomogeneous electron gas". *Phys. Rev.* **136**, B864. DOI: 10.1103/PhysRev.136.B864.

Huzinaga, S. (1965). "Gaussian-type functions for polyatomic systems. I". *J. Chem. Phys.* **42**, 1293. DOI: 10.1063/1.1696113.

Hylleraas, E. A. (1929). "Neue berechnung der energie des heliums im grundzustande, sowie des tiefsten terms von ortho-helium". *Zeitschrift für Physik* **54**, 347. DOI: 10.1007/BF01375457.

Ishida, K. et al. (1977). "The intrinsic reaction coordinate. An ab initio calculation for HNC $\rightarrow$ HCN and $H^- + CH_4 \rightarrow CH_4 + H^-$". *J. Chem. Phys.* **66**, 2153. DOI: 10.1063/1.434152.

Jensen, F. (1994). "Transition structure modeling by intersecting potential energy surfaces". *J. Comput. Chem.* **15**, 1199. DOI: 10.1002/jcc.540151103.

Jensen, F. (2017). *Introduction to computational chemistry, 3rd Edition*. John Wiley & Sons, Ltd.

Jónsson, H. et al. (1998). "Nudged elastic band method for finding minimum energy paths of transitions". In: *Classical and Quantum Dynamics in Condensed Phase Simulations*, 385. DOI: 10.1142/9789812839664_0016.

Kassel, L. S. (1928). "Studies in homogeneous gas reactions. I". *J. Chem. Phys.* **32**, 225. DOI: 10.1021/j150284a007.

Keith, J. A. et al. (2021). "Combining machine learning and computational chemistry for predictive insights into chemical systems". *Chem. Rev.* **121**, 9816. DOI: 10.1021/acs.chemrev.1c00107.

King, D. A. (1975). "Thermal desorption from metal surfaces: a review". *Surf. Sci.* **47**, 384. DOI: https://doi.org/10.1016/0039-6028(75)90302-7.

Klopper, W. et al. (2002). "Explicitly correlated second-order Møller-Plesset methods with auxiliary basis sets". *J. Chem. Phys.* **116**, 6397. DOI: 10.1063/1.1461814.

Koch, W. et al. (2015). *A chemist's guide to density functional theory*. John Wiley & Sons, Ltd. DOI: 10.1002/3527600043.

Kohn, W. et al. (1965). "Self-Consistent Equations Including Exchange and Correlation Effects". *Phys. Rev.* **140**, A1133. DOI: 10.1103/PhysRev.140.A1133.

Kolasinski, K. W. (2012). *Surface science: foundations of catalysis and nanoscience*. John Wiley & Sons. DOI: 10.1002/9781119941798.

Kresse, G. et al. (1996). "Efficient iterative schemes for ab initio total-energy calculations using a plane-wave basis set". *Phys. Rev. B* **54**, 11169. DOI: 10.1103/PhysRevB.54.11169.

Krishnan, R. et al. (1980). "Self-consistent molecular orbital methods. XX. A basis set for correlated wave functions". *J. Chem. Phys.* **72**, 650. DOI: doi:10.1063/1.438955.

Kruse, H. et al. (2012). "A geometrical correction for the inter- and intra-molecular basis set superposition error in Hartree-Fock and density functional theory calculations for large systems". *The Journal of Chemical Physics* **136**, 154101. DOI: 10.1063/1.3700154.

Kumar, A. et al. (2020). "Explicitly correlated coupled cluster method for accurate treatment of open-shell molecules with hundreds of atoms". *J. Chem. Phys.* **153**, 094105. DOI: 10.1063/5.0012753.

Kutzelnigg, W. (1985). "r$_{12}$-Dependent terms in the wave function as closed sums of partial wave amplitudes for large *l*". *Theor. Chem. Acc.* **68**, 445. DOI: `10.1007/BF00527669`.

Lee, K. et al. (2010). "Higher-accuracy van der Waals density functional". *Phys. Rev. B* **82**, 081101. DOI: `10.1103/PhysRevB.82.081101`.

Lewars, E. G. (2016). *Computational chemistry: introduction to the theory and applications of molecular and quantum mechanics*. Springer.

Marcus, R. A. (1952). "Unimolecular dissociations and free radical recombination reactions". *J. Chem. Phys.* **20**, 359. DOI: `10.1063/1.1700424`.

Mardirossian, N. et al. (2017). "Thirty years of density functional theory in computational chemistry: an overview and extensive assessment of 200 density functionals". *Mol. Phys.* **115**, 2315. DOI: `10.1080/00268976.2017.1333644`.

Maseras, F. et al. (1995). "IMOMM: A new integrated ab initio + molecular mechanics geometry optimization scheme of equilibrium structures and transition states". *J. Comput. Chem.* **16**, 1170. DOI: `10.1002/jcc.540160911`.

Meyer, W. (1973). "PNO–CI Studies of electron correlation effects. I. Configuration expansion by means of nonorthogonal orbitals, and application to the ground state and ionized states of methane". *J. Chem. Phys.* **58**, 1017. DOI: `10.1063/1.1679283`.

Minissale, M. et al. (2022). "Thermal desorption of interstellar ices: a review on the controlling parameters and their implications from snowlines to chemical complexity". *ACS Earth Space Chem.* **6**, 597. DOI: `10.1021/acsearthspacechem.1c00357`.

Møller, C. et al. (1934). "Note on an approximation treatment for many-electron systems". *Phys. Rev.* **46**, 618. DOI: `10.1103/PhysRev.46.618`.

Monkhorst, H. J. et al. (1976). "Special points for Brillouin-zone integrations". *Phys. Rev. B* **13**, 5188. DOI: `10.1103/PhysRevB.13.5188`.

Muñoz Caro, G. M. et al. (2010). "New results on thermal and photodesorption of CO ice using the novel InterStellar Astrochemistry Chamber (ISAC)". *Astron. Astrophys.* **522**, A108. DOI: `10.1051/0004-6361/200912462`.

Neese, F. (2004). "Definition of corresponding orbitals and the diradical character in broken symmetry DFT calculations on spin coupled systems". *J. Phys. Chem. Solids* **65**, 781. DOI: `10.1016/j.jpcs.2003.11.015`.

Neese, F. (2009). "Prediction of molecular properties and molecular spectroscopy with density functional theory: from fundamental theory to exchange-coupling". *Coord. Chem. Rev.* **253**, 526. DOI: `10.1016/j.ccr.2008.05.014`.

Neese, F. (2022). "Software update: The ORCA program system-version 5.0". *Wiley Interdiscip. Rev. Comput. Mol. Sci.* **12**, e1606. DOI: `10.1002/wcms.1606`.

Neugebauer, H. et al. (2023). "Assessment of DLPNO-MP2 approximations in double-hybrid DFT". *J. Chem. Theory Comput.* **19**, 7695. DOI: `10.1021/acs.jctc.3c00896`.

Noodleman, L. (1981). "Valence bond description of antiferromagnetic coupling in transition metal dimers". *J. Chem. Phys.* **74**, 5737. DOI: `10.1063/1.440939`.

Okoshi, M. et al. (2015). "Revisiting the extrapolation of correlation energies to complete basis set limit". *J. Comp. Chem.* **36**, 1075. DOI: `10.1002/jcc.23896`.

Paizs, B. et al. (1998). "Comparative study of BSSE correction methods at DFT and MP2 levels of theory". *J. Comput. Chem.* **19**, 575. DOI: `10.1002/(SICI)1096-987X(19980430)19:6<575::AID-JCC1>3.0.CO;2-O`.

Perdew, J. P. et al. (2001). "Jacob's ladder of density functional approximations for the exchange-correlation energy". *AIP Conf. Proc.* **577**, 1. DOI: `10.1063/1.1390175`.

Perdew, J. P. et al. (2005). "Prescription for the design and selection of density functional approximations: More constraint satisfaction with fewer fits". *J. Chem. Phys.* **123**, 062201. DOI: `10.1063/1.1904565`.

Perrero, J. et al. (2023a). "Quantum mechanical modelling of the grain-surface formation of acetaldehyde on H$_2$O:CO dirty ice surfaces". *Mon. Not. R. Astron. Soc.* **525**, 2654. DOI: 10.1093/mnras/stad2459.

Perrero, J. et al. (2023b). "Theoretical modelling of the adsorption of neutral and charged sulphur-bearing species on to olivine nanoclusters". *Mon. Not. R. Astron. Soc.* **527**, 10697. DOI: 10.1093/mnras/stad3896.

Perrero, J. et al. (2024a). "Binding energies and vibrational spectral features of S$_n$ species on amorphous water-ice mantles: a quantum mechanical study". *Astrophys. J.* **971**, 36. DOI: 10.3847/1538-4357/ad5548.

Perrero, J. et al. (2024b). "Synthesis of urea on the surface of interstellar water ice clusters. A quantum chemical study". *Icarus* **410**, 115848. DOI: 10.1016/j.icarus.2023.115848.

Perrero, J. et al. (2022a). "Binding energies of interstellar relevant S-bearing species on water ice mantles: a quantum mechanical investigation". *Astrophys. J.* **938**, 158. DOI: 10.3847/1538-4357/ac9278.

Perrero, J. et al. (2022b). "Non-energetic formation of ethanol via CCH reaction with interstellar H$_2$O ices. A computational chemistry study". *ACS Earth Space Chem.* **6**, 496. DOI: 10.1021/acsearthspacechem.1c00369.

Perrero, J. et al. (2024c). "Binding energies of ethanol and ethylamine on interstellar water ices: synergy between theory and experiments". *Phys. Chem. Chem. Phys.* **26**, 18205. DOI: 10.1039/D4CP01934B.

Pople, J. A. et al. (1954). "Self-consistent orbitals for radicals". *J. Chem. Phys.* **22**, 571. DOI: 10.1063/1.1740120.

Pracht, P. et al. (2020). "Automated exploration of the low-energy chemical space with fast quantum chemical methods". *Phys. Chem. Chem. Phys.* **22**, 7169. DOI: 10.1039/C9CP06869D.

Rappe, A. K. et al. (1992). "UFF, a full periodic table force field for molecular mechanics and molecular dynamics simulations". *J. Am. Chem. Soc.* **114**, 10024. DOI: 10.1021/ja00051a040.

Redhead, P. (1962). "Thermal desorption of gases". *Vacuum* **12**, 203. DOI: https://doi.org/10.1016/0042-207X(62)90978-8.

Rice, O. K. et al. (1927). "Theories of unimolecular gas reactions at low pressures". *J. Am. Chem. Soc.* **49**, 1617. DOI: 10.1021/ja01406a001.

Rimola, A. et al. (2021). "Computational surface modelling of ices and minerals of interstellar interest - Insights and perspectives". *Minerals* **11**, 26. DOI: 10.3390/min11010026.

Roothaan, C. C. J. (1951). "New developments in molecular orbital theory". *Rev. Mod. Phys.* **23**, 69. DOI: 10.1103/RevModPhys.23.69.

Rothman, M. J. et al. (1980). "Analysis of an energy minimization method for locating transition states on potential energy hypersurfaces". *Chem. Phys. Lett.* **70**, 405. DOI: 10.1016/0009-2614(80)85361-9.

Salomon-Ferrer, R. et al. (2013). "An overview of the Amber biomolecular simulation package". *Wiley Interdiscip. Rev. Comput. Mol. Sci.* **3**, 198. DOI: https://doi.org/10.1002/wcms.1121.

Sauer, J. et al. (1994). "Theoretical study of van der Waals complexes at surface sites in comparison with the experiment". *Chem. Rev.* **94**, 2095.

Schrödinger, E. (1926). "An undulatory theory of the mechanics of atoms and molecules". *Phys. Rev.* **28**, 1049. DOI: 10.1103/PhysRev.28.1049.

Shavitt, I. (1977). "The method of configuration interaction". In: *Methods of Electronic Structure Theory*. Ed. by H. F. Schaefer. Boston, MA: Springer US, 189. DOI: 10.1007/978-1-4757-0887-5_6.

Sherrill, C. D. et al. (1999). "The configuration interaction method: advances in highly correlated approaches". *Adv. Quantum Chem.* **34**, 143. DOI: 10.1016/S0065-3276(08)60532-8.

Slater, J. C. (1930). "Note on Hartree's method". *Phys. Rev.* **35**, 210. DOI: 10.1103/PhysRev.35.210.2.

Spicher, S. et al. (2020). "Robust atomistic modeling of materials, organometallic, and biochemical systems". *Angew. Chem. Int. Ed.* **59**, 15665. DOI: https://doi.org/10.1002/anie.202004239.

Stöhr, M. et al. (2019). "Theory and practice of modeling van der Waals interactions in electronic-structure calculations". *Chem. Soc. Rev.* **48**, 4118. DOI: 10.1039/C9CS00060G.

Sure, R. et al. (2013). "Corrected small basis set Hartree-Fock method for large systems". *J. Comput. Chem.* **34**, 1672. DOI: 10.1002/jcc.23317.

Suter, M. T. et al. (2006). "Argon collisions with amorphous water ice surfaces". *Chem. Phys.* **326**, 281. DOI: 10.1016/j.chemphys.2006.02.012.

Svensson, M. et al. (1996). "ONIOM: a multilayered integrated MO + MM method for geometry optimizations and single point energy predictions. A test for Diels-Alder reactions and Pt(P(t-Bu)$_3$)$_2$ + H$_2$ oxidative addition". *J. Phys. Chem.* **100**, 19357. DOI: 10.1021/jp962071j.

Szabo, A. et al. (1996). *Modern quantum chemistry: introduction to advanced electronic structure theory*. Courier Corporation, Honolulu HI USA.

Tait, S. L. et al. (2005). "n-alkanes on MgO(100). II. Chain length dependence of kinetic desorption parameters for small n-alkanes". *J. Chem. Phys.* **122**. 164708, 164708. DOI: 10.1063/1.1883630.

Tatewaki, H. et al. (1980). "A systematic preparation of new contracted Gaussian-type orbital sets. III. Second-row atoms from Li through Ne". *J. Comput. Chem.* **1**, 205. DOI: 10.1002/jcc.540010302.

Tkatchenko, A. et al. (2009). "Accurate molecular van der Waals Interactions from ground-state electron density and free-atom reference data". *Phys. Rev. Lett.* **102**, 073005. DOI: 10.1103/PhysRevLett.102.073005.

Tkatchenko, A. et al. (2012). "Accurate and efficient method for many-body van der Waals interactions". *Phys. Rev. Lett.* **108**, 236402. DOI: 10.1103/PhysRevLett.108.236402.

Valeev, E. F. (2004). "Improving on the resolution of the identity in linear R12 ab initio theories". *Chem. Phys. Lett.* **395**, 190. DOI: 10.1016/j.cplett.2004.07.061.

van Duin, A. C. T. et al. (2001). "ReaxFF: a reactive force field for hydrocarbons". *J. Phys. Chem. A* **105**, 9396. DOI: 10.1021/jp004368u.

Vydrov, O. A. et al. (2009). "Nonlocal van der Waals density functional made simple". *Phys. Rev. Lett.* **103**, 063004. DOI: 10.1103/PhysRevLett.103.063004.

Vydrov, O. A. et al. (2012). "Benchmark assessment of the accuracy of several van der Waals density functionals". *J. Chem. Theory Comput.* **8**, 1929. DOI: 10.1021/ct300081y.

Wang, J. et al. (2004). "Development and testing of a general amber force field". *J. Comput. Chem.* **25**, 1157. DOI: https://doi.org/10.1002/jcc.20035.

Weigend, F. et al. (2005). "Balanced basis sets of split valence, triple zeta valence and quadruple zeta valence quality for H to Rn: Design and assessment of accuracy". *Phys. Chem. Chem. Phys.* **7**, 3297. DOI: 10.1039/B508541A.

Werner, H.-J. et al. (2007). "General orbital invariant MP2-F12 theory". *J. Chem. Phys.* **126**, 164102. DOI: 10.1063/1.2712434.

Williams, I. H. et al. (1982). "Use and abuse of the distinguished-coordinate method for transition-state structure searching". *J. Mol. Struct.* **89**, 365. DOI: 10.1016/0166-1280(82)80095-X.

Zheng, J. et al. (2011). "Minimally augmented Karlsruhe basis sets". *Theor. Chem. Acc.* **128**, 295. DOI: 10.1007/s00214-010-0846-z.

Zicovich-Wilson, C. M. et al. (1998a). "On the use of symmetry-adapted crystalline orbitals in SCF-LCAO periodic calculations. I. The construction of the symmetrized orbitals". *Int. J. Quantum Chem.* **67**, 299. DOI: `10.1002/(SICI)1097-461X(1998)67:5<299::AID-QUA3>3.0.CO;2-Q`.

Zicovich-Wilson, C. M. et al. (1998b). "On the use of symmetry-adapted crystalline orbitals in SCF-LCAO periodic calculations. II. Implementation of the self-consistent-field scheme and examples". *Int. J. Quantum Chem.* **67**, 311. DOI: `10.1002/(SICI)1097-461X(1998)67:5<311::AID-QUA4>3.0.CO;2-Y`.

Part II

Adsorption

Chapter 3

Binding Energies of S-bearing species on H$_2$O ice mantles

Introduction

The study of sulphur chemistry, with the aim of shedding light on the puzzling S-depletion problem, has been a recurring theme throughout my predoctoral research. As detailed in Section 1.2.1, the environments where sulphur depletion is more pronounced are dense molecular clouds (Fuente et al., 2023). These clouds are characterized by the presence of carbonaceous and silicaceous dust grains coated by icy mantles, constituted mainly of water (McClure et al., 2023). For this reason, it is important to understand the adsorption behaviour of S-bearing species onto water ice mantles, represented by crystalline and amorphous water ice models.

In '*Binding energies of interstellar relevant S-bearing species on water ice mantles: a quantum mechanical investigation*' (Perrero et al., 2022, *ApJ*, **938**, 158), the BEs of 17 S-bearing species were computed, selecting small molecules that either have been detected in the ISM or are likely candidates. The list includes closed-shell (CS, C$_3$S, CH$_3$SH, H$_2$CS, H$_2$S, H$_2$S$_2$, OCS, SO$_2$) and open-shell species (HS, HS$_2$, and NS with a doublet ground state; C$_2$S, C$_4$S, S, S$_2$, and SO with a triplet ground state). Notably, approximately half of these species exhibit an open-shell configuration, a characteristic attributed to the rarefied conditions of the ISM, which allows the survival of reactive and unstable species.

Furthermore, in '*Binding energies and vibrational spectral features of S$_n$ species on amorphous water-ice mantles: a quantum mechanical study*' (Perrero et al., 2024, *ApJ*, **971**, 36), the BEs and the vibrational spectral features of sulphur allotropes from S$_2$ to S$_8$ were characterised. This class of species has garnered a lot of interest in recent years, largely due to their potential role as S-reservoir candidates.

Results

The S-bearing species characterised in these works can be classified depending on the type of interaction they establish with the ice model.

- H-bond donors and H-bond acceptors: CH$_3$SH, H$_2$CS, H$_2$S, H$_2$S$_2$, HCS, HS, and HS$_2$.

- Only H-bond acceptors: OCS, SO$_2$, NS, and SO.

- Molecules with a carbene-like terminal carbon atom (thus, resembling the Lewis structure of a carbene): CS, C$_2$S, C$_3$S, and C$_4$S.
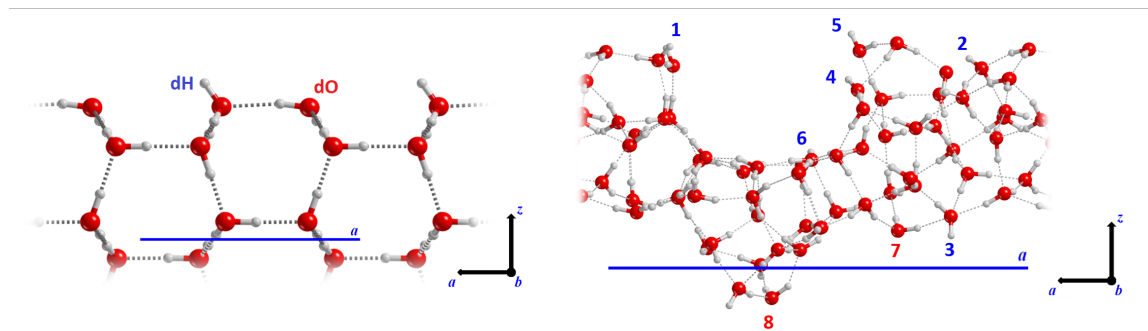
Figure 3.1: Side view of the crystalline (010) water P-ice slab model (left panel) and of the amorphous water ice surface model (right panel). The numbers identify the adsorption sites: those in blue represent dangling hydrogen atoms (dH), while those in red represent dangling oxygen atoms (dO).

- Species interacting mainly through dispersive interactions: S, S_2, S_3, S_4, S_5, S_6, S_7, and S_8.

The calculations were conducted using CRYSTAL17 (Dovesi et al., 2018) employing three DFT functionals: the hybrid B3LYP-D3(BJ) for closed-shell species; the hybrid meta-GGA M06-2X for open-shell species; and the hybrid BHLYP-D3(BJ) for S_n ($n = 2-8$) species. These functionals were combined with an Ahlrichs triple zeta valence quality basis set supplemented with a double set of polarisation functions (Ahlrichs-VTZ*, Schäfer et al., 1992). Two periodic water ice models were adopted to mimic the ice mantle (see Figure 3.1): a 2×1 supercell (010) slab model cut from the bulk of a proton-ordered crystalline ice (CI, Casassa et al., 1997), and an amorphous water ice surface (ASW), built by joining three amorphous water clusters and applying PBCs to the structure (Ferrero et al., 2020).

The CI model offers two binding sites, constituted by the dangling H and the dangling O exposed by the (010) surface. In contrast, the ASW model presents numerous binding sites, eight of which were selected based on their H-bonding capability (dH1–dH6 as H-bond donors and dO7–dO8 as H-bond acceptors). The initial geometries were manually constructed, adhering to the principle of electrostatic complementarity between the adsorbate and the ice model. For the large and nonpolar species ranging from S_3 to S_8, the investigation was limited to two surface binding sites, representing the cavity region (between dH4 and dH6 sites) and the flat portion of the model (between dH3 and dO7 sites). This limitation was due to their interactions, primarily governed by London dispersion forces, which depend on the contact between the adsorbate and the surface. In contrast, electronic effects, such as electrostatic, polarisation and quantum exchange-repulsion interactions, played a minor role.

The analysis of the collected data highlights the critical importance of accurately describing London dispersion interactions to characterise the behaviour of S-bearing species, especially when the number of S atoms increases (as in the S_n species sequence). In general, weak interactions typically constitute at least 50% of the BE(0)s, with few exceptions such as H_2S and SO_2, where two H-bonds can be established with the dH and dO atoms of the surface. This observation aligns with the higher atomic polarisability of third-period atoms compared to C, N, and O containing molecules, resulting in weaker interactions of S-bearing species with ice. Consequently, their surface mobility is also affected, with species possessing lower BE(0)s expected to diffuse faster than those with higher BE(0)s, setting up constrains on the reactions feasible on an icy surface (Cuppen et al., 2017;
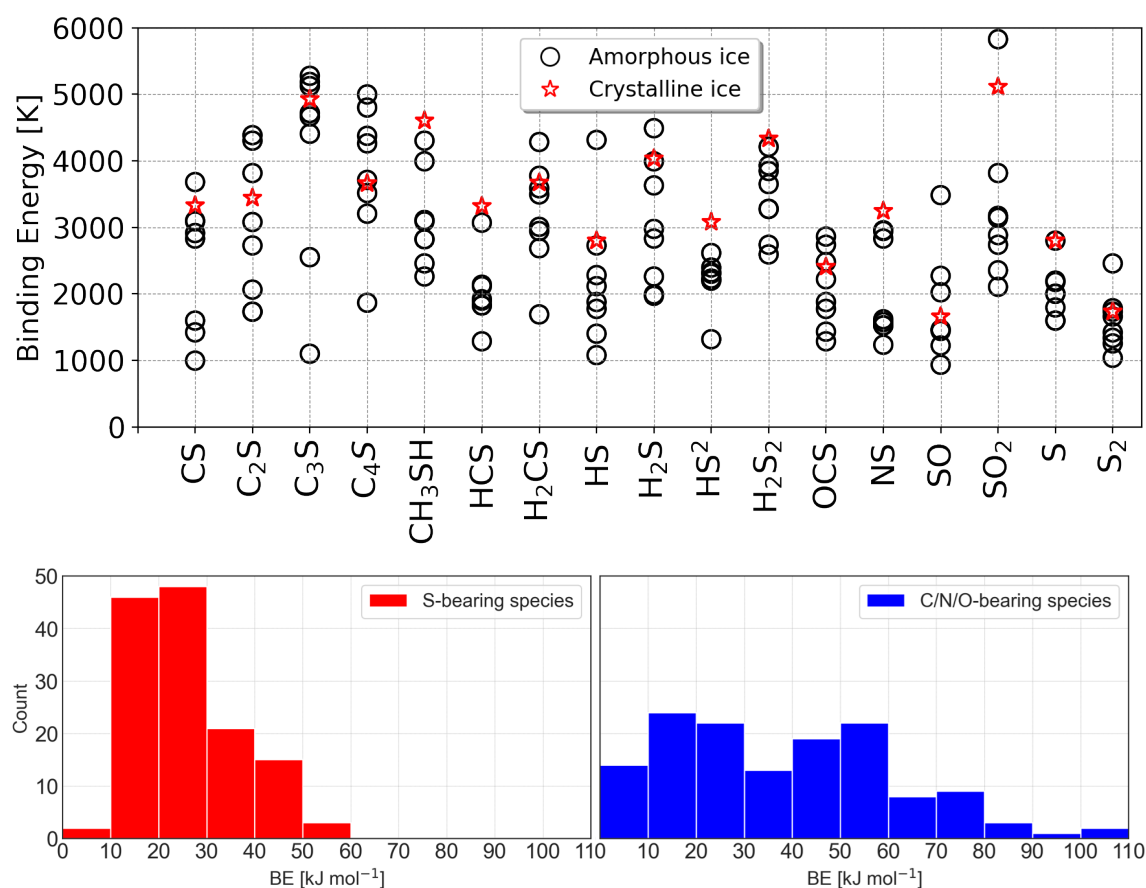
Figure 3.2: *Top panel*: computed BE(0)s (in Kelvin). For each species, black circles represent ZPE-corrected BEs computed onto the amorphous ice model, while red stars correspond to the ZPE-corrected BEs obtained for the crystalline ice model. *Bottom panel*: distribution of BE(0)s (in kJ mol^{-1}) computed on the amorphous ice model for S-bearing species (red) and the C/N/O-bearing species characterised in Ferrero et al. (2020).

Kouchi et al., 2020).

On average, the dispersion contributions to the BE(0)s are higher when the adsorption takes place on ASW than on CI due to the closer contact of the adsorbate with the ice surface. While in the CI model the H-bond chains extend to infinity ensuring a reinforcement of the H-bonding strength (cooperativity effect), this is not the case for the ASW model. In ASW, the random organisation of the water molecules breaks the H-bonds chain extensions, reducing the H-bonding cooperativity and, therefore, its strength. This, in turn, also affects the H-bonding strength exhibited by the terminal OH groups involved in the interactions with the adsorbates, decreasing the corresponding BE(0) values, as can be observed in the top panel of Figure 3.2.

In the periodic table, sulphur belongs to the third period, has a larger radius, and is more polarisable with respect to C/N/O second-period atoms. The computation of BE(0)s of S-bearing species was preceded by a similar work in which C/N/O-bearing species were targeted (Ferrero et al., 2020). Accordingly, the distributions of BE(0)s for the two sets of molecules were compared, highlighting how the simple presence of one heavier atom in a molecule can modify the adsorption properties and related parameters, such as the BE(0) values. The distribution of BE(0)s on the ASW ice in Ferrero et al. (2020) has
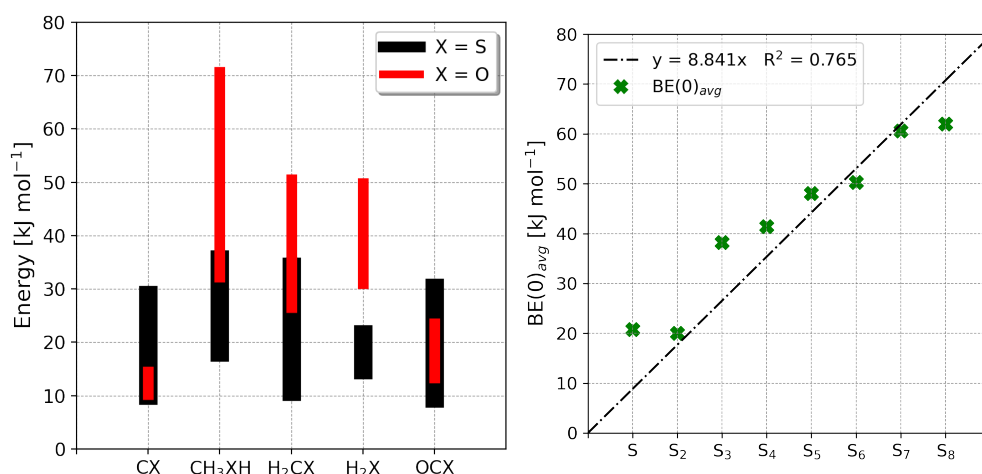
Figure 3.3: *Left panel*: comparison between selected BE(0)s (in kJ mol^{-1}) of S-bearing species vs. O-bearing species adsorbed onto the crystalline ice surface. *Right panel*: correlation between the BE(0)$_{avg}$ (in kJ mol^{-1}) and the number n of atoms of each S_n species. The linear fit does not seem appropriate to define the trend, as it appears that the increase in BE(0) happens in steps every couple of species.

a bimodal character (see bottom panel of Figure 3.2), indicating two different adsorption behaviours in the set of the considered species: a group of low BE(0)s (characterised by dispersive interactions), and a group of high BE(0)s (amphiprotic and larger species involved in the H-bond). In contrast, S-containing species span a much narrow range of BE(0)s, suggesting a common adsorption feature, despite the diverse chemical structures. The analysis of the dispersive and pure electrostatic contributions to the BE(0)s of these species indicates that weak interactions are the most relevant and crucial forces in the description of the adsorption of S-containing species on ices and, thus, they are also responsible for the similarity in the BE(0)s of the pool of S-bearing species characterised.

In addition to these general considerations, a punctual comparison between S-bearing and O-bearing species on CI can be drawn for some cases in order to highlight a few exceptions to the general behaviour of the set of molecules (see left panel of Figure 3.3). As a rule of thumb, one would expect S-bearing molecules to exhibit lower BE(0)s than the corresponding O-bearing ones. However, notable exceptions exist, such as the CS/CO pair, where an opposite trend is observed, and the OCS/CO_2 pair, which instead shows significant similarities. CS exhibits a larger BE(0) and a lower percentage of dispersive energy than its O-analog, CO, due to the dipole moment of these species. Indeed, CS has a large dipole moment (1.9 D), at variance with the negligible one of CO. This causes CS to lay closer to surface and enhances the interaction between the S atom and the dangling O atoms available on the two sides of the molecules.

In Figure 3.4, it is possible to observe the shorter distances between CS and the ice with respect to CO, and how the positively charged portion of the adsorbate is oriented towards the negatively charged zones of the surface. On the other hand, despite differing in the electrostatic/dispersion contribution of their BE(0), both OCS and CO_2 interacts similarly with the ice mantle: they have a linear geometry, an almost null dipole, and they establish a weak H-bond with a dangling H of the ice surface.

The obtained BE ensembles for the ASW model matches well with both the experimental and the computed BEs listed in the literature, often bridging the discrepancies between
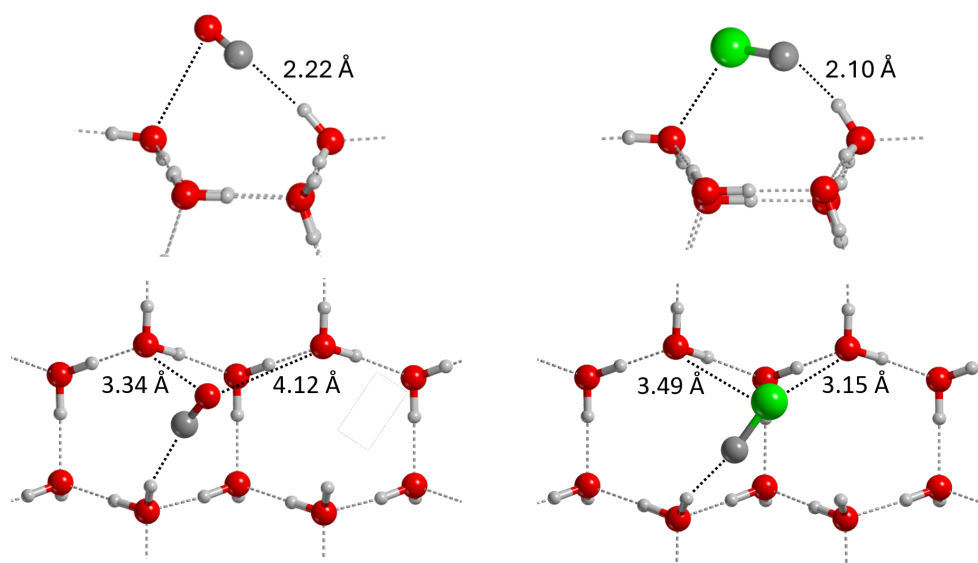
Figure 3.4: Adsorption geometry of S-bearing vs. O-bearing species at crystalline P-ice (010) surface, detail of CO (adapted from Ferrero et al., 2020) and CS adsorption. Top panels show the lateral view, whereas bottom panels display the top view. Distances between atoms are given in Å.

the single values provided in different studies (Wakelam et al., 2017; Penteado et al., 2017; Das et al., 2018). S_n species present a unique case, as the only reported values in the literature have been partly determined from experiments and partly extrapolated using the linear addition method (e.g., Penteado et al., 2017; Cazaux et al., 2022). As depicted in the right panel of Figure 3.3, the average binding energy of each species, $BE(0)_{avg} = (BE(0)_{cavity} + BE(0)_{flat})/2$, plotted against the number of S atoms of the adsorbate shows that the increase in BE(0)s with the number of S atoms does not simply scale linearly. Rather, it seems that close couples (S_1–S_2, S_3–S_4, S_5–S_6 and S_7–S_8) exhibit almost the same BE(0). While the first increase between pairs is steep (20 kJ mol^{-1}), the others are more moderate (10 kJ mol^{-1}). This seems to be due to the number of S atoms facing the ice surface (three S atoms for S_5–S_6, four S atoms for S_7–S_8 cases), significantly changing the dispersive contributions to the BE(0)s. This highlights the necessity of considering binding sites characterised by diverse atomistic environments in order to achieve a more accurate description of a real ice mantle. Moreover, BE(0) distributions are essential in providing robust parameters for numerical models describing the chemical evolution of the Universe.

Regarding the simulation of vibrational spectral features of the S_n species, both IR and Raman spectra were computed with the aim of providing spectroscopic data for these species adsorbed onto an ice surface, and finding some diversity between gas-phase species and adsorbed ones. The spectra analysis revealed that a discernible shift can only be measured for the open-chain S_2, S_3, and S_4 species, whereas larger rings exhibit minimal shifts attributable to interactions with the ice surface, rendering the distinction between free and adsorbed molecules a challenging task (see Figure 3.5).

In principle, the present outcome may guide the interpretation of the JWST spectra detection of interstellar ice, at least as far as the IR spectra are concerned. However, the absolute intensity of each IR vibrational mode is an important parameter as it regulates the likelihood of the observation. The results show many IR peaks with almost negligible intensities, which become smaller as the S-chain length increase, due to their almost null dipole perturbations. Unfortunately, Raman spectra of the interstellar matter cannot be
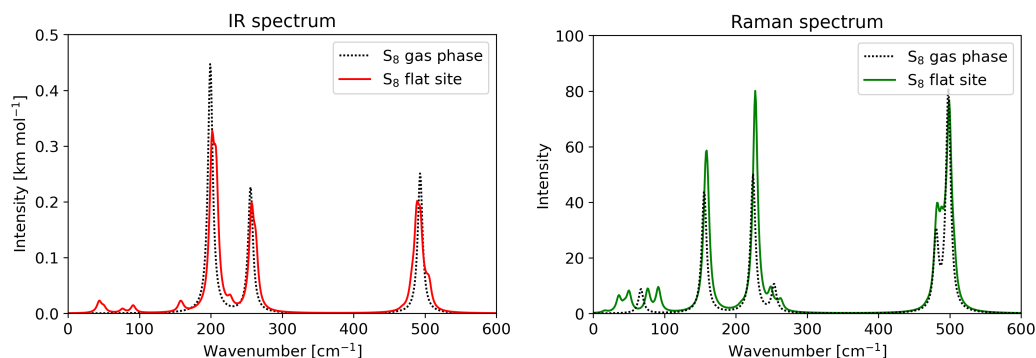
Figure 3.5: IR and Raman spectra of S_8 computed at BHLYP-D3(BJ)/A-VTZ* level of theory. The gas-phase features (dotted line) are compared against those of the molecule adsorbed on the flat region of the amorphous ice model (solid line). IR intensities are in km mol^{-1}, while Raman intensities are provided in arbitrary units. Different vibrational modes are active in the two spectra.

observed with the current technology, although they emerge as the preferred technique for the detection of these species in the mid-infrared window, as the Raman intensities are quite high, depending on the polarisability of the molecule (Shingledecker et al., 2020). Indeed, S is a large and easily polarisable atom, imparting high polarisability to the S_n species. For the time being, Raman can be adopted in terrestrial experiments to characterise S-bearing species.

Future perspectives

The computational procedure adopted in these works shows some limitations. For instance, the modelled amorphous water surface was not exhaustively explored with an unbiased procedure, thus possibly affecting the resulting ensemble of BEs. Moreover, the few binding sites characterised do not allow us to define a true statistical distribution with a mean value and standard deviation. In our group, the ACO-FROST scheme was developed to overcome these limitations. The code enables the construction of an ice cluster by random addition of water molecules up to 1000 units, thus sampling the binding sites offered by such model without any user bias (Germain et al., 2022). Thanks to the use of an ONIOM(QMHigh/QMLow) approach to compute the BE of a species at each binding site, this procedure allows to compute BE distributions at the accurate DLPNO-CCSD(T) level of theory. This workflow has been applied to NH_3 and H_2O (Tinacci et al., 2022; Tinacci et al., 2023), and more recently to H_2S (Bariosco et al., 2024).

Another interesting point concerns the simulation of IR and Raman spectra. The literature offers highly accurate theoretical simulations of gas-phase S-bearing species vibrational features, in very good agreement with the experimental spectra. Such studies help providing features for the detection of these species in the gas phase, but also assigning each feature to the specific atomic motion that caused the emergence of vibrational bands in the spectra. The focus of the study was to determine whether the adsorption of a species onto the ice could be responsible for a shift in its IR and Raman absorption bands, without aiming at reproducing the experimentally measured gas-phase features. Therefore, an effort could be done in improving the accuracy of the computed data, in addition to enlarging the pool of species characterised spectroscopically. This could provide useful data for the identification of these species, in view of the huge quantity of spectra that are being

measured by the JWST and other facilities, regarding not only gas-phase species, but also ice mantles composition (McClure et al., 2023; Rocha et al., 2024).

References

Bariosco, V. et al. (2024). "The binding energy distribution of H₂S: why it is not the major sulphur reservoir of the interstellar ices". *Mon. Not. R. Astron. Soc.* **531**, 1371. DOI: `10.1093/mnras/stae1210`.

Casassa, S. et al. (1997). "Proton-ordered models of ordinary ice for quantum-mechanical studies". *J. Chem. Phys.* **106**, 8030.

Cazaux, S. et al. (2022). "Photoprocessing of H₂S on dust grains. Building S chains in translucent clouds and comets". *Astron. Astrophys.* **657**, A100. DOI: `10.1051/0004-6361/202141861`.

Cuppen, H. M. et al. (2017). "Grain surface models and data for astrochemistry". *Space Sci. Rev.* **212**, 1. DOI: `10.1007/s11214-016-0319-3`.

Das, A. et al. (2018). "An approach to estimate the binding energy of interstellar species". *Astrophys. J. Suppl. Ser.* **237**, 9. DOI: `10.3847/1538-4365/aac886`.

Dovesi, R. et al. (2018). "Quantum-mechanical condensed matter simulations with CRYSTAL". *Wiley Interdiscip. Rev. Comput. Mol. Sci.* **8**, e1360. DOI: `10.1002/wcms.1360`.

Ferrero, S. et al. (2020). "Binding energies of interstellar molecules on crystalline and amorphous models of water ice by ab initio calculations". *Astrophys. J.* **904**, 11. DOI: `10.3847/1538-4357/abb953`.

Fuente, A. et al. (2023). "Gas phase Elemental abundances in Molecular cloudS (GEMS). VII. Sulfur elemental abundance". *Astron. Astrophys.* **670**, A114. DOI: `10.1051/0004-6361/202244843`.

Germain, A. et al. (2022). "Computer generated realistic interstellar icy grain models: physicochemical properties and interaction with NH₃". *ACS Earth Space Chem.* **6**, 1286. DOI: `10.1021/acsearthspacechem.2c00004`.

Kouchi, A. et al. (2020). "Direct measurements of activation energies for surface diffusion of CO and CO₂ on amorphous solid water using in situ transmission electron microscopy". *Astrophys. J. Lett.* **891**, L22. DOI: `10.3847/2041-8213/ab78a2`.

McClure, M. K. et al. (2023). "An Ice Age JWST inventory of dense molecular cloud ices". *Nat. Astron.* **7**, 431. DOI: `10.1038/s41550-022-01875-w`.

Penteado, E. M. et al. (2017). "Sensitivity analysis of grain surface chemistry to binding energies of ice species". *Astrophys. J.* **844**, 71. DOI: `10.3847/1538-4357/aa78f9`.

Perrero, J. et al. (2024). "Binding energies and vibrational spectral features of Sₙ species on amorphous water-ice mantles: a quantum mechanical study". *Astrophys. J.* **971**, 36. DOI: `10.3847/1538-4357/ad5548`.

Perrero, J. et al. (2022). "Binding energies of interstellar relevant S-bearing species on water ice mantles: a quantum mechanical investigation". *Astrophys. J.* **938**, 158. DOI: `10.3847/1538-4357/ac9278`.

Rocha, W. et al. (2024). "JWST Observations of Young protoStars (JOYS+): Detecting icy complex organic molecules and ions - I. CH₄, SO₂, HCOO⁻, OCN⁻, H₂CO, HCOOH, CH₃CH₂OH, CH₃CHO, CH₃OCHO, and CH₃COOH". *Astron. Astrophys.* **683**, A124. DOI: `10.1051/0004-6361/202348427`.

Schäfer, A. et al. (1992). "Fully optimized contracted Gaussian basis sets for atoms Li to Kr". *J. Chem. Phys.* **97**, 2571. DOI: `10.1063/1.463096`.

Shingledecker, C. et al. (2020). "Isomers in interstellar environments. I. The case of Z- and E-cyanomethanimine". *Astrophys. J.* **897**, 158. DOI: `10.3847/1538-4357/ab94b5`.

Tinacci, L. et al. (2022). "Theoretical distribution of the ammonia binding energy at interstellar icy grains: a new computational framework". *ACS Earth Space Chem.* **6**, 1514. DOI: 10.1021/acsearthspacechem.2c00040.

Tinacci, L. et al. (2023). "Theoretical water binding energy distribution and snowline in protoplanetary disks". *Astrophys. J.* **951**, 32. DOI: 10.3847/1538-4357/accae8.

Wakelam, V. et al. (2017). "Binding energies: new values and impact on the efficiency of chemical desorption". *Mol. Astrophys.* **6**, 22. DOI: 10.1016/j.molap.2017.01.002.

Binding Energies of Interstellar Relevant S-bearing Species on Water Ice Mantles: A Quantum Mechanical Investigation

Jessica Perrero[1,2] ⓘ, Joan Enrique-Romero[1] ⓘ, Stefano Ferrero[1] ⓘ, Cecilia Ceccarelli[3] ⓘ, Linda Podio[4] ⓘ, Claudio Codella[3,4] ⓘ, Albert Rimola[1] ⓘ, and Piero Ugliengo[2] ⓘ

[1] Departament de Química, Universitat Autònoma de Barcelona, Bellaterra, E-08193, Catalonia, Spain; albert.rimola@uab.cat
[2] Dipartimento di Chimica and Nanostructured Interfaces and Surfaces (NIS) Centre, Università degli Studi di Torino, via P. Giuria 7, I-10125, Torino, Italy
piero.ugliengo@unito.it
[3] Univ. Grenoble Alpes, CNRS, Institut de Planétologie et d'Astrophysique de Grenoble (IPAG), F-38000 Grenoble, France
[4] INAF, Osservatorio Astrofisico di Arcetri, Largo E. Fermi 5, I-50125 Firenze, Italy
Received 2022 July 6; revised 2022 September 12; accepted 2022 September 14; published 2022 October 24

Abstract

Binding energies (BEs) are one of the most important parameters for astrochemical modeling determining, because they govern whether a species stays in the gas phase or is frozen on the grain surfaces. It is currently known that, in the denser and colder regions of the interstellar medium, sulfur is severely depleted in the gas phase. It has been suggested that it may be locked into the grain icy mantles. However, which are the main sulfur carriers is still a matter of debate. This work aims to establish accurate BEs of 17 sulfur-containing species on two validated water ice structural models, the proton-ordered crystalline (010) surface and an amorphous water ice surface. We adopted density functional theory-based methods (the hybrid B3LYP-D3(BJ) and the hybrid meta-GGA M06-2X functionals) to predict structures and energetics of the adsorption complexes. London's dispersion interactions are shown to be crucial for an accurate estimate of the BEs due to the presence of the high polarizable sulfur element. On the crystalline model, the adsorption is restricted to a very limited number of binding sites with single valued BEs, while on the amorphous model, several adsorption structures are predicted, giving a BE distribution for each species. With the exception of a few cases, both experimental and other computational data are in agreement with our calculated BE values. A final discussion on how useful the computed BEs are with respect to the snow lines of the same species in protoplanetary disks is provided.

Unified Astronomy Thesaurus concepts: Interstellar dust (836); Surface ices (2117); Interstellar molecules (849); Dense interstellar clouds (371); Interstellar medium (847); Solid matter physics (2090); Interstellar dust processes (838); Computational methods (1965)

1. Introduction

Stars like our Sun begin their journey in the interstellar medium (ISM), where star formation takes place in dense (10^3–10^4 cm^{-3}) and cold (10 K) regions, the so-called molecular clouds. In the past, it was thought that the ISM was too harsh an environment for molecules to survive and thrive. However, almost 80 yr ago, the first diatomic molecules (the methylidyne radical CH, its cation CH$^+$, and the cyano radical CN) were detected by means of optical and ultraviolet spectroscopy (Swings & Rosenfeld 1937; McKellar 1940; Douglas & Herzberg 1942), which indeed indicated that chemistry is present and has an important role in the ISM.

At present, we count more than 270 detected gas-phase species (McGuire 2021), a number that constantly increases given the enhanced performances of the observational facilities (e.g., Yebes 40 m, IRAM 30 m, NOEMA, the Atacama Large Millimeter/submillimeter Array (ALMA), and Green Bank Telescope (GBT)), and the expectation of the new results provided by the James Webb Space Telescope. As a consequence of these thrilling discoveries, curiosity concerning the chemistry of the ISM has been growing more and more keen.

The characteristic densities and temperatures of molecular clouds allow (i) the molecules to survive, since the external UV fields are highly diminished, and (ii) the formation of thick icy mantles coating the surfaces of dust grains, due to the adsorption and in situ synthesis of species and their subsequent hydrogenation. The resulting icy mantles are dominated by water, but they also contain other volatile species like CO, CO$_2$, CH$_3$OH, and NH$_3$, and hence are referred to as "dirty ices" (Boogert et al. 2015).

The phenomena occurring on the icy mantle surfaces are of paramount importance from a chemical point of view. Indeed, ice mantles are thought to facilitate the occurrence of reactions taking place at their surfaces, primarily exhibiting three functions: (i) as pre-concentrators of chemical species, especially relevant in the low-density environments of molecular clouds, where the rate of collision between gas-phase species is extremely small, (ii) as chemical catalysts, by decreasing the activation energies of the reactions, and hence overcoming the energy barriers under the interstellar conditions (Zamirri et al. 2019b), and (iii) as third bodies, by absorbing the large energy excess released by exothermic reactions, without undermining the stability of the newly formed products (Pantaleone et al. 2020, 2021). The first and the third points are the keys to successful recombination reactions.

For a grain surface reaction to take place, at least one of the two reactants needs to be adsorbed on the grain. The adsorption is regulated by two variables: the dust temperature, and the binding energy (BE) of the adsorbed species. The latter quantity defines how strong the interaction between the species and the surface is, and dictates the chance that a given adsorbed

species can be ejected into the gas phase: the higher the BE, the higher the temperature required to thermally desorb. In the current astrochemical models, BE values are important input parameters, not only to consider likely desorption events (e.g., Penteado et al. 2017) but to simulate diffusion processes on the surfaces, as the diffusion barriers are usually assumed to be a fraction of the BE (Mispelaer et al. 2013; Karssemeijer & Cuppen 2014; Ghesquiere et al. 2015; Lauck et al. 2015; Cuppen et al. 2017; He et al. 2017, 2018; Cooke et al. 2018; Kouchi et al. 2020; Maté et al. 2020). Therefore, BEs are crucial parameters in determining the ISM chemistry and its resulting composition (Penteado et al. 2017; Wakelam et al. 2017; Ferrero et al. 2020; Enrique-Romero et al. 2021).

1.1. Previous Studies of the BEs

Determining BEs is a challenging task (Minissale et al. 2022). From an experimental point of view, effective and coverage-dependent BEs are obtained via temperature programmed desorption (TPD) experiments. TPD consists of two steps: first, the substrate, maintained at a constant temperature, is exposed to the adsorption of the species; then, the temperature is increased until the desorption of the species, which is collected and analyzed by a mass spectrometer. The BEs are then extracted by applying the direct inversion method through the Polanyi–Wigner equation (e.g., Dohnálek et al. 2001). Despite its great usefulness, this technique shows two limitations: (i) the obtained BEs depend not only on the morphology and the composition of the substrate but also on the regimes in which the experiments are performed, i.e., submonolayer, monolayer, or multilayer (e.g., Noble et al. 2012; He et al. 2016; Chaabouni et al. 2018) and will return coverage-dependent BEs, and (ii) it measures a desorption enthalpy, a quantity that is equal to the BE only in the absence of other activated processes, like ice restructuring, usually assumed to be negligible (He et al. 2016).

Despite the numerous literature studies that have investigated the desorption processes by means of TPD (e.g., Collings et al. 2004; Noble et al. 2012; Dulieu et al. 2013; Fayolle et al. 2016; He et al. 2016; Smith et al. 2016), only a limited variety of molecules has been considered, in particular, stable closed-shell species, in contrast to the large variety of interstellar species. Moreover, the employed substrates are almost invariably water ices.

A possible alternative to TPD is to adopt state-of-the-art computational chemistry to simulate the adsorption process. The simulation can handle both closed- and open-shell species, allotting some extra care for the latter. The main limitation is the trade-off between the system size (the icy grain model) and the accuracy of the calculation. A number of computational studies have reported the BEs of important astrochemical species like H, H_2, N, O, HF, CO, and CO_2 on icy surfaces modeled by periodic/cluster crystalline/amorphous systems (e.g., Al-Halabi & Van Dishoeck 2007; Karssemeijer & Cuppen 2014; Zamirri et al. 2017; Shimonishi et al. 2018; Zamirri et al. 2019a; Bovolenta et al. 2020; Ferrero et al. 2020). Other works addressed the BEs of a large number of species, adopting very approximated models for the substrate. Two examples are the works of Wakelam et al. (2017) and Das et al. (2018), in which the ice surface simulated by water clusters of minimal nuclearity allowed the prediction of the BEs for 100 species. In Wakelam et al. (2017), a single water molecule was adopted to represent the ice surface, while recovering the

missing components of the BEs through a clever fitting procedure against selected experimental BE values. In Das et al. (2018), the adoption of clusters from one to six water molecules allowed them to study the BE of 16 species, with the puzzling result that water tetramer was found to be the best model for ice.

One way to generate computer models for amorphous ices is by using water clusters cut out from a crystalline ice, heating them up by molecular dynamics runs and by quenching at low temperatures (Shimonishi et al. 2018; Rimola et al. 2021b). Another approach is to refer to a model repeated in space by the periodic boundary conditions. This allows for the simulation of both the crystalline ice (here adopting an already studied proton-ordered model by Casassa et al. 1997) and an amorphous one. In the latter case, the usual procedure is starting from a large unit cell of a crystalline ice and performing a number of heating/freezing cycles to arrive to an amorphous ice model. Another strategy, recently proposed by the ACO-FROST scheme (Germain et al. 2022), consists of growing icy clusters by a random step-by-step addition of molecular water molecules.

More recently, Ferrero et al. (2020) computed a large set of BEs for 21 astrochemically relevant species, on both crystalline and amorphous surfaces of water ice. Both models ensured that hydrogen-bond cooperativity (of fundamental relevance to obtain accurate BE values) is fully taken into account, at variance with the small ice clusters adopted by Wakelam et al. (2017) and Das et al. (2018). For the crystalline icy model, only very few adsorption sites were available, limiting the BEs to one or two distinct values per species. For the amorphous ice model, however, the complex surface morphology allowed the calculation of multiple BE values for each species, resulting in a BE range better describing the variety of binding sites expected on real amorphous ice mantles.

In the present work, we apply the methodology of Ferrero et al. (2020) in order to enlarge the set of BEs. The focus here is on the adsorption of 17 interstellar relevant S-bearing species, namely: CS, $C_2S^{\bullet\bullet}$, C_3S, $C_4S^{\bullet\bullet}$, CH_3SH, H_2CS, $HS^{\bullet}$, H_2S, $HS_2^{\bullet}$, H_2S_2, $NS^{\bullet}$, OCS, $S^{\bullet\bullet}$, $S_2^{\bullet\bullet}$, $SO^{\bullet\bullet}$, and SO_2 (dots indicate the unpaired electrons). The chosen species satisfy two criteria: (i) they are neutral species, since positive ions become neutral when landing on negatively charged dust grains (Walmsley et al. 2004; Ceccarelli & Dominik 2005; Rimola et al. 2021a) as long recognized (Draine & Sutin 1987; Rae et al. 2004; Mason et al. 2014), and (ii) they envisage at most six atoms to ensure relatively compact structures needed to properly probe the largest number of adsorption sites on ice models with relatively small unit cells.

1.2. The Sulfur Depletion

The choice of studying the BEs of S-bearing species is due to a long standing issue in the field of astrochemistry: the sulfur depletion problem. In dense clouds, sulfur is severely depleted from the gas phase (e.g., Tieftrunk et al. 1994; Ruffle et al. 1999; Wakelam et al. 2004; Phuong et al. 2018; Vastel et al. 2018; van't Hoff et al. 2020) by more than 2 orders of magnitude with respect to the solar system S abundance ([S]/[H] = 1.8×10^{-5}; Anders & Grevesse 1989; Woods et al. 2015). Therefore, sulfur may freeze out on dust grains after its hydrogenation, or react with other species in a similar way as atomic oxygen. H_2S was expected to be the main sink of sulfur on dust grains (Garrod et al. 2007; Jiménez-Escobar & Muñoz Caro 2011), but it has

never been directly detected on interstellar ices yet. The only species detected in the ice mantles are OCS and, tentatively, SO_2 (Boogert et al. 2015). Accordingly, the most important S-carriers are still unknown. Nowadays, the most likely species that act as reservoirs of S are thought to be organosulfur compounds (Laas & Caselli 2019) and polysulphanes (H_2S_n; Druard & Wakelam 2012). These are refractory species that, once trapped on the mantles or in the core of the grains, cannot desorb and, therefore, become undetectable (Woods et al. 2015). In the last three years, seven new gas-phase S-bearing species were identified, most of them in TMC-1 (Cernicharo et al. 2021; Rodríguez-Almeida et al. 2021), and characterized by a C–S chemical bond.

A recent review of the laboratory experiments performed on the chemistry of sulfur in the condensed phase has highlighted that the formation of SO_2, SO_3, hydrates of H_2SO_4, and related species is very common when performing photolysis, proton-irradiation, and radiolysis of mixed ices. However, neutral–neutral reactions have yet to be deeply explored. Moreover, gas-phase chemistry is likely to be a major contributor in sulfur astrochemistry (Mifsud et al. 2021).

The formation of organosulphur molecules was observed experimentally for the first time in the work of Ruf et al. (2019), where a 2:1:1 mixture of $H_2O:CH_3OH:NH_3$ ice was bombarded with S^{7+} ions, although showing a possible source of compounds relative to more evolved environments, like icy moons, Kuiper Belt objects, comets, and their building blocks.

In diffuse clouds, sulfur is mostly present in its ionized atomic form S^+, and close to the cosmic abundance (Jenkins 2009), it progressively depletes as the cloud evolves (Hily-Blant et al. 2022). Sulfur depletion in protoplanetary disks and later stages can be explained by the presence of refractory sulfide minerals, such as FeS, in the grains (Keller et al. 2002; Kama et al. 2019).

With the present work, thus, we aim to contribute to this puzzling subject by providing a set of accurate BE values of several S-bearing species, which can be used in numerical modeling studies aimed at rationalizing observations and laboratory experiments.

2. Methodology

Since the calculations follow the same procedure as Ferrero et al. (2020), we refer to this work for the equations used here to compute the BEs of the S-bearing species set. Moreover, the reader can find details on these expressions in Appendix A. A thorough guide to the computation of BEs is available in the Supplementary Material.

2.1. Computational Details

We adopted a periodic approach to model the water ice surfaces and the adsorption of the 17 S-bearing species on them. The calculations were performed with the periodic ab initio code CRYSTAL17 developed by Dovesi et al. (2018), which adopts localized Gaussian functions as basis sets. This code exploits the local combination of atomic orbitals (LCAO) approximation, expanding the Bloch functions of periodic systems as a linear combination of atom-centered Gaussian functions. This software implements both the Hartree–Fock (HF) and Kohn–Sham self-consistent field methods to solve the electronic Schrödinger equation, taking advantage of the symmetry of the system, when present. Thanks to its capability to simulate systems with periodicity ranging from zero

(molecules) to three (solid bulks) dimensions, it allows us to rigorously define true slabs to modeling surfaces without the need of artificial replica along the direction perpendicular to the slab plane, as usually implemented in codes adopting plane waves basis sets.

On the crystalline model, the hybrid B3LYP (Becke 1988, 1993; Lee et al. 1988) and the hybrid meta-GGA M06-2X (Zhao & Truhlar 2008) density functionals were used in the geometry optimizations and in computing the BEs of closed-shell and open-shell species, respectively. To account for dispersion interactions, the hybrid B3LYP functional was combined with the Grimme's D3 empirical correction with the Becke–Johnson (BJ) damping scheme (i.e., B3LYP-D3(BJ)) (Grimme et al. 2010, 2011; Sure & Grimme 2013). The hybrid meta-GGA M06-2X functional was used together with a spin-unrestricted formalism (Pople et al. 1995) to model the adsorption of open-shell species (with one or two unpaired electrons) because it better describes their adsorption properties (Ferrero et al. 2020) due to its higher percentage of exact exchange (54% compared to the 20% of B3LYP). Note that for M06-2X, the D3(BJ) correction for dispersion was not applied because, for this functional, the description of the dispersion component is already included in its definition. For this reason, the contribution of the dispersion component to the BEs can be worked out only for the closed-shell species (computed at B3LYP-D3(BJ)). The two density functional theory (DFT) methods have been used in combination with the Ahlrichs triple zeta valence quality basis set supplemented with a double set of polarization functions (i.e., A-VTZ*; Schäfer et al. 1992). Thus, for the crystalline models, the BEs were computed from the DFT energies that resulted from the DFT optimized structures. This scheme is hereafter referred to as DFT//DFT. All of the BEs were corrected for the basis set superposition error (BSSE) through the counterpoise correction method by Boys & Bernardi (1970).

Finally, in order to check for the accuracy of the DFT//DFT BEs and without the aim of performing a benchmarking study, a refinement at the CCSD(T) level was performed by applying the ONIOM2 scheme as proposed by Dapprich et al. (1999) to a number of species representative of the set. Given the dependency of CCSD(T) method on the basis set, the Dunning (1989) correlation consistent family of *cc-pVnZ* basis sets (where *n* is 2, 3, 4, 5,... and corresponds to a ζ of D, T, Q, 5,…) was employed. This allows us to perform an extrapolation of the desired property, here the BE, by plotting it against $1/n^3$. We checked that the numbers thus obtained approached the values given by DFT//DFT. The Jun-cc-pVnZ basis set (with $n = 2$, 3, and 4) was chosen to perform the calculations, with the exception of SO_2, for which the aug-cc-pVnZ basis set (where one more diffuse function is added to all of the atoms, including H) was adopted to recover the whole interaction between SO_2 and the two water molecules of the *model* system. See Appendix A for more details on the BSSE correction and on the ONIOM2 scheme.

On the amorphous ice model, the DFT//DFT scheme can hardly be carried out due to the larger unit cell size compared with the crystalline one. Therefore, we adopted the computationally cheaper semiempirical HF-3c method for the adsorption on the amorphous ice surface model. HF-3c is an HF-based method adopting a minimal basis set (MINI-1; Tatewaki & Huzinaga 1980), to which three empirical corrections (3c) are added (Sure & Grimme 2013): (i) the dispersion energy

Perrero et al.

(D3(BJ)) for noncovalent interactions (Grimme et al. 2010); (ii) a short range bond correction to recover the systematically overestimated covalent bond lengths for electronegative elements, due to the MINI-1 basis set (Grimme et al. 2011; Brandenburg et al. 2013); and (iii) the geometrical counterpoise (gCP) method developed by Grimme (Kruse & Grimme 2012) to a priori remove the BSSE. On the optimized HF-3c geometries, DFT single-point energy calculations were performed to compute the BEs (this procedure is hereafter referred to as DFT//HF-3c), which were also corrected for BSSE. Before adopting DFT//HF-3c for the amorphous system, we proved its accuracy compared to DFT//DFT for the crystalline ice, resulting in an excellent match.

For both the crystalline and amorphous systems, geometry optimizations were carried out by relaxing both the internal atomic positions inside the unit cell and the cell parameters.

Each stationary point was characterized by means of harmonic frequency calculations at the Γ point by diagonalizing the mass-weighted Hessian matrix of the second-order energy derivatives with respect to atomic displacements (Pascale et al. 2004; Zicovich-Wilson et al. 2004). Each Hessian matrix element was computed numerically by means of a six-point formula based on two displacements of ± 0.003 Å from the minimum along each Cartesian coordinate. For the crystalline ice, computed at the DFT level, only a portion of the system constituted by the adsorbed species plus the two closest water molecules to the adsorbate was considered to build the Hessian matrix. In the case of the amorphous ice, the entire system was considered, and the full Hessian matrix was computed at the HF-3c level. For this later case, however, the frequencies were only used to check that the complexes are actual minima of the potential energy surfaces (all of the frequencies are real), since they are expected to not be accurate enough because of the approximated HF-3c methodology. In contrast, from the DFT frequencies computed for the fragments, we computed the zero-point vibrational energy (ZPE) corrections to: (i) correct the electronic BEs for the crystalline ice by including the corresponding ZPE contributions, and (ii) derive a scaling factor to apply to the BEs computed on the amorphous ice model to arrive at ZPE-corrected values without the need to explicitly run a full DFT frequency calculation (see Appendix B for more details on these two points).

2.2. Ice Models

Interstellar ices are thought to be mostly formed by amorphous solid water (Watanabe & Kouchi 2008; Boogert et al. 2015). However, as a starting point of our study, we have chosen a crystalline model (see the top panel of Figure 1). This choice is due to two main reasons: (i) crystalline structures are well defined due to symmetry constraints and are computationally cheap, and (ii) no definite structure for amorphous ice models is available. Moreover, regions rich in crystalline ices have been observed in protoplanetary disks and stellar outflows (Molinari et al. 1999; Terada & Tokunaga 2012). Our ice surface model is derived from the bulk of the proton-ordered P-ice, which was cut along the (010) surface defining a 2D periodic slab model (Casassa et al. 1997; Zamirri et al. 2018). The thickness of the ice (10.9 Å) was enough to converge the corresponding surface energy. We adopted a 2×1 supercell slab model, consisting of 12 atomic layers and cell parameters of $|a| = 8.980$ Å and $|b| = 7.082$ Å (at B3LYP-D3(BJ)/A-VTZ* level), which are large enough to
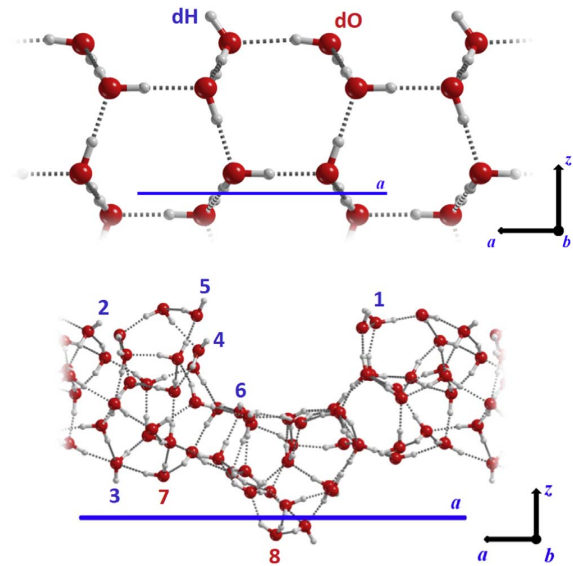
Figure 1. Top panel: side view of the crystalline (010) water P-ice slab model (along the b lattice vector). Bottom panel: side view of the amorphous water ice slab model (along the b lattice vector). Numbers identify the different adsorption sites: those in blue represent dangling hydrogen atoms (dH), while those in red represent dangling oxygen atoms (dO).

avoid lateral interactions between the adsorbed molecules in different replicas of the ice cell, thereby simulating the adsorption of isolated species. The supercell shows two dangling hydrogen (dH) atoms and two dangling oxygen (dO) atoms as binding sites (top panel of Figure 1). The structure of the ice is such that it ensures a null electric dipole along the nonperiodic z-axis. This is a direct consequence of the symmetry of the system, which shows two identical faces both at the top and at the bottom of the model. Therefore, the adsorption was modeled only on the top face of the system.

The more realistic amorphous model, already used in Ferrero et al. (2020; see bottom panel of Figure 1) consists of 60 water molecules per unit cell. The cell parameters are $|a| = 20.355$ Å, $|b| = 10.028$ Å, and $|\gamma| = 102°.983$ (at HF-3c). The different structural features between the upper and lower surfaces are responsible for the presence of a small electric dipole moment across the nonperiodic direction, and also for the presence of a variety of different binding sites. Therefore, to model the adsorption of the S-bearing species, we selected eight characteristic adsorption sites (highlighted in the bottom panel of Figure 1). The sites are chosen as follows: cases 1, 2, and 5 are located on the top surface of the ice, case 4 and 6 are inside the cavity of the model, and case 3, 7, and 8 are on the bottom-surface of the model. Binding sites from 1–6 are dH, while 7 and 8 are dO.

3. Results

In this work, the adsorption of 17 S-bearing species (shown in Figure 2) has been simulated, of which eight are closed-shell species and nine open-shell species (with unpaired electrons as indicated by the dots in Figure 2). For the open-shell species, the electronic ground state of each one was checked and found to be in agreement with those reported by Woon & Herbst (2009) and Das et al. (2018). Therefore, NS$^\bullet$, HS$^\bullet$, HS$_2^\bullet$, and
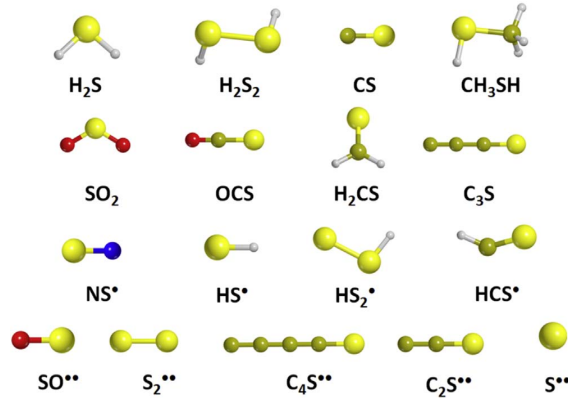
Figure 2. Set of 17 S-bearing species considered in this work. Dots represent unpaired electrons.

HCS$^{\bullet}$ are doublets (with one unpaired electron) and S$^{\bullet\bullet}$, SO$^{\bullet\bullet}$, S$_2^{\bullet\bullet}$, C$_2$S$^{\bullet\bullet}$, and C$_4$S$^{\bullet\bullet}$ are triplets (with two unpaired electrons). Each species was placed manually on the ice surface models according to the molecule/surface electrostatic potential complementarity, and from these manually built systems, geometry optimizations were performed.

3.1. BEs on Crystalline Ice

3.1.1. DFT//DFT BEs

Table 1 reports the computed BE values as described in the computational section.

The role of the dispersion interactions to the BEs was assessed by considering the D3(BJ) contribution only to the BE. In other words, for each full B3LYP-D3(BJ) optimized structure, we split the B3LYP-D3(BJ) total energy in a pure electronic DFT term coming from the B3LYP and the pure dispersive D3(BJ) one. This approach maximizes the weight of the dispersion because the attractive nature of the D3(BJ) term brings the adsorbates as close as possible to the icy surface, which, in turn, boosts the D3(BJ) value. A different approach would be to optimize the geometries at B3LYP only and then evaluate the D3(BJ) term through a single-point energy evaluation (referred to as the B3LYP-D3(BJ)//B3LYP scheme). The missing D3(BJ) term during the geometry optimization causes both an elongation of the average distance and important changes in the spatial arrangement of the adsorbate compared to the full B3LYP-D3(BJ) cases. Therefore, the dispersion contribution for the B3LYP-D3(BJ)//B3LYP is expected to be smaller (underestimated) than the one from the full B3LYP-D3(BJ) optimization calculation. We checked both approaches (data not reported) for two sets of molecules, O-bearing (CO, H₂O, CO₂, CH₃OH, and H₂CO) and S-bearing (CS, H₂S, OCS, CH₃SH, and H₂CS) adsorbed on the P-ice crystalline surface. We found the B3LYP structures involving CS and, especially OCS, to be rather different from the corresponding B3LYP-D3(BJ) ones. The same was found for the CO and CH₃OH cases. Nonetheless, the percentage average difference in the dispersion between the two approaches is a modest 11% in favor of the B3LYP-D3(BJ), as expected. In this work, we were interested in establishing the relative weight of dispersion (*rwd*) between S- and O-containing species, rather than its absolute value. For the

cases described above, we computed an *rwd* percentage average difference between B3LYP-D3(BJ)//B3LYP and a fully optimized B3LYP-D3(BJ) of only 4%, without any order reverting in the dispersion weight. Therefore, in agreement with this test case, the data shown in this work are relative to the full B3LYP-D3(BJ) approach, aware that the role of dispersion may be overestimated.

At the DFT//DFT level, computed *BE disp* values span a range from 2400–6900 K, depending on the kind of interaction that the adsorbate experiences with the ice surface, i.e., hydrogen bonds, interactions between both permanent and instantaneous dipole moments, and dispersive interactions. According to that, we can distribute the molecules in four different groups:

Molecules of Group I: (CH₃SH, H₂CS, H₂S, H₂S₂, HCS$^{\bullet}$, HS$^{\bullet}$, and HS$_2^{\bullet}$): these molecules contain groups that can act as H-bond donors and H-bond acceptors. It is worth noting that in the cases of H₂CS and HCS$^{\bullet}$, the H-bond donor groups are weak.
Molecules of Group II: (OCS, SO₂, NS$^{\bullet}$, and SO$^{\bullet\bullet}$): these molecules feature only H-donor acceptor groups because they contain atoms that are more electronegative than S.
Molecules of Group III: (CS, C₂S$^{\bullet\bullet}$, C₃S, and C₄S$^{\bullet\bullet}$): molecules that can establish one H-bond interaction with their C-end atom and a surface dH.
Molecules of Group IV: (S$^{\bullet\bullet}$ and S$_2^{\bullet\bullet}$): species consisting of only S atoms so that dispersive interactions are expected to be the main binding driving forces.

The molecule with the smallest dispersion contribution to its BE is H₂S (of Group I), which, like water, is capable of acting as both an H-bond donor and acceptor, hence involving two water molecules of the ice surface in its adsorption. H₂S, H₂S₂, H₂CS, and CH₃SH (of the same Group I) show this same adsorption feature. However, the presence of an S–S or a C–S bond enhances the contribution of dispersion forces, which can reach up to circa 70% of the BE, as in H₂S₂. The open-shell species HS$^{\bullet}$ and HS$_2^{\bullet}$ (also of Group I) have smaller BEs than their hydrogenated counterparts due to the absence of one H atom.

For molecules of Group II, the sulfur atom interacts through dispersive forces with dO of the nearest surface water molecules. SO₂, thanks to its two oxygen atoms that act as H-bond acceptors, presents the highest BE of the entire set of tested molecules (6880 K). OCS, which shows an almost null dipole moment, presents the largest dispersion contribution to the BE of the entire set (>90%), hence being one of the species less bound to the ice.

Molecules of Group III indeed form an H-bond between their C-ends and a surface dH. This interaction, moreover, is enhanced due to the dipole moment of the C chains and to the carbene-like character of the C-end atom. Furthermore, these species can bind strongly to the surface thanks to the onset of dispersive forces that become stronger with the size of the molecule. Despite these premises, the BEs of these species are similar (4000–4500 K), with the exception of C₃S, which has a higher BE (6723 K at the most) because of its adsorption geometry. That is, once C₃S adsorbs on the surface, it is arranged in rows with a distance of only 3.1 Å between the S-end and the C-end of two neighboring molecules, therefore maximizing favorable head-to-tail interactions between dipoles. This results in an energetic gain due to the lateral interactions

Table 1
Computed Binding Energies (*BE disp*, in kelvin, and without ZPE Corrections) of the S-bearing Species Set at the P-ice (010) (2 × 1) Supercell

| | *BEs on the Crystalline Water Ice* | | | | | |
| | DFT//DFT | | | DFT//HF-3c | | |
Species	*BE Disp*	*BE No Disp*	*Disp (%)*	*BE Disp*	*BE No Disp*	*Disp (%)*
CS	4582	1600	2982(65%)	3861	1239	2622(68%)
C_3S	6038/6723	1564/2129	4474(74%)/4594(68%)	5713/6146	421/1443	5292(93%)/4703(77%)
CH_3SH	6182	2959	3223(52%)	5340	2081	3259(61%)
H_2CS	4847/6242	2225/2850	2622(54%)/3392(54%)	4258/5641	1792/2417	2466(58%)/3223(57%)
H_2S	5268	3332	1936(37%)	4679	2862	1816(39%)
H_2S_2	5436/6158	1624/1936	3813(70%)/4222(69%)	5027	1527	3500(70%)
OCS	3007/3440	-229/325	3235(107%)/3115(90%)	2790	132	2658 (95%)
SO_2	6880	3608	3271(48%)	5929	2502	3428(58%)
HCS$^{\bullet}$	4113			3849		
HS$^{\bullet}$	4270			3247		
HS$_2^{\bullet}$	4270/4763/4871			3572/3139		
NS$^{\bullet}$	4330			3765		
$C_2S^{\bullet\bullet}$	4089/4691			3993/4498		
$C_4S^{\bullet\bullet}$	4366/4414			4246		
S$^{\bullet\bullet}$	3921			3247		
S$_2^{\bullet\bullet}$	2393			2009		
SO$^{\bullet\bullet}$	3861			1924		

Note. The first column refers to the adsorbed species. Columns (2)–(4) contain the values computed at the DFT//DFT level of theory. The last three columns report the same values computed at the DFT//HF-3c level of theory. For the closed-shell species (computed at the B3LYP-D3(BJ) level), the BE contributions arising from the nondispersive (*no disp*) and the dispersive (*disp*) forces, together with their percentage (%), are listed. For the open-shell species (computed at the M06-2X level), the *BE no disp* and *disp* contributions cannot be separated. Whenever more than one adsorption geometry was found, all of the *BEs* are listed and separated by a slash.

between adsorbate molecules in different replicas of the cell that enhance the BE, a phenomenon that does not happen for $C_2S^{\bullet\bullet}$ and $C_4S^{\bullet\bullet}$. In fact, we would expect $C_4S^{\bullet\bullet}$ to show larger BEs, but its elongated structure makes it challenging to maximize its contact area with the ice surface, hence interacting mostly through the C-end and pointing the S-end upward.

Finally, for molecules of Group IV, even though $S_2^{\bullet\bullet}$ is heavier and larger than S$^{\bullet\bullet}$, its interaction with the ice is the weakest of the entire set of the tested molecules. $S_2^{\bullet\bullet}$ has an electronic triplet ground state (like O_2) and is the only homonuclear molecule of the set. Its dipole moment is zero, but not its quadrupole moment, which allows for the onset of a quadrupolar interaction between the S–S bond region and a dH of the ice surface. However, its BE is lower (2393 K) than that for S$^{\bullet\bullet}$ (3921 K).

3.1.2. ONIOM2-corrected BEs

For some species, BEs computed at DFT//DFT have been refined at a CCSD(T) level by applying the ONIOM2 methodology by Dapprich et al. (1999), considering that most of the BE contribution arises from the local interactions between the adsorbed species and a small number of nearby water molecules. These calculations were performed on the following seven S-bearing species: CH_3SH, CS, H_2CS, OCS, SO_2, NS$^{\bullet}$, and $S_2^{\bullet\bullet}$. These molecules have been chosen because they well represent both closed- and open-shell species and sample the entire range of BEs of the 17 species of this work.

Figure 3 (panel (a)), plots the ONIOM2-corrected BEs against the DFT//DFT ones, showing a very good fit that confirms the accuracy and reliability of the DFT//DFT scheme adopted so far, with the latter slightly overestimated compared to the ONIOM2-corrected one.

3.1.3. DFT//HF-3c BEs

To cope with the larger size of the amorphous ice model, we tested the performance of the cheaper DFT//HF-3c scheme on the crystalline ice model to assess its applicability also for the amorphous ice.

Starting from the previously optimized DFT structures, we re-optimized the geometries at HF-3c level. In general, the HF-3c optimized geometries are comparable with the DFT ones, with the exception of very few cases, such as the SO_2 adsorption complex (see below). However, by comparing the HF-3c//HF-3c BEs with the DFT//DFT ones, the resulting correlation is rather coarse (see Figure 3, panel (b), blue symbols and line).

However, a much better agreement is shown by the DFT// HF-3c BEs (the linear correlation improves notably, see Figure 3, panel (b), orange symbols and line). Such an agreement was already shown in Ferrero et al. (2020), and the accuracy of the DFT//HF-3c scheme was also exhibited in molecular crystals (Cutini et al. 2016), polypeptides (Cutini et al. 2017), and pure-silica zeolites (Cutini et al. 2019). These results, thus, extend the application of the DFT//HF-3c scheme to derive accurate BEs for S-bearing molecules adsorbed on ice surfaces.

HF-3c//HF-3c data (blue symbols) of Figure 3 reveal an outlier (for SO_2, around 7000 K), the HF-3c//HF-3c BE being 25% higher than the DFT//DFT one, while the DFT//HF-3c value is about 15% smaller than the DFT//DFT value.

This effect is because HF-3c optimized geometries show shorter distances between the adsorbate and the ice model, which, when computing the single-point energy at the DFT level, will increase both the dispersive interactions and the exchange repulsion contributions. For instance, HF-3c reduces the distance between the S atom of SO_2 and an O atom of the ice surface to 2.25 Å, compared to the 2.48 Å of the B3LYP-D3

(a)

(b)
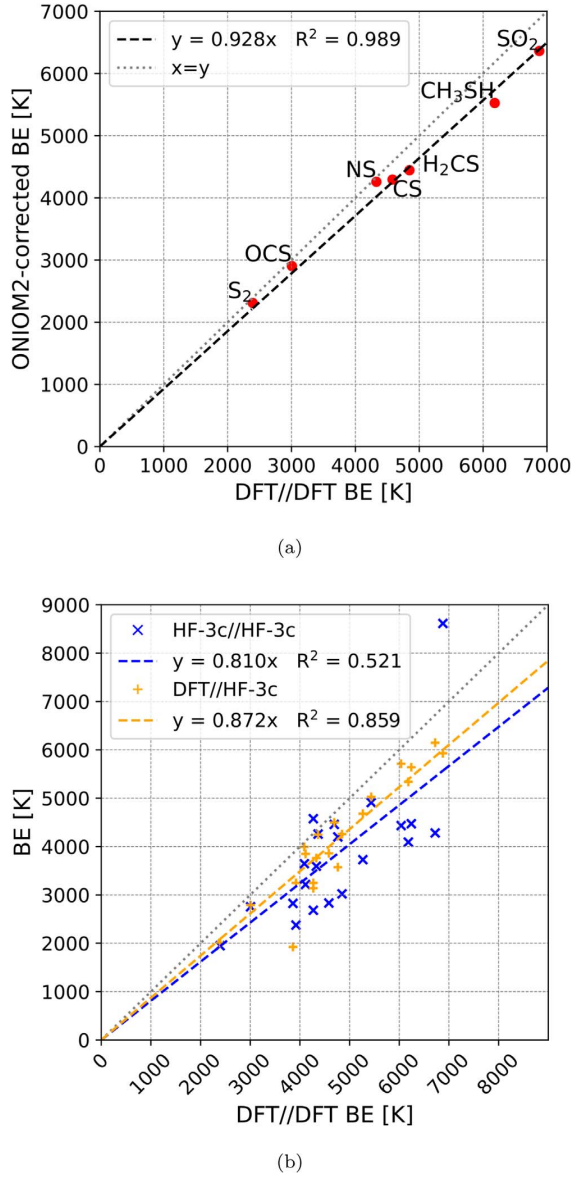
Figure 3. (a) Best linear fit between the DFT//DFT and the ONIOM2-corrected BEs for the crystalline ice systems. (b) Best linear fit between the DFT//DFT BEs and the HF-3c//HF-3c (in blue) and the DFT//HF-3c (in orange) schemes, for the crystalline ice systems. BEs are in kelvin.

(BJ) optimization. Moreover, by looking at the *BE disp* values of Table 1, we notice that the percentage of dispersion in DFT//HF-3c BE values is almost always larger than that of DFT//DFT BEs.

Finally, HF-3c can be critical for radical species like NS$^{\bullet}$. The NS$^{\bullet}$ experimental bond length value is 1.494 Å (Peebles & Marshall 2002), while the calculated ones are 1.480 Å with M06-2X and 1.651 Å with HF-3c. The charge and spin density distributions are also different, with 76% and 59% spin density on nitrogen at HF-3c and at M06-2X, respectively. The higher spin localization of HF-3c causes the lengthening of the bond,

which, when adsorbed, shrinks to 1.633 Å, resulting in a gain in energy of about 10 kJ mol^{-1} (at DFT//HF-3c). As this behavior is systematic (for both free and adsorbed molecules), it cancels out when computing the BE. In conclusion, HF-3c can be used as a cheap level of theory provided that a careful check is exerted for species with uncommon structures and electronic configurations (especially open-shell ones).

3.2. BEs on Amorphous Ice

The amorphous ice shows a richer variety of adsorption sites causing a distribution of BE values for the considered molecules. We characterized eight surface binding sites (dH1-6 as H-bond donors and dO7-8 as H-bond acceptors), which were chosen as a function of their H-bonding ability. We manually built up the starting geometry, exposing the amorphous solid water (ASW) electrophilic regions (due to dangling OH bonds, while their counterparts correspond to exposed O atoms) to the nucleophilic ones of the adsorbates and vice versa (following the principle of electrostatic complementarity). The distance between the adsorbate and the surface was set up as the sum of the van der Waals radii of the corresponding closest atoms, by means of computer graphics manipulation. By proceeding this way, we obtained a total of 136 adsorption complexes. As explained in Section 2.1, the complexes were first optimized at the HF-3c level followed by a harmonic frequency calculation to confirm all structures as minima. Table 2 shows the BEs value at the final DFT//HF-3c level. The mean ($\langle BE \rangle$) and standard deviation (σ) for the BEs are also provided, although we recommend that the reader not consider them as representative of the ensemble of BEs here listed, given the limited sampling of binding sites performed in this study, far from being suitable for a statistical treatment.

From the analysis of our data, it stands out that dH4 and dH6 sites, residing in the cavity domain of the ice model, exhibit the highest BE values due to the close proximity of the surrounding water molecules. The reverse happens for dO7 and dO8, placed on the bottom and as the outermost water molecules of the model, which are the least favorable binding sites.

On average, the dispersion contributions to the BEs are higher when the adsorption takes place at the amorphous ice than at the crystalline ice due to closer contact of the adsorbate with the ice surface. While in the crystalline proton-ordered P-ice model, the H-bond chains extend to infinity ensuring a reinforcement of the H-bonding strength (cooperativity effect), this is not the case for the ASW model. In ASW, the random organization of the water molecules breaks the H-bonding chain extensions, reducing the H-bonding cooperativity and, therefore, its strength. This, in turn, also affects the H-bonding strength exhibited by the chain terminal ice OH groups involved in the interactions with the adsorbates, decreasing the corresponding BE values. This is shown clearly by the higher BE values computed for adsorption on the crystalline P-ice with respect to the ASW model, in agreement with previous literature data (Ferrero et al. 2020). However, other effects, like the easier structure deformation for the amorphous ice, accommodates the adsorbates getting closer to the ice surface, maximizing both the H-bond strength and the dispersive contribution, overcoming the loss of H-bonding cooperativity.

The above interpretation can explain the presence of some very high BE values, which depart from the rest of the BEs of

Table 2
Summary of the DFT//HF-3c *BEs* (in kelvin, and without ZPE Corrections) of the 17 S-bearing Species at the Amorphous Ice Periodic Model

	Amorphous Ice BE Values									
Species	dH1	dH2	dH3	dH4	dH5	dH6	dO7	dO8	$\langle BE \rangle$	σ
CS	4270	1852	3596	3283	3380	3584	1155	1648	2846	1054
C_3S	5472	6014	6122	5412	5112	5941	1275	2959	4788	1630
CH_3SH	3608	4991	3584	3271	3271	4630	2622	2850	3603	769
H_2CS	4161	4967	3416	3488	4378	4053	1960	3115	3692	859
H_2S	3452	5208	3283	4210	4630	2622	2285	2309	3500	1026
H_2S_2	3007	4234	4558	4462	3801	3801	3175	4883	3990	623
OCS	2875	1491	2574	2177	1660	3320	2057	3175	2416	637
SO_2	3344	3175	3644	6759	3680	4426	2730	2442	3775	1263
$HCS^{\bullet}$	2117	2225	2454	2117	1491	3560	2478	2201	2330	545
$HS^{\bullet}$	3163	2454	2057	2646	5003	2177	1624	1251	2547	1080
$HS_2^{\bullet}$	2562	1527	2586	3031	2670	2550	2778	2694	2550	413
$NS^{\bullet}$	3283	1431	1828	1768	3416	3428	1768	1876	2350	805
$C_2S^{\bullet\bullet}$	4426	3163	5088	3572	2009	4991	2009	2393	3456	1193
$C_4S^{\bullet\bullet}$	5075	2165	5797	3716	4943	5569	4306	4077	4456	1097
$S^{\bullet\bullet}$	3247	2081	2550	2321	2526	2321	1852	1852	2344	425
$S_2^{\bullet\bullet}$	1924	1455	2850	1552	2009	2069	1648	1203	1839	472
$SO^{\bullet\bullet}$	4041	1082	2634	1419	1696	2345	1672	1696	2073	874

Note. For each species, eight BE values, alongside their mean ($\langle BE \rangle$) and standard deviation (σ), are provided.

the corresponding ensembles. This happens for CH_3SH, C_3S, H_2CS, H_2S, H_2S_2, $C_2S^{\bullet\bullet}$, and $C_4S^{\bullet\bullet}$, adsorbed in the dH2 and dH5 sites (located at the edges of the top surface). In these cases, a dramatic structural rearrangement of the amorphous ice takes place, with a global energy gain that can reach 2400 K, contributing to the "anomalous" high BEs. In practice, the species/ice interactions cause a large restructuring of the amorphous ice, whose new structure has a lower energy than the initial ice taken as a reference.

This phenomenon is not usual when dealing with rigid structures (e.g., metal surfaces, oxides, and graphene); however, soft matter like water ice is held together by the same kind of interactions keeping the adsorbate attached at the surface. Therefore, the geometrical relaxation induced by the adsorption can rearrange the structure in such a way that, once optimized, it falls in a new minimum with a lower energy with respect to the reference system. A full analysis of this phenomenon has been recently described in Tinacci et al. (2022).

To cope with this "artificial" increment of the BE, we adopted the new ice structure as a reference for the calculation of the BE, which are now coherent with the general BE ensembles. We think this is an important issue, not common in the adsorption phenomena on metallic, ionic, or covalent surfaces, which are dominated by stronger forces than those occurring with soft matter like water ices. This problem would be mitigated only by enlarging the ice model at an increasing computational cost.

3.3. Zero-point Energy (ZPE) Corrections

As anticipated in Section 2.1, the ZPE corrections were computed following two different schemes, depending on the adopted surface models. For the adsorption on the crystalline ice, we computed the harmonic frequencies of a fragment consisting of the S-bearing species and the two closest water molecules of the ice with the assumption that deformation occurs only in the proximity of the adsorption site. The ΔZPE is computed following the advice described in Appendix B to arrive at a ZPE-corrected BE, i.e., BE(0). Figure 4 shows a
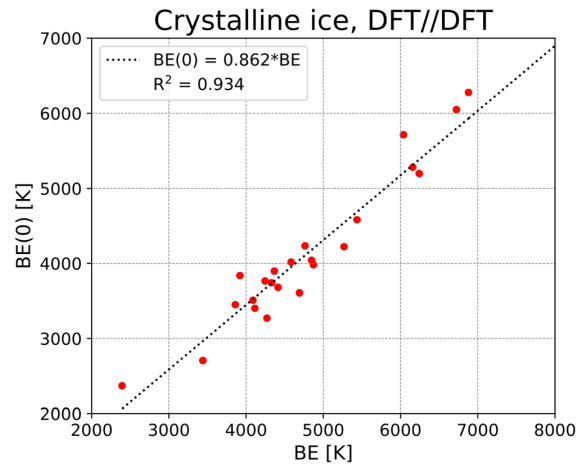
Figure 4. Analysis of ZPE corrections. Correlation between DFT//DFT BE(0) and BE for the adsorption at the crystalline ice. The intercept is set to zero.

good linear correlation between BE and BE(0), showing the average ZPE correction is about 14% of the BE.

The final BE(0) values for all of the adsorption complexes at the amorphous ice have, therefore, been computed by multiplying the DFT//HF-3c BEs by a scale factor of 0.862 (see Figure 4, panel (a)).

4. Discussion

4.1. Comparison with BEs for Non-S-bearing Adsorbates

In the recent work by Ferrero et al. (2020), the adsorption of 17 closed-shell and four open-shell species was simulated. The list included: (i) nondipolar molecules with significant quadrupole moments (i.e., H_2, N_2, and O_2) or higher-order multiple moments (i.e., CH_4), hence interacting weakly with the ice; (ii) molecules that, besides exhibiting a quadrupole moment, established H-bonds with surface dH atoms (i.e., CO, OCS, and

(a)

(b)
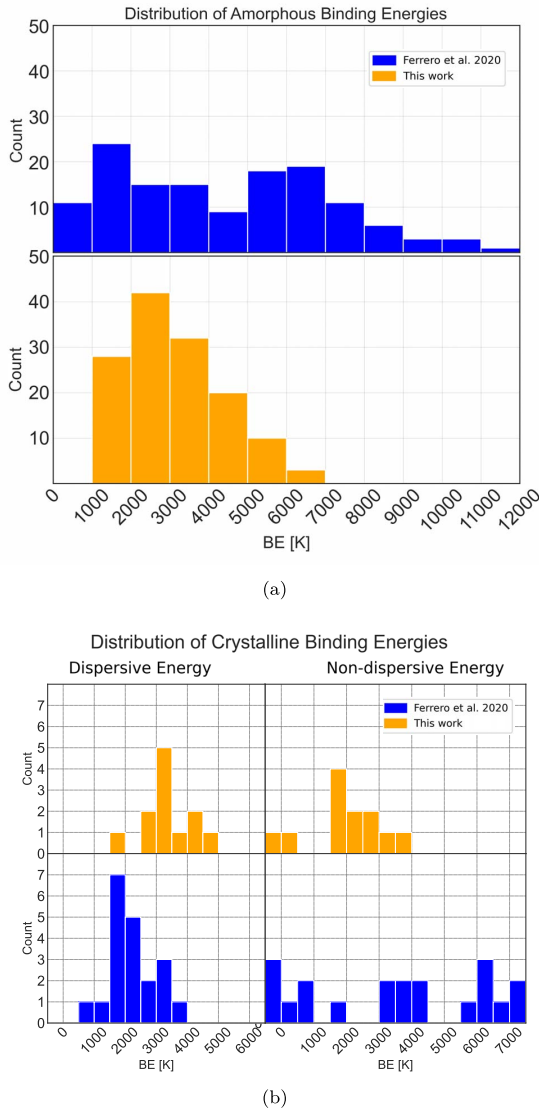
Figure 5. (a) Distribution of BEs computed on the amorphous ice model for S-bearing species (orange) and the species of Ferrero et al. (2020; blue). (b) Distribution of the dispersive (left panel) and nondispersive (right panel) contributions to the crystalline BEs for closed-shell species.

CO_2); (iii) amphiprotic molecules, which are both H-bond acceptors and donors (i.e., NH_3, H_2O, HCl, HCN, and H_2S); (iv) larger molecules that are capable of establishing a greater number of interactions with the surface due to the presence of several functional groups, hence giving rise to the highest BE values of the set (i.e., CH_3OH, CH_3CN, H_2CO, $HCONH_2$, and HCOOH); and (v) the open-shell species $OH^•$, $NH_2^•$, $CH_3^•$, and $HCO^•$, the two former ones forming strong H-bonds with dH and dO sites, at variance with the two latter ones.

Figure 5 compares the BEs of the S-bearing species with those of Ferrero et al. (2020). The distribution of BEs in Ferrero et al. (2020) has a bimodal character (see panel (a)), indicating two different adsorption behaviors in the set of the considered species: a group of low BEs (characterized by dispersive

interactions), and a group of high BEs (amphiprotic and larger species involved in the H-bond). In contrast, S-containing species span a much narrow range of BEs, suggesting a common adsorption feature, despite the diverse chemical structures.

Deeper insights into the contributions to the BE of these two sets of species arise from the analysis of the closed-shell species adsorbed at the crystalline ice model. Each BE can be decomposed in dispersive and nondispersive contributions (see panel (b) of Figure 5) for all considered species.

The distribution of the dispersive contributions highlights two main facts: (i) this term is more important when heavy atoms (like sulfur) belong to the adsorbed species; (ii) the mean value of the distribution for S-bearing species (ca. 3500 K) is higher than that of the nondispersive terms (ca. 2000 K), as dispersion accounts for more than 50% of the BEs provided in this work. Therefore, weak interactions are the most relevant and crucial forces in the description of the adsorption of S-containing species on ices and, thus, they need to be carefully accounted for to properly describe the sulfur chemistry on icy mantles. The above considerations are not surprising due to higher atomic polarizability of second-row atoms compared to C-, N-, and O-containing molecules.

The different behaviors of the two sets of species will have consequences on their chemistry. Considering the BE ensembles, one can argue S-containing species show higher desorption temperatures compared to weakly interacting molecules, like O_2, CH_4, or CO. On the contrary, S-bearing species interact more weakly than amphiprotic molecules with ice. The same inference applies to their surface mobility. As usually, the barriers for diffusion are taken as an arbitrary fraction of the BEs (Cuppen et al. 2017; Kouchi et al. 2020), so we can assume that species with lower BEs will diffuse faster than those with higher BEs, setting up constrains on the reactions that can take place on an icy surface. The particularly low BEs of $S_2^{••}$ (the weakest bounded S-bearing species) also implies its highest mobility. In the hypothesis that polysulphanes could be a reservoir of sulfur, the high mobility of $S_2^{••}$ could favor their encounter and reaction, forming chains and cyclic sulfur species (Druard & Wakelam 2012; Mifsud et al. 2021) that hardly desorb due to the very large dispersive contribution to their BE.

4.2. S-bearing versus O-bearing Species

In addition to these general considerations, a punctual comparison between S-bearing and O-bearing species can be drawn for some cases in order to highlight a few exceptions to what we generally understood about our set of molecules.

In Table 3 we compare the contributions to the BE(0) values of some S-bearing species with their oxygen analogs. As a rule of thumb, we would expect molecules containing sulfur to always show a BE(0) lower than the corresponding O-bearing ones, with the dispersive interactions being larger for the former group. However, by considering case by case, we notice that there are some exceptions to this behavior (see Figures 7–9 in Appendix C) For the pair CS/CO, the trend is the opposite, while the OCS/CO_2 pair shows many similarities.

Indeed, CS exhibits a larger BE(0) and a lower percentage of dispersive energy than its O-analog, CO. This can be explained by looking at the dipole moments of these species. CS shows a large dipole moment (1.9 D), at variance with the negligible one of CO. The H-bonding interaction of the two species with a

Table 3
Contribution to Selected BE(0) (in kelvin) for S-bearing Species vs. O-bearing Species Adsorption at Crystalline Ice

Sulfur Bearing Species				Oxygen Bearing Species				
Species	BE(0)	No Disp	Disp (%)	μ	Species	BE(0)	No Disp	Disp(%)	μ
CS	2453	785	1668(68%)	1.9	CO	1663	50	1613(97%)	0.1
CH_3SH	4603	1795	2808(61%)	1.5	CH_3OH	7385	5391	1994(27%)	1.7
H_2CS	4267	1792	2475(58%)	1.7	H_2CO	5187	3268	1919(37%)	4.6
H_2S	4033	2460	1573(39%)	1.1	H_2O	7200	5832	1368(19%)	2.0
OCS	2405	120	2285(95%)	0.8	CO_2	2568	796	1772(69%)	0.0

Note. The latter are taken from Ferrero et al. (2020). The BE(0) are decomposed into *no disp* and *disp* contributions, applying the percentage of dispersion (%) obtained for each species. The dipole moment μ (in Debye) of the free molecules is computed at the B3LYP-D3(BJ)/A-VTZ* level of theory. When more than one BE was present, the average value is reported.

dangling OH is therefore stronger for CS, as it is the dispersive interaction of the S atom with the water molecule of the surface (see Figure 7 in Appendix C).

Both OCS and CO_2 have a linear geometry, an almost null dipole, and interact through an H-bond with a dangling OH of the surface. While OCS exhibits a larger dispersion interaction, for CO_2, the electrostatic component makes up about 30% of the BE, yielding a comparable BE(0) for the two molecules.

On the other hand, the other pairs behave as we expected, as described in Section 4.1. The adsorption geometries show some similarities between the two members of each pair, with the most important differences due to the presence and strength of the H-bonds. Specifically, CH_3SH/CH_3OH and H_2S/H_2O exhibit the same number of H-bonds, while for H_2CS/H_2CO, only the latter establishes an H-bond with the surface through the C=O group.

4.3. Comparison with the Literature

Before comparing the present results with literature experimental data, some general considerations are at hand. In the ISM, the water ice mantle is the result of the in situ water formation through surface reactions. Therefore, the final ice structure is the result of the energetic locally hot spots injected in the mantle where intermediates (e.g., OH$^{\bullet}$ and HOO$^{\bullet}$) and final products are formed. As the injected energy is large, it locally heats up the ice, shaping the final structure of the grain in a complex way, difficult to attain through laboratory experiments. In the terrestrial laboratories, ice is prepared directly by deposition from vapor water molecules, with a certain kinetics, on cold metal fingers (Penteado et al. 2017). The final ice can be amorphous (either compact or porous) or crystalline, depending on the kinetics of adsorption and processing temperature. Unfortunately, the detailed structure of amorphous ice can only be partly inferred indirectly by spectroscopic measurements, therefore limiting our knowledge of the atomistic details. The same difficulty occurs for computer modeling: indeed, we are not aware of computer simulations reacting hydrogen and oxygen atoms step by step up to form a sizable icy grain, even if a simpler attempt to form a single water molecule on the forsterite surface has been recently reported (Molpeceres et al. 2019).

As a function of the adopted ice models in computer simulation, the external surface may show a variety of different kinds of adsorption sites, giving rise to different BEs (Song & Kastner 2017). When very few sites are available, like in the proton-ordered ice model adopted here, no more than two different BE values resulted. For the amorphous model, instead, a significant variability of binding sites resulted,

giving rise to an ensemble of BEs. As reported in detail by Ferrero et al. (2020) and not repeated here, extra care should be exerted when comparing the computed BEs with those from experiments.

For instance, while BEs are straightforwardly calculated by computer simulations (see Appendix B), experimental BEs are never directly observed in the thermal desorption, as TPD peaks are usually interpreted through the Redhead (1962) method or more sophisticated techniques, through which desorption adsorption energies (DAEs) are worked out. As DAEs may be a function of the surface coverage θ, the comparison with the theoretical BEs is not straightforward (for a recent review, see Minissale et al. 2022). For instance, the ice structure is sensitive to both temperature and adsorption/ desorption processes (at variance with surfaces from covalent/ ionic solids) as its layers are held together by weaker interactions (e.g., H-bonds in water ices or dispersion in CO ices), which are similar in strength to the BE values. Obviously, ice restructuring processes may affect the final value of the DAEs.

In Table 4, our BEs are compared with those from Penteado et al. (2017; see Figure 6). These authors showed a list of recommended BEs, collecting data from previous works and providing an uncertainty range for each value. For H_2S, OCS, and SO_2, the BEs are derived a posteriori from the experimental TPD measurements of Collings et al. (2004), using the empirical relationship of

$$\text{BE}(X): T_{\text{des}}(X) = \text{BE}(H_2O): T_{\text{des}}(H_2O) \qquad (1)$$

where X is the considered chemical species, and T_{des} is the desorption temperature of the species deposited on a water ice extrapolated from the TPD measurements of Collings et al. (2004). The reference $\text{BE}(H_2O)$ is set to 4800 K from previous works (see Penteado et al. 2017 for more details). The uncertainty assigned to the BE values of H_2S, OCS, and SO_2 was 3.5%. For the other species, the provided data are based on the work of Hasegawa & Herbst (1993), which in turn were based on previous works, including Allen & Robinson (1977). In the latter, the BE of a molecule was treated as the sum of the BEs of the constituent atoms to infer the interaction energy of several species on SiO_2 surfaces, which was subsequently scaled by an empirical factor to obtain BEs on water ice. The uncertainty of these values is set to half the BE for species whose BE is less than 1000 K, and set to 500 K for all other cases.

The comparison between our computed BEs for the crystal-line ice and the literature data shows, as expected,

Table 4
Summary of the Computed BE(0) Values (in kelvin) in Comparison with Data from the Literature

					Binding Energies					
		This Work						Literature		
	Crystalline	Amorphous				Computed		Database		Various
Species	BE(0)	Min	Max	⟨BE⟩	σ	Das	Wakelam	KIDA	UMIST	Penteado
CS	2453	995	3680	2453	909	2217	3200	3200	1900	1800 ± 500
C₃S	4925/5298	1099	5277	4128	1405			3500	3500	3000 ± 500
CH₃SH	4603	2260	4302	3106	663		4200			
H₂CS	3670/4863	1690	4282	3183	740	3110	4400	4400	2700	2025 ± 500
H₂S	4033	1970	4489	3017	884	2556	2900	2700	2743	2290 ± 90
H₂S₂	4333	2592	4209	3439	537	4368		3100	3100	2600 ± 500
OCS	2405	1286	2861	2083	549	1571	2100	2400	2888	2325 ± 95
SO₂	5111	2105	5827	3254	1089	3745	5000	3400	5330	3010 ± 110
HCS˙	3318	1286	3069	2009	469	2713	2900	2900	2350	2000 ± 500
HS˙	2799	1078	4313	2195	931	2221	2700	2700	1500	1350 ± 500
HS₂˙	2706/3079	1317	2613	2198	356	4014		2650	2650	2300 ± 500
NS˙	3245	1234	2955	2026	694	2774		1900	1900	1800 ± 500
C₂S˙˙	3442/3877	1731	4385	2979	1028	2447		2700		2500 ± 500
C₄S˙˙	3660	1866	4997	3841	945			4300	4300	3500 ± 500
S˙˙	2799	1579	2799	2020	366	1428	2600	2600	1100	985 ± 495
S₂˙˙	1732	1037	2457	1644	1585	407		2200	2200	2000 ± 500
SO˙˙	1658	933	3483	2128	1787	754	2900	2800	2600	1800 ± 500

Note. The second column contains the BEs on the crystalline P-ice (010) model, the third and the fourth columns contain the minimum and maximum BE values, respectively, found for the amorphous ice, the fifth and the sixth columns list the mean (⟨BE⟩) and the standard deviation (σ), respectively, relative to the amorphous BEs, while columns (7)–(11) report BEs from the literature, respectively, from computed data (Das et al. 2018 and Wakelam et al. 2017), from databases (KIDA; Wakelam et al. 2015; and UMIST; McElroy et al. 2013) and from experiments (Penteado et al. 2017). The BE(0) values were obtained by applying the Equation (0).862*BE = BE(0) (see the text for more details).
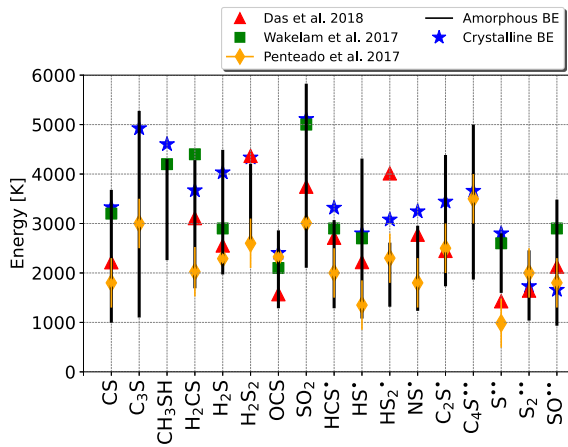
Figure 6. Computed and literature BEs (in kelvin). For each species, the solid black line covers the min/max ZPE-corrected BE values for the amorphous ice model, while blue stars correspond to the ZPE-corrected BEs on the crystalline ice model.

discrepancies. However, comparison of the range provided in Penteado et al. (2017) with our BE ensemble reveals that disagreement is only for S˙˙. The additive principle applied by Allen & Robinson (1977) implies that S₂˙˙ BE must be twice the value of the isolated S˙˙ atom. However, we have seen that S˙˙ and S₂˙˙ showed a very similar distribution of BEs, due to the same nature of their interaction with the surface. For the other species, the ranges provided by Penteado et al. (2017) lay within our ensembles, especially for H₂S, OCS, and SO₂, which have a very narrow distribution of BEs. However, computed BEs for crystalline ice compare poorly with the

average values provided by Penteado et al. (2017), showing that the additive principle is not suitable for the description of the interactions between polyatomic species and extended ice models.

In addition to the experimental data, comparison is carried out with recent BEs from computational works for a large number of species, some of which contain sulfur (see Figure 6).

In Wakelam et al. (2017), a single water molecule was adopted as an ice model (the M06-2X/aug-cc-pVTZ theory level; with neither ZPE nor BSSE corrections). The lost contributions from a real ice surface were somehow recovered by a clever fit between computed BEs and experimental ones for a subset of species. The resultant fitted parameters were used to derive all other BE values. Comparison between our crystalline BEs with those of Wakelam et al. (2017) shows a difference of about 30% of the value. A better agreement with Wakelam et al. (2017) values is shown by the BE range spanned by our amorphous BE ensembles.

Das et al. (2018) computed the BEs for a molecular set including 100 species, adopting a water tetramer and, in few cases, a water hexamer as the ice model, at the MP2/aug-cc-pVDZ theory level, without BSSE and ZPE corrections. Among the S-bearing molecules, only H₂S and OCS were adsorbed on a water hexamer. The ice models employed in Das et al. (2018) still lack the effect of H-bond cooperativity (present in our periodic models) and could be the reason of the small values of BEs for the S-containing species, even lower than those estimated by Wakelam et al. (2017). Moreover, H₂S and OCS BEs show an increment when changing the model from the water tetramer to the water hexamer, and it is not clear for how long this trend would continue before reaching a converged value. The Das et al. (2018) values are within the BE ensembles computed for the amorphous ice. Altogether,

this indicates that the choices of the ice model and of the computational method have a strong relevance on the predicted BEs. Thus, more studies are needed to fully characterize BE distributions, by using larger models and exploring more binding sites.

4.4. Binding Energies and Snow Lines in Protoplanetary Disks

As mentioned in Section 1, the BEs of the species on ice mantles have a profound impact on the interstellar chemistry and, more specifically, on the chemical composition of the regions where planetary systems, like our own, are formed. A very important case is represented by the gaseous versus solid chemical composition in protoplanetary disks, which are the sites where planets, asteroids, and comets eventually form. If a species is in the solid form, then it will likely be incorporated in the (aforementioned) formation of rocky objects, whereas, if it is in the gaseous form, it will only enrich the giant gaseous forming planets of the elements contained in the species (e.g., Öberg & Bergin 2021). Sulfur, on the other hand, seems to be a very important element for terrestrial life and, perhaps, even a key element for its emergence (e.g., Shalayel et al. 2020).

As discussed in Section 1, the major reservoirs of sulfur in cold molecular clouds (Section 1.2, from where the evolution toward a planetary system starts) are unknown, though they are suspected to be in solid organosulfur compounds and polysulphates (Druard & Wakelam 2012; Laas & Caselli 2019). During the evolution, the quantity of sulfur in the gaseous phase changes by orders of magnitude, so that it is very important to know it in the protoplanetary disks. So far, there are no measurements for solid, and only very few for gaseous, S-bearing species in protoplanetary disks (see below). The locus where the transition of a species from the solid to the gas phase takes place is usually called "snow-line" in astrophysical jargon, particularly so in the protoplanetary disks, which are objects that are relatively cold and dense (e.g., Öberg & Bergin 2021). Then, one efficient way to measure the solid versus gaseous content of S-bearing species in protoplanetary disks is to observe where the species disappear from the gas phase, because they freeze onto the dust grain water-rich mantles, namely, to measure their snow lines. Two major parameters determine where the snow line lies: the temperature of the dust, and the BE of the species. In general, the larger the distance from the disk center (heated by the central forming star), the colder the dust. Therefore, species with lower BEs remain gaseous at larger disk radii.

The ALMA-DOT survey of young disks provides the first preliminary observational constraints on the position of the snow lines of some of the S- and O-bearing molecules considered in this study (Podio et al. 2020a). In particular, ALMA-DOT observed a protoplanetary disk, IRAS 04302 +2247, seen edge-on, which makes it ideal to constrain the snow lines of different species. These observations show that the molecular emission is bright in an intermediate disk layer (the so-called molecular layer; Aikawa & Herbst 1999), while it decreases in the disk midplane due to molecular freeze-out onto the dust grains. More relevant to this work, CS, H₂CO, and H₂CS show a similar spatial distribution, and a sharp decrease of their emission is observed at smaller radii than CO (Codella et al. 2020; Podio et al. 2020b). The estimated snow line is at 25 au for H₂CO (and consequently H₂CS and CS) and 100 au for CO (van't Hoff et al. 2020). The larger snow-line radius of CS with respect to that of CO is generally in agreement with

the two estimated BEs: 995–3680 K (CS; this work) versus 1109–1869 K (CO; Ferrero et al. 2020). On the other hand, the observations suggest similar snow lines for CS, H₂CO, and H₂CS, while the estimated BEs of H₂CO and H₂CS are larger than that of CS: 3071–6194 K (H₂CO; Ferrero et al. 2020) and 1690–4282 K (H₂CS; this work) versus 995–3680 K (CS; this work). We emphasize, however, that the ALMA-DOT observations are unable to resolve the inner 25 au of the disk. Therefore, higher spatial resolution observations are needed to constrain the snow lines of species with large BEs, such as H₂CO and H₂CS.

In conclusion, the admittedly scarce observations so far available seem to be in agreement with the estimated BEs obtained through theoretical quantum chemical calculations as provided in Ferrero et al. (2020) and this work, which encourage us to pursue the work to a larger sample of species, both S- and N-bearing and the so-called interstellar complex organic molecules (Ceccarelli et al. 2017).

5. Conclusions

In the present work, the BEs of 17 astrochemically relevant S-bearing species adsorbed on periodic water ice models have been computed using DFT based on the hybrid B3LYP-D3(BJ) (for closed-shell species) and hybrid meta-GGA M06-2X (for open-shell species) with an Ahlrichs-VTZ* double-zeta polarized Gaussian basis sets. We adopted either a crystalline proton-ordered ice model or a more realistic amorphous ice model, both treated within the periodic boundary conditions. The adopted DFT results have also been refined toward a CCSD(T) level through the ONIOM2 approach carried out on the crystalline model, showing a very good convergence between the DFT BEs and those refined with the ONIOM2 scheme. As full DFT is too costly for the simulation of adsorption on the amorphous ice, we checked the reliability of the cheaper HF-3c method by contrasting the BEs with that at the DFT level for the crystalline ice. While HF-3c BEs poorly correlate with the DFT ones, the BEs at the single-point DFT// HF-3c level give an excellent correlation with full DFT values. The validated DFT//HF-3c method was used to study the adsorption process on the amorphous ice model, in which the richness of adsorption sites (up to eight) implies a BE ensemble for each species. We also showed the ZPE correction to the electronic BE to be around 14% of the BE itself irrespective of the adsorbed species, and provided a scale factor to obtain the BE(0) for adsorption complexes at the amorphous ice model. This is important, as it allows for skipping the expensive frequency calculation by simple scaling of the electronic BEs. The analysis of the obtained data showed that, in order to properly describe the behavior of S-bearing species, special care must be taken in the description of the dispersive interactions, which gain more importance as the number of large and heavy atoms, like sulfur, increases. When considering the amorphous ice model, which provides enough richness of sites, the resulting BE ensembles match both the experimental and the literature computed BEs. We posit BE distributions rather than single BE values to be essential for providing robust parameters to be adopted in numerical models of chemical evolution in the universe.

Regarding the sulfur depletion problem, our calculations do not solve the open questions. Nonetheless, we provide strong and relatively accurate BE values, which can elucidate the features of S-bearing species in comparison with S-free

molecules when adsorbed on icy mantles. An important clue is provided by the $S_2^{\cdot\cdot}$ case in which the lowest BE implies higher diffusivity and increasing reactivity toward the formation of higher-weight S-containing rings strongly bound to the ice through dispersion interactions. The CS molecule also shows some counterintuitive results when compared to the analog CO molecule, due to a higher dipole moment and dispersion contribution. The present work also highlights the utility of accurately computing BE values to be correlated with snow lines in protoplanetary disks.

Appendix A
Computational Details

For optimization and frequency calculations, we refer to the computational parameters adopted in the work of Ferrero et al. (2020): the threshold parameters for the evaluation of the Coulomb and exchange bielectronic integrals (TOLINTEG) were set to 7, 7, 7, 7, and 14 when working with crystalline ice, while for the amorphous ice to 7, 7, 7, 7, and 25, which facilitates the convergence of the self-consistent field (SCF), especially when adsorbing open-shell species.

Some species required a careful treatment to describe properly their electronic state. The use of the BROYDEN accelerator (Johnson 1988) and the broken-(spin)-symmetry *ansatz* (Neese 2004, 2009) was necessary to obtain an optimal convergence of the SCF procedure.

For the numerical evaluation of bielectronic integrals (Becke 1988), the standard pruned grid, composed of 75 radial points and a maximum of 974 angular points, was used. To sample the reciprocal space, we adopted the Pack–Monkhorst mesh (Pack & Monkhorst 1977), with a shrinking factor of 2, which generates 4 k points in the first Brillouin zone. The only exception is for the adsorption of atomic sulfur on the crystalline ice model, which required a shrinking factor of 3, generating 5 k points, in order to avoid numerical noise in the results.

The Broyden–Fletcher–Goldfarb–Shanno algorithm (Broyden 1970; Fletcher 1970; Goldfarb 1970; Shanno 1970) was used to carry out geometric optimizations.

Appendix B
Calculation of the Binding Energies

When using a finite basis set of localized Gaussian functions to describe our systems, BSSEs arise. This is the case in our BEs computed at both DFT//DFT and DFT//HF-3c. Thus, the a posteriori counterpoise (CP) correction of Boys & Bernardi (1970) was applied to compensate for this error, and our BEs are therefore defined as the opposite of the CP-corrected interaction energies (ΔE^{CP}), that is,

$$BE = -\Delta E^{CP} \quad \text{(B1)}$$

$$\Delta E^{CP} = \Delta E - BSSE \quad \text{(B2)}$$

where the non-CP-corrected interaction energy ΔE is given by the sum of the deformation-free interaction energy (ΔE^*), the deformation energy of the slab (δE_S), the deformation energy of the molecule (δE_μ), and the lateral interaction (E_L) between adsorbate molecules in different replicas of the cell. This quantity corresponds to the common definition of interaction energy, which in this case is the energy of the complex to which energies of the isolated species and isolated ice model are subtracted.

$$\Delta E = \Delta E^* + \delta E_S + \delta E_\mu + E_L$$
$$= E_{complex} - E_{ice} - E_{species}. \quad \text{(B3)}$$

For the crystalline systems, inclusion of the ZPE corrections to the BE are performed according to the equation BE(0) = BE − ΔZPE, where

$$\Delta ZPE = ZPE_{complex} - ZPE_{ice} - ZPE_{species}. \quad \text{(B4)}$$

For the amorphous case, inclusion of ZPE corrections was done by applying a scaling factor derived from a linear correlation between BE and BE(0) in the crystalline systems, that is, BE(0) = 0.862*BE.

Finally, to check for accuracy and refine DFT BEs for our crystalline ice model, the single- and double-electronic excitation coupled-cluster method with an added perturbative description of triple excitations (CCSD(T)) was used, in combination with a correlation consistent basis set extrapolated to the largest possible basis set. These calculations have been performed with the Gaussian16 software package (Frisch et al. 2016). These refinements were performed through the ONIOM2 approach (Dapprich et al. 1999), dividing the systems into two parts (*model* and *real* systems), which are described by two different levels of theory (*high* and *low*). The *model* system (represented by the adsorbate and the two closest water molecules) was described by the *high* level of theory, CCSD(T). The *real* system (that is, the whole system) was described by the corresponding DFT (*low*) level of theory.

The ONIOM2-corrected BE is:

$$BE(ONIOM2) = BE(low, real)$$
$$+ BE(high, model) - BE(low, model). \quad \text{(B5)}$$

In this way, the ΔE = BE(high, model) − BE(low, model) represents the correction term to the energy of the *real* system due to the improved description at the *high* level. This

procedure ensures that if the *low* level of theory is improved to arrive at the *high* level of theory or if the *model* system is enlarged to become the *real* system, the energy of the whole system is that at the higher level of theory.

In this work, for the calculation of the ONIOM2-corrected BEs, BE(ONIOM2), Equation (B5) can be rewritten as

$$
\begin{aligned}
BE(ONIOM2) = {} & BE(DFT; \mu - ice) \\
& + BE(CCSD(T); \mu - 2H_2O) \\
& - BE(DFT; \mu - 2H_2O) \quad \quad (B6)
\end{aligned}
$$

where BE(DFT; $\mu - $ ice) is the BE computed at DFT//DFT, while the BEs of the model system ($\mu - 2H_2O$) are computed through single-point energy calculations at CCSD(T).

A thorough guide to the computation of BEs is available in the Supplementary Material.

Appendix C
S-bearing versus O-bearing Species
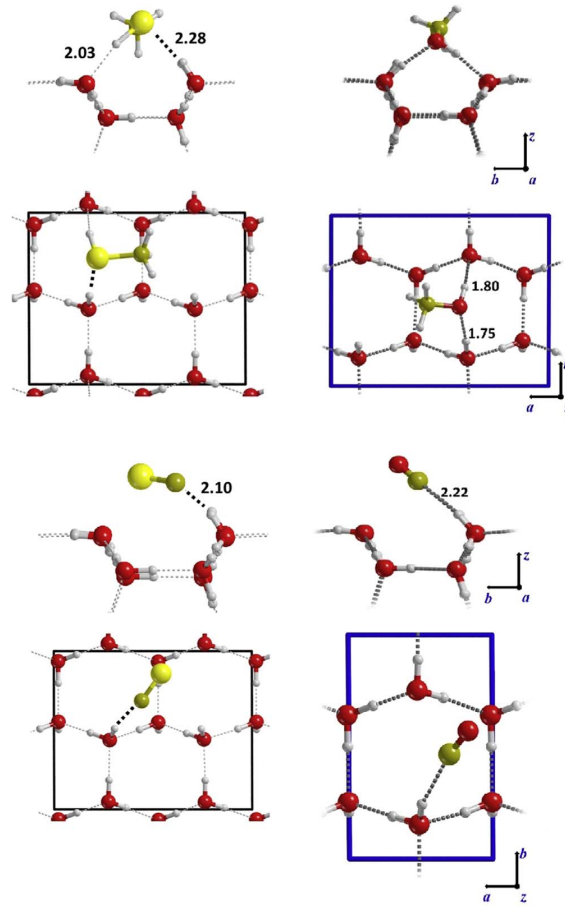
Figure 7. Adsorption geometry of S-bearing vs. O-bearing species at P-ice (010) surface. Side view is at the top; the top view is at the bottom. Complexes on the right (O-bearing species) are adapted from Ferrero et al. (2020). Distances are given in angstrom units. (i) CH$_3$SH vs. CH$_3$OH; (ii) CS vs. CO.
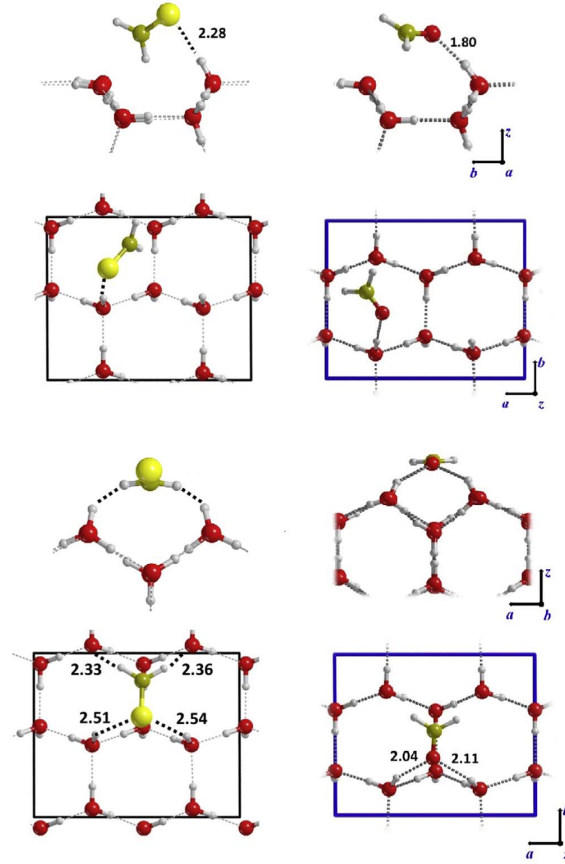
Figure 8. Adsorption geometry of S-bearing vs. O-bearing species at P-ice (010) surface. Side view is at the top; the top view is at the bottom. Adsorption complexes on the right (O-bearing species) are adapted from Ferrero et al. (2020). Distances are given in angstrom units. (i) First and (ii) second adsorption geometry of H$_2$CS vs. H$_2$CO.

15
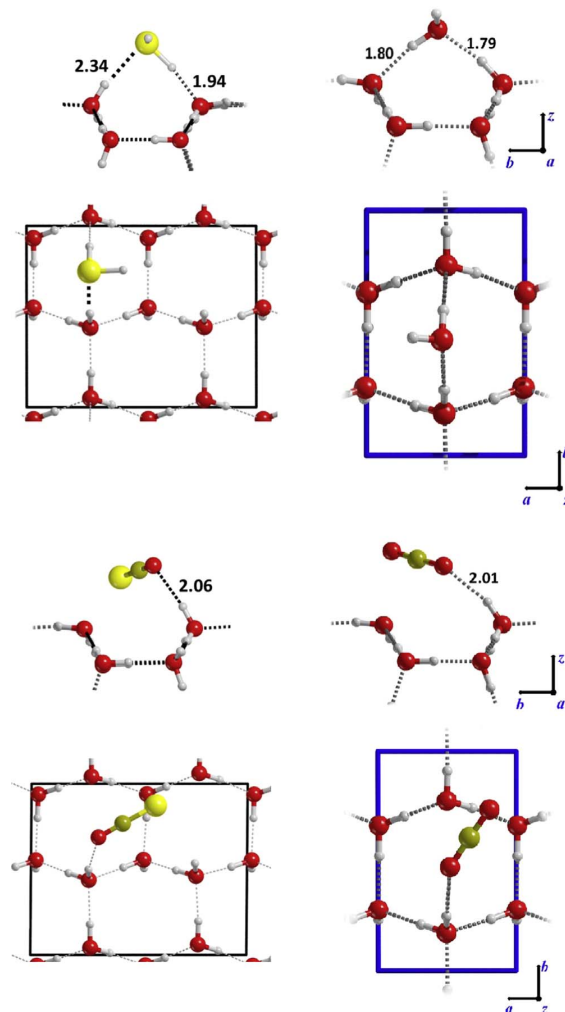
Figure 9. Adsorption geometry of S-bearing vs. O-bearing species at P-ice (010) surface. Side view is at the top; the top view is at the bottom. Adsorption complexes on the right (O-bearing species) are adapted from Ferrero et al. (2020). Distances are given in angstrom units. (i) H$_2$S vs. H$_2$O; (ii) adsorption geometry of OCS vs. CO$_2$.

ORCID iDs

Jessica Perrero ● https://orcid.org/0000-0003-2161-9120
Joan Enrique-Romero ● https://orcid.org/0000-0002-2147-7735
Stefano Ferrero ● https://orcid.org/0000-0001-7819-7657
Cecilia Ceccarelli ● https://orcid.org/0000-0001-9664-6292
Linda Podio ● https://orcid.org/0000-0003-2733-5372
Claudio Codella ● https://orcid.org/0000-0003-1514-3074
Albert Rimola ● https://orcid.org/0000-0002-9637-4554
Piero Ugliengo ● https://orcid.org/0000-0001-8886-9832

References

Aikawa, Y., & Herbst, E. 1999, A&A, 351, 233
Al-Halabi, A., & Van Dishoeck, E. F. 2007, MNRAS, 382, 1648
Allen, M., & Robinson, G. W. 1977, ApJ, 212, 396
Anders, E., & Grevesse, N. 1989, GeCoA, 53, 197
Becke, A. D. 1988, PhRvA, 38, 3098

Becke, A. D. 1993, JChPh, 98, 5648
Boogert, A. A., Gerakines, P. A., & Whittet, D. C. 2015, ARA&A, 53, 541
Bovolenta, G., Bovino, S., Vöhringer-Martinez, E., et al. 2020, MolAs, 21, 100095
Boys, S., & Bernardi, F. 1970, MolPh, 19, 553
Brandenburg, J. G., Alessio, M., Civalleri, B., et al. 2013, JPCA, 117, 9282
Broyden, C. G. 1970, JApMa, 6, 76
Casassa, S., Ugliengo, P., & Pisani, C. 1997, JChPh, 106, 8030
Ceccarelli, C., Caselli, P., Fontani, F., et al. 2017, ApJ, 850, 176
Ceccarelli, C., & Dominik, C. 2005, A&A, 440, 583
Cernicharo, J., Cabezas, C., Agúndez, M., et al. 2021, A&A, 648, L3
Chaabouni, H., Diana, S., Nguyen, T., & Dulieu, F. 2018, A&A, 612, A47
Codella, C., Podio, L., Garufi, A., et al. 2020, A&A, 644, A120
Collings, M. P., Anderson, M. A., Chen, R., et al. 2004, MNRAS, 354, 1133
Cooke, I. R., Öberg, K. I., Fayolle, E. C., Peeler, Z., & Bergner, J. B. 2018, ApJ, 852, 75
Cuppen, H. M., Walsh, C., Lamberts, T., et al. 2017, SSRv, 212, 1
Cutini, M., Civalleri, B., Corno, M., et al. 2016, J. Chem. Theory Comput., 12, 3340
Cutini, M., Civalleri, B., & Ugliengo, P. 2019, ACS Omega, 4, 1838

Perrero et al.

Cutini, M., Corno, M., & Ugliengo, P. 2017, J. Chem. Theory Comput., 13, 370
Dapprich, S., Komáromi, I., Byun, K. S., Morokuma, K., & Frisch, M. J. 1999, Comput. Theor. Chem., 461, 1
Das, A., Sil, M., Gorai, P., Chakrabarti, S. K., & Loison, J. C. 2018, ApJS, 237, 9
Dohnálek, Z., Kimmel, G. A., Joyce, S. A., et al. 2001, JPCB, 105, 3747
Douglas, A. E., & Herzberg, G. 1942, CJRes, 20a, 71
Dovesi, R., Erba, A., Orlando, R., et al. 2018, WIREs Comput. Mol. Sci., 8, e1360
Draine, B. T., & Sutin, B. 1987, ApJ, 320, 803
Druard, C., & Wakelam, V. 2012, MNRAS, 426, 354
Dulieu, F., Congiu, E., Noble, J., et al. 2013, NatSR, 3, 1338
Dunning, T. H. 1989, JChPh, 90, 1007
Enrique-Romero, J., Ceccarelli, C., Rimola, A., et al. 2021, A&A, 655, A9
Fayolle, E. C., Balfe, J., Loomis, R., et al. 2016, ApJL, 816, L28
Ferrero, S., Zamirri, L., Ceccarelli, C., et al. 2020, ApJ, 904, 11
Fletcher, R. 1970, CompJ, 13, 317
Frisch, M. J., Trucks, G. W., Schlegel, H. B., et al. 2016, Gaussian 16 Revision C.01 (Wallingford, CT: Gaussian Inc.), https://gaussian.com
Garrod, R. T., Wakelam, V., & Herbst, E. 2007, A&A, 467, 1103
Germain, A., Tinacci, L., Pantaleone, S., Ceccarelli, C., & Ugliengo, P. 2022, ESC, 6, 1286
Ghesquiere, P., Mineva, T., Talbi, D., et al. 2015, PCCP, 17, 11455
Goldfarb, D. 1970, MaCom, 24, 23
Grimme, S., Antony, J., Ehrlich, S., & Krieg, H. 2010, JChPh, 132, 154104
Grimme, S., Ehrlich, S., & Goerigk, L. 2011, JCoCh, 32, 1456
Hasegawa, T. I., & Herbst, E. 1993, MNRAS, 261, 83
He, J., Acharyya, K., & Vidali, G. 2016, ApJ, 825, 89
He, J., Emtiaz, S. M., & Vidali, G. 2017, ApJ, 837, 65
He, J., Emtiaz, S. M., & Vidali, G. 2018, ApJ, 863, 156
Hily-Blant, P., Pineau des Forêts, G., Faure, A., & Lique, F. 2022, A&A, 658, A168
Jenkins, E. B. 2009, ApJ, 700, 1299
Jiménez-Escobar, A., & Muñoz Caro, G. M. 2011, A&A, 536, A91
Johnson, D. D. 1988, PhRvB, 38, 12807
Kama, M., Shorttle, O., Jermyn, A. S., et al. 2019, ApJ, 885, 114
Karssemeijer, L. J., & Cuppen, H. M. 2014, A&A, 569, A107
Keller, L. P., Hony, S., Bradley, J. P., et al. 2002, Natur, 417, 148
Kouchi, A., Furuya, K., Hama, T., et al. 2020, ApJL, 891, L22
Kruse, H., & Grimme, S. 2012, JChPh, 136, 154101
Laas, J. C., & Caselli, P. 2019, A&A, 624, A108
Lauck, T., Karssemeijer, L., Shulenberger, K., et al. 2015, ApJ, 801, 118
Lee, C., Yang, W., & Parr, R. G. 1988, PhRvB, 37, 785
Mason, N. J., Nair, B., Jheeta, S., & Szymanska, E. 2014, FaDi, 168, 235
Maté, B., Cazaux, S., Satorre, M. Á., et al. 2020, A&A, 643, A163
McElroy, D., Walsh, C., Markwick, A. J., et al. 2013, A&A, 550, A36
McGuire, B. A. 2022, ApJS, 259, 30
McKellar, A. 1940, PASP, 52, 187
Mifsud, D. V., Kaňuchová, Z., Herczku, P., et al. 2021, SSRv, 217, 14
Minissale, M., Aikawa, Y., Bergin, E., et al. 2022, ESC, 6, 597
Mispelaer, F., Theulé, P., Aouididi, H., et al. 2013, A&A, 555, A13
Molinari, S., Ceccarelli, C., White, G. J., et al. 1999, ApJL, 521, L71
Molpeceres, G., Rimola, A., Ceccarelli, C., et al. 2019, MNRAS, 482, 5389
Neese, F. 2004, JPCS, 65, 781
Neese, F. 2009, Coord. Chem. Rev., 253, 526
Noble, J. A., Theule, P., Mispelaer, F., et al. 2012, A&A, 543, A5

Öberg, K. I., & Bergin, E. A. 2021, PhR, 893, 1
Pack, J. D., & Monkhorst, H. J. 1977, PhRvB, 16, 1748
Pantaleone, S., Enrique-Romero, J., Ceccarelli, C., et al. 2020, ApJ, 897, 56
Pantaleone, S., Enrique-Romero, J., Ceccarelli, C., et al. 2021, ApJ, 917, 49
Pascale, F., Zicovich-Wilson, C. M., Lopez Gejo, F., et al. 2004, JCoCh, 25, 888
Peebles, L. R., & Marshall, P. 2002, CPL, 366, 520
Penteado, E. M., Walsh, C., & Cuppen, H. M. 2017, ApJ, 844, 71
Phuong, N. T., Chapillon, E., Majumdar, L., et al. 2018, A&A, 616, L5
Podio, L., Garufi, A., Codella, C., et al. 2020a, A&A, 644, A119
Podio, L., Garufi, A., Codella, C., et al. 2020b, A&A, 642, L7
Pople, J. A., Gill, P. M. W., & Handy, N. C. 1995, IJQC, 56, 303
Rae, J. G. L., Hartquist, T. W., Lepp, S. H., O'Neill, P. T., & Williams, D. A. 2004, A&A, 413, 1
Redhead, P. 1962, Vacuu, 12, 203
Rimola, A., Ceccarelli, C., Balucani, N., & Ugliengo, P. 2021a, FrASS, 8, 655405
Rimola, A., Ferrero, S., Germain, A., Corno, M., & Ugliengo, P. 2021b, Mine, 11, 26
Rodríguez-Almeida, L. F., Jiménez-Serra, I., Rivilla, V. M., et al. 2021, ApJL, 912, L11
Ruf, A., Bouquet, A., Boduch, P., et al. 2019, ApJL, 885, L40
Ruffle, D. P., Hartquist, T. W., Caselli, P., & Williams, D. A. 1999, MNRAS, 306, 691
Schäfer, A., Horn, H., & Ahlrichs, R. 1992, JChPh, 97, 2571
Shalayel, I., Youssef-Saliba, S., Vazart, F., et al. 2020, EurJOC, 2020, 3019
Shanno, D. F. 1970, MaCom, 24, 647
Shimonishi, T., Nakatani, N., Furuya, K., & Hama, T. 2018, ApJ, 855, 27
Smith, R. S., May, R. A., & Kay, B. D. 2016, JPCB, 120, 1979
Song, L., & Kästner, J. 2017, ApJ, 850, 118
Sure, R., & Grimme, S. 2013, JCoCh, 34, 1672
Swings, P., & Rosenfeld, L. 1937, ApJ, 86, 483
Tatewaki, H., & Huzinaga, S. 1980, JCoCh, 1, 205
Terada, H., & Tokunaga, A. T. 2012, ApJ, 753, 19
Tieftrunk, A., Pineau des Forets, G., Schilke, P., & Walmsley, C. M. 1994, A&A, 289, 579
Tinacci, L., Germain, A., Pantaleone, S., et al. 2022, ESC, 6, 1514
van't Hoff, M. L. R., van Dishoeck, E. F., Jørgensen, J. K., & Calcutt, H. 2020, A&A, 633, A7
Vastel, C., Quénard, D., Le Gal, R., et al. 2018, MNRAS, 478, 5514
Wakelam, V., Caselli, P., Ceccarelli, C., Herbst, E., & Castets, A. 2004, A&A, 422, 159
Wakelam, V., Loison, J.-C., Herbst, E., et al. 2015, ApJS, 217, 20
Wakelam, V., Loison, J.-C., Mereau, R., & Ruaud, M. 2017, MolAs, 6, 22
Walmsley, C. M., Flower, D. R., & Pineau des Forêts, G. 2004, A&A, 418, 1035
Watanabe, N., & Kouchi, A. 2008, PrSS, 83, 439
Woods, P. M., Occhiogrosso, A., Viti, S., et al. 2015, MNRAS, 450, 1256
Woon, D. E., & Herbst, E. 2009, ApJS, 185, 273
Zamirri, L., Casassa, S., Rimola, A., et al. 2018, MNRAS, 480, 1427
Zamirri, L., Corno, M., Rimola, A., & Ugliengo, P. 2017, ESC, 1, 384
Zamirri, L., Pantaleone, S., & Ugliengo, P. 2019a, JChPh, 150, 064702
Zamirri, L., Ugliengo, P., Ceccarelli, C., & Rimola, A. 2019b, ESC, 3, 1499
Zhao, Y., & Truhlar, D. G. 2008, Theor. Chem. Acc., 120, 215
Zicovich-Wilson, C. M., Pascale, F., Roetti, C., et al. 2004, JCoCh, 25, 1873

Binding Energies and Vibrational Spectral Features of S_n Species on Amorphous Water-ice Mantles: A Quantum Mechanical Study

Jessica Perrero[1,2] , Leire Beitia-Antero[3,4] , Asunción Fuente[5] , Piero Ugliengo[2] , and Albert Rimola[1]

[1] Departament de Química, Universitat Autònoma de Barcelona, Bellaterra, 08193 Catalonia, Spain; albert.rimola@uab.cat

[2] Dipartimento di Chimica and Nanostructured Interfaces and Surfaces (NIS) Centre, Università degli Studi di Torino, via P. Giuria 7, 10125, Torino, Italy; piero.ugliengo@unito.it

[3] AEGORA Research Group—Joint Center for Ultraviolet Astronomy, Universidad Complutense de Madrid, Plaza de Ciencias 3, 28040 Madrid, Spain

[4] Departamento de Estadística e Investigación Operativa, Fac. de CC. Matemáticas, Plaza de Ciencias 3, 28040 Madrid, Spain

[5] Centro de Astrobiología (CSIC/INTA), Ctra.de Torrejón a Ajalvir km 4, E-28806 Torrejón de Ardoz, Spain

Received 2024 March 14; revised 2024 May 14; accepted 2024 June 5; published 2024 August 5

Abstract

In the denser and colder regions of the interstellar medium (ISM), gas-phase sulfur is depleted by 2 or 3 orders of magnitude with respect to its cosmic abundance. Thus, which species are the main carriers of sulfur is an open question. Recent studies have proposed S_n species as potential sulfur reservoirs. Among the various sulfur allotropes, the most stable one is the S_8 ring, detected in the asteroid Ryugu and Orgueil meteorite. Shorter species, namely S_3 and S_4, have been found in the comet 67P/C-G, but their presence in the ISM remains elusive. In this study, we compute the binding energies (BEs) of S_n ($n = 1$–8) species on an amorphous water-ice surface model and analyze their infrared (IR) and Raman spectral features to provide data for their identification in the ISM. Our computations reveal that these species exhibit lower BEs than previously assumed and that their spectral features experience minimal shifts when adsorbed on water ice, because of the weak and nonspecific S_n–ice interactions. Furthermore, these species display very low IR band intensities and, therefore, very accurate instruments operating in the mid-IR range are required for detecting the presence of these species in dense interstellar environments.

Unified Astronomy Thesaurus concepts: Surface ices (2117); Interstellar dust (836); Interstellar molecules (849); Dense interstellar clouds (371); Interstellar medium (847); Solid matter physics (2090); Computational methods (1965); Interstellar dust processes (838)

1. Introduction

Sulfur chemistry has garnered significant interest in astrochemistry, particularly since sulfur depletion in the interstellar medium (ISM) was first acknowledged in the 1970s (Spitzer & Jenkins 1975; Gondhalekar 1985). Although the abundance of sulfur in the gas phase of the diffuse medium is consistent with the cosmic value, $[S]/[H] = 1.5 \times 10^{-5}$ cm^{-3} (Jenkins 2009), more evolved environments such as translucent clouds and dense clouds are characterized by an environment-dependent depletion of 1 or 2 orders of magnitude (Fuente et al. 2023). Initially, the sulfur missing from the gas phase was expected to yield H_2S on the icy grain mantles (Caselli et al. 1994), similar to the freezing of oxygen atoms yielding H_2O. However, the abundance of S-bearing species observed in the ice mantle (OCS and tentatively SO_2) and the upper limits estimated for H_2S account for less than 5% of the sulfur budget in the solid phase (Boogert et al. 2022; McClure et al. 2023). For this reason, the main reservoirs of sulfur are still unknown, and its chemistry is being extensively investigated.

Sulfur is known to present different molecular allotropes, forming chains and rings up to 20 atoms, as it easily tends to react with itself even in a diluted medium. In the last 20 yr, the interest in the S_n species (with $2 \leqslant n \leqslant 8$) has grown exponentially in the field of astrochemistry, after being first proposed as S-reservoirs (Wakelam et al. 2004). Several experiments have shown the production of these species,

together with H_2S_n (with $n \geqslant 2$), after the photoprocessing of H_2S-containing ices (e.g., Ferrante et al. 2008; Jiménez-Escobar & Caro 2011; Jiménez-Escobar et al. 2014; Cazaux et al. 2022). When including proper reaction pathways, astrochemical models also predict their formation (Laas & Caselli 2019). In particular, when considering cosmic-ray-driven radiation chemistry and fast nondiffusive reactions for bulk radicals, pure sulfur allotropes are one of the main products (Shingledecker et al. 2020). So far, the only molecule characterized by an S–S bond was detected in the Horsehead nebula, a moderately UV-irradiated environment, where gas-phase S_2H was found (Fuente et al. 2017). On the other hand, S_3 and S_4 have been detected in the comet 67P/C-G (beside sulfides and sulfur oxides) by Calmonte et al. (2016). In the same source, Altwegg et al. (2022) have also detected ammonium sulfide, which is the most abundant salt of the comet. S_n species have also been found in other bodies of the solar system, such as the Ryugu asteroid and the Orgueil meteorite, which contain low and high abundances of S_8, respectively (Aponte et al. 2023).

The formation mechanism of S_n species is suspected to depend on the environment. Translucent cloud conditions are more likely to favor the formation of long-S_n species (Cazaux et al. 2022), as Ruffle et al. (1999) suggested that the negative grain charge distribution could be responsible for enhancing S^+ accretion on the core of the grains. On the other hand, laboratory experiments predict the formation of short S_n species due to the UV photoprocessing of H_2S ice, along with the formation of H_2S_n species (Jiménez-Escobar & Caro 2011; Jiménez-Escobar et al. 2014). The abundance ratio between the species that are formed depends on the shielding effect of the

H₂S ice (Cazaux et al. 2022). S_n ($n > 4$) species would be more refractory as n increases, so that they could not desorb from the core of the grains in hot cores/hot corinos, but could be released in shock regions. On the other hand, S_n ($2 \leqslant n \leqslant 4$) species could potentially be observed in less harsh environments, and hence the need for providing spectroscopic data for their identification.

With the launch of JSWT in 2021 December and the beginning of the EUCLID mission in 2023 July, numerous spectra will be collected, not only for gas-phase species, but also for interstellar ices, and the interpretation of the spectra will need both experimental and computational data.

From a theoretical point of view, there are several studies on the S_n-free molecules that elucidate their geometrical features and electronic states (e.g., Raghavachari et al. 1990; McCarthy et al. 2004a, 2004b). Their infrared (IR) and Raman spectra have been recorded experimentally in the gas phase or with matrix isolation in the solid argon technique, depending on which was more feasible for each species, which are collected in reviews (Eckert & Steudel 2003; Trofimov et al. 2009). Gas-phase S_3 and S_4 have also been characterized by means of rotational spectroscopy in the millimeter regions, providing valuable data for their detection and identification in the ISM (McCarthy et al. 2004a, 2004b). However, to the best of our knowledge, no previous studies have been conducted on S_n interacting with water ice. Thus, in this work, we focus on the adsorption of S_n ($n = 1$–8) species on interstellar water ices (here modeled as an extended periodic amorphous surface) with the aim of providing their binding energies (BEs) and vibrational spectroscopic (IR and Raman) properties computed at a quantum mechanical level. BEs are important parameters used in astrochemical models to describe the chemical evolution of planet-forming environments. Since BEs appear in exponential terms, their accuracy is mandatory to provide sensible results. Additionally, the perturbation of the vibrational IR and Raman bands of the S_n species due to the adsorption at ice will be of great value for their experimental detection in ISM ices (at least for the IR spectra). In Section 2, we describe the methodology applied in the simulations, and in Section 3 we present the results and a discussion of their implications in the field of astrochemistry. Finally, in Section 4, we summarize our conclusions.

2. Methodology

All the calculations were performed with the periodic ab initio code CRYSTAL17 (Dovesi et al. 2018), which allows the simulation of systems from zero to three periodic dimensions (i.e., molecules, polymers, surfaces, and bulks) and describes the atoms with Gaussian-type orbitals instead of plane waves (as commonly employed in periodic codes). Due to such a feature, our surfaces are slab models, to which periodic boundary conditions (PBCs) along two directions have been applied, presenting a finite thickness in the nonperiodic direction.

After finding the most stable conformer and electronic state of each gas-phase S_n species, we computed their adsorption on a periodic amorphous-like water-ice surface (see Figure 1). This model was designed by Ferrero et al. (2020b), by joining three amorphous water clusters and applying the PBCs, thus cutting the obtained bulk ice model along the (010) plane to yield a periodic surface. The resulting slab was characterized by edges and cavities, with binding sites possessing different
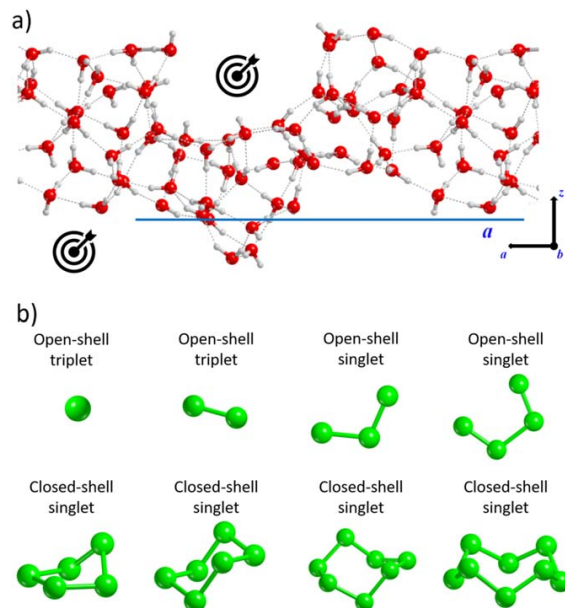
Figure 1. (a) The amorphous periodic water-ice model adopted in this work. The target icon indicates the binding sites considered for the adsorption of species from S to S_8. Color code: red, oxygen; and gray, hydrogen. (b) Species characterized in this work with the corresponding electronic ground state. Species from S to S_4 are linear chains (top row), while species from S_5 to S_8 are cyclic rings (bottom row).

adsorption strengths. The distinct morphologies of the upper and lower surfaces are responsible for the presence of a small electric dipole moment across the nonperiodic direction. The unit cell has 180 atoms and its cell parameters are $a = 20.275$ Å, $b = 10.052$ Å, and $\gamma = 103°442$ within the adopted density functional theory (DFT) level (see below).

The geometry optimizations of the gas-phase S_n species and their adsorption complexes were performed with the hybrid DFT BHLYP functional (Becke 1993; Lee et al. 1988), supplemented with the D3(BJ) dispersion correction by Grimme et al. (2010) and combined with the Ahlrichs-VTZ* (A-VTZ*) basis set, previously adopted in Ferrero et al. (2020b) and Perrero et al. (2022). The choice of this functional was justified by the need to treat both closed-shell and open-shell species at the highest cost-effective ratio. Thus, we relied on the known good performance of the B3LYP functional in similar previous publications (Ferrero et al. 2020b; Perrero et al. 2022) and chose to use a higher percentage of exact exchange (50%) to properly describe open-shell species, resulting in the adoption of the BHLYP-D3(BJ)/A-VTZ* methodology.

The adsorption complexes were computed by relaxing both the internal atomic positions and the unit cell parameters. We selected two binding sites on the amorphous ice model in order to represent the two main binding sites that this model offers: (i) the cavity region; and (ii) a flat portion of the surface. In the previous works of Ferrero et al. (2020b) and Perrero et al. (2022), more binding sites were probed, with the aim of defining BE ranges for a larger set of species that were, however, relatively small in size. In this case, since large nonpolar species are involved (interacting mainly through weak nonspecific forces), we suppose these two binding sites to be

representative of the range of interactions between the molecule and the ice surface. We expect larger BEs for species adsorbed in the cavity region than in the flat region because of the larger contact surface between the adsorbate and the ice-water molecules (and hence larger interactions) in the former case.

The final BEs, BE(0), were computed through the equation:

$$BE(0) = BE - \Delta ZPE = -(\Delta E - BSSE) - \Delta ZPE, \quad (1)$$

where the interaction energy $\Delta E = E_{complex} - E_{ice} - E_{species}$ was corrected for the basis set superposition error (BSSE; arising from the finiteness of the basis set) and for the zero-point energy ($\Delta ZPE = ZPE_{complex} - ZPE_{ice} - ZPE_{species}$) computed at 0 Kelvin. The ice surface taken as reference is the one optimized after the desorption of the adsorbate, this way neglecting spurious effects in the BE(0)s due to an over-deformation of the ice structure induced by the presence of the adsorbate and caused by the finite thickness of the ice model. Indeed, our experience indicates that an amorphous ice surface, contrary to a rigid crystalline one, can dramatically reconstruct locally to better accommodate the adsorbate (Perrero et al. 2022, 2023). The significant deformation observed is the result of fully relaxing the geometry of the systems (both internal atomic positions and unit cell parameters), which is compulsory for ensuring that the adsorption complexes are actual minima stationary points and hence for accurately computing IR and Raman spectra. Consequently, during the optimization process, the ice unit cell may contract or expand, contrary to what would happen on a real ice surface. To address this discrepancy, we opted to derive BEs from simulations of desorption processes. Basically, we simulate a desorption process rather than an adsorption one, in which, on the latter, the reference surface is the pristine one, while for the former it is the one left after desorption. The different terms that contribute to the BE(0) are analyzed and explained in Appendix B, and for their detailed explanation, we refer the reader to the works of Ferrero et al. (2020b) and Perrero et al. (2022).

Frequency calculations on the BHYLP-D3(BJ)/A-VTZ*-optimized geometries were run on the adsorption complexes with a twofold aim: (i) of confirming the nature of the minima on the potential energy surface (PES); and (ii) of computing the IR and Raman spectra. The Hessian matrix was calculated considering only the displacements of the S$_n$ adsorbed species, while the rest of the system is kept at fixed geometry. We previously checked that the exclusion of water molecules did not have a significant influence on the fragment Hessian matrix and, therefore, on the final vibrational spectra. For each coordinate, two displacements along each of the three cartesian coordinates were computed, with a step of 0.001 Å and a tolerance on the SCF energy of 10^{-11} atomic units. Both the IR and Raman intensities were computed through a coupled-perturbed Hartree–Fock/Kohn–Sham approach (Pascale et al. 2004; Zicovich-Wilson et al. 2004), which allows for a completely analytical calculation of Born charges, IR intensities, and dielectric and Raman tensors. Please note that although we used a fragment to calculate the frequencies involving only the S atoms of the S$_n$ species, the IR and Raman intensities are unaffected by this approach. Indeed, for the IR spectra, the transition dipole moment governing their intensities is calculated through a wave function encompassing the whole system, which accordingly accounts for the polarization effects

of the ice. This is also the case for the Raman intensities, as the transition polarizability is calculated with the complete wave function. The vibrational modes were classified through the analyzer implemented in CRYSTAL17. The software decomposes the motion of each couple of atoms into three components: the first along the two atoms; the second on the plane containing a third atom; and the third out of the abovementioned plane. Finally, it uses this information to classify the modes as stretching (S), bending (B), or other (O). The IR and Raman spectra were calculated by a raw superposition of Lorentzian peaks, with an FWHM of 8 cm^{-1}, applying a Lorentzian broadening to the peaks after computing their relative intensities (Maschio et al. 2013a, 2013b).

3. Results and Discussion

3.1. Gas-phase S$_n$ Species

Numerous studies in the literature have delved into the various molecular allotropes of sulfur. These investigations focused not only on the structural features and electronic states of the S$_n$ species but also on their spectroscopic properties. The electronic ground state of atomic sulfur and S$_2$ is a triplet (like atomic oxygen and O$_2$), while species with n $\geqslant$ 6 are closed-shell monocyclic rings, which have been characterized by X-ray crystallography and IR spectroscopy (Eckert & Steudel 2003). However, the S$_3$, S$_4$, and S$_5$ systems have sparked debates regarding their configuration as either chains or rings, prompting extensive research (e.g., Meyer & Stroyer-Hansen 1972; McCarthy et al. 2004a, 2004b; Thorwirth et al. 2005). Figure 1 shows the most stable structures and their electronic states found with our computational methodology. In the following, we provide a comparison between our results and literature data. The singlet and triplet state energies of each species can be found in Appendix A.

In their quantum chemical investigation, Raghavachari et al. (1990) showed that the most stable conformation for S$_3$ was a chain, in a singlet electronic state. Our calculations agree with this hypothesis when an open-shell singlet electronic configuration is assumed. Moreover, we find that the second most stable configuration is the closed-shell singlet spin state, closely followed by a ring structure with a closed-shell singlet electronic state.

For S$_4$, DFT calculations have revealed six possible isomers, involving both chains and rings, which can be detected under nonequilibrium conditions (Eckert & Steudel 2003). The open-chain structure with C$_{2v}$ symmetry and an open-shell singlet electronic state was reported as the most stable isomer (McCarthy et al. 2004b), which is in agreement with our calculations at the BHLYP-D3(BJ) level of theory.

S$_5$ is a minority species in sulfur vapor at all temperatures and pressures (Steudel et al. 2003), and it is the least-characterized structure, for which no spectral information is available. Only one minimum can be found on the PES of S$_5$, corresponding to the envelope conformation, while the half-chair conformation is a saddle point (Cioslowski et al. 2001). In our calculations, we find that the energy difference between the two conformations is 0.7 kJ mol^{-1} at the DFT level of theory, and the presence of an imaginary frequency for the half-chair conformation confirms that the envelope structure is the correct minimum.

Rings as S$_6$ and larger can also be found in the solid phase. S$_6$ is a highly symmetric homocycle, the most stable conformer

Perrero et al.

Table 1
BE(0) in Kilojoules per Mole for S_n Species Adsorbed on the Two Binding Regions of the Amorphous Ice Model, Computed at the BHLYP-D3(BJ)/A-VTZ* Level of Theory

BE(0)	Surface	S	S_2	S_3	S_4	S_5	S_6	S_7	S_8
Flat (this work)	Comput., periodic H_2O ice	16.4	17.8	31.5	41.8	43.2	47.9	57.5	52.7
Cavity (this work)	Comput., periodic H_2O ice	25.5	22.2	44.9	41.0	53.0	52.7	64.0	71.2
Perrero et al. (2022)	Comput., periodic H_2O ice	13.1–23.3	8.6–20.4	...	...	...	...	...	...
Cazaux et al. (2022)	Exp., H_2S ice	...	28.2[a]	49.9[a]	70.6[a]	89.8[b]	109.7[b]	129.7[b]	149.7[b]
Penteado et al. (2017)	Exp. and Comput.	8.2 ± 4.1	16.6 ± 4.1						
Wakelam et al. (2017)	Comput., 1 H_2O	21.6	...	...	...	...	...	...	...
Das et al. (2018)	Comput., $(H_2O)_4$ cluster	11.9	13.7	...	...	...	...	...	...
KIDA (Wakelam et al. 2015)	...	...	21.6[c]	18.3[d]	...	...	...	...	...
UMIST (McElroy et al. 2013)	...	...	9.1[d]	18.3[d]	...	...	...	...	...

Notes. Values from the literature are listed for comparison.
[a] Values derived from laboratory experiments.
[b] Extrapolated values (see the main text for details).
[c] Value from Wakelam et al. (2017).
[d] Values from Hasegawa et al. (1992).

being the chair conformation, in analogy to cyclohexane. S_7 is better known for existing in four bulk allotropic forms, while a ring with C_s symmetry is the favored conformer in the gas phase. S_8 constitutes the most thermodynamically stable and thus the common form of sulfur, and it has been determined to adopt a crown-shaped geometry in the gas phase (Raghavachari et al. 1990).

In summary, the ground states of the species targeted in this study are open-shell triplets for S and S_2, open-shell singlets for the chains S_3 and S_4, and closed-shell singlets for the rings from S_5 to S_8, all in agreement with previous literature data.

3.2. S_n–Ice Adsorption Complexes and BEs

For each S_n species, we consider two adsorption complexes on the amorphous ice model, initially locating the species on regions either geometrically flat or in the small surface cavity (highlighted by the target icon in Figure 1). Table 1 reports the computed BE(0) values and Figure 2 plots a comparative trend of the BE(0)s when the S_n species are adsorbed in either the cavity or on the flat regions. The terms contributing to the BE(0) values are reported in Table 2.

The interaction between the S_n species and the ice is almost entirely due to: (i) electronic effects (contributed by electrostatic interaction, Pauli repulsion, and orbital interaction due to charge transfer and polarization effects); and (ii) London dispersion interactions. The percentages of the dispersion interactions' contribution to each BE value (see Table 2) show their dominance, with the exception of atomic sulfur, for which 40%–50% of the ΔE is due to the electronic contribution. For the S_2 and S_4 cases, dispersion interactions even compensate for the slight repulsion from the pure electronic interactions ΔE. Therefore, the BE is dominated by dispersion interactions, which are governed by the mutual polarizability of the interacting species (ice grains and the S_n species). Indeed, the S_n species exhibit a high polarizability, but negligible electric multipoles provide a small contribution to the electrostatic component of the BE. For the same reasons, the charge transfer contribution is also very small. Accordingly, we obtain dispersion contributions ranging between 70%–100% of the total BE.

The BE(0) values reported in Table 1 indicate that S and S_2 are the two S-bearing species with lower BE(0)s, obviously due to the more limited electronic and dispersion contributions.

Remarkably, in the cavity region, atomic S interacts more strongly than S_2, as occurs for H and O compared to their corresponding (more inert and stable) diatomic H_2 and O_2 species (Ferrero et al. 2020a, 2020b; Minissale et al. 2022). From S_2 to S_8, the BE(0)s (and in particular the ΔE^* terms, free from the deformation energies; see Table 2) increase with the number of S atoms, as each atomic S addition gives further interactions in the S_n–ice complexes. That is, although the dispersion forces are weak, the sum of several small contributions can result in large interaction energies, especially when the adsorbate has several atoms due to establishing a large contact area with the surface. This effect is responsible for the increase of the BE with the number of S atoms in the adsorbed species, even in the absence of local interactions, such as hydrogen bonds.

The morphology of the surface binding site affects the resulting BE(0). Indeed, in most cases, the BE(0) in the cavity region is larger than that on the flat region (see panel (a)) of Figure 2. There is a good fit between the two sets of BE(0)s, revealing an increase of about 18% of the BE(0) when passing from the flat to cavity regions. As outlined before, the dispersion forces, responsible for the S_n–ice interactions, strongly depend on the contact area between the adsorbates and the surface water molecules, becoming larger as the surface contact area increases, due to the higher polarizability effects on the S_n species. In the amorphous cavity regions, almost every S atom of the adsorbed species interacts with the surface water molecules, while on the flat region, only some atoms of the adsorbate are directly facing the water molecules of the surface, the rest being oriented toward the gas phase. This results in a higher weight of dispersion interactions for species adsorbed in the cavity region (see panels (b) and (c) of Figure 2). The only exception is S_4 (with similar BE(0)s for the two regions), because the interaction of S_4 with the cavity is associated with a large deformation of the cavity surface region (listed in Table 2).

The adsorption of large rings in the cavity means, to some extent, a structural rearrangement of the surface to fit the molecule in the cavity. This is reflected by the increment of the surface deformation energy (δE_S) with the increase of the number of S atoms, in particular for the S_7 and S_8 cases. In contrast, the deformation of the adsorbed species (δE_μ) is of a
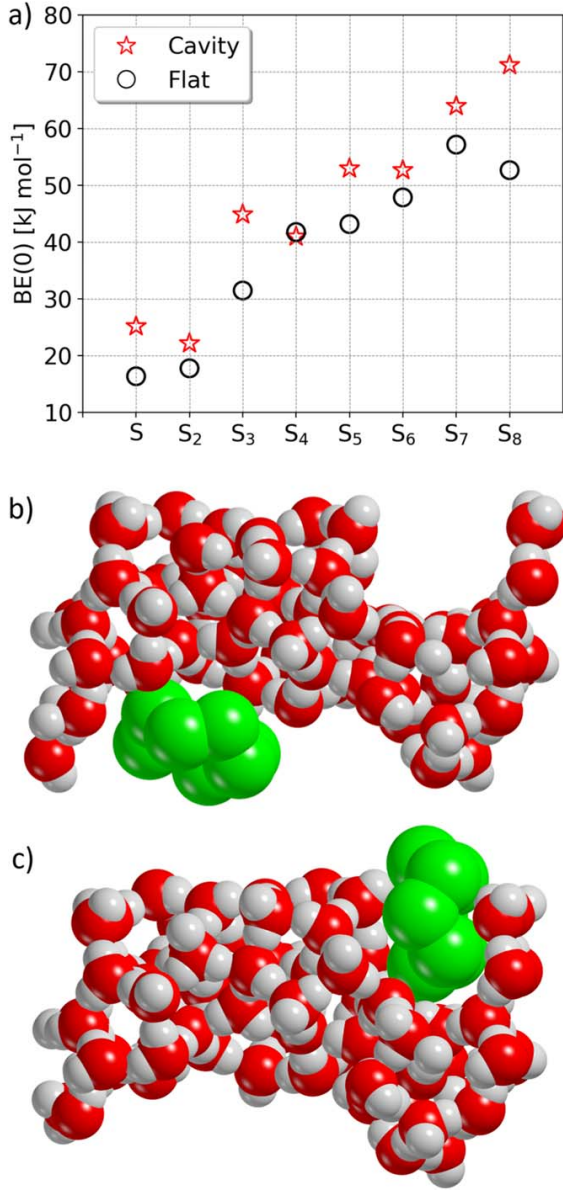
Figure 2. (a) BEs (BE(0), in kilojoules per mole) of S-chains at the BHLYP-D3(BJ)/A-VTZ* level of theory adsorbed onto the amorphous model (cavity site: star; and flat site: circle). Adsorption geometries of S_8 onto the amorphous ice surface: (b) flat region; and (c) cavity region.

few kJ mol^{-1}, since they do not suffer from structural modifications due to their weak interactions with the ice.

The lateral interaction energy (δE_L) between adsorbates in adjacent cells (whose absolute value is mainly below 2 kJ mol^{-1}; see Table 2), is indicative of the adequate dimensions of the unit cells for the simulation of the freeze-out of an isolated S_n species.

In the literature, the only previous study on the BEs of species from S_3 to S_8 is based on an experimental work by Cazaux et al. (2022; see Table 1). The BEs of S_2–S_4 are estimated from temperature-programmed desorption

experiments, based on the empirical rule defined in Luna et al. (2017), while the BEs of S_5–S_8 are extrapolated based on the trend obtained for S_2–S_4. However, the species were formed by H_2S photoprocessing, and therefore their BE data are not relative to the adsorption on water ice, but rather are the result of self-interactions among the different sulfur species formed during the experiment. For this reason, the comparison between the BEs computed in this work and those estimated and/or extrapolated in Cazaux et al. (2022) is not straightforward. A new set of experiments performed on water ice would be necessary to compare the data obtained from our calculations. From our own computed data, we plot the average BE of each species, BE(0)$_{avg}$ = (BE(0)$_{cavity}$ + BE(0)$_{flat}$)/2, against the number of S atoms of the adsorbate (see Figure 3). Clearly, the increase in BE(0)s with the number of S atoms does not simply scale linearly. Rather, it seems that close couples (S_1–S_2, S_3–S_4, S_5–S_6, and S_7–S_8) exhibit almost the same BE(0). Although the first increase between pairs is steep (20 kJ mol^{-1}), the others are more moderate (10 kJ mol^{-1}). This seems to be due to the same number of S atoms facing the ice surface (three S atoms for S_5–S_6 and four S atoms for the S_7–S_8 cases), significantly changing the dispersive interactions. Even if quite rough for the above reasons, the linear best fit of Figure 3 gives an increment of about 9 kJ mol^{-1} to the BE(0)$_{avg}$ for each added S atom. This increment is approximately half of the value proposed in the literature, which was set to 20 kJ mol^{-1} per S atom (see Cazaux et al. 2022). Therefore, we would like to raise awareness about the magnitude of the BEs reported in the literature, as its use in astrochemical modeling has a significant impact on the desorption rates. To have deeper insights into this point (namely, the influence of an error in the BE on the desorption rate constant), we calculated the ratio between desorption rates, r_{des} with an error δ on the BE, that is:

$$r_{des} = \frac{k_{des}(BE)}{k_{des}(BE + \delta)} = \exp\left(\frac{\delta}{RT}\right). \qquad (2)$$

Note that r_{des} does not depend on the BE itself. Larger errors will have a major impact at low temperatures, while they will be smeared out at high temperatures, bringing the δ/RT term toward zero. Considering the limit of chemical accuracy, the error is $\delta = 4$ kJ mol^{-1}, meaning that at $T = 10$ K, such an error implies a difference of 20 orders of magnitude on the k_{des}. At such low temperatures, however, thermal desorption of sulfur allotropes is negligible and the impact of our estimations on the gas chemistry would be moderate. In contrast, thermal desorption can be dominant in warmer regions, around young protostars. In these environments, dust temperatures are >50 K and some volatile compounds can be sublimated. At these temperatures, an error of $\delta = 4$ kJ mol^{-1} reduces the difference on the k_{des} to ~4 orders of magnitude, with a significant impact in the abundances of these species in the gas phase. Thus, the impact of minor inaccuracies in the BE on the results of a chemical model depends on the specific conditions of the region under study. The same absolute error on different BE values will have the same impact on the desorption rate, in which such an impact depends in turn on the considered environment.

As for atomic S and S_2 molecules, ab initio literature calculations have been performed to compute their BEs on interstellar ice mantles. For atomic S, Wakelam et al. (2017) used one water molecule to simulate the ice mantle, while Das

Table 2
Contributions to the BE(0)s (in Kilojoules per Mole) of the Adsorption Complexes Modeled on the Flat Region and in the Cavity Region of the Amorphous Ice Model, Computed at the BHLYP-D3(BJ)/A-VTZ* Level of Theory

Flat Region	S	S_2	S_3	S_4	S_5	S_6	S_7	S_8
ΔE	−18.3	−23.3	−39.3	−53.0	−50.9	−60.2	−68.0	−63.7
ΔE_{elect}	−7.1	+0.5	−9.4	+0.9	−20.1	−1.4	−12.1	−8.7
ΔE_{disp} (%)	−11.2 (61)	−23.8 (102)	−29.9 (76)	−54.0 (102)	−30.9 (61)	−58.8 (98)	−55.9 (82)	−55.0 (86)
δE_S	0.7	0.9	5.1	3.0	5.2	13.7	4.7	3.8
δE_μ	0.0	0.3	3.3	9.0	0.5	0.5	0.4	1.2
δE_L	0.0	−0.3	−0.1	−0.1	−0.4	−0.6	−1.0	−1.5
ΔE^*	−19.0	−24.2	−47.6	−65.0	−56.1	−73.8	−72.1	−67.2
BSSE	−1.9	−4.3	−6.0	−8.9	−5.8	−10.5	−8.5	−9.5
Cavity Region	**S**	**S_2**	**S_3**	**S_4**	**S_5**	**S_6**	**S_7**	**S_8**
ΔE	−27.6	−28.3	−53.8	−51.5	−63.4	−64.6	−78.3	−87.7
ΔE_{elect}	−14.0	+1.7	−15.2	+0.8	−11.3	+0.9	−6.3	−2.8
ΔE_{disp} (%)	−13.6 (49)	−30.0 (106)	−38.7 (66)	−52.3 (102)	−52.1 (82)	−65.5 (101)	−72.0 (92)	−85.0 (97)
δE_S	5.0	1.6	2.3	10.7	8.3	6.4	10.3	9.7
δE_μ	0.0	0.0	0.0	0.0	0.6	0.3	0.4	0.7
δE_L	0.0	0.0	−0.1	−0.3	−0.4	−0.4	−0.7	−1.4
ΔE^*	−32.7	−29.9	−56.0	−62.0	−71.9	−70.9	−88.3	−96.8
BSSE	−2.4	−4.8	−6.9	−8.7	−8.4	−10.3	−12.2	−14.7

Note. The equations showing how the terms add up are reported and explained in Appendix B. ΔE is the bare interaction energy, split into the electronic ΔE_{elect} and dispersive ΔE_{disp} contributions, the latter also in percentage; δE_S is the deformation energy of the surface; δE_μ is the deformation energy of the adsorbate; δE_L is the lateral interaction energy; ΔE^* is the deformation-free interaction energy; and the BSSE is the basis set superposition error.
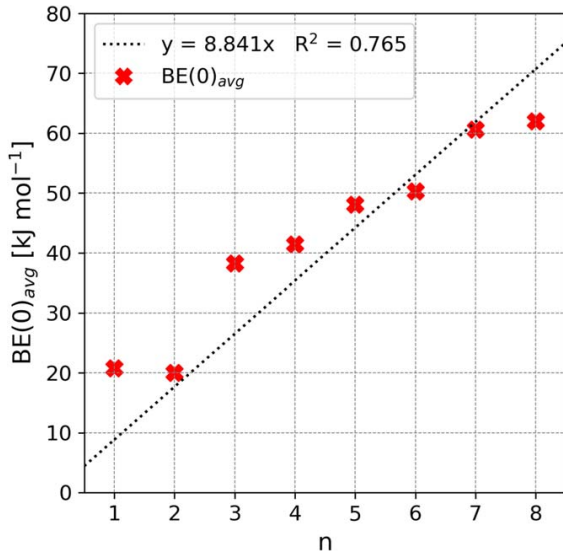
Figure 3. Correlation between the BE(0)$_{avg}$ and the number n of atoms of each S_n species. The linear fit does not seem appropriate for defining the trend, as it appears that the increase of BE(0) happens in steps every couple of species.

et al. (2018) used a water tetramer as an ice analog for studying S and S_2 adsorptions. An estimate of the BE of S and S_2 was provided by Penteado et al. (2017), in a review collecting values from both theoretical and experimental works. Other values of the BEs are tabulated in the UMIST and KIDA databases (McElroy et al. 2013; Wakelam et al. 2015). We also contributed, in a recent work (Perrero et al. 2022), to the BEs of S and S_2, while giving a range of BEs (computed at the M062X-D3/A-VTZ*//HF-3c level of theory) for each species on eight different binding sites available in the amorphous ice model of this work. Interestingly, the BEs computed in the

present work for S and S_2 cover the upper and lower limits of the ranges provided in Perrero et al. (2022). The computed BEs of S_2 were in agreement with previous literature values, while for atomic S, the weakest tail of the calculated BE range did not include the even smaller values proposed by Penteado et al. (2017) and by the UMIST database (McElroy et al. 2013). All the BE values reported in the literature are collected in Table 1.

3.3. Vibrational Spectroscopic Features

Here, we focus on the calculation of the frequencies (ν) of the S_n species (for $n = 2$–8) as gas-phase and as adsorbed complexes, for IR and Raman spectra. Table 3 shows the whole set of computed vibrational frequencies for the considered cases, while Figure 4 shows the comparison between the largest S_8 molecules in the gas phase and when adsorbed on the flat region.

Several studies have measured experimentally or simulated theoretically the spectra of these species, both in the gas phase or in the condensed phase. The reviews of Eckert & Steudel (2003) and Trofimov et al. (2009) are particularly useful for gathering detailed information. The main vibrational features available in the literature are reported in Table 3. It is worth noting that the comparison between the frequencies reported in the literature and those computed in this work is not always satisfying. For example, Lenain et al. (1988) report a stretching vibration for S_2 of 715 cm^{-1}, while our calculations give a value of 747 cm^{-1}. For S_3, Brabson et al. (1991) and Picquenard et al. (1993) give 281 cm^{-1} (Raman) for the bending and 581 cm^{-1} (Raman) and 680 (IR) cm^{-1} for the symmetric and antisymmetric stretching, respectively, while we find values of 254, 520, and 639 cm^{-1}. We can immediately see that the differences are large, even considering that highly accurate quantum chemical calculations have been performed, in agreement with what is reported in the literature (Steudel et al. 2003).

Table 3
Vibrational Frequencies in Inverse Centimeters Computed at the Full BHLYP-D3(BJ)/A-VTZ* Level

Specie	Gas Phase	Cavity Region	Flat Region	Type	IR	Raman	Tabulated Freq.	Type	Source
S_2	747	745	746	S	...	X	715	S	Raman
S_3	254	267	264	B	...	X	281	B	Raman
	520	518	556	S	...	X	581	S sym	Raman
	639	643	711	S	X	X	680	S antsym	IR
S_4	140	151	171	B	...	X	...	...	...
	310	315	330	B	...	X	303[a]	B	Raman
	322	336	458	B	X	X	...	...	...
	656	655	669	S	X	...	575[a]	S	Raman
	662	665	670/681	S	...	X	680[a]/683	S	Raman/IR
S_5	245	254	253	O	X	X	...	...	...
	306	308	307	B	X	X	...	...	...
	416	426/436	427	S	...	X	...	...	...
	423	426	423	S	X	...	...	...	...
	460	467	466	S	X	X	...	...	...
	525	516	524	S	X	...	...	...	...
	528	516/535	524	S	...	X	...	...	...
S_6	167	175	176	O	X	...	180	O	IR
	215	219	219	O	X (no gas)	X	...	...	...
	274	278	277	O	...	X	...	...	...
	329	333	333	O	X	...	313	B	IR
	...	441	444	S	X	...	...	...	...
	486	490	490	S	X	X	463	S	IR
	504	505	504	S	...	X	...	...	...
S_7	160	169	165	O	...	X	...	...	...
	181	186	187	O	X (no gas)	X	...	...	...
	243	251	247	B	X	X	235	B	IR
	285	290	288	B	X	...	270	B	IR
	300	298	303	B	...	X	...	...	...
	411	410	409	S	X	X	400	S	IR
	451	464	459	S	X	X	480	S	IR
	506	504	507	S	X	X	513	S	IR
	536	527	526	S	...	X	...	...	...
S_8	...	...	...	...	...	...	90	O	IR/Raman
	155	162	159	B	...	X	150–250	B	IR/Raman
	199	207	202	O	X	...	...	...	...
	224	230	227	O	...	X	...	...	...
	253	255	249	O	...	X	...	...	...
	256	261	257	O	X	...	...	...	...
	481	488	482	S	...	X	410–480	S	IR/Raman
	493	494	489	S	X	...	...	...	...
	498	501	499	S	...	X	...	...	...

Notes. The first seven columns are dedicated to computed values, while the last three columns are dedicated to literature values. The second column reports the frequencies computed for the gas-phase molecule, while the third and fourth columns report the ones for the adsorbate in the cavity and on the flat region of the amorphous model. The peaks are classified as stretching (S), bending (B), or other (O; representing different types of torsion), and it is indicated if they are IR- or Raman-active. S sym and S antsym indicate symmetric and asymmetric stretching, respectively. The literature values are taken from Eckert & Steudel (2003), with the exception of S_4, for which we refer to the work of Picquenard et al. (1993).
[a] For the sake of clarity, only strong bands for each species are reported. Origin of the spectra: S_2 was recorded in the gas phase; S_3 from sulfur vapors and matrix isolation in solid argon; and S_4 in saturated and unsaturated sulfur vapor—solid S_6, α-S_7, and α-S_8 were used to record their spectra. For a complete list of all the features, we refer the reader to Eckert & Steudel (2003) and Trofimov et al. (2009).

It is worth noting that no scaling was applied to our computed frequencies. Nevertheless, the absolute prediction of the vibrational frequencies is not the focus of this work; we are rather interested in highlighting the frequency shifts of the S_n species' vibrational modes with respect to the gas-phase values due to their interaction with the ice.

As mentioned above, the interaction between the S_n species and the water-ice surfaces is almost totally governed by London dispersion forces, which are very weak forces based on permanent dipole–induced dipole moments and therefore are nonspecific and nondirectional (at variance with the H-bonding). In our case, the dispersion contribution arises

from the interaction between the permanent dipole moment of the water surface molecules and the temporary or induced dipoles of the S_n adsorbates. The fact that dispersion forces are nonspecific and do not establish vibrational coupling with the water surface causes the adsorption of S_n species to be either only slightly perturbed or to have a null effect on the vibrational modes of the adsorbates. Consequently, the IR spectra are almost unperturbed with respect to the free S_n species. Additionally, the shifts observed when comparing gas-phase and adsorbed species' vibrational features further decrease with the molecular size of the adsorbate. This is in agreement with the decreasing contribution of the electronic
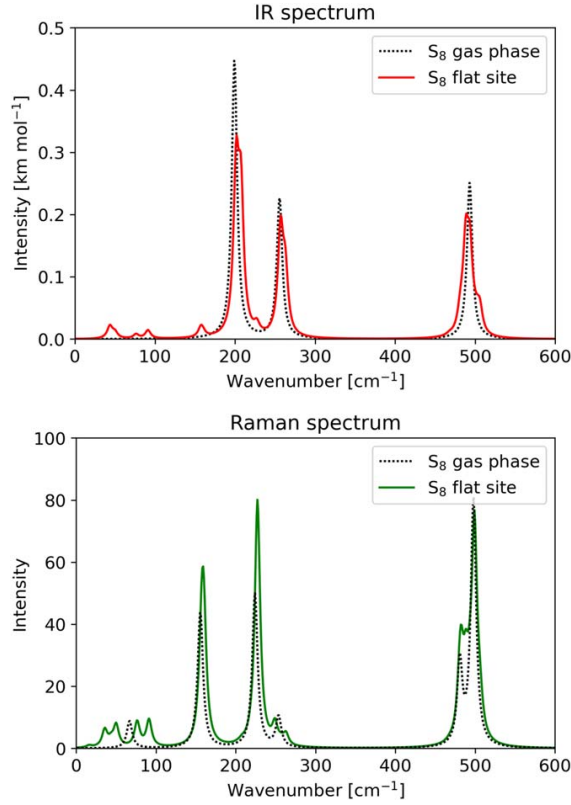
Figure 4. IR and Raman spectra of S$_8$ computed at the BHLYP-D3(BJ)/A-VTZ* level of theory. Dotted lines: gas-phase species. Solid lines: adsorbed species. IR intensities are in kilometers per mole, while Raman intensities are given in arbitrary units.

component of the BE(0) with the molecular size and the increasing role of the nonspecific London-type interactions. In general, we notice that both IR and Raman peaks suffer a small hypsochromic shift, due to a slight increase in the bond strength. We notice such an effect on S$_3$, whose bond lengths change from 1.951 Å in the gas phase to 1.901 and 1.930 Å for the adsorbed molecule on the flat and cavity regions of the ice. Such variations correspond to a hypsochromic shift of $\Delta\nu = 70$ cm^{-1} on the asymmetric stretching vibration (the only active IR mode). However, such a strong variation is observed only for S$_3$ (and S$_4$; see below), while for the other species, the caused change is much smaller (about $\Delta\nu = 0$–10 cm^{-1}). S$_2$ experiences no shift due to adsorption, as evidenced by the unaltered bond length (1.899 Å), and is consistent with its weak interaction with ice. While the S$_2$ stretching peak is active in Raman spectroscopy, in the IR spectra it is possible to distinguish between the gas-phase and the adsorbed cases. For symmetry, no bands are observed in the gas phase, while the interaction with the ice slightly activates this mode. The same phenomenon has been documented for CH$_4$ and NH$_4$SH, whose IR spectral features are affected by the presence of an amorphous water-ice matrix interacting with the adsorbate (Escribano et al. 2014; Hudson et al. 2015). Finally, for S$_4$, an interesting aspect appears: while there is no significant difference between the gas-phase and cavity region spectra, this is juxtaposed by a large change in the vibrational features

on the flat region. That is, the $\Delta\nu$ of the first two bending modes is 20–30 cm^{-1}, and $\Delta\nu > 100$ cm^{-1} for the third vibrational mode. The explanation can be found in the geometrical features of the molecule: for all the cases (gas phase and on both ice regions), the optimized conformer of S$_4$ falls into the C$_{2v}$ symmetry. The gas-phase S–S bond length of 2.201 Å shortens to 2.193 Å when adsorbed on the cavity, with a corresponding hypsochromic shift of $\Delta\nu = 20$–30 cm^{-1}. Even more so, when adsorbed on the flat region, the S–S bond length decreases to 2.056 Å, with a large hypsochromic shift of its stretching frequency ($\Delta\nu > 100$ cm^{-1}).

In principle, the present outcome may guide the interpretation of JWST spectra detection of interstellar ice, at least concerning the IR spectra. However, the absolute intensity of each IR vibrational mode is an important parameter, as it regulates the chance of being observed. Our results show many IR peaks with almost negligible intensities (which become smaller as the length of the S-chain increases), as the dipole changes during vibration are almost negligible for the homonuclear S$_n$ rings. It is a pity that Raman spectra of the interstellar matter cannot, unfortunately, be observed with the present technology, as the Raman intensities, depending on the polarizability of the molecule, are rather high. Indeed, sulfur is a large and easily polarizable atom, imparting high polarizability to the S$_n$ species. For the time being, Raman can be adopted in terrestrial experiments of the kind reported by Cazaux et al. (2022) to characterize the S-bearing species.

Ices in interstellar environments are primarily identified by their vibrational transitions in the near-to-far IR. In general, the 1–3 μm wavelength region contains combination and overtone modes, the 3–6 μm region comprehends the stretching vibrations, the 6–30 μm region the bending and libration vibrations, while the 25–300 μm region represents torsional and intermolecular (lattice) modes (Boogert et al. 2015).

The frequencies covered by the vibrational modes of the investigated S$_n$ species span the 150–750 cm^{-1} range, corresponding to a wavelength range of 13.3–66.6 μm. Above 30 μm, the availability and capability of the instrumentation are limited, e.g., JSWT is designed to observe in the wavelength range from 0.6 to 27 μm (Rauscher & Ressler 2005). In addition, both amorphous and crystalline olivine and forsterite exhibit bending and torsional modes within the 14–24 μm region (Boogert et al. 2015; Zamirri et al. 2019), and libration modes of water cover the region around 10–12 μm (Gibb et al. 2000; McClure et al. 2023).

Therefore, the forest of vibrational bands located in that region of the spectra, along with the weak intensities of the vibrational S$_n$ peaks, may render their IR detection rather difficult. When moving to terrestrial laboratory experiments, the seminal work of Anderson & Loh (1969) suggested that Raman spectroscopy is ideal for the characterization of sulfur allotropes, due to the ability to distinguish and assign several active vibration modes, as also shown in Table 3 from the computed ones. Thus, the Raman bands simulated here can serve as proxies for the detection of the S$_n$ species adsorbed on the ices in terrestrial laboratory experiments. This would be the case, for instance, for the stretching modes around 500 cm^{-1}, which are all active in Raman while invisible in IR.

4. Conclusions

In this work, we have computed the zero-point-corrected BEs (BE(0)s) and the vibrational features (both IR and Raman

spectra inclusive of absolute intensities) of the adsorption complexes of S_n species ($n = 1$–8) on an amorphous water-ice surface model by means of quantum chemical simulations. The ice model had already been proposed by Ferrero et al. (2020b) and Perrero et al. (2022) to study the interaction of many different molecules of astrochemical interest.

We adopted ab initio periodic calculations based on the BHLYP-D3(BJ)/A-VTZ* model chemistry for both the geometry optimization and the computation of IR and Raman spectra in the harmonic approximation (for frequencies and intensities). To simplify the modeling due to the large size of the S_n species, we focused on two different regions of the amorphous ice model. The first exhibits a cavity, mimicking some ice porosity in which the contact between the adsorbate and the ice surface is at its maximum. The second is a flat region, which represents a portion of dense icy dust grains. This limits the number of BEs (mainly two) that we obtain, but we expect these values to well represent the upper and lower limits of the range that one would obtain by conducting a broader sampling of binding sites. The BE(0)s of the S_n species were about 18% higher for the cavity region than for the flat one, as expected due to the nonspecific nature of the interactions. These two situations likely represent the tail limits of a complete BE(0)s distribution that can be computed on much larger (and not feasible with our computational facilities) icy grain models. Currently, a few chemical models exist where more than one BE value for each species can be included. Moreover, several works are focusing on the computation of BE distribution histograms—e.g., Bovolenta et al. (2022); Tinacci et al. (2022, 2023)—as being more representative of the variety of binding sites that a real amorphous ice mantle could offer. A distribution of values with a statistical meaning allows the determination of a mean BE and a standard deviation for each species. However, if we were to suggest a single BE value to be adopted in chemical models, the average between the two BEs computed for each species should be a reasonable choice. Nonetheless, we are aware that a more meticulous sampling of the ice model would be necessary in order to provide statistically meaningful data.

We found that the BE(0) values of the S_n species increase with the number of S atoms, and that their interaction with the ice is mainly driven by dispersion-like (London) interactions. Only for the single S atom was a major electronic effect contribution detected. We found only a rough linear correlation between the averaged BE(0) values of the two surface regions and the number of sulfur atoms, with an increment by each S atom of about 9 kJ mol⁻¹, which may be useful for guessing the BE(0) for even larger sulfur polymorphs by simple addition. A deeper analysis revealed that close couples (S_1–S_2, S_3–S_4, S_5–S_6, and S_7–S_8) exhibit almost the same BE(0). From the analysis of the IR and Raman spectra, it is not possible to easily distinguish between gas-phase and adsorbed species, given that the perturbations suffered by the vibrational features of the adsorbed species are small and, overall, their amount becomes smaller with the increasing size of the S_n species. Thus, the species exhibiting significative vibrational frequency perturbations upon adsorption are S_n with $n = 2$–4. The intensities of the IR and Raman peaks suggest Raman spectroscopy (due to the large polarizability of sulfur and its allotropic forms) to be the technique of election for the

detection of S_n species in terrestrial laboratory experiments, as Raman cannot, unfortunately, be used for studying the ISM spectral features.

Appendix A
S_n Species Details

We computed the energy gaps between the different spin states of the S_n species characterized in this work. In the case of S and S_2, their ground state is a triplet spin state. The singlet and the triplet spin states are well separated in energy (see Table A1).

In contrast, S_3, S_4, and S_5 are more elusive and present electronic states closed in energy (see Table A2). The ground state of S_3 and S_4 is an open-shell singlet. For S_3, the closed-shell chain structure is only 10 kJ mol⁻¹ less stable than the ground state, followed closely by the ring (in the closed-shell singlet state). In the case of S_4, the second most stable configuration is the triplet spin state chain. The cyclic form of S_4 is the less favored conformer. S_5 most stable conformed has a ring structure and a singlet ground state. This species has also been modeled as a chain, but it is almost 70 kJ mol⁻¹ less stable than the ring, when in the state of triplet or open-shell singlet. The closed-shell singlet configuration is remarkably unfavored due to its planar geometry.

Table A1
Energy Gaps (in Kilojoules per Mole) of Atomic and Diatomic Sulfur Species

Species	Closed-shell Singlet	Triplet
S	431	0
S_2	274	0

Note. The most stable structure is taken as the reference zero-energy structure.

Perrero et al.

Table A2
Energy Gaps (in Kilojoules per Mole) of Sulfur Allotropes Computed in This Work

Species	Closed-shell Singlet	Open-shell Singlet	Triplet	Ring
S_3	10	0	101	17
S_4	43	0	21	60
S_5	162	68	67	0

Note. The most stable structure is taken as the reference zero-energy structure. The ring conformer possesses a closed-shell singlet spin state. For S_5, the ring conformer consists of the envelope conformation.

Finally, it is well established that S_6, S_7, and S_8 are ring structures with a closed-shell singlet ground state, thus we do not provide additional details regarding their electronic spin states.

Appendix B
Calculation of the BEs

In the following, we report the detailed calculation of the BEs.

We are interested in the counterpoise-deformation-corrected interaction energy, where the BSSE correction is included to make up for the error that arises when using a finite basis set of localized Gaussian functions to describe a chemical system:

$$\Delta E^{\mathrm{CP}} = \Delta E^* + \delta E_S + \delta E_\mu + \delta E_L - \mathrm{BSSE} = \Delta E - \mathrm{BSSE}. \quad (B1)$$

From this equation, it appears that the non-counterpoise-corrected interaction energy ΔE is given by the sum of the deformation-free interaction energy (ΔE^*), the deformation energy of the slab (δE_S) and the molecule (δE_μ), and the lateral interaction (E_L) between adsorbate molecules in a different replica of the cell. This quantity corresponds to the common definition of interaction energy, which is the difference between the energy of the complex and the energies of the isolated species and isolated ice model:

$$\Delta E = \Delta E^* + \delta E_S + \delta E_\mu + \delta E_L = E_{\mathrm{complex}} - E_{\mathrm{ice}} - E_{\mathrm{species}}. \quad (B2)$$

The lateral interaction energy δE_L is due to the interactions experienced by each adsorbate with its images on the replicated unit cells. This term becomes particularly relevant for high adsorbate coverage, as the distances between adsorbate molecules in neighbor cells will become shorter with increasing coverage. Here, we are interested in minimizing the δE_L term, to arrive at a ΔE representative of the sole interaction between the adsorbate and the ice surface. This requires the adoption of a large enough unit cell to minimize the δE_L term.

By convention, the BE is simply the opposite of ΔE^{CP}:

$$\mathrm{BE} = -\Delta E^{\mathrm{CP}}. \quad (B3)$$

Therefore, the BE(0), which is the adsorption enthalpy at 0 K, can be obtained by simply subtracting the zero-point energy correction from the BE. In this work, we adopted $\Delta \mathrm{ZPE} = \mathrm{ZPE}_{\mathrm{complex}} - \mathrm{ZPE}_{\mathrm{species}}$, where $\mathrm{ZPE}_{\mathrm{complex}}$ was computed only for a fragment of the system constituted by the adsorbed species. In this way, we are considering the same atoms in the two zero-point energy terms:

$$\mathrm{BE}(0) = \mathrm{BE} - \mathrm{ZPE}. \quad (B4)$$

ORCID iDs

Jessica Perrero ⃝ https://orcid.org/0000-0003-2161-9120
Leire Beitia-Antero ⃝ https://orcid.org/0000-0003-0833-4075
Asunción Fuente ⃝ https://orcid.org/0000-0001-6317-6343
Piero Ugliengo ⃝ https://orcid.org/0000-0001-8886-9832
Albert Rimola ⃝ https://orcid.org/0000-0002-9637-4554

References

Altwegg, K., Combi, M., Fuselier, S. A., et al. 2022, MNRAS, 516, 3900
Anderson, A., & Loh, Y. T. 1969, CaJCh, 47, 879
Aponte, J. C., Dworkin, J. P., Glavin, D. P., et al. 2023, EPS, 75, 28
Becke, A. D. 1993, JChPh, 98, 1372
Boogert, A., Brewer, K., Brittain, A., & Emerson, K. 2022, ApJ, 941, 32
Boogert, A. A., Gerakines, P. A., & Whittet, D. C. 2015, ARA&A, 53, 541
Bovolenta, G. M., Vogt-Geisse, S., Bovino, S., & Grassi, T. 2022, ApJS, 262, 17
Brabson, G. D., Mielke, Z., & Andrews, L. 1991, JPhCh, 95, 79
Calmonte, U., Altwegg, K., Balsiger, H., et al. 2016, MNRAS, 462, S253
Caselli, P., Hasegawa, T., & Herbst, E. 1994, ApJ, 421, 206
Cazaux, S., Carrascosa, H., Caro, G. M., et al. 2022, A&A, 657, A100
Cioslowski, J., Szarecka, A., & Moncrieff, D. 2001, JPCA, 105, 501
Das, A., Sil, M., Gorai, P., Chakrabarti, S. K., & Loison, J. C. 2018, ApJS, 237, 9
Dovesi, R., Erba, A., Orlando, R., et al. 2018, WIREs Comput. Mol. Sci., 8, e1360
Eckert, B., & Steudel, R. 2003, in Molecular Spectra of Sulfur Molecules and Solid Sulfur Allotropes, ed. R. Steudel (Berlin: Springer), 31
Escribano, R., Timón, V., Gálvez, O., et al. 2014, PCCP, 16, 16694
Ferrante, R. F., Moore, M. H., Spiliotis, M. M., & Hudson, R. L. 2008, ApJ, 684, 1210
Ferrero, S., Martínez-Bachs, B., Enrique-Romero, J., & Rimola, A. 2020a, in Computational Science and Its Applications—ICCSA 2020, ed. O. Gervasi et al. (Cham: Springer), 553
Ferrero, S., Zamirri, L., Ceccarelli, C., et al. 2020b, ApJ, 904, 11
Fuente, A., Goicoechea, J. R., Pety, J., et al. 2017, ApJL, 851, L49
Fuente, A., Rivière-Marichalar, P., Beitia-Antero, L., et al. 2023, A&A, 670, A114
Gibb, E. L., Whittet, D. C. B., Schutte, W. A., et al. 2000, ApJ, 536, 347
Gondhalekar, P. M. 1985, MNRAS, 217, 585
Grimme, S., Antony, J., Ehrlich, S., & Krieg, H. 2010, JChPh, 132, 154104
Hasegawa, T. I., Herbst, E., & Leung, C. M. 1992, ApJS, 82, 167
Hudson, R. L., Gerakines, P. A., & Loeffler, M. J. 2015, PCCP, 17, 12545
Jenkins, E. B. 2009, ApJ, 700, 1299
Jiménez-Escobar, A., & Caro, G. M. 2011, A&A, 536, A91
Jiménez-Escobar, A., Muñoz Caro, G. M., & Chen, Y.-J. 2014, MNRAS, 443, 343
Laas, J. C., & Caselli, P. 2019, A&A, 624, A108
Lee, C., Yang, W., & Parr, R. G. 1988, PhRvB, 37, 785
Lenain, P., Picquenard, E., Corset, J., Jensen, D., & Steudel, R. 1988, Berichte der Bunsengesellschaft für physikalische Chemie, 92, 859
Luna, R., Luna-Ferrándiz, R., Millán, C., et al. 2017, ApJ, 842, 51
Maschio, L., Kirtman, B., Rérat, M., Orlando, R., & Dovesi, R. 2013a, JChPh, 139, 164101
Maschio, L., Kirtman, B., Rérat, M., Orlando, R., & Dovesi, R. 2013b, JChPh, 139, 164102
McCarthy, M. C., Thorwirth, S., Gottlieb, C. A., & Thaddeus, P. 2004a, JAChS, 126, 4096
McCarthy, M. C., Thorwirth, S., Gottlieb, C. A., & Thaddeus, P. 2004b, JChPh, 121, 632
McClure, M. K., Rocha, W. R. M., Pontoppidan, K. M., et al. 2023, NatAs, 7, 431
McElroy, D., Walsh, C., Markwick, A. J., et al. 2013, A&A, 550, A36
Meyer, B., & Stroyer-Hansen, T. 1972, JPhCh, 76, 3968
Minissale, M., Aikawa, Y., Bergin, E., et al. 2022, ESC, 6, 597
Pascale, F., Zicovich-Wilson, C. M., López Gejo, F., et al. 2004, JCoCh, 25, 888
Penteado, E. M., Walsh, C., & Cuppen, H. M. 2017, ApJ, 844, 71
Perrero, J., Enrique-Romero, J., Ferrero, S., et al. 2022, ApJ, 938, 158
Perrero, J., Ugliengo, P., Ceccarelli, C., & Rimola, A. 2023, MNRAS, 525, 2654
Picquenard, E., Boumedien, M., & Corset, J. 1993, JMoSt, 293, 63

Raghavachari, K., Rohlfing, C. M., & Binkley, J. S. 1990, JChPh, 93, 5862

Rauscher, B. J., & Ressler, M. E. 2005, ExA, 19, 149

Ruffle, D. P., Hartquist, T. W., Caselli, P., & Williams, D. A. 1999, MNRAS, 306, 691

Shingledecker, C. N., Lamberts, T., Laas, J. C., et al. 2020, ApJ, 888, 52

Spitzer, L., & Jenkins, E. B. 1975, ARA&A, 13, 133

Steudel, R., Steudel, Y., & Wong, M. W. 2003, in Speciation and Thermodynamics of Sulfur Vapor, ed. R. Steudel (Berlin: Springer), 117

Thorwirth, S., McCarthy, M. C., Gottlieb, C. A., et al. 2005, JChPh, 123, 054326

Tinacci, L., Germain, A., Pantaleone, S., et al. 2022, ESC, 6, 1514

Tinacci, L., Germain, A., Pantaleone, S., et al. 2023, ApJ, 951, 32

Trofimov, B., Sinegovskaya, L., & Gusarova, N. 2009, J. Sulfur Chem., 30, 518

Wakelam, V., Castets, A., Ceccarelli, C., et al. 2004, A&A, 413, 609

Wakelam, V., Loison, J.-C., Herbst, E., et al. 2015, ApJS, 217, 20

Wakelam, V., Loison, J.-C., Mereau, R., & Ruaud, M. 2017, MolAs, 6, 22

Zamirri, L., Maciá Escatllar, A., Mariñoso Guiu, J., Ugliengo, P., & Bromley, S. T. 2019, ESC, 3, 2323

Zicovich-Wilson, C. M., Pascale, F., Roetti, C., et al. 2004, JCoCh, 25, 1873

Chapter 4

Adsorption of neutral and charged S-bearing species onto olivine nanoclusters

Introduction

The study of sulphur chemistry was extended to the processes occurring in diffuse clouds, environments where the formation of prestellar star cores has not yet started. In these warm and rarefied clouds, permeated by radiation, gas-phase species are mainly atomic or ionic, although some molecules can be found. The solid phase is characterised by bare dust grains that expose their core to the gas-phase environment. The majority of sulphur resides in the gas-phase as S^+, with an abundance close to the reference value, $[S^+]/[H]$ = 1.66×10^{-5} (Esteban et al., 2004). Indeed, the depletion of gas-phase sulphur occurs in more evolved environments, such as dense clouds and protoplanetary disks.

The presence of sulphur in the form of minerals found in comets and meteorites motivates the study of the interaction between gaseous S-bearing species and the mineral surface of grain cores at early evolutionary stages (Trigo-Rodríguez, 2012; Brownlee, 2014). A strong interaction could explain the formation of refractory species, which would be unable to desorb in warm regions (such as hot cores and hot corinos) as they would be tightly bound to the grain core, and therefore more difficult to be unambiguously detected. In '*Theoretical modelling of the adsorption of neutral and charged sulphur-bearing species on to olivine nanoclusters*' (Perrero et al., 2023, *MNRAS*, **527**, 10697), the adsorption complexes of some key S-bearing species, both neutral and charged, on the core of dust grains, represented by olivine nanoclusters, were modelled.

Results

The silicate core of dust grains is mainly amorphous and constituted by pyroxenes and olivines with chemical composition $Mg_xFe_{(1-x)}SiO_3$ and $Mg_{2x}Fe_{(2-2x)}SiO_4$ (x = 0−1, Henning, 2010). The cluster models adopted in this work represent olivines, one of the most abundant family of interstellar silicates. The $Mg_3FeSi_2O_8$ and $Mg_4Si_2O_8$ nanoclusters were modelled with a top-down approach following the work of Serra-Peralta et al. (2022), where the water formation reaction catalysed by Fe^{2+} on both olivine clusters and periodic surfaces was studied.

Here, the Mg end-member forsterite cluster was considered in addition to the Fe-containing ones, due to the interest in drawing a comparison between S-bearing species interacting with Mg^{2+} and with Fe^{2+}. Depending on the position (X, Y, and Z) occupied
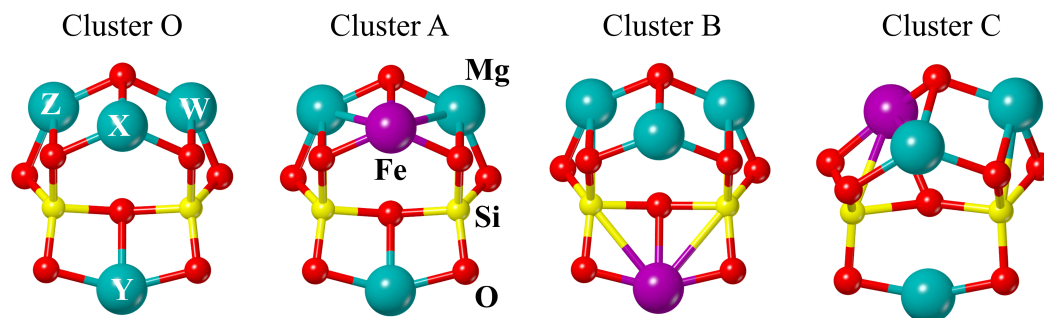
Figure 4.1: Forsterite (O) and olivine (A, B, and C) clusters representing the core of dust grains. The atom labels in cluster O identify adsorption sites. In clusters O, A, and B, sites Z and W are equivalent for symmetry.

by Fe^{2+}, the different clusters represented in Figure 4.1 (A, B, and C, respectively) are obtained.

The presence of Fe^{2+} introduces unpaired electrons in the model, whose most stable electronic spin state is the quintet state, followed by the triplet and finally the singlet states, as reported by previous studies (Navarro-Ruiz et al., 2014; Navarro-Ruiz et al., 2016).

The adsorption complexes of nine S-bearing species, both neutral and charged, were modelled: CS, H$_2$S, H$_2$S$^+$, HS, HS$^+$, S, S$^+$, SO, and SO$^+$. The calculations were performed with ORCA 5.0.3 (Neese, 2022) and divided in three parts: i) a benchmark study on clusters stability; ii) a benchmark study on the adsorption of CS, CO, H$_2$S, and H$_2$O on the binding sites offered by each cluster; and iii) the characterisation of the BE ensembles of the set of S-bearing species targeted in this work.

In the benchmark studies, the performance of B3LYP-D3(BJ)/6-311G(d,p), r^{2}SCAN-3c, ωB97M-V/def2-TZVP, and BHLYP-D3(BJ)/def2-TZVP against the respective single point energies at DLPNO-CCSD(T)/aug-cc-pVTZ level of theory was evaluated. ωB97M-V/def2-TZVP appeared as the most accurate methodology to compute the stability of the clusters and to model the adsorption complexes of CS, CO, H$_2$S, and H$_2$O, with an absolute error below 4 kJ mol^{-1}, within the chemical accuracy.

CS and CO interact with the metal centres through the carbon atom, where their dipole moment exhibits a concentration of electronic charge. The two species prefer to interact with Fe rather than Mg, owing to the π-electron back donation effect of Fe. As was previously observed for water ice, the larger dipole of CS is responsible for a stronger BE with respect to CO (Perrero et al., 2022).

The adsorption of H$_2$X (X = O, S) upon forsterite resulted, in a few cases, in their spontaneous dissociation. Their chemisorption was not only dependent on the binding site, but also on the level of theory adopted in the calculation. In fact, the simulation of the minimum energy path connecting the reactant (physisorbed complex) and the product (chemisorbed complex) at ωB97M-V level of theory returned very small dissociation barriers, which approached zero when corrected for the ZPE (see Figure 4.2). This indicated that the chemisorption of H$_2$X may occur onto forsterite, due to the Mg^{2+} cations acting as a Lewis acid and the O^{2-} anions behaving as Lewis bases, thus causing the cleavage of H$_2$X into HX$^-$ and H$^+$.

To ensure that H$_2$X dissociation was not an artefact of the low-coordinated metal centres exposed by the cluster, the same process was simulated on periodic forsterite surfaces, where metal centres possess higher coordination due to the extended nature of the slabs
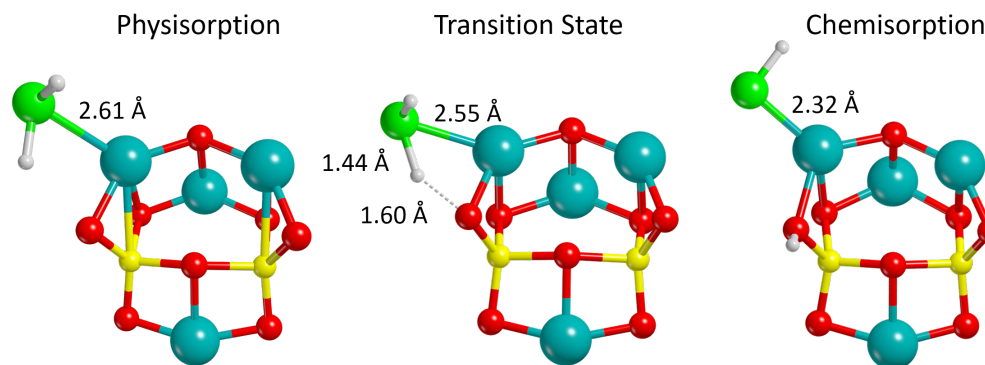
Figure 4.2: The dissociation of H_2S on the forsterite cluster, characterised at the ωB97M-V/def2-TZVP level of theory, exhibits an almost null potential energy barrier.

(Zamirri et al., 2017; Bancone et al., 2023). Molecular physisorption was found on the most stable forsterite surfaces, (120) and (001), while the less stable (101), (111), (021), and (110) slabs caused H_2S dissociative chemisorption. Therefore, corners and edges of dust grains, where metal centres are less coordinated, represent suitable binding sites for the chemisorption of these species.

The benchmark indicated that cluster C is the most stable olivine model, characterised by the presence of Fe^{2+} at position Z, which breaks the symmetry of the nanoclusters and results in the emergence of an additional binding site. Therefore, the BE ensembles of the set of S-bearing species listed above were computed on cluster C. The morphology of the adsorption complexes revealed primarily that the Fe−S interaction is stronger than Mg−S for all the species interacting with the olivine metal centres through the S atom. However, there are two exceptions to this trend: SO and SO^+. These species interact with the metal centre through oxygen, which in this case is the most electronegative atom. Therefore, the Mg−O interaction results stronger than Fe−O, as observed also for the couple H_2S/H_2O.

The adsorption of an open-shell species on Fe^{2+} may cause part of its spin density to transfer from the sulphur atom to the metal, increasing the BE as in the case of S and HS. Furthermore, the presence of a charge dramatically increases the BE, as the four ions included in this study demonstrate (see top panel of Figure 4.3). The adsorption of H_2S^+ and HS^+ on Fe^{2+} results in their deprotonation, whereas only physisorption occurs when they interact with Mg^{2+}.

Some of the species addressed in this work were also the subject of the study presented in Chapter 3, which allows to make a comparison between the binding energies computed onto the ASW surface and the olivine nanoclusters (see Figure 4.3). Despite the differences in the computational methodology (cluster *versus* periodic approach, and a different combination of functional and basis set) employed to determine the BEs, the pronounced discrepancies between the derived values suggest that the substrate on which the species are adsorbed exerts a pivotal influence on the strength of the interaction. In the case of ASW, the interactions are weak and controlled mainly by dispersion forces. In contrast, the BEs obtained for olivine clusters are large and determined mostly by electrostatic interactions, to which occasionally electron transfer phenomena add up.

The consequence of such a strong interaction between sulphur and the mineral surface is that S-containing species have a high probability to freeze out onto the core of dust grains and be unable to desorb into the gas phase even at the temperatures found in diffuse clouds (T $\simeq$ 100 K). In these environments, the presence of charged gas-phase species
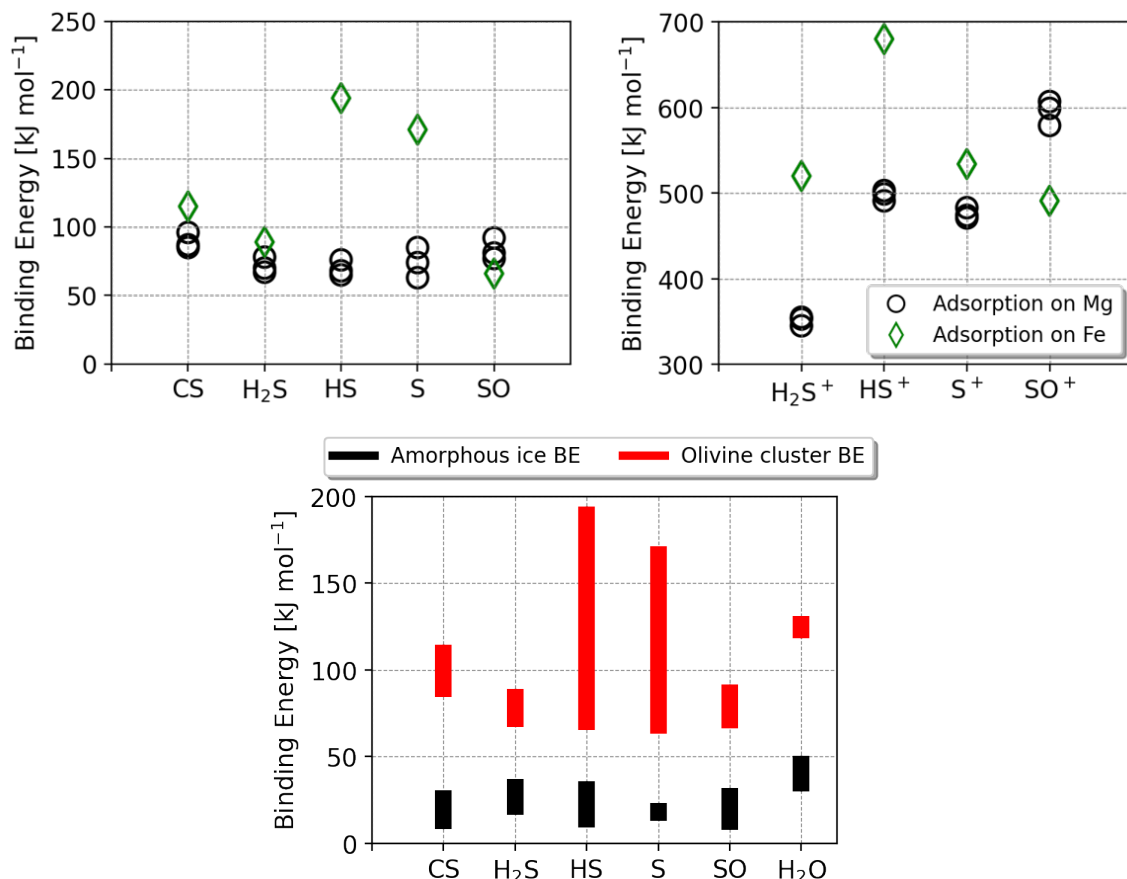
Figure 4.3: *Top panel*: BEs (in kJ mol^{-1}) of neutral species (on the left) and cations (on the right) adsorbed upon cluster C. *Bottom panel*: BE ranges (in kJ mol^{-1}) covered by CS, H$_2$S, HS, S, SO and H$_2$O adsorbed on amorphous ice (Ferrero et al., 2020; Perrero et al., 2022) and on olivine clusters.

should also favour the adsorption process as long as the grains are negatively charged (Cazaux et al., 2022; Fuente et al., 2023). Even if the grain particles were mostly neutrals or positively charged, the accretion of neutral sulphur species on the grain surfaces could enhance the number of sulphur atoms in refractories.

As it appears in the bottom panel of Figure 4.3, H$_2$O adsorption on olivine is more energetic than H$_2$S adsorption, meaning that water is more likely (and probable) than hydrogen sulphide to form a stable interaction with the mineral. However, S-bearing species, weakly adsorbed on water ice, have the possibility to diffuse towards regions of the grain not coated by the ice mantle, thus exposing part of the mineral surface where to be strongly adsorbed. The assumption that S-bearing species become part of the grain core, rather than interacting with the icy mantles, would be in agreement with the fact that they are usually used as shock tracers (e.g., Sato et al., 2022; Zhang et al., 2023). The harsh conditions of the shock would therefore provide enough energy to break the strong interaction between sulphur and the mineral surface, allowing its transformation into H$_2$S and its successive ejection in the gas phase (Holdship et al., 2017).

Finally, the tendency of species such as H$_2$S, HS$^+$, and H$_2$S$^+$ to chemisorb onto olivine nanoclusters plants the seed for the formation of the Fe$-$S bond present in sulphide minerals such as troilite and pentlandite. Indeed, approximately 90% of the sulphur is predicted to be locked in the refractory residue of protoplanetary disks, followed by sulphur chains S$_n$ (Kama et al., 2019). The material of the protoplanetary disk would then be subjected to

processing and modifications until yielding the actual compositions of comets, asteroids and meteorites, where more sulphur compounds are found (Calmonte et al., 2016; Aponte et al., 2023).

Future perspectives

The size of the olivine nanocluster models adopted to simulate the core of dust grains represents a limitation. Despite comparing the adsorption process on both cluster and periodic surfaces to prevent the low-coordination of the metal centres from being responsible for H_2S dissociation, we are aware that enlarging the cluster size would enhance the accuracy of the computed BEs. For most properties considered, significant discrepancies with respect to the bulk limit are observed when employing small clusters, thereby reinforcing the shortcomings of a top-down approach for the description of these structures (Macià Escatllar et al., 2019). Therefore, it would become of primary importance to enlarge the cluster, adopting the $Mg_{6-x}Fe_xSi_3O_{12}$ nanoclusters modelled by Serra-Peralta et al. (2022), or more extended models constituted by several silicate units (e.g., Zamirri et al., 2019). The latter option would be more suitable especially when simulating reaction mechanisms or the adsorption of larger species.

The evidence that some S-bearing species may chemisorb onto the core of dust grains, which is exposed to the gas phase both in diffuse and, to a lesser extent, in dense clouds, raises the discussion about their reactivity. Furthermore, the presence of sulphide minerals in the small bodies of the Solar System poses questions regarding their origin. Moreover, it is currently not clear if S-chains like S_3 and S_4, detected in comets, asteroid and meteorites (Calmonte et al., 2016; Aponte et al., 2023), are the product of S and S_2 addition or that of larger rings (e.g., S_8) destruction (Ruffle et al., 1999).

Dust grains were assumed to be neutral in the simulations, although some models predict them to be positively charged in the diffuse medium and negatively charged in denser environments (Ibáñez-Mejía et al., 2019). If this was the case, the interaction between gas-phase cations and positively charged grains in diffuse clouds would clearly be hampered by electrostatic repulsion. However, the results concerning positively charged sulphur-bearing species adsorbed on neutral dust grain cores would hold true for the case in which neutral gas-phase species interact with charged dust grains. Therefore, the interaction energies should be of the same order of magnitude, since the presence of a charge in the system would still be the main driving force of the interaction. Nevertheless, the atomistic details of the system would vary due to the presence of a charge on the olivine nanocluster, paving the way for successive investigations similar to those performed for charged water ice cluster (Rimola et al., 2021).

References

Aponte, J. C. et al. (2023). "PAHs, hydrocarbons, and dimethylsulfides in Asteroid Ryugu samples A0106 and C0107 and the Orgueil (CI1) meteorite". *Earth Planets Space* **75**, 28. DOI: `10.1186/s40623-022-01758-4`.

Bancone, N. et al. (2023). "Adsorption of HCN on cosmic silicates: a periodic quantum mechanical study". *Phys. Chem. Chem. Phys.* **25**, 26797. DOI: `10.1039/D3CP01459B`.

Brownlee, D. (2014). "The Stardust mission: analyzing samples from the edge of the Solar System". *Annu. Rev. Earth Planet. Sci.* **42**, 179. DOI: `10.1146/annurev-earth-050212-124203`.

Calmonte, U. et al. (2016). "Sulphur-bearing species in the coma of comet 67P/Churyumov-Gerasimenko". *Mon. Not. R. Astron. Soc.* **462**, S253. DOI: `10.1093/mnras/stw2601`.

Cazaux, S. et al. (2022). "Photoprocessing of H_2S on dust grains. Building S chains in translucent clouds and comets". *Astron. Astrophys.* **657**, A100. DOI: `10.1051/0004-6361/202141861`.

Esteban, C. et al. (2004). "A reappraisal of the chemical composition of the Orion nebula based on Very Large Telescope echelle spectrophotometry". *Mon. Not. R. Astron. Soc.* **355**, 229. DOI: `10.1111/j.1365-2966.2004.08313.x`.

Ferrero, S. et al. (2020). "Binding energies of interstellar molecules on crystalline and amorphous models of water ice by ab initio calculations". *Astrophys. J.* **904**, 11. DOI: `10.3847/1538-4357/abb953`.

Fuente, A. et al. (2023). "Gas phase Elemental abundances in Molecular cloudS (GEMS). VII. Sulfur elemental abundance". *Astron. Astrophys.* **670**, A114. DOI: `10.1051/0004-6361/202244843`.

Henning, T. (2010). "Cosmic silicates". *Annu. Rev. Astron. Astrophys.* **48**, 21. DOI: `10.1146/annurev-astro-081309-130815`.

Holdship, J. et al. (2017). "UCLCHEM: A gas-grain chemical code for clouds, cores, and C-shocks". *Astron. J.* **154**, 38. DOI: `10.3847/1538-3881/aa773f`.

Ibáñez-Mejía, J. C. et al. (2019). "Dust charge distribution in the interstellar medium". *Mon. Not. R. Astron. Soc.* **485**, 1220. DOI: `10.1093/mnras/stz207`.

Kama, M. et al. (2019). "Abundant refractory sulfur in protoplanetary disks". *Astrophys. J.* **885**, 114. DOI: `10.3847/1538-4357/ab45f8`.

Macià Escatllar, A. et al. (2019). "Structure and properties of nanosilicates with olivine $(Mg_2SiO_4)_N$ and pyroxene $(MgSiO_3)_N$ compositions". *ACS Earth Space Chem.* **3**, 2390. DOI: `10.1021/acsearthspacechem.9b00139`.

Navarro-Ruiz, J. et al. (2016). "Does Fe^{2+} in olivine-based interstellar grains play any role in the formation of H_2? Atomistic insights from DFT periodic simulations". *Chem. Comm.* **52**, 6873. DOI: `10.1039/c6cc02313d`.

Navarro-Ruiz, J. et al. (2014). "B3LYP periodic study of the physicochemical properties of the nonpolar (010) Mg-pure and Fe-containing olivine surfaces". *J. Phys. Chem. A* **118**, 5866. DOI: `10.1021/jp4118198`.

Neese, F. (2022). "Software update: The ORCA program system-version 5.0". *Wiley Interdiscip. Rev. Comput. Mol. Sci.* **12**, e1606. DOI: `10.1002/wcms.1606`.

Perrero, J. et al. (2023). "Theoretical modelling of the adsorption of neutral and charged sulphur-bearing species on to olivine nanoclusters". *Mon. Not. R. Astron. Soc.* **527**, 10697. DOI: `10.1093/mnras/stad3896`.

Perrero, J. et al. (2022). "Binding energies of interstellar relevant S-bearing species on water ice mantles: a quantum mechanical investigation". *Astrophys. J.* **938**, 158. DOI: `10.3847/1538-4357/ac9278`.

Rimola, A. et al. (2021). "Interaction of HCO^+ cations with interstellar negative grains. Quantum chemical investigation and astrophysical implications". *Front. Astron. Space Sci.* **8**. DOI: `10.3389/fspas.2021.655405`.

Ruffle, D. P. et al. (1999). "The sulphur depletion problem". *Mon. Not. R. Astron. Soc.* **306**, 691. DOI: `10.1046/j.1365-8711.1999.02562.x`.

Sato, M. T. et al. (2022). "APEX and NOEMA observations of H_2S in nearby luminous galaxies and the ULIRG Mrk 231 - A possible relation between dense gas properties and molecular outflows". *Astron. Astrophys.* **660**, A82. DOI: `10.1051/0004-6361/202141260`.

Serra-Peralta, M. et al. (2022). "Water formation on interstellar silicates: the role of Fe^{2+}/H_2 interactions in the $O + H_2 \rightarrow H_2O$ reaction". *Phys. Chem. Chem. Phys.* **24**, 28381. DOI: `10.1039/d2cp04051d`.

Trigo-Rodríguez, J. M. (2012). *Meteoritos, Colección ¿Qué sabemos de?* Editorial Catarata-CSIC, Madrid.

Zamirri, L. et al. (2017). "Forsterite surfaces as models of interstellar core dust grains: computational study of carbon monoxide adsorption". *ACS Earth Space Chem.* **1**, 384. DOI: `10.1021/acsearthspacechem.7b00041`.

Zamirri, L. et al. (2019). "What can infrared spectra tell us about the crystallinity of nano-sized interstellar silicate dust grains?" *ACS Earth Space Chem.* **3**, 2323. DOI: `10.1021/acsearthspacechem.9b00157`.

Zhang, Z. E. et al. (2023). "The Perseus ALMA Chemistry Survey (PEACHES). II. Sulfur-bearing species and dust polarization revealing shocked regions in protostars in the Perseus molecular cloud". *Astrophys. J.* **946**, 113. DOI: `10.3847/1538-4357/acbdf7`.

Theoretical modelling of the adsorption of neutral and charged sulphur-bearing species on to olivine nanoclusters

Jessica Perrero [1,2] Leire Beitia-Antero [3,4] Asunción Fuente [5] Piero Ugliengo [2]★
and Albert Rimola [1]★

[1]*Departament de Química, Universitat Autònoma de Barcelona, Bellaterra, E-08193 Catalonia, Spain*
[2]*Dipartimento di Chimica and Nanostructured Interfaces and Surfaces (NIS) Centre, Università degli Studi di Torino, via P. Giuria 7, I-10125 Torino, Italy*
[3]*AEGORA Research Group – Joint Center for Ultraviolet Astronomy, Universidad Complutense de Madrid, Plaza de Ciencias 3, E-28040 Madrid, Spain*
[4]*Departamento de Estadística e Investigación Operativa, Fac. de CC. Matemáticas, Plaza de Ciencias 3, E-28040 Madrid, Spain*
[5]*Centro de Astrobiología (CSIC/INTA), Ctra.deTorrejón a Ajalvir km 4, E-28806 Torrejón de Ardoz, Spain*

ABSTRACT

Sulphur depletion in the interstellar medium (ISM) is a long-standing issue, as only 1 per cent of its cosmic abundance is detected in dense molecular clouds (MCs), while it does not appear to be depleted in other environments. In addition to gas phase species, MCs also contain interstellar dust grains, which are irregular, micron-sized, solid aggregates of carbonaceous materials, and/or silicates. Grains provide a surface where species can meet, accrete, and react. Although freeze-out of sulphur on to dust grains could explain its depletion, only OCS and, tentatively, SO_2 were observed on their surfaces. Therefore, it is our aim to investigate the interaction between sulphur-containing species and the exposed mineral core of the grains at a stage prior to when sulphur depletion is observed. Here, the grain core is represented by olivine nanoclusters, one of the most abundant minerals in the ISM, with composition $Mg_4Si_2O_8$ and $Mg_3FeSi_2O_8$. We performed a series of quantum mechanical calculations to characterize the adsorption of nine S-bearing species, both neutral and charged, on to the nanoclusters. Our calculations reveal that the Fe–S interaction is preferred to Mg–S, causing sometimes the chemisorption of the adsorbate. These species are more strongly adsorbed on the bare dust grain silicate cores than on water ice mantles, and hence therefore likely sticking on the surface of grains forming part of the grain core. This demonstrates that the interaction of bare grains with sulphur species in cloud envelopes can determine the S-depletion observed in dense molecular clouds.

Key words: astrochemistry – molecular processes – solid state: refractory – methods: numerical – ISM: molecules.

1 INTRODUCTION

On Earth, sulphur is one of the key elements that contributes to the engine of life. It is an essential component of our bodies, as it is found in amino acids such as cysteine and methionine, in coenzyme A, in vitamin B1 and biotin, in antioxidants as glutathione, and in many more molecules (Voet, Voet & Pratt 2008). However, sulphur played an important role long before life appeared on Earth, and its chemistry in the interstellar medium (ISM), the environment where stars and planets are formed, is nowadays a challenge for the astronomical and the astrochemical community. Sulphur is the 10th most abundant element in the Universe. Its cosmic abundance, [S]/[H] = 1.8×10^{-5} (Anders & Grevesse 1989), equal to an S/O ratio of 1/37, is used as a reference for measuring sulphur abundance during the several stages of the evolution of a planetary system. While in diffuse clouds the majority of sulphur resides in the gas-phase as S^+ (Jenkins 2009), it is not clear which forms it assumes in translucent and dense clouds (also called molecular clouds, MCs; Woods et al. 2015; Laas & Caselli 2019). Hily-Blant et al. (2022) suggests that

in chemically young cores, atomic sulphur is still the main carrier, which however could not be directly observed. Moreover, it would gradually deplete as the cloud evolves, as also inferred in Fuente et al. (2023). The phenomenon of freeze-out that occurs in MCs could be responsible for the adsorption of gas-phase sulphur on to the surface of icy grains (Caselli, Hasegawa & Herbst 1994), a case in which the presence of H_2S on their surface would be expected. However, only the OCS and, tentatively, the SO_2 molecules were observed in MCs and young stellar object (YSO) ices (Boogert, Gerakines & Whittet 2015; Boogert et al. 2022; McClure et al. 2023), and only upper limits have been estimated for H_2S (Smith 1991; McClure et al. 2023). More recent studies suggest that sulphur is mostly contained in organic species (Laas & Caselli 2019) or in a refractory residue composed of species characterized by the S–S chemical bond (like H_2S_n with $2 \le n \le 3$, and chains of S_n with $3 \le n \le 8$), along with complex species such as hexathiepan (S_6CH_2), which are products of ice processing, as experiments indicate (Ferrante et al. 2008; Jiménez-Escobar & Caro 2011; Cazaux et al. 2022). Nevertheless, numerous sulphur-bearing species (S_2, S_3, and S_4, CH_3SH, C_2H_6SH, together with the most common H_2S, OCS, SO, S_2, SO_2, and CS_2) are detected in comets as 67P/Churyumov–Gerasimenko (Calmonte

★ E-mail: albert.rimola@uab.cat (AR); piero.ugliengo@unito.it (PU)

et al. 2016), whose composition seems to be inherited from the prestellar and protostellar evolutionary phases (Drozdovskaya et al. 2019). Comets contain a record of the chemical composition of the primitive Solar Nebula at the place where they formed, 4.6 Gyr ago (Altwegg, Balsiger & Fuselier 2019). The same applies to a particular type of meteorites, in which sulphur is found in the form of minerals containing iron and nickel (Trigo-Rodríguez 2012). Among the variety of existing meteorites, chondrites represent fairly well the material that surrounded the young Sun and from which the planets formed. Ordinary chondrites contain S mostly in the form of troilite FeS (a variety of pyrrhotite, $Fe_{(1-x)}S$; Kallemeyn et al. 1989), while carbonaceous chondrites contain also pentlandite $(Fe,Ni)_9S_8$, and some inorganic sulphates and aromatic organic compounds (Gao & Thiemens 1993; Yabuta et al. 2007; Trigo-Rodríguez 2012). On the other hand, enstatite chondrites are rich in sulphides like niningerite, alabandite, and other alkaline sulphides (Sears, Kallemeyn & Wasson 1982).

Thus, there seems to be a missing piece of the puzzle between the gas-phase S-bearing species present in diffuse clouds and the solid sulphides found in the remnants of the protoplanetary discs. To understand the fate of sulphur, we aim to investigate what can happen in diffuse clouds, when some simple sulphur species interact with bare dust grains, a system that already contains the atomic ingredients necessary to form the sulphides observed in more evolved environments. Depending on the C/O ratio of the asymptotic giant branch (AGB) stars where they are formed, dust grains are formed by carbonaceous materials or silicates and represent 1 per cent of the ISM mass (Potapov & McCoustra 2021). The main families of interstellar silicates are pyroxenes and olivines with chemical composition $Mg_xFe_{(1-x)}SiO_3$ and $Mg_{2x}Fe_{(2-2x)}SiO_4$ (with x = 0–1; Henning 2010). These nanometre to micrometre-sized non-spherical, porous dust particles lock up nearly 30 per cent of oxygen and 100 per cent of silicon, magnesium, and iron available in the ISM (Van Dishoeck, Herbst & Neufeld 2013). Commonly, interstellar grain silicates are structurally amorphous, although Mg-rich crystalline silicates have also been observed around young stars (Molster & Kemper 2005; Spoon et al. 2022).

In this work, we modelled dust grains as olivine nanoclusters, as in a recent work (Serra-Peralta, Domínguez-Dalmases & Rimola 2022). In the latter, both cluster and periodic approaches were considered to study the formation of water, and were previously adopted by Navarro-Ruiz et al. (2014, 2016) to study the formation of H_2. To our knowledge, the only study of S-bearing species interacting with an olivine surface is a paper by some of us (Rimola, Trigo-Rodríguez & Martins 2017) in which butan-1-sulphonic acid was adsorbed on the (010) surface of forsterite (Fo; Mg_2SiO_4) to seek the correlation between binding energies and measured abundances of a class of soluble organic compounds found in carbonaceous meteorites. Here, we decided to focus on the cluster approach, firstly developing a reliable computational methodology to simulate olivine clusters, using here the adsorption of H_2S as a test case. We then characterized the adsorption on the Mg and Fe sites of olivine clusters of other sulphur bearing species, both neutral and charged: S, S^+, CS, SH, SH^+, SO, SO^+, H_2S, and H_2S^+. For each species, we computed the reaction energy, which can be recast as interaction energy, ΔE, which is a negative quantity for an exothermic reaction. Usually, in the context of astrochemical numerical models, it is the binding energy BE (BE = $-\Delta E$) the quantity that defines the strength of the interaction between the species and the surface. The BE, as defined above, is computed by using the electronic energies of the involved species, assuming that the nuclei are immobile. Quantum mechanics imposes that even at 0 K the nuclei undergo a vibrational motion,
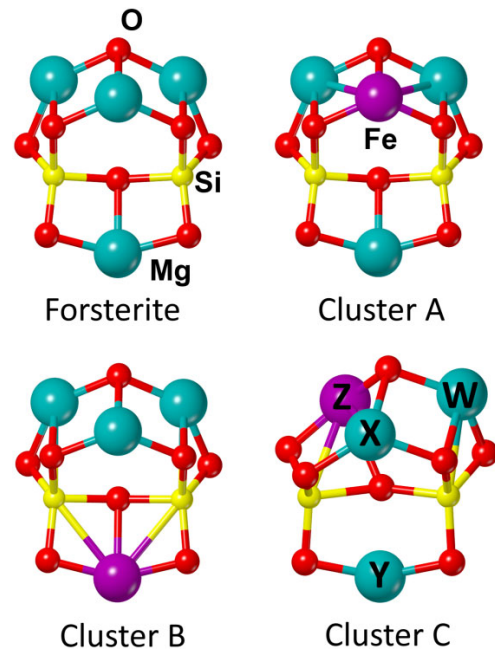
Figure 1. Fo and olivine clusters used in this work as dust grains models. The labels in cluster C are useful to identify adsorption sites.

which contributes to the electronic energy through the zero point energy (ZPE). It is, therefore the BE(0) = BE − ΔZPE, the key parameter to be used in astrochemical models, determining whether desorption phenomena can take place (Penteado, Walsh & Cuppen 2017), and also governing the diffusion process, as diffusion barriers are usually assumed to be a fraction of the BE(0) (e.g. Karssemeijer & Cuppen 2014; Cuppen et al. 2017; Kouchi et al. 2020; Maté, Belén et al. 2020).

The work is organized as follows: in Section 2, we describe the methodology used in the study, Section 3 contains the results, and in Section 4, we discuss our finding and their implications in the sulphur depletion problem. Finally, Section 5 summarizes the conclusions.

2 METHODS

The olivine clusters presented in Serra-Peralta, Domínguez-Dalmases & Rimola (2022) and their Fo parent cluster developed by Escatllar et al. (2019) were adopted to model the core of a dust grain. Each model consists of a cluster of two silicate units with composition $Mg_{(4-x)}Fe_xSi_2O_8$ (with x = 0–1). Clusters A, B, and C are characterized by the presence of a Fe atom at positions X, Y, and Z, respectively (see Fig. 1). Please, note that W and Z positions are equivalent by symmetry. The free Fe^{2+} electronic valence configuration is $4s^0\,3d^6$, allowing the system to exist in three different spin states: singlet, triplet, and quintet. As reported in the literature (Navarro-Ruiz et al. 2014, 2016), the most stable configuration is that showing the maximum spin multiplicity, therefore the quintet, followed by the triplet and the singlet states at higher energies.

We first performed a benchmark study with the aim of finding a suitable methodology to describe the adsorption of S-bearing species on to olivine clusters. All the calculations were run with the ORCA programme v.5.0.3 (Neese 2022). We optimized (using default settings) clusters A, B, and C in the quintet, triplet, and singlet

Table 1. Relative energies (ΔE in the text) of olivine clusters optimized with different DFT functionals and their DLPNO-CCSD(T) single energy point calculations. Cluster C is the most stable one and is taken as a reference to compute the ΔE of clusters A and B.

Quintet	r²SCAN-3c	DLPNO// r²SCAN-3c	ωB97M-V	DLPNO// ωB97M-V	BHLYP-D3(BJ)	DLPNO// BHLYP-D3(BJ)	B3LYP-D3(BJ)	DLPNO// B3LYP-D3(BJ)
Cluster A	31.5	28.3	32.6	29.1	34.4	27.1	34.0	32.6
Cluster B	10.0	10.8	12.9	11.7	9.6	9.4	14.0	11.9
Error (per cent)	9.3	–	11.1	–	14.1	–	17.5	–
Singlet	r²SCAN-3c	DLPNO// r²SCAN-3c	ωB97M-V	DLPNO// ωB97M-V	BHLYP-D3(BJ)	DLPNO// BHLYP-D3(BJ)	B3LYP-D3(BJ)	DLPNO// B3LYP-D3(BJ)
Cluster A	18.1	10.5	13.3	11.5	7.1	10.8	14.2	12.1
Cluster B	22.9	13.2	17.5	13.6	18.3	13.5	19.8	13.6
Error (per cent)	72.9	–	21.9	–	35.2	–	31.5	–
Average error (per cent)	41.1	–	16.5	–	24.7	–	24.5	–

spin states with different density functional theory (DFT) methods, that is: (i) the methodology adopted in Serra-Peralta, Domínguez-Dalmases & Rimola (2022), namely the B3LYP-D3(BJ) method (Becke 1988, 1993b; Lee, Yang & Parr 1988) combined with the 6–311++G(d,p) basis set (Hehre, Ditchfield & Pople 1972; Hariharan & Pople 1973); (ii) the meta-generalized-gradient approximation (meta-GGA) r²SCAN-3c method, which goes with its own tailored triple zeta quality basis set (Grimme et al. 2021), (iii) the range-separated hybrid meta-GGA ωB97M-V method (Mardirossian & Head-Gordon 2017), and (iv) the hybrid BHLYP-D3(BJ) method, which features 50 per cent of exact exchange (Lee, Yang & Parr 1988; Becke 1993a). The last two methods were combined with the def2-TZVP basis set (Weigend & Ahlrichs 2005). The calculations were performed with the spin-unrestricted formalism in case of open-shell systems (Pople, Gill & Handy 1995). The accuracy of these DFT methods was tested against the domain-based local pair natural orbital the coupled cluster theory with single-, double-, and per-turbative triple-excitations (DLPNO-CCSD(T)). We compared the energy values obtained at DFT level against DLPNO-CCSD(T)/aug-cc-pVTZ (Guo et al. 2018) single energy calculations on each DFT optimized geometry. The calculations were carried out with a tight-PNO set-up and the default settings for the self consistent field (SCF).

The second part of the benchmark involved the characterization of the adsorption of H_2S and H_2O on the Fo grain nanoclusters, starting from four complexes manually built to allow the two species to interact with sites X, W, Y, and with neighbouring oxygen atoms of site W (which as mentioned above is equal to site Z). Adsorbing H_2S with r²SCAN-3c and B3LYP-D3(BJ) results in some cases in its spontaneous dissociation. Thus, we used the nudged elastic band (NEB) algorithm to find the minimum energy path connecting the reactant (physisorbed complex) and the product (chemisorbed complex). The algorithm generates a number of configurations of the atoms, referred to as images of the system (in our case we chose eight images) that link the two minima with the aim of finding the image with the highest energy. Subsequently, the latter structure is optimized as a transition state following the eigenvector associated with the eigenvalue of the Hessian matrix.

Once we selected an appropriate level of theory, we initially characterized the binding sites of the four olivine clusters by adsorbing H_2S, H_2O, CS, and CO. Because of symmetry, we identified three adsorption sites (X, W, Y) for Fo cluster, cluster A and cluster B, while in cluster C the Fe substitution at position Z causes a loss of symmetry and the emergence of an additional binding site. We then characterized the adsorption of the nine S-bearing species on cluster C, which is the most stable structure and presents the largest number

of binding sites. Each species was described in its ground state: CS, H_2S, and SH^+ as singlets, S^+, SH, SO^+, and H_2S^+ as doublets, and finally S and SO as triplets. Combining the spin states of the S-bearing species with the ground state of cluster C, i.e. the quintet, we obtained adsorption complexes of CS, H_2S, and SH^+ in the quintet state, S^+, SH, SO^+, and H_2S^+ in the sextet state and S and SO in the septet state. For each complex, the full set of harmonic frequencies was computed to establish each structure to be a true minimum on the potential energy surface (PES). From them, the zero point vibrational energy, ZPE, correction was computed to correct the binding energy, BE, a quantity defined as the opposite of the interaction energy, obtained with the equation:

$$BE = -\Delta E_{int} = -E_{complex} + E_{cluster} + E_{adsorbate}, \qquad (1)$$

to be corrected for the ZPE as:

$$BE(0) = BE - \Delta ZPE, \qquad (2)$$

where $\Delta ZPE = ZPE_{complex} - ZPE_{cluster} - ZPE_{adsorbate}$.

3 RESULTS

3.1 Benchmark

Clusters A, B, and C were optimized to characterize their stability from both a structural and an electronic point of view. Data on the quintet and the singlet states are reported in Table 1, while those concerning the triplet state were excluded due to some convergence problems that arose during the optimization of the structures. We did not aim to compare the energy difference between clusters of different spin states, as we know that DFT is not reliable for treating systems in their excited states, but we compared the relative energies between different clusters with the same spin multiplicity (ΔE). Cluster C was the most stable of the group and it was taken as a reference to calculate the ΔE of cluster A and B. Among the four functionals tested in the benchmark, ωB97M-V showed the smallest error when compared to DLPNO-CCSD(T), with an average error of 11.1 per cent for the quintet and of 21.9 per cent for the singlet spin states. Although the percentage error appeared to be large, the absolute errors corresponded to a few kJ mol⁻¹, which are always <4 kJ mol⁻¹ for ωB97M-V, therefore, in the limit of chemical accuracy. BHLYP-D3(BJ) performed similarly to ωB97M-V, followed by B3LYP-D3(BJ), while r²SCAN-3c, lacking of exact exchange, was the less suitable functional. However, it is worth pointing out the surprising performance of r²SCAN-3c in

Table 2. Adsorption energies (ΔE_{int} in the text) of H_2S and H_2O on the Fo cluster optimized with different DFT functionals and their DLPNO-CCSD(T) single energy point calculations. Complex I and II differ for the orientation of the adsorbate with respect to the binding site (#). The asterisk (∗) indicates the cases in which spontaneous dissociation takes place. The percentage error is obtained as the average over those computed for each DFT method against the DLPNO//DFT energy value. The average error (in %) is done over the four complexes of both H_2O and H_2S together.

Adsorption of H_2S	Metal centre	r^2SCAN-3c	DLPNO// r^2SCAN-3c	ωB97M-V	DLPNO// ωB97M-V	B3LYP-D3(BJ)	DLPNO// B3LYP-D3(BJ)
Complex I	13	−79.5	−74.5	−74.1	−76.2	−84.4	−84.5
Complex II	13#	−90.9	−92.1	−86.6	−92.3	−101.5	−101.2
Complex III	10	−185.8∗	−176.0∗	−77.0	−80.0	−88.2	−89.3
Complex IV	6	−183.0∗	−174.5∗	−70.3	−72.8	−194.7∗	−186.1∗
Adsorption of H_2O	**Metal centre**	**r^2SCAN-3c**	**DLPNO// r^2SCAN-3c**	**ωB97M-V**	**DLPNO// ωB97M-V**	**B3LYP-D3(BJ)**	**DLPNO// B3LYP-D3(BJ)**
Complex I	13	−119.5	−124.5	−122.9	−125.4	−127.7	−135.4
Complex II	13#	−119.4	−124.6	−124.3	−126.5	−126.5	−139.0
Complex III	10	−168.1	−157.1	−167.0	−167.8	−178.1	−177.5
Complex IV	6	−153.5∗	−161.3∗	−114.5	−115.3	−174.5∗	−172.4∗
Average error	–	4.8	–	2.6	–	3.4	–

the description of the quintet spin state, despite the presence of unpaired electrons, with an error of only 9.3 per cent. Nevertheless, the representation of the singlet spin state was not satisfying, showing an error of 72.9 per cent. In general, the energies of the clusters in the singlet spin state were affected by larger errors than those of the structures in the quintet ground state, confirming that DFT does not represent a suitable choice when describing excited states. Nevertheless, the stability order documented in the literature was well-reproduced with every functional adopted in the benchmark. In terms of the description of the band gap of the system, the outcome largely depends on the percentage of exacts exchange included in the definition of the functional. Indeed, for r^2SCAN-3c, in which exact exchange is not accounted for, the band gap was almost zero, sometimes responsible for convergence problems, as in the case of the triplet spin state.

To expand our benchmark, we considered the adsorption of H_2S and H_2O on the Fo cluster. The two species were manually placed on the Fo and the obtained complexes were optimized with ωB97M-V, B3LYP-D3, and r^2SCAN-3c functionals. When comparing the interaction energies computed with the three different functionals against their respective DLPNO-CCSD(T) single energy points, ωB97M-V/def2-TZVP resulted again in the best-performing level of theory (see Table 2). In this case, the percentage errors were much lower than in the previous benchmark due to the larger adsorption energies involved compared to ΔE. However, at least for ωB97M-V, the absolute error remained below 4 kJ mol^{-1}. We also point out the great improvement in the performance of r^2SCAN-3c, justified by the absence of unpaired electrons in the system.

When modelling the adsorption of H_2S on Fo, we noticed an interesting phenomenon. A spontaneous dissociation of H_2S was observed in complexes III and IV at r^2SCAN-3c level of theory, while only complex IV caused the dissociation of the adsorbate at B3LYP-D3(BJ) level of theory, and no dissociation occurred with the ωB97M-V functional. In these two complexes (III and IV), H_2S interacts with the Mg cation located in sites W and X, respectively. The dissociated complexes obtained with r^2SCAN-3c are stable enough, so that a subsequent optimization with ωB97M-V did not change their structure. The chemisorbed structures were more stable than the physisorbed ones by about 100 kJ mol^{-1}. Thus, we computed the energy barrier for the dissociation process at ωB97M-V (that in which spontaneous dissociation is not observed), obtaining a value of 0.2 kJ mol^{-1} for complex III and 7.2 kJ mol^{-1} for complex

IV. When considering the ZPE correction, the dissociation barriers at 0 K became −3.4 and 3.9 kJ mol^{-1} for complexes III and IV, respectively. The frequency associated with the imaginary mode of the transition state is $231i$ cm^{-1} for complex III and $192i$ cm^{-1} for complex IV. In Fig. 2, the reactant, the transition state structure, and the product are shown in the case of complex III, together with a plot of the PES along the reaction coordinate. The dissociation barriers are indeed very small, in one case even submerged below zero, indicating that the cleavage of H_2S into HS$^-$ and H$^+$ is likely to occur on to Fo cluster, once the molecule is adsorbed on the Mg sites. When adsorbing H_2O on Mg, we observed the spontaneous dissociation of the O–H bond in complex IV, in which the oxygen atom interacts with the Mg cation of site X at both r^2SCAN-3c and B3LYP-D3(BJ) levels of theory. We did not computed the PES of the dissociation at ωB97M-V level of theory, however, we assume that a small barrier for the process is present, as for H_2S. Thus, we can conclude that the dissociation barrier depends on the methodology and that can either be submerged below zero or be a few kJ mol^{-1}. The two benchmark studies indicate ωB97M-V/def2-TZVP to be the best-performing methodology with an average error of 16.5 per cent on the relative stability of olivine clusters and of 2.6 per cent on H_2S and H_2O adsorption energies, becoming this functional our choice for the following calculations.

3.2 Cluster versus periodic approach

The computational approach adopted in this work to study the interaction of S-bearing species with the silicate core of the grains may appear too simplistic due to the limited size of the cluster models. The exposure of the metal centres could be responsible for their higher reactivity, which could influence the outcomes of the calculations. Enlarging the cluster model to increase the coordination of the metal centres is not practical due to the steep increase of the computational cost of the calculations. Therefore, we adopted a periodic approach to model different extended Fo slab surfaces, with the closest level of theory to that of the cluster. The periodic approach represents the opposite situation compared to the cluster, as the metal center binding sites (albeit at the surfaces) possess the highest coordination due to the extended nature of the slabs. The cluster-based adsorption complexes described in Table 2 were optimized at the DFT PBE method, combined with the def2-TZVP basis set. For the periodic calculations, H_2S was adsorbed on to the (001), (021),
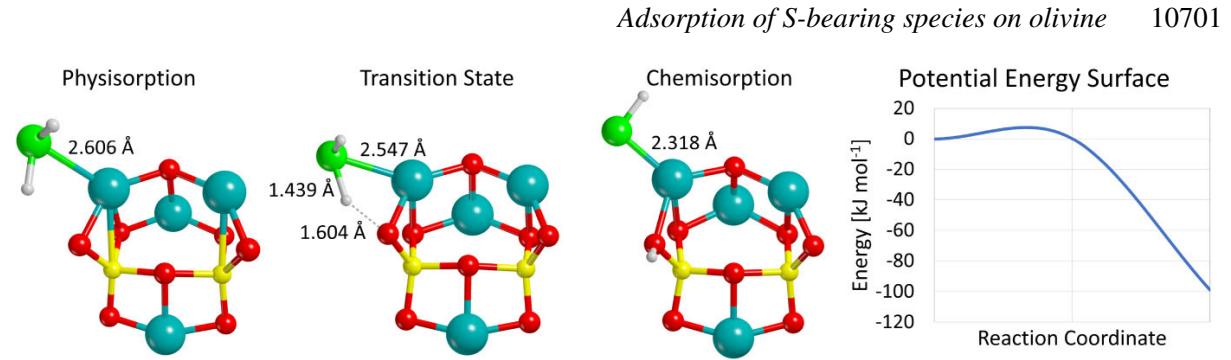
Figure 2. The dissociation of H_2S on the Fo cluster (complex III) characterized at the ωB97M-V/def2-TZVP level of theory. It exhibits a small potential energy barrier and becomes barrierless when taking into account the ZPE corrections.

(101), (110), (111), and (120) Fo surfaces, which were previously characterized in Zamirri et al. (2017) and Bancone et al. (2023). The periodic adsorption complexes were also optimized at PBE, and the Fo atoms were described with the basis set proposed by Bruno et al. (2014), while H_2S with the same def2-TZVP basis set adopted for the cluster calculations. We did not include dispersion interactions in the description of the system, as it was not possible to reproduce the desired level of theory (D2 with customized dispersion coefficient for the Mg atom) in both the cluster and the periodic calculations due to specific implementation of the D2 coding in the ORCA programme. Despite the missing dispersion term, the calculations show that H_2S still spontaneously dissociates on the Fo cluster, in complexes I, II, III, and IV. On the periodic systems, molecular physisorption is found on the most stable Fo surfaces, (120) and (001), while on the less stable (101), (111), (021), and (110), H_2S dissociative chemisorption takes place. Therefore, we can thus conclude that H_2S chemisorption is not simply an artefact of the size of the cluster that exposes low-coordinated metal centres. Depending on the surface and on the specific adsorption site, it is possible to have spontaneous dissociation of H_2S also on large and extended surfaces in which the ion coordination is more complete than in the cluster. We remark that the level of theory chosen to characterize the system may be responsible for the presence or absence of a small barrier for the dissociation process.

3.3 Characterization of the nanocluster binding sites

We characterized the binding sites of each nanocluster (Fo and the olivines) by adsorbing H_2S, CS, and their oxygen analogues. H_2S and H_2O are species with an electronegative atom (S and O) that preferentially interacts with the positively charged metal center, and two hydrogen atoms that can interact via H-bond with the oxygen atoms of the silicate unit, when geometrically feasible. On the other hand, CS and CO are species whose dipole shows a concentration of electronic charge on the carbon atom, and accordingly this atom is the one interacting with the metal center. The bond length of CS in the gas-phase is 1.523 Å, and when it is adsorbed on Mg it shortens to 1.500 Å, due to the electron donation coming from the CS σ orbitals with moderate antibonding character to Mg. When CS is adsorbed on Fe, the bond length becomes 1.509 Å, due to the π-electron back donation effect of Fe on the antibonding orbitals of CS. The same occurs with CO, in which the CO bond lengths in the Mg- and Fe-adsorbed complexes are 1.117 and 1.120 Å, respectively, shorter than that in the gas-phase molecule (1.123 Å). Remarkably, the largest CS bond shortening compared to CO, together with the differences in their dipole moments (0.1 and 1.9 Debye for CO and

Table 3. BEs (in kJ mol^{-1}) of H_2S, H_2O, CS, and CO adsorbed on Fo and olivine clusters. BE ranges result from the presence of different adsorption sites on the same cluster.

Cluster	Site	H_2S	H_2O	CS	CO
Fo	Mg	70–77	115–167	89–91	48–50
A	Fe	68	94	121	66
A	Mg	76–78	121–125	92–93	50–52
B	Fe	73	98	109	62
B	Mg	72–74	119–122	91–93	49–51
C	Fe	97	127	120	70
C	Mg	74–85	118–131	90–91	46–54

CS, respectively), causes the BE of CS to be almost doubled with respect to CO. We previously observed the same phenomenon when characterizing the interaction of CO and CS on water ice (Perrero et al. 2022), where the larger dipole of CS caused an increase in BE of 50 per cent with respect to the CO BE value. This further strikes the difference in the chemical behaviour of CO and CS.

Table 3 shows a summary of the results. We obtained a range of values for the adsorption on to Mg centres and one value for each Fe. It appears that CS and CO prefer to interact with Fe rather than Mg, while H_2O clearly shows a larger affinity with Mg rather than with Fe. However, the behaviour of H_2S is not straightforward. The interaction with both metals seems to be comparable in clusters A and B, but cluster C represents an exception. In fact, there is a notable difference between the 74–85 kJ mol^{-1} BE values computed when H_2S interacts with Mg and the BE value of 97 kJ mol^{-1} computed for the adsorption on to Fe. An overall look at the values, particularly the BEs obtained for the Fe site at different positions (X, W, Y, and Z) hints at a possible role of the coordination of the metal centre in determining the binding strength. Indeed, sites W and Z (cluster C) are the most exposed and less coordinated, and they tend to give the highest BE, while site X (cluster A) is the most coordinated and is usually the weakest one. In general, cluster C, in addition to being the most stable structure and offering the largest number of binding sites, is also covering the entire set of binding energies obtained with the entire set of nanoclusters. All of these reasons are in favour of choosing this structure (cluster C) for the investigation of the adsorption of the whole set of S-bearing species.

3.4 Adsorption of S-bearing species

The set of the adsorbed species includes CS, H_2S, H_2S^+, HS, HS$^+$, S, S$^+$, SO, and SO$^+$. These species have been selected for being the most abundant sulphur carriers in diffuse clouds and the external
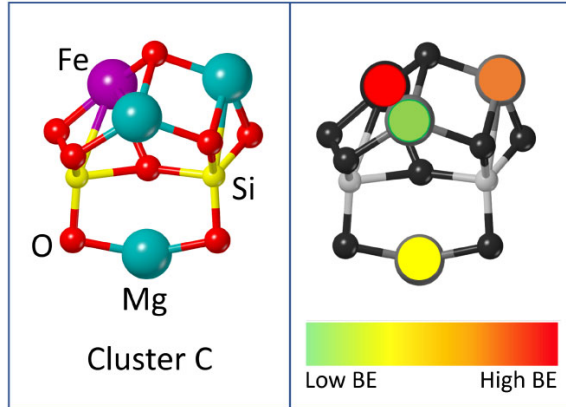
Figure 3. Intensity map showing the strength of each binding site from weaker (–) to stronger (++), depending on which species has been adsorbed. It is valid for all the species characterized in this work, with the exception of SO and SO^+, for which the Fe is the weakest binding site. In the case of H_2S^+ and HS^+, the cation dissociate when adsorbed onto Fe.

Table 4. Calculated binding energies [BE and BE(0), in kJ mol^{-1}] for all the considered S-bearing species on the cluster C.

	BE		BE(0)	
	Mg	Fe	Mg	Fe
CS	90–100	120	85–96	115
H_2S	74–85	97	67–78	89
H_2S^+	354–364	538	345–355	520
HS	70–80	203	65–76	194
HS^+	498–508	698	491–503	680
S	64–87	175	63–85	171
S^+	470–481	534	471–483	534
SO	80–96	69	77–92	66
SO^+	586–616	499	579–607	491

layers of photon-dominated regions (PDR) where the water ice has not been formed yet, either in the cloud envelopes or the dense PDRs formed in the vicinity of recently formed young massive stars (Fuente et al. 2003, 2023; Neufeld et al. 2015; Goicoechea et al. 2021). We modelled four adsorption complexes for each species, from which some common characteristics emerged: (i) we can draw a colour map (see Fig. 3) to highlight the strength of the adsorption sites which is valid for all the species; (ii) the Fe–S interaction is stronger than the Mg–S one (see Table 4). Although we may attribute part of the reason to the coordination of the metal centre, it is not the only explanation to such differences; (iii) SO and SO^+ interact with the metal centre through oxygen, which in this case is the most electronegative atom. This is responsible for the differences in the adsorption energies listed in Table 4; (iv) the presence of a charge dramatically increases the BE, as we observed for the four ions included in this study, (H_2S^+, HS^+, S^+, and SO^+).

From the calculations, we found that H_2S^+ and HS^+ are physisorbed on Mg, but chemisorbed on Fe, in which the proton transfers to one of the oxygen atoms belonging to the closest silicate unit (similarly to what we observed for H_2S on Fo), and the charge is distributed on to the entire system. Moreover, when an open-shell species adsorbs on Fe, part of its spin density transfers from the sulphur atom to the metal, increasing the binding energy as in the case of S and HS. On the other hand, this effect is prevented for

Table 5. Binding energies [BE(0), in kJ mol^{-1}] of five S-bearing species and water on amorphous ice (Ferrero et al. 2020; Perrero et al. 2022) and on olivine.

Species	BE(0) on amorphous ice	BE(0) on olivine
CS	8.3–30.6	84.4–114.6
H_2S	16.4–37.3	67.1–89.0
HS	9.0–35.9	65.4–194.4
S	13.1–23.3	63.0–171.2
SO	7.8–32.0	66.3–91.8
H_2O	30.0–50.8	118.2–131.0
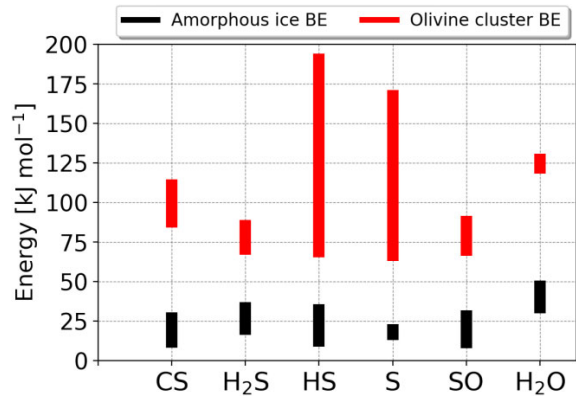
Figure 4. Binding energies [BE(0), in kJ mol^{-1}] ranges covered by CS, H_2S, HS, S, SO, and H_2O adsorbed on amorphous ice (Ferrero et al. 2020; Perrero et al. 2022) and on olivine.

SO, whose two unpaired electrons remain localized on to the radical species, due to the adsorption through the oxygen atom. The BEs of both SO and SO^+ can be explained by looking at the behaviour of H_2O, in which the interaction with the metal center takes place through oxygen and for which the interaction Mg–O is favoured over the Fe–O one. Finally, the inclusion of the ΔZPE correction in computing the BE(0) does not alter the trend derived from the analysis of the BEs.

4 DISCUSSION AND ASTROPHYSICAL IMPLICATIONS

In a previous work by some of us (Perrero et al. 2022), the BEs of 17 S-bearing species adsorbed on to crystalline and amorphous water ice were computationally studied adopting a periodic approach and DFT//HF-3c levels of theory. The B3LYP-D3 functional was used to compute the energy of closed-shell systems (such as CS and H_2S), while for open-shell species (such as HS, S, and SO) M06-2X was adopted. These functionals were combined with an Ahlrichs triple zeta valence quality basis set, supplemented with a double set of polarization functions (Schäfer, Horn & Ahlrichs 1992). Although the computational approach adopted in Perrero et al. (2022) differs from this work, it does not justify the large differences between the BE(0) values of the same set of species on the amorphous ice surface and the olivine nanoclusters (see Table 5 and Fig. 4). While in the first case the interactions are weak and controlled mainly by the dispersion forces, BE(0)s computed in this work are large and determined mostly by electrostatic interactions, to which occasionally electron transfer phenomena add up.

The consequences of such a strong interaction between sulphur and the mineral surface is that S-containing species have a high chance to freeze out on to the core of dust grains and not be able to desorb into the gas-phase even at the temperatures found in a diffuse cloud (around 100 K). In those environments, the presence of charged gas-phase species should also favour the adsorption process as long as the grains are negatively charged (Cazaux et al. 2022; Fuente et al. 2023). Even if the grain particles are mostly neutrals or positively charged, the accretion of neutral sulphur species on the grain surfaces could enhance the number of sulphur atoms in refractories. On the other hand, it should be considered that dust grains in dense clouds are not completely covered by the ice mantle, therefore still exposing part of their mineral surface into the gas (Potapov & McCoustra 2021). As it clearly appears in Fig. 4, H_2O adsorption on olivine is more energetic than H_2S, meaning that water is more likely (and probable) than hydrogen sulphide to form a stable interaction with the mineral. However, the modest interaction between sulphur-containing species and water ice allows these molecules to diffuse on its surface and likely move towards the portion of exposed core of the grains. Therefore, whether considering the physical conditions of a diffuse or those of a dense cloud, S-bearing species would have a certain chance either to directly stick on to the grain core or diffuse from the mantle towards the exposed fraction of the core grain where they become strongly chemisorbed.

Another interesting issue is the tendency of certain species, namely H_2S, HS^+, and H_2S^+, to chemisorb on to olivine nanoclusters, planting the seed for the formation of the Fe–S bond present in sulphide minerals such as troilite and pentlandite. In the work of Kama et al. (2019), approximately 90 per cent of the sulphur is predicted to be locked in the refractory residue of protoplanetary discs, the main carriers being precisely sulphide minerals, followed by sulphur chains S_n, through to the study of the photospheres of a sample of young stars. However, chemical models (Druard & Wakelam 2012) and laboratory experiments (Woods et al. 2015) predict a scarce abundance of sulphur chains in these environments, reason why sulphide minerals are considered the major reservoir of refractory sulphur in the protoplanetary disc. These two minerals are also found in cometary dust and meteoritic rocks (Kallemeyn et al. 1989; Trigo-Rodríguez 2012). From a thermodynamic point of view, Fe–S is also more favoured than Mg–S, as the latter is only found in the less common enstatite chondrites, that due to their formation in reducing conditions, are rich in alkaline sulphides like the Mg-containing niningerite and alabandite (Sears, Kallemeyn & Wasson 1982).

In this work, we did not consider charged dust grains, even though the model of Ibáñez-Mejía et al. (2019) predicted them to be positively charged in a diffuse medium and negatively charged in denser environments. If this was the case, the interaction between gas-phase cations and positively charged grains in diffuse clouds would clearly be hampered by electrostatic repulsion. However, our results concerning positively charged sulphur-bearing species adsorbed on neutral dust grain cores hold true for the case in which neutral gas-phase species interact with charged dust grains. Although the atomistic details of the system should vary due to the presence of a charge on the olivine nanocluster, the interaction energies should be of the same order of magnitude, since the presence of a charge in the system would still be the main driving force of the interaction. On the other hand, Fuente et al. (2023) argue that sulphur would remain ionized in the gaseous medium until grains are expected to be negatively charged. If this was the case, the electrostatic interactions would be responsible for an increased sulphur depletion effect.

According to what Hily-Blant et al. (2022) suggested, the fact that sulphur depletion increases progressively as the core evolves could be in agreement with the fact that during the evolution, atomic S

freezes out on the surface of grains and, depending on which surface it reaches, it can either become part of the mineral core or as Cazaux et al. (2022) propose, it can fall on the ice mantle and be subjected to photoprocessing, thus reacting and forming a refractory residue.

Our calculations are also relevant to understand the sulphur chemistry in the dense PDRs formed on the molecular cloud/HII regions interfaces. It has been considered that in these dense warm regions (dust temperature $\sim$100 K), the chemistry is well explained with gas-phase networks since freeze-out on grain surfaces is negligible. Our new calculations suggest that this may not be the case since the binding energies of sulphur species is up to a factor of $\sim$10 in bare grains. This means that gas–grain interactions need to be considered in these warm environments.

Finally, the assumption that S-bearing species become part of the grain core, rather than interacting with the icy mantles, would be in agreement with the fact that they are usually used as shock tracers (e.g. Sato, M. T. et al. 2022; Zhang et al. 2023). In shock regions, which are caused by the impact of stellar outflows with the quiescent surrounding gas, H_2S can be sputtered off the grains and enter in the gas-phase, where it marks the zone that has been affected by such an impact (Woods et al. 2015). The harsh conditions of the shock would therefore provide enough energy to break the strong interaction between sulphur and the mineral surface, allowing its transformation in H_2S and successive ejection in the gas-phase (Holdship et al. 2017).

5 CONCLUSIONS

In this work, we studied the interaction of nine S-bearing species, CS, H_2S, H_2S^+, HS, HS^+, S, S^+, SO, and SO^+, which include both neutral and charged, as well as closed-shell and open-shell systems. We characterized their adsorption complexes and computed the corresponding binding energies on olivine nanoclusters (Fo and the Fe-containing analogues) by means of quantum mechanical calculations, to simulate the interaction of a gas-phase species with the surface of a silicate bare dust grain in the diffuse interstellar medium. Our main findings are that: (i) from a thermodynamic point of view, the Fe–S interaction is more stable than Mg–S, while when the oxygen end is interacting with the metal centre we notice the opposite trend; (ii) S-bearing species are adsorbed much more strongly on the core of bare dust grains than on their icy mantles (represented by pure amorphous water ice surfaces); (iii) the metal centres of the olivine clusters can be responsible for the dissociation of hydrogenated S-bearing species, especially if the latter are positively charged; and (iv) the dissociation of H_2S on Fo cluster presents a small barrier, that is likely to be overcome when considering the energy liberated by the adsorption process. The implications of such findings are that sulphur species have a high probability of sticking on to the surfaces of bare dust grains and becoming part of their core in the form of refractory materials, as predicted by a number of experimental and observational studies, in addition to chemical models. Indeed, more investigations are needed in order to finally unveil sulphur chemistry in the ISM. However, the trapping of sulphur into the grain cores in the early stages of the evolution of a prestellar core could, in part, account for the S-depletion in dense cores.

ACKNOWLEDGEMENTS

DATA AVAILABILITY

The data underlying this article are freely available in Zenodo at https://zenodo.org/doi/10.5281/zenodo.8363882.

REFERENCES

Altwegg K., Balsiger H., Fuselier S. A., 2019, ARA&A, 57, 113
Anders E., Grevesse N., 1989, Geochim. Cosmochim. Acta, 53, 197
Bancone N., Pantaleone S., Ugliengo P., Rimola A., Corno M., 2023, Phys. Chem. Chem. Phys., 25, 26797
Becke A. D., 1988, Phys. Rev. A, 38, 3098
Becke A. D., 1993a, J. Chem. Phys., 98, 1372
Becke A. D., 1993b, J. Chem. Phys., 98, 5648
Boogert A. A., Gerakines P. A., Whittet D. C., 2015, ARA&A, 53, 541
Boogert A., Brewer K., Brittain A., Emerson K., 2022, ApJ, 941, 32
Bruno M., Massaro F. R., Prencipe M., Demichelis R., De La Pierre M., Nestola F., 2014, J. Phys. Chem. C, 118, 2498
Calmonte U. et al., 2016, MNRAS, 462, S253
Caselli P., Hasegawa T., Herbst E., 1994, ApJ, 421, 206
Cazaux S., Carrascosa H., Caro G. M., Caselli P., Fuente A., Navarro-Almaida D., Riviére-Marichalar P., 2022, A&A, 657, A100
Cuppen H. M., Walsh C., Lamberts T., Semenov D., Garrod R. T., Penteado E. M., Ioppolo S., 2017, Space Sci. Rev., 212, 1
Drozdovskaya M. N., van Dishoeck E. F., Rubin M., Jørgensen J. K., Altwegg K., 2019, MNRAS, 490, 50
Druard C., Wakelam V., 2012, MNRAS, 426, 354
Escatllar A. M., Lazaukas T., Woodley S. M., Bromley S. T., 2019, ACS Earth Space Chem., 3, 2390
Ferrante R. F., Moore M. H., Spiliotis M. M., Hudson R. L., 2008, ApJ, 684, 1210
Ferrero S., Zamirri L., Ceccarelli C., Witzel A., Rimola A., Ugliengo P., 2020, ApJ, 904, 11
Fuente A., Rodrıguez-Franco A., Garcıa-Burillo S., Martın-Pintado J., Black J. H., 2003, A&A, 406, 899
Fuente A. et al., 2023, A&A, 670, A114
Gao X., Thiemens M. H., 1993, Geochim. Cosmochim. Acta, 57, 3159
Goicoechea J. R. et al., 2021, A&A, 647, A10
Grimme S., Hansen A., Ehlert S., Mewes J.-M., 2021, J. Chem. Phys., 154, 064103
Guo Y., Riplinger C., Becker U., Liakos D. G., Minenkov Y., Cavallo L., Neese F., 2018, J. Chem. Phys., 148, 011101
Hariharan P. C., Pople J. A., 1973, Theor. Chim. Acta, 28, 213
Hehre W. J., Ditchfield R., Pople J. A., 1972, J. Chem. Phys., 56, 2257

Henning T., 2010, ARA&A, 48, 21
Hily-Blant P., Pineau des Forêts G., Faure A., Lique F., 2022, A&A, 658, A168
Holdship J., Viti S., Jiménez-Serra I., Makrymallis A., Priestley F., 2017, AJ, 154, 38
Ibáñez-Mejía J. C., Walch S., Ivlev A. V., Clarke S., Caselli P., Joshi P. R., 2019, MNRAS, 485, 1220
Jenkins E. B., 2009, ApJ, 700, 1299
Jiménez-Escobar A., Caro G. M., 2011, A&A, 536, A91
Kallemeyn G. W., Rubin A. E., Wang D., Wasson J. T., 1989, Geochim. Cosmochim. Acta, 53, 2747
Kama M., Shorttle O., Jermyn A. S., Folsom C., Furuya K., Bergin E., Walsh C., Keller L., 2019, ApJ, 885, 114
Karssemeijer L. J., Cuppen H. M., 2014, Astron. Astrophys., 569, A107
Kouchi A., Furuya K., Hama T., Chigai T., Kozasa T., Watanabe N., 2020, ApJ, 891, L22
Laas J. C., Caselli P., 2019, A&A, 624, A108
Lee C., Yang W., Parr R. G., 1988, Phys. Rev. B, 37, 785
Mardirossian N., Head-Gordon M., 2017, Mol. Phys., 115, 2315
Belén Maté, Stéphanie Cazaux, Miguel Ángel Satorre, Germán Molpeceres, Juan Ortigoso, Carlos Millán, Carmina Santonja, 2020, Astron. Astrophys., 643, A163
McClure M. K. et al., 2023, Nat. Astron., 7, 431
Molster F., Kemper C., 2005, Space Sci. Rev., 119, 3
Navarro-Ruiz J., Ugliengo P., Rimola A., Sodupe M., 2014, J. Phys. Chem. A, 118, 5866
Navarro-Ruiz J., Ugliengo P., Sodupe M., Rimola A., 2016, Chem. Comm., 52, 6873
Neese F., 2022, WIREs Comput. Mol. Sci., 12, e1606
Neufeld D. A. et al., 2015, A&A, 577, A49
Penteado E. M., Walsh C., Cuppen H. M., 2017, ApJ, 844, 71
Perrero J., Enrique-Romero J., Ferrero S., Ceccarelli C., Podio L., Codella C., Rimola A., Ugliengo P., 2022, ApJ, 938, 158
Pople J. A., Gill P. M. W., Handy N. C., 1995, Int. J. Quantum Chem., 56, 303
Potapov A., McCoustra M., 2021, Int. Rev. Phys. Chem., 40, 299
Rimola A., Trigo-Rodríguez J. M., Martins Z., 2017, PCCP, 19, 18217
Sato M. T. et al., 2022, A&A, 660, A82
Schäfer A., Horn H., Ahlrichs R., 1992, J. Chem. Phys., 97, 2571
Sears D. W., Kallemeyn G. W., Wasson J. T., 1982, Geochim. Cosmochim. Acta, 46, 597
Serra-Peralta M., Domínguez-Dalmases C., Rimola A., 2022, PCCP, 24, 28381
Smith R. G., 1991, MNRAS, 249, 172
Spoon H. et al., 2022, ApJS, 259, 37
Trigo-Rodríguez J. M., 2012, Meteoritos, Colección ¿Qué sabemos de?. Editorial Catarata-CSIC, Madrid, Spain
Van Dishoeck E. F., Herbst E., Neufeld D. A., 2013, Chem. Rev., 113, 9043
Voet D., Voet J. G., Pratt C. W., 2008, Principles of Biochemistry. John Wiley & Sons, Hoboken, New Jersey, USA
Weigend F., Ahlrichs R., 2005, PCCP, 7, 3297
Woods P. M., Occhiogrosso A., Viti S., Kaňuchová Z., Palumbo M. E., Price S., 2015, MNRAS, 450, 1256
Yabuta H., Williams L. B., Cody G. D., Alexander C. M. O., Pizzarello S., 2007, Meteorit. Planet. Sci., 42, 37
Zamirri L., Corno M., Rimola A., Ugliengo P., 2017, ACS Earth Space Chem., 1, 384
Zhang Z. E., lun Yang Y., Zhang Y., Cox E. G., Zeng S., Murillo N. M., Ohashi S., Sakai N., 2023, ApJ, 946, 113

This paper has been typeset from a TEX/LATEX file prepared by the author.

Chapter 5

A theoretical and experimental combined study of ethanol and ethylamine binding energies on H_2O ice surfaces

Introduction

Finally, the investigation of adsorption processes led to a collaboration between computational and experimental chemists. During the visit to the LERMA laboratory of CY Cergy Paris Université,[1] under the guide of Professor F. Dulieu and of his PhD student J. Vitorino, I had the opportunity to learn how experiments are conducted and how the expertise in different fields can be combined to understand the chemical processes occurring in the ISM.

Ethanol (CH_3CH_2OH) and ethylamine ($CH_3CH_2NH_2$) may be expected to show a similar behaviour in the ISM, due to their atomic composition. Both molecules are COMs, therefore, they are related to molecules of prebiotic importance. $CH_3CH_2NH_2$ has been detected only in a few comets and tentatively toward a galactic centre cloud, which is a region of active star formation (Goesmann et al., 2015; Zeng et al., 2021). In contrast, CH_3CH_2OH has been observed in several comets and in both cold and warm ISM environments (e.g., Altwegg et al., 2019; Agúndez et al., 2023). For this reason, ethanol has been extensively characterised in the scientific literature, whereas little information is available regarding ethylamine.

The two molecules are likely to be formed on the icy mantles covering dust grains in dark clouds, however, only ethanol has been detected in the ice matrix (Rocha et al., 2024). The cause of such inconsistency could be due to multiple motivations, among which a smaller abundance and thus production of N-bearing species, a higher reactivity of ethylamine, and differences in the adsorption/desorption behaviour. The latter was the focus of this investigation.

In '*Binding energies of ethanol and ethylamine on interstellar water ices: synergy between theory and experiments*' (Perrero et al., 2024, *PCCP*, **26**, 18205) it has been studied how these two COMs interact with themselves and with the icy mantles of dust grains, from both a computational and an experimental perspective. Through this work, it clearly appears how the two fields not only mutually support each other, but also serve as complementary tools to overcome their respective limitations.

---

[1] https://lerma.labo.cyu.fr/DR/

Results

The quantities measured and computed in this section may generate some confusion due to their sign. The binding energy (BE) is defined as the opposite of the adsorption energy, while the desorption energy (E_{des}) represents the energy required to facilitate the desorption of the adsorbate. For their definition and in case of adsorption being thermodinamically favoured, both quantities are positive. Conversely, the cohesive energy (E_C) denotes the energy released from the system upon the formation of a surface or a bulk structure and is a negative quantity. In the following, these values will be compared in reason of their absolute value.

Experimentally, the E_{des} was determined by depositing fixed amounts of each adsorbate on a surface and subsequently analysing the data obtained from TPD experiments, performed in the VENUS interstellar chamber (Congiu et al., 2020). Each species was adsorbed on three types of surfaces: bare gold, amorphous ice (ASW), and crystalline ice (CI).

The first set of experiments aimed at the determination of the E_{des} of pure CH_3CH_2OH and $CH_3CH_2NH_2$ deposited on a bare gold surface. The temperature at which the desorption peak is registered and the heating ramp used in the TPD experiment are necessary to compute the pre-exponential factor needed to extract the desorption energy (see left panel of Figure 5.1). A mathematical model based on the Polanyi-Wigner equation (see Section 2.7) returns E_{des} = 53.6 kJ mol^{-1} for CH_3CH_2OH and E_{des} = 41.6−43.2 kJ mol^{-1} for $CH_3CH_2NH_2$.

The second set of experiments consisted of the deposition of submonolayer quantities of CH_3CH_2OH and $CH_3CH_2NH_2$ on 10 ML of ASW and 10 ML of CI. In all the experiments and for both molecules, co-desorption of the adsorbate with water is observed. During the TPD, the energy provided when raising the temperature causes the crystallisation of the ASW (characterised by the appearance of a shoulder in the desorption curve, see the left panel of Figure 5.2). In the case of ethanol, the phase change of the ice seems to enhance the desorption of the adsorbate, indicating a stronger interaction of CH_3CH_2OH with ASW with respect to CI (see the right panel of Figure 5.2). In contrast, ethylamine does not show such behaviour. In these experiments, the co-desorption precludes the determination of the E_{des} of the adsorbate, because the interaction between the water molecules of the surface is weaker than that between the adsorbate and the ice surface. Thus, the desorption temperature of the adsorbate is established by that of water. For this reason, all species whose E_{des} is larger than that of water ice exhibit such behaviour and do not allow the determination of their E_{des} from TPD experiments (Collings et al., 2004; Burke et al., 2015). Nevertheless, computational chemistry can provide the missing data.

The last set of experiments concerned the deposition of a multilayer of CH_3CH_2OH and $CH_3CH_2NH_2$ on 10 ML of ASW. The TPD curve presents multiple desorption peaks, among which one can distinguish a variety of interactions. The TPD curve of $CH_3CH_2NH_2$ shows three distinct peaks due to: i) molecules desorbing from the multilayer (thus, not in direct contact with water), ii) molecules ejected during the crystallisation of the ASW surface, and iii) molecules co-desorbing with the water ice surface. In the TPD curve of CH_3CH_2OH, the first two peaks are merged. It is not possible to extract any additional information on the E_{des} from these profiles, due to their complexity. However, calculations offer an explanation to what has been observed experimentally.

From a computational standpoint, the BEs were computed by simulating the adsorption geometry of each adsorbate on both an ASW and a CI periodic models, using CRYSTAL17 code (Dovesi et al., 2018). In the case of CI, different coverages were also simulated.
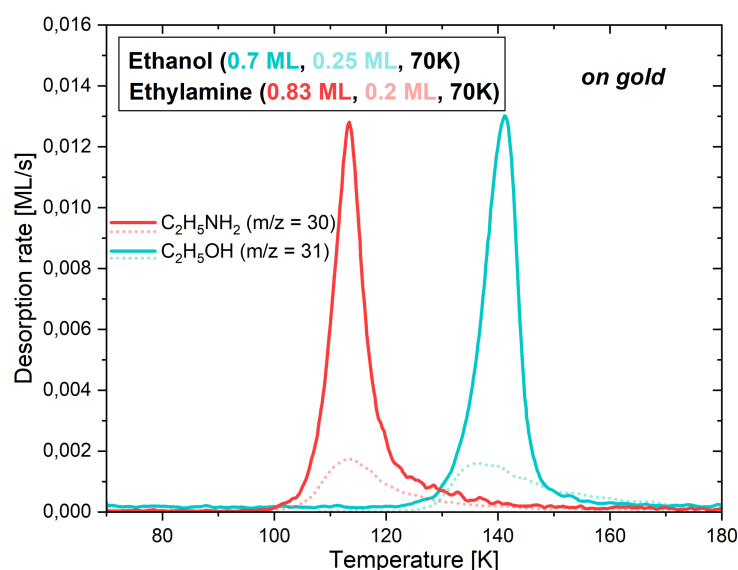
Figure 5.1: TPD of pure CH$_3$CH$_2$OH and CH$_3$CH$_2$NH$_2$ adsorbed on a bare gold surface. From the maximum of ethylamine (in red, at 113 K) and ethanol (in light blue, at 141 K) desorption curves, the desorption energy is determined.

Furthermore, the crystal structure of the adsorbates was characterised, with particular interest in their most stable surfaces and in the adsorption of each adsorbate onto the respective surface.

The ASW ice was modelled as an amorphous-like surface characterised by edges and cavities (left panel of Figure 5.3), where nine distinct binding sites were chosen to compute the adsorption of CH$_3$CH$_2$OH and CH$_3$CH$_2$NH$_2$, with the aim of obtaining an ensemble accounting for the presence of both weak and strong adsorption sites. The calculations returned BE = 26.0−59.1 kJ mol^{-1} for CH$_3$CH$_2$OH and BE = 19.1−71.1 kJ mol^{-1} for CH$_3$CH$_2$NH$_2$.

Two or three adsorption complexes were considered on the CI model, whose BEs is included in the ensemble computed on the ASW model (see Figure 5.4). Additionally, the BEs computed in the case of a higher surface coverage on the CI increase when two
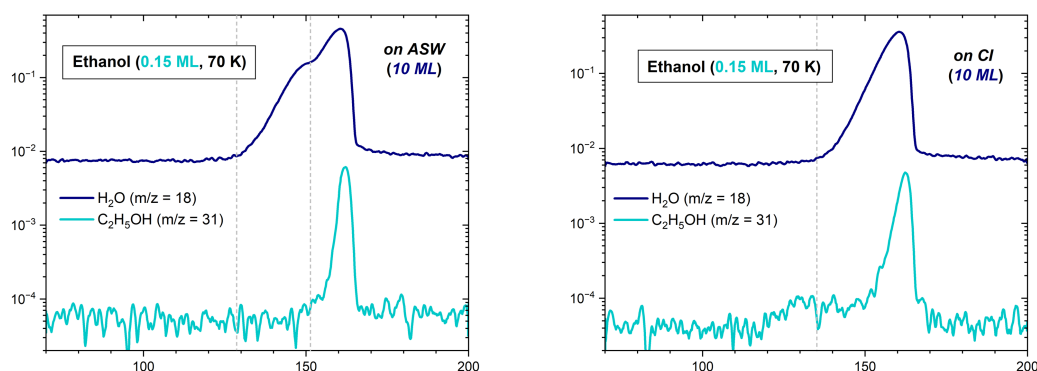
Figure 5.2: TPD of a submonolayer coverage of CH$_3$CH$_2$OH deposited on 10 ML of ASW (left) and CI (right) ices. The dark blue curve traces the desorption of water (in the left panel, the shoulder on the left is due to the crystallisation of ASW). The light blue curve traces the desorption of ethanol, that co-desorbs with water.
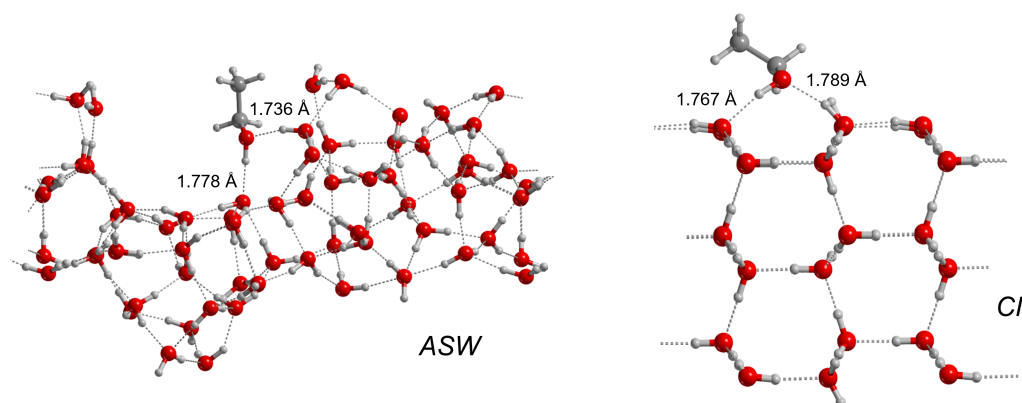
Figure 5.3: Adsorption complexes of CH_3CH_2OH on ASW (left) and CI (right) periodic ice models. Through computational chemistry it is possible to determine the BE of ethanol on a water ice surface.

molecules per cell are adsorbed, whereas they decrease in case of adsorbing four molecules per cell. Such behaviour is due to how easily the molecules can accommodate on the ice surface and whether their interaction with the ice and between themselves is maximised (2 molecules/cell) or hindered (4 molecules/cell).

Furthermore, the cohesive energy (E_C, see equation 2.59) of the bulk and of the most stable surfaces obtained from the crystal structures of ethanol and ethylamine was computed. The values obtained range from -53.4 to -40.3 kJ mol^{-1} for ethanol and from -44.0 to -30.3 kJ mol^{-1} for ethylamine, where the most negative value corresponds to the E_C of the bulk and the least negative is referred to the E_C of the least stable surface.

Finally, the adsorption of CH_3CH_2OH on the (010) ethanol surface returned BE = $20.9-41.8$ kJ mol^{-1}, whereas the corresponding simulation involving $CH_3CH_2NH_2$ and the (100) ethylamine surface yielded BE = $21.4-43.0$ kJ mol^{-1}.

Joining the information retrieved from the two approaches led to a detailed interpretation of what was observed in the experiments. The desorption energies experimentally determined for pure CH_3CH_2OH and $CH_3CH_2NH_2$ deposited on a gold surface closely align with the cohesive energies of crystalline bulks of ethanol and ethylamine, along with their most stable surfaces.

The E_{des} for submonolayer coverages of CH_3CH_2OH and $CH_3CH_2NH_2$ deposited on CI and ASW surfaces cannot be determined experimentally due to co-desorption of the adsorbate with the surface, but can be provided by the theoretical simulation, which returns a larger BE range for $CH_3CH_2NH_2$ with respect to CH_3CH_2OH. The upper values were consistent with the co-desorption behaviour, being larger than the E_C of water ice (-55.8 kJ mol^{-1} for CI). The lower limits of the ensemble are peculiar to the calculations, which allow for the characterisation of the BE of isolated molecules adsorbed on weak binding sites. In fact, the E_{des} provided by the experiments do not usually cover the lower limit of the BE distribution obtained with the calculations, as the deposition of sub-monolayer quantities of adsorbate is not comparable with the adsorption of a single species (Minissale et al., 2022).

In the TPD experiment, the adsorbate is likely to diffuse on the surface thanks to the constant thermal energy provided to the molecules during the analysis and either bind a stronger site than that initially occupied or interact with neighbouring adsorbed species. In the latter case, the measured desorption energy would be given by a combination of the real binding site strength plus a contribution depending on the lateral interactions.
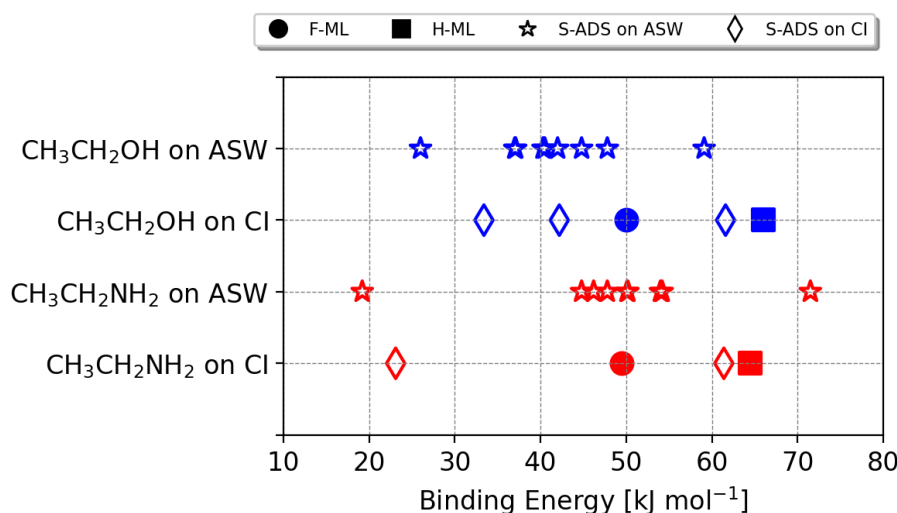
Figure 5.4: BE values computed for the adsorption of CH_3CH_2OH (blue) and $CH_3CH_2NH_2$ (red) on ASW and CI models. Different adsorption scenarios are included: single adsorption (S-ADS), half monolayer coverage (H-ML) and full monolayer coverage (F-ML). Higher coverages have only been simulated on the CI model.

Therefore, the E_{des} provided by the experiments do not usually cover the lower limit of the BE distribution obtained with the calculations.

The TPD of a multilayer coverage of CH_3CH_2OH and $CH_3CH_2NH_2$ on ASW highlights that the temperature at which the first ethylamine molecules of the multilayer desorb is higher than that of pure ethylamine, owing to the presence of the water ice surface. In contrast, for ethanol, it is not possible to distinguish the two behaviours as the corresponding peaks are overlapping. The theoretical results show that molecules in the bulk structure of crystalline ethanol ($E_C = -53.4$ kJ mol^{-1}) are characterised by a stronger interaction compared to those of crystalline ethylamine ($E_C = -44.0$ kJ mol^{-1}), but similar to those of proton ordered water ice ($E_C = -55.8$ kJ mol^{-1}). The comparison of these cohesive energies elucidates the reason why ethanol does not desorb prior to water, whereas this does not apply to ethylamine.

In conclusion, the E_{des} of both CH_3CH_2OH and $CH_3CH_2NH_2$ increases when the substrate changes from bare gold to ASW and CI. Indeed, their behaviour would not suggest large discrepancies in their detection. While the presence of ethanol in the icy mantle of dust grains has been confirmed, ethylamine has not been observed (Rocha et al., 2024). Moreover, gas-phase ethanol has been detected in several environments, while the observation of ethylamine remains tentative. Such diversity could result from a number of factors. One possibility is that ethylamine may be less abundant than ethanol due to the absence of efficient synthetic pathways. Another hypothesis is that ethylamine may exhibit higher reactivity leading to rapid consumption upon entering the gas phase. Alternatively, it may be characterised by spectral features that overlap with those of other molecules, hampering its detection.

Furthermore, the BEs of the species on water ice mantles have a profound impact on the chemical composition of the regions where a planetary system eventually forms. The snow-line of a species is defined as the zone where adsorption and desorption mechanisms are at work to regulate its permanence in the gas phase or in the solid phase (Öberg et al., 2021). These data suggest that a fraction of CH_3CH_2OH and $CH_3CH_2NH_2$ may still

reside on the grains when the majority of the water has already sublimated, available to be incorporated in the planetesimals that are future constituents of rocky planets.

The findings of this study demonstrate the pivotal role of computational chemistry in the interpretation of experimental data, as well as its capacity to yield insights that cannot be obtained through conventional experimental techniques.

Future perspectives

This study offers a nice example of how experiments and computations can mutually support each other to overcome their inherent limitations. Nevertheless, enhancements can be made on both fronts to more accurately reflect the scenarios that are the focus of this investigation.

From an experimental point of view, conducting experiments with lower surface coverages of adsorbates and slower heating ramps would probably represent a step forward toward the simulations, although still constituting a very different scenario with respect to the systems modelled via computational chemistry. The study clearly highlights that ethanol and ethylamine are unlikely to desorb via thermal desorption. From an experimental point of view, the application of alternative techniques to the study of the desorption process could provide details regarding the non-thermal desorption mechanisms. A review of the literature reveals some examples of studies conducted with MALDI-TOF MS, LDPI TOF-MS and PSD-REMPI techniques that address astrochemistry-related topics (Gudipati et al., 2012; Bossa et al., 2015; Watanabe et al., 2020). The listed acronyms represents procedures in which photodesorption and photochemistry processes are investigated by combining matrix-assisted laser desorption-ionization (MALDI), laser desorption postionisation (LDPI), or photostimulated desorption (PSD) with resonance-enhanced multiphoton ionisation (REMPI) and time-of-flight (TOF) mass spectrometry (MS).

Conversely, the simulations could be better adapted to the experiment. By increasing the number of molecules adsorbed on the ice surface (or alternatively, on a large cluster, as in Tinacci et al., 2022), it could be possible to account for the energetic effects (commonly defined as lateral interactions) caused by the presence of additional adsorbed species in adjacent binding sites. Additionally, the desorption process could be simulated in spite of the adsorption one. The BE values obtained from such simulations could provide an explanation for the absence of a low tail of BEs in the experiments (V. Bariosco, private communication).

References

Agúndez, M. et al. (2023). "Detection of ethanol, acetone, and propanal in TMC-1. New O-bearing complex organics in cold sources". *Astron. Astrophys.* **673**, A34. DOI: 10.1051/0004-6361/202346076.

Altwegg, K. et al. (2019). "Cometary chemistry and the origin of icy solar system bodies: the view after rosetta". *Annu. Rev. Astron. Astrophys.* **57**, 113. DOI: 10.1146/annurev-astro-091918-104409.

Bossa, J.-B. et al. (2015). "Methane ice photochemistry and kinetic study using laser desorption time-of-flight mass spectrometry at 20 K". *Phys. Chem. Chem. Phys.* **17** (26), 17346. DOI: 10.1039/C5CP00578G.

Burke, D. J. et al. (2015). "Trapping and desorption of complex organic molecules in water at 20 K". *J. Chem. Phys.* **143**, 164704. DOI: 10.1063/1.4934264.

Collings, M. P. et al. (2004). "A laboratory survey of the thermal desorption of astrophysically relevant molecules". *Mon. Not. R. Astron. Soc.* **354**, 1133. DOI: 10.1111/j.1365-2966.2004.08272.x.

Congiu, E. et al. (2020). "A new multi-beam apparatus for the study of surface chemistry routes to formation of complex organic molecules in space". *Rev. Sci. Instrum.* **91** (12), 124504. DOI: 10.1063/5.0018926.

Dovesi, R. et al. (2018). "Quantum-mechanical condensed matter simulations with CRYSTAL". *Wiley Interdiscip. Rev. Comput. Mol. Sci.* **8**, e1360. DOI: 10.1002/wcms.1360.

Goesmann, F. et al. (2015). "Organic compounds on comet 67P/Churyumov-Gerasimenko revealed by COSAC mass spectrometry". *Science* **349**, aab0689. DOI: 10.1126/science.aab0689.

Gudipati, M. S. et al. (2012). "In-situ probing of radiation-induced processing of organics in astrophysical ice analogs - Novel LASER desorption LASER ionization time-of-flight mass spectroscopic studies". *Astrophys. J. Lett.* **756**, L24. DOI: 10.1088/2041-8205/756/1/L24.

Minissale, M. et al. (2022). "Thermal desorption of interstellar ices: a review on the controlling parameters and their implications from snowlines to chemical complexity". *ACS Earth Space Chem.* **6**, 597. DOI: 10.1021/acsearthspacechem.1c00357.

Öberg, K. I. et al. (2021). "Astrochemistry and compositions of planetary systems". *Phys. Rep.* **893**, 1. DOI: 10.1016/j.physrep.2020.09.004.

Perrero, J. et al. (2024). "Binding energies of ethanol and ethylamine on interstellar water ices: synergy between theory and experiments". *Phys. Chem. Chem. Phys.* **26**, 18205. DOI: 10.1039/D4CP01934B.

Rocha, W. et al. (2024). "JWST Observations of Young protoStars (JOYS+): Detecting icy complex organic molecules and ions - I. CH$_4$, SO$_2$, HCOO$^-$, OCN$^-$, H$_2$CO, HCOOH, CH$_3$CH$_2$OH, CH$_3$CHO, CH$_3$OCHO, and CH$_3$COOH". *Astron. Astrophys.* **683**, A124. DOI: 10.1051/0004-6361/202348427.

Tinacci, L. et al. (2022). "Theoretical distribution of the ammonia binding energy at interstellar icy grains: a new computational framework". *ACS Earth Space Chem.* **6**, 1514. DOI: 10.1021/acsearthspacechem.2c00040.

Watanabe, N. et al. (2020). "Experimental approach to physicochemical hydrogen processes on cosmic ice dust". *J. Phys. Soc. Jpn.* **89**, 051015. DOI: 10.7566/JPSJ.89.051015.

Zeng, S. et al. (2021). "Probing the chemical complexity of amines in the ISM: detection of vinylamine (C$_2$H$_3$NH$_2$) and tentative detection of ethylamine (C$_2$H$_5$NH$_2$)". *Astrophys. J. Lett.* **920**, L27. DOI: 10.3847/2041-8213/ac2c7e.

PCCP

FEATURE ARTICLE

Binding energies of ethanol and ethylamine on interstellar water ices: synergy between theory and experiments†

Jessica Perrero, [ID] [ab] Julie Vitorino, [ID] [c] Emanuele Congiu, [ID] [c] Piero Ugliengo, [ID] *[b] Albert Rimola [ID] *[a] and François Dulieu [ID] *[c]

Experimental and computational chemistry are two disciplines used to conduct research in astro-chemistry, providing essential reference data for both astronomical observations and modeling. These approaches not only mutually support each other, but also serve as complementary tools to overcome their respective limitations. Leveraging on such synergy, we characterized the binding energies (BEs) of ethanol (CH_3CH_2OH) and ethylamine ($CH_3CH_2NH_2$), two interstellar complex organic molecules (iCOMs), on crystalline and amorphous water ices through density functional theory (DFT) calculations and temperature-programmed desorption (TPD) experiments. Experimentally, CH_3CH_2OH and $CH_3CH_2NH_2$ behave similarly, in which desorption temperatures are higher on the water ices than on a bare gold surface. Computed cohesive energies of pure ethanol and ethylamine bulk structures allow describing of the BEs of the pure species deposited on the gold surface, as extracted from the TPD curve analyses. The BEs of submonolayer coverages of CH_3CH_2OH and $CH_3CH_2NH_2$ on the water ices cannot be directly extracted from TPD due to their co-desorption with water, but they are computed through DFT calculations, and found to be greater than the cohesive energy of water. The behaviour of CH_3CH_2OH and $CH_3CH_2NH_2$ is different when depositing adsorbate multilayers on the amorphous ice, in that, according to their computed cohesive energies, ethylamine layers present weaker interactions compared to ethanol and water. Finally, from the computed BEs of ethanol, ethylamine and water, we can infer that the snow-lines of these three species in protoplanetary disks will be situated at different distances from the central star. It appears that a fraction of ethanol and ethylamine is already frozen on the grains in the water snow-lines, causing their incorporation in water-rich planetesimals.

1 Introduction

In astrochemistry, ethanol (CH_3CH_2OH) and ethylamine ($CH_3CH_2NH_2$) belong to a class of compounds called interstellar complex organic molecules (iCOMs). These are compounds that contain between 6–12 atoms, in which at least one is carbon, also bearing non-metal heteroatoms, like N, O, S or P.[1–3] These molecules are the simplest organic compounds synthesised in space, and hence they are thought to represent the dawn of organic chemistry. Additionally, they are thought to

be precursors of more complex organic molecules, which can be of biological relevance, such as amino acids, nucleobases and sugars.[4]

Ethylamine is thought to be the precursor of the alanine amino acid, just as methylamine is supposed to be the parent of glycine.[5,6] Methylamine and ethylamine have been observed in the coma of comet 67P/C-G together with glycine.[7] Furthermore, they have also been detected, together with a handful of amino acids, in comet 81P/Wild2 by the Stardust mission.[8] In the interstellar medium (ISM), ethylamine has only been tentatively detected towards the Galactic center cloud G+0.693-0.027.[9] On the other hand, ethanol has been detected in several comets (*e.g.*, 67P/C-G,[10] Lovejoy,[11] and Hale–Bopp[12]) and in both warm (*e.g.*, Sgr B2,[13] Orion,[14,15] and SVS-13[16]) and cold (*e.g.*, L483,[17] and TMC-1[18]) environments of the ISM. Recently, it has also been identified in icy mantles.[19,20]

The presence of a complex molecule such as CH_3CH_2OH in warm sources was surprising, but plausible due to the environmental temperatures. However, its detection in cold regions

[a] Departament de Química, Universitat Autònoma de Barcelona, Bellaterra, 08193, Catalonia, Spain. E-mail: albert.rimola@uab.cat

[b] Dipartimento di Chimica and Nanostructured Interfaces and Surfaces (NIS) Centre, Università degli Studi di Torino, via P. Giuria 7, 10125, Torino, Italy. E-mail: piero.ugliengo@unito.it

[c] CY Cergy Paris Université, Observatoire de Paris, PSL University, Sorbonne Université, CNRS, LERMA, F-95000 Cergy, France. E-mail: francois.dulieu@cyu.fr

† Electronic supplementary information (ESI) available. See DOI: https://doi.org/10.1039/d4cp01934b

This journal is © the Owner Societies 2024

Phys. Chem. Chem. Phys., 2024, **26**, 18205–18222 | **18205**

challenged astrochemists. The interest in ethanol grew after a correlation between the abundances of glycolaldehyde and ethanol in the protostellar shock region L1157-B1 was evidenced.[21] Consequently, a series of gas-phase reactions starting from ethanol and leading to glycolaldehyde were proposed, beginning with a H-abstraction step operated by Cl or OH radicals. From this neutral–neutral gas-phase mechanism, it appeared that ethanol could be the parent molecule of formic acid (HCOOH) and other iCOMs, such as glycolaldehyde (HCOCH$_2$OH), acetic acid (CH$_3$COOH), and acetaldehyde (CH$_3$CHO).[22]

The reactivity of CH$_3$CH$_2$NH$_2$, due to its scarce detection in the ISM, has been poorly explored. The UV irradiation and thermal processing of methylamine-containing ices yielded a variety of products, such as formamide, ethylamine, methylcyanide and N-heterocycles, showing how molecular complexity can increase upon methylamine processing.[23] The production of CH$_3$CH$_2$NH$_2$ is usually attributed to the reaction between ammonia and C-bearing species on the ice mantle. The exposure of NH$_3$ and CH$_4$/C$_2$H$_6$ ices to cosmic ray radiation at 5 K resulted in the formation of CH$_3$NH$_2$ and CH$_3$CH$_2$NH$_2$, respectively.[5] At higher temperatures, photolysis of C$_2$H$_2$ + NH$_3$ between 180 and 300 K produced ethylamine (among other products), with a yield proportional to temperature.[24]

Formation of ethanol, in contrast, has been more explored. Experimentally, both energetic and non-energetic pathways have been identified: UV irradiation of CO$_2$-rich and H$_2$O-rich ices;[25] UV irradiation and radiolysis of C$_2$H$_2$:H$_2$O ices;[26,27] O addition to ethane;[28] and exposure of C$_2$H$_2$:O$_2$ ice to H atoms.[29] Computational works also characterized ethanol formation, proposing synthetic routes on dust grains at low temperatures and through almost barrierless pathways. The radical–radical coupling between CH$_3$ and CH$_2$OH on water ice was postulated as a promising mechanism, since its competitive channel (a H-abstraction yielding CH$_4$ and H$_2$CO) was found to be highly disfavoured.[30] The reaction of CCH + H$_2$O (where water is a component of the ice mantle), passing through the formation of vinyl alcohol, can yield ethanol after some hydrogenation steps that, in the case of presenting a barrier, can proceed *via* tunnelling.[31] More recently, two works investigated the reactivity of atomic carbon on CO-rich and H$_2$O-rich ices, suggesting that the two scenarios can lead to the formation of iCOMs in a non-energetic way, especially ethanol, when species characterized by a C=C=O skeleton are fully hydrogenated.[32,33] Clearly, the discrepancy in the quantity of studies regarding these two molecules is linked to their detection. Numerous factors may contribute to the elusive nature of ethylamine to astronomers. For instance, it might predominantly reside in ice mantles rather than in the gas phase; it could exhibit higher reactivity leading to rapid consumption upon entering the gas phase; or it may have spectral features that overlap with those of other molecules. To streamline our investigation, we focused on the first point. The adsorption and desorption processes are determined by the binding energy (BE), a pivotal parameter that quantifies the strength of the interaction between a molecule and a surface.[34] It also regulates whether diffusion processes can take place, since diffusion barriers are usually assumed to be a fraction of the BE, *e.g.*, ref. 35–38. The first estimates of CH$_3$CH$_2$OH and CH$_3$CH$_2$NH$_2$ BEs were made by Garrod,[39] who proposed BE = 65.5 kJ mol^{-1} for ethylamine and BE = 52.0 kJ mol^{-1} for ethanol, in order to introduce them in astrochemical models. In 2011, Lattelais *et al.*[40] determined the BE of CH$_3$CH$_2$OH on water ice to be 56.5 kJ mol^{-1}. More recently, Etim *et al.*[41] computed the BE of ethanol using the methodology introduced by Wakelam *et al.*,[42] that is, simulating the ice with one water molecule and calculating the BE (in Kelvin) using the scaling BE$_{ice}$ = 289.019 + (1.65174 × BE$_{1H_2O}$), this way obtaining a value between 37.4 kJ mol^{-1} and 40.7 kJ mol^{-1}, with an uncertainty in the final result of 30%. To the best of our knowledge, no other estimates are available.

For this reason, we characterized both experimentally and computationally the BEs of ethanol and ethylamine adsorbed on crystalline and amorphous water ice (CI and ASW, respectively). In order to interpret the results of the experiments, we also computed the bulk and surface cohesive energies of ethanol and ethylamine crystals, as well as the BEs of each species on the most stable surface formed during the growth of the corresponding crystal.

BEs, in addition to being a key parameter in astrochemical models, are also one of the two quantities needed to compare the theoretical calculations with the desorption energy E_{des} extracted from the experiments, together with the pre-exponential factor ν.[34] The latter is often defined as the vibrational frequency of a given species in its surface potential well, and it takes into account the entropic effects of the desorption process. The pre-exponential factor is entered into the equation that determines the thermal desorption rate, together with E_{des}, which accounts for the enthalpic contribution. There are two main ways to determine ν: one is to adopt the approximated approach of Hasegawa and Herbst,[43] the alternative consists of exploiting the transition-state theory within the immobile adsorbate approximation, as Tait *et al.*[44] suggested. In this work, we adopted the latter approach to determine ν, with the aim to derive E_{des} from the experimental data.

The work is organized as follows: in Section 2 we present the computational results, while Section 3 is dedicated to the laboratory experiments. Discussion of the obtained results through the two approaches is provided in Section 4, along with their astrophysical implications. Finally, we summarized the most important findings of the work in Section 5.

2 Theoretical simulations

For the sake of clarity, we adopted the following notation to distinguish between the molecular adsorbates and the solid-state phases: CH$_3$CH$_2$OH and CH$_3$CH$_2$NH$_2$ refer to the adsorbates, while the bulk and surfaces of ethanol and ethylamine are identified as EtOH and EtNH$_2$. Accordingly, the adsorption of ethanol on an ethanol surface is referred to as CH$_3$CH$_2$OH on an EtOH surface.

PCCP

2.1 Methodology

Quantum chemical periodic calculations were performed with the CRYSTAL17 code, which is suitable for treating systems with zero (molecules), one (polymers), two (slab surfaces), and three (bulks) periodic dimensions. It uses localized Gaussian functions as basis sets, contrary to the plane waves adopted by most of the periodic codes.[45] This allows us to rigorously define true periodic 2D models, and avoid having to build replicas of the system along the non-periodic direction. In this work, we modelled 3D (bulks) and 2D (slabs) systems for H$_2$O, EtOH and EtNH$_2$ ices.

2.1.1 Computational details.

All the geometry optimizations and frequency calculations were run with the semi-empirical HF-3c method, a Hartree–Fock-based method adopting a minimal basis set (MINI-1),[46] to which three empirical corrections (3c) are added to make up for the smallness of the basis set:[47] (i) the Grimme's D3 empirical term with the Becke–Johnson (BJ) damping scheme (D3(BJ)[48,49]) to account for dispersion energy arising from noncovalent interactions; (ii) a short-range bond correction to recover the systematically overestimated covalent bond lengths for electronegative elements;[50] and (iii) the geometrical counterpoise (gCP) method developed by Kruse and Grimme[51] to *a priori* remove the BSSE.

To compute the BEs, DFT single-point energy calculations were performed on each optimized HF-3c geometry (hereafter referred to as DFT//HF-3c). The hybrid B3LYP functional[52–54] combined with the D3(BJ) correction for the dispersion energy was used, a methodology already tested and applied for closed-shell species.[55,56] B3LYP-D3(BJ) was combined with an Ahlrichs triple-zeta-valence-quality basis set supplemented with a double set of polarization functions, defined as A-VTZ*.[57]

All the structures (bulks, surfaces and adsorption complexes) were characterized by HF-3c harmonic frequency calculations performed on the entire system. This serves to confirm the nature of the stationary points and to compute the zero-point-energy (ZPE) correction that accounts for the kinetic vibrational energy at 0 K.

2.1.2 Water ice surface models and calculation of the BEs.

Two periodic water ice models previously used in ref. 55 and 56 (see Fig. 1) were used to compute the adsorption of ethanol and ethylamine. To simulate the surfaces, we adopted the slab model, in which a slab of a given thickness is cut out from the bulk ice model. The first structure is a crystalline ice model, represented by the (010) surface cut out from the bulk of the proton-ordered P-ice.[58] The unit cell is characterized by the cell parameters $|a|$ = 9.065 Å and $|b|$ = 7.153 Å and it consists of twelve atomic layers. However, interstellar ices are mostly amorphous in nature;[19,59] therefore, we adopted a more realistic model consisting of 60 disordered water molecules per unit cell. The structure possesses a cavity and several edges, thereby showing multiple different binding sites. Its cell parameters are: $|a|$ = 20.355 Å, $|b|$ = 10.028 Å, and $|\gamma|$ = 103.0°.

The adsorption complexes were manually constructed placing the adsorbates on the binding sites present in the ice models, following the principle of electrostatic complementarity between the adsorbate and the surface, and fully optimizing the structures. On the crystalline ice model, we characterized three situations: (i) single molecule adsorption (S-ADS), represented by one molecule adsorbed per unit cell; (ii) a half-monolayer (H-ML) coverage, simulated by adsorbing two molecules per unit cell; and (iii) a full monolayer (F-ML) coverage, modelled by adsorbing four molecules per unit cell. Alternatively, on the amorphous ice model, a range of single adsorptions were characterized with the aim to obtain BEs describing the adsorbate/ice interactions of different strengths. Nine positions suitable to adsorb CH$_3$CH$_2$OH and CH$_3$CH$_2$NH$_2$ were identified, among which seven are dangling H atoms (dH) and the remaining two are dangling O atoms (dO). Given the presence of both H-bond acceptor and donor groups in the adsorbates, such an ensemble of binding sites allows the establishment of both types of interactions.

The final binding energy, BE(0), defined as a positive quantity in the case of a favourable interaction, results from subtracting the basis set superposition error (BSSE), arising from the finiteness of the basis set, and adding the HF-3c ZPE
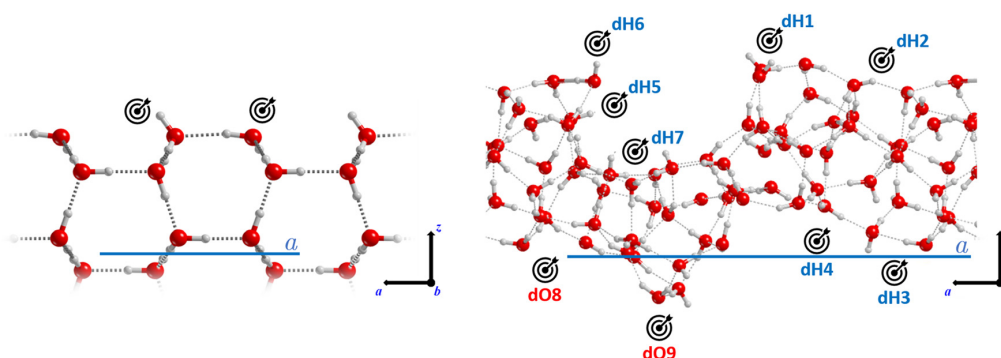
Fig. 1 Crystalline (left) and amorphous (right) periodic water ice models adopted in this work. The target icon indicates the binding sites considered for the adsorption of CH$_3$CH$_2$OH and CH$_3$CH$_2$NH$_2$. On the amorphous model, the sites have been labelled as dangling hydrogen atoms (dH1–dH7) and dangling oxygen atoms (dO8–dO9). Colour code: red, oxygen; grey, hydrogen. The unit cell parameter is also highlighted (in blue).

This journal is © the Owner Societies 2024

Phys. Chem. Chem. Phys., 2024, **26**, 18205–18222 | **18207**

correction at 0 Kelvin ($\Delta ZPE = ZPE_{complex} - ZPE_{ice} - ZPE_{species}$) to the bare interaction energy ($\Delta E = E_{complex} - E_{ice} - E_{species}$).

$$BE(0) = BE - \Delta ZPE = -(\Delta E - BSSE) - \Delta ZPE \quad (1)$$

Each BE value can be decomposed in a purely electronic contribution extracted from the pure DFT calculation and a fraction due to purely dispersive interactions, estimated with the D3(BJ) term. We are aware that this approach is not rigorous, thus our estimates should be taken as indicative. A detailed explanation of the computation of the BE(0)s and their energetic contributions can be found in the ESI† and in previously published works.[55,56]

2.1.3 Modeling of EtOH and EtNH₂ ices. The EtOH and EtNH₂ ice bulk structures were modeled by fully optimizing their crystalline structures determined by X-ray diffraction.[60,61] Subsequently, several low-Miller-index surfaces were generated to characterize their stability. For each slab, the internal atomic positions were optimized while keeping the unit cell parameters frozen at the bulk values. The thickness of each slab was determined in such a way that their surface energy converged to a plateau.

The surface energy (E_S, in J m^{-2}) is the energy required to cut out a slab from the bulk. The most stable surfaces are characterized by the lowest surface energies. E_S is calculated through the equation:

$$E_S = \frac{E_{slab} - N \cdot E_{bulk}}{2A}, \quad (2)$$

where E_{slab} is the energy of the surface, E_{bulk} is the energy of the bulk, $N = z_{slab}/z_{bulk}$ with z being the number of molecules contained in the unit cells of slab and bulk, and A is the surface area. The factor 2 accounts for the existence of two equal surfaces of the slab.

The cohesive energy (E_C, in kJ mol^{-1}) of the bulk (or a surface) results from the equation:

$$E_C = \frac{E_{bulk(slab)}}{z} - E_{mol}, \quad (3)$$

where E_{mol} is the energy of the fully optimized isolated molecule in the gas phase.

The extraction energy (E_X) of a molecule from a surface is the energy cost to extract the molecule from the surface. It is obtained by calculating the energy of the structure that follows the removal of one surface molecule without re-optimization of the structure, and is repeated for each molecule located in the external layer of the surface:

$$E_X = E_{carved} + E_{mol} - E_{slab} + \Delta ZPE_{extr}, \quad (4)$$

where E_{carved} is the energy of the surface upon molecule extraction, and ΔZPE_{extr} accounts for the contribution of the ZPE to the extraction processes, which is approximated to $\Delta ZPE_{extr} = ZPE_{surface}/N - ZPE_{mol}$.

The most stable surface of a crystal is the most extended one, and is characterized by the lowest E_S and the highest E_C values. In principle, it should also possess the highest E_X, since it is more difficult to extract a molecule from a well-packed

structure. The (010) EtOH and the (100) EtNH₂ surfaces satisfy these criteria.

Therefore, we simulated the adsorption of CH₃CH₂OH and CH₃CH₂NH₂ onto these surfaces, identifying three binding sites per adsorbate.

2.2 Results

This section is organized as follows: Section 2.2.1 addresses the modeling of bulks and surfaces of EtOH and EtNH₂ crystals; Section 2.2.2 regards the computation of the BE(0)s obtained on such surfaces; Section 2.2.3 presents the BE(0)s for the S-ADS scenario on the crystalline and amorphous water ice surface models; and Section 2.2.4 shows the results for the H-ML and F-ML coverages.

2.2.1 EtOH and EtNH₂ crystal and surface ices. The bulk and surface ice models for EtOH and EtNH₂ were simulated taking as a reference their experimental structures. The crystal structure of EtNH₂ ($P2_1/C$ space group) was determined by X-ray diffraction at 150 K through *in situ* crystallization from the liquid,[61] while single crystals of ethanol (P_C space group) were grown at 156 K and analyzed through X-ray diffraction at 87 K.[60]

In the asymmetric unit, both EtOH and EtNH₂ present two crystallographically independent molecules, while the unit cells contain four molecules (see Fig. 2a and d). In both cases, two types of intermolecular interactions can be distinguished: H-bonding between the NH₂ (for EtNH₂) and OH (for EtOH) groups, and CH₃···CH₃ dispersion. The conformation around the C–C bond is staggered in both molecules. In EtOH, the OH group is differently oriented so that both the *trans* and the *gauche* conformers are present in the unit cell. The optimization at the HF-3c level of theory results in a reduction of the cell parameters, and consequently of the cell volume by 7% for EtOH and by 13% for EtNH₂ (see Table 1).

The (010), (100), (001), (110), (101), (011), and (111) surfaces were generated from the EtOH and EtNH₂ bulk structures, the thicknesses of which satisfy the surface energy convergence condition.[62] Special care was paid to the resulting dipole moment across the non-periodic direction of each slab, discarding those with $|\mu| > 5$ D. The stability order of the surfaces was determined primarily on their E_S value, and in the second instance on their E_C and E_X values (shown in Table 2). For both EtOH and EtNH₂, the slabs present very small E_S values, in agreement with their weakly bound molecular crystal natures. The extraction energy was computed for each molecule laying in the external layer of each surface. Thus, two to four values were computed for each slab. The (100) slabs represent the only exception for both systems, as the molecules defining the top layer are related by symmetry (a glide reflection in EtOH, and a screw rotation in EtNH₂) hence providing only one value.

Six EtOH surfaces (see Table 2) were found to comply with the dipole moment constraint. The ladder of stability is (from more to less stable): (010)$^{A-layer}$ > (100) > (101) > (110) > (011) > (010)$^{B-layer}$ (the definition of A-layer and B-layer is explained below). The cohesive energies obtained for these slabs ranges from −49.4 kJ mol^{-1} (010)$^{A-layer}$ to −40.3 kJ mol^{-1}

18208 | *Phys. Chem. Chem. Phys.*, 2024, **26**, 18205–18222
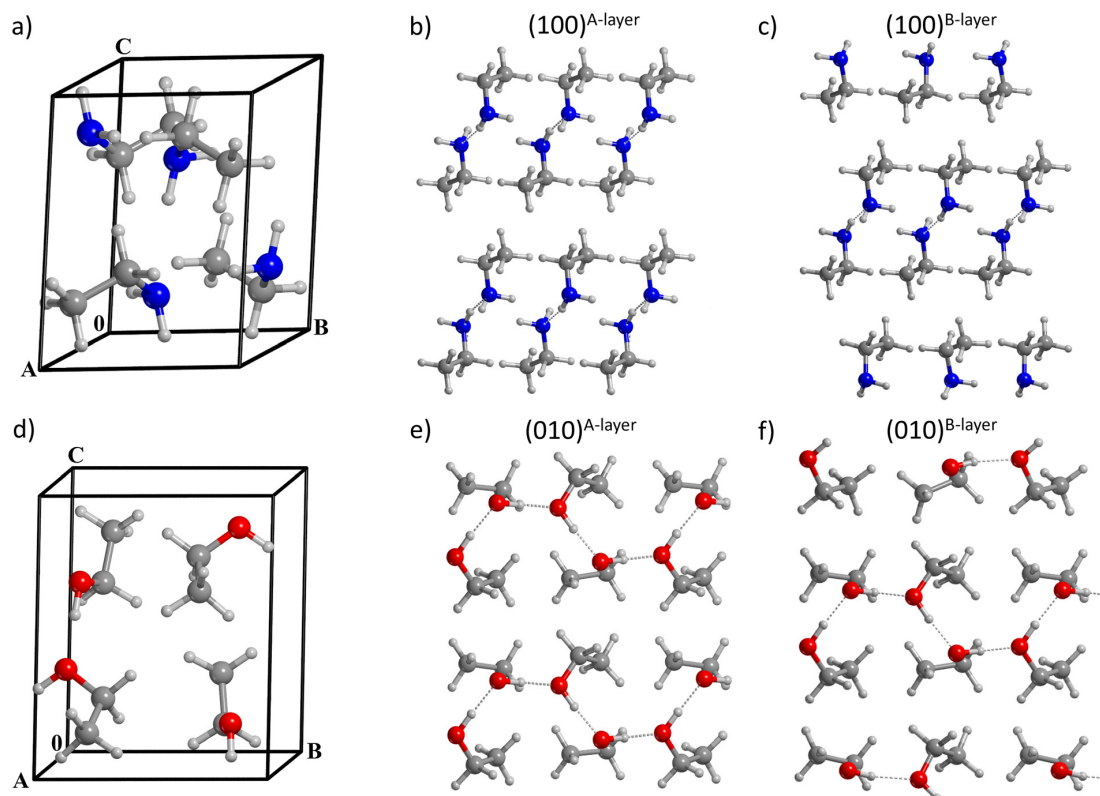
This journal is © the Owner Societies 2024

Fig. 2 Unit cell of the bulk structures of EtNH$_2$ (a) and EtOH (d). Lateral view of the (100) EtNH$_2$ (b) and (010) EtOH (e) slabs, the most stable surfaces cut out from the respective bulks, exposing their apolar backbone to the external environment (A-layer type). Lateral view of the (100) EtNH$_2$ (c) and (010) EtOH (f) slabs, which were generated by cutting out the surface in order to expose the polar moieties to the external environment (B-layer).

Table 1 Experimental[60,61] and computed (at the HF-3c level of theory) cell parameters of ethanol and ethylamine bulk structures. a, b and c are in Å, α, β and γ are in degrees, and the volumes are in Å^3

	Ethanol		Ethylamine	
	Exp.	Comput.	Exp.	Comput.
a	5.377	5.179	8.263	7.856
b	6.882	6.773	7.310	6.949
c	8.255	8.146	5.532	5.315
α	90.0	90.0	90.0	89.9
β	102.2	104.8	99.1	100.0
γ	90.0	90.0	90.0	89.8
Volume	298.6	276.2	329.9	285.8

Table 2 Dipole moment across the slab (μ, in D), surface energy (E_S, in J m^{-2}), cohesive energy (E_C, in kJ mol^{-1}), and extraction energy (E_X, in kJ mol^{-1}) of EtOH and EtNH$_2$ surfaces at the B3LYP-D3(BJ)/A-VTZ* level of theory. E_C, E_S, and E_X are corrected for the ZPE

Surface	μ	E_S	E_C	E_X
EtOH				
(010)$^{A\text{-layer}}$	$+7.2 \times 10^{-4}$	0.0761	-49.4	104.1–108.2
(100)	-3.3	0.0994	-47.9	106.0
(101)	-1.7	0.1053	-45.7	62.0–113.7
(110)	-2.9	0.1594	-44.0	59.0–116.6
(011)	$+3.5$	0.1616	-40.3	60.0–95.2
(010)$^{B\text{-layer}}$	-1.8×10^{-1}	0.1857	-42.0	58.9–60.0
EtNH$_2$				
(100)$^{A\text{-layer}}$	$+1.3 \times 10^{-4}$	0.0673	-40.4	71.5
(001)	$+2.4 \times 10^{-3}$	0.0797	-39.9	64.8–69.3
(010)	$+2.5 \times 10^{-4}$	0.0790	-38.9	65.0–69.4
(111)	-1.2×10^{-3}	0.0962	-35.7	63.3–80.4
(101)	$+1.2 \times 10^{-3}$	0.1034	-33.8	36.0–63.5
(110)	$+1.8$	0.1295	-36.7	68.1–84.3
(011)	$+8.8 \times 10^{-4}$	0.1319	-30.0	37.5–60.4
(100)$^{B\text{-layer}}$	-1.5×10^{-3}	0.1857	-34.1	45.6

(011), while the extraction energy spans the range from 59 to 115 kJ mol^{-1}.

For EtNH$_2$, eight surfaces were characterized (see Table 2), and their stability order is: (100)$^{A\text{-layer}}$ > (001) > (010) > (111) > (101) > (110) > (011) > (100)$^{B\text{-layer}}$. All of them have an almost null dipole, with the exception of the (110) slab (μ = 1.8 D), which is responsible for the large E_S. The E_C values range between -40.4 kJ mol^{-1} (100)$^{A\text{-layer}}$ and -30.0 kJ mol^{-1} (011), and E_X covers the range between 35 and 85 kJ mol^{-1}, which makes ethylamine slightly less bound than ethanol.

Two types of cuts (A-layer and B-layer) were modeled for the (010) EtOH and the (100) EtNH$_2$ surfaces, the former one being the most stable slab cut. In the EtOH-(010) and EtNH$_2$-(100)

This journal is © the Owner Societies 2024

Phys. Chem. Chem. Phys., 2024, **26**, 18205–18222 | **18209**

Feature Article

surfaces, a couple of layers held together by a network of H-bonds is alternated with another couple governed by dispersive forces. Depending on the type of interlayer interaction preserved by the cut, the resulting surface can be characterized by the polar moieties being completely segregated inwards to the slab (A-layer, see Fig. 2b and e) or totally exposed to the exterior (B-layer, see Fig. 2c and f). The presence of polar groups exposed to the surface causes the B-layer cut to be less stable than the A-layer cut, resulting in EtOH-(010)$^{B-layer}$ and EtNH₂-(100)$^{B-layer}$ being characterized by the largest E_S. The natural consequence is that B-layer type surfaces will yield larger BE(0)s for the adsorption of CH₃CH₂OH and CH₃CH₂NH₂.

2.2.2   Binding energies on pure EtOH and EtNH₂ surfaces. We computed three BE(0)s for each species, two on the EtNH₂-(100)$^{A-layer}$ and EtOH-(010)$^{A-layer}$ surfaces, and one on the EtNH₂-(100)$^{B-layer}$ and EtOH-(010)$^{B-layer}$ surfaces. The structures are available at https://zenodo.org/records/11103454.

On the EtOH-(010)$^{A-layer}$ surface, we identified two adsorption complexes characterized by a different orientation of the adsorbate with respect to the surface. In the first case, the driving force of the interaction is represented by the dispersive interactions between the aliphatic chains, resulting in the ethanol molecule laying parallel to the surface, with BE(0) = 20.9 kJ mol^{-1}. In the second case, the molecule is placed perpendicularly to the surface to establish a H-bond interaction with one of the partially exposed hydroxyl groups. Dispersive forces also play an important role in the value of BE(0), which is as high as 30.9 kJ mol^{-1}.

On the EtNH₂-(100)$^{A-layer}$ surface, we found two very similar adsorption complexes with a BE(0) of 21.4 kJ mol^{-1}

and 21.6 kJ mol^{-1}, due to the symmetry of the surface. They are entirely dominated by dispersive forces, the adsorbate molecule laying parallel to the surface in the two cases. The small difference between the two complexes is due to a slight change in the orientation of the ethylamine with respect to the EtNH₂ surface.

The adsorption complex obtained on the EtNH₂-(100)$^{B-layer}$ and EtOH-(010)$^{B-layer}$ slabs are characterized by the –OH and –NH₂ groups of the adsorbate accepting a H-bond from the surface, resulting in BE(0) = 41.8 kJ mol^{-1} for CH₃CH₂OH and BE(0) = 43.0 kJ mol^{-1} for CH₃CH₂NH₂.

2.2.3   Binding energies on the crystalline and amorphous water ice models. The theoretical results on the single adsorption (S-ADS) of CH₃CH₂OH and CH₃CH₂NH₂ on the crystalline ice (CI) and amorphous solid water (ASW) surfaces are presented here.

We identified three adsorption complexes of CH₃CH₂OH onto the CI surface, characterized by a different orientation of the adsorbate with respect to the surface (see bottom panel of Fig. 3). Each complex is characterized by the presence of at least one H-bond. In the weakest bound complex (BE(0) = 33.4 kJ mol^{-1}), CH₃CH₂OH only acts as a H-bond acceptor, in favour of the interaction of the aliphatic chain with the ice. In the other two complexes, both the O and H atoms of CH₃CH₂OH are involved in H-bonds, but the orientation of the adsorbate, in the most stable case (BE(0) = 61.6 kJ mol^{-1}), precisely interacts with uncoordinated surface-exposed H₂O sites, while, in the other (BE(0) = 42.2 kJ mol^{-1}), a rearrangement of surface-dangling OH groups is required to establish two (longer) H-bonds.
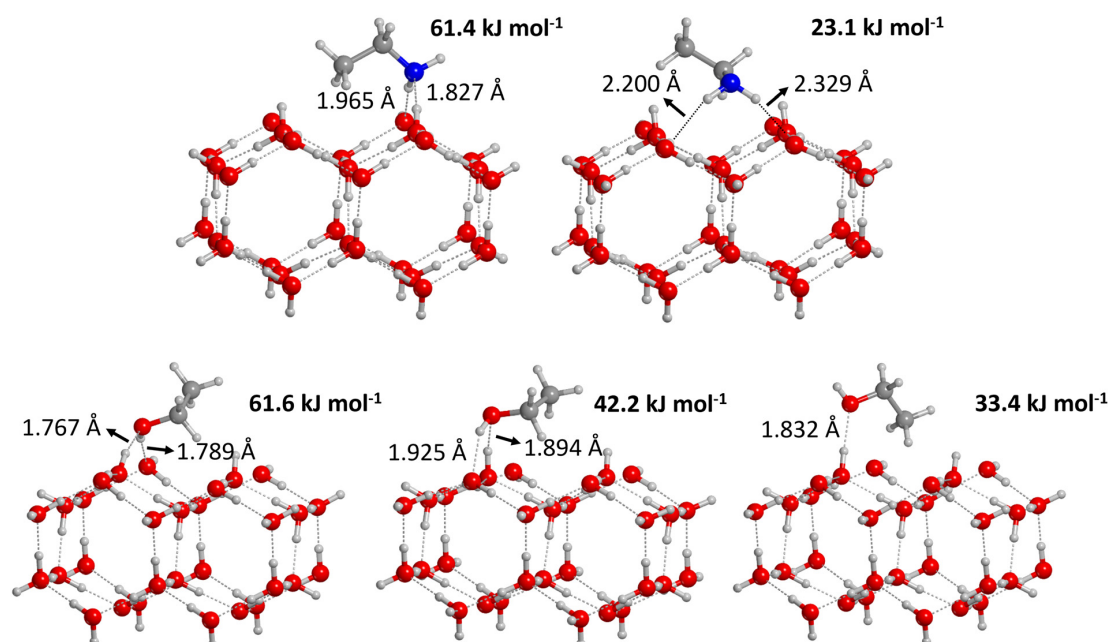

Fig. 3 Optimized geometries of the adsorption complexes of ethylamine (top) and ethanol (bottom) on the crystalline water ice surface model. The corresponding computed BE(0)s are also given.

Table 3 Computed binding energies (BE(0), in kJ mol^{-1}) of ethanol and ethylamine on the ASW ice surface model. See Fig. 1 for the definition of the binding sites

Binding site	CH$_3$CH$_2$OH	CH$_3$CH$_2$NH$_2$
dH1	37.0	50.1
dH2	44.8	47.8
dH3	40.3	54.0
dH4	42.0	54.2
dH5	40.5	44.8
dH6	47.8	50.2
dH7	59.1	71.5
dO8	26.0	19.2
dO9	37.1	46.2

For CH$_3$CH$_2$OH on the ASW surface, nine binding sites were sampled. The majority of the BE(0) values range from 37 to 48 kJ mol^{-1} (see Table 3), with two exceptions. In the dO8 site, the ethanol OH group only acts as a (weak) H-bond donor towards the dO atom and hence BE(0) = 26.0 kJ mol^{-1}. In contrast, in the dH7 site, ethanol is located in the cavity of the ASW and establishes three H-bonds, two involving the O atom and one the H atom of the OH moiety, and hence BE(0) = 59.1 kJ mol^{-1}.

The adsorption of CH$_3$CH$_2$NH$_2$ on the CI surface model resulted in two adsorption complexes, each characterized by the presence of two H-bonds (see top panel of Fig. 3). In the most stable complex, CH$_3$CH$_2$NH$_2$ is accepting a H-bond through the N atom and donating another H-bond through a H atom of the amino group, resulting in BE(0) = 61.4 kJ mol^{-1}, where the contribution of weak forces is reduced to 40%. In the second (less stable) complex, the two H atoms of the amino group act as H-bond donors, thus resulting in a weaker complex with BE(0) = 23.1 kJ mol^{-1}), where the dispersion interactions of the aliphatic chains are responsible for the larger contribution (almost 90%) to the final BE(0).

For CH$_3$CH$_2$NH$_2$ on the ASW surface, similar to what was observed for CH$_3$CH$_2$OH, the nine BE(0)s range from 45 to 55 kJ mol^{-1}, with the exception of those computed for sites dO8 and dH7, with BE(0) = 19.2 kJ mol^{-1} and 71.5 kJ mol^{-1}, respectively. The reasons are also weak a H-bond donation for the first case and a very strong interaction dominated by three H-bonds involving each atom of the NH$_2$ group for the second case.

2.2.4 Half and full monolayers on crystalline water ice. The simulation of higher surface coverages consisted of the adsorption of two (H-ML) or four (F-ML) molecules per cell. The adsorbates were manually placed with the NH$_2$ and OH moieties pointing towards the surface to optimize their interaction with the ice.

For both species, the H-ML BE(0) values per molecule are slightly larger than those obtained in the S-ADS regime: 66.0 kJ mol^{-1} (*versus* 61.6 kJ mol^{-1}) for CH$_3$CH$_2$OH, and 64.5 kJ mol^{-1} (*versus* 61.4 kJ mol^{-1}) for CH$_3$CH$_2$NH$_2$. Instead, the F-ML BE(0) values per molecule are smaller, 50.0 kJ mol^{-1} for CH$_3$CH$_2$OH and 49.5 kJ mol^{-1} for CH$_3$CH$_2$NH$_2$. This is due to the fact that, in the H-ML cases, two molecules can still easily be accommodated in the cell and find the most favourable

geometry to maximize their interactions with the surface. In contrast, in the F-ML cases, the four molecules struggle to fit in the cell and lay with the aliphatic chain pointing upwards, minimizing the interaction with the ice and being surrounded only by the other adsorbates. The lateral interaction between the adsorbates, one of the terms favourably contributing to the BE(0), is mostly based on weak London forces, increasing the weight of dispersive interactions in the final BE(0): from 43% and 44% in the H-ML conditions, to 68% and 79% in the F-ML ones, for CH$_3$CH$_2$OH and CH$_3$CH$_2$NH$_2$, respectively.

Despite the compromises made by our models and the simplified procedures, the present results are guidelines for understanding the process of approaching a monolayer coverage in a real system. That is, the first adsorbate molecules occupy the strongest surface adsorption sites, and then, by increasing the number of adsorbates, surface sites from the strongest to the weakest ones become occupied, until the formation of a monolayer occurs. This assumption holds true in the case of molecules that wet the surface, like ethanol and ethylamine.

3 Laboratory experiments

The desorption energies (E_{des}) of CH$_3$CH$_2$OH and CH$_3$CH$_2$NH$_2$ have been estimated by means of experimental procedures, and dividing the work into two parts: determination of the monolayer (ML) of ethanol and ethylamine, and temperature-programmed desorption (TPD) measurements to determine the E_{des} of the adsorbates on crystalline and amorphous water ice films.

3.1 Methodology

3.1.1 Experimental setup. All of the experiments were hereby conducted with the VENUS apparatus located at LERMA-CY laboratory in Cergy-Pontoise, France, and described extensively in Congiu *et al.*[63] VENUS consists of an ultra-high vacuum (UHV) stainless steel main chamber with a base pressure of 2 × 10^{-10} mbar, containing a 9 mm in diameter gold-coated copper sample holder. The latter is attached to the cold head of a closed-cycle He cryostat, that allows the temperature to be varied between 6 K and 350 K *via* a computer-controlled resistive heater.

Ethanol is liquid at room temperature, while ethylamine needs to be diluted in water to be stable (with about 66–72% of CH$_3$CH$_2$NH$_2$ in H$_2$O‡). The two species were first converted into gas in the central molecular beamline of VENUS. The beam has an aperture of approximately 3 mm and a residual pressure of 10^{-7} mbar. By means of differential pumping through two intermediate stainless steel chambers, the gases were then sent towards the cold surface. The species were deposited on the surface, which was maintained at a constant temperature of 70 K. During this process, the base pressure of the main

‡ Ethylamine; SDS No. 295442 [Print]; Merck Life Science S.A.S.: Saint-Quentin-Fallavier, France, Feb 16, 2023. **https://www.sigmaaldrich.com/FR/fr/product/aldrich/471208** (accessed Nov 9, 2023).

This journal is © the Owner Societies 2024

Phys. Chem. Chem. Phys., 2024, **26**, 18205–18222 | 18211

Feature Article

chamber remains low (up to 5×10^{-10} mbar), ensuring a focalization of the molecules onto the sample and negligible gas–gas interactions above the cold head. During this phase, it is possible to monitor the evolution of the ice *in situ via* reflection absorption infrared spectroscopy (RAIRS) performed with a Vertex-70 Fourier Transform infrared (FT-IR) spectrometer over a spectral range from 800 to 4500 cm^{-1} (from 12.5 to 2.22 nm). The production of a mean spectrum is non-destructive and takes place every two minutes, corresponding to 256 scans of the ice.

Once the deposition phase is completed, the desorption of the species from the surface is monitored *via* temperature-programmed desorption (TPD). After positioning the Hiden 51/3F Quadrupole Mass Spectrometer (QMS) 5 mm in front of the cold head, the surface temperature is gradually increased with a rate of $\beta = 0.15$ K s^{-1} = 9 K min^{-1} up to 200 K. Throughout the heating process, the different chemical species progressively sublimate from the surface and desorb at a temperature that depends on their nature and on the binding energy with each site offered by the surface. This results in a TPD spectrum where the abundance of each atomic mass unit (amu) is monitored against its thermal desorption temperature. Indeed, the electrons produced by the hot filament of the QMS will likely induce the fragmentation of the molecules hitting its head into several ions. The statistic repartition of the ions, called the cracking pattern, is specific for each species and depends on the ionization energy (set at 30 eV in this work). Each desorption curve can be described with the Polanyi–Wigner equation following an Arrhenius relationship.

$$r(N, E_{des}, T) = -\frac{dN}{dt} = \frac{A}{\beta}N^n e^{\frac{-E_{des}}{RT}}, \qquad (5)$$

where the desorption rate r (molecules cm^{-2} s^{-1}) depends on the number density of molecules adsorbed on the surface N (molecules cm^{-2}), the desorption energy of a molecule on the surface E_{des} (J mol^{-1}), and the temperature of the surface T (K). In eqn (5), A is the pre-exponential factor (s^{-1}), β is the heating rate, R is the ideal gas constant (J mol^{-1} K^{-1}), and n is the order of the desorption process. The zeroth-order represents desorption kinetics that are independent of the amount of available adsorbate, such as the case of thick films consisting of multilayers. The first-order kinetics corresponds to the desorption of an adsorbate whose coverage is lower or equal to one monolayer, and implies that the desorption rate is proportional to the number of molecules present on the surface. The fitting of the TPD results allows us to determine N and E_{des}, provided that the pre-exponential factor A is fairly constrained.

3.1.2 Growth of the molecular films. In this work, ethanol and ethylamine have been sent towards the surface with the central molecular beam of VENUS. They have been deposited either on bare gold or on a film of water ice (see Section 3.1.3 for more details). In all the cases, the surface was held at 70 K. The VENUS setup has been optimized for the study of very thin layers (from sub-monolayer up to one monolayer) of adsorbates, although systems of thicker ices, whether pure or mixed,

can be investigated as well (usually under 100 monolayers). In order to determine the amount of molecules present on the cold head, two methods can be used and mutually confirm each other.

The first method can be performed *in situ via* infrared measurements during the deposition. The column density N (molecules cm^{-2}) of deposited or newly formed species can be calculated *via* a modified Lambert–Beer equation,

$$N = 2\frac{\int A(\lambda)d\lambda}{f}, \qquad (6)$$

where the constant 2 is determined specifically for the VENUS setup,[63] $\int A(\lambda)d\lambda$ is the integrated area of the infrared absorption feature (cm^{-1}), and f is the corresponding band strength. In the case of ethanol, the calculation shows that the monolayer is reached after approximately 21 minutes, using a band strength of $f = 1.41 10^{-17}$ cm × molecules^{-1} at 1055 cm^{-1}.[64] For ethylamine, the only band-strength values available have been calculated very recently.[6] As there are no other available values, most experimental works involving ethylamine (*i.e.*, Danger *et al.*[65]) adopted the band strength of methylamine, which was first communicated in 2005 without any known source.[66] With the corresponding band strength of amorphous ethylamine $f = 3.69 10^{-18}$ cm × molecules^{-1} at 1395 cm^{-1},[6] one monolayer of $CH_3CH_2NH_2$ appears to be reached after 24 minutes of deposition.

The other way is *via* the TPD measurements as described by Noble *et al.*[67] A monolayer (ML) is defined by the theoretical filling of all available sites on the gold surface, corresponding to approximately 10^{15} molecules cm^{-2}. During the deposition phase, as the dose is gradually increased, the available sites are progressively filled, beginning from high-depth sites towards low-energy ones, until the deposited amount reaches 1 ML. In the case of ethanol, the values obtained with TPD and infrared measurements match well, giving a ML completion after $\sim$20 minutes. This is easily determinable with the desorption profile of CH_3CH_2OH. Ethylamine, however, has a more complex desorption profile, making the monolayer determination more ambiguous. The areas under the main fragment curves of ethylamine and ethanol are not directly comparable, due to their different ionization cross-sections at 30 eV. At this ionization energy, there is no record of an ionization cross-section measurement for ethylamine. The value of $\sigma^{tot}_{CH_3CH_2NH_2} = 9$ Å^2 has been used in studies of 67P/C-G[7,68] but is only valid at 70 eV. In this work, we chose to use the ionization cross-section of dimethylamine ($\sigma^{tot}_{CH_3NHCH_3} = 6.68$ Å^2 at 30 eV), which also has a 9 Å^2 value at 70 eV.[69] Considering this, it is possible to demonstrate once again the time of ML completion for ethanol (20 minutes) and ethylamine (24 minutes). Table 4 reports the list of experiments performed.

3.1.3 Growth of water ice films. Water can be grown on the sample either *via* a molecular beam identical to the one used for ethanol and ethylamine, or *via* a water vapor delivery manifold controlled by a needle valve. In this work, the latter technique was used. It allows water vapor to leak directly into

18212 | *Phys. Chem. Chem. Phys.*, 2024, **26**, 18205–18222

This journal is © the Owner Societies 2024

Table 4 List of the experiments performed with the VENUS setup

Deposited molecule	Quantity deposited (ML)	Substrate type	Substrate thickness (ML)
Ethanol (C_2H_5OH)	0.25; 0.5; 0.6; 0.7; 0.75; 1.5	Gold	—
	0.15; 0.25; 0.7; 2.1	Amorphous H_2O	10; 6.5; 10; 10
	0.15	Crystalline H_2O	10
Ethylamine ($C_2H_5NH_2$)	0.2; 0.33; 0.4; 0.7; 0.83; 1.25	Gold	—
	0.08; 0.13; 0.4; 1.25	Amorphous H_2O	10; 10; 10; 10
	0.13	Crystalline H_2O	10

the main chamber, sufficiently far from the cold head for a monolayer to be grown in approximately 5 minutes. This method is also called "background deposition" and enables the possibility to use water as a matrix, or as a thick ice substrate. In the experiments of this work, we deposited 10 ML of water on the sample, with the exception of one experiment, in which a more accurate recalculation of the ice thickness yielded 6.5 ML (see last column of Table 4).

Depending on the temperature and modality of water deposition, different morphologies can be obtained. In our experimental conditions, non-porous amorphous solid water (ASW) – mimicking a compact ice bulk – is easily formed by leaving the cold finger at a steady temperature of 110 K during the deposition. Once a thickness of 10 ML is reached, the sample is cooled down to 70 K in order to deposit one of the molecules of interest. The procedure to form crystalline ice (CI) requires more steps, as a thermal treatment has to be performed on the 10 ML formerly deposited. The ice is first warmed to 140 K at a rate of 9 K min^{-1}, then to 142.5 K at a rate of 6 K min^{-1}. The process of crystallization can be monitored *via* RAIRS (stopped once the entire ice is crystalline, proved by a major change in the band shape), as well as *via* QMS to quantify the desorbing H_2O until this value remains constant.

The quantity of H_2O on the surface can directly be estimated during the deposition by monitoring the partial pressure of water inside the main chamber. Otherwise, it can be verified using the same methods as for ethanol and ethylamine.

3.2 Results

The experiments performed in this work can be divided into two categories: (i) sub-monolayer depositions of the adsorbates on ASW or CI films; and (ii) multilayer depositions of the adsorbates on an ASW film. For each adsorbate, CH_3CH_2OH and $CH_3CH_2NH_2$, three sub-monolayer depositions were carried out on ASW and one on CI. Only one multilayer deposition of each species was performed on amorphous H_2O. See Table 4 for the experimental details.

With this experimental study, our aim is to investigate the modification of the desorption profiles of CH_3CH_2OH and $CH_3CH_2NH_2$ depending on the surface type on which they are deposited (gold, ASW and CI), and on the surface coverage (sub-monolayer, monolayer and multilayer). In order to compare these results with the theoretical ones, the desorption energy of the adsorbates was also derived from the TPD curves using software developed in-house.

In the figures of this section, for the sake of clarity, we only display the most abundant molecular ion for each species: m/z = 18 for water ($[H_2O]^+$), m/z = 31 for ethanol ($[CH_2OH]^+$), and m/z = 30 for ethylamine ($[CH_2NH_2]^+$). Moreover, as no clear conclusion can be drawn from the infrared spectra produced during the experiments, except for the monolayer calibration (see Section 3.1.2), we chose not to display them in this paper.

3.2.1 Sub-monolayer depositions

3.2.1.1 On a gold substrate. Firstly, the behaviour of CH_3CH_2OH and $CH_3CH_2NH_2$ on the bare gold surface was studied to assess the adsorbate/surface interactions, which will be compared with those established when the surface consists of water ice (described in the following subsections). The experiments were initially performed to calibrate the flux to use for each of the two adsorbates. Fig. 4 represents the TPD curves for the m/z = 31 ethanol fragment and the m/z = 30 ethylamine fragment, which desorb at different deposition times. To avoid any ambiguity, and since the deposition times account for the quantities deposited, they have been converted to monolayers (MLs).

While CH_3CH_2OH exhibits a noticeable site-filling behaviour, starting with the strongest binding sites, this is not the case for $CH_3CH_2NH_2$. The start, end, and maximum of the desorption occurs at 122, 170 and 141 K for 0.7 ML of ethanol, and at 97, 160 and 113 K for 0.83 ML of ethylamine. In the case of the lowest coverages, represented by the dotted fainter lines,
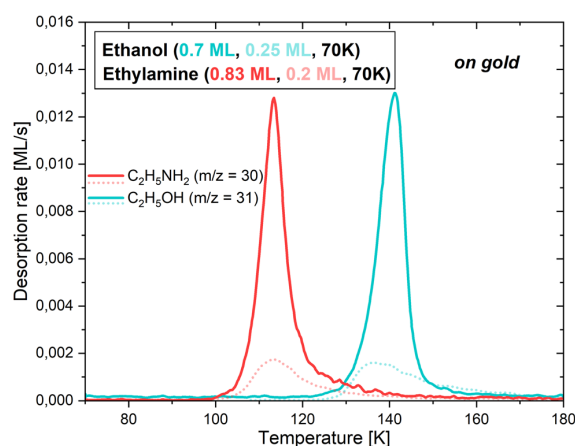

Fig. 4 TPD curves for the deposition of 0.7 ML (solid blue line) and 0.25 ML (dotted blue line) of ethanol, and 0.83 ML (solid red line) and 0.2 ML (dotted red line) of ethylamine, on the gold substrate. The most abundant molecular ion is displayed for each molecule.

This journal is © the Owner Societies 2024

Phys. Chem. Chem. Phys., 2024, **26**, 18205–18222 | **18213**

Feature Article

the start of the desorptions is slightly shifted towards higher temperatures. This is explained by the propensity of the adsorbates to attach to the most favourable binding sites, therefore needing more thermal energy to sublimate into the gas phase. As soon as more molecules are present on the surface, they occupy less favourable binding sites until all of them are used. This moment defines the monolayer, as additional molecules would directly stick to the first layer, and not to the bare gold. It is worth noting that the calibration curve pattern matches the time estimated for the monolayer completion in the previous section.

For these conditions, it is possible to extract the desorption energy of each of the adsorbates on the gold substrate, following the method outlined in Section 3.2.3.

3.2.1.2 On amorphous solid water. In the case of the sub-monolayer depositions of CH₃CH₂OH, namely 0.15, 0.25 and 0.7 ML, on a slab of 10 ML of ASW, the desorption curves and behaviours are all fairly comparable, as seen in the left panels of Fig. 5 and 6.

The TPD profiles differ in their integrated area, the latter being proportional to the quantity of molecules deposited on

the bulk of H₂O. In the case of the 0.15 and 0.25 ML CH₃CH₂OH depositions, a common pattern is visible, with the adsorbate starting to desorb at 147 K and 144 K, respectively, along with the crystallization of water. On the other hand, with the 0.7 ML CH₃CH₂OH deposition, the adsorbate starts to desorb together with amorphous water already at ~130 K. We note here that the quantity of water under the 0.25 ML deposition of ethanol was lower due to the use of a lower flux. The additional noise, visible on $m/z = 18$ and $m/z = 31$, is due to a poor following of the heating ramp after a change of the thermometer. This resulted in small recurrent surges of desorption, and in the partial crystallization of water before the expected temperature. However, this behaviour does not change the essence of the results. In all cases, the rest of the ethanol desorption follows the water pattern, with T_{peak} slightly shifted by about 1–2 K after the maximum of water desorption, and the desorption of both molecules ending mutually. This suggests that CH₃CH₂OH stays bound to the water surface until the H₂O molecules leave the surface completely. The moment ethanol starts desorbing can be explained by a stronger binding energy with ASW compared to CI in the case (see below) of the lowest
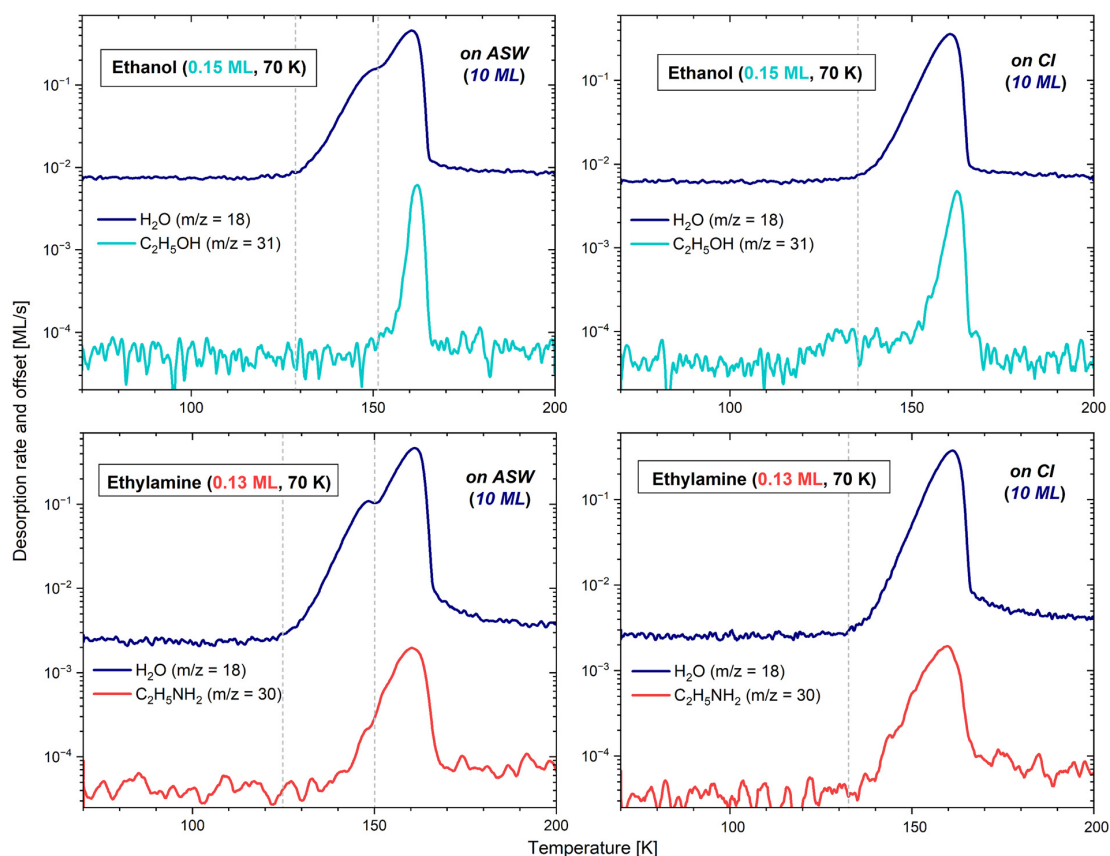
Fig. 5 TPD curves for the deposition of 0.15 ML of ethanol on 10 ML of ASW (top left) and of CI (top right), and 0.13 ML of ethylamine on 10 ML of ASW (bottom left) and of CI (bottom right). The most abundant molecular ion is displayed for each molecule. A logarithmic scale is used for better data readability, and grey vertical lines indicate the start of the water desorption and its crystallization.

18214 | *Phys. Chem. Chem. Phys.*, 2024, **26**, 18205–18222

This journal is © the Owner Societies 2024

Fig. 6 TPD curves for the deposition of 0.7 ML of ethanol (top left), 0.4 ML of ethylamine (bottom left), 2.1 ML of ethanol (top right) and 1.25 ML of ethylamine (bottom right) on 10 ML of ASW. The most abundant molecular ion is displayed for each molecule. A logarithmic scale is used for better data readability, and grey vertical lines indicate the start of the water desorption and its crystallization.
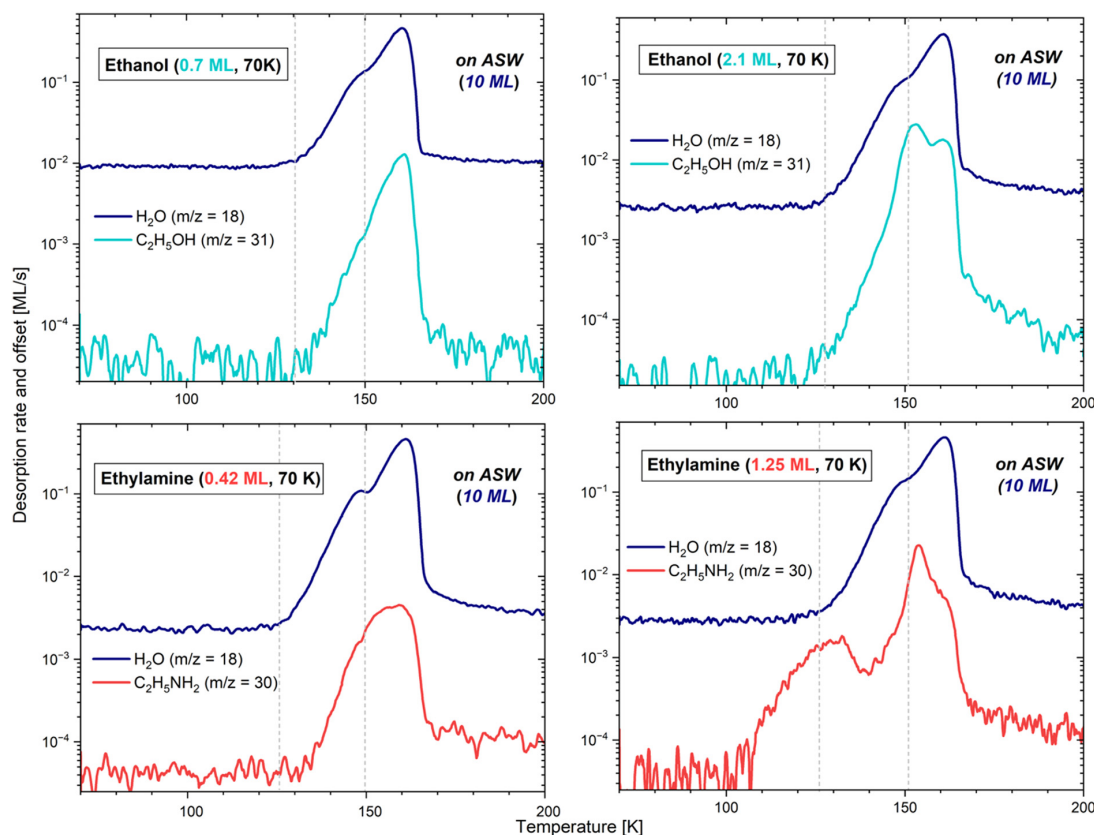
coverages, leading CH_3CH_2OH to stay bound to water until it changes configuration by crystallizing. Please refer to Section 3.2.1.3 for further details about the crystallization processes.

The sub-monolayer depositions of $CH_3CH_2NH_2$ (0.08, 0.13, and 0.4 ML) on the slab of 10 ML of ASW have common characteristics with the ethanol depositions. For instance, the ethylamine and H_2O desorptions end mutually, and the integrated areas of the TPD profiles of ethylamine are also proportional to the surface coverage. However, the maximum of the desorption of $CH_3CH_2NH_2$ is reached 1 K before that of water, except for the coverage of 0.08 ML, where both ethylamine and water show their maximum peak concomitantly. Additionally, in all cases, ethylamine starts desorbing before the crystallization of water at, respectively, 138, 140 and 132 K. Contrary to ethanol, it seems that $CH_3CH_2NH_2$ binds with water in the same way, regardless of the configuration of the ice. The lowest temperature would here simply reflect the higher concentration of molecules, consequently desorbing earlier due to the unavailability of the most favourable binding sites.

However, the comparison of TPDs registered after short deposition times of both ethanol and ethylamine highlights that both molecules sublimate far later when adsorbed on water ice rather than when deposited on the gold surface, due to their more favourable and stronger interaction with the ASW ice.

3.2.1.3 On crystalline ice. The above interpretations of a stronger binding energy of the adsorbate with ASW than with CI, in the case of low coverage for ethanol, are demonstrated experimentally by depositing 0.15 ML of CH_3CH_2OH and 0.13 ML of $CH_3CH_2NH_2$ on 10 ML of CI. The H_2O ice was crystallized *via* the process described in Section 3.1.3, and the results are displayed in the right panels of Fig. 5.

In the case of ethylamine, the desorption curve is identical to that on ASW. The start, end, and maximum of the desorption occur at the same temperatures, and the integrated areas are equivalent, attesting that the deposition conditions are extremely similar, apart from the configuration of the H_2O substrate. Thus, it seems that there is no influence of the ice structural state in the desorption energy of $CH_3CH_2NH_2$ on water ice.

In the case of ethanol, however, the *m/z* = 31 signal differs fairly significantly whether deposited on ASW or on CI. On CI,

although most of the sublimation into the gas phase takes place at the very end of the water desorption at T_{peak} = 162 K (as expected from the results obtained on ASW), a small fraction of molecules starts desorbing before water, from ∼117 K to ∼145 K. This corresponds better to the temperature range observed in the case of a deposition exclusively on gold. The curve shape suggests that when H₂O is completely crystalline, the ethanol molecules either bond slightly less (explaining their pre-desorption), or tend to agglomerate one onto each other, favouring a behaviour close to that of a multilayer regime. With any of the above solutions, the conclusion remains that in a sub-monolayer regime, ethanol has a different behaviour on ASW and on CI, further demonstrating its ejection from the surface during the phase change of water.

3.2.2 Multilayer depositions. The desorption process of the adsorbates in a multilayer regime (*i.e.*, 2.1 ML of CH₃CH₂OH and 1.25 ML of CH₃CH₂NH₂) deposited onto a film of 10 ML of ASW were also performed. The corresponding TPD curves are displayed on the right panels of Fig. 6. The desorption profile of ethanol shows two clearly distinguishable peaks, while that of ethylamine exhibits the contribution of three desorption peaks. They all attest that there are different kinds of molecular interactions.

In both species, the shoulder monitored at higher temperature at the end of the H₂O desorption, furthest to the right, is comparable to the results obtained from the sub-monolayer depositions. In other words, the molecules of ethanol and ethylamine that are directly in contact with the highest energy binding sites keep being bonded very strongly with water, even when the latter is desorbing. They are therefore sublimating together with the very last water molecules.

In the case of ethylamine, the first peak observable even before the start of the water desorption corresponds to a fraction of molecules that are not directly interacting with the bulk of H₂O, but rather with the less strongly bonded multilayer. Indeed, these CH₃CH₂NH₂ molecules start desorbing at 102 K, corresponding well to the behaviour exhibited when a multilayer regime is deposited solely on gold, with the addition of a slight water-binding contribution, explaining the signal persistence up to ∼150 K (visible if using an extrapolation). The interaction between layers of CH₃CH₂NH₂ is thus weaker than that between the adsorbate and the ASW ice film. In the case of ethanol, in contrast, this first peak characteristic of a multilayer regime does not appear prior to the desorption of water, but is instead blended with the intermediate peak (described in the next paragraph). Indeed, on gold, multilayers of CH₃CH₂OH only start to desorb around 120 K. This temperature mingles with that of the start of water desorption, therefore making the multilayer contribution indistinguishable from the second peak, when the adsorbate is deposited on H₂O.

Lastly, for both adsorbates, the largest contribution to the desorption peaks occurs at the moment of the H₂O phase change. This would correspond to the ejection of ethanol and ethylamine from the surface when water is undergoing a morphological change. In a multilayer regime, both adsorbates

consequently appear to bond more strongly with ASW than with CI.

3.2.3 Desorption energy derivation. The desorption conditions on water ice do not allow us to easily extract the desorption energies, E_{des}, of the adsorbates. Indeed, in most of the cases, the interaction between the adsorbates and water ice is stronger than that of water with itself, resulting in a co-desorption of H₂O and the adsorbates, or in a late desorption of the adsorbates, together with the last H₂O molecules present on the sample. Since water starts sublimating first, calculating the E_{des} values of the adsorbates on water ice is therefore unfeasible.[34] Likewise, the multiple peaks found when several adsorbate layers are deposited also prevent a clear derivation of the adsorbate/water E_{des}.

However, obtaining E_{des} values is possible by using the sub-monolayer and monolayer depositions of CH₃CH₂OH and CH₃CH₂NH₂ on the bare gold substrate (see above). The mathematical model, based on eqn (5) and developed by Chaabouni *et al.*,[70] was employed to fit the experimental results. The code returns different populations (N) of molecules sublimating into the gas phase with a certain desorption energy (E_{des}), all together contributing to the final TPD curve. The best fit of the experimental data is obtained when the calculated curve matches well the experimental results, which is satisfied when the three parameters (A_{TST}; E_{des}, N) are well constrained.

The pre-exponential factors needed to obtain the curves and the populations were calculated with an equation derived from transition state theory[44] (further details can be found in the ESI†), yielding A_{TST} = 3.31 × 10¹⁸ s⁻¹ for ethanol, and A_{TST} = 2.04 × 10¹⁸ s⁻¹ for ethylamine.

The model returns E_{des} = 53.6 kJ mol⁻¹ (6450 K) for CH₃CH₂OH and E_{des} = 41.6–43.2 kJ mol⁻¹ (5000–5200 K) for CH₃CH₂NH₂, as displayed in Fig. 7 (right panels), where the best fits of the simulated TPD (in red) match well the ones measured in the experiments (represented by the black dots). Each simulated curve is given by the combination of a number of TPDs, each corresponding to the different E_{des} obtained in the population graph (left panel of Fig. 7). For ethanol, we do not obtain an actual distribution, as more than 80% of the molecules are characterized by one main energy value. On the other hand, ethylamine shows a proper distribution with almost 70% of the population having E_{des} between 41.6–43.2 kJ mol⁻¹ (5000–5200 K), followed by about 15% of the population with E_{des} between 44.9–46.6 kJ mol⁻¹ (5400–5600 K) and the remaining population in which each E_{des} has a progressively smaller weight until reaching a negligible contribution.

4 Discussion

4.1 Pure CH₃CH₂OH and CH₃CH₂NH₂ depositions

All the quantities computed in this work have been reported in Table 5. The desorption of CH₃CH₂OH and CH₃CH₂NH₂ deposited on the bare gold surface resulted in a TPD with a T_{peak} of 141 K and 113 K, respectively. From there, E_{des} = 53.6 kJ mol⁻¹ for ethanol and E_{des} = 41.6–43.2 kJ mol⁻¹ for ethylamine were
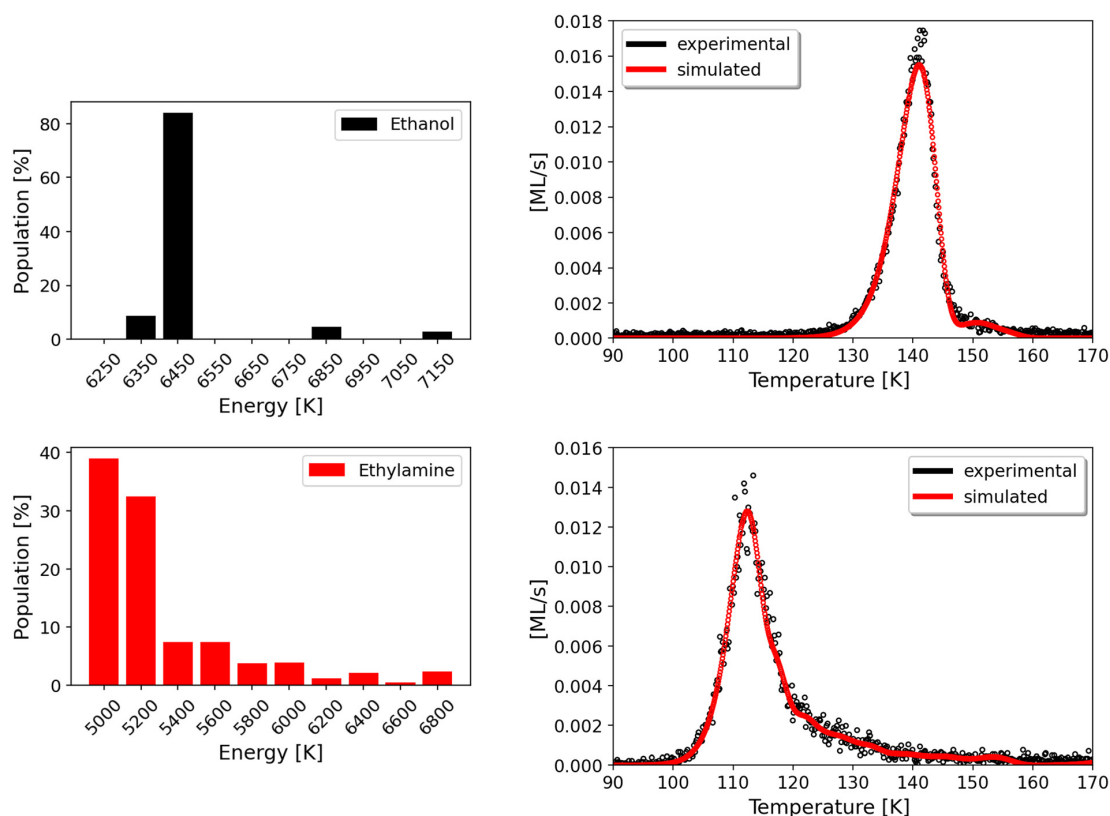
PCCP **Feature Article**

Fig. 7 Comparison between the measured and reproduced TPD profiles and relative populations of 0.7 ML of CH_3CH_2OH adsorbed on gold (top panel, 8 TPDs) and 0.4 ML of $CH_3CH_2NH_2$ adsorbed on gold (bottom panel, 10 TPDs), considering the calculated pre-exponential factor.

Table 5 Summary of all the computed quantities. All quantities are ZPE-corrected and are provided in kJ mol^{-1} and in Kelvin. BE(0) = binding energy; E_C = cohesive energy; E_X = extraction energy; CI = crystalline ice; ASW = amorphous solid water; S-ADS = single adsorption; H-ML = half monolayer; F-ML = full monolayer. Multiple values are separated by a slash, while ranges are represented by their endpoints

	kJ mol^{-1}				Kelvin			
	CH_3CH_2OH	$CH_3CH_2NH_2$	CI	ASW	CH_3CH_2OH	$CH_3CH_2NH_2$	CI	ASW
Bulk E_C	−53.4	−44.0	−55.8		−6423	−5292	−6711	
Surface E_C	−49.4 to −40.3	−40.4 to −30.3	−49.5	−44.9	−5941 to −4847	−4859 to −3644	−5953	−5400
Surface E_X	58.9 to 116.6	36.0 to 84.3			7084 to 14024	4330 to 10139		
BE(0) on (010) EtOH	20.9/30.9/41.8				2514/3716/5027			
BE(0) on (100) EtNH$_2$		21.4/21.6/43.0				2574/2598/5172		
BE(0) S-ADS on CI	33.4/42.2/61.6	23.1/61.4			4017/5075/7409	2778/7385		
BE(0) H-ML on CI	66.0	64.5			7938	7758		
BE(0) F-ML on CI	50.0	49.5			6014	5953		
BE(0) S-ADS on ASW	26.0 to 59.1	19.1 to 71.7			3127 to 7108	2297 to 8624		

derived, along with the respective pre-exponential factors ν. From a computational point of view, this scenario can be reproduced in two ways: (i) by modeling the bulk and the surfaces of EtOH and EtNH₂ crystals; or (ii) by adsorbing CH_3CH_2OH and $CH_3CH_2NH_2$ on the most stable EtOH and EtNH₂ surfaces. The quantity that determines the strength of the interaction between the molecules forming the crystals is

the cohesive energy E_C of the bulk (−53.4 kJ mol^{-1} for EtOH and −44.0 kJ mol^{-1} for EtNH₂) and of the most stable surfaces (−49.4 kJ mol^{-1} for EtOH and −40.4 kJ mol^{-1} for EtNH₂). It should be noted that the negative values taken by E_C are due to its definition, which is the opposite of that of the BE(0). Therefore, a more negative value indicates a more stable structure. We also simulated the adsorption of CH_3CH_2OH on

the (010) EtOH surface, and CH₃CH₂NH₂ on the (100) EtNH₂ surface, to compute the relative binding energy, which resulted in a range covering similar values for the two species (20.9–41.8 kJ mol⁻¹ for CH₃CH₂OH and 21.4–43.0 kJ mol⁻¹ for CH₃CH₂NH₂). Despite the similarity of the BE(0)s, the first calculations suggest that the interaction between organized ethanol molecules is stronger than that between ethylamine molecules. This is in agreement with the E_{des} of ethanol and ethylamine estimated experimentally. Remarkably, the E_C of the bulk and of the most stable EtOH and EtNH₂ surfaces seems to be the quantity that better describes what we observe in the experiment, supposing that small quantities of adsorbate, when deposited on the gold finger, or during the heating phase, could aggregate and order themselves into structures that resemble the order present in the crystal.

4.2 Sub-monolayer depositions

The experiments performed in this work cannot provide an experimental measurement of the E_{des} of CH₃CH₂OH and CH₃CH₂NH₂ adsorbed on water ice. This is because the interpretation of the TPD profiles is hindered by the presence of co-desorption phenomena, and occasionally the emergence of multiple desorption peaks. This occurred as well in previous experimental studies (*e.g.*, Lattelais *et al.*[40]) investigating the desorption of ethanol from water ice. For this reason, Burke *et al.*[71] classified ethanol as a complex water-like molecule, in that it wets the ice surface and co-desorbs with water (which moreover affects the water crystallization process), like methanol, acetic acid, and other iCOMs. Minissale *et al.*[34] also mentioned that the species capable of establishing several H-bonds with water are likely to be strongly bound with the ice and behave like ethanol, thereby making impracticable the determination of their E_{des} values from a TPD experiment. From our calculations, this phenomenon can be explained by the presence of BE(0) values of CH₃CH₂OH and CH₃CH₂NH₂ that are responsible for an interaction between the adsorbate and water that is stronger than the cohesive energy of water ice (−55.8 kJ mol⁻¹ in the case of CI bulk, and slightly inferior for ASW and CI surfaces).

Moreover, the experiments show that CH₃CH₂NH₂ binds with ASW and CI with similar strength, regardless of their different structural states. On the contrary, CH₃CH₂OH seems to have stronger binding energies with ASW compared to CI in the case of low coverages (0.15 and 0.25 ML). This aspect does not clearly emerge from the calculations, because the differences in the BE(0) ensembles of ASW and CI are limited. While the BE(0) values computed for ethylamine cover almost the same range for ASW (19.1–71.7 kJ mol⁻¹) and CI (23.1/61.4 kJ mol⁻¹), ethanol can experience lower BE(0)s on ASW (26.0–59.1 kJ mol⁻¹) rather than on CI (33.4/42.2/61.6 kJ mol⁻¹), thus in disagreement with the experimental data.

Additionally, an aspect that must be considered in the comparison of experimental and theoretical results is that, in a sub-monolayer deposition TPD experiment, constant thermal energy is provided to the molecules, which is used to diffuse and move toward stronger binding sites, where the system is

more stable, this way neglecting the least favourable binding sites. Moreover, the experiments measure desorption energies, accounting for desorption effects that cannot be reproduced in the calculations. Therefore, the E_{des} values provided by the experiments do not usually cover the lower limit of the BE(0) distribution obtained with calculations.

In this sense, quantum chemical calculations offer the possibility to compute the quantities that cannot be determined experimentally. Despite their structural similarity, CH₃CH₂OH and CH₃CH₂NH₂ show differences in their chemical behaviour, due to the H-bond capabilities of the OH and NH₂ groups. NH₂ is a stronger H-bond acceptor than OH, but it is a weaker H-bond donor. This results in CH₃CH₂NH₂ spanning a larger BE(0) range than CH₃CH₂OH when adsorbed on the ASW model (19.1–71.7 kJ mol⁻¹ *vs.* 26.0–59.1 kJ mol⁻¹, respectively) since the strength of the interaction depends on the atom establishing the H-bond with the binding site of the ice. Such a difference can also partially be observed with the CI model, where the lowest BE(0), due to H-bond donation from the adsorbate to the surface, is 23.1 kJ mol⁻¹ for ethylamine and 33.4 kJ mol⁻¹ for ethanol. The values obtained for the CI can represent in part the BE ensemble obtained on the ASW, although two or three values are not sufficient to account for the diversity of binding sites available on the amorphous model.

The BE(0) values obtained for CH₃CH₂OH and CH₃CH₂NH₂ on CI and ASW mostly agree with those proposed in the literature. Garrod[39] suggested BE = 65.5 kJ mol⁻¹ for CH₃CH₂NH₂ and BE = 52.0 kJ mol⁻¹ for CH₃CH₂OH, highlighting the stronger interaction of ethylamine, compared to ethanol, with the ice. To the best of our knowledge, no other BEs have been documented for CH₃CH₂NH₂ on water ice. At variance, ethanol has been the object of a number of investigations. Lattelais *et al.*[40] computed the adsorption of ethanol onto the same crystalline proton-ordered ice model of this work, using the PW91 functional in combination with plane waves, with the VASP code, obtaining BE = 56.5 kJ mol⁻¹, close to the value of Garrod.[39] Due to the use of plane waves, the BE computed by Lattelais *et al.*[40] does not suffer from the BSSE. However, at variance with our calculations, both the ZPE and the dispersion corrections are lacking, probably explaining the discrepancy with the value computed in this work for the same adsorption complex (BE(0) = 61.6 kJ mol⁻¹). On the contrary, the values provided by Etim *et al.*,[41] in which ethanol is interacting with only one water molecule, range from 37.4 to 40.7 kJ mol⁻¹, which lie within the intermediate range of our BE(0) ensemble. Clearly, the latter estimate cannot reproduce the largest BE(0)s, due to the impossibility of capturing the essence of the interaction between CH₃CH₂OH and water ice when approximating its structure with only one water molecule. The choice of the ice model appears to be crucial, especially when the adsorbate is large enough to interact with more than one water molecule. Thus, the values proposed in this work represent an extension of those already available in the literature, additionally describing a tail of weaker BE(0) values that can only be simulated when using extended amorphous ice models characterized by a rich structural variability.

The simulation of the H-ML and F-ML scenarios by adsorbing a larger number of molecules on the surface yields slightly

larger and lower BE(0)s compared to the S-ADS case, respectively. In the calculations, we directly modeled the adsorption of a layer of molecules, which results in the determination of a single BE(0) value for all the species adsorbed. This does not faithfully represent what happens in the experiment, where the species approach the surface in different moments and start occupying binding sites starting from the strongest and then to the weakest, resulting in a distribution of BEs. However, the BE(0)s obtained from the simulation of different surface coverages represents a useful alternative to understand the variation in the BE(0) values resulting from the occupation of an increasing number of surface binding sites.

4.3 Multilayer depositions

The deposition of 1.25 ML of $CH_3CH_2NH_2$ on ASW results in multiple desorption peaks, in which the desorption of the adsorbate alone can be discerned from its co-desorption with water. The first desorption peak (starting at 102 K, before water desorption) corresponds to ethylamine molecules that are not in direct contact with the water surface. The interaction between layers of $CH_3CH_2NH_2$ is thus weaker than that between $CH_3CH_2NH_2$ and the ASW film. However, in the TPD of 2.1 ML of CH_3CH_2OH on ASW, the peak corresponding to the multilayer desorption is blended with that caused by the desorption of the ethanol in direct contact with water ice due to crystallization of the latter. This causes the two types of desorption to be indistinguishable. Such a discrepancy between $CH_3CH_2NH_2$ and CH_3CH_2OH can be justified by comparing, once again, the E_C of the species under investigation. The computed cohesive energies of ASW and CI surfaces (-49.5 and -44.9 kJ mol^{-1}, respectively) are comparable with those of ethanol surfaces (between -49.4 and -40.3 kJ mol^{-1}), but larger than those of ethylamine surfaces (between -40.4 and -30.3 kJ mol^{-1}). Based on these numbers, we can assume that even in the presence of larger quantities of ethanol on the water ice surface, both ethanol and water likely desorb in the same temperature range: the multilayer desorption is regulated by the cohesive energy, while the desorption of those ethanol molecules in direct contact with water is determined by the BE(0) of CH_3CH_2OH on ASW.

4.4 Astrophysical implications

The experiments performed in this work reveal that ethanol and, in part, ethylamine co-desorb with water ice. Computational data confirm and complement the experimental results, providing an ensemble of BE(0)s accounting for the upper and lower limits. Usually, the weakest interactions between the adsorbate and the surface cannot be measured by TPD experiments, but need to be considered when determining the regions of the ISM in which a species is available in the gas phase, rather than segregated on the ice grains. Despite this, the presence of ethanol, as well as other iCOMs in general, in the cold (<20 K) outskirts of prestellar cores requires non-thermal desorption processes to be explained.

In contrast, ethylamine has only been tentatively detected towards the Galactic center cloud G+0.693-0.027,[9] raising doubts regarding its absence elsewhere. This work suggests that both CH_3CH_2OH and $CH_3CH_2NH_2$ should be found in warm regions, like hot cores and hot corinos, where the ice mantles sublimate due to the presence of a warm central object.

The E_{des} of the species on water ice mantles have a profound impact on the chemical composition of the regions where planetary systems eventually form. A very important case is represented by the gaseous-versus-solid chemical composition of protoplanetary disks. If a species is in the solid form, it will likely be incorporated in rocky planets, asteroids and comets, whereas, if it resides in the gas phase, it will only enrich the giant gaseous planets. The transition of a species from the gas phase to the solid phase (when moving away from the central object) is identified by its snow-line.[72]

If we compare the BE(0) ranges spanned by ethanol (26.0–59.1 kJ mol^{-1}), ethylamine (19.1–71.7 kJ mol^{-1}) and water (14.2–61.6 kJ mol^{-1}, peaking at 35.2 kJ mol^{-1}),[73] we can have clues on the composition of the icy mantles on the protoplanetary disks, dictating whether a species is incorporated in water-rich planetesimals or not. By looking at the maximum BE(0) values of CH_3CH_2OH and $CH_3CH_2NH_2$, we can infer that at least a fraction of these species will remain on the grains in regions where up to 96% of water has completely sublimated (corresponding to BE(0) $\simeq$ 54.0 kJ mol^{-1}). Ethanol and ethylamine could therefore be incorporated in the planetesimals that will form rocky bodies.

Theoretical calculations indicate that the BE(0) ensembles of CH_3CH_2OH and $CH_3CH_2NH_2$ on water ice span similar ranges. Accordingly, if ethanol is detected in the ice,[19] ethylamine should also be detected. However, this is not the case. Thus, the reason behind the presence of ethanol and the absence of ethylamine in ISM regions points towards their synthetic pathways. As mentioned in Section 1, ethanol synthesis on water ices has been proposed via reactivity between CCH and H_2O followed by hydrogenation.[31] The analogue reaction for ethylamine would be thus initiated by CCH + NH_3. However, ammonia is much less abundant than water, causing a meager production of $CH_3CH_2NH_2$. Hydrogenation of icy acetaldehyde (CH_3CHO), which can form by the HCO + CH_3 radical–radical coupling on water ice,[74] is an alternative route towards ethanol formation. The analogue pathway for ethylamine is the hydrogenation of acetonitrile (CH_3CN), which can form previously through HCN + CH_3 or CN + CH_3 reactions. However, HCN is chemically inert in cold environments,[75] while the likelihood of CH_3CN undergoing hydrogenation is doubtful, due to the intrinsic stability (and consequent inertness) of nitriles.[76] Moreover, detection of CH_3CN in ices still remains elusive.[19] Additionally, at variance with ethanol, ethylamine could form salts due to the basicity of the amino moiety. In general, O-bearing species are more abundant than N-bearing species, a fact directly linked to the cosmic abundances of oxygen and nitrogen,[77–79] although such a discrepancy cannot fully account for the differences in the detection of these two iCOMs, especially considering the extremely articulated network of chemical reactions taking place in the ISM.

This journal is © the Owner Societies 2024

Phys. Chem. Chem. Phys., 2024, 26, 18205–18222 | 18219

Feature Article

5 Conclusions

In this work, the interaction of CH_3CH_2OH and $CH_3CH_2NH_2$ on water ice has been studied by means of a computational (periodic DFT simulations) and an experimental (TPD measurements) approach.

First, E_{des} values for pure CH_3CH_2OH and $CH_3CH_2NH_2$ deposited on a gold surface were determined experimentally, which closely align with the cohesive energies of crystalline bulks of EtOH and $EtNH_2$, along with their most stable surfaces.

The E_{des} values for submonolayer coverages of CH_3CH_2OH and $CH_3CH_2NH_2$ deposited on crystalline and amorphous water ice surfaces cannot be determined experimentally due to the complexity of their desorption profiles, where multiple desorption peaks are occasionally present, in addition to the co-desorption of the adsorbate with water. Theoretical calculations fill this gap by providing a comprehensive set of BE(0) values for CH_3CH_2OH and $CH_3CH_2NH_2$ on both crystalline and amorphous surface ice models. Notably, these calculations reveal weak binding sites that are elusive in traditional TPD experiments. Nevertheless, the TPD of a submonolayer deposition of ethanol on crystalline ice reveals a very small fraction of molecules desorbing from the surface prior to its crystallization, indicating a weaker interaction of ethanol with crystalline ice compared to the amorphous one. The deposition of a multilayer of adsorbate can provide additional information, due to the occupation of all the binding sites available on the water surface and the formation of multiple layers of adsorbate, avoiding a direct interaction with the water ice. The temperature at which the first ethylamine molecules of the multilayer desorb is higher than that of pure ethylamine, owing to the presence of the water ice surface. After desorption of the multilayer, the TPD profile resembles that of a submonolayer deposition. Conversely, for ethanol, it is not possible to distinguish the two behaviours as the corresponding peaks are overlapping. The theoretical results corroborate these findings, in that the cohesive energy of the bulk and surfaces of crystalline $EtNH_2$ is smaller compared to that of EtOH, which in turn is comparable with that of crystalline and amorphous water ice. This disparity explains why ethylamine multilayers desorb before water, while ethanol multilayers do not.

The desorption energies of CH_3CH_2OH and $CH_3CH_2NH_2$ play a critical role in determining their presence in the gas or in the solid phase of the ISM, thus influencing the chemical composition of celestial bodies formed from protoplanetary disks, as delineated by snow-lines. The high BE(0) values of ethanol rationalize its presence in interstellar ices. However, the non-detection of ethylamine cannot be explained by its BE(0) values, and likely stems from the lack of favourable reaction pathways responsible for its formation. Nevertheless, the scarcity of gas-phase $CH_3CH_2NH_2$ in the ISM and the presence of CH_3CH_2OH in the gas phase of cold objects, the latter usually elucidated by invoking non-thermal desorption mechanisms, need further investigation.

This work exemplifies the way in which computational chemistry can not only support laboratory experiments, but the two disciplines can complement each other in order to provide reference data as the input for astrochemical models.[80]

Data availability

Computational models available at **https://zenodo.org/records/11103454**.

Author contributions

Conflicts of interest

There are no conflicts to declare.

Acknowledgements

18220 | *Phys. Chem. Chem. Phys.*, 2024, **26**, 18205–18222

This journal is © the Owner Societies 2024

Notes and references

1 E. Herbst and E. F. van Dishoeck, *Annu. Rev. Astron. Astrophys.*, 2009, **47**, 427–480.

2 E. Herbst, *Int. Rev. Phys. Chem.*, 2017, **36**, 287–331.

3 C. Ceccarelli, P. Caselli, F. Fontani, R. Neri, A. López-Sepulcre, C. Codella, S. Feng, I. Jiménez-Serra, B. Lefloch, J. E. Pineda, C. Vastel, F. Alves, R. Bachiller, N. Balucani, E. Bianchi, L. Bizzocchi, S. Bottinelli, E. Caux, A. Chacón-Tanarro, R. Choudhury, A. Coutens, F. Dulieu, C. Favre, P. Hily-Blant, J. Holdship, C. Kahane, A. J. Al-Edhari, J. Laas, J. Ospina, Y. Oya, L. Podio, A. Pon, A. Punanova, D. Quenard, A. Rimola, N. Sakai, I. R. Sims, S. Spezzano, V. Taquet, L. Testi, P. Theulé, P. Ugliengo, A. I. Vasyunin, S. Viti, L. Wiesenfeld and S. Yamamoto, *Astrophys. J.*, 2017, **850**, 176.

4 P. Caselli and C. Ceccarelli, *Astron. Astrophys. Rev.*, 2012, **20**, 56.

5 M. Förstel, A. Bergantini, P. Maksyutenko, S. Góbi and R. I. Kaiser, *Astrophys. J.*, 2017, **845**, 83.

6 R. L. Hudson, Y. Y. Yarnall and P. A. Gerakines, *Astrobiology*, 2022, **22**, 452–461.

7 F. Goesmann, H. Rosenbauer, J. H. Bredehöft, M. Cabane, P. Ehrenfreund, T. Gautier, C. Giri, H. Krüger, L. L. Roy, A. J. MacDermott, S. McKenna-Lawlor, U. J. Meierhenrich, G. M. M. Caro, F. Raulin, R. Roll, A. Steele, H. Steininger, R. Sternberg, C. Szopa, W. Thiemann and S. Ulamec, *Science*, 2015, **349**, aab0689.

8 D. P. Glavin, J. P. Dworkin and S. A. Sandford, *Meteorit. Planet. Sci.*, 2008, **43**, 399–413.

9 S. Zeng, I. Jiménez-Serra, V. M. Rivilla, J. Martn-Pintado, L. F. Rodrguez-Almeida, B. Tercero, P. de Vicente, F. Rico-Villas, L. Colzi, S. Martn and M. A. Requena-Torres, *Astrophys. J., Lett.*, 2021, **920**, L27.

10 K. Altwegg, H. Balsiger and S. A. Fuselier, *Annu. Rev. Astron. Astrophys.*, 2019, **57**, 113–155.

11 N. Biver, D. Bockelée-Morvan, R. Moreno, J. Crovisier, P. Colom, D. C. Lis, A. Sandqvist, J. Boissier, D. Despois and S. N. Milam, *Sci. Adv.*, 2015, **1**, e1500863.

12 J. Crovisier, D. Bockelée-Morvan, P. Colom, N. Biver, D. Despois, D. C. Lis and the Team for target-of-opportunity radio observations of comets, *Astron. Astrophys.*, 2004, **418**, 1141–1157.

13 B. Zuckerman, B. E. Turner, D. R. Johnson, F. O. Clark, F. J. Lovas, N. Fourikis, P. Palmer, M. Morris, A. E. Lilley, J. A. Ball, C. A. Gottlieb, M. M. Litvak and H. Penfield, *Astrophys. J., Lett.*, 1975, **196**, L99–L102.

14 M. Ohishi, S. Yamamoto, S. Saito, K. Kawaguchi, H. Suzuki, N. Kaifu, S.-I. Ishikawa, S. Takano, T. Tsuji and W. Unno, *Astrophys. J.*, 1988, **329**, 511.

15 J. C. Pearson, K. V. L. N. Sastry, E. Herbst and F. C. D. Lucia, *Astrophys. J.*, 1997, **480**, 420.

16 E. Bianchi, C. Codella, C. Ceccarelli, F. Vazart, R. Bachiller, N. Balucani, M. Bouvier, M. De Simone, J. Enrique-Romero, C. Kahane, B. Lefloch, A. López-Sepulcre, J. Ospina-Zamudio, L. Podio and V. Taquet, *Mon. Not. R. Astron. Soc.*, 2019, **483**, 1850–1861.

17 M. Agúndez, N. Marcelino, J. Cernicharo, E. Roueff and M. Tafalla, *Astron. Astrophys.*, 2019, **625**, A147.

18 M. Agúndez, J. C. Loison, K. M. Hickson, V. Wakelam, R. Fuentetaja, C. Cabezas, N. Marcelino, B. Tercero, P. de Vicente and J. Cernicharo, *Astron. Astrophys.*, 2023, **673**, A34.

19 M. K. McClure, W. Rocha, K. Pontoppidan, N. Crouzet, L. E. Chu, E. Dartois, T. Lamberts, J. Noble, Y. Pendleton and G. Perotti, *et al.*, *Nat. Astron.*, 2023, **7**, 431–443.

20 W. R. M. Rocha, E. F. van Dishoeck, M. E. Ressler, M. L. van Gelder, K. Slavicinska, N. G. C. Brunken, H. Linnartz, T. P. Ray, H. Beuther, A. Caratti o Garatti, V. Geers, P. J. Kavanagh, P. D. Klaassen, K. Justtanont, Y. Chen, L. Francis, C. Gieser, G. Perotti,. Tychoniec, M. Barsony, L. Majumdar, V. J. M. le Gouellec, L. E. U. Chu, B. W. P. Lew, T. Henning and G. Wright, *Astron. Astrophys.*, 2024, **683**, A124.

21 B. Lefloch, C. Ceccarelli, C. Codella, C. Favre, L. Podio, C. Vastel, S. Viti and R. Bachiller, *Mon. Not. R. Astron. Soc.: Lett.*, 2017, **469**, L73–L77.

22 D. Skouteris, N. Balucani, C. Ceccarelli, F. Vazart, C. Puzzarini, V. Barone, C. Codella and B. Lefloch, *Astrophys. J.*, 2018, **854**, 135.

23 H. Carrascosa, C. González Daz, G. M. Muñoz Caro, P. C. Gómez and M. L. Sanz, European Planetary Science Congress, 2021, pp. EPSC2021-51.

24 T. C. Keane, *Origins Life Evol. Biospheres*, 2017, **47**, 223–248.

25 R. L. Hudson and M. J. Loeffler, *Astrophys. J.*, 2013, **773**, 109.

26 C. Robert Wu, D. Judge, B.-M. Cheng, W.-H. Shih, T.-S. Yih and W. Ip, *Icarus*, 2002, **156**, 456–473.

27 K.-J. Chuang, G. Fedoseev, G. Scirè, G. A. Baratta, C. Jäger, T. Henning, H. Linnartz and M. E. Palumbo, *Astron. Astrophys.*, 2021, **650**, A85.

28 J. B. Bergner, K. I. Öberg and M. Rajappan, *Astrophys. J.*, 2019, **874**, 115.

29 K.-J. Chuang, G. Fedoseev, D. Qasim, S. Ioppolo, C. Jäger, T. Henning, M. E. Palumbo, E. F. van Dishoeck and H. Linnartz, *Astron. Astrophys.*, 2020, **635**, A199.

30 J. Enrique-Romero, A. Rimola, C. Ceccarelli, P. Ugliengo, N. Balucani and D. Skouteris, *Astrophys. J., Suppl. Ser.*, 2022, **259**, 39.

31 J. Perrero, J. Enrique-Romero, B. Martnez-Bachs, C. Ceccarelli, N. Balucani, P. Ugliengo and A. Rimola, *ACS Earth Space Chem.*, 2022, **6**, 496–511.

32 S. Ferrero, C. Ceccarelli, P. Ugliengo, M. Sodupe and A. Rimola, *Astrophys. J.*, 2023, **951**, 150.

33 S. Ferrero, C. Ceccarelli, P. Ugliengo, M. Sodupe and A. Rimola, *Astrophys. J.*, 2024, **960**, 22.

34 M. Minissale, Y. Aikawa, E. Bergin, M. Bertin, W. A. Brown, S. Cazaux, S. B. Charnley, A. Coutens, H. M. Cuppen, V. Guzman, H. Linnartz, M. R. S. McCoustra, A. Rimola, J. G. Schrauwen, C. Toubin, P. Ugliengo, N. Watanabe, V. Wakelam and F. Dulieu, *ACS Earth Space Chem.*, 2022, **6**, 597–630.

35 L. J. Karssemeijer and H. M. Cuppen, *Astron. Astrophys.*, 2014, **569**, A107.

This journal is © the Owner Societies 2024

Phys. Chem. Chem. Phys., 2024, **26**, 18205–18222 | **18221**

Chapter 5. A theoretical and experimental combined study of ethanol and ethylamine binding energies on H₂O ice surfaces

153

Feature Article

36 H. M. Cuppen, C. Walsh, T. Lamberts, D. Semenov, R. T. Garrod, E. M. Penteado and S. Ioppolo, *Space Sci. Rev.*, 2017, **212**, 1–58.

37 A. Kouchi, K. Furuya, T. Hama, T. Chigai, T. Kozasa and N. Watanabe, *Astrophys. J., Lett.*, 2020, **891**, L22.

38 B. Maté, S. Cazaux, M. Á. Satorre, G. Molpeceres, J. Ortigoso, C. Millán and C. Santonja, *Astron. Astrophys.*, 2020, **643**, A163.

39 R. T. Garrod, *Astrophys. J.*, 2013, **765**, 60.

40 M. Lattelais, M. Bertin, H. Mokrane, C. Romanzin, X. Michaut, P. Jeseck, J.-H. Fillion, H. Chaabouni, E. Congiu, F. Dulieu, S. Baouche, J.-L. Lemaire, F. Pauzat, J. Pilmé, C. Minot and Y. Ellinger, *Astron. Astrophys.*, 2011, **532**, A12.

41 E. E. Etim, P. Gorai, A. Das, S. K. Chakrabarti and E. Arunan, *Adv. Space Res.*, 2018, **61**, 2870–2880.

42 V. Wakelam, J.-C. Loison, R. Mereau and M. Ruaud, *Mol. Astrophys.*, 2017, **6**, 22–35.

43 T. I. Hasegawa and E. Herbst, *Mon. Not. R. Astron. Soc.*, 1993, **263**, 589–606.

44 S. L. Tait, Z. Dohnálek, C. T. Campbell and B. D. Kay, *J. Chem. Phys.*, 2005, **122**, 164708.

45 R. Dovesi, A. Erba, R. Orlando, C. M. Zicovich-Wilson, B. Civalleri, L. Maschio, M. Rérat, S. Casassa, J. Baima, S. Salustro and B. Kirtman, *Wiley Interdiscip. Rev.: Comput. Mol. Sci.*, 2018, **8**, e1360.

46 H. Tatewaki and S. Huzinaga, *J. Comput. Chem.*, 1980, **1**, 205–228.

47 R. Sure and S. Grimme, *J. Comput. Chem.*, 2013, **34**, 1672–1685.

48 S. Grimme, J. Antony, S. Ehrlich and H. Krieg, *J. Chem. Phys.*, 2010, **132**, 154104.

49 S. Grimme, S. Ehrlich and L. Goerigk, *J. Comput. Chem.*, 2011, **32**, 1456–1465.

50 J. G. Brandenburg, M. Alessio, B. Civalleri, M. F. Peintinger, T. Bredow and S. Grimme, *J. Phys. Chem. A*, 2013, **117**, 9282–9292.

51 H. Kruse and S. Grimme, *J. Chem. Phys.*, 2012, **136**, 154101.

52 A. D. Becke, *Phys. Rev. A: At., Mol., Opt. Phys.*, 1988, **38**, 3098–3100.

53 A. D. Becke, *J. Chem. Phys.*, 1993, **98**, 5648–5652.

54 C. Lee, W. Yang and R. G. Parr, *Phys. Rev. B: Condens. Matter Mater. Phys.*, 1988, **37**, 785–789.

55 S. Ferrero, L. Zamirri, C. Ceccarelli, A. Witzel, A. Rimola and P. Ugliengo, *Astrophys. J.*, 2020, **904**, 11.

56 J. Perrero, J. Enrique-Romero, S. Ferrero, C. Ceccarelli, L. Podio, C. Codella, A. Rimola and P. Ugliengo, *Astrophys. J.*, 2022, **938**, 158.

57 A. Schäfer, H. Horn and R. Ahlrichs, *J. Chem. Phys.*, 1992, **97**, 2571–2577.

58 S. Casassa, P. Ugliengo and C. Pisani, *J. Chem. Phys.*, 1997, **106**, 8030–8040.

59 A. C. A. Boogert, P. A. Gerakines and D. C. B. Whittet, *Annu. Rev. Astron. Astrophys.*, 2015, **53**, 541–581.

60 P. G. Jönsson, *Acta Crystallogr., Sect. B: Struct. Crystallogr. Cryst. Chem.*, 1976, **32**, 232–235.

61 A. G. P. Maloney, P. A. Wood and S. Parsons, *CrystEngComm*, 2014, **16**, 3867–3882.

62 M. Corno and P. Ugliengo, in *Surface Modeling of Ceramic Biomaterials*, ed. B. Bhushan, Springer, Netherlands, Dordrecht, 2014, pp. 1–13.

63 E. Congiu, A. Sow, T. Nguyen, S. Baouche and F. Dulieu, *Rev. Sci. Instrum.*, 2020, **91**, 124504.

64 R. L. Hudson, *Spectrochim. Acta, Part A*, 2017, **187**, 82–86.

65 G. Danger, J.-B. Bossa, P. De Marcellus, F. Borget, F. Duvernay, P. Theulé, T. Chiavassa and L. d'Hendecourt, *Astron. Astrophys.*, 2011, **525**, A30.

66 P. D. Holtom, C. J. Bennett, Y. Osamura, N. J. Mason and R. I. Kaiser, *Astrophys. J.*, 2005, **626**, 940.

67 J. A. Noble, F. Dulieu, E. Congiu and H. J. Fraser, *Astrophys. J.*, 2011, **735**, 121.

68 K. Altwegg, H. Balsiger, A. Bar-Nun, J.-J. Berthelier, A. Bieler, P. Bochsler, C. Briois, U. Calmonte, M. R. Combi and H. Cottin, *et al.*, *Sci. Adv.*, 2016, **2**, e1600285.

69 R. Singh, M. Kumar and S. Pal, *J. Electron Spectrosc. Relat. Phenom.*, 2018, **226**, 22–25.

70 H. Chaabouni, S. Diana, T. Nguyen and F. Dulieu, *Astron. Astrophys.*, 2018, **612**, A47.

71 D. J. Burke, F. Puletti, P. M. Woods, S. Viti, B. Slater and W. A. Brown, *J. Chem. Phys.*, 2015, **143**, 164704.

72 K. I. Öberg and E. A. Bergin, *Phys. Rep.*, 2021, **893**, 1–48.

73 L. Tinacci, A. Germain, S. Pantaleone, C. Ceccarelli, N. Balucani and P. Ugliengo, *Astrophys. J.*, 2023, **951**, 32.

74 J. Enrique-Romero, C. Ceccarelli, A. Rimola, D. Skouteris, N. Balucani and P. Ugliengo, *Astron. Astrophys.*, 2021, **655**, A9.

75 I. W. M. Smith, D. Talbi and E. Herbst, *Astron. Astrophys.*, 2001, **369**, 611–615.

76 T. Nguyen, I. Fourré, C. Favre, C. Barois, E. Congiu, S. Baouche, J.-C. Guillemin, Y. Ellinger and F. Dulieu, *Astron. Astrophys.*, 2019, **628**, A15.

77 J. A. Cardelli, J. S. Mathis, D. C. Ebbets and B. D. Savage, *Astrophys. J., Lett.*, 1993, **402**, L17.

78 D. M. Meyer, M. Jura and J. A. Cardelli, *Astrophys. J.*, 1998, **493**, 222.

79 E. Jenkins, *Astrophys. J.*, 2009, **700**, 1299–1348.

80 R. C. Fortenberry, *J. Phys. Chem. A*, 2024, **128**, 1555–1565.

18222 | *Phys. Chem. Chem. Phys.*, 2024, **26**, 18205–18222

This journal is © the Owner Societies 2024

Part III

Reactivity

Chapter 6

Formation of urea and ethanol on pure H$_2$O ice clusters

Introduction

Complex organic molecules (COMs) are ubiquitous in the ISM and their synthetic pathways are a matter of debate, as discussed in Section 1.2.2. In addition to the two main paradigms proposed for the synthesis of COMs, consisting of networks of gas-phase reactions and of radical-radical couplings occurring on the surface of dust grains, other mechanisms have been proposed in recent years. Around 40% of the species detected in the ISM are COMs, and consequently there is plenty of possible formation mechanisms to be investigated. For this reason, a thorough study requires focussing on a particular process. In this thesis, urea (NH$_2$CONH$_2$) and ethanol (CH$_3$CH$_2$OH) have been the subjects of two investigations aimed at providing details onto their grain-surface synthesis. These species were elected because they are related to prebiotic molecules. Thus, there is interest in knowing the conditions in which they form and whether they can be inherited through the process that culminates in the formation of a planetary system. Urea is characterised by two C−N bonds and is one of the key ingredients required in the synthesis of purines and pirimidines, the building blocks of the nucleotides that constitute both RNA and DNA. Ethanol is also related to prebiotic molecules, as its gas-phase processing can yield glycolaldehyde, from which ethylene glycol, the simplest sugar alcohol, can be obtained.

On the surface of dust grains, 'closed-shell + closed-shell' schemes tipically exhibit a reaction barrier, resulting from the necessity of breaking bonds. Conversely, 'radical + radical' recombination reactions are often considered to be barrierless, due to the absence of such constraints. However, in the latter scheme, diffusion barriers and side reactions may compete with the formation of the product of interest (Enrique-Romero et al., 2022). For this reason, the 'radical + closed-shell' scheme originally proposed for the synthesis of formamide, which involved the reaction of $^\bullet$CN with a water molecule of the ice mantle (Rimola et al., 2018), was applied to the reaction of $^\bullet$CCH + H$_2$O. This pathway, followed by three hydrogenation steps, brings to the formation of ethanol in an almost barrierless fashion, as presented in '*Non-energetic formation of ethanol via CCH reaction with interstellar H$_2$O ices. A computational chemistry study*' (Perrero et al., 2022, *ACS Earth Space Chem.*, **6**, 496).

A slightly different strategy was adopted in '*Synthesis of urea on the surface of interstellar water ice clusters. A quantum chemical study*' (Perrero et al., 2024, *Icarus*, **410**, 115848), where two 'radical + closed-shell' pathways (involving the H$_2$NCO$^\bullet$ and $^\bullet$NH$_2$ radicals) were tested along with other schemes to identify the most promising urea formation mechanism. Additionally, in this case none of the reactants belonged to the modelled mantle
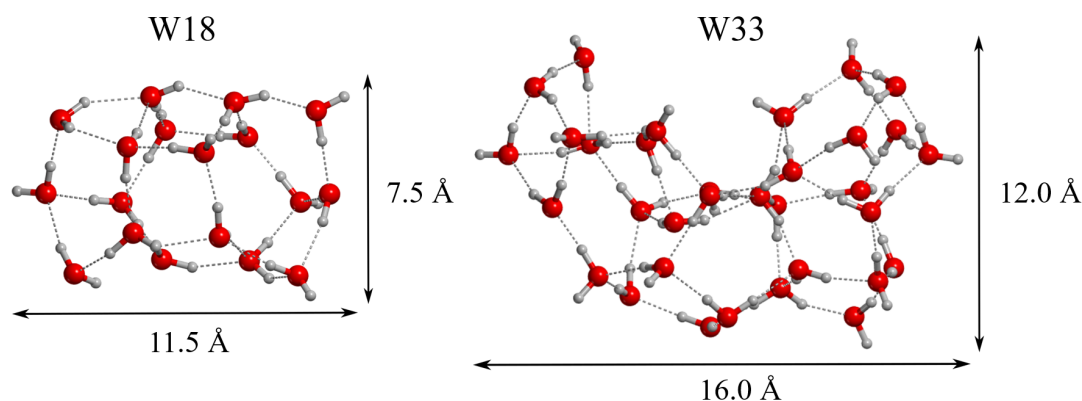
Figure 6.1: Structures of the 18 and 33 water molecules clusters.

structure, in that they were adsorbed on the surface of the model, simulating a Langmuir-Hinshelwood mechanism. The role of the ice surface in each reaction depends on the specific mechanism considered.

Results

In these studies, the ASW ice coating interstellar grains was simulated with two cluster models: W18, representing a compact flat water ice surface, and W33, characterised by the presence of a cavity structure of about 6 Å (see Figure 6.1). Such strategy was adopted to perform the calculations at a high theory level, focussing on the atomistic details of the reactions. The calculations were performed with ORCA 5.0.3 (Neese, 2022, for the formation of urea) and with GAUSSIAN16 (Frisch et al., 2016, for the formation of ethanol).

The few detections of urea in the gas phase (Belloche et al., 2019; Zeng et al., 2023) and its stability against UV irradiation in laboratory experiments (Herrero et al., 2022) suggest that this molecule resides preferably in the grain mantles. Consequently, there is interest in characterising its grain-surface formation. Isocyanic acid, HNCO, and formamide, NH$_2$CHO, which are widely detected species, have been proposed as urea precursors in experimental studies (Raunier et al., 2004; Förstel et al., 2016). From a computational perspective, a number of reaction pathways from formamide to urea was investigated by Slate et al. (2020), while our investigation focusses on the reactivity of isocyanic acid.

The reactions were performed at B3LYP-D3(BJ)/ma-def2-TZVP level of theory, resulting in three main outcomes: i) the assessment of the role of the ice surface in the 'closed-shell + closed-shell' scheme (HNCO + NH$_3$), ii) the evaluation of the probability of salt formation (NH$_4^+$OCN$^-$), and iii) the search for a kinetically favoured grain-surface reaction pathway (H$_2$NCO$^\bullet$ + $^\bullet$NH$_2$). The reliability of the adopted methodology was tested by a gas-phase benchmarking against CCSD(T)-F12 and DLPNO-CCSD(T)-F12 results. Furthermore, the accuracy of the energy barriers obtained for the 'closed-shell + closed-shell' scheme and the salt formation on W18 was determined by comparing DFT results against DLPNO-CCSD(T)-F12 single energy point calculations.

The reaction between HNCO and NH$_3$ was modelled in presence of 0, 1, and 18 water molecules, the latter case represented by the W18 cluster. In the gas phase, the reaction takes place in a concerted fashion and encompasses the formation of a C−N bond simultaneously to a proton transfer from the nitrogen atom of NH$_3$ to that of HNCO, with
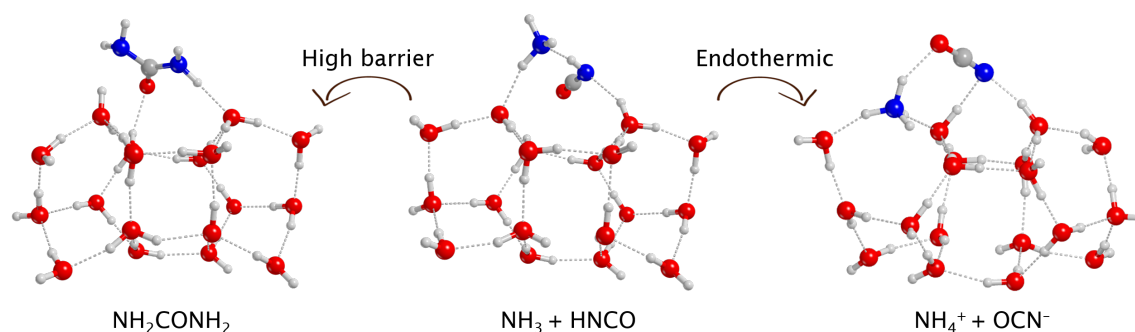
Figure 6.2: Once HNCO and NH$_3$ are adsorbed on the ice, the formation of urea has to overcome a large barrier (~ 100 kJ mol^{-1}, left panel), while their conversion into ammonium cyanate is not thermodynamically favoured (ΔH > 0, right panel).

a barrier of ~ 140 kJ mol^{-1}. The corresponding TS structure is a highly strained four-membered ring that changes to a less hindered six-membered structure when one water molecule is introduced in the reaction. Consequently, thanks to the water molecule that mediates the proton transfer, the barrier reduces to ~ 50 kJ mol^{-1}. The reproduction of the same mechanism on the W18 cluster results in the proton transfer being mediated by four water molecules, linked by the network of H-bonds established in the reactant complex. However, this process is characterised by a reaction barrier of ~ 100 kJ mol^{-1}. The large number of water molecules offered by the surface improves the proton transfer mechanism with respect to the gas-phase process, but the strong interaction (which requires to be weakened to favour reaction) of the adsorbates with the ice appears to be an even greater drawback.

The reaction between the acid HNCO and the basis NH$_3$ on water ice can also yield ammonium cyanate (NH$_4^+$OCN$^-$, represented in Figure 6.2). Previous laboratory experiments and theoretical calculations reported the formation of the ion pair in conditions where solvation effects are at work, as for example in the ice bulk. In this case, the adsorption of HNCO and NH$_3$ does not guarantee enough stabilisation of the ion pair to promote the formation of the salt, which is endothermic and shows a barrier ranging from 19.0 to 29.0 kJ mol^{-1} depending on the number of water molecules involved in the proton transfer.

Finally, the large barrier of the 'closed-shell + closed-shell' scheme on the W18 motivated the search for alternative reaction pathways yielding urea. The 'radical + closed-shell' scheme HNCO + $^\bullet$NH$_2$ (which requires a subsequent hydrogenation step to yield urea) and the 'radical + radical' recombination H$_2$NCO$^\bullet$ + $^\bullet$NH$_2$ were the best candidates. The 'radical + closed-shell' mechanism presents an energy barrier of ~ 80 kJ mol^{-1}, being only slightly more favoured than the 'closed-shell + closed-shell' scheme. Both HNCO and $^\bullet$NH$_2$ are tightly bound to the surface, which in this process assumes the role of reactant supplier and, eventually, third body.

The most promising mechanism to form NH$_2$CONH$_2$ consists of the 'radical + radical' scheme, although it is in competition with a H-abstraction reaction. The formation of urea is favoured over the H-abstraction both kinetically and termodynamically, despite the fact that the orientation of the reactants plays a crucial role in determining the outcome of the reaction. The barrier of approximately 4 kJ mol^{-1} computed for the radical-radical recombination (due to the diffusion of the reactants) corresponds to a half-life time of the reactants of 27 years at T = 10 K, which lowers to 0.03 s at 20 K. This indicates a very fast reaction, whose velocity quickly increases with the temperature (see Figure 6.3). However,
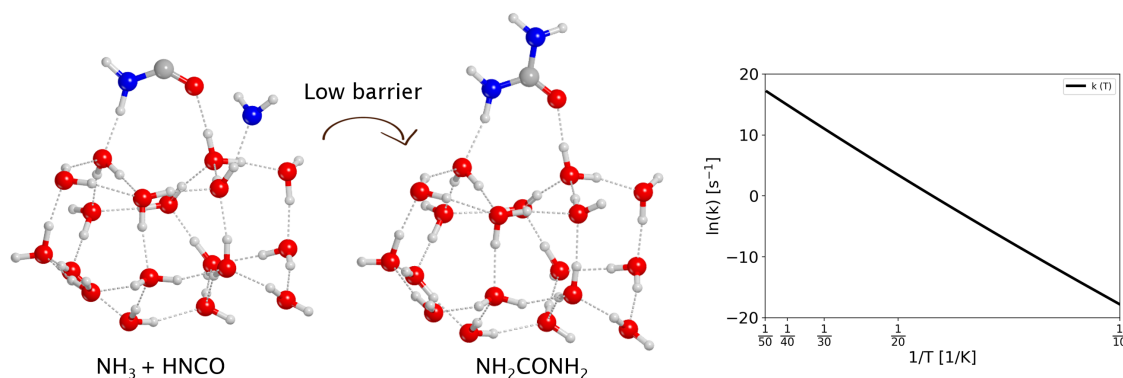
Figure 6.3: The radical-radical recombination of $H_2NCO^{\bullet}$ and $^{\bullet}NH_2$ has a barrier of ~ 4 kJ mol^{-1} and is characterised by fast kinetics at the low temperatures of the ISM (10-20 K).

it must be considered that the H-abstraction reaction leading to HNCO + NH$_3$, despite having a barrier of ~ 20 kJ mol^{-1}, could eventually proceed via tunnelling effect, thus competing with the formation of urea. In the 'radical + radical' reactions, the ice surface assumes the role of a reactant supplier and third body.

In addition to radical-radical recombination reactions, charged pathways also represent a promising mechanism to explain the formation of complex molecules such as urea (Brigiano et al., 2018; Slate et al., 2020; Kerkeni et al., 2023). Their activation barriers are generally lower than those of reactions between closed-shell species, making these pathways feasible in the cold and rarefied environments of the ISM. The presence of an ice surface would be crucial also in this case, especially to provide a third body able to dissipate the energy liberated by the reaction of energetic species such as cations.

In the case of urea formation, the 'radical + closed-shell' scheme is kinetically impeded, while the 'radical + radical' recombination competes with a side reaction. In general, the latter scheme has an additional limitation: the reactions can only occur in the coupling temperature window, resulting from the delicate trade-off between the diffusion and the desorption of the radicals on the ice surface (Enrique-Romero et al., 2021).

Conversely, in the synthesis of ethanol, the $^{\bullet}CCH + H_2O$ reaction represents a particular case in which the 'radical + closed-shell' scheme yields the almost barrierless formation of a COM. The process was characterised on the W18 and W33 clusters using the DFT functional ωB97X-D3 combined with the 6-311++G(d,p) basis set to optimise the structures and with the 6-311++G(2df,2pd) basis set to refine the energies. Both the binding energies and the reaction barriers were benchmarked against CCSD(T)/aug-cc-pVTZ level of theory.

The BE values computed for the adsorption of $^{\bullet}CCH$ on W18 are 23.7, 37.9, and 49.9 kJ mol^{-1}. Each value is representative of a particular interaction, the first corresponding to an adsorption complex in which $^{\bullet}CCH$ establishes two H-bonds with W18, the second and the third relative to complexes in which the $^{\bullet}CCH$ interacts with water through a hemibond. This particular interaction, which takes place between two centres (a carbon and an oxygen atom) and three electrons (the unpaired electron of $^{\bullet}CCH$ and a pair of electrons of the O atom of water), is the key towards the formation of COMs.

The adsorption geometry also affects the resulting products: from the H-bonded complex, a H-abstraction yields HCCH + $^{\bullet}OH$ barrierlessly (R1 in Figure 6.4), whereas the hemibonded complex promotes the formation of a C$-$O bond followed by a H-transfer step along the H-bonds network involving 1 to 4 extra water molecules, similarly to what
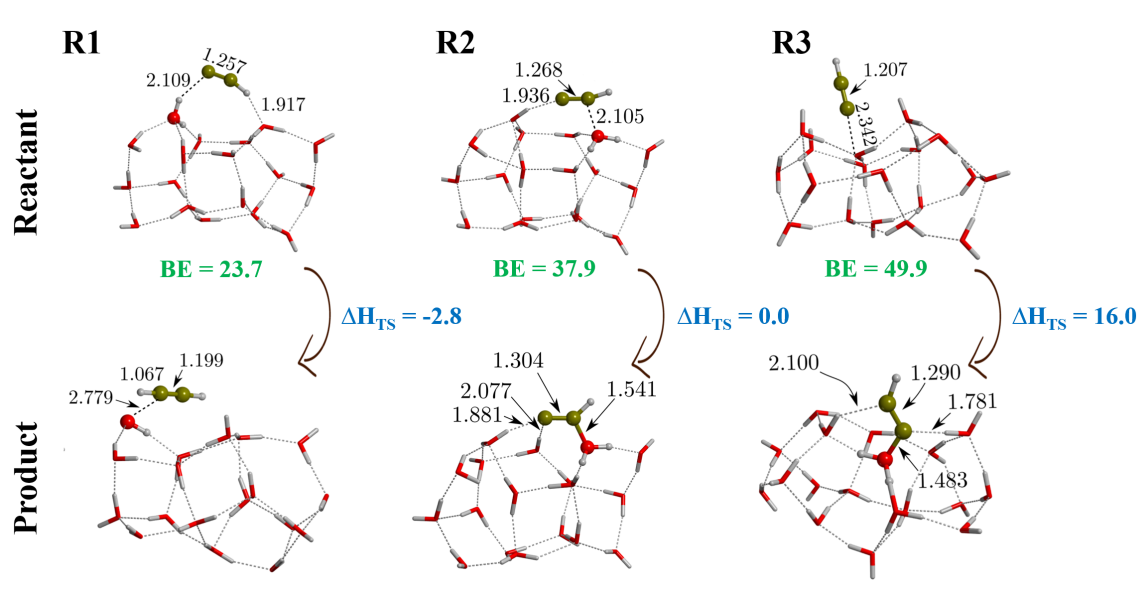
Figure 6.4: The products formed as a consequence of the different adsorption geometries of •CCH onto W18. ΔH_{TS} corresponds to the ZPE-corrected ΔE_{TS}, where a $\Delta E_{TS} > 0$ allowed for the identification of the TS structure.

has been described in the formation of urea (R2 and R3 in Figure 6.4). The reaction on the central carbon atom of •CCH is the most favourable one, as the coordination sphere of the reacting water molecule is not affected by the formation of the C−O bond. Additionally, the successive H-transfer step is also barrierless, therefore representing an entirely non-energetic pathway to form •HCCHOH, the precursor of vinyl alcohol.

From •HCCHOH to CH_3CH_2OH, three hydrogenation steps are required. The first and the third fall in the category of radical-radical recombination reactions involving a hydrogen atom, which can easily diffuse on the ice surface and react in a barrierless fashion. However, the second hydrogenation step, $H_2CCHOH + H^\bullet$, is a 'radical + closed-shell' reaction, whose energy barrier was computed with the same basis sets as the previous reaction steps, combined with the MPWB1K-D3(BJ) functional. Depending on which carbon atom of the vinyl alcohol (H_2CCHOH) is hydrogenated, the process presents $\Delta H_{TS} = 7-15 \text{ kJ mol}^{-1}$. The calculated quantum tunnelling crossover temperature associated with the two barriers is situated between 118 and 174 K, indicating that tunnelling effect may play a role in this reaction. Vinyl alcohol could also isomerise into acetaldehyde, which is the thermodynamically favoured product. The tautomerization involves a H-transfer through a H-bonds network which extends over four water molecules, characterised by $\Delta H_{TS} = 60-75 \text{ kJ mol}^{-1}$. Despite the hydrogenation reaction being more probable, this path cannot be completely excluded due to quantum tunnelling effects.

In conclusion, the hemibond interaction (for the C−O bond formation) and quantum tunnelling effects (for the hydrogenation steps) are the two fundamental ingredients to promote the non-energetic formation of ethanol on the ice mantle of dust grains. The comparison of the reaction mechanisms taking place on W18 and W33 demonstrates that the effect of the cavity is almost insignificant for the energetics of the path, which follows the same steps as for the W18 cluster. Our findings complement and furnish atomistic details of the synthetic routes explored in the experiments, where C_2H_2/H_2O ices need to be processed to trigger reactivity, probably to generate reactive radical species (e.g.,
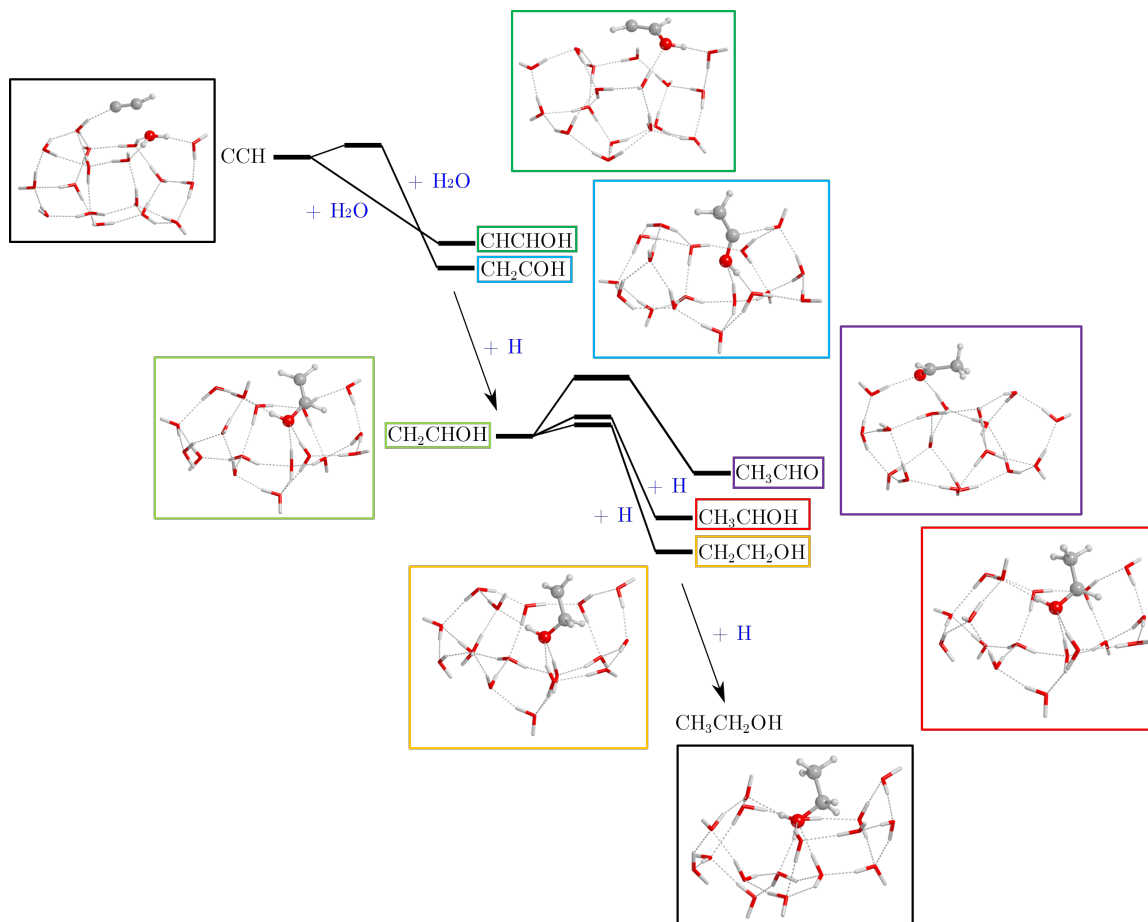
Figure 6.5: The sequence of reactions linking •CCH to CH₃CH₂OH involves the formation of a hemibonded complex which promotes the barrierless formation of a C-O bond, followed by three hydrogenation steps that go through the formation of vinyl alcohol, an isomer of acetaldehyde. However, the isomerization process is less favoured than the subsequent hydrogenation. Ethanol can therefore be produced in a non-energetic way on the icy mantles coating dust grains.

Hudson et al., 2013; Chuang et al., 2021). This mechanism provides an explanation for the presence of ethanol in the coldest regions of the ISM and also as a component of the ices (McClure et al., 2023; Rocha et al., 2024), although its desorption remains a missing step linking the presence of ethanol in both solid and gas phase.

Future perspectives

For a few years, radical-radical recombination reactions have been seen as the optimal explanation for the formation of COMs on the cold icy mantles covering the dust grains of dense clouds. However, it is now well established that these processes are also characterised by energy barriers, primarily as a consequence of the requirement of the radicals to diffuse across the surface in order to meet and react with each other. In a water-dominated ice mantle, polar species are mostly affected by diffusion barriers, as these depend on the interaction energy of the species with the surface. Several alternatives have been proposed, yet the chemistry of cold environments continues to present significant challenges not only for the formation but also for the desorption of COMs. The search for promising COMs reaction mechanisms has been extended to the reaction of single atoms and charged

species (e.g. Ferrero et al., 2023; Jayaweera et al., 2024).

There are several issues regarding the chemistry of the ISM, in particular of COMs formation, that yet require an explanation. Intersystem crossing processes, which allow species to jump between stationary and low-lying excited states, are an interesting phenomenon that may explain part of the chemical complexity of the ISM. Furthermore, a deeper understanding of non-thermal desorption processes could also shed light on the substantial presence of COMs in the gas phase. Thanks to the continuous improvement of both experimental and computational techniques, the number of studies focussing on these topics is constantly increasing, as it is the number of COMs detected in the ISM, providing an endless source of new challenges.

References

Belloche, A. et al. (2019). "Re-exploring molecular complexity with ALMA (ReMoCA): interstellar detection of urea". *Astron. Astrophys.* **628**, A10. DOI: `10.1051/0004-6361/201935428`.

Brigiano, F. S. et al. (2018). "The formation of urea in space - I. Ion-molecule, neutral-neutral, and radical gas-phase reactions". *Astron. Astrophys.* **610**, A26. DOI: `10.1051/0004-6361/201731610`.

Chuang, K.-J. et al. (2021). "Formation of complex organic molecules in molecular clouds: acetaldehyde, vinyl alcohol, ketene, and ethanol via the 'energetic' processing of C_2H_2 ice". *Astron. Astrophys.* **650**, A85. DOI: `10.1051/0004-6361/202140780`.

Enrique-Romero, J. et al. (2021). "Theoretical computations on the efficiency of acetaldehyde formation on interstellar icy grains". *Astron. Astrophys.* **655**, A9. DOI: `10.1051/0004-6361/202141531`.

Enrique-Romero, J. et al. (2022). "Quantum mechanical simulations of the radical–radical chemistry on icy surfaces". *Astrophys. J. Suppl. Ser.* **259**, 39. DOI: `10.3847/1538-4365/ac480e`.

Ferrero, S. et al. (2023). "Formation of complex organic molecules on interstellar CO ices? Insights from computational chemistry simulations". *Astrophys. J.* **951**, 150. DOI: `10.3847/1538-4357/acd192`.

Förstel, M. et al. (2016). "Synthesis of urea in cometary model ices and implications for Comet 67P/Churyumov–Gerasimenko". *Chem. Commun.* **52** (4), 741. DOI: `10.1039/C5CC07635H`.

Frisch, M. J. et al. (2016). *Gaussian16 Revision C.01*. Gaussian Inc. Wallingford CT.

Herrero, V. J. et al. (2022). "Stability of urea in astrophysical ices. A laboratory study of VUV irradiation and high-energy electron bombardment". *Mon. Not. R. Astron. Soc.* **517**, 1058. DOI: `10.1093/mnras/stac2658`.

Hudson, R. L. et al. (2013). "Ketene formation in interstellar ices: a laboratory study". *Astrophys. J.* **773**, 109. DOI: `10.1088/0004-637X/773/2/109`.

Jayaweera, A. P. et al. (2024). "On the mechanism and quantum tunneling of the CO_2 + OH anion reaction in ice: a computational study". *ACS Earth Space Chem.*, accepted. DOI: `10.1021/acsearthspacechem.4c00073`.

Kerkeni, B. et al. (2023). "Peptide bonds in the interstellar medium: facile catalytic formation from nitriles on water–ice grains". *J. Phys. Chem. A* **127**, 5382. DOI: `10.1021/acs.jpca.3c00719`.

McClure, M. K. et al. (2023). "An Ice Age JWST inventory of dense molecular cloud ices". *Nat. Astron.* **7**, 431. DOI: `10.1038/s41550-022-01875-w`.

Neese, F. (2022). "Software update: The ORCA program system-version 5.0". *Wiley Interdiscip. Rev. Comput. Mol. Sci.* **12**, e1606. DOI: 10.1002/wcms.1606.

Perrero, J. et al. (2024). "Synthesis of urea on the surface of interstellar water ice clusters. A quantum chemical study". *Icarus* **410**, 115848. DOI: 10.1016/j.icarus.2023.115848.

Perrero, J. et al. (2022). "Non-energetic formation of ethanol via CCH reaction with interstellar H$_2$O ices. A computational chemistry study". *ACS Earth Space Chem.* **6**, 496. DOI: 10.1021/acsearthspacechem.1c00369.

Raunier, S. et al. (2004). "Tentative identification of urea and formamide in ISO-SWS infrared spectra of interstellar ices". *Astron. Astrophys.* **416**, 165. DOI: 10.1051/0004-6361:20034558.

Rimola, A. et al. (2018). "Can formamide be formed on interstellar ice? An atomistic perspective". *ACS Earth Space Chem.* **2**, 720. DOI: 10.1021/acsearthspacechem.7b00156.

Rocha, W. et al. (2024). "JWST Observations of Young protoStars (JOYS+): Detecting icy complex organic molecules and ions - I. CH$_4$, SO$_2$, HCOO$^-$, OCN$^-$, H$_2$CO, HCOOH, CH$_3$CH$_2$OH, CH$_3$CHO, CH$_3$OCHO, and CH$_3$COOH". *Astron. Astrophys.* **683**, A124. DOI: 10.1051/0004-6361/202348427.

Slate, E. C. S. et al. (2020). "Computational studies into urea formation in the interstellar medium". *Mon. Not. R. Astron. Soc.* **497**, 5413. DOI: 10.1093/mnras/staa2436.

Zeng, S. et al. (2023). "Amides inventory towards the G+0.693-0.027 molecular cloud". *Mon. Not. R. Astron. Soc.* **523**, 1448. DOI: 10.1093/mnras/stad1478.
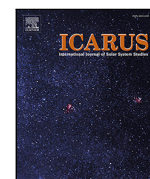
Synthesis of urea on the surface of interstellar water ice clusters. A quantum chemical study

J. Perrero [a,b,*], A. Rimola [a,*]

[a] *Departament de Química, Universitat Autònoma de Barcelona, Bellaterra, 08193, Catalonia, Spain*
[b] *Dipartimento di Chimica and Nanostructured Interfaces and Surfaces (NIS) Centre, Università degli Studi di Torino, Torino, 10125, Italy*

ARTICLE INFO

ABSTRACT

Urea is a prebiotic molecule that has been detected in few sources of the interstellar medium (ISM) and in Murchison meteorite. Being stable against ultraviolet radiation and high-energy electron bombardment, urea is expected to be present in interstellar ices. Theoretical and experimental studies suggest that isocyanic acid (HNCO) and formamide (NH_2CHO) are possible precursors of urea. However, uncertainties still exist regarding its formation routes. Previous computational works characterised urea formation in the gas phase or in presence of few water molecules by reaction of formamide with nitrogen-bearing species. In this work, we investigated the reaction of $HNCO + NH_3$ on an 18 water molecules ice cluster model mimicking interstellar ice mantles by means of quantum chemical computations. We characterised different mechanisms involving both closed-shell and open-shell species at B3LYP-D3(BJ)/ma-def2-TZVP level of theory, in which the radical–radical $H_2NCO + NH_2$ coupling has been found to be the most favourable one due to being almost barrierless. In this path, the presence of the icy surfaces is crucial for acting as reactant concentrators/suppliers, as well as third bodies able to dissipate the energy liberated during the urea formation.

1. Introduction

Nowadays, about 300 gas-phase molecules have been detected in the interstellar medium (ISM), out of which a few are amides, e.g., formamide, acetamide, N-methylformamide or urea (Belloche et al., 2017; Müller et al., 2001; Ligterink et al., 2022; Zeng et al., 2023). The latter has the particularity to possess two C–N bonds and is one of the key ingredients required in the synthesis of purines and pirimidines (Robertson and Miller, 1995; Becker et al., 2019; Menor Salván et al., 2020). These nucleobases are the building blocks of the nucleotides that constitute both the RNA and the DNA (Kolb, 2014). These characteristics make urea one of the key species in the field of astrochemistry and origin of life studies.

Urea, NH_2CONH_2, was first detected in the Murchinson meteorite (Hayatsu et al., 1975), and more recently it was observed towards Sagittarius B2(N1) by Belloche et al. (2019), towards G+0.693-0.027 giant molecular cloud by both Jiménez-Serra et al. (2020) and Zeng et al. (2023), and tentatively detected by Raunier et al. (2004a) in NGC 7538 IRS9 and by Remijan et al. (2014) in Sagittarius B2(N-LMH). However, observations dedicated to determine the inventory of interstellar amides towards the class 0 protostar SMM1-a in Serpens cloud (Ligterink et al., 2022) did not report the presence of urea.

Laboratory experiments carried out by Herrero et al. (2022) on the irradiation of NH_2CONH_2 and NH_2CONH_2:H_2O ices show that urea is stable against ultraviolet irradiation and high-energy electron bombardment in cold molecular clouds and hot cores, thereby suggesting that grain mantles could be a reservoir of urea in the ISM.

Despite the numerous studies on its synthetic pathways, there are still uncertainties regarding urea formation in the ISM. Previous experimental and theoretical investigations have proposed two precursors of urea: isocyanic acid, HNCO, and formamide, NH_2CHO.

HNCO can be considered a molecule of prebiotic interest and it was first detected in 1972 in the ISM (Snyder and Buhl, 1972), in cometary comae (Winnewisser and Kramer, 1999), and in external galaxies (Nguyen-Q-Rieu et al., 1991). Jiménez-Escobar et al. (2014) obtained solid HNCO by UV irradiation of H_2O:NH_3:CO and H_2O:HCN ice mixtures. A successive experimental study of Nourry et al. (2015) suggested that the reaction of N + CO on water icy mantles could be responsible for its production. Alternatively, in translucent and dense clouds, HNCO (together with NH_3) was proposed to be produced by co-deposition of N, H and CO (Fedoseev et al., 2014).

HNCO was first proposed as a urea precursor by Raunier et al. (2004a), in which vacuum ultraviolet irradiation of pure HNCO ice at 10 K produced ammonium cyanate ($NH_4^+OCN^-$), formamide and

* Corresponding authors at: Departament de Química, Universitat Autònoma de Barcelona, Bellaterra, 08193, Catalonia, Spain.
E-mail addresses: jessica.perrero@uab.cat (J. Perrero), albert.rimola@uab.cat (A. Rimola).

urea. The formation of ammonium cyanate can possess an activation barrier or be spontaneous depending on the chemical environment of the reactants. While Raunier et al. (2003) described the spontaneous deprotonation of HNCO embedded in NH_3/H_2O ice mixtures, Mispelaer et al. (2012) observed that thermal processing of $HNCO:NH_3$ ices is necessary to overcome the small barrier of the acid–base reaction. Nevertheless, the deprotonation of isocyanic acid could explain why it has never been detected in icy mantles, while the OCN^- feature has been documented (Boogert et al., 2015; McClure et al., 2023).

Another hypothesis postulates formamide as a precursor of urea (Förstel et al., 2016), in which the irradiation of $NH_3:CO$ ices first forms formamide and then urea. Meijer et al. (2019) and Slate et al. (2020) characterised by means of computational chemistry calculations the mechanisms proposed in Förstel et al. (2016). The calculations showed that the concerted reaction between formamide and ammonia, as well as the two reactions obtained by converting one of the reactants into a radical, are not feasible under ISM conditions. Thus, an alternative set of reactions involving radicals and charged species was proposed, both in the gas phase and in the presence of very few (e.g., three) water molecules as minimal cluster models mimicking an ice mantle. These pathways show no or very low barriers. Another set of reactions involving formamide was characterised by Brigiano et al. (2018), who studied several pathways to form urea in the gas phase. The majority of them possess high activation barriers, hence being unfeasible in the ISM. In this work, again, charged species provided a solution to the lack of energy input of the ISM, with $HCONH_2 + NH_2OH_2^+$ being the most favourable reaction.

Given the presence of a thorough computational study on formamide reactions, in this work we investigated the reactivity of HNCO and derivatives, focussing in particular on the effect that ice mantles can have on their reactions. Icy grains can play multiple roles in astrochemical reactions: (i) they can act as a chemical catalyst, reducing energy barriers and accelerating reactions (Potapov and McCoustra, 2021), (ii) they can serve as reactant concentrators and even suppliers, and (iii) they can exert the third body effect, dissipating the energy released by exothermic processes, hence stabilising the products formed (e.g., Pantaleone et al., 2020, 2021; Ferrero et al., 2023). The presence of the ice surface can be crucial for the positive outcome of a reaction which, otherwise, would be unfeasible in the gas phase. For example, in previous theoretical works by us, we investigated the reactivity of a radical (CN and CCH) with a component of the ice mantle (H_2O), resulting in the synthesis of formamide and ethanol with small or no barriers (Rimola et al., 2018; Perrero et al., 2022).

In the present work, we modelled different synthetic routes for urea formation using HNCO as reactant (instead of NH_2CHO, the main reactant in previous theoretical works), by simulating different processes on the surface of an 18 H_2O molecules cluster, a robust model to mimic interstellar water ice surfaces for chemical reactions (Zamirri et al., 2019; Rimola et al., 2020).

We first considered the reactivity between HNCO and NH_3 (closed-shell/closed-shell reaction), that is:

$$HNCO + NH_3 \longrightarrow NH_2CONH_2 \tag{1}$$

However, this reaction has a competitive channel, the formation of the $NH_4^+OCN^-$ ion pair by proton transfer from HNCO to NH_3:

$$HNCO + NH_3 \longrightarrow NH_4^+OCN^- \tag{2}$$

The formation of the ion pair cannot be overlooked given that it can be favoured by the presence of the water ice surfaces, because of the ability of water to stabilise charged species.

As a second possible channel for the formation of urea, we also simulated the reactivity of HNCO with NH_2 (closed-shell/radical reaction), giving $NHCONH_2$ (an urea radical precursor), whose successive hydrogenation yields the actual urea molecule:

$$HNCO + NH_2 \longrightarrow NHCONH_2 \tag{3}$$

$$NHCONH_2 + H \longrightarrow NH_2CONH_2 \tag{4}$$

Finally, we considered a third route, the radical–radical reaction between H_2NCO and NH_2. However, this can have two outcomes, depending on the orientation of the reactants: direct formation of urea (for which we also computed the kinetics) or formation of HNCO and NH_3 by direct H-transfer from H_2NCO to NH_2. That is:

$$H_2NCO + NH_2 \longrightarrow NH_2CONH_2 \tag{5}$$

$$H_2NCO + NH_2 \longrightarrow NH_3 + HNCO \tag{6}$$

In this work, we present the results obtained for the simulation of these reactions by means of quantum chemical calculations.

2. Methods

All calculations were performed with the ORCA (v.5.0.3) programme suite (Neese, 2022). We ran geometry optimisations and frequency calculations with the hybrid DFT functional B3LYP (Lee et al., 1988; Becke, 1988, 1993) including the Grimme's D3 empirical correction using the Becke–Johnson (BJ) damping scheme (Grimme et al., 2010, 2011) and combined with the ma-def2-TZVP basis set (Zheng et al., 2011).

We identified the reactants and the products of each reaction, and, if necessary, the transition states through to the nudged elastic band (NEB) method. Frequency calculations were carried out to confirm the nature of the stationary points, namely, reactants and products as minima and transition states as first-order saddle points of the potential energy surfaces. B3LYP-D3(BJ)/ma-def2-TZVP potential energies were corrected with the vibrational zero-point energy (ZPE) term for each stationary point, thus obtaining enthalpy variations at 0 K according to the equation, e.g., for energy barriers, $\Delta H_{TS} = \Delta E_{TS} + \Delta ZPE$.

To assess the accuracy of the B3LYP-D3(BJ)/ma-def2-TZVP methodology, we performed single point energy calculations on the optimised structures at a higher level of theory, that is, the 'gold standard' of quantum chemistry CCSD(T) (Raghavachari et al., 1989) with the inclusion of explicitly correlated terms in the wave function to account for electron correlation effects: the so-called CCSD(T)-F12 method (Adler et al., 2007, and references therein). The calculations are performed with a combination of correlation consistent basis sets, in our case cc-pVTZ-F12 as the main basis set, with cc-pVTZ-F12-CABS, aug-cc-pVTZ, and aug-cc-pVQZ/C as auxiliary basis sets. The benchmark has been done for reaction (1) both in the gas phase (i.e., absence of water) and in the presence of one water molecule.

Additionally, to improve the accuracy of the results obtained for the reactions occurring on the cluster model at a feasible computational cost, we used the domain based local pair natural orbital coupled cluster theory with single-, double-, and perturbative triple-excitations, DLPNO-CCSD(T) (Riplinger et al., 2016), to which the same F12 approximation is added (Pavošević et al., 2017). This methodology was applied to the reaction (1) when simulated on the water ice cluster model.

Reactions (3), (4), (5), and (6) involve structures that are open-shell in nature. Thus, the calculations were performed within the unrestricted formalism. For radical–radical reactions, additionally, we used the broken-(spin)-symmetry *ansatz* to correctly describe the open-shell singlet state of the system (Neese, 2004; Abe, 2013), allowing two unpaired electrons with opposite spin to occupy different orbitals, to avoid forcing the recombination between the two radicals. The stability of the wave function so obtained was verified prior to the geometry optimisation step. This methodological strategy was also verified by some of us for the treatment of the electronic structure of biradical systems (Enrique-Romero et al., 2022), including a comparison of the
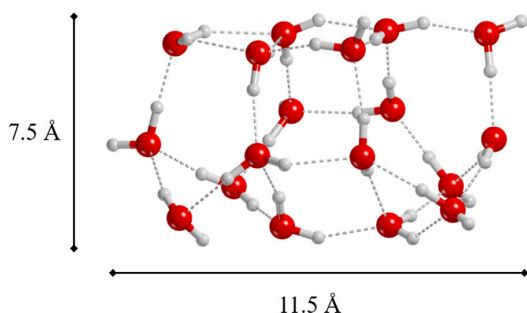
Fig. 1. The 18 water molecules cluster, optimised at the B3LYP-D3(BJ)/ma-def2-TZVP level of theory.

broken symmetry approach with CASPT2 calculations (Enrique-Romero et al., 2020).

The computational requirements needed to perform single point energy calculations at the DLPNO-CCSD(T)-F12 level of theory on open-shell systems exceeded our resources, so they were calculated at the B3LYP-D3(BJ)/ma-def2-TZVP level of theory. However, DLPNO-CCSD(T)-F12 calculations were possible for closed-shell systems (reactions (1) and (2)), and demonstrated the reliability of the DFT methodology.

Additionally, we calculated the unimolecular rate constant and half-life time for reaction (5) using the classical transition state theory, following the Eyring's equation:

$$k(T) = \kappa \frac{k_B T}{h} e^{\frac{-\Delta G\ddagger}{RT}} \qquad (7)$$

where κ is the tunnelling transmission coefficient (which in our case is assumed to be 1 since tunnelling effects are not operative due to the non-participation of light atoms like H but heavy entities), k_B is the Boltzmann constant, T is the temperature, h is the Planck constant, $\Delta G\ddagger$ is the Gibbs free energy barrier (computed at a given temperature) and R is the gas constant. Once obtained the rate constant, one can compute the half-life time of the reactants through the equation $t_{1/2}(T) = ln(2)/k(T)$, which is defined as the time for the reactants to be half consumed.

Finally, our water ice cluster model consists of 18 H₂O molecules (see Fig. 1) and has been used in previous studies by some of us (Rimola et al., 2014, 2018; Enrique-Romero et al., 2019; Perrero et al., 2022). The structure represents a compact, amorphous, and flat water ice surface, whose size is a compromise between a more realistic extended model and one that allows to adopt a high level of theory at a reasonable computational cost.

3. Results and discussion

As mentioned above, we first characterised the reaction between HNCO and NH₃, in the gas phase. Because these molecules are closed-shell, we expect to find a high energy barrier for the formation of urea, which is confirmed by our calculations. The gas-phase reaction between isocyanic acid and ammonia takes place in a concerted fashion and goes through the formation of the C–N bond simultaneously to a proton transfer from the nitrogen atom of NH₃ to that of HNCO (see Fig. 2A). The transition state structure presents a four-membered ring, which is a highly strained geometry, and hence the energy barrier is as high as 136.0 kJ mol⁻¹ (at B3LYP-D3(BJ) level of theory). By introducing one water molecule into the reaction, the transition state structure presents a six-membered ring. This is a geometrically less strained structure because of the participation of the added water molecule in the proton transfer. That is, the water molecule assists the H-transfer by receiving a proton from ammonia and donating one of its protons

to the NH moiety of isocyanic acid (see Fig. 2B). This water-assisted proton transfer mechanism has a large impact on the energy barrier, as it decreases to 46.3 kJ mol⁻¹ (at B3LYP-D3(BJ) theory level).

As mentioned in Section 2, these closed-shell/closed-shell processes have also been used to perform a benchmark study to calibrate the adequacy of the B3LYP-D3(BJ)/ma-def2-TZVP level of theory. The results are summarised in Table 1 and, as can be seen, indicate a very good performance of B3LYP-D3(BJ)/ma-def2-TZVP compared to CCSD(T)-F12. The relative errors of the potential energy barriers at B3LYP-D3(BJ) with respect to CCSD(T)-F12 are 0.6% and 11% in the absence and in the presence of the water assisting molecule, respectively. The energies computed at DLPNO-CCSD(T)-F12 slightly improve the quality reached by B3LYP-D3(BJ), with relative errors of 1% and 3% in absence and in the presence of water with respect to CCSD(T)-F12.

Given the previous results, we simulated the same reaction on the water ice cluster model, since a larger number of water molecules assisting the proton transfer step could reduce the energy barrier even more.

The adsorption geometry of HNCO and NH₃ on the flat surface of the cluster does not seem to point towards the formation of urea, since we found a number of complexes characterised by a H-bond between the hydrogen of HNCO and the nitrogen of NH₃. Most likely, this orientation yields ammonium cyanate, rather than urea. Additionally, we also found some reaction pathways in which the formation of urea occurred without involving the water molecules at the surface, with transition states resembling four-membered ring structures. However, we found a mechanism involving icy water molecules in the proton transfer event similarly to the reaction in the presence of one water molecule (see Fig. 3). Here, to form the C–N bond, a subtle rotation of the HNCO is needed to bring the C atom close to ammonia, and four water molecules participate in the proton transfer, which takes place through the network of H-bonds established in the reactant complex. However, the strong interaction between the reactants and the ice is against the reaction, which presents a barrier of 97.8 kJ mol⁻¹, significantly higher than that obtained in the presence of one water molecule (46.3 kJ mol⁻¹). Therefore, the large number of water molecules offered by the surface improves the proton transfer mechanism with respect to the gas-phase process, but the strong interaction of the adsorbates with the ice seems to be an even greater drawback.

None of the HNCO + NH₃ + ice adsorption complexes yielded the spontaneous formation of the NH₄⁺OCN⁻ ion pair. Furthermore, geometry optimisations considering the ion pair already formed as initial structures evolved towards the formation of HNCO and NH₃, meaning that complexes in which the NH₄⁺ and OCN⁻ ions interact directly are not stable. On the other hand, the water molecules of the ice surface can stabilise the charges of the two isolated ions, due to H-bonds. Therefore, we searched for adsorption geometries in which HNCO and NH₃ were separated by some water molecules to avoid their direct interaction and, at the same time, interact with them, thus favouring the formation and survival of the NH₄⁺OCN⁻ ion pair. We found two structures in which HNCO and NH₃ are separated, by one and two water molecules, respectively (see Fig. 4). Thus, we computed the formation of the ion pair in which the proton transfer takes place through the H₂O molecules that separate HNCO and NH₃. In both cases, the processes are not spontaneous and present a barrier of 19.0 and 28.8 kJ mol⁻¹ when one and two H₂O molecules are involved, respectively. Moreover, the reactions are endothermic and hence the processes are thermodynamically disfavoured.

In relation to the formation of the NH₄⁺OCN⁻ ion pair, several studies are available in the literature. While both Raunier et al. (2003) and Theule et al. (2011) found a barrier for the dissociation process of HNCO in water ice, Raunier et al. (2004b) found that the formation of NH₄⁺OCN⁻ is spontaneous when HNCO is embedded in a mixture of NH₃:H₂O ice, meaning that the formation of the NH₄⁺OCN⁻ ion pair is more favourable than the formation of OCN⁻ in pure water. On the other hand, Mispelaer et al. (2012) studied the formation of NH₄⁺OCN⁻
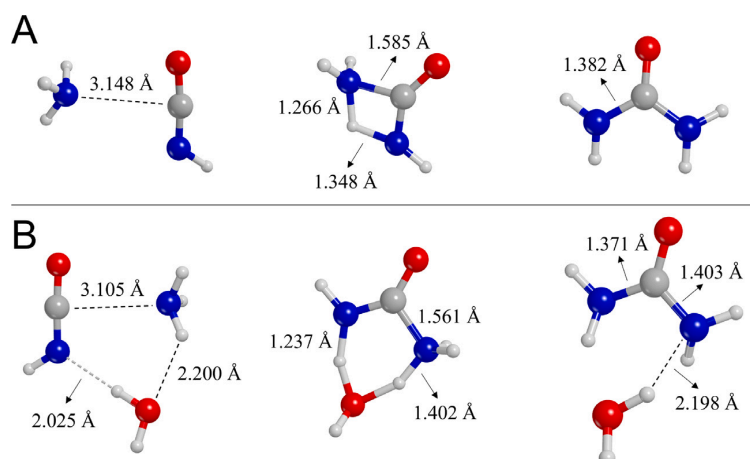
Fig. 2. Structures (from left to right) of reactant, transition state and product for the gas phase reaction in absence (A) and in presence (B) of one water molecule. Structures are optimised at B3LYP-D3(BJ)/ma-def2-TZVP level of theory, bond distances are in Å.

Table 1
Gas phase benchmark. Optimised geometries and the ZPE correction are computed at the B3LYP-D3(BJ)/ma-def2-TZVP level of theory. Energies in kJ mol^{-1}.

HNCO + NH$_3$	Potential energies			Enthalpies		
	B3LYP-D3(BJ)	DLPNO-F12	CCSD(T)-F12	B3LYP-D3(BJ)	DLPNO-F12	CCSD(T)-F12
Reactant	0.0	0.0	0.0	0.0	0.0	0.0
Transition state	136.0	136.5	135.2	140.1	140.6	139.2
Product	−75.9	−80.4	−81.1	−57.9	−62.4	−63.1
HNCO + NH$_3$ + H$_2$O	B3LYP-D3(BJ)	DLPNO-F12	CCSD(T)-F12	B3LYP-D3(BJ)	DLPNO-F12	CCSD(T)-F12
Reactant	0.0	0.0	0.0	0.0	0.0	0.0
Transition state	46.3	53.3	51.9	49.9	56.9	55.5
Product	−75.4	−81.3	−81.8	−58.6	−64.5	−65.0

Fig. 3. B3LYP-D3(BJ) optimised structures for the reactant (left), transition state (centre), and product (right) of the HNCO + NH$_3$ → NH$_2$CONH$_2$ reaction on the water ice cluster model.

by thermally treating a mixture of HNCO and NH$_3$ ice and found a small barrier for the process (0.4 kJ mol^{-1}, in Table 2). From the calculations of Raunier et al. (2004b) it appears that the barrierless ion pair formation is due to the solvation of both HNCO and NH$_3$ on behalf of three or more water molecules. Our results are in line with all these findings, because from previous work it seems clear that the spontaneous formation of the NH$_4^+$OCN$^-$ ion pair can take place in the bulk of the ice, where the number of water molecules interacting with the reactants is larger than those offered by the surface. Indeed, on the latter, the species tend to be adsorbed and do not experience bulk water solvation effects, and accordingly the stabilisation inferred by the surface molecules is not sufficient to guarantee the spontaneous formation of the ion pair.

Interestingly, the reactions studied so far involve closed-shell species, and hence we were able to compute the potential energy

barriers at DLPNO-CCSD(T)-F12 level of theory. By comparing these coupled cluster results with those obtained at B3LYP-D3(BJ) level (see Table 3), we can see that B3LYP-D3(BJ) slightly underestimates the barriers with an average error of about 16%. In view of this fairly agreement between the two methods, we proceeded with the rest of the calculations at the B3LYP-D3(BJ) theory level. The remaining reactions involve open-shell species that increase their computational cost.

We characterised the two proposed alternative pathways involving radical species, in a way similar to Slate et al. (2020), that is, reactions (3) and (5). Considering the enhanced reactivity of radicals, we expect the barriers of these processes to be lower than those involving only the closed-shell species.

Firstly, we characterised reaction (3), which is between HNCO and the NH$_2$ amino radical, yielding NHCONH$_2$. The calculated energy barrier is 78.8 kJ mol^{-1}, only 20 kJ mol^{-1} less than the closed-shell/closed-shell reaction. The reactants are tightly bound (well-stabilised) to the
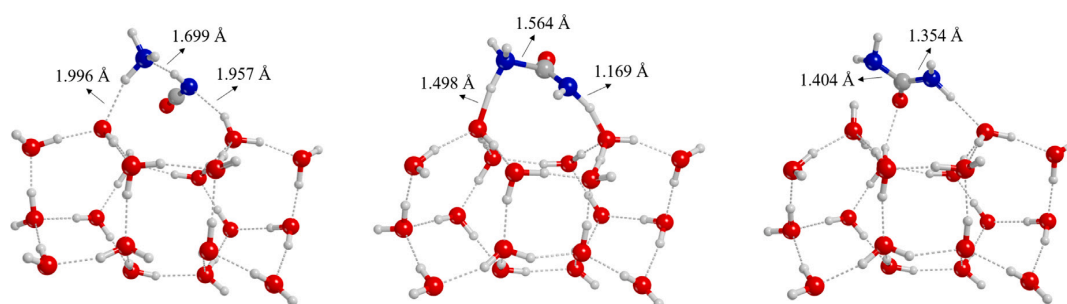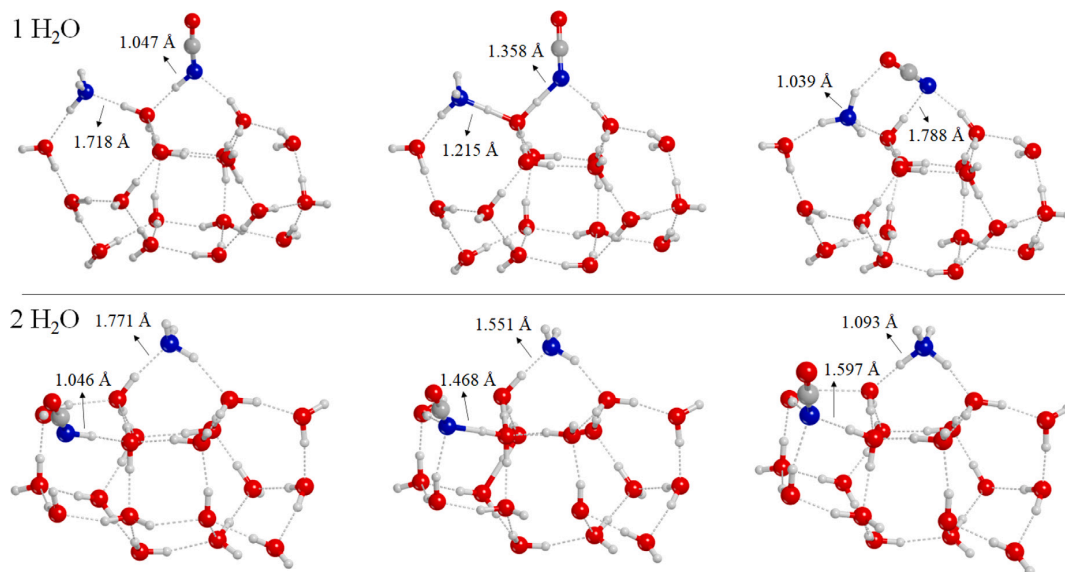
Fig. 4. B3LYP-D3(BJ) optimised structures for the reactant (left), transition state (centre), and product (right) of the HNCO + NH₃ → NH₄⁺OCN⁻ reaction mediated by one (top) and two (bottom) water molecules.

Table 2
Enthalpy variations at 0 K (in kJ mol⁻¹) of the reactions modelled on the water ice cluster at B3LYP-D3(BJ)/ma-def2-TZVP level of theory, compared with literature data. References: (a) Mispelaer et al. (2012), (b) Raunier et al. (2004b), (c) Slate et al. (2020).

Literature	Barrier	Reference	Present work	ΔH_{TS}	ΔH_{prod}
			HNCO + NH₃ → NH₂CONH₂	97.8	−28.8
HNCO + NH₃ $\xrightarrow{\Delta}$ NH₄⁺OCN⁻	0.4	experiments (a)	HNCO + NH₃ $\xrightarrow{1H_2O}$ NH₄⁺OCN⁻	19.0	8.0
HNCO + NH₃ → NH₄⁺OCN⁻ (*)	no	theory (b)	HNCO + NH₃ $\xrightarrow{2H_2O}$ NH₄⁺OCN⁻	28.8	34.5
			HNCO + NH₂ → NHCONH₂	78.8	−21.7
H₂NCO + NH₂ → NH₂CONH₂	4.0	theory (c)	H₂NCO + NH₂ → NH₂CONH₂	3.9	−357.2
			H₂NCO + NH₂ → NH₃ + HNCO	≈ 20.0	−290.9

* The reaction is performed on a 3 H₂O cluster.

Table 3
Potential energy barriers (ΔE_{TS}, in kJ mol⁻¹) of the closed-shell reactions performed on the water ice cluster model. Energies obtained with B3LYP-D3(BJ)/ma-def2-TZVP (DFT) are compared with single point energy calculations at DLPNO-CCSD(T)-F12 (DLPNO) level of theory.

Reaction	DFT	DLPNO
HNCO + NH₃ → NH₂CONH₂	106.4	116.6
HNCO + NH₃ $\xrightarrow{1H_2O}$ NH₄⁺OCN⁻	31.6	39.2
HNCO + NH₃ $\xrightarrow{2H_2O}$ NH₄⁺OCN⁻	40.2	50.8

surface, and hence the energy barrier is prohibitive in the ISM. We also noticed that, in this reaction, no proton transfer takes place, therefore the water ice is uniquely participating as reactant concentrator/supplier and, in view of the released reaction energy (−21.7 kJ mol⁻¹), as energy dissipator. In order to finally form urea, a final H-addition to NHCONH₂ is necessary. This process can be barrierless depending on the orientation of the two partners. If the H atom is not pointing towards the NH moiety, it has to overcome a small diffusion barrier to react, which moreover can occur via quantum tunnelling. In agreement with that, in this final H-addition, by optimising the initial states in the triplet electronic state, we found two different positions for the H atoms (see the yellow- and green-represented H atom in Fig. 5, left panel). When changing to the singlet electronic state, the yellow H atom yielded the product barrierlessly, but this is not the case for the green one. For this case, to assess the energetics of the H-addition, we performed a scan calculation along the N–H distance (Fig. 5, right panel), in which the potential energy is almost constant at a N–H distance between 3 Å and

4 Å (i.e., when the hydrogen atom is approaching the reactive site), and falls down into the potential well at shorter distances, this way forming the product. This indicates that, although the initial state is stable and apparently does not react spontaneously, in practice the hydrogenation reaction evolves towards the formation of urea in a non-energetic way.

Finally, the radical–radical reaction between H₂NCO and NH₂ was investigated. It presents a much lower energy barrier compared to the other two reactions, but it has a competitive channel that yields HNCO + NH₃ through an H-abstraction. The occurrence of one process or the other depends on the geometry of the adsorption complex. This was also found in Enrique-Romero et al. (2022) by studying a well-suited pair of radical–radical couplings forming different interstellar complex organic molecules. From a thermodynamic point of view, reaction (5) is more exothermic than reaction (6). In relation to the energy barriers, we performed scan calculations along the C–N (forming urea) and the H–N (forming HNCO + NH₃) distances to estimate and compare the potential energy profiles of the two reactions. In Fig. 6 we observe that the highest energy point of reaction (5) reaches ≈ 5 kJ mol⁻¹, while for reaction (6) it is located at ≈ 20 kJ mol⁻¹. For the former reaction, we were able to localise the transition state structure, presenting an actual ZPE-corrected energy barrier of 3.9 kJ mol⁻¹. For the latter reaction, any attempt to localise the actual transition state structure failed, probably because of hysteresis effects caused by the high mobility of the H atom. Despite this, the distinguished energy profiles clearly indicate that the radical–radical coupling is, in terms of energy barriers, more favourable than the H-abstraction. Thus, as shown in these results (alongside the thermodynamics), the formation of urea seems to be
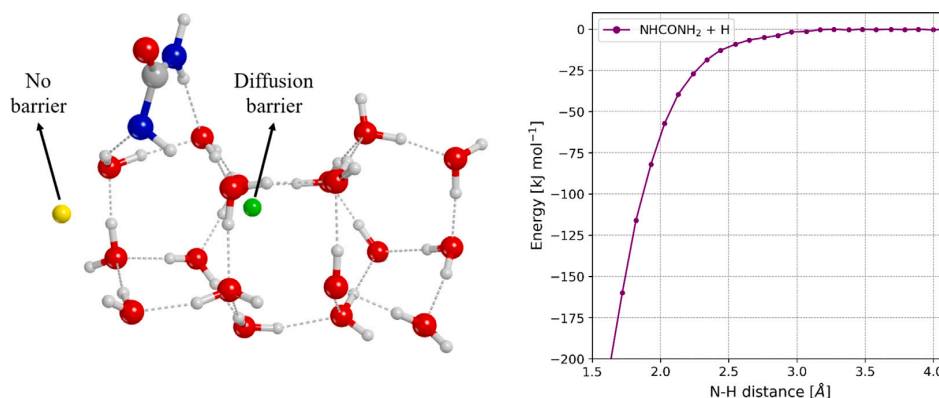
Fig. 5. Left panel: there are two possible initial positions for H atoms (represented as yellow and green atoms) through which the H-addition to NH_2CONH can take place. The yellow position evolves spontaneously to form urea, whereas the green position does not. Right panel: distinguished potential energy profile obtained by scanning the N-H distance from the green-represented H atom. (For interpretation of the references to colour in this figure legend, the reader is referred to the web version of this article.)
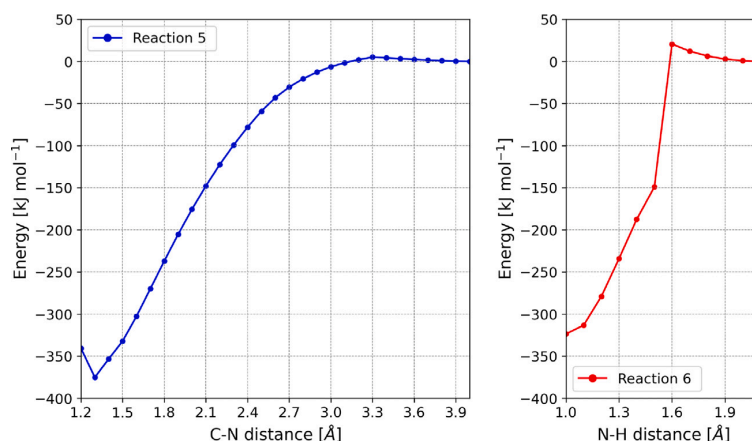

Fig. 6. Scan profile for reactions (5) and (6) in which the energy along the reaction coordinate (the C-N distance in the first case and the N-H distance in the second case) is followed. The reaction that yields $HNCO + NH_3$ (reaction (6)) has a higher barrier to overcome to yield the product with respect to the formation of urea (reaction (5)). (For interpretation of the references to colour in this figure legend, the reader is referred to the web version of this article.)

Table 4
Unimolecular rate constants (in s^{-1}) and half-life times (in s) computed for reaction (5) between 10 and 50 K with the classical Eyring equation.

T (K)	k (s^{-1})	$t_{1/2}$ (s)
10	8.0×10^{-10}	8.6×10^{8}
15	7.5×10^{-3}	9.2×10^{1}
20	2.5×10^{1}	2.8×10^{-2}
25	3.4×10^{3}	2.0×10^{-4}
30	9.5×10^{4}	7.3×10^{-6}
35	1.0×10^{6}	6.6×10^{-7}
40	6.5×10^{6}	1.1×10^{-7}
45	2.7×10^{7}	2.5×10^{-8}
50	8.7×10^{7}	8.0×10^{-9}

the most favourable path through this radical–radical coupling path. However, the H-abstraction can also be facilitated by tunnelling effects so that this competitive channel cannot be totally excluded and should not be overlooked.

In reaction (5), the ice surface does not actively participate in the mechanism, but (as postulated in the closed-shell/radical reaction) it encompasses the role of reactant concentrator/supplier and third body. The radical H_2NCO can be obtained from the reaction of CN

+ H_2O (Rimola et al., 2018), but is also the radical of formamide, as suggested by Slate et al. (2020). In the latter work, the authors found a barrier of 4 kJ mol⁻¹ for reaction (5), which is in agreement with our results (see Table 2). However, the authors also argued that the positive outcome of the reaction depends on the chance of an electronic spin change of the system because the most stable electronic state is the (unreactive) triplet, at variance with the less stable (reactive) singlet. This also holds for our simulations. However, during the long-life time of interstellar molecular clouds, events like photon and/or cosmic ray incidence and thermal/shock waves can indeed induce triplet-to-singlet electronic state changes, this way enabling the occurrence of the radical–radical couplings.

Assuming this, we performed a kinetic study on reaction (5) to know at which temperature the reaction can overcome the ZPE-corrected energy barrier of 3.9 kJ mol⁻¹. We computed the $\Delta G‡$ from 10 to 50 K and we obtained the unimolecular rate constant of the reaction (see Fig. 7), together with the half-life time of the reactants (see Table 4). At a temperature of 10 K, it takes 8.6×10^8 s (corresponding to 27 years) for the reactant to be half consumed, so the reaction is very slow. However, at 20 K the half-life time becomes 0.03 s, indicative of a very fast reaction, which enhances its velocity as the temperature increases. Therefore, we can conclude that a barrier of 3.9 kJ mol⁻¹ does not
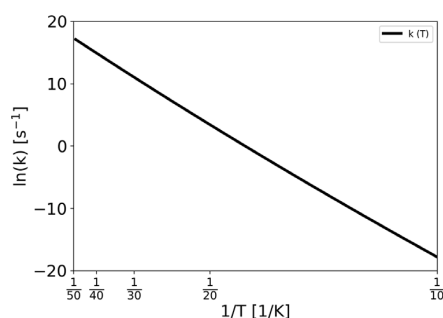
Fig. 7. Arrhenius plot of the rate constant (in s^{-1}) obtained with the classical Eyring equation for reaction (5) between 10 and 50 K..

hamper this reaction under ISM conditions. However, a factor that should be considered is the availability and proximity of the radicals in order to yield the product.

4. Conclusion

In this work, we investigated the formation of urea on an 18 H_2O molecules ice cluster through different chemical reactions that involve both closed-shell and open-shell species. We first characterised the reaction between HNCO and NH_3 (closed-shell/closed-shell) in absence and in presence of one H_2O molecule, with the aim of testing the accuracy of the B3LYP-D3(BJ)/ma-def2-TZVP methodology by comparing it with the reference CCSD(T)-F12. We then characterised the same reaction on the 18 H_2O molecules cluster model, finding that although water ice participates in the proton transfer step necessary to yield urea (hence exerting some catalytic effects), the energy barrier of the process is $\approx$ 100 kJ mol^{-1}, hampering the reaction to take place in the ISM. We also studied a radical/closed-shell (HNCO + NH_2) and a radical–radical (H_2NCO + NH_2) pathways, to assess if they were a more favourable process. We summarise our findings for these open-shell reactions in the following: (i) the radical/closed-shell reaction has an energy barrier of about $\approx$ 80 kJ mol^{-1}, and therefore it can also be discarded in the ISM; (ii) the radical–radical reaction is almost barrierless, but it has a competitive channel (H-abstraction forming HNCO + NH_3) which, however, is characterised by an energy barrier of $\approx$ 20 kJ mol^{-1} (although tunnelling effects can be operative); (iii) in view of the nature of the reactions and their large and negative reaction energies, the role of the icy grains in these reactions is of reactant concentrators/suppliers and energy dissipators. In the closed-shell/closed-shell reaction, the water ice surface participates in the proton transfer, while in the radical/closed-shell and radical–radical reactions it simply binds the reactants. In all reactions, the strong interaction of HNCO and NH_3 with the ice surface can represent an obstacle to the course of the reaction. As some authors suggest (Brigiano et al., 2018; Slate et al., 2020; Kerkeni and Simmie, 2023), in addition to radical–radical reactivity, charged pathways also represent a promising mechanism to explain the formation of complex molecules such as urea. Their activation barriers are generally lower than those of reactions between closed-shell species, making these pathways feasible in the cold and rarefied environments of the ISM. In conclusion, the presence of the ice would be crucial also in this case, especially to provide a third body able to dissipate the energy liberated by the reaction of energetic species like cations.

Declaration of competing interest

The authors declare that they have no known competing financial interests or personal relationships that could have appeared to influence the work reported in this paper.

Data availability

The data underlying this article are freely available in Zenodo at https://doi.org/10.5281/zenodo.8285735.

References

Abe, M., 2013. Diradicals. Chem. Rev. 113, 7011–7088. http://dx.doi.org/10.1021/cr400056a.

Adler, T.B., Knizia, G., Werner, H.J., 2007. A simple and efficient CCSD(T)-F12 approximation. J. Chem. Phys. 127, 221106. http://dx.doi.org/10.1063/1.2817618.

Becke, A.D., 1988. Density-functional exchange-energy approximation with correct asymptotic behavior. Phys. Rev. A 38, 3098–3100. http://dx.doi.org/10.1103/PhysRevA.38.3098.

Becke, A.D., 1993. Density-functional thermochemistry. III. The role of exact exchange. J. Chem. Phys. 98, 5648–5652. http://dx.doi.org/10.1063/1.464913.

Becker, S., Feldmann, J., Wiedemann, S., Okamura, H., Schneider, C., Iwan, K., Crisp, A., Rossa, M., Amatov, T., Carell, T., 2019. Unified prebiotically plausible synthesis of pyrimidine and purine rna ribonucleotides. Science 366, 76–82. http://dx.doi.org/10.1126/science.aax2747.

Belloche, A., Garrod, R.T., Müller, H.S.P., Menten, K.M., Medvedev, I., Thomas, J., Kisiel, Z., 2019. Re-exploring molecular complexity with ALMA (ReMoCA): interstellar detection of urea. Astron. Astrophys. 628, A10. http://dx.doi.org/10.1051/0004-6361/201935428.

Belloche, A., Meshcheryakov, A.A., Garrod, R.T., Ilyushin, V.V., Alekseev, E.A., Motiyenko, R.A., Margulès, L., Müller, H.S.P., Menten, K.M., 2017. Rotational spectroscopy, tentative interstellar detection, and chemical modeling of N-methylformamide. Astron. Astrophys. 601, A49. http://dx.doi.org/10.1051/0004-6361/201629724.

Boogert, A.A., Gerakines, P.A., Whittet, D.C., 2015. Observations of the icy universe. Annu. Rev. Astron. Astrophys. 53, 541–581. http://dx.doi.org/10.1146/annurev-astro-082214-122348.

Brigiano, F.S., Jeanvoine, Y., Largo, A., Spezia, R., 2018. The formation of urea in space - I. Ion-molecule, neutral-neutral, and radical gas-phase reactions. Astron. Astrophys. 610, A26. http://dx.doi.org/10.1051/0004-6361/201731610.

Enrique-Romero, J., Álvarez-Barcia, S., Kolb, F.J., Rimola, A., Ceccarelli, C., Balucani, N., Meisner, J., Ugliengo, P., Lamberts, T., Kästner, J., 2020. Revisiting the reactivity between HCO and CH_3 on interstellar grain surfaces. Mon. Not. R. Astron. Soc. 493, 2523–2527. http://dx.doi.org/10.1093/mnras/staa484.

Enrique-Romero, J., Rimola, A., Ceccarelli, C., Ugliengo, P., Balucani, N., Skouteris, D., 2019. Reactivity of HCO with CH_3 and NH_2 on water ice surfaces. A comprehensive accurate quantum chemistry study. ACS Earth Space Chem. 3, 2158–2170. http://dx.doi.org/10.1021/acsearthspacechem.9b00156.

Enrique-Romero, J., Rimola, A., Ceccarelli, C., Ugliengo, P., Balucani, N., Skouteris, D., 2022. Quantum mechanical simulations of the radical-radical chemistry on icy surfaces. Astrophys. J. Suppl. Ser. 259, 39. http://dx.doi.org/10.3847/1538-4365/ac480e.

Fedoseev, G., Ioppolo, S., Zhao, D., Lamberts, T., Linnartz, H., 2014. Low-temperature surface formation of NH_3 and HNCO: hydrogenation of nitrogen atoms in CO-rich interstellar ice analogues. Mon. Not. R. Astron. Soc. 446, 439–448. http://dx.doi.org/10.1093/mnras/stu2028.

Ferrero, S., Pantaleone, S., Ceccarelli, C., Ugliengo, P., Sodupe, M., Rimola, A., 2023. Where does the energy go during the interstellar NH_3 formation on water ice? A computational study. Astrophys. J. 944, 142. http://dx.doi.org/10.3847/1538-4357/acae8e.

Förstel, M., Maksyutenko, P., Jones, B.M., Sun, B.J., Chang, A.H.H., Kaiser, R.I., 2016. Synthesis of urea in cometary model ices and implications for comet 67P/Churyumov–Gerasimenko. Chem. Commun 52, 741–744. http://dx.doi.org/10.1039/C5CC07635H.

Grimme, S., Antony, J., Ehrlich, S., Krieg, H., 2010. A consistent and accurate ab initio parametrization of density functional dispersion correction (DFT-D) for the 94 elements H-Pu. J. Chem. Phys. 132, 154104. http://dx.doi.org/10.1063/1.3382344.

Grimme, S., Ehrlich, S., Goerigk, L., 2011. Effect of the damping function in dispersion corrected density functional theory. J. Chem. Phys. 32, 1456–1465. http://dx.doi.org/10.1002/jcc.21759.

Hayatsu, R., Studier, M.H., Moore, L.P., Anders, E., 1975. Purines and triazines in the murchison meteorite. Geochim. Cosmochim. Acta 39, 471–488. http://dx.doi.org/10.1016/0016-7037(75)90101-5.

Herrero, V.J., Tanarro, I., Jiménez-Serra, I., Carrascosa, H., Muñoz Caro, G.M., Maté, B., 2022. Stability of urea in astrophysical ices. A laboratory study of VUV irradiation and high-energy electron bombardment. Mon. Not. R. Astron. Soc. 517, 1058–1070. http://dx.doi.org/10.1093/mnras/stac2658.

Jiménez-Escobar, A., Giuliano, B.M., Caro, G.M.M., Cernicharo, J., Marcelino, N., 2014. Investigation of HNCO isomer formation in ice mantles by UV and thermal processing: an experimental approach. Astrophys. J. 788, 19. http://dx.doi.org/10.1088/0004-637X/788/1/19.

Jiménez-Serra, I., Martín-Pintado, J., Rivilla, V.M., Rodríguez-Almeida, L., Alonso Alonso, E.R., Zeng, S., Cocinero, E.J., Martín, S., Requena-Torres, M., Martín-Domenech, R., Testi, L., 2020. Toward the RNA-world in the interstellar medium—Detection of Urea and Search of 2-Amino-oxazole and Simple Sugars. Astrobiology 20, 1048–1066. http://dx.doi.org/10.1089/ast.2019.2125, arXiv:2004.07834.

Kerkeni, B., Simmie, J.M., 2023. Peptide bonds in the interstellar medium: facile catalytic formation from nitriles on water–ice grains. J. Phys. Chem. A 127, 5382–5389. http://dx.doi.org/10.1021/acs.jpca.3c00719.

Kolb, V.M., 2014. Astrobiology: An Evolutionary Approach. CRC Press, Boca Raton, http://dx.doi.org/10.1201/b17348.

Lee, C., Yang, W., Parr, R.G., 1988. Development of the Colle-Salvetti correlation-energy formula into a functional of the electron density. Phys. Rev. B 37, 785–789. http://dx.doi.org/10.1103/PhysRevB.37.785.

Ligterink, N.F.W., Ahmadi, A., Luitel, B., Coutens, A., Calcutt, H., Tychoniec, H., Jørgensen, J.K., Garrod, R.T., Bouwman, J., 2022. The prebiotic molecular inventory of serpens SMM1: II. The building blocks of peptide chains. ACS Earth Space Chem. 6, 455–467. http://dx.doi.org/10.1021/acsearthspacechem.1c00330.

McClure, M.K., Rocha, W., Pontoppidan, K., Crouzet, N., Chu, L.E., Dartois, E., Lamberts, T., Noble, J., Pendleton, Y., Perotti, G., et al., 2023. An ice age JWST inventory of dense molecular cloud ices. Nat. Astron. 7, 431–443. http://dx.doi.org/10.1038/s41550-022-01875-w.

Meijer, A.J.H.M., Slate, E.C.S., Barker, R., Euesden, R.T., Revels, M.R., 2019. On the formation of urea in the ISM. Proc. Int. Astron. Union 15, 363–364. http://dx.doi.org/10.1017/S1743921319007828.

Menor Salván, C., Bouza, M., Fialho, D.M., Burcar, B.T., Fernández, F.M., Hud, N.V., 2020. Prebiotic origin of pre-RNA building blocks in a urea warm little pond scenario. ChemBioChem 21, 3504–3510. http://dx.doi.org/10.1002/cbic.202000510.

Mispelaer, F., Theule, P., Duvernay, F., Roubin, P., Chiavassa, T., 2012. Kinetics of OCN^- formation from the HNCO + NH_3 solid-state thermal reaction. Astron. Astrophys. 540, A40. http://dx.doi.org/10.1051/0004-6361/201117128.

Müller, H.S.P., Thorwirth, S., Roth, D.A., Winnewisser, G., 2001. The cologne database for molecular spectroscopy, CDMS. Astron. Astrophys. 370, L49–L52. http://dx.doi.org/10.1051/0004-6361/20010367.

Neese, F., 2004. Definition of corresponding orbitals and the diradical character in broken symmetry DFT calculations on spin coupled systems. J. Phys. Chem. Solids 65, 781–785. http://dx.doi.org/10.1016/j.jpcs.2003.11.015.

Neese, F., 2022. Software update: the ORCA program system—version 5.0. Wiley Interdiscip. Rev. Comput. Mol. Sci. 12, e1606. http://dx.doi.org/10.1002/wcms.1606.

Nguyen-Q-Rieu, Henkel, C., Jackson, J.M., Mauersberger, R., 1991. Detection of HNCO in external galaxies.. Astron. Astrophys. 241, L33, https://ui.adsabs.harvard.edu/abs/1991A&A.241L.33N.

Nourry, S., Zins, E.L., Krim, L., 2015. Formation of HNCO from carbon monoxide and atomic nitrogen in their fundamental states. Investigation of the reaction pathway in conditions relevant to the interstellar medium. Phys. Chem. Chem. Phys. 17, 2804–2813. http://dx.doi.org/10.1039/C4CP03876B.

Pantaleone, S., Enrique-Romero, J., Ceccarelli, C., Ferrero, S., Balucani, N., Rimola, A., Ugliengo, P., 2021. H_2 formation on interstellar grains and the fate of reaction energy. Astrophys. J. 917, 49. http://dx.doi.org/10.3847/1538-4357/ac0142.

Pantaleone, S., Enrique-Romero, J., Ceccarelli, C., Ugliengo, P., Balucani, N., Rimola, A., 2020. Chemical desorption versus energy dissipation: insights from ab initio molecular dynamics of $HCO^.$ formation. Astrophys. J. 897, 56. http://dx.doi.org/10.3847/1538-4357/ab8a4b.

Pavošević, F., Peng, C., Pinski, P., Riplinger, C., Neese, F., Valeev, E.F., 2017. SparseMaps—A systematic infrastructure for reduced scaling electronic structure methods. V. Linear scaling explicitly correlated coupled-cluster method with pair natural orbitals. J. Chem. Phys. 146, 174108. http://dx.doi.org/10.1063/1.4979993.

Perrero, J., Enrique-Romero, J., Martínez-Bachs, B., Ceccarelli, C., Balucani, N., Ugliengo, P., Rimola, A., 2022. Non-energetic formation of ethanol via CCH reaction with interstellar H_2O ices. A computational chemistry study. ACS Earth Space Chem. 6, 496–511. http://dx.doi.org/10.1021/acsearthspacechem.1c00369.

Potapov, A., McCoustra, M., 2021. Physics and chemistry on the surface of cosmic dust grains: A laboratory view. Int. Rev. Phys. Chem. 40, 299–364. http://dx.doi.org/10.1080/0144235X.2021.1918498.

Raghavachari, K., Trucks, G.W., Pople, J.A., Head-Gordon, M., 1989. A fifth-order perturbation comparison of electron correlation theories. Chem. Phys. Lett. 157, 479–483. http://dx.doi.org/10.1016/S0009-2614(89)87395-6.

Raunier, S., Chiavassa, T., Duvernay, F., Borget, F., Aycard, J.P., Dartois, E., d'Hendecourt, L., 2004a. Tentative identification of urea and formamide in ISO-SWS infrared spectra of interstellar ices. Astron. Astrophys. 416, 165–169. http://dx.doi.org/10.1051/0004-6361:20034558.

Raunier, S., Chiavassa, T., Marinelli, F., Allouche, A., Aycard, J., 2003. Reactivity of HNCO with NH_3 at low temperature monitored by FTIR spectroscopy: formation of $NH_4^+OCN^-$. Chem. Phys. Lett. 368, 594–600. http://dx.doi.org/10.1016/S0009-2614(02)01919-X.

Raunier, S., Chiavassa, T., Marinelli, F., Aycard, J.P., 2004b. Experimental and theoretical study on the spontaneous formation of OCN^- ion: reactivity between HNCO and NH_3/H_2O environment at low temperature. Chem. Phys 302, 259–264. http://dx.doi.org/10.1016/j.chemphys.2004.04.013.

Remijan, A.J., Snyder, L.E., McGuire, B.A., Kuo, H.L., Looney, L.W., Friedel, D.N., Golubiatnikov, G.Y., Lovas, F.J., Ilyushin, V.V., Alekseev, E.A., Dyubko, S.F., McCall, B.J., Hollis, J.M., 2014. Observational results of a multi-telescope campaign in search of interstellar urea $[(NH_2)_2CO]$. Astrophys. J. 783, 77. http://dx.doi.org/10.1088/0004-637X/783/2/77.

Rimola, A., Ferrero, S., Germain, A., Corno, M., Ugliengo, P., 2020. Computational surface modelling of ices and minerals of interstellar interest—insights and perspectives. Minerals 11, 26. http://dx.doi.org/10.3390/min11010026.

Rimola, A., Skouteris, D., Balucani, N., Ceccarelli, C., Enrique-Romero, J., Taquet, V., Ugliengo, P., 2018. Can formamide be formed on interstellar ice? An atomistic perspective. ACS Earth Space Chem. 2, 720–734. http://dx.doi.org/10.1021/acsearthspacechem.7b00156.

Rimola, A., Taquet, V., Ugliengo, P., Balucani, N., Ceccarelli, C., 2014. Combined quantum chemical and modeling study of CO hydrogenation on water ice. Astron. Astrophys. 572, A70. http://dx.doi.org/10.1051/0004-6361/201424046.

Riplinger, C., Pinski, P., Becker, U., Valeev, E.F., Neese, F., 2016. Sparse maps—A systematic infrastructure for reduced-scaling electronic structure methods. II. Linear scaling domain based pair natural orbital coupled cluster theory. J. Chem. Phys. 144, 024109. http://dx.doi.org/10.1063/1.4939030.

Robertson, M.P., Miller, S.L., 1995. An efficient prebiotic synthesis of cytosine and uracil. Nature 375, 772–774. http://dx.doi.org/10.1038/375772a0.

Slate, E.C.S., Barker, R., Euesden, R.T., Revels, M.R., Meijer, A.J.H.M., 2020. Computational studies into urea formation in the interstellar medium. Mon. Not. R. Astron. Soc. 497, 5413–5420. http://dx.doi.org/10.1093/mnras/staa2436.

Snyder, L.E., Buhl, D., 1972. Interstellar isocyanic acid. Astrophys. J. 177 (619), http://dx.doi.org/10.1086/151739.

Theule, P., Duvernay, F., Ilmane, A., Hasegawa, T., Morata, O., Coussan, S., Danger, G., Chiavassa, T., 2011. Kinetics of the OCN^- and HOCN formation from the HNCO + H_2O thermal reaction in interstellar ice analogs. Astron. Astrophys. 530, A96. http://dx.doi.org/10.1051/0004-6361/201016051.

Winnewisser, G., Kramer, C., 1999. Spectroscopy between the stars. Space Sci. Rev. 90, 181–202. http://dx.doi.org/10.1023/A:1005254216488.

Zamirri, L., Ugliengo, P., Ceccarelli, C., Rimola, A., 2019. Quantum mechanical investigations on the formation of complex organic molecules on interstellar ice mantles. Review and perspectives. ACS Earth Space Chem. 3, 1499–1523. http://dx.doi.org/10.1021/acsearthspacechem.9b00082.

Zeng, S., Rivilla, V.M., Jiménez-Serra, I., Colzi, L., Martín-Pintado, J., Tercero, B., de Vicente, P., Martín, S., Requena-Torres, M.A., 2023. Amides inventory towards the G+0.693-0.027 molecular cloud. Mon. Not. R. Astron. Soc. 523, 1448–1463. http://dx.doi.org/10.1093/mnras/stad1478.

Zheng, J., Xu, X., Truhlar, D.G., 2011. Minimally augmented karlsruhe basis sets. Theor. Chem. Acc. 128, 295–305. http://dx.doi.org/10.1007/s00214-010-0846-z.
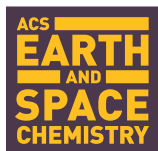
Non-energetic Formation of Ethanol via CCH Reaction with Interstellar H₂O Ices. A Computational Chemistry Study

Jessica Perrero, Joan Enrique-Romero,* Berta Martínez-Bachs, Cecilia Ceccarelli, Nadia Balucani, Piero Ugliengo, and Albert Rimola*

Read Online

ACCESS | Metrics & More | Article Recommendations | Supporting Information

ABSTRACT: Ethanol (CH₃CH₂OH) is a relatively common molecule, often found in star-forming regions. Recent studies suggest that it could be a parent molecule of several so-called interstellar complex organic molecules (iCOMs). However, the formation route of this species remains under debate. In the present work, we study the formation of ethanol through the reaction of CCH with one H₂O molecule belonging to the ice as a test case to investigate the viability of chemical reactions based on a "radical + ice component" scheme as an alternative mechanism for the synthesis of iCOMs, beyond the usual radical–radical coupling. This has been done by means of DFT calculations adopting two clusters of 18 and 33 water molecules as ice models. Results indicate that CH₃CH₂OH can potentially be formed by this proposed reaction mechanism. The reaction of CCH with H₂O on the water ice clusters can be barrierless (because of the help of boundary icy water molecules acting as proton-transfer assistants), leading to the formation of vinyl alcohol precursors (H₂CCOH and CHCHOH). Subsequent hydrogenation of vinyl alcohol yielding ethanol is the only step presenting a low activation energy barrier. We finally discuss the astrophysical implications of these findings.

KEYWORDS: *interstellar medium, astrochemistry, DFT, iCOMs, grains*
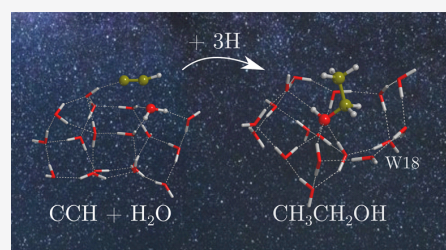
■ INTRODUCTION

Interstellar complex organic molecules (iCOMs) are compounds between 6 and 12/13 atoms, in which at least one is carbon, conferring the organic character.[1−3] These molecules are important because (i) they can be considered as the simplest organic compounds that are synthesized in space (hence representing the dawn of organic chemistry) and (ii) they are the precursors of more complex organic molecules, which can be of biological relevance, such as amino acids, nucleobases, and sugars. Indeed, there is robust evidence that the iCOMs formed in the interstellar medium (ISM) were inherited by small objects of the solar system[4−8] (*e.g.*, carbonaceous chondrites), which upon alteration mechanisms (*e.g.*, hydrothermal) can be converted into more evolved organic species,[9−12] thereby providing a potential contribution to the emergence of life on Earth.

The first detection of iCOMs took place in 1971 in massive star formation regions,[13] but we had to wait for the beginning of this century for detections in regions that could eventually evolve in solar-like planetary systems.[6,14] Currently, complex organic molecules have been detected in different astrophysical environments such as prestellar cores, protostellar outflows, protoplanetary disks, and even external galaxies.[3,8,15−18]

Two different prevailing paradigms have been postulated for the formation of iCOMs: one based on gas-phase reactions[19−24] and the other based on radical−radical couplings

occurring on grain surfaces,[25,26] although other paradigms have been postulated, like those based on the condensation of atomic C,[27,28] excited O atom insertion,[29,30] or the formation of HCO on surfaces as a parent precursor of other iCOMs.[31,32] Both prevailing reaction models have the same initial step: formation of hydrogenated species (*e.g.*, CH₃OH, NH₃, H₂CO, and CH₄) by H-addition on icy grain surfaces in the cold prestellar phase. In the gas-phase paradigm, the process follows with the desorption of these species, either thermally when the grain surface reaches *ca.* 100 K like in hot cores/corinos, nonthermally by photodesorption because of UV incidence on the grains,[33−35] by chemical desorption once they are formed,[36−41] or induced by cosmic rays (CRs).[42−45] In the gas phase they react with other gaseous species forming iCOMs. In the on-grain paradigm, the hydrogenated species act as parent species of molecular radicals (*e.g.*, CH₃, HCO, and NH₂) formed by the irradiation of UV photons and/or energetic ions, partial hydrogenation, and H-abstraction

reactions[2,25,26,46−50] during the cold preprotostellar stage. Later on, these radicals, because of the warm up of the protostar surroundings (*ca.* 30 K), can diffuse on the icy surfaces and encounter each other to couple and form the iCOMs.
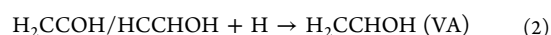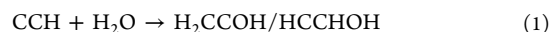
These two reaction paradigms have been largely used in combined observational/astrochemical modeling studies to rationalize the presence of iCOMs in the given sources (*e.g.,* see refs 3 and 51−53). Additionally, they have also been assumed to study the formation of iCOMs by means of quantum chemical simulations.[54−57] By compiling all the available works, it seems that both paradigms are necessary to explain the presence, distribution, and abundance of the wide and rich organic chemistry in the ISM. Thus, knowing whether the formation of an iCOM is dominated by surface or gas-phase chemistry is a case-by-case problem. It depends on the nature of the iCOMs, and each one has to be addressed as a particular case.

With the different quantum chemical studies addressing on-grain radical−radical couplings, some drawbacks of this paradigm have been identified. One is that the chance for the coupling is a delicate trade-off between the diffusion of the radicals and their desorption. That is, the temperature increase that enables the radical diffusion must be lower than their desorption temperatures. This can give rise to a small temperature window in which the coupling can take place, because this *coupling temperature window* is defined by the lowest diffusion temperature and the lower desorption temperature between the two radicals. For instance, in acetaldehyde formation by the coupling of CH$_3$ and HCO, the coupling temperature window was found to be between the temperatures at which CH$_3$ becomes mobile on the surface (between 9 and 15 K, depending on the adopted diffusion barrier) and the temperature at which the methyl radical would desorb (30 K).[55] Another drawback is that radical−radical couplings are often assumed to be barrierless because they are driven by the coupling of the opposite electronic spins of the radicals. However, the reactions can exhibit energy barriers because the radicals, to proceed with the coupling, need to break the interactions with the icy surfaces. Obviously, as a rule of thumb, the stronger the interaction, the higher the energy barrier. A third limitation of this paradigm is that radical−radical couplings can have competitive channels inhibiting the efficiency of the iCOM formation. The competitive reactions are based on H-abstractions from one radical to the other. For instance, the CH$_3$ + HCO coupling can give CH$_3$CHO (acetaldehyde as iCOM) but also CH$_4$ + CO (the H-abstraction product).

In a previous work by some of us,[58] an alternative on-grain mechanism different from the radical−radical coupling was proposed. It is based on the reaction of a radical (coming from the gas phase or generated by UV irradiation) with neutral, entire components of the ice, *i.e.,* H$_2$O and CO as the most abundant components. In that work, this mechanism was tested to form formamide (NH$_2$CHO) through the reaction of the radical CN with a water molecule belonging to the ice, *i.e.,* CN + H$_2$O(ice) → NH$_2$CO, in which the resulting species can be easily hydrogenated to form formamide. This alternative mechanism overcomes the problems of (i) the coupling temperature window (the diffusion of the radical is not needed because it reacts with an abundant ice component, thus increasing the chance of the encountering among the two reactants) and (ii) the competitive channel (they *a priori* do

not present any other possible reaction). However, they present energy barriers because the reaction is between a radical and a neutral closed-shell species.

The present work aims to investigate this alternative on-grain mechanism by simulating with quantum chemical computations the reactivity of the CCH radical with a water molecule of the ice. The goal is to study the possibility of forming ethanol (EtOH), with the formation of vinyl alcohol (VA) as intermediate species, through the following reactions:

$$CCH + H_2O \rightarrow H_2CCOH/HCCHOH \qquad (1)$$

$$H_2CCOH/HCCHOH + H \rightarrow H_2CCHOH \; (VA) \qquad (2)$$

$$H_2CCHOH + 2H \rightarrow CH_3CH_2OH \; (EtOH) \qquad (3)$$

We consider this path toward ethanol because the electronic structure of CCH is isoelectronic with CN, hence exhibiting a similar reactivity with water as shown in Rimola *et al.*[58]

CCH was one of the first interstellar polyatomic molecules to be detected.[59] It is a fundamental and common carbon chain (in fact, the simplest) species in the ISM. It is found in regions near UV sources, the so-called photon dominated regions (PDRs) (*e.g.,* see refs 60 and 61); in diffuse and translucent clouds (*e.g.,* see refs 62 and 63); in protostellar objects;[64,65] and in the cavities of protostellar outflows.[66,67] In addition, CCH has been detected in protoplanetary disks[30,68−71] and external galaxies (*e.g.,* see ref 72) probably in their PDR regions/skins. CCH is also abundant toward the lukewarm (≤40 K) envelopes of the so-called warm carbon chain chemistry (WCCC) objects, which are young class 0/I sources characterized by higher abundances of carbon chains and lower abundances of iCOMs than those observed in hot corinos (see for example ref 65). CCH appears at scales of a few thousand AU around the protostellar center at densities of some 10^6 cm^{-3} (*e.g.,* see ref 73). Particularly relevant to this work, CCH is also relatively abundant in cold molecular clouds (*e.g.,* see refs 74 and 75) and prestellar cores.[76] Typical CCH column densities range from 10^{12}−10^{15} cm^{-2},[61,77] with the greatest values in PDRs.[61] In molecular clouds, the CCH column density is around 10^{14} cm^{-2}, equivalent to abundances of ∼10^{-9}−10^{-8}.[74,75] Similar abundances are found in prestellar cores, as CCH probably resides in the least depleted zone, similar to the molecular clouds.[76,78,79] In summary, CCH is abundant (∼10^{-9}−10^{-8}) in cold (≤20 K) regions where the interstellar dust grains are enveloped by icy mantles. Thus, it is worth investigating the possibility that it interacts with the water molecules of the ice to form ethanol, following the path described above (reactions 1−3).

The reaction of CCH + H$_2$O has been studied as a gas-phase process at high temperatures, both experimentally and theoretically. Seminal experiments by Van Look and Peeters[80] suggested that the outcome of the reaction was not the result of a direct H-abstraction forming HCCH + OH, and hence, the authors proposed a mechanism based on, first, an association between the two reactive partners, forming H$_2$C═CHOH or HC≡CHOH, followed by an elimination giving rise to H$_2$CCO + H and/or HCCH + OH. Subsequent theoretical calculations,[81] however, indicated that among the different reactive channels, the direct H-abstraction was the most kinetically favorable one, in detriment to the association−elimination mechanism. Investigations regarding this reaction ended with a combined experimental/theoretical study carried out by some of the first paper's authors, concluding that the H-
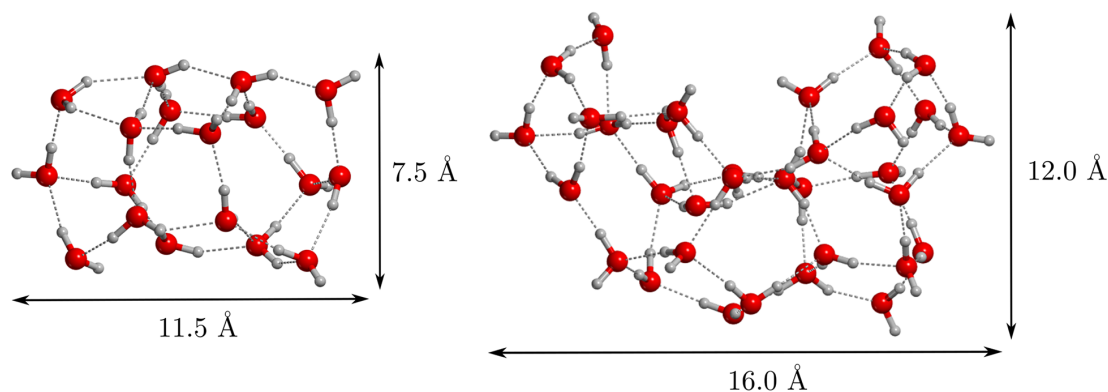
Figure 1. Structures of the 18 and 33 water molecule clusters, optimized at the ωB97X-D3/6-311++G(d,p) level of theory.

abstraction producing HCCH + OH is indeed the most facile chemical reaction.[82]

In contrast, to the best of our knowledge, no experimental works exist on the reactivity of CCH with water ices. However, the addition of OH radicals to C_2H_2 ices (isoelectronic with CCH + H_2O) at temperatures below 20 K, followed by H-additions, has been studied by several authors, resulting in the formation of several products, among them vinyl alcohol and ethanol. This reactivity usually involves an energetic preprocessing of the ice analogues (*i.e.*, irradiation with ions, electrons, and photons) to generate the OH radicals. Among these works, we can find (1) ion radiolysis experiments (MeV protons) that generate mainly CO, CO_2, methanol and ethanol;[83] (2) MeV protons and far UV photon irradiation that yield vinyl alcohol formation;[84] (3) UV irradiation and proton radiolysis of the ices that form vinyl alcohol, acetaldehyde, ketene, and ethanol;[85] (4) ice irradiation with extreme UV photons that leads to the formation of some iCOMs like ethane, methanol, and ethanol, together with some simpler species (*e.g.*, CO, CO_2, and methane);[86] and (5) radiolysis of the C_2H_2:H_2O ices with less energetic protons (200 keV) at 17 K that produce several iCOMs, like vinyl alcohol, acetaldehyde, ketene and ethanol, and some other species, such as C_2H_4, C_2H_6, C_4H_2, and C_4H_4.[87] In this later work, it was proposed that once vinyl alcohol is formed by the attack of an OH radical to C_2H_2, two possible situations may take place: either an intramolecular isomerization step forming acetaldehyde or successive H-additions on vinyl alcohol to form ethanol. More recently, nonenergetic processes have also been explored, in which C_2H_2:O_2 ices exposed to H atoms at 10 K produce most of the products found in Chuang *et al.*,[87] including acetaldehyde, vinyl alcohol, ketene, and ethanol. Other experiments indicate that vinyl alcohol and acetaldehyde can also be formed through other chemical reactions. That is, the O addition to C_2H_2 mainly results in ketene formation,[30,85,88,89] while the O addition to more saturated hydrocarbons (acetylene, ethane, and ethylene) leads to the formation of different iCOMs (ketene, ethanol and acetaldehyde, and acetaldehyde and ethylene oxide, respectively).[30,90]

Ethanol formation has recently received much attention because it has been postulated to be a parent molecule through which other iCOMs can be formed by different gas-phase reactions, such as acetaldehyde, glycolaldehyde, formic acid, acetic acid, and formaldehyde (the so-called genealogical tree of ethanol; see refs 23, 24, and 91). Because of this

significance, this work focuses on the formation of this ancestor molecule following reactions 1−3 on water ice surfaces by means of quantum chemical simulations to determine if they are energetically feasible.

■ METHODOLOGY

All the calculations were based on density functional theory (DFT) and run with the Gaussian16 software package.[92] Geometry optimizations and frequency calculations were all performed by combining the DFT methods with the Pople-based 6-311++G(d,p) basis set.[93,94] These energies were subsequently refined at the 6-311++G(2df,2pd)[95] level by performing single-point energy calculations on the optimized geometries. In order to identify the DFT method that better describes our systems (and hence to use it for the reaction simulations on the water ice surface models), we carried out a preliminary benchmarking study using the CCH + H_2O and CH_2CHOH + H gas-phase reactions as models. Five different hybrid DFT methods were used, which were corrected with Grimme's D3 term or, if possible, with the D3(BJ) version[96−98] to account for dispersion interactions. The tested DFT-D methods were BHLYP-D3(BJ),[99,100] M062X-D3,[101] MPWB1K-D3(BJ),[102] PW6B95-D3(BJ),[103] and ωB97X-D3.[104] By comparing the results with those obtained with single energy points at the CCSD(T)/aug-cc-pVTZ[105] level of theory, known as the "gold-standard" in quantum chemistry, we found that the ωB97X-D3 method showed the best performance when modeling the water addition to CCH, while MPWB1K-D3(BJ) described better the hydrogenation of CH_2CHOH (see Results). Accordingly, the CCH + H_2O and the CH_2CHOH + H reactions on the water ice cluster models were computed at the ωB97X-D3/6-311++G-(2df,2pd)//ωB97X-D3/6-311++G(d,p) and MPWB1K-D3(BJ)/6-311++G(2df,2pd)//MPWB1K-D3(BJ)/6-311++G-(d,p) theory levels, respectively.

All the stationary points of the potential energy surfaces (PESs) were characterized by their analytical calculation of the harmonic frequencies as minima (reactants, products, and intermediates) and saddle points (transition states). When needed, intrinsic reaction coordinate (IRC) calculations at the level of theory adopted in the geometry optimizations were carried out to ensure that a given transition state actually connects with the corresponding minima. Thermochemical corrections to the potential energy values were carried out using the standard rigid rotor/harmonic oscillator formulas to
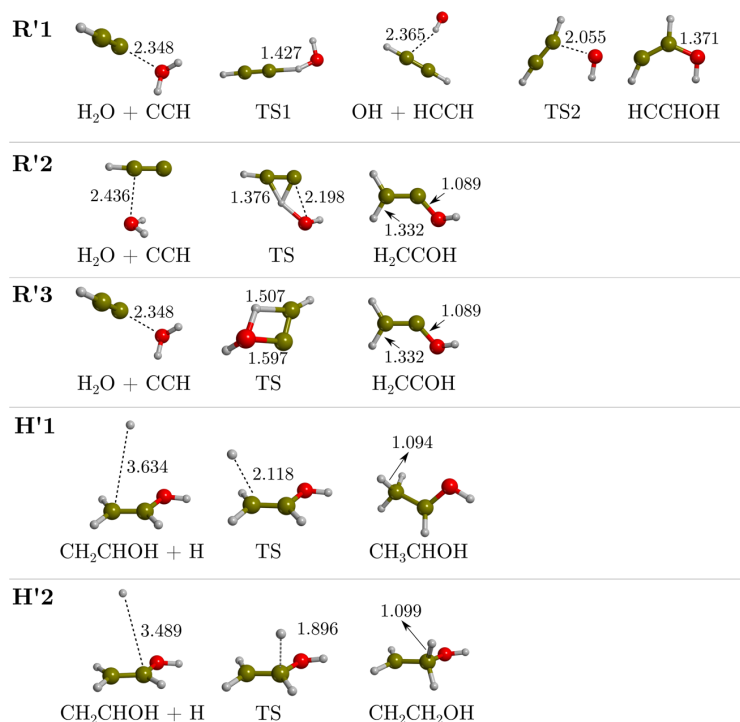
Figure 2. Stationary points identified in the benchmarking study. Reaction pathways **R′1**, **R′2**, and **R′3** refer to gas-phase CCH + H₂O reaction and are optimized at ωB97X-D3. **H′1** and **H′2** correspond to the two hydrogenation pathways of vinyl alcohol, optimized at MPWB1K-D3(BJ). Distances are in Å.

compute the zero-point energy (ZPE) corrections.[106] Because the systems are open-shell in nature, calculations were performed within the unrestricted formalism.

We additionally calculated the tunnelling crossover temperatures, *i.e.*, the temperature below which quantum tunnelling becomes the main mechanism for trespassing the potential energy barriers. To this end, we used eq 4,[107] where $\Delta H^{\ddagger}$ is the ZPE-corrected barrier height, $\omega^{\ddagger}$ is the frequency associated with the TS, and k_B and $\hbar$ are the Boltzmann's and reduced Planck's constants. This temperature indicates what reactions may actually have an important role at low temperatures despite having an activation barrier.

$$T_c = \frac{\hbar \omega^{\ddagger} \Delta H^{\ddagger} / k_B}{2\pi \Delta H^{\ddagger} - \hbar \omega^{\ddagger} \ln(2)} \qquad (4)$$

The surfaces of amorphous solid water (ASW) ice coating interstellar grains were simulated by two different cluster models: one consisting of 18 water molecules and the other consisting of 33 water molecules (hereafter termed W18 and W33; Figure 1). While the former represents a compact, flat water ice surface, the latter presents a cavity structure of about 6 Å. For more details, we refer the reader to refs 54, 58, and 108.

For the calculation of the binding energies (BEs) of CCH interacting with the H₂O ice surface models (*i.e.*, CCH/surf complexes), we adopted the same electronic structure methodology as for reactivity, namely, for each CCH/surf complex and corresponding isolated components, geometry optimizations and frequency calculations (and hence ZPE corrections) were computed at the ωB97X-D3/6-311++G-

(d,p) level, followed by single-point energy calculations at the improved ωB97X-D3/6-311++G(2df,2pd) level. Basis set superposition error (BSSE) was corrected following the Boys and Bernardi counterpoise method. The final, corrected, adsorption energy (ΔE_{ads}^{CP}) was calculated as

$$\Delta E_{ads}^{CP}(CCH/surf)$$
$$= \Delta E_{ads} + BSSE(CCH) + BSSE(surf) + \Delta ZPE \qquad (5)$$

where $\Delta E_{ads} = E(CCH/surf) - E(CCH) - E(surf)$ refers to the BSSE-noncorrected adsorption energy. Note that we used the same sign convention as in ref 54; namely, the adsorption energy is the negative of the binding energy: $\Delta E_{ads}^{CP} = -BE$.

■ RESULTS

Benchmarking Study. As mentioned above, we carried out a preliminary benchmarking analysis for the reactivity using two gas-phase model reactions, CCH + H₂O and CH₂CHOH + H, to find the DFT method that describes better the reaction properties. For CCH + H₂O, we found three possible reaction pathways, labeled as **R′1**, **R′2**, and **R′3**, the stationary points of which are shown in Figure 2.

R′1 follows a stepwise mechanism: the first step involves the formation of acetylene (HCCH) and the hydroxyl radical (OH) as intermediate species, and the second step consists of the condensation of these intermediates to form the HCCHOH radical. In contrast, both **R′2** and **R′3** adopt a concerted mechanism. These two reactions involve a C−O bond formation followed by a H-transfer to the other C atom to form the H₂CCOH radical (isomer of HCCHOH, the product of **R′1**). The difference between **R′2** and **R′3** is that,

Table 1. Relative Energies (in kJ mol^{-1}) of the Stationary Points Involved in the Reaction Pathways Found for the Gas-Phase CCH + H$_2$O Reaction Model (R′1, R′2, and R′3) and for the Gas-Phase Hydrogenation (H′1 and H′2) for All the DFT-D Methods and the CCSD(T) Method Used for the Benchmarking Study[a]

reaction	step	BHLYP-D3(BJ)	M062X-D3	MPWB1K-D3(BJ)	PW6B95-D3(BJ)	ωB97X-D3	CCSD(T)
R′1	H$_2$O + CCH	0.0	0.0	0.0	0.0	0.0	0.0
	TS1	28.5	8.9	25.6	19.6	29.0	29.1
	OH + HCCH	−91.6	−57.0	−72.5	−63.0	−62.3	−69.0
	TS2	−68.5	−62.8	−60.2	−61.1	−53.5	−51.5
	HCCHOH	−217.0	−222.0	−217.7	−203.6	−205.9	−193.8
	TS1 % R′1	2.1	69.5	11.8	32.6	0.4	
	TS2 % R′1	33.2	22.1	17.0	18.8	4.0	
	Avg % R′1	20.0	30.9	11.5	16.3	5.1	
R′2	H$_2$O + CCH	0.0	0.0	0.0	0.0	0.0	0.0
	TS1	117.4	107.5	96.4	90.8	108.0	99.5
	H$_2$CCOH	−249.3	−246.8	−266.3	−253.2	−247.8	−241.1
	TS % R′2	18.0	8.1	3.1	8.7	8.5	
	Avg % R′2	10.7	5.2	6.8	6.9	5.6	
R′3	H$_2$O + CCH	0.0	0.0	0.0	0.0	0.0	0.0
	TS	120.3	87.7	98.6	123.5	113.0	105.4
	H$_2$CCOH	−240.3	−244.8	−241.9	−228.8	−229.7	−214.1
	TS % R′3	16.7	16.8	6.5	17.1	7.2	
	Avg % R′3	14.5	15.6	9.7	12.0	7.2	
	Global Avg %	15.1	17.2	9.3	11.7	6.0	
H′1	CH$_2$CHOH + H	0.0	0.0	0.0	0.0	0.0	0.0
	TS	0.3		4.1	2.3	11.4	6.5
	CH$_3$CHOH	−192.6		−183.3	−177.1	−188.1	−176.0
	TS % H′1	116.4		43.6	78.5	93.0	
	Avg % H′1	62.9		23.9	39.6	49.9	
H′2	CH$_2$CHOH + H	0.0	0.0	0.0	0.0	0.0	0.0
	TS	8.0		14.2	12.5	21.6	15.9
	CH$_2$CH$_2$OH	−157.9		−143.0	−177.1	−149.0	−142.0
	TS % H′2	54.2		11.9	23.7	38.5	
	Avg % H′2	32.7		6.3	24.1	21.7	
	Global Avg %	47.8		15.1	31.8	35.8	

[a]See Methodology for more details. Rows indicated as "TS % RX" show the unsigned error (in percent) relative to the predicted energy of the TS. Rows indicated as "Avg % RX" show the averaged unsigned errors (in percent and accounting for all the stationary points) of each DFT-D method with respect to the CCSD(T)//ωB97X-D3 for R′1, R′2, and R′3 and CCDS(T)//MPWB1K-D3(BJ) for H′1 and H′2 reference values. The last row indicates the global averaged unsigned error (in percent).

in the former, the H-transfer comes first, followed then by a spontaneous C−O bond formation, while in the latter, the C−O bond formation and the proton transfer evolve in a synchronized way.

The computed energetics of these reaction pathways using the different quantum chemical methods are shown in Table 1. The optimized geometries of the stationary points are available in the Supporting Information. As can be seen, the overall best functional for these reactions of water addition to CCH is ωB97X-D3, with an average unsigned error of ∼5% in the energy barriers and ∼6% in the whole energetics. The performance of the other functionals is, from better to worse, MPWB1K-D3(BJ), PW6B95-D3(BJ), BHLYP-D3(BJ), and M062X-D3.

For the hydrogenation steps (reactions 2 and 3), we considered only the hydrogenation of vinyl alcohol, namely, CH$_2$CHOH + H, because it is the unique step that can exhibit an energy barrier due to involving a closed-shell molecule (vinyl alcohol) with a radical (H atom). In contrast, the other steps consist of the hydrogenation of radical species, which are barrierless processes because of the spontaneous spin−spin coupling. For this H-addition reaction, we found two possible pathways (labeled as **H′1** and **H′2** in Figure 2), leading to two

different products (CH$_3$CHOH and CH$_2$CH$_2$OH, respectively), depending on which C atom the H addition takes place. **H′1** and **H′2** share a similar mechanism, in which the H atom in the reactant structures is located at *ca.* 3.5 Å from the C atom with which it will react. Results show that path **H′1** is more favorable than **H′2**, both for the stability of the product and for presenting a lower activation energy barrier (see Table 1). This is because the **H′1** product (CH$_3$CHOH) exhibits a better delocalization of the unpaired electron with respect to the **H′2** product (CH$_2$CH$_2$OH). Among the used DFT methods, the functional with the smallest average unsigned error compared to CCSD(T) single-point energy calculations is MPWB1K-D3(BJ). The performance of the other functionals, from better to worse, is PW6B95-D3(BJ), ωB97X-D3, and BHLYP-D3(BJ). M062X-D3 was discarded for convergence problems of the reactant structures. Therefore, according to this benchmarking study, the ωB97X-D3 DFT method has been chosen to simulate the addition of water to CCH on the W18 and W33 cluster models, and MPWB1K-D3(BJ) has been adopted for the hydrogenation step of vinyl alcohol.

Adsorption of CCH on Water Ice and Binding Energies. The complexes formed when CCH adsorbs on

W18 and W33 are shown in the R structures of Figures 3 and 4, respectively. Table 2 reports the computed binding energies and the different contributions, as detailed in Methodology.

In most of the cases, a nonclassical hemibond between the CCH species and an H_2O of the ice is established because of the formation of a two-center, three-electron system between the unpaired electron of CCH and a lone pair of H_2O. This interaction is highlighted by the computed spin density values
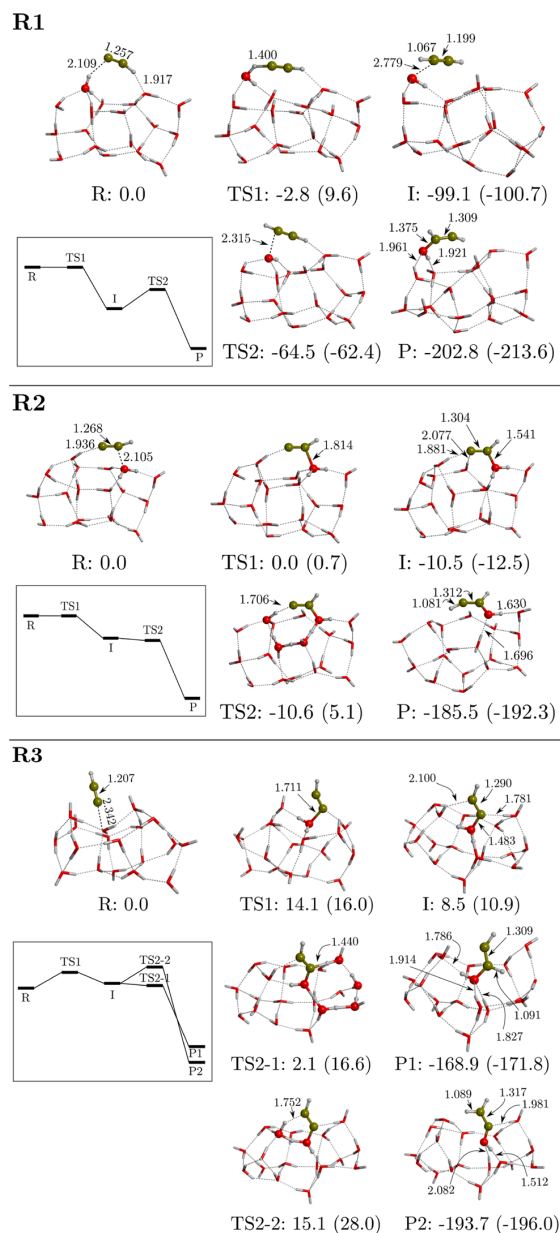
R1

R: 0.0   TS1: -2.8 (9.6)   I: -99.1 (-100.7)

TS2: -64.5 (-62.4)   P: -202.8 (-213.6)

R2

R: 0.0   TS1: 0.0 (0.7)   I: -10.5 (-12.5)

TS2: -10.6 (5.1)   P: -185.5 (-192.3)

R3

R: 0.0   TS1: 14.1 (16.0)   I: 8.5 (10.9)

TS2-1: 2.1 (16.6)   P1: -168.9 (-171.8)

TS2-2: 15.1 (28.0)   P2: -193.7 (-196.0)

Figure 3. Computed potential energy surfaces (PESs) of the reactions **R1-3** between CCH and the W18 ASW ice cluster model. Bare energy values correspond to relative ZPE-corrected values, while values in parentheses correspond to those missing this correction. The miniature panels sketch the ZPE-corrected PESs. Energies are in kJ mol^{-1}, and distances are in Å.

and maps, which clearly indicate a delocalization of the unpaired electron between the two centers (see data in the Supporting Information). The distances of these hemibonds vary between 2.1 and 2.3 Å (see the R structures of the **R2**, **R3**, **R2-1**, and **R2-2** sequences of Figures 3 and 4). The only exception not presenting a hemibonded complex is the structure R of **R1** (Figure 3), in which classical, weak hydrogen bond (H-bond) interactions are established between CCH and the W18 ice model. Interestingly, any attempt to find a pure H-bonded complex (i.e., without any hemibonded interaction) on W33 failed, with the geometry optimizations collapsing into the hemibonded structures. This reinforces the idea that the more surface water molecules, the higher the possibility to form hemibonded complexes, although most of the hemi-bonded complexes also present H-bond interactions. This is because the outermost water molecules of the cluster are unsaturated in terms of H-bonds, presenting H- and O-dangling atoms ready to establish H-bond and hemibonded interactions, respectively. Remarkably, hemibonded systems also form in the reactant structures of the gas-phase reactions (see above). However, these gas-phase systems present a lower hemibonded character than the complexes on W18 and W33 because the spin is less delocalized between the two centers (see spin density values and maps in the Supporting Information).

As expected, hemibonded complexes present BE values larger than those of H-bonded ones (see Table 2). The difference in the BEs between the complexes shown in **R2** and **R3** (i.e., on W18) arises from the orbital occupied by the CCH unpaired electron. In the former, the unpaired electron belongs to the π system of the CCH (the spin density is shared between the two C atoms, and the linearity of CCH becomes broken upon hemibond formation), while in the latter it belongs to a σ orbital of the C-end of CCH, in both cases interacting with a lone pair of H_2O to form the hemibond. As the orbital overlap is more efficient in σ orbitals than in π orbitals, the latter complex presents a larger BE than the former (49.9 and 37.9 kJ mol^{-1}, respectively). On W33, both hemibonded complexes have similar BE values (89.7 and 86.0 kJ mol^{-1}) because in both systems the unpaired electron occupies a π orbital. Remarkably, the values on W33 are notably higher than those on W18, and we investigated what might be the cause. We checked for a correlation between the BE and the number of water molecules forming the cluster, carving several structures from our W33 model, that is, by removing water molecules from the edges of the model in order to build a set of water clusters with decreasing dimensions (and blocking some O atoms of the cluster to prevent the cavity from collapsing). By proceeding in this way, we found evidence that the increasing number of interactions between CCH and the ice, together with the cooperativity of H-bonds, is responsible for the increment of the BE. Data of this analysis are provided in the Supporting Information.

Finally, it is worth mentioning that we performed a preliminary benchmarking study on the binding energies of the dimeric CCH/H_2O system. Results (available in the Supporting Information) indicate that while the H-bonded dimer is very well described by most of the DFT methods, this is not the case for the hemibonded one. However, for the particular case of ωB97X-D3, the computed binding energies are somewhat overestimated, belonging to the group of the functionals that better compare with CCSD(T). Accordingly, the computed binding energies of the hemibonded complexes
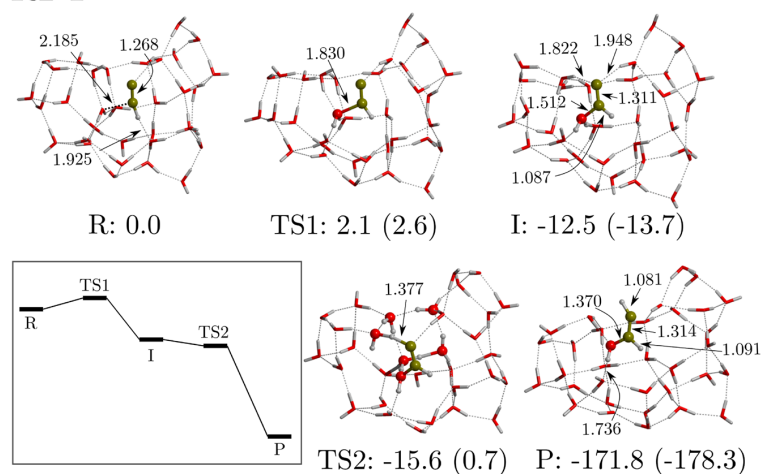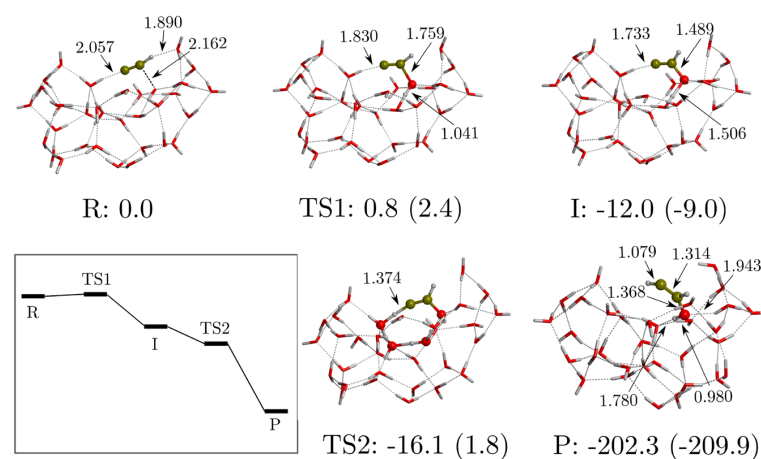
Figure 4. Computed potential energy surfaces (PESs) of the reactions **R2-1** and **R2-2** between CCH and W33 ASW ice cluster model. Bare energy values correspond to relative ZPE-corrected values, while values in parentheses correspond to those missing this correction. The miniature panels sketch the ZPE-corrected PESs. Energies are in kJ mol⁻¹, and distances are in Å.

Table 2. Binding Energy (BE) Values (in kJ mol⁻¹) of CCH on the W18 and W33 Cluster Models According to the Computed Complexes Shown in Figures 3 and 4 (the R Structures of the Reactions (Rx) R1, R2, R3, R2-1, and R2-2)[a]

surface	Rx	ΔE_{ads}	ΔE_{disp}	ΔZPE	$\Delta BSSE$	BE
W18	R1	−21.2	−3.3	−0.6	1.4	23.7
	R2	−32.8	−10.1	3.0	2.1	37.9
	R3	−32.2	−22.1	2.2	2.2	49.9
W33	R2-1	−97.1	−7.2	11.2	3.3	89.7
	R2-2	−81.6	−19.0	11.2	3.5	86.0

[a]The contributions from the pure potential energy values (ΔE_{ads}), dispersion corrections (ΔE_{disp}), zero-point energy corrections (ΔZPE), and BSSE corrections ($\Delta BSSE$) are also shown.

arising from CCH in interaction with W18 and W33 should be considered overestimated by some amount. Despite this drawback, we would like to stress that the main scope of the work is on the reactivity between CCH and H₂O followed by H-additions and that the used DFT methods are actually accurate enough for this purpose, as shown above. In this case, the error in the binding energies self-canceled when deriving the energy features (energy barriers and reaction energies) of the reactions.

Reactivity between CCH and H₂O on the Ice Surface Models. *W18 ASW Ice Cluster Model.* Following the three reaction types found in the benchmark study, we tried to reproduce them on top of the W18 ice cluster model. However, significant differences in the mechanisms have been found, precisely because they occur on the ice model. Indeed,

the larger number of water molecules indicates that (i) there are no concerted mechanisms at work and (ii) water-assisted proton-transfer reactions are operative. Water-assisted proton-transfer mechanisms were elucidated theoretically in the latter years of the last century[109] and can induce important decrease in the energy barriers with respect to the nonwater-assisted analogues. This is because the assisting water molecules bridge the accepting/donating proton processes with their neighboring molecules and, at the same time, reduce the strain of the rings in the transition-state structures. Hence, this mechanism is also called proton-transport catalysis. Such catalytic effects have also been observed in processes of interstellar interest in icy surfaces.[58,110,111] It is worth mentioning that the water-assisted proton transfers, to be catalytically effective, need a proper H-bond connectivity among the bridging water molecules, from the first to the last proton transfer. This means that, if the H-bonding network is truncated because of the presence of interstitial unpurities, the mechanism is not operative. This is an aspect not to overlook in interstellar ices because they contain minor volatile species in the ices that can obstruct the chained proton relays. Remarkably, it is worth stressing that the catalytic transfers involve H atoms with a proton character and not atomic radicals. This is because the H species exchanged during the transfers are proton-like atoms chemically bonded to a more electronegative O atom.

Because the identified reaction channels on W18 differ significantly from the gas-phase ones, we redefine the **R′1-3** model channels into **R1-3**, which adopt the following simplified mechanistic steps:
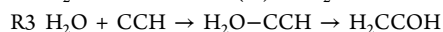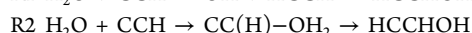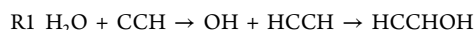
R1 $H_2O + CCH \rightarrow OH + HCCH \rightarrow HCCHOH$
R2 $H_2O + CCH \rightarrow CC(H)-OH_2 \rightarrow HCCHOH$
R3 $H_2O + CCH \rightarrow H_2O-CCH \rightarrow H_2CCOH$

The stationary points and the energy profiles of these reaction pathways are shown in Figure 3.

The **R1** path remains the same as the **R′1** one, namely, formation of HCCH and OH as intermediate species by H-transfer from the reactive H_2O molecule to CCH, and then coupling of the OH to HCCH to form the HCCHOH radical as vinyl alcohol precursor. Both **R2** and **R3** start with the formation of the hemibonded systems (see the Supporting Information for their spin densities). However, because the involved C atoms are different, the pathways proceed in a different way as well. The hemibonded structure of **R2** evolves toward the formation of the $CC(H)-OH_2$ intermediate, which is followed by a proton transfer, from the OH_2 moiety and adopting a water-assisted proton-transfer mechanism, to form the final HCCHOH radical. In contrast, the hemibonded structure of **R3** transforms into H_2O-CCH as the intermediate species. From this intermediate, two different paths are possible, namely, from the OH_2 moiety, a proton transfer to (i) the central C atom (TS2-1) or (ii) the terminal C atom (TS2-2), forming HCCHOH or H_2CCOH, respectively. Interestingly, both paths proceed through a water-assisted proton-transfer mechanism. The fact that **R3** exhibits these two paths is because there are well-oriented H-bonds in the water cluster allowing for the water-assisted mechanism in two directions, while this is not possible in **R2** because of the geometry of the intermediate structure.

In relation to the energetics (see also Figure 3), the first steps (TS1) of paths **R1** and **R2** become submerged below the energy of reactants once they are ZPE-corrected. The same happens for the second step (TS2) of path **R2**. This means

that **R2** is an overall effectively barrierless reaction on W18. In contrast, **R1** has a low-energy intermediate (associated with the formation of HCCH), and consequently, the second step (TS2) encounters a relatively high energy barrier of 34.6 kJ mol^{-1} (with respect to the intermediate). For **R3**, the first step already presents a non-negligible energy barrier, even when it is ZPE-corrected (14.1 kJ mol^{-1}). For the second steps, TS2-1 has an energy lower than that of TS2-2 because the geometry associated with the latter saddle point is more strained, because the cycle created by the water assistant molecules is smaller. All the reaction paths present negative and very large reaction energies, indicating that the formed vinyl alcohol radicals are more stable than the reactant states. We observed that, in some cases, the ZPE corrections added to the potential energies are very large (see, for instance, TS1 in **R1**, TS2 in **R2**, and TS2-1 and TS2-2 in **R3**). Interestingly, these transition states involve the motion of H atoms of the water molecules, either as a direct proton transfer (case of TS1 in **R1**) or as a water-assisted proton-transfer mechanism (cases of TS2 in **R2** and TS2-1 and TS2-2 in **R3**). In contrast, when a C−O bond is formed (namely, without involving any proton motion) it results in a slight ZPE correction. In order to understand this behavior, we simulated the IR spectra of R, TS1, I, and TS2-1 of **R3** (see the Supporting Information). The spectra of R and TS1, where only the C−O bond forms, show mostly common features, with the exception of a couple of bands around 3000 cm^{-1}, because of O−H stretching of the water molecules surrounding the CCH. On the other hand, comparing the spectrum of TS2-1 with R highlights the presence of a number of features at a shorter wavenumber, arising from the water-assisted proton-transfer. Given that the ZPE arises from the sum of the energy of all the vibrational modes, the shorter wavelength features of TS2-1 explain why its ZPE is smaller than R and hence why the resulting ΔZPE is negative.
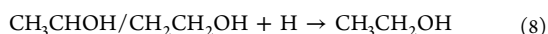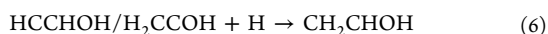
As a final comment, we stress the influence of the saturated state (in terms of H-bonding) of the reacting water molecule in the energy barriers. Indeed, according to the potential energy values, the TS1 barrier in **R2** is actually lower than that in **R3**, 0.7 and 16.0 kJ mol^{-1}, respectively (see Figure 3). This is because, in the former, TS1 is more reactant-like than in the latter because, in the R structure of **R2**, the reacting water molecule is not fully saturated by H-bonds (i.e., 2 H-bonds as donor +1 H-bond as acceptor) while this is the case in **R3** (i.e., 2 H-bonds as donor +2 H-bonds as acceptor). The lack of the H-bond in R of the **R2** reaction allows the water "unsaturated" lone pair to form the hemibonded system with CCH, in which the C−O bond is half-formed. Thus, to reach the TS1 structure, no significant energy requirements and geometrical changes are needed, and hence the low energy barrier. In contrast, in **R3**, to form TS1 from the R structure, the reacting water molecule has to break one of the H-bonds to form the new C−O bond, implying a more energetic cost and relevant geometrical changes. Nevertheless, the associated quantum tunnelling crossover temperature is rather high (244 K), indicating that this channel could be relevant at interstellar temperatures.

W33 ASW Ice Cluster Model. After modeling the reaction on the flat surface of W18, we set out to investigate the possible effects of a cavity structure like that of W33. We tried to reproduce the same three reaction paths as those taking place on W18, but we found only two mechanisms, and both are similar to **R2**; hence, they are termed **R2-1** and **R2-2**. The stationary points and the energy profiles of these reaction

pathways are shown in Figure 4. It is worth mentioning that, to model the reaction path **R2-2**, it was necessary to fix the position of some of the oxygen atoms placed at the edge of the model because full geometry relaxation led to the collapse of the cavity.

In both cases, CCH is located in the cavity, with the central C atom interacting with the oxygen atom of the reactant water molecule of the surface, forming the aforementioned hemibonded systems (see the Supporting Information for spin densities). Along the reactions, these structures evolve to form the $CC(H)-OH_2$ intermediate. For both cases, this step has a very low ZPE-corrected energy barrier (2.1 and 0.8 kJ mol⁻¹ for TS1 and TS2, respectively). The second step involves, for both paths, the proton transfer from the OH_2 moiety to the terminal C atom forming the HCCHOH radical, also by means of a water-assisted proton-transfer mechanism. The two paths lead to the same radical because the H-bond network enables the water-assisted proton-transfer to connect with the terminal C atom and not the central one. These second steps are energetically below the corresponding intermediates (by including ZPE corrections), and accordingly, the water-assisted proton transfers proceed in a barrierless fashion. Because the reaction energies are very large and negative, the computed reactions on W33 are energetically very favorable, similarly to the **R2** reaction occurring on W18.

Toward the Formation of Ethanol: Hydrogenation of Vinyl Alcohol. As shown above, reaction of CCH with an icy water molecule leads to the formation of CHCHOH and H₂CCOH. From these species, to reach ethanol, a set of hydrogenation steps are necessary, as sketched in reactions 6−8.

$$HCCHOH/H_2CCOH + H \rightarrow CH_2CHOH \quad (6)$$

$$CH_2CHOH + H \rightarrow CH_3CHOH/CH_2CH_2OH \quad (7)$$

$$CH_3CHOH/CH_2CH_2OH + H \rightarrow CH_3CH_2OH \quad (8)$$

The first hydrogenation forms vinyl alcohol (VA). As this H-addition is a radical−radical coupling, we consider it as barrierless. The second hydrogenation step is the H-addition to the VA. It involves the reactivity between a closed-shell species (namely, VA) with a radical (H), and accordingly, it is expected to have an activation barrier. Interestingly, depending on the C in which the H-addition takes place, the species formed is either CH₃CHOH or CH₂CH₂OH. The third and final hydrogenation step leads to the formation of ethanol, irrespective of the initial radical species. This H-addition is, again, a radical−radical coupling, and accordingly, it is expected to be barrierless in a similar fashion as the first hydrogenation. According to this reactive scheme, to investigate on ethanol formation, we simulated only reaction 7 on the W18 ice model.

We identified two reaction paths, termed **H1** and **H2** (see Figure 5), the difference of which being the C atom that undergoes the H-addition, in analogy to the gas-phase **H′1** and **H′2** reactions (see Figure 2). Both reactions start from a prereactant structure in which the H atom is *ca.* 3.3 Å from the VA because of the weak interactions between the two partners. The computed potential energy surfaces indicate that the two hydrogenation reactions present a non-negligible energy barrier. In agreement with gas-phase results, the path leading to the formation of CH₃CHOH is more favorable than that resulting with CH₂CH₂OH, in terms of both energy barriers
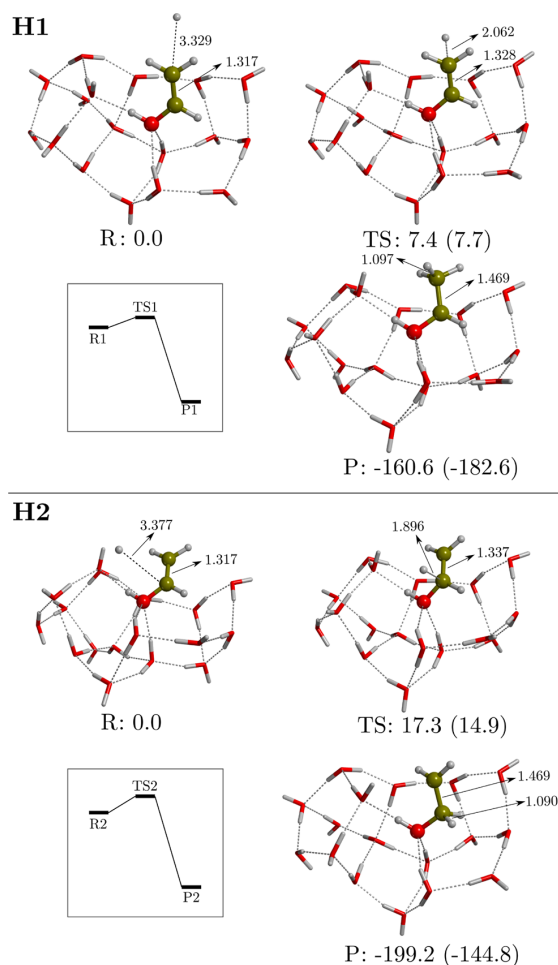

H1

R: 0.0   TS: 7.4 (7.7)

P: -160.6 (-182.6)

H2

R: 0.0   TS: 17.3 (14.9)

P: -199.2 (-144.8)

Figure 5. Computed potential energy surfaces (PESs) of the hydrogenation reactions **H1** and **H2** on W18 ASW ice cluster model. Bare energy values correspond to relative ZPE-corrected values, while values in parentheses correspond to those missing this correction. The miniature panels sketch the ZPE-corrected PESs. Energies are in kJ mol⁻¹, and distances are in Å.

and reaction energies. Remarkably, the computed energy barriers on W18 are higher (3−4 kJ mol⁻¹) than those obtained in the gas-phase. This is probably because the adsorption of VA with the surface induces an enhanced stabilization of the former due to the intermolecular forces between VA and the icy surface. Thus, chemically strictly speaking, the surface does not act as a chemical catalyst but slightly inhibits the process. However, it is worth highlighting that the **H1** reaction presents a very low potential energy barrier and, because of the involvement of a H atom and the very low temperatures of the ISM, tunneling effects can operate as well. Indeed, its associated quantum tunnelling crossover temperature is 118 K. For reaction **H2**, the crossover temperature is slightly higher, 174 K; therefore, quantum tunneling could also play a role.

Isomerization between Vinyl Alcohol and Acetaldehyde. Vinyl alcohol and acetaldehyde are tautomers (*i.e.*, structural isomers), and therefore, we have here considered the

conversion from one to the other according to reaction 9. This isomerization reaction has been computed at the MPWB1K-D3(BJ)//6-311++G(2df,2pd)//MPWB1K-D3(BJ)//6-311++G(d,p) level for consistency with the methodology applied to the hydrogenation of vinyl alcohol.

$$CH_2CHOH \Leftrightarrow CH_3CHO \qquad (9)$$

Among them, acetaldehyde is the most stable isomer (by ~41 kJ mol⁻¹). In the gas phase, the barrier connecting vinyl alcohol with acetaldehyde is very high (237.9 kJ mol⁻¹, see the Supporting Information). This is because the mechanism involves an intramolecular H-transfer from the OH of vinyl alcohol to the terminal C atom, with a highly strained transition state.

If we now consider this reaction to take place through the water molecules of W18, as shown in Figure 6, we can see that a water-assisted proton-transfer mechanism can take place, lowering the activation energy barrier down to 73.5 kJ mol⁻¹ when the reaction starts from vinyl alcohol (**I1**) and to 57.7 kJ mol⁻¹ when it starts from its less hydrogenated precursor (**I2**). The latter reaction produces CH₂CHO, which can be successively hydrogenated to form acetaldehyde. The difference in the two activation barriers is probably due to the structure of the ring through which the proton is transferred; that is, in **I1** it is more strained. This is a great example of how interstellar ices act as chemical catalysts. However, computed energy barriers are very high to be surmountable under interstellar conditions, and accordingly, these channels seem unlikely. Nevertheless, we note that the barrier of **I2** is narrower and lower than that of **I1** (with barriers widths of about 1.6 and 2.2 Å, respectively, assuming the asymmetric Eckart barrier model; see ref 112). Therefore, **I2** would be the most efficient mechanism among the two, if assuming that quantum tunneling does play a role.

■ DISCUSSION AND ASTROPHYSICAL IMPLICATIONS

CCH is a highly reactive species that easily reacts with water. Because it is a C-centered radical and contains both donor and acceptor H-bond atoms (the H and the C-end atoms, respectively), it tends to form H-bonded and hemibonded complexes with water ice molecules. The most relevant computed energetics of CCH reactivity on our ASW ice models are summarized in Table 3. On W18, **R3** presents an activation barrier of 14.4 kJ mol⁻¹, and accordingly, it is not *a priori* an efficient path to form vinyl alcohol, although it could still be relevant if quantum tunnelling effects work. The first step of **R1** is barrierless to form HCCH + OH, but the reaction stops at this stage. This is because the second step has an intrinsic energy barrier of 34.6 kJ mol⁻¹ (the energy difference between TS2 and I; see Figure 3). Moreover, the energy released by the first reaction step will no longer be available for the second step, as water ices tend to efficiently dissipate chemical energy fast.[113,114] Therefore, **R1** will lead to the formation of a highly stabilized acetylene, which will hardly react with OH remaining stuck on the ice. However, this reaction can be an effective channel toward the formation of OH radicals on the ice surfaces without the need of a direct energy processing. This can be of importance because the generated OH could participate in further surface reactions in the form of OH additions. **R2**, at variance with the other two reactions, is an effective barrierless reaction path toward vinyl alcohol formation. Because of that, this reaction has also been
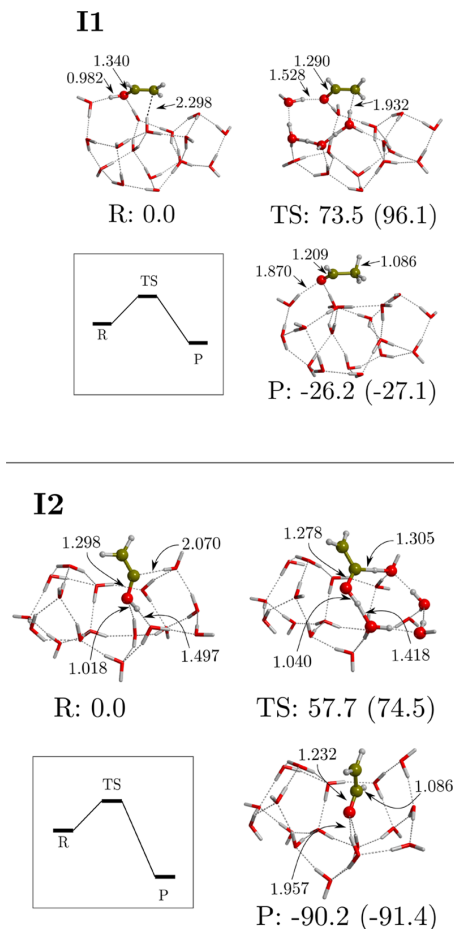

I1

R: 0.0   TS: 73.5 (96.1)

P: −26.2 (−27.1)

I2

R: 0.0   TS: 57.7 (74.5)

P: −90.2 (−91.4)

Figure 6. Computed potential energy surfaces (PESs) of the isomerization between vinyl alcohol and acetaldehyde (**I1**) and the analogue reaction involving their precursor, *i.e.*, the product P2 of R3 (**I2**) on W18 ice cluster model at MPWB1K-D3(BJ)/6-311+G(2df,2pd)//MPWB1K-D3(BJ)/6-311++G(d,p). Bare energy values correspond to relative ZPE-corrected values, while values in parentheses correspond to those missing this correction. The miniature panel sketches the ZPE-corrected PESs. Energies are in kJ mol⁻¹, and distances are in Å.

Table 3. Summary of the Energetics of the Simulated Reactions and Their Products

	reaction	barrier	product
W18	R1	NO	HCCH + OH
	R2	NO	HCCHOH
	R3	14.4 kJ mol⁻¹	H₂CCOH/HCCHOH
W33	R2-1	2.1 kJ mol⁻¹	HCCHOH
	R2-2	0.8 kJ mol⁻¹	HCCHOH
W18	H1	7.4 kJ mol⁻¹	CH₃CH₂OH
	H2	17.3 kJ mol⁻¹	CH₃CH₂OH

modeled on W33 to study the effects of the cavity on the reactivity. On W33, we found that the reactions are no more barrierless, although the two identified paths present low activation barriers (2.1 and 0.8 kJ mol⁻¹ for **R2-1** and **R2-2**,

respectively). Because these two pathways are equivalent to **R2** on W18, the effect of the cavity is almost insignificant for the energetics of the path. Therefore, we can consider that the mechanistic steps represented by the **R2**, **R2-1**, and **R2-2** pathways constitute the most likely channel to form vinyl alcohol.

The hydrogenation of vinyl alcohol on grains leads to the formation of ethanol, as occurring in methanol formation from CO[115−119] and ethane formation from C$_2$H$_2$ and C$_2$H$_4$.[120−122] The H-addition to vinyl alcohol is the only hydrogenation step not involving a barrierless radical−radical coupling and presents an energy barrier of 7.4 and 17.3 kJ mol^{-1} for the **H1** and **H2** channel (see Table 3). Thus, **H1** is the most energetically favored pathway for the formation of the ethanol radical precursor. Despite the computed relatively high energy barriers considering very low temperatures, these reactions can proceed through tunneling and are accordingly operative in the reaction chain starting from the adsorption of CCH on water ice.

These quantum chemical results can partly be related to the experimental findings mentioned in the Introduction. Indeed, part of the experimental synthetic routes have been simulated here, providing an atomistic interpretation (including the energetics) for the formation of vinyl alcohol followed by it hydrogenation to form ethanol. The main difference between the experiments and our computations is that, in the experiments, the C$_2$H$_2$/H$_2$O ices need to be processed to trigger reactivity (probably due to generating the radical reactive species like CCH and OH), while in our simulations the assumption is that the reaction does not require energetic processing of ices, because the CCH is readily available in the gas phase in a wide variety of environments.

We also considered the isomerization of vinyl alcohol into acetaldehyde (and the same for their less hydrogenated precursors), because in the experiments these reactions were suggested to explain the presence of both vinyl alcohol and acetaldehyde. According to our calculations, however, these reactions, although being catalyzed by the surfaces thanks to a water-assisted proton-transfer mechanism, present high energy barriers, rendering them poorly competitive to the final H additions. However, experimental authors pointed out that the isomerization could take place thanks to the exothermicity of the previous steps, in which the energy released along the reaction steps can be used to overcome the isomerization energy barrier. Our computed energetic data is consistent with this view. The very favorable reaction energies shown by the reactions indicate that the energy barriers of the isomerization processes lay below the prereactive asymptotic states, and therefore, they can be overcome by making use of the nascent reaction energies. However, one should bear in mind that water ice surfaces are extraordinary third bodies[113,114] and accordingly, the direct transfer of the previous reaction energies to surmount the isomerization energy barriers is doubtful. To shed some light on this topic, dedicated *ab initio* molecular dynamics simulations are needed, which is outside scope of the present work.

Finally, results presented in this work are very relevant in the framework of cold astrochemistry. The presence of abundant (∼10^{-9}−10^{-8}) gaseous CCH radicals in cold (≤20 K) regions, where water ices envelope the refractory cores of the interstellar dust grains (see Introduction), can lead to the formation of vinyl alcohol and ethanol in addition to HCCH and OH through a competitive reaction channel. Remarkably,

at variance with most of the experimentally proposed mechanisms (see Introduction), the formation of the aforementioned products does not require the energetic processing of interstellar ices. Regarding the formation of iCOMs, our proposal complements the nonenergetic reaction scheme of Chuang *et al.*,[123] in which OH radicals attack C$_2$H$_2$ to form iCOMs. We note that CCH (and the other intermediate radicals) could also be destroyed by other competitive surface reactions, *e.g.*, by H-abstraction reactions with H$_2$, or H-additions. This will be considered in the future.

In general, the astrochemical processes in cold regions such as the ones described in this work are important to improve our understanding of the presence of complex species detected in the cold (<20 K) outskirts of prestellar cores during the past decade (*e.g.*[16,124−128]). In this vein, ethanol has recently gained some attention, as it has been advocated to be the precursor of several iCOMs formed by cold gas-phase reactions (the genealogical tree of ethanol[23,91]). Indeed, the correlation of glycoladehyde and acetaldehyde abundances observed toward a number of interstellar sources has been shown to follow very well the theoretical predictions when their synthesis takes place through this gas-phase scheme.[24] In the present work, we showed that an efficient path exists for the formation of ethanol on the surfaces of interstellar ices. However, the nonthermal desorption of ethanol (and of the other products) remains as a crucial missing step in the sequential events linking the chemistry of iCOMs occurring on the surface of grains and in the gas phase in cold regions; this issue is undoubtedly a central matter of further investigation.

■ CONCLUSIONS

Interstellar complex organic molecules (iCOMs) have been detected in different astrophysical environments. However, the chemistry leading to their formation is not unambiguously known. Two prevailing paradigms have been largely used to rationalize their presence in the interstellar medium: one advocates reaction in the gas-phase, whereas the other presents reaction on the surface of icy grains. In this work, we focused on the latter by computing the reaction of CCH with a H$_2$O molecule forming part of the ice structure, leading to vinyl alcohol (CH$_2$CHOH), which upon hydrogenation is converted into ethanol (CH$_3$CH$_2$OH). This reaction is proposed as an alternative synthetic route for iCOMs beyond the commonly assumed radical−radical couplings. Investigations have been performed by means of DFT quantum chemical simulations and adopting cluster models of 18 and 33 water molecules (W18 and W33) to mimic the icy surfaces. For the reaction of CCH with H$_2$O, three different reaction pathways have been elucidated, leading to the formation of HCCH + OH, CHCHOH, and H$_2$CCOH. Some cases present small activation barriers, but in others the reactions are barrierless when zero-point energy corrections are accounted for. Hydrogenation of vinyl alcohol on the W18 cluster has been found to present activation barriers of a certain significance but, for these reactions, quantum tunneling is likely to be at work, speeding them up. Isomerization between vinyl alcohol and acetaldehyde have also been simulated on W18, with the results indicating that, despite the strong catalytic role played by the water ice, they have a barrier of significant height. Additionally, the direct H-abstraction from the water molecule to CCH leading to the formation of HCCH and the OH radical on the surface has been found to be an energetically competitive channel. It is worth mentioning that a chemical

kinetics treatment of these results is underway in order to compute the rate constants (including tunneling effects explicitly) for each of the proposed reactive channels and hence elucidate branching ratios and formation efficiencies of the simulated paths.

In summary, results from our calculations indicate that the reaction of CCH with water ice can lead to the formation of vinyl alcohol and, lately, to the production of ethanol, and likely acetaldehyde, without the need of ice energy processing. This conclusion is of relevance in the context of iCOM formation because, according to the genealogical tree of ethanol, this species is the parent molecule through which different iCOMs (*e.g.*, formic acid, formaldehyde, glycolaldehyde, and others) can form by means of gas-phase processes.[23,24] Thus, in this work, we provide quantum chemical evidence on the feasibility of our mechanistic proposal, in which ethanol can be formed on interstellar icy grain surfaces, hence linking the two paradigms in the synthesis of iCOMs, at least in this particular case. The missing link between on-grain and gas-phase chemistry stands in the nonthermal desorption of ethanol and its precursors, which should be a subject for further investigation.

■ ASSOCIATED CONTENT

Ⓢ Supporting Information

The Supporting Information is available free of charge at https://pubs.acs.org/doi/10.1021/acsearthspace-chem.1c00369.

> Structures and errors of the benchmarking study; energetics relative to the CCH + H₂O reactions on W18 and W33; contributions to the binding energies of CCH on W18 and W33; Mulliken spin densities and spin density maps of the complexes CCH + H₂O in the gas phase and on W18 and W33; energetics relative to the hydrogenation of vinyl alcohol; energetics relative to the isomerization of vinyl alcohol into acetaldehyde (PDF)

■ AUTHOR INFORMATION

Corresponding Authors

Joan Enrique-Romero − *Univ. Grenoble Alpes, CNRS, Institut de Planétologie et d'Astrophysique de Grenoble (IPAG), 38000 Grenoble, France; Departament de Química, Universitat Autònoma de Barcelona, Bellaterra 08193 Catalonia, Spain;* ⓘ orcid.org/0000-0002-2147-7735; Email: juan.enrique-romero@univ-grenoble-alpes.fr

Albert Rimola − *Departament de Química, Universitat Autònoma de Barcelona, Bellaterra 08193 Catalonia, Spain;* ⓘ orcid.org/0000-0002-9637-4554; Email: albert.rimola@uab.cat

Authors

Jessica Perrero − *Departament de Química, Universitat Autònoma de Barcelona, Bellaterra 08193 Catalonia, Spain; Dipartimento di Chimica and Nanostructured Interfaces and Surfaces (NIS) Centre, Università degli Studi di Torino, 10125 Torino, Italy*

Berta Martínez-Bachs − *Departament de Química, Universitat Autònoma de Barcelona, Bellaterra 08193 Catalonia, Spain*

Cecilia Ceccarelli − *Univ. Grenoble Alpes, CNRS, Institut de Planétologie et d'Astrophysique de Grenoble (IPAG), 38000 Grenoble, France;* ⓘ orcid.org/0000-0001-9664-6292

Nadia Balucani − *Dipartimento di Chimica, Biologia e Biotecnologie, Università di Perugia, 06123 Perugia, Italy; Univ. Grenoble Alpes, CNRS, Institut de Planétologie et d'Astrophysique de Grenoble (IPAG), 38000 Grenoble, France; Osservatorio Astrosico di Arcetri, 50125 Firenze, Italy;* ⓘ orcid.org/0000-0001-5121-5683

Piero Ugliengo − *Dipartimento di Chimica and Nanostructured Interfaces and Surfaces (NIS) Centre, Università degli Studi di Torino, 10125 Torino, Italy;* ⓘ orcid.org/0000-0001-8886-9832

Complete contact information is available at:
https://pubs.acs.org/10.1021/acsearthspacechem.1c00369

Notes

The authors declare no competing financial interest.

■ REFERENCES

(1) Herbst, E.; van Dishoeck, E. F. Complex Organic Interstellar Molecules. *Annu. Rev. Astron. Astrophys.* **2009**, *47*, 427−480.

(2) Herbst, E. The synthesis of large interstellar molecules. *Int. Rev. Phys. Chem.* **2017**, *36*, 287−331.

(3) Ceccarelli, C.; et al. Seeds Of Life In Space (SOLIS): The Organic Composition Diversity at 300−1000 au Scale in Solar-type Star-forming Regions. *Astrophys. J.* **2017**, *850*, 176.

(4) Caselli, P.; Ceccarelli, C. Our astrochemical heritage. *Astron. Astrophys. Rev.* **2012**, *20*, 56.

(5) Ceccarelli, C.; Caselli, P.; Bockelée-Morvan, D.; Mousis, O.; Pizzarello, S.; Robert, F.; Semenov, D. Deuterium Fractionation: The Ariadne's Thread from the Precollapse Phase to Meteorites and Comets Today. In *Protostars and Planets VI*; 2014. DOI: 10.2458/azu_uapress_9780816531240-ch037

(6) Cazaux, S.; Tielens, A. G. G. M.; Ceccarelli, C.; Castets, A.; Wakelam, V.; Caux, E.; Parise, B.; Teyssier, D. The Hot Core around the Low-Mass Protostar IRAS 16293−2422: Scoundrels Rule! *Astrophys. J.* **2003**, *593*, L51−L55.

(7) Ligterink, N. F. W.; Calcutt, H.; Coutens, A.; Kristensen, L. E.; Bourke, T. L.; Drozdovskaya, M. N.; Müller, H. S. P.; Wampfler, S. F.; van der Wiel, M. H. D.; van Dishoeck, E. F.; Jørgensen, J. K. The ALMA-PILS survey: Stringent limits on small amines and nitrogen-oxides towards IRAS 16293−2422B. *Astron. Astrophys.* **2018**, *619*, A28.

(8) Bianchi, E.; Codella, C.; Ceccarelli, C.; Vazart, F.; Bachiller, R.; Balucani, N.; Bouvier, M.; De Simone, M.; Enrique-Romero, J.; Kahane, C.; Lefloch, B.; López-Sepulcre, A.; Ospina-Zamudio, J.; Podio, L.; Taquet, V. The census of interstellar complex organic molecules in the Class I hot corino of SVS13-A. *Mon. Not. R. Astron. Soc.* **2019**, *483*, 1850−1861.

(9) Alexander, C. M. O.; Cody, G. D.; Kebukawa, Y.; Bowden, R.; Fogel, M. L.; Kilcoyne, A. L. D.; Nittler, L. R.; Herd, C. D. K. Elemental, isotopic, and structural changes in Tagish Lake insoluble organic matter produced by parent body processes. *Meteorit. Planet. Sci.* **2014**, *49*, 503−525.

(10) Rotelli, L.; Trigo-Rodríguez, J. M.; Moyano-Cambero, C. E.; Carota, E.; Botta, L.; di Mauro, E.; Saladino, R. The key role of meteorites in the formation of relevant prebiotic molecules in a formamide/water environment. *Sci. Rep.* **2016**, *6*, 38888.

(11) Yabuta, H.; Williams, L. B.; Cody, G. D.; Alexander, C. M. O. D.; Pizzarello, S. The insoluble carbonaceous material of CM chondrites: A possible source of discrete organic compounds under hydrothermal conditions. *Meteorit. Planet. Sci.* **2007**, *42*, 37−48.

(12) Callahan, M. P.; Smith, K. E.; Cleaves, H. J.; Ruzicka, J.; Stern, J. C.; Glavin, D. P.; House, C. H.; Dworkin, J. P. Carbonaceous meteorites contain a wide range of extraterrestrial nucleobases. *Proc. Natl. Acad. Sci. U. S. A.* **2011**, *108*, 13995−13998.

(13) Rubin, R. H.; Swenson, J. G. W.; Benson, R. C.; Tigelaar, H. L.; Flygare, W. H. Microwave Detection of Interstellar Formamide. *Astrophys. J.* **1971**, *169*, L39.

(14) Ceccarelli, C.; Loinard, L.; Castets, A.; Faure, A.; Lefloch, B. Search for glycine in the solar type protostar IRAS 16293−2422. *Astron. Astrophys.* **2000**, *362*, 1122−1126.

(15) McGuire, B. A. 2018 Census of Interstellar, Circumstellar, Extragalactic, Protoplanetary Disk, and Exoplanetary Molecules. *Astrophys. J.s* **2018**, *239*, 17.

(16) Bacmann, A.; Taquet, V.; Faure, A.; Kahane, C.; Ceccarelli, C. Detection of complex organic molecules in a prestellar core: a new challenge for astrochemical models. *Astron. Astrophys.* **2012**, *541*, L12.

(17) Arce, H. G.; Santiago-García, J.; Jørgensen, J. K.; Tafalla, M.; Bachiller, R. Complex Molecules in the L1157 Molecular Outflow. *Astrophys. J.* **2008**, *681*, L21.

(18) Muller, S.; Beelen, A.; Black, J. H.; Curran, S. J.; Horellou, C.; Aalto, S.; Combes, F.; Guélin, M.; Henkel, C. A precise and accurate determination of the cosmic microwave background temperature at z = 0.89. *Astron. Astrophys.* **2013**, *551*, A109.

(19) Charnley, S. B.; Tielens, A. G. G. M.; Millar, T. J. On the Molecular Complexity of the Hot Cores in Orion A: Grain Surface Chemistry as "The Last Refuge of the Scoundrel. *Astrophys. J.* **1992**, *399*, L71.

(20) Charnley, S. B.; Tielens, A. G. G. M.; Rodgers, S. D. Deuterated Methanol in the Orion Compact Ridge. *Astrophys. J.* **1997**, *482*, L203−L206.

(21) Taquet, V.; Wirström, E. S.; Charnley, S. B. Formation and Recondensation of Complex Organic Molecules during Protostellar Luminosity Outbursts. *Astrophys. J.* **2016**, *821*, 46.

(22) Balucani, N.; Ceccarelli, C.; Taquet, V. Formation of complex organic molecules in cold objects: the role of gas-phase reactions. *Mon. Not. R. Astron. Soc.* **2015**, *449*, L16−L20.

(23) Skouteris, D.; Balucani, N.; Ceccarelli, C.; Vazart, F.; Puzzarini, C.; Barone, V.; Codella, C.; Lefloch, B. The Genealogical Tree of Ethanol: Gas-phase Formation of Glycolaldehyde, Acetic Acid, and Formic Acid. *Astrophys. J.* **2018**, *854*, 135.

(24) Vazart, F.; Ceccarelli, C.; Balucani, N.; Bianchi, E.; Skouteris, D. Gas-phase formation of acetaldehyde: review and new theoretical computations. *Mon. Not. R. Astron. Soc.* **2020**, *499*, 5547−5561.

(25) Garrod, R. T.; Herbst, E. Formation of methyl formate and other organic species in the warm-up phase of hot molecular cores. *Astron. Astrophys.* **2006**, *457*, 927−936.

(26) Garrod, R. T.; Weaver, S. L. W.; Herbst, E. Complex Chemistry in Star-forming Regions: An Expanded Gas-Grain Warm-up Chemical Model. *Astrophys. J.* **2008**, *682*, 283−302.

(27) Ruaud, M.; Loison, J. C.; Hickson, K. M.; Gratier, P.; Hersant, F.; Wakelam, V. Modelling complex organic molecules in dense regions: Eley-Rideal and complex induced reaction. *Mon. Not. R. Astron. Soc.* **2015**, *447*, 4004−4017.

(28) Krasnokutski, S. A.; Jäger, C.; Henning, T. Condensation of Atomic Carbon: Possible Routes toward Glycine. *Astrophys. J.* **2020**, *889*, 67.

(29) Bergner, J. B.; Öberg, K. I.; Rajappan, M. Methanol Formation via Oxygen Insertion Chemistry in Ices. *Astrophysical Journal* **2017**, *845*, 29.

(30) Bergner, J. B.; Öberg, K. I.; Rajappan, M. Oxygen Atom Reactions with C₂H₆, C₂H₄, and C₂H₂ in Ices. *Astrophys. J.* **2019**, *874*, 115.

(31) Fedoseev, G.; Cuppen, H. M.; Ioppolo, S.; Lamberts, T.; Linnartz, H. Experimental evidence for glycolaldehyde and ethylene glycol formation by surface hydrogenation of CO molecules under dense molecular cloud conditions. *Mon. Not. R. Astron. Soc.* **2015**, *448*, 1288−1297.

(32) Simons, M. A. J.; Lamberts, T.; Cuppen, H. M. Formation of COMs through CO hydrogenation on interstellar grains. *Astron. Astrophys.* **2020**, *634*, A52.

(33) Bertin, M.; Fayolle, E. C.; Romanzin, C.; Poderoso, H. A. M.; Michaut, X.; Philippe, L.; Jeseck, P.; Öberg, K. I.; Linnartz, H.; Fillion, J.-H. Indirect Ultraviolet Photodesorption from CO:N2 Binary Ices − an Efficient Grain-gas Process. *Astrophys. J.* **2013**, *779*, 120.

(34) Bertin, M.; Romanzin, C.; Doronin, M.; Philippe, L.; Jeseck, P.; Ligterink, N.; Linnartz, H.; Michaut, X.; Fillion, J.-H. UV Photo-desorption of Methanol in Pure and CO-rich Ices: Desorption Rates of the Intact Molecule and of the Photofragments. *Astrophys. J. Lett.* **2016**, *817*, L12.

(35) Fayolle, E.; Bertin, M.; Romanzin, C.; Michaut, X.; Oberg, K.; Linnartz, H.; Fillion, J. H. Photodesorption of interstellar ice analogues: a wavelength-dependent study. In *The Molecular Universe*; 2011; p 157.

(36) Duley, W. W.; Williams, D. A. The formation of H2 on interstellar dust. *Mon. Not. R. Astron. Soc.* **1993**, *260*, 37−42.

(37) Garrod, R. T.; Wakelam, V.; Herbst, E. Non-thermal desorption from interstellar dust grains via exothermic surface reactions. *Astron. Astrophys.* **2007**, *467*, 1103−1115.

(38) Minissale, M.; Dulieu, F. Influence of surface coverage on the chemical desorption process. *J. Chem. Phys.* **2014**, *141*, No. 014304.

(39) Minissale, M.; Dulieu, F.; Cazaux, S.; Hocuk, S. Dust as interstellar catalyst I. Quantifying the chemical desorption process. *Astron. Astrophys.* **2016**, *585*, A24.

(40) Takahashi, J.; Williams, D. A. Chemical Desorption of CO in the Vicinity of H₂ Forming Sites on Dust. In *The Physics and Chemistry of the Interstellar Medium*; 1999; p 375.

(41) Vasyunin, A. I.; Herbst, E. Reactive Desorption and Radiative Association as Possible Drivers of Complex Molecule Formation in the Cold Interstellar Medium. *Astrophys. J.* **2013**, *769*, 34.

(42) Leger, A.; Jura, M.; Omont, A. Desorption from interstellar grains. *Astron. Astrophys.* **1985**, *144*, 147−160.

(43) Hasegawa, T. I.; Herbst, E. Three-Phase Chemical Models of Dense Interstellar Clouds - Gas Dust Particle Mantles and Dust Particle Surfaces. *Mon. Not. R. Astron. Soc.* **1993**, *263*, 589.

(44) Kalvāns, J. Temperature Spectra of Interstellar Dust Grains Heated by Cosmic Rays. I. Translucent Clouds. *Astrophys. J., Suppl. Ser.* **2016**, *224*, 42.

(45) Dartois, E.; Chabot, M.; Id Barkach, T.; Rothard, H.; Augé, B.; Agnihotri, A. N.; Domaracka, A.; Boduch, P. Cosmic ray sputtering yield of interstellar H₂O ice mantles. Ice mantle thickness depend-ence. *Astron. Astrophys.* **2018**, *618*, A173.

(46) Shingledecker, C. N.; Tennis, J.; Gal, R. L.; Herbst, E. On Cosmic-Ray-driven Grain Chemistry in Cold Core Models. *ApJ.* **2018**, *861*, 20.

(47) Shingledecker, C. N.; Herbst, E. A general method for the inclusion of radiation chemistry in astrochemical models. *Phys. Chem. Chem. Phys.* **2018**, *20*, 5359−5367.

(48) Taquet, V.; Ceccarelli, C.; Kahane, C. Multilayer modeling of porous grain surface chemistry: I. The GRAINOBLE model. *A&A* **2012**, *538*, A42.

(49) Minissale, M.; Moudens, A.; Baouche, S.; Chaabouni, H.; Dulieu, F. Hydrogenation of CO-bearing species on grains: unexpected chemical desorption of CO. *Mon. Not. R. Astron. Soc.* **2016**, *458*, 2953−2961.

(50) Jin, M.; Garrod, R. T. Formation of Complex Organic Molecules in Cold Interstellar Environments through Nondiffusive Grain-surface and Ice-mantle Chemistry. *Astrophys. J., Suppl. Ser.* **2020**, *249*, 26.

(51) Codella, C.; et al. Seeds of Life in Space (SOLIS). II. Formamide in protostellar shocks: Evidence for gas-phase formation. *Astron. Astrophys.* **2017**, *605*, L3.

(52) Ligterink, N. F. W.; Calcutt, H.; Coutens, A.; Kristensen, L. E.; Bourke, T. L.; Drozdovskaya, M. N.; Müller, H. S. P.; Wampfler, S. F.; van der Wiel, M. H. D.; van Dishoeck, E. F.; Jørgensen, J. K. The ALMA-PILS survey: Stringent limits on small amines and nitrogen-oxides towards IRAS 16293−2422B. *Astron. Astrophys.* **2018**, *619*, A28.

(53) McGuire, B. A.; Shingledecker, C. N.; Willis, E. R.; Burkhardt, A. M.; El-Abd, S.; Motiyenko, R. A.; Brogan, C. L.; Hunter, T. R.; Margulès, L.; Guillemin, J.-C.; Garrod, R. T.; Herbst, E.; Remijan, A. J. ALMA Detection of Interstellar Methoxymethanol (CH₃OCH₂OH). *Astrophys. J.* **2017**, *851*, L46.

(54) Enrique-Romero, J.; Rimola, A.; Ceccarelli, C.; Ugliengo, P.; Balucani, N.; Skouteris, D. Reactivity of HCO with CH₃ and NH₂ on Water Ice Surfaces. A Comprehensive Accurate Quantum Chemistry Study. *ACS Earth Space Chem.* **2019**, *3*, 2158−2170.

(55) Enrique-Romero, J.; Ceccarelli, C.; Rimola, A.; Skouteris, D.; Balucani, N.; Ugliengo, P. Theoretical computations on the efficiency of acetaldehyde formation on interstellar icy grains. *Astron. Astrophys.* **2021**, *655*, A9.

(56) Enrique-Romero, J.; Álvarez-Barcia, S.; Kolb, F. J.; Rimola, A.; Ceccarelli, C.; Balucani, N.; Meisner, J.; Ugliengo, P.; Lamberts, T.; Kästner, J. Revisiting the Reactivity between HCO and CH₃ on Interstellar Grain Surfaces. *Mon. Not. R. Astron. Soc.* **2020**, *493*, 2523−2527.

(57) Lamberts, T.; Markmeyer, M. N.; Kolb, F. J.; Kästner, J. Formation of Acetaldehyde on CO-Rich Ices. *ACS Earth Space Chem.* **2019**, *3*, 958−963.

(58) Rimola, A.; Skouteris, D.; Balucani, N.; Ceccarelli, C.; Enrique-Romero, J.; Taquet, V.; Ugliengo, P. Can Formamide Be Formed on Interstellar Ice? An Atomistic Perspective. *ACS Earth Space Chem.* **2018**, *2*, 720−734.

(59) Tucker, K. D.; Kutner, M. L.; Thaddeus, P. The Ethynyl Radical C₂H-A New Interstellar Molecule. *Astrophys. J. Lett.* **1974**, *193*, L115.

(60) Teyssier, D.; Fossé, D.; Gerin, M.; Pety, J.; Abergel, A.; Roueff, E. Carbon budget and carbon chemistry in Photon Dominated Regions. *Astron. Astrophys.* **2004**, *417*, 135−149.

(61) Bouvier, M.; López-Sepulcre, A.; Ceccarelli, C.; Kahane, C.; Imai, M.; Sakai, N.; Yamamoto, S.; Dagdigian, P. J. Hunting for hot corinos and WCCC sources in the OMC-2/3 filament. *A&A* **2020**, *636*, A19.

(62) Lucas, R.; Liszt, H. S. Comparative chemistry of diffuse clouds. I. C_2H and C_3H_2. *Astron. Astrophys.* **2000**, *358*, 1069−1076.

(63) Gerin, M.; Kaźmierczak, M.; Jastrzebska, M.; Falgarone, E.; Hily-Blant, P.; Godard, B.; de Luca, M. The tight correlation of CCH, and c-C₃H₂ in diffuse and translucent clouds. *Astron. Astrophys.* **2011**, *525*, A116.

(64) Sakai, N.; Sakai, T.; Hirota, T.; Yamamoto, S. Abundant Carbon-Chain Molecules toward the Low-Mass Protostar IRAS 04368 + 2557 in L1527. *Astrophys. J.* **2008**, *672*, 371−381.

(65) Sakai, N.; Yamamoto, S. Warm Carbon-Chain Chemistry. *Chem. Rev.* **2013**, *113*, 8981−9015.

(66) Oya, Y.; Sakai, N.; Sakai, T.; Watanabe, Y.; Hirota, T.; Lindberg, J. E.; Bisschop, S. E.; Jørgensen, J. K.; van Dishoeck, E. F.; Yamamoto, S. A Substellar-Mass Protostar and Its Outflow of IRAS 15398−3359 Revealed by Subarcsecond-Resolution Observations of H₂ CO and CCH. *ApJ.* **2014**, *795*, 152.

(67) Zhang, Y.; Higuchi, A. E.; Sakai, N.; Oya, Y.; López-Sepulcre, A.; Imai, M.; Sakai, T.; Watanabe, Y.; Ceccarelli, C.; Lefloch, B.; Yamamoto, S. Rotation in the NGC 1333 IRAS 4C Outflow. *ApJ.* **2018**, *864*, 76.

(68) Kastner, J. H.; Hily-Blant, P.; Rodriguez, D. R.; Punzi, K.; Forveille, T. Unbiased Millimeter-Wave Line Surveys of TW Hya and V4046 Sgr: The Enhanced C₂H and CN Abundances of Evolved Protoplanetary Disks. *ApJ.* **2014**, *793*, 55.

(69) Kastner, J. H.; Qi, C.; Gorti, U.; Hily-Blant, P.; Oberg, K.; Forveille, T.; Andrews, S.; Wilner, D. A Ring of C₂H in the Molecular Disk Orbiting TW Hya. *ApJ.* **2015**, *806*, 75.

(70) Miotello, A.; Facchini, S.; van Dishoeck, E. F.; Cazzoletti, P.; Testi, L.; Williams, J. P.; Ansdell, M.; van Terwisga, S.; van der Marel, N. Bright C ₂ H emission in protoplanetary discs in Lupus: high volatile C/O > 1 ratios. *A&A* **2019**, *631*, A69.

(71) Guzmán, V. V.; et al. Molecules with ALMA at Planet-forming Scales (MAPS). VI. Distribution of the Small Organics HCN, C ₂ H, and H ₂ CO. *Astrophys. J., Suppl. Ser.* **2021**, *257*, 6.

(72) Meier, D. S.; Turner, J. L. Spatially Resolved Chemistry in Nearby Galaxies. I. The Center of IC 342. *ApJ.* **2005**, *618*, 259−280.

(73) Sakai, N.; et al. A Chemical View of Protostellar-Disk Formation in L1527. *ApJ.* **2014**, *791*, L38.

(74) Friberg, P.; Madden, S. C.; Hjalmarson, A.; Irvine, W. M. Methanol in dark clouds. *Astron. Astrophys.* **1988**, *195*, 281−289.

(75) Dickens, J. E.; Irvine, W. M.; Snell, R. L.; Bergin, E. A.; Schloerb, F. P.; Pratap, P.; Miralles, M. P. A Study of the Physics and Chemistry of L134N. *Astrophys. J.* **2000**, *542*, 870−889.

(76) Padovani, M.; Walmsley, C. M.; Tafalla, M.; Galli, D.; Müller, H. S. P. C{2}H in prestellar cores. *Astron. Astrophys.* **2009**, *505*, 1199−1211.

(77) Higuchi, A. E.; Sakai, N.; Watanabe, Y.; López-Sepulcre, A.; Yoshida, K.; Oya, Y.; Imai, M.; Zhang, Y.; Ceccarelli, C.; Lefloch, B.; Codella, C.; Bachiller, R.; Hirota, T.; Sakai, T.; Yamamoto, S. Chemical Survey toward Young Stellar Objects in the Perseus Molecular Cloud Complex. *Astrophys. J., Suppl. Ser.* **2018**, *236*, 52.

(78) Liu, X. C.; Wu, Y.; Zhang, C.; Liu, T.; Yuan, J.; Qin, S. L.; Ju, B. G.; Li, L. X. C₂H N = 1 - 0 and N₂H⁺ J = 1 - 0 observations of Planck Galactic cold clumps. *Astron. Astrophys.* **2019**, *622*, A32.

(79) Taniguchi, K.; Plunkett, A.; Herbst, E.; Dobashi, K.; Shimoikura, T.; Nakamura, F.; Saito, M. Investigation of chemical differentiation among the NGC 2264 cluster-forming clumps. *Mon. Not. R. Astron. Soc.* **2020**, *493*, 2395−2409.

(80) Van Look, H.; Peeters, J. Rate Coefficients of the Reactions of C₂H with O₂, C₂H₂, and H₂O between 295 and 450 K. *J. Chem. Phys. A* **1995**, *99*, 16284−16289.

(81) Ding, Y.-h.; Zhang, X.; Li, Z.-s.; Huang, X.-r.; Sun, C.-c. Is the C2H+H2O Reaction Anomalous? *J. Chem. Phys. A* **2001**, *105*, 8206−8215.

(82) Carl, S. A.; Minh Thi Nguyen, H.; Elsamra, R. M. I.; Tho Nguyen, M.; Peeters, J. Pulsed Laser Photolysis and Quantum Chemical-Statistical Rate Study of the Reaction of the Ethynyl Radical with Water Vapor. *J. Chem. Phys.* **2005**, *122*, 114307.

(83) Moore, M. H.; Hudson, R. L. Infrared Study of Ion-Irradiated Water-Ice Mixtures with Hydrocarbons Relevant to Comets. *Icarus* **1998**, *135*, 518−527.

(84) Hudson, R. L.; Moore, M. H. Solid-Phase Formation of Interstellar Vinyl Alcohol. *Astrophys. J.* **2003**, *586*, L107−L110.

(85) Hudson, R. L.; Loeffler, M. J. Ketene Formation in Interstellar Ices: A Laboratory Study. *Astrophys. J.* **2013**, *773*, 109.

(86) Wu, C. R.; Judge, D.; Cheng, B.-M.; Shih, W.-H.; Yih, T.-S.; Ip, W. Extreme ultraviolet photon-induced chemical reactions in the C_2H_2–H_2O mixed ices at 10 K. *Icarus* **2002**, *156*, 456−473.

(87) Chuang, K. J.; Fedoseev, G.; Scirè, C.; Baratta, G. A.; Jäger, C.; Henning, T.; Linnartz, H.; Palumbo, M. E. Formation of complex organic molecules in molecular clouds: acetaldehyde, vinyl alcohol, ketene, and ethanol via the "energetic" processing of C_2H_2 ice. *Astron. Astrophys.* **2021**, *650*, A85.

(88) Haller, I.; Pimentel, G. C. Reaction of Oxygben Atoms with Acetylene to Form Ketene. *J. Am. Chem. Soc.* **1962**, *84*, 2855−2857.

(89) Zasimov, P. V.; Ryazantsev, S. V.; Tyurin, D. A.; Feldman, V. I. Radiation-induced chemistry in the C_2H_2-H_2O system at cryogenic temperatures: a matrix isolation study. *Mon. Not. R. Astron. Soc.* **2019**, *491*, 5140−5150.

(90) Bennett, C. J.; Osamura, Y.; Lebar, M. D.; Kaiser, R. I. Laboratory Studies on the Formation of Three C_2H_4O Isomers-Acetaldehyde (CH_3CHO), Ethylene Oxide (c-C_2H_4O), and Vinyl Alcohol (CH_2CHOH)-in Interstellar and Cometary Ices. *Astrophys. J.* **2005**, *634*, 698−711.

(91) Vazart, F. Can Interstellar CH_3OCH_3 + H^+ Lead to Protonated Acetaldehyde CH_3CHOH^+? *19th International Conference on Computational Science and Its Applications, ICCSA 2019*, Saint Petersburg, Russia, July 1−4, 2019, Part VII. 2019; pp 138−139.

(92) Frisch, M. J. et al. *Gaussian 16*, Rev C.01; Gaussian Inc.: Wallingford CT, 2016.

(93) Hehre, W. J.; Ditchfield, R.; Pople, J. A. Self—Consistent Molecular Orbital Methods. XII. Further Extensions of Gaussian—Type Basis Sets for Use in Molecular Orbital Studies of Organic Molecules. *J. Chem. Phys.* **1972**, *56*, 2257−2261.

(94) Hariharan, P. C.; Pople, J. A. The influence of polarization functions on molecular orbital hydrogenation energies. *Theor. Chim. Acta* **1973**, *28*, 213−222.

(95) Krishnan, R.; Binkley, J. S.; Seeger, R.; Pople, J. A. Self-consistent molecular orbital methods. XX. A basis set for correlated wave functions. *J. Chem. Phys.* **1980**, *72*, 650−654.

(96) Grimme, S. Semiempirical GGA-type density functional constructed with a long-range dispersion correction. *J. Comput. Chem.* **2006**, *27*, 1787−1799.

(97) Grimme, S.; Antony, J.; Ehrlich, S.; Krieg, H. A consistent and accurate ab initio parametrization of density functional dispersion correction (DFT-D) for the 94 elements H-Pu. *J. Chem. Phys.* **2010**, *132*, 154104.

(98) Grimme, S.; Ehrlich, S.; Goerigk, L. Effect of the damping function in dispersion corrected density functional theory. *J. Comput. Chem.* **2011**, *32*, 1456−1465.

(99) Becke, A. D. A new mixing of Hartree−Fock and local density-functional theories. *J. Chem. Phys.* **1993**, *98*, 1372−1377.

(100) Lee, C.; Yang, W.; Parr, R. G. Development of the Colle-Salvetti correlation-energy formula into a functional of the electron density. *Phys. Rev. B* **1988**, *37*, 785−789.

(101) Zhao, Y.; Truhlar, D. The M06 suite of density functionals for main group thermochemistry, thermochemical kinetics, noncovalent interactions, excited states, and transition elements: Two new functionals and systematic testing of four M06 functionals and 12 other functionals. *Theor. Chem. Acc.* **2008**, *119*, 525.

(102) Zhao, Y.; Truhlar, D. G. Hybrid Meta Density Functional Theory Methods for Thermochemistry, Thermochemical Kinetics, and Noncovalent Interactions: The MPW1B95 and MPWB1K Models and Comparative Assessments for Hydrogen Bonding and van der Waals Interactions. *J. Phys. Chem. A* **2004**, *108*, 6908−6918.

(103) Zhao, Y.; Truhlar, D. G. Design of Density Functionals That Are Broadly Accurate for Thermochemistry, Thermochemical Kinetics, and Nonbonded Interactions. *J. Phys. Chem. A* **2005**, *109*, 5656−5667. PMID: 16833898

(104) Chai, J.-D.; Head-Gordon, M. Systematic optimization of long-range corrected hybrid density functionals. *J. Chem. Phys.* **2008**, *128*, No. 084106.

(105) Raghavachari, K.; Trucks, G. W.; Pople, J. A.; Head-Gordon, M. A fifth-order perturbation comparison of electron correlation theories. *Chem. Phys. Lett.* **1989**, *157*, 479−483.

(106) McQuarrie, D. A. *Statistical mechanics*; Harper & Row New York, 1975.

(107) Fermann, J. T.; Auerbach, S. Modeling proton mobility in acidic zeolite clusters: II. Room temperature tunneling effects from semiclassical rate theory. *J. Chem. Phys.* **2000**, *112*, 6787−6794.

(108) Rimola, A.; Taquet, V.; Ugliengo, P.; Balucani, N.; Ceccarelli, C. Combined Quantum Chemical and Modeling Study of CO Hydrogenation on Water Ice. *Astron. Astrophys.* **2014**, *572*, A70.

(109) Chalk, A. J.; Radom, L. Proton-Transport Catalysis:A Systematic Study of the Rearrangement of the Isoformyl Cation to the Formyl Cation. *J. Am. Chem. Soc.* **1997**, *119*, 7573−7578.

(110) Molpeceres, G.; Kästner, J.; Fedoseev, G.; Qasim, D.; Schömig, R.; Linnartz, H.; Lamberts, T. Carbon Atom Reactivity with Amorphous Solid Water: H2O-Catalyzed Formation of H2CO. *J. Phys. Chem. Lett.* **2021**, *12*, 10854−10860. PMID: 34727500

(111) Rimola, A.; Sodupe, M.; Ugliengo, P. Deep-space glycine formation via Strecker-type reactions activated by ice water dust mantles. A computational approach. *Phys. Chem. Chem. Phys.* **2010**, *12*, 5285−5294.

(112) Peters, P. S.; Duflot, D.; Faure, A.; Kahane, C.; Ceccarelli, C.; Wiesenfeld, L.; Toubin, C. Theoretical Investigation of the Isomer-ization of trans-HCOH to H2CO: An Example of a Water-Catalyzed Reaction. *J. Phys. Chem. A* **2011**, *115*, 8983−8989.

(113) Pantaleone, S.; Enrique-Romero, J.; Ceccarelli, C.; Ugliengo, P.; Balucani, N.; Rimola, A. Chemical Desorption versus Energy Dissipation: Insights from Ab Initio Molecular Dynamics of HCO· Formation. *Astrophys. J.* **2020**, *897*, 56.

(114) Pantaleone, S.; Enrique-Romero, J.; Ceccarelli, C.; Ferrero, S.; Balucani, N.; Rimola, A.; Ugliengo, P. H2 Formation on Interstellar Grains and the Fate of Reaction Energy. *Astrophys. J.* **2021**, *917*, 49.

(115) Hidaka, H.; Watanabe, M.; Kouchi, A.; Watanabe, N. Reaction Routes in the CO-H2CO-dn-CH3OH-dmSYSTEM Clarified from H(D) Exposure of Solid Formaldehyde at Low Temperatures. *Astrophys. J.* **2009**, *702*, 291−300.

(116) Watanabe, N.; Kouchi, A. Efficient Formation of Form-aldehyde and Methanol by the Addition of Hydrogen Atoms to CO in H2O-CO Ice at 10 K. *Astrophys. J.* **2002**, *571*, L173−L176.

(117) Osamura, Y.; Roberts, H.; Herbst, E. On the possible interconversion between pairs of deuterated isotopomers of methanol, its ion, and its protonated ion in star-forming regions. *Astron. Astrophys.* **2004**, *421*, 1101−1111.

(118) Nagaoka, A.; Watanabe, N.; Kouchi, A. H-D Substitution in Interstellar Solid Methanol: A Key Route for D Enrichment. *Astrophys. J.* **2005**, *624*, L29−L32.

(119) Fuchs, G. W.; Cuppen, H. M.; Ioppolo, S.; Romanzin, C.; Bisschop, S. E.; Andersson, S.; van Dishoeck, E. F.; Linnartz, H. Hydrogenation reactions in interstellar CO ice analogues - A combined experimental/theoretical approach. *Astron. Astrophys.* **2009**, *505*, 629−639.

(120) Bennett, J. E.; Mile, B. Studies of radical−molecule reactions using a rotating cryostat. Reactions of hydrogen atoms with organic substrates at 77 K. *J. Chem. Soc., Faraday Trans. 1* **1973**, *69*, 1398−1414.

(121) Hiraoka, K.; Takayama, T.; Euchi, A.; Handa, H.; Sato, T. Study of the Reactions of H and D Atoms with Solid C2H2, C2H4, and C2H6at Cryogenic Temperatures. *Astrophysical Journal* **2000**, *532*, 1029−1037.

(122) Kobayashi, H.; Hidaka, H.; Lamberts, T.; Hama, T.; Kawakita, H.; KĂˇstner, J.; Watanabe, N. Hydrogenation and Deuteration of C2H2and C2H4on Cold Grains: A Clue to the Formation Mechanism of C2H6with Astronomical Interest. *Astrophysical Journal* **2017**, *837*, 155.

(123) Chuang, K. J.; Fedoseev, G.; Qasim, D.; Ioppolo, S.; Jäger, C.; Henning, T.; Palumbo, M. E.; van Dishoeck, E. F.; Linnartz, H. Formation of complex molecules in translucent clouds: acetaldehyde,

vinyl alcohol, ketene, and ethanol via "nonenergetic" processing of C2H2 ice. *Astron. Astrophys.* **2020**, *635*, A199.

(124) Cernicharo, J.; Marcelino, N.; Roueff, E.; Gerin, M.; Jiménez-Escobar, A.; Muñoz Caro, G. M. Discovery of the Methoxy Radical, CH₃O, toward B1: Dust Grain and Gas-phase Chemistry in Cold Dark Clouds. *Astrophys. J.* **2012**, *759*, L43.

(125) Vastel, C.; Ceccarelli, C.; Lefloch, B.; Bachiller, R. The Origin of Complex Organic Molecules in Prestellar Cores. *Astrophys. J.* **2014**, *795*, L2.

(126) Jaber, A. A.; Ceccarelli, C.; Kahane, C.; Caux, E. The Census of Complex Organic Molecules in the Solar-type Protostar IRAS16293−2422. *Astrophys. J.* **2014**, *791*, 29.

(127) Jiménez-Serra, I.; Vasyunin, A. I.; Caselli, P.; Marcelino, N.; Billot, N.; Viti, S.; Testi, L.; Vastel, C.; Lefloch, B.; Bachiller, R. The Spatial Distribution of Complex Organic Molecules in the L1544 Prestellar Core. *Astrophys. J.* **2016**, *830*, L6.

(128) Scibelli, S.; Shirley, Y. Prevalence of Complex Organic Molecules in Starless and Prestellar Cores within the Taurus Molecular Cloud. *Astrophys. J.* **2020**, *891*, 73.

Chapter 7

Formation of acetaldehyde on H_2O:CO dirty ice surfaces

Introduction

To complete the work on the formation pathways of COMs, the synthesis of acetaldehyde (CH_3CHO) on the surface of a periodic model of dirty ice was investigated. Acetaldehyde is one of the most commonly detected COMs, found in cold pre-stellar cores, hot cores and hot corinos, protostellar molecular shocks, young disks, and also in comets. Both gas-phase and grain-surface chemistry are thought to play a crucial role in its synthesis. While in warm environments the ethanol genealogical tree is currently the most promising explanation for its presence (Skouteris et al., 2018), it is unclear whether this is the only mechanism at work in cold regions or grain-surface processes contribute as well. The $HCO^{\bullet}$ + $^{\bullet}CH_3$ radical-radical recombination reaction has some drawbacks. The pathway leading to acetaldehyde has a diffusion barrier and, additionally, it presents a competitive channel yielding CO + CH_4 (Enrique-Romero et al., 2016; Lamberts et al., 2019). Furthermore, an increase in the mobility of the radicals causes a decrease in the acetaldehyde formation efficiency (Enrique-Romero et al., 2021).

In '*Quantum mechanical modelling of the grain-surface formation of acetaldehyde on H_2O:CO dirty ice surfaces*' (Perrero et al., 2023, *MNRAS*, **525**, 2654), the formation of acetaldehyde was investigated by applying the 'radical + closed-shell' scheme characterised in previous works (Rimola et al., 2018; Perrero et al., 2022). The novelty of this study regards the adoption of a periodic ice model formed by 25% of CO and 75% of H_2O, defined as 'dirty ice', whose composition reflects the two most abundant species contained in icy mantles. Moreover, CO constitutes the closed-shell species involved in the reaction, at variance with previous investigations, in which water was the mantle component involved in the reaction.

Results

The synthesis of acetaldehyde was simulated via a two-step process: i) $^{\bullet}CH_3$ + $CO_{(ice)} \rightarrow CH_3CO^{\bullet}$; and ii) $CH_3CO^{\bullet}$ + $H^{\bullet} \rightarrow CH_3CHO$. The $CO_{(ice)}$ belongs to dirty ice surfaces that were prepared *ad hoc* for this study. The H_2O:CO surfaces were modelled from the bulk of a crystalline P-ice water, after substituting 25% of H_2O molecules with CO in the bulk and cutting along the (001), (010), and (100) planes. Three amorphous-like surfaces, characterised by the presence of clathrate-like cages of H_2O surrounding CO molecules, were obtained, as shown in Figure 7.1. All the calculations were performed with CRYSTAL17 (Dovesi et al., 2018), with the exception of post-HF refinements of the reaction energetics, for which GAUSSIAN16 was employed (Frisch et al., 2016).
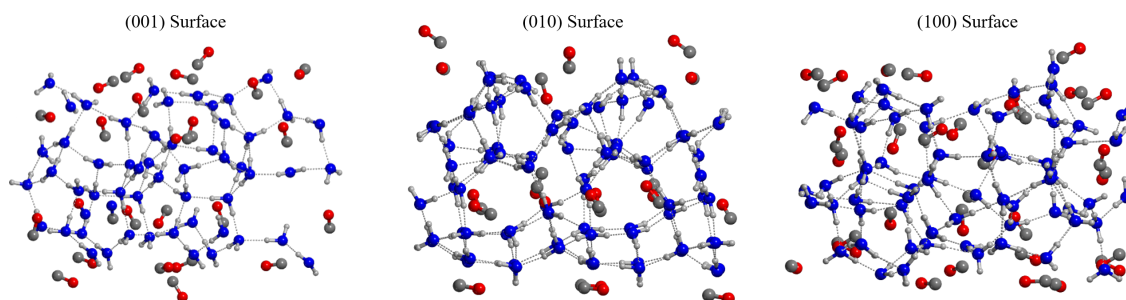
Figure 7.1: Structures of the (001), (010), and (100) ice surfaces, optimised at HF-3c level of theory. Color code: H, white; C, grey; O atoms belonging to H$_2$O, blue; O atoms belonging to the CO, red.

The size of the surface models, containing approximately 200 atoms per unit cell, rendered impracticable the adoption of a high level of theory to characterise the reaction profiles. For this reason, two benchmark studies were conducted with the purpose of identifying the most appropriate methodology at this scope and of evaluating the quality of the obtained results.

The first benchmark concerned the $^\bullet$CH$_3$ + CO $\rightarrow$ CH$_3$CO$^\bullet$ gas-phase reaction. BHLYP-D3(BJ)/6-311G(d,p)//HF-3c, hereafter DFT//HF-3c, was the most suitable methodology to describe the energy barrier of the reaction, when compared against CCSD(T)/aug-cc-PVTZ//BHLYP-D3(BJ)/6-311G(d,p), hereafter CCSD(T)//DFT.

The second benchmark compared the performance of the DFT//HF-3c scheme against CCSD(T)/CBS//DFT when in presence of a surface. Three models were selected for this benchmark: a cluster of 20 CO molecules, and two periodic crystalline ice models where only one surface H$_2$O molecule was replaced with a CO. In this case, the refinement at CCSD(T) level of theory was performed only on a small fragment extracted from the cluster/periodic system, applying the ONIOM2 scheme with the OAN(C) equation to obtain a CBS limit quality reaction energy (see Sections 2.2.4 and 2.6.4 for a detailed explanation of these techniques). The computational resources required for these calculations were not sufficient to characterize the reaction on additional surface models, and thus obtaining a correction factor to improve the DFT//HF-3c data was outside the scope of the benchmarking. The data relative to the three models shown in Figure 7.2 clearly highlight that the DFT//HF-3c methodology underestimates the barriers of $\simeq$ 50% compared to CCSD(T)/CBS//DFT, suggesting that DFT//HF-3c data should be carefully interpreted.

On the dirty ice amorphous-like surfaces previously modelled, both a Langmuir-Hinshelwood (LH) and an Eley-Rideal (ER) mechanisms were simulated. The LH reaction mechanism consisted in the adsorption of $^\bullet$CH$_3$ onto different binding sites of each surface and its subsequent diffusion toward CO, to form the acetyl radical. In total, the reaction mechanism was simulated nine times, resulting in a LH potential energy barrier (ΔE$_{TS}$, where the ZPE is not included) that ranges from 5.8 to 36.8 kJ mol^{-1}, depending on the local morphology of the reactive site.

The reaction profile characterised by the lowest barrier was chosen to perform the hydrogenation step, which consisted in the adsorption of the H atom in five different positions around the acetyl radical. The formation of CH$_3$CHO is a barrierless radical-radical recombination when the H atom is well oriented toward the CO moiety of CH$_3$CO. Alternatively, even in cold molecular clouds (MCs), H atoms have enough mobility to jump on the surface and find the proper orientation to react, provided that the two reactants are
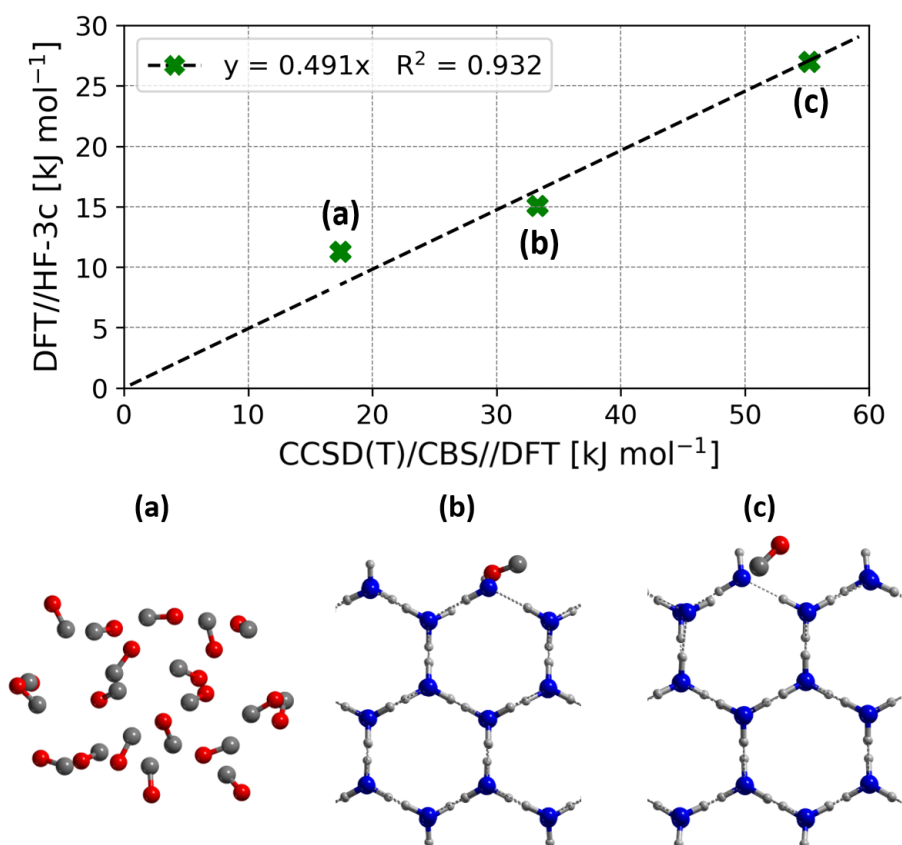
Figure 7.2: Plot of the DFT//HF-3c against CCSD(T)/CBS//DFT potential energy barriers of the reaction $^\bullet$CH$_3$ + CO$_{(ice)}$ → CH$_3$CO$^\bullet$ performed on three test models (a cluster made of 20 CO molecules (a), and two crystalline periodic H$_2$O ice models where a water molecule exposing a dangling hydrogen atom (b), and one exposing a dangling oxygen atom (c) where substituted with a CO molecule). From this plot, it appears that DFT//HF-3c methodology underestimates the barriers compared to CCSD(T)/CBS//DFT of a factor two.

in an electronic spin state that enables the formation of a chemical bond. Otherwise, an intersystem crossing could take the system from the ground triplet spin state to an excited open-shell singlet state, ultimately allowing the formation of acetaldehyde.

At variance, the ER mechanism was modelled by simulating the progressive approach of $^\bullet$CH$_3$ to a CO molecule belonging to the outer layer of the surface, avoiding any thermalisation, and thus directly reacting to yield CH$_3$CO$^\bullet$. The two-dimensional PES of the process is characterised by a local minimum due to the formation of a van der Waals complex, followed by a maximum that represents the TS leading to CH$_3$CO$^\bullet$. In this case, ΔE_{TS} $\simeq$ 8.5 kJ mol^{-1}, whereas the energy difference between the van der Waals minimum and the TS maximum is $\simeq$ 16 kJ, comparable with the average LH reaction barrier (see Figure 7.3). Despite presenting a smaller barrier than the LH mechanism, the ER reaction should not have an energy barrier in order to effectively yield CH$_3$CO$^\bullet$.

The hydrogenation step was performed in a similar fashion to the previous reaction, and resulted in a repulsive interaction as the distance between the reactants in a triplet electronic spin state decreases. However, if the electronic spin state of the system is an open-shell singlet, the radical-radical recombination reaction occurs barrierlessly, yielding acetaldehyde.

Finally, the H$^\bullet$ + CO → HCO$^\bullet$ reaction could represent a competitive channel against

acetyl hydrogenation. This process is known to have a small barrier of $\simeq 5$ kJ mol^{-1} and to occur through tunnelling (Rimola et al., 2014; Pantaleone et al., 2020). However, both the high abundance of H atoms and the barrierless nature of acetyl hydrogenation are in favour of the latter reaction rather than the formation of HCO$^\bullet$.

From the second benchmark performed in this study (see Figure 7.2), one can roughly assume that the values computed for the formation of acetyl on the surface have to be doubled (ΔE_{TS} = 11.6$-$73.6 kJ mol^{-1}) to be fairly compared with the gas-phase reaction barrier (ΔE_{TS} = 17.9 kJ mol^{-1}). It follows that grain-surface reactions are less favourable than the gas-phase process in the majority of the characterised cases and are in general unlikely to take place in cold MCs. Warmer environments, where the thermal energy would allow overcoming the reaction barrier, would instead cause the sublimation of the reactants, preventing acetyl, and consequently acetaldehyde, to form (Enrique-Romero et al., 2021).
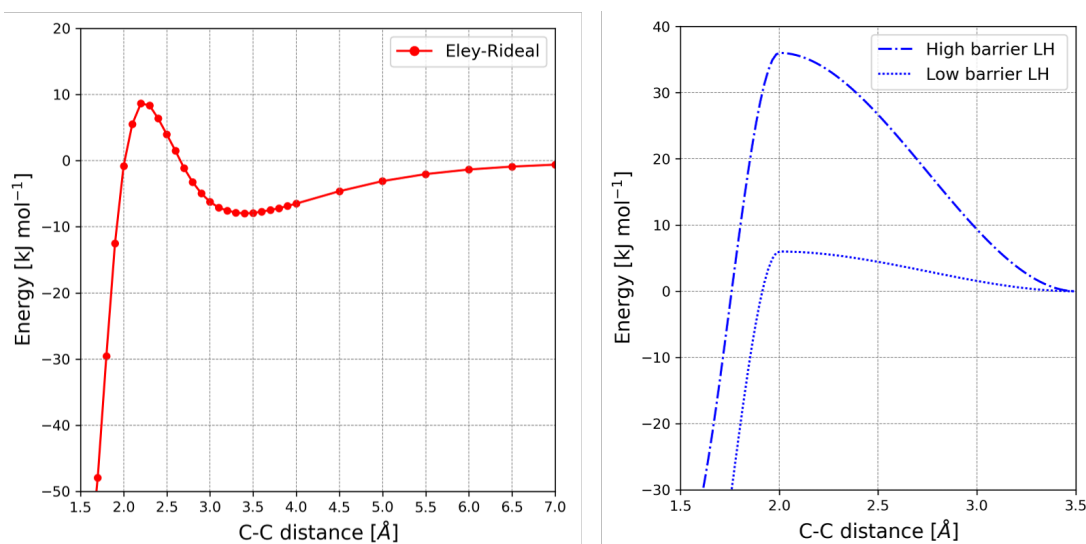

Figure 7.3: Energy profiles (in kJ mol^{-1}) for the $^\bullet$CH$_3$ + CO $\rightarrow$ CH$_3$CO$^\bullet$ reaction via the Eley-Rideal (left) and Langmuir-Hinshelwood (right) mechanisms. The C–C distance is given in Å. Only the two Langmuir-Hinshelwood profiles with the largest (dash-dotted) and the smallest (dotted) barriers are represented.

In summary, both the LH and ER mechanisms do not represent feasible pathways to form acetaldehyde on the surface of dust grains in cold environments. The CO embedded in the dirty ice model does not appear to be activated by the surrounding water molecules, as their interaction is based on dispersive and quadrupolar forces that make the CO rather hydrophobic. Furthermore, it seems that the presence of the surface provides an additional, although modest, interaction between the $^\bullet$CH$_3$ and the surface that needs to be broken in order to allow the formation of the C$-$C bond. In contrast, the ice surface is well known to favour hydrogenation reactions by acting as a reactant concentrator and as a third body.

The numerous studies carried out so far, including experimental and modelling ones, tend to agree that acetaldehyde is unlikely to be a grain-surface product (Simons et al., 2020; Gutiérrez-Quintanilla et al., 2021). Although this COM can be formed in the gas-phase as a product of ethanol processing, consequent to the formation of $^\bullet$CH$_2$CH$_2$OH and $^\bullet$CH$_3$CHOH radicals, followed by reaction with atomic oxygen (Skouteris et al., 2018), its

recent detection in the interstellar ice mantles points toward the presence of a favourable grain-surface synthetic pathway. In protostar IRAS 2A, a gas-phase CH_3CH_2OH/CH_3CHO ratio close to that of the solid phase suggests acetaldehyde to be a product of surface chemistry (Rocha et al., 2024). However, a two-step reaction process characterised by Martínez-Bachs et al. (2023) shows that the conversion of CH_3CH_2OH into CH_3CHO is not favoured on the ice mantle. Reactions started by both the C atom and the CCO radical, characterised from both a theoretical and an experimental standpoint, might be promising candidates to explain the presence of COMs in the ice mantles, although they appear to be at work only in PDRs, where C atoms and CO ice are simultaneously present (Fedoseev et al., 2022; Ferrero et al., 2023). In conclusion, the grain-surface formation of acetaldehyde still represents a challenge for the astrochemical community.

Future perspectives

Our current knowledge regarding interstellar ice mantles concerns their composition rather than their morphology. This lack of information hampers the characterisation of surface models of true dirty ices, i.e., H_2O mixed with traces of CO, CO_2, NH_3, CH_3OH, etc. At present, only the H_2O:CO models proposed in this work and those prepared by Zamirri et al. (2018), with the aim of characterising the CO infrared fingerprint in interstellar water ice models, have been designed. Currently, H_2O:CO_2 mixed ice models aimed at infrared spectra simulation are being prepared by M. Andersen[1] and T. Lamberts[2]. As well as for H_2O:CO mixed ice, the major issue arising during the preparation of such models is the segregation of the polar and apolar fractions of the ice, consequent to the global optimisation of their structure (T. Lamberts, private communication). Nonetheless, this kind of models are very important, because the interaction of minor species with water ice molecules can lead to their activation, increasing their propensity to react, in addition to influencing the strength of the interaction between the adsorbates and the ice. Usually, the activation of a species is investigated by modelling its adsorption onto pure water ice surfaces, however, it is not comparable with the case in which such species forms part of the ice network (Rimola et al., 2021).

This work paves the way for the development of new models of dirty ice incorporating additional species. Building an amorphous dirty ice model requires including several atoms in its structure. The main limitation of using large (periodic) models to simulate reactions is that it does not allow to perform high theory level calculations. A valid strategy could be exploiting ONIOM methodologies to treat large structures at a low theory level and at the same time to accurately model the specific zone of the system in which the reactivity takes place. The development of increasingly efficient ML potentials and the incoming information from JWST (M. K. McClure et al., 2023; Dartois et al., 2024) could find fertile ground to promote the study of these systems.

References

Dartois, E. et al. (2024). "Spectroscopic sizing of interstellar icy grains with JWST". *Nat. Astron.* **8**, 359. DOI: 10.1038/s41550-023-02155-x.

Dovesi, R. et al. (2018). "Quantum-mechanical condensed matter simulations with CRYSTAL". *Wiley Interdisc. Rev. Comput. Mol. Sci.* **8**, e1360. DOI: 10.1002/wcms.1360.

---

[1] https://aias.au.dk/aias-fellows/mie-andersen
[2] https://www.universiteitleiden.nl/en/staffmembers/thanja-lamberts#tab-1

Enrique-Romero, J. et al. (2016). "The (impossible?) formation of acetaldehyde on the grain surfaces: insights from quantum chemical calculations". *Mon. Not. R. Astron. Soc.* **459**, L6. DOI: 10.1093/mnrasl/slw031.

Enrique-Romero, J. et al. (2021). "Theoretical computations on the efficiency of acetaldehyde formation on interstellar icy grains". *Astron. Astrophys.* **655**, A9. DOI: 10.1051/0004-6361/202141531.

Fedoseev, G. et al. (2022). "Hydrogenation of accreting C atoms and CO molecules - simulating ketene and acetaldehyde formation under dark and translucent cloud conditions". *Astrophys. J.* **924**, 110. DOI: 10.3847/1538-4357/ac3834.

Ferrero, S. et al. (2023). "Where Does the Energy Go during the Interstellar NH_3 Formation on Water Ice? A Computational Study". *The Astrophysical Journal* **944**, 142. DOI: 10.3847/1538-4357/acae8e.

Frisch, M. J. et al. (2016). *Gaussian16 Revision C.01*. Gaussian Inc. Wallingford CT.

Gutiérrez-Quintanilla, A. et al. (2021). "iCOM formation from radical chemistry: a mechanistic study from cryogenic matrix coupled with IR and EPR spectroscopies". *Mon. Not. R. Astron. Soc.* **506**, 3734. DOI: 10.1093/mnras/stab1850.

Lamberts, T. et al. (2019). "Formation of acetaldehyde on CO-rich ices". *ACS Earth Space Chem.* **3**, 958. DOI: 10.1021/acsearthspacechem.9b00029.

Martínez-Bachs, B. et al. (2023). "Gas-phase vs. grain-surface formation of interstellar complex organic molecules: a comprehensive quantum-chemical study". *Int. J. Mol. Sci.* **24**, 16824. DOI: 10.3390/ijms242316824.

McClure, M. K. et al. (2023). "An Ice Age JWST inventory of dense molecular cloud ices". *Nat. Astron.* **7**, 431. DOI: 10.1038/s41550-022-01875-w.

Pantaleone, S. et al. (2020). "Chemical desorption versus energy dissipation: insights from ab initio molecular dynamics of HCO· formation". *Astrophys. J.* **897**, 56. DOI: 10.3847/1538-4357/ab8a4b.

Perrero, J. et al. (2023). "Quantum mechanical modelling of the grain-surface formation of acetaldehyde on H_2O:CO dirty ice surfaces". *Mon. Not. R. Astron. Soc.* **525**, 2654. DOI: 10.1093/mnras/stad2459.

Perrero, J. et al. (2022). "Non-energetic formation of ethanol via CCH reaction with interstellar H_2O ices. A computational chemistry study". *ACS Earth Space Chem.* **6**, 496. DOI: 10.1021/acsearthspacechem.1c00369.

Rimola, A. et al. (2014). "Combined quantum chemical and modeling study of CO hydrogenation on water ice". *Astron. Astrophys.* **572**, A70. DOI: 10.1051/0004-6361/201424046.

Rimola, A. et al. (2018). "Can formamide be formed on interstellar ice? An atomistic perspective". *ACS Earth Space Chem.* **2**, 720. DOI: 10.1021/acsearthspacechem.7b00156.

Rimola, A. et al. (2021). "Computational surface modelling of ices and minerals of interstellar interest - Insights and perspectives". *Minerals* **11**, 26. DOI: 10.3390/min11010026.

Rocha, W. et al. (2024). "JWST Observations of Young protoStars (JOYS+): Detecting icy complex organic molecules and ions - I. CH_4, SO_2, $HCOO^-$, OCN^-, H_2CO, HCOOH, CH_3CH_2OH, CH_3CHO, CH_3OCHO, and CH_3COOH". *Astron. Astrophys.* **683**, A124. DOI: 10.1051/0004-6361/202348427.

Simons, M. A. J. et al. (2020). "Formation of COMs through CO hydrogenation on interstellar grains". *Astron. Astrophys.* **634**, A52. DOI: 10.1051/0004-6361/201936522.

Skouteris, D. et al. (2018). "The genealogical tree of ethanol: gas-phase formation of glycolaldehyde, acetic acid, and formic acid". *Astrophys. J.* **854**, 135. DOI: 10.3847/1538-4357/aaa41e.

Zamirri, L. et al. (2018). "IR spectral fingerprint of carbon monoxide in interstellar water-ice models". *Mon. Not. R. Astron. Soc.* **480**, 1427. DOI: 10.1093/mnras/sty1927.

Quantum mechanical modelling of the grain-surface formation of acetaldehyde on H$_2$O:CO dirty ice surfaces

Jessica Perrero,[1,2] Piero Ugliengo [ORCID],[2] Cecilia Ceccarelli [ORCID][3] and Albert Rimola [ORCID][1]★

[1]*Departament de Química, Universitat Autònoma de Barcelona, E-08193 Bellaterra, Catalonia, Spain*
[2]*Dipartimento di Chimica and Nanostructured Interfaces and Surfaces (NIS) Centre, Università degli Studi di Torino, via P. Giuria 7, I-10125 Torino, Italy*
[3]*CNRS, Institut de Planétologie et d'Astrophysique de Grenoble (IPAG), Université Grenoble Alpes, F-38000 Grenoble, France*

ABSTRACT

Acetaldehyde (CH$_3$CHO) is one of the most detected interstellar complex organic molecules (iCOMs) in the interstellar medium (ISM). These species have a potential biological relevance, as they can be precursors of more complex species from which life could have emerged. The formation of iCOMs in the ISM is a challenge and a matter of debate, whether gas-phase, grain-surface chemistry, or both are needed for their synthesis. In the gas-phase, CH$_3$CHO can be efficiently synthesized from ethanol and/or ethyl radical. On the grain-surfaces, radical–radical recombinations were traditionally invoked. However, several pitfalls have been recently identified, such as the presence of energy barriers and competitive side reactions (i.e. H abstractions). Here, we investigate a new grain-surface reaction pathway for the formation of acetaldehyde, namely the reaction between CH$_3$ and a CO molecule of a dirty water/CO ice followed by hydrogenation of its product, CH$_3$CO. To this end, we carried out *ab initio* computations of the reaction occurring on an ice composed of 75 per cent water and 25 per cent CO molecules. We found that the CH$_3$ + CO$_{(ice)}$ reaction exhibits barriers difficult to overcome in the ISM, either adopting a Langmuir–Hinshelwood or an Eley–Rideal mechanism. The subsequent hydrogenation step is found to be barrierless, provided that the two reacting species have the correct orientation. Therefore, this pathway seems unlikely to occur in the ISM.

Key words: astrochemistry – molecular processes – ISM: molecules.

1 INTRODUCTION

Acetaldehyde is one of the most common detected interstellar complex organic molecules (iCOMs), which are chemical compounds defined as molecules with six or more atoms that contain at least one carbon atom (Herbst & van Dishoeck 2009; Ceccarelli et al. 2017; Herbst 2017). Since their detection in star-forming regions, iCOMs rose the interest of scientists. There is evidence that some iCOMs formed in the interstellar medium (ISM) were inherited by the small objects of the Solar system (Cazaux et al. 2003; Caselli & Ceccarelli 2012; Ceccarelli et al. 2014; Ligterink et al. 2018; Bianchi et al. 2019; Drozdovskaya et al. 2019). These species, after thermal and hydrothermal alterations, can be converted into more complex organic species (Yabuta et al. 2007; Callahan et al. 2011; Alexander et al. 2014; Rotelli et al. 2016), therefore potentially paving the way to the emergence of life on Earth.

Acetaldehyde was first detected in Sagittarius B2 by Gottlieb (1973), Fourikis et al. (1974), and Gilmore et al. (1976). Some years later, it was also detected in cold clouds, TMC-1 and L134N, by Matthews, Friberg & Irvine (1985). This molecule has been found in a large number of environments: cold pre-stellar cores (Bacmann et al. 2012; Scibelli & Shirley 2020), hot cores (Blake et al. 1987; Law et al. 2021), hot corinos (Cazaux et al. 2003; Chahine et al. 2022), protostellar molecular shocks (Lefloch et al. 2017; De Simone et al.

2020), young discs (Codella et al. 2018; Lee et al. 2019), and also in comets (Crovisier et al. 2004; Biver et al. 2021).

The presence of acetaldehyde (CH$_3$CHO) and other iCOMs in cold pre-stellar cores demonstrates that their synthesis cannot be the result of grain-surface reactions involving migration of species (i.e. radicals) other than H and O (e.g. Bacmann et al. 2012; Ceccarelli et al. 2022).

The reaction pathways that lead to iCOMs are still a matter of debate, as both gas-phase and grain-surface chemistry are invoked to play a crucial role in their synthesis (e.g. Garrod, Weaver & Herbst 2008; Balucani, Ceccarelli & Taquet 2015; Ceccarelli et al. 2022). Several paradigms for the formation of iCOMs were proposed in the literature, the most popular being schemes based on gas-phase reactions (e.g. Charnley, Tielens & Millar 1992; Charnley, Tielens & Rodgers 1997; Balucani et al. 2015; Taquet, Wirström & Charnley 2016; Skouteris et al. 2018; Vazart et al. 2020) and a network of radical–radical couplings occurring on the surface of grains (e.g. Garrod & Herbst 2006; Garrod et al. 2008; Jin & Garrod 2020). Other paradigms include a mechanism based on the condensation of atomic C (Ruaud et al. 2015; Krasnokutski, Jäger & Henning 2020), on the excited O-atom insertion (Bergner, Öberg & Rajappan 2017, 2019), or on the formation of HCO radical on ice surfaces as a parent precursor of other iCOMs (Fedoseev et al. 2015; Simons, Lamberts & Cuppen 2020).

For what concerns acetaldehyde, several works investigated its formation routes from an experimental and theoretical point of view. In the gas-phase, the reaction between ethyl radical and atomic

★ E-mail: albert.rimola@uab.cat

oxygen was proposed to yield CH_3CHO by Charnley (2004), as well as the insertion of CH into methanol (Vasyunin et al. 2017). In KIDA (Wakelam et al. 2012) and UMIST (McElroy et al. 2013) data bases, an ionic route involving protonated acetaldehyde (obtained from dimethyl ether) is present. Finally, in 2018, the idea that acetaldehyde (and other iCOMs) can arise from the chemical transformation of ethanol in the gas-phase was proposed (Skouteris et al. 2018). In this chemical network, called the genealogical tree of ethanol, the latter is the precursor (the parent molecule) that give rise to different iCOMs such as glycolaldehyde, acetic acid, formic acid, and acetaldehyde, among others. More recently, Vazart et al. (2020) carried out a systematic study of all gas-phase reactions present in the literature, which lead to the formation of acetaldehyde, and performed new *ab initio* computations for reactions having only guessed product and rate constants. These authors confirmed the pathways starting from ethyl radical (Charnley 2004) and ethanol (Skouteris et al. 2018) and discarded the others (as they used incorrect product or rate constants). In their study, Vazart et al. (2020) also showed that the ethanol genealogical tree is currently the most promising explanation for the synthesis of acetaldehyde in warm objects. Perrero et al. (2022a) proposed that ethanol would be formed on the grain-surface by the reaction of CCH with a water molecule of the ice, followed by hydrogenation of the produced vinyl alcohol. Remarkably, the presence of frozen ethanol has been tentatively detected by *JWST* observations (although needs confirmation) (Yang et al. 2022; McClure et al. 2023), supporting the hypothesis of the ethanol being the mother of acetaldehyde.

On the grain surfaces, experimental results are in some cases contradictory. Acetaldehyde was formed in ices containing H_2O, CO, CH_4, and CH_3OH processed by UV-irradiation (Moore & Hudson 1998; Bennett et al. 2005; Öberg et al. 2009, 2010; Paardekooper, Bossa & Linnartz 2016; Martín-Doménech, Öberg & Rajappan 2020). In the experiments by Chuang et al. (2021), a number of iCOMs were obtained by irradiating with 200 keV H^+ ions C_2H_2:H_2O ices, including acetaldehyde. However, in experiments using a matrix isolation technique of UV-illuminated methanol ices, where the presence of radicals could be monitored, Gutiérrez-Quintanilla et al. (2021) found that several iCOMs were formed, except acetaldehyde. Finally, the experiments by Fedoseev et al. (2022) produced acetaldehyde and its precursor, ketene, via a non-energetic pathway, where CO is co-deposited with C, H, and H_2O at 10 K.

From a theoretical point of view, the radical–radical coupling of HCO and CH_3 was proposed by Garrod & Herbst (2006) to yield CH_3CHO on icy grain surfaces, as it was supposed that the reaction is barrierless due to taking place between two radical species. However, successive studies showed that not only this reaction has an energy barrier (because the radicals are physisorbed on the ice surface and have to break the intermolecular forces with the surface to react), but it also presents a competitive channel leading to the formation of CH_4 + CO (Enrique-Romero et al. 2019, 2020). The same reaction simulated on a model of CO ice gave similar results, culminating in one of these three outcomes: formation of CH_3CHO, H-abstraction yielding CH_4 + CO, or no reaction taking place (Lamberts et al. 2019). A recent study by Enrique-Romero et al. (2021) concluded that the efficiency of acetaldehyde formation via radical coupling is a strong function of the mobility of the radicals on the grain surface (and, consequently, of the grain temperature), in which the easier the diffusion of HCO and CH_3, the less the acetaldehyde formation efficiency. Finally, recent kinetic calculations of Ben Chouikha et al. (2022) on the reaction between atomic carbon and methanol proposed by Singh, Tandon & Misra (2019) show the presence of a slow

reaction step preceding the barrierless formation of acetaldehyde from the radicals HCO and CH_3. However, at low temperature, the product can be formed due to tunnelling effects. We notice, however, that the simultaneous presence of methanol and atomic carbon on the grain-surfaces is unlikely, as methanol is mostly formed by the hydrogenation of frozen CO, i.e. when carbon is prevalently locked into CO.

In summary, there is evidence that, in hot cores/corinos, acetaldehyde is formed in the gas-phase by reactions occurring in the warm gas, but it is still unclear whether this is the only mechanism at work, especially in cold environments. In light of this situation, in this work, we decided to delve into the non-energetic formation of acetaldehyde on the surface of dust grains, when radicals cannot diffuse.

When dealing with surface reactions, several mechanisms can operate: (i) Langmuir–Hinshelwood (LH: Langmuir 1922; Hinshelwood 1930) reactions, which are efficient in the case where one of the reactants can easily diffuse on the surface of the grains (Hasegawa & Herbst 1993); (ii) Eley–Rideal (ER: Eley & Rideal 1940) reactions, in which species from the gas-phase directly react with surface molecules, avoiding diffusion, but are efficient only if there are sufficient reactive species on the grain surface and if the reactions do not possess an activation energy (Ruaud et al. 2015); (iii) Harris–Kasemo hot atom reactions, in which a high-energy species has enough energy to overcome the diffusion barriers and travels on the surface until all excess energy is lost or it reacts (Harris & Kasemo 1981); (iv) reactions of suprathermal species generated by the excitation and/or ionization caused by cosmic ray bombardment (Shingledecker et al. 2018; Shingledecker & Herbst 2018; Paulive, Shingledecker & Herbst 2020).

In this work, we investigated the acetaldehyde formation through a two-step mechanism based on a 'radical + ice' reaction, as done for the synthesis of formamide (CN + $H_2O_{(ice)}$: Rimola et al. 2018)) and of vinyl alcohol/ethanol (CCH + $H_2O_{(ice)}$: Perrero et al. 2022a)). Here, we propose the reaction of a methyl radical, CH_3, with a CO molecule belonging to the ice mantle of the grain, thus avoiding competitive reactions as H-abstractions, followed by a hydrogenation step:

$$CH_3 + CO \rightarrow CH_3CO \qquad (1)$$

$$CH_3CO + H \rightarrow CH_3CHO \qquad (2)$$

In the first step, which involves the coupling of the methyl radical CH_3 with $CO_{(ice)}$, we assume that either CH_3 is adsorbed close to the CO and diffuses to react with it (LH mechanism) or that it lands directly on the CO, reacting immediately with it (ER mechanism). The second step consists in the hydrogenation of the acetyl (CH_3CO) radical so formed, which is expected to be almost barrierless as it involves an H atom reacting with a radical, whether it diffuses on the surface (LH) or it comes from the gas-phase (ER).

This work is organized as follows: in Section 2 we report the methodology (including benchmark studies); in Section 3 we present the results and Section 4 is dedicated to their discussion and comparison with other studies. Section 5 concludes the article.

2 METHODOLOGY

2.1 Computational details

We employed CRYSTAL17 (Dovesi et al. 2018) and GAUSSIAN16 (Frisch et al. 2016) software packages, to execute periodic and molecular calculations, respectively. CRYSTAL17, at variance with other periodic codes, adopts localized Gaussian functions as basis

2656   *J. Perrero et al.*

sets (in a similar approach to that for GAUSSIAN16), and it works with systems that range from zero to three periodic dimensions, avoiding the fake 3D replica of surface models that would arise when working with plane waves basis sets.

To reduce the computational cost of the periodic simulations, all the structures were optimized using the approximated HF-3c method followed by a single point energy calculation at the density functional theory (DFT) level, hereafter referred to as DFT//HF-3c. To check the accuracy of this scheme, we performed a benchmark study, which splits in two phases: (i) we compared the performance of DFT//HF-3c (CRYSTAL17) versus CCSD(T)//DFT in the gas-phase (GAUSSIAN16) to select the best-performing DFT functional, and (ii) we applied the ONIOM2 correction (Dapprich et al. 1999) with the extrapolation scheme of Okoshi, Atsumi & Nakai (2015) in order to compare DFT//HF-3c against ONIOM2//DFT on the surface.

The HF-3c method was used in the most time-consuming periodic calculations, namely, geometry optimizations and frequency calculations (Sure & Grimme 2013). HF-3c is based on the Hartree–Fock (HF) method computed with a minimal basis set (MINIX, Tatewaki & Huzinaga 1980), in which three empirical corrections (3c) were added: the dispersion energy D3(BJ) (Grimme et al. 2010), the basis set superposition error (BSSE) correction with the geometrical counterpoise (Kruse & Grimme 2012), and the short-range bond correction to fix overestimated covalent bond lengths for electronegative elements (Grimme, Ehrlich & Goerigk 2011; Brandenburg et al. 2013). Subsequently, the energies were refined with single point calculations on to the HF-3c optimized structures at the desired DFT level of theory, following an approach that provided accurate results in several cases, from molecular crystals (Cutini et al. 2016), polypeptides (Cutini, Corno & Ugliengo 2017), pure-silica zeolites (Cutini, Civalleri & Ugliengo 2019) to the computation of binding energies on crystalline and amorphous pure water ice (Ferrero et al. 2020; Perrero et al. 2022b).

In the periodic calculations, all the stationary points of a potential energy surfaces (PES) were characterized by the calculation of the harmonic frequencies at Γ point as minima (reactants, products) or first-order saddle points (transition states). Each Hessian matrix element was computed numerically by means of a three-point formula based on two displacements of 0.003 Å from the minimum along each Cartesian coordinate. The zero-point energy correction was computed with the standard rigid rotor/harmonic oscillator formalism (McQuarrie 1975). Since the systems are open-shell in nature, calculations were performed within the unrestricted formalism. The threshold parameters for the evaluation of the Coulomb and exchange bi-electronic integrals were set equal to 10^{-7}, 10^{-7}, 10^{-7}, 10^{-7}, and 10^{-25}. The sampling of the reciprocal space was conducted with a Pack–Monkhorst mesh (Pack & Monkhorst 1977), with a shrinking factor of 2, which generates 4k points in the first Brillouin zone.

2.2 H₂O:CO ice surface models

The H₂O:CO surfaces employed in this study were obtained from a bulk model of the pure H₂O crystalline P-ice (Casassa, Ugliengo & Pisani 1997), in which one every four water molecules was replaced by CO (Fig. 1). Three surfaces were cut along the planes (001), (010), (100) (see Fig. 2) and then fully relaxed at HF-3c level of theory, optimizing both cell parameters and atomic positions, which led to a heavy reorganization of each structure. Although we imposed a lattice to the system through periodic boundary conditions, we modelled large unit cells of H₂O:CO dirty ice (within P1 space symmetry) whose geometry relaxation resulted in an amorphous-like surface model. The cell parameters, the dipole, and the number of atoms
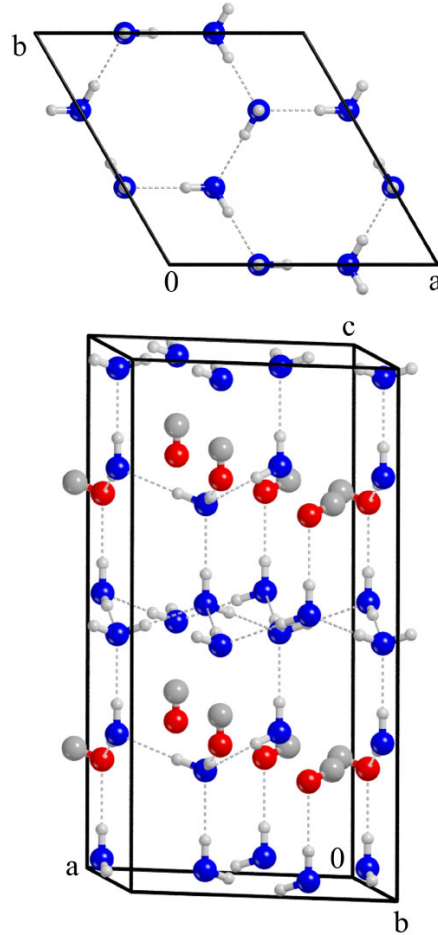
Figure 1. Top and lateral view of the dirty ice bulk model where one every four water molecules was replaced by CO. Colour code: H, white; C, grey; O atoms belonging to water, blue; O atoms belonging to the CO, red.

of each structure can be found in Table 1. The (001) surface has the smallest number of atoms (192) and the smallest dipole moment across the z-axis (-0.87 D at BHLYP-D3(BJ) level of theory). The H₂O and the CO molecules broke the symmetric structure of the bulk, creating clathrate-like cages in which CO molecules are surrounded by a network of water molecules engaged in hydrogen bonds (H-bonds). The outer layers of each surface are characterized by the presence of faintly interacting CO molecules that, depending on the coverage percentage, form a relatively complete monolayer of CO. Mixed ice models with a similar behaviour were reported in the theoretical work of Zamirri et al. (2018), in which CO adsorption, entrapment, and mixture within H₂O ices was studied. There, it emerged that dispersive and quadrupolar forces have a prominent role in determining the structural features of these ice mixtures, and are responsible for the hydrophobic behaviour of CO. Indeed, when CO is entrapped in the ice structure, it causes large rearrangements of the network of hydrogen bonds, while when it is adsorbed on the top of the surfaces, it forms ordered layers. This gives rise to sections of the surface characterized by different electrostatic potential surfaces depending on the local arrangement of the carbon monoxide molecules.
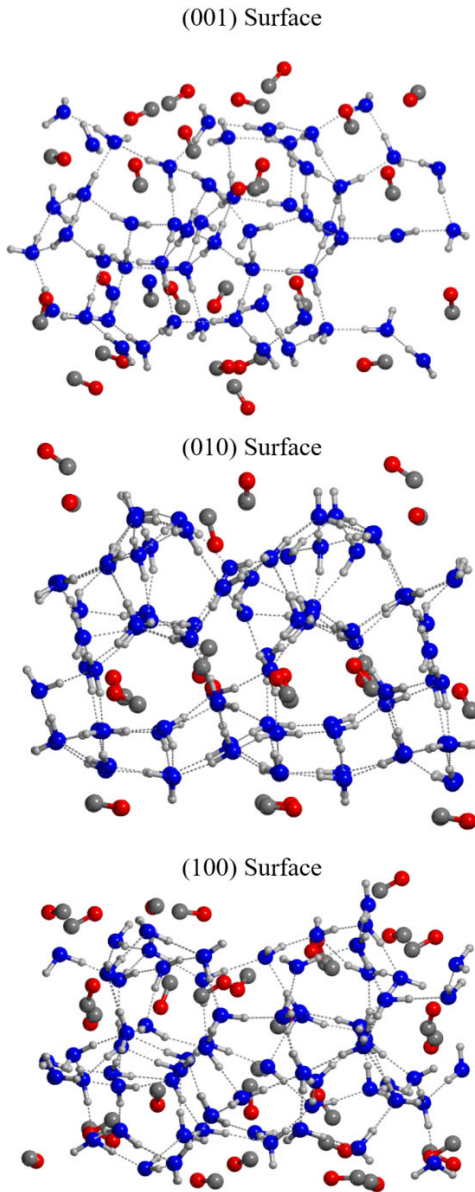
(001) Surface

(010) Surface

(100) Surface

Figure 2. Structures of the (001), (010), and (100) ice surfaces, optimized at the HF-3c level of theory. Colour code: H, white; C, grey; O atoms belonging to water, blue; O atoms belonging to the CO, red.

Table 1. Cell parameters (a and b in Å, and γ in deg) of the three ice surfaces optimized at HF-3c level. Dipole moment (μ, in Debye) across the non-periodic z-axis of the surfaces calculated at HF-3c and BHLYP-D3(BJ) (DFT) level of theory. The number of water and carbon monoxide molecules of each surface per unit cell (H_2O:CO) is also reported.

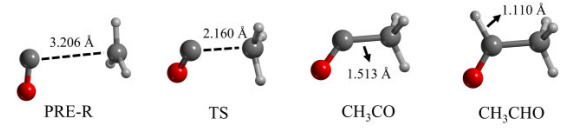| Surfaces	a	b	γ	μ(HF-3c)	μ(DFT)	H_2O:CO
(100)	14.718	12.718	101.294	−1.78	−1.72	56:24
(010)	14.289	12.478	107.261	3.13	3.10	64:16
(001)	12.776	14.604	128.338	−1.52	−0.87	48:24

Figure 3. Stationary points of Reactions 1 and 2, computed at BHLYP-D3(BJ)/6-311G(d,p)//HF-3c level of theory. Distances are in Å.

In our model, the quantity of CO is not sufficient to give rise to a complete monolayer of CO, but the bottom face of (010) surface shows a neat arrangement of CO molecules. We notice very few cases in which CO molecules are engaged in short H-bonds with water molecules (<2.4 Å). This is because the water molecules tend to form an H-bond network between them and minimize the number of dangling H atoms pointing towards CO. Moreover, the majority of H-bond interactions take place through the O-end of the CO molecule and not through the C-end.

This phenomenon is probably driven by the small energy difference between the two interactions at HF-3c level of theory, for which the H-bond through C atom is favoured over the H-bond through the O atom by only 0.3 kJ mol⁻¹ (see Fig. B1). The C···H interaction is also longer (2.390 Å) than the O···H one (2.212 Å), although the results are comparable with those given by B3LYP-D3(BJ)/6-311G(d,p).

3 RESULTS

3.1 Preliminary benchmark studies

3.1.1 Gas-phase benchmark calculations

In order to select the most appropriate DFT level of theory with which executing the periodic simulations, we first performed a benchmark analysis of the reactions 1 and 2 in the gas-phase (namely, in the absence of the whole icy surfaces). For the sake of reliability of the benchmark study adopting these gas-phase reactions, geometry optimizations were performed at HF-3c level in CRYSTAL17, while the subsequent single point energies were computed with six different DFT methods, which were corrected with the Grimme's D3 or, when available, the D3(BJ) terms (Grimme et al. 2010, 2011) to account for dispersion interactions. Thus, the employed methods are BHLYP-D3(BJ) (Lee, Yang & Parr 1988; Becke 1993a), B3LYP-D3(BJ) (Becke 1988, 1993b; Lee et al. 1988), M062X-D3 (Zhao & Truhlar 2008), M052X-D3 (Zhao, Schultz & Truhlar 2006), MPWB1K-D3(BJ) (Zhao & Truhlar 2004), and ωB97X-D3 (Chai & Head-Gordon 2008). They were used in conjunction with the Pople-based 6–311G(d,p) basis set. Diffuse functions were neglected because their small exponents can cause high linear dependencies in the wavefunction of the periodic systems we aim to work with (Klahn & Bingel 1977; VandeVondele & Hutter 2007; Peintinger, Oliveira & Bredow 2013; Vilela Oliveira et al. 2019).

The DFT//HF-3c results were compared with those obtained by performing optimizations at the same DFT/6-311G(d,p) levels, followed by single point energy calculations at single and double electronic excitation coupled-cluster method with an added perturbative description of triple excitations (CCSD(T)) combined with Dunning's aug-cc-pVTZ basis set in GAUSSIAN16 (Raghavachari et al. 1989). The reaction path is represented in Fig. 3. Reaction 1 presents a barrier due to being the coupling of the radical CH₃ with the closed-shell CO. Reaction 2 is a radical–radical coupling and therefore is barrierless in the gas-phase.

2658   *J. Perrero et al.*

The results of this benchmark study for the gas-phase reaction models are shown in Table 2. The different CCSD(T)//DFT calculations return comparable energy values, meaning that results are almost unaffected by the small differences in the optimized geometries obtained with the different DFT methods. Thus, we only report here the results computed at CCSD(T)//BHLYP-D3(BJ), which can be taken as reference values. The error percentages on the energy barriers are high when comparing the DFT//HF-3c results with the CCSD(T)//BHLYP-D3(BJ) ones. To have deeper insights into that, we have analysed the resulting optimized structures with each method. Table 3 reports the pivotal bond lengths of each species, where one can observe that HF-3c does not reproduce well the structures for the pre-reactant (PRE-R) and the transition state (TS) structures compared with the DFT methods. In the PRE-R and in the TS, the C—C length at HF-3c versus any DFT level shows differences going from 0.1 to 0.3 Å and, indeed, have a decisive impact on the energies that are computed afterwards at single point DFT.

Energetic results indicate that B3LYP-D3(BJ) is the least suitable functional (99.3 per cent error on the potential energy barrier for Reaction 1), while BHLYP-D3(BJ) is the best one (20.6 per cent error though, corresponding to an absolute error of −4.6 kJ mol⁻¹). The BHLYP-D3(BJ) method also gives the smallest error percentage in the reaction energies for the formation of the CH₃CO radical. On the other hand, every functional describes well the reaction of CH₃CO with H.

3.1.2 Grain-surface benchmark calculations

Based on the error percentage on the energy of the gas-phase TS, we chose BHLYP-D3(BJ) to compute the reactions on the surface. However, although BHLYP-D3(BJ)//HF-3c performs globally well compared with CCSD(T)//BHLYP-D3(BJ), one has to pay special care when modelling the transition state of Reaction 1, which is the pivotal step to determine whether the reaction is feasible or not in the ISM. As probably the same discrepancies can affect the periodic calculations, we also benchmarked them to assess the quality of the employed methods. Indeed, it is clear that we need to improve the quality of our data directly on the periodic surface, where the interaction between the reactants and the ice could change again the geometrical features of the interaction between CH₃ and CO, and therefore draw more discrepancies between HF-3c, BHLYP-D3(BJ) and CCSD(T) results.

A possible solution to this problem should be performing ONIOM2 calculations (Dapprich et al. 1999) combining BHLYP-D3(BJ) with CCSD(T), as low and high energy levels. This methodology has been previously applied to the computation of binding energies (Ferrero et al. 2020; Perrero et al. 2022b). However, this would require obtaining optimized structures at BHLYP-D3(BJ) of the full periodic systems, which in our case is not feasible due to the high number of atoms present in the unit cells. Instead, we selected three test model cases for simulating the acetaldehyde formation and computing the energies applying the ONIOM2 refinement, in order to compare the performance of BHLYP-D3(BJ)//HF-3c against the ONIOM2-corrected values on the reaction barrier.

The test cases are based on two pure H₂O crystalline periodic ice models, in which one water molecule is replaced by a CO, and a molecular cluster of pure CO ice. They are shown in Fig. A1 and are represented by the 2x1 supercell of the (010) P-ice surface in which (i) a water molecule exposing a dangling oxygen atom (H₂O Ice (a)) and (ii) a water molecule exposing a dangling hydrogen atom (H₂O Ice (b)) were substituted

Table 2. Relative energies (in kJ mol⁻¹) of the stationary points of the gas-phase reactions 1 and 2 for all the DFT/6-311G(d,p) methods (computed with CRYSTAL17) and the CCSD(T)/aug-cc-pVTZ method (computed with GAUSSIAN16). R stands for isolated reactants, PRE-R for pre-reactant complex, TS for transition state, and P for product. The data are not ZPE-corrected.

Reaction	Step	A/H†	B/H†	C/H†	D/H†	E/H†	F/H†	CCSD(T)//A†
R1: CO + CH₃ → CH₃CO	R	0.03	−0.03	4.84	6.58	1.32	1.35	2.03
	PRE-R	0.0	0.0	0.0	0.0	0.0	0.0	0.0
	TS	17.9	0.2	9.4	15.6	4.8	3.5	22.5
	P	−54.3	−66.4	−58.0	−51.1	−74.9	−71.6	−56.1
	err% TS R1	20.6 per cent	99.3 per cent	58.4 per cent	30.9 per cent	78.6 per cent	84.3 per cent	
	err% P R1	3.1 per cent	18.5 per cent	3.4 per cent	8.9 per cent	33.5 per cent	27.7 per cent	
	mean err% R1	11.9 per cent	58.9 per cent	30.9 per cent	19.9 per cent	56.1 per cent	56.0 per cent	
R2: CH₃CO + H → CH₃CHO	R	0.0	0.0	0.0	0.0	0.0	0.0	0.0
	P	−390.7	−388.0	−394.8	−396.8	−383.0	−402.6	−396.1
	err % P R2	1.4 per cent	2.0 per cent	0.3 per cent	0.2 per cent	3.3 per cent	1.6 per cent	

Note. † A=BHLYP-D3(BJ), B = B3LYP-D3(BJ), C = M052X-D3, D = M062X-D3, E = MPWB1K-D3(BJ), F = ωB97X-D3, H = HF-3c

Table 3. Distances (in Å) of selected bonds in the structures of the pre-reactants (PRE-R), transition state (TS), and products (CH$_3$CO and CH$_3$CHO) of the gas-phase reaction models 1 and 2 computed at different theory levels.

Structure	BHLYP-D3(BJ)	B3LYP-D3(BJ)	M052X-D3	M062X-D3	MPWB1K-D3(BJ)	ωB97X-D3	HF-3c
CO	1.114	1.127	1.120	1.121	1.116	1.125	1.135
C—C (PRE-R)	3.369	3.190	3.211	3.206	3.431	3.294	3.154
C—C (TS)	2.146	2.238	2.171	2.147	2.243	2.209	2.015
C—C (CH$_3$CO)	1.505	1.515	1.513	1.517	1.498	1.513	1.552
C—O (CH$_3$CO)	1.166	1.180	1.174	1.173	1.167	1.177	1.187
C—H (CH$_3$CHO)	1.513	1.114	1.106	1.110	1.105	1.113	1.107
C—O (CH$_3$CHO)	1.177	1.204	1.200	1.199	1.191	1.200	1.208

Table 4. Potential energy barrier (in kJ mol^{-1}) of Reaction 1 computed on the three test cases for the grain-surface benchmark. DFT stands for BHLYP-D3(BJ)/6-311G(d,p).

Structure	*real*		*model*		*final*
	DFT//HF-3c	DFT//DFT	DFT	CBS	ONIOM2
H$_2$O Ice (a)	27.0	49.5	13.8	19.6	55.2
H$_2$O Ice (b)	15.1	40.1	9.0	2.3	33.3
CO Ice	11.3	15.0	18.0	20.4	17.4

by a CO molecule, and (iii) a cluster model made of 20 CO molecules.

Each system was divided in two parts (*model* and *real* systems), described by two different levels of theory (*high* and *low*). The *model* system (represented by the CH$_3$ and the CO) was described by the *high* level of theory, CCSD(T). The *real* system (that is, the whole system) was described by the *low* level of theory, BHLYP-D3(BJ). In this ONIOM correction, CCSD(T) was used in combination with the Dunning's aug-cc-pVNZ (with N = D,T) basis sets (Dunning 1989) and, with these data, the OAN(C) extrapolation scheme to the complete basis set (CBS) limit was applied (Okoshi et al. 2015).

The ONIOM2-corrected energy barrier (ΔE_{TS}) was computed as

$$\Delta E_{TS(ONIOM2)} = \Delta E_{TS}(low, real) +$$
$$\Delta E_{TS}(high, model) - \Delta E_{TS}(low, model), \quad (3)$$

where the $\Delta E_{corr} = \Delta E_{TS}(high,model) - \Delta E_{TS}(low,model)$ represents the correction term to the energy of the *real* system.

In this work, for the calculation of the ONIOM2-corrected barriers, ΔE_{ONIOM2}, equation (3) can be rewritten as

$$\Delta E_{TS(ONIOM2)} = \Delta E_{TS}(DFT; all) +$$
$$\Delta E_{TS}(CCSD(T)/CBS; fragm) - \Delta E_{TS}(DFT; fragm), \quad (4)$$

where $\Delta E_{TS}(DFT; all)$ is the activation barrier computed at DFT//DFT. The ΔE_{TS} of the model system (CH$_3$ + CO; *fragm*) is computed through single point energy calculations at CCSD(T)/aug-cc-pVNZ with n = D,T and extrapolated to the CBS limit due to the OAN(C) equation.

$$E_{CBS}^{OAN(C)} = \frac{3^3 E(T) - s^3 E(D)}{3^3 - s^3} \quad (5)$$

In this equation, s = 2.091 based on the choice of method and basis set, E(T) is the energy calculated with the aug-cc-pVTZ basis set, and E(D) corresponds to that computed with the aug-cc-pVDZ basis set.

We performed Reaction 1 on the three test models, both at BHLYP-D3(BJ)//HF-3c level of theory and at the ONIOM2 scheme, chosen as reference. Data are available in Table 4.
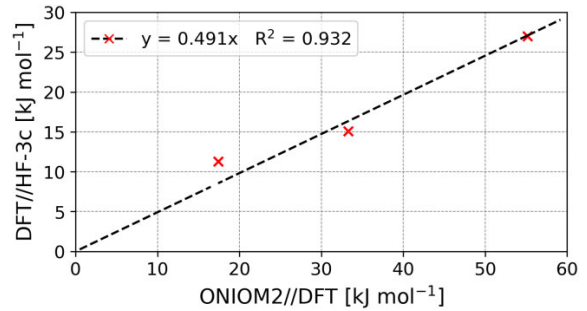
Figure 4. Plot of the DFT//HF-3c against ONIOM2//DFT potential energy barriers of Reaction 1 performed on the three test models (the CO molecular cluster and the two crystalline periodic H$_2$O models with a CO substitution).

In the plot of Fig. 4, we compare the ONIOM2//DFT results against the DFT//HF-3c ones. The regression line (DFT//HF-3c = 0.491·ONIOM2//DFT, R^2 = 0.932) shows that the method of choice for the periodic calculations, DFT//HF-3c, underestimates the reaction barrier, as already emerging from the gas-phase benchmark study.

Since we have very few cases, we do not aim to adopt the slope as a correction factor. On the other hand, computing the reactions on the dirty ice surface models at full BHLYP-D3(BJ) level is almost unpractical. This benchmark study, however, allows to figure out the error bar associated with the present periodic calculations.

3.2 Grain-surface reactions adopting an LH mechanism

Once we have checked and chosen a reasonably suitable methodology to calculate Reactions 1 and 2, we simulated them on the dirty H$_2$O:CO icy surface models.

To this end, we first adsorbed the CH$_3$ on the ice models by manually placing the radical in positions characterized by different local environments. Only the atomic positions were relaxed, while the cell parameters were kept frozen, to be consistent during the successive steps of the reaction and avoid structural deformations of the ice surface models. To calculate the binding energy (BE) of CH$_3$ on the mixed H$_2$O:CO surfaces, we followed the same computational scheme as in Ferrero et al. (2020) and Perrero et al. (2022b), that is, by correcting the adsorption energy $\Delta E_{ads} = E_{complex} - E_{ice} - E_{CH_3}$ for the BSSE (which generates from using a finite basis set) through the counterpoise method by Boys & Bernardi (1970).

$$BE = -\Delta E_{ads} + BSSE \quad (6)$$

For each case we computed the deformation energies of the surface and of the radical to verify that heavy structural rearrangements were not affecting our models during the geometry optimizations. We also

computed the BE(0) at 0 K, by correcting the BE for the ΔZPE as in equation (7).

$$BE(0) = BE - \Delta ZPE \qquad (7)$$

To identify the transition states, we adopted the distinguished reaction coordinate (DRC) procedure by performing a scan calculation along the C—C length. The maximum energy structure of the DRC pseudo-PES was used to localize and optimize the actual TS structure (as implemented in the CRYSTAL code, Rimola et al. 2010). In the DRC process, we avoided using internal redundant coordinates. Instead, we selected a mixed coordinate system made up of a set of selected valence internal parameters (bond lengths, angles, and dihedrals) plus the full set of symmetry adapted fractional displacements and elastic distortions (evoked by the keyword INTLMIXED in CRYSTAL17). This represents an advantage both in reducing the number of valence internal parameters that are automatically generated for the system and in solving the quasi-linear dependencies that arise in systems with a lack of connectivity, which are reflected in a very high condition number of the Wilson B-Matrix. The latter condition usually makes the optimization either to fail or to exhibit an erratic behaviour (Dovesi et al. 2018).

To simulate Reaction 2, we selected one newly formed CH₃CO/ice complex, and we manually placed the hydrogen atom to simulate its adsorption. We first set up five starting geometries and optimized the structures as open-shell triplets (the two unpaired electrons with the same sign), which were then optimized as open-shell singlets (the two unpaired electrons with opposite signs). When the orientation of H was in favour of the formation of the C—H bond, but no acetaldehyde was obtained spontaneously, we performed DRC calculations to characterize the PES of the process.

3.2.1 Adsorption of methyl radical on the dirty ices

For each surface, CH₃ was adsorbed in four different positions (two on the top-face and two on the bottom-face) to sample different binding sites. The adsorption structures at the (100) surface are shown in Fig. 5. Table 5 summarizes the computed BEs and their contribution, along with the adsorption enthalpy BE(0). The same Table 5 presents the nomenclature adopted for each binding site.

The methyl radical possesses an unpaired electron localized on the carbon atom, and its electrostatic potential surface is neutral
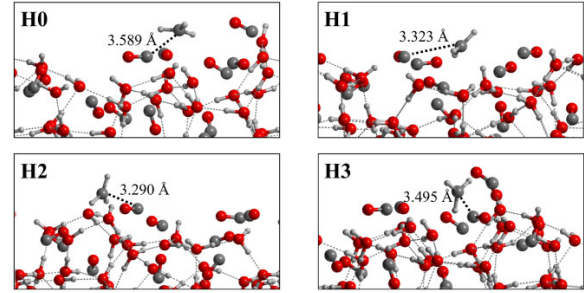

Figure 5. Structures of the CH₃ adsorption complexes on the (100) surface, optimized at HF-3c level. Distances are in Å.

almost everywhere. Therefore, this species will not form strong electrostatic interactions with the surface, especially with the polar water molecules. Thus, dispersion interactions are the key to explain the behaviour of the methyl on to the surface. The BSSE can be as large as 50 per cent of the BE, due to the fact that the 6–311G(d,p) basis set has a rather small number of functions.

The BSSE-non-corrected adsorption energies vary between -13 and -40.3 kJ mol⁻¹. Considering the BSSE, the resulting BEs range from 5.9 to 33.4 kJ mol⁻¹. In nine out of the 12 characterized binding sites, the BEs are between 6 and 14 kJ mol⁻¹, while in two cases a value of 18.5 kJ mol⁻¹ is found. These values are similar to those obtained by Ferrero et al. (2020), where the BE computed on the crystalline water ice is 18.2 kJ mol⁻¹, and on the amorphous water span the 9.2 to 13.8 kJ mol⁻¹ range, indicating a similar interaction of methyl radical with the two ice models. However, in the case of the binding site referred to as L3, the BE overcomes 30 kJ mol⁻¹. This is the only adsorption complex in which the interaction would be attractive even if we were not accounting for the dispersion. Indeed, while in all other cases the interaction would be repulsive, here the hydrogen atoms of the CH₃ are sufficiently close to the oxygen atoms of both CO and H₂O, therefore determining an advantageous electrostatic interaction of 8.8 kJ mol⁻¹. The ZPE correction is in the range 4–5 kJ mol⁻¹ in all the cases, as we would expect from the limited rearrangement of both the surface and the radical upon adsorption.

Table 5. Binding energy (BE) values (in kJ mol⁻¹) of CH₃ on different surface sites of the dirty H₂O:CO ice model. The contributions from the pure potential energy values (ΔE_{ads}), the BSSE corrections ($\Delta BSSE$), the dispersive (Disp) and the non-dispersive (No Disp) terms of the BE, the zero-point energy corrections (ΔZPE), and the resulting adsorption enthalpy (BE(0)) are shown.

Surface	Binding site	ΔE_{ads}	$\Delta BSSE$	BE	Disp	No disp	ΔZPE	BE(0)
(100)	H0	-15.2	-5.9	9.3	15.0	-5.7	4.0	5.3
	H1	-18.8	-8.9	9.8	17.8	-8.0	4.7	5.1
	H2	-17.4	-6.8	10.7	13.3	-2.6	3.7	7.0
	H3	-22.2	-10.8	11.3	20.2	-8.8	4.7	6.7
(010)	K0	-27.3	-13.4	14.0	19.8	-5.8	4.5	9.5
	K1	-14.5	-6.2	8.3	12.9	-4.6	4.4	3.9
	K2	-31.8	-13.4	18.4	18.8	-0.4	4.7	13.7
	K3	-29.4	-11.0	18.5	16.9	1.5	4.3	14.1
(001)	L0	-13.8	-7.3	6.5	6.7	-0.2	5.5	1.0
	L1	-13.0	-7.1	5.9	27.9	-22.0	6.6	-0.7
	L2	-18.9	-7.6	11.3	14.7	-3.3	3.9	7.4
	L3	-40.3	-6.9	33.4	24.5	8.8	4.3	29.1

Table 6. ZPE-corrected potential energy barriers ($\Delta H(0)_{TS}$, in kJ mol^{-1}) for the formation of acetyl on different binding sites of each surface. The internal potential energy values (ΔE_{TS}) and the zero-point energy corrections (ΔZPE_{TS}) are displayed.

Surface	Binding site	ΔE_{TS}	ΔZPE_{TS}	$\Delta H(0)_{TS}$
(100)	H1	11.7	10.7	22.4
	H2	13.4	11.3	24.7
	H3	5.8	11.0	16.8
(010)	K1	11.6	10.3	21.9
	K2	23.7	10.0	33.7
	K3	36.8	10.1	46.9
(001)	L1	10.8	10.8	21.6
	L2	14.5	12.3	26.8
	L3	14.4	11.9	26.5
Gas-phase	-	17.9	10.8	28.7

3.2.2 Acetyl radical formation

We modelled the formation of acetyl on a selected number of structures (see Fig. C1 for an example). For each surface, we chose the three adsorption complexes characterized by the largest differences in the chemical environment of CH$_3$. The purpose of this choice is to probe the effect of the chemical environment on the potential energy barrier of the reaction. According to the LH mechanism, the CH$_3$ diffuses towards the closest CO on the surface to form the chemical bond. In all the nine cases analysed (see Table 6), a potential energy barrier has to be overcome in order to form the acetyl radical. The average barrier is around 10–15 kJ mol^{-1}, with some exceptions. On the (100) surface, the complex **H3** has a barrier of only 5.8 kJ mol^{-1}. We notice that in this case, in the scan calculation, it is the CO that approaches the CH$_3$ and not vice versa, as we observed in the other simulations. We suppose that the particular geometry of this surface allows an easy diffusion of the CO, turning into a low potential energy barrier. On the other hand, on the (010) surface, we found two unfavourable mechanisms, **K2** and **K3**, presenting energy barriers up to 36.8 kJ mol^{-1}. In **K2**, an H-bond between the carbon of the CO and a water molecule of the surface needs to break to make CO available for the reaction with CH$_3$. In **K3**, the large distance (3.9 Å) between the reactants is the responsible of the high barrier.

When adding the ZPE contributions, according to the equation $\Delta H_{TS} = \Delta E_{TS} + \Delta ZPE$, each barrier increases by about 11 kJ mol^{-1}. For the gas-phase reaction, we found barriers of $\Delta E_{TS} = 17.9$ kJ mol^{-1} and $\Delta H_{TS} = 28.7$ kJ mol^{-1}, meaning a $\Delta ZPE_{TS} = 10.8$ kJ mol^{-1}, very close to that obtained on the surface. If we focus solely on the energy barrier, in seven cases out of nine the barriers of the surface reactions are lower than the gas-phase one. However, the grain-surface benchmark calculations warn us that these barriers are underestimated and therefore it is highly probable that only the grain-surface **H3** case is slightly more favourable than the gas-phase reaction.

3.2.3 Acetaldehyde formation

Among the different acetyl products obtained, we selected the **H1** case to model Reaction 2. The reason for this choice is that, in this structure, the acetyl is bound to a water molecule through an H-bond involving the oxygen of the carbonyl group, which means the carbon atom of interest is not hindered because it is pointing towards the gas-phase (it is not facing the inner side of the surface), and thus it is prone to react with a hydrogen atom diffusing on the surface (see Fig. C2).

The adsorption of atomic hydrogen followed by the optimization of the CH$_3$CO + H complex in an open-shell triplet spin state resulted, as expected, in no reaction. However, a change of the electronic spin state to an open-shell singlet brought to the spontaneous formation of acetaldehyde in two (out of five) complexes without harming the H-bond interaction between the carbonyl moiety and the H$_2$O$_{(ice)}$. We noticed that if the H atom is at a maximum distance of 3.5 Å from the CO moiety and it is correctly oriented (meaning that it approaches the CO from the less hindered side), the radical coupling is barrierless.

In the other cases, either the H atom is hindered by the methyl moiety, or it has to overcome a small diffusion barrier to get close enough to the reactive centre. With the methodology chosen for the optimization, we notice that a very small diffusion barrier, of about 1 kJ mol^{-1}, is limiting the free diffusion of the hydrogen on the surface, as the gradient in the optimization process falls to zero and a minimum is found.

3.3 Grain-surface reactions adopting an ER mechanism

In the ER mechanism, the CH$_3$ gas-phase species directly reacts with a surface CO icy component. To simulate this, we generated, with a Python script, several geometries in which the distance between the approaching CH$_3$ from the gas-phase and the reactive CO of the surface progressively decreases. We ran the optimization of these structures without relaxing the geometry of the surface to avoid its thermalization during the approach of the CH$_3$. Only after the product forms, the entire system was relaxed. Therefore, we provide the energy profiles for Reactions 1 and 2 without characterizing the actual transition states but only giving an estimate. This is because, due to the geometrical constraints applied to the surface, we would obtain high-order stationary points with imaginary frequencies associated with the motion of the frozen atoms of the surface. For the same reason, we also do not provide the ZPE-corrected profiles for these processes. We simulated both steps of the reaction assuming an ER mechanism. We chose the (100) surface as the reactive one, focusing on the **H1** binding site. We did so in order to compare LH and ER mechanisms for steps 1 and 2, but also because the CO involved in the C—C bond formation is exposing the C-end towards the gas-phase, therefore being available for this type of reactivity. The energy profile of CH$_3$ + CO is plotted in Fig. 6. Both the profile computed at HF-3c level and the one refined at BHLYP-D3(BJ) level are shown. One can clearly see the disagreement between the two methodologies in terms of energetics. The BHLYP-D3(BJ) profile shows that below 5 Å of distance there is an attractive interaction between the methyl radical and the CO. The presence of a van der Waals complex well in the energy profile appears at a distance of 3.3 Å. When getting close to 2 Å, we find the maximum energy point, whose value is about 8.5 kJ mol^{-1} compared with the energy at infinite distance. The ΔE between the minimum and maximum energy point is 16 kJ mol^{-1}, which is compatible with the barrier computed for the LH mechanism. According to these results, with both the formation of such complex and the presence of a barrier, the reaction will hardly yield acetyl.

On the other hand, considering that acetyl is already on the surface and a hydrogen atom approaches from the gas-phase, two situations can take place (see Fig. 7). If the overall spin of the system is a triplet, no coupling takes place and the energy of the system becomes highly repulsive as the distance between the two reactants increase. In contrast, if the system is in a singlet open-shell electronic state, the formation of the C—H bond occurs spontaneously. We also simulated the competitive reaction, in which H falls on to the surface and
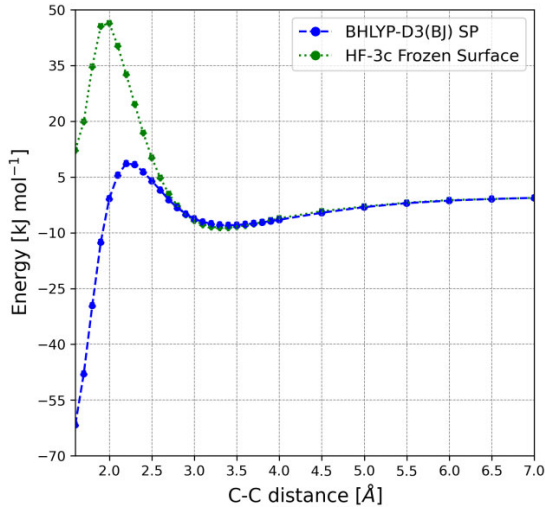
2662   *J. Perrero et al.*

Figure 6. Eley–Rideal reaction profile of CH_3 + CO. Energy is given in kJ mol^{-1}, C—C distance in Å. The reaction is computed keeping the surface frozen at HF-3c level of theory (green). We also provide the single point energy computed at BHLYP-D3(BJ)/6-311G(d,p) level of theory (blue) on HF-3c geometries.
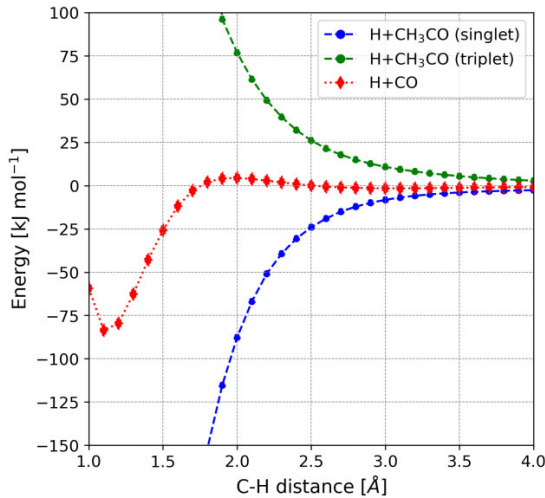

Figure 7. Eley–Rideal reaction profile of H + CH_3CO and its competitive reaction H + CO at BHLYP-D3(BJ)/6-311G(d,p) level of theory. Energy is given in kJ mol^{-1}, C—H distance in Å. H + CO presents a small barrier (red), H + CH_3CO in the triplet spin state (green) becomes repulsive, while in the singlet spin state (blue) yields the product barrierlessly.

reacts with an adjacent surface CO molecule (considering an overall triplet spin state) forming the HCO radical with a small barrier of 4.5 kJ mol^{-1}. Thus, in case of an H atom approaching the surface, the formation of acetaldehyde via H addition to acetyl is the most probable reaction.

4 DISCUSSION AND ASTROPHYSICAL IMPLICATIONS

In this work, we simulated the formation of acetaldehyde on H₂O:CO dirty ice surfaces models through the reaction of a methyl radical with a CO belonging to the ice surface, in which, subsequently, the newly formed acetyl radical gets hydrogenated to yield acetaldehyde. We performed these two-step process on the basis of both LH and ER surface mechanisms.

Due to this 'radical + ice' reaction mechanism, step 1 has no competitive reactions, at variance with the prevailing radical–radical coupling mechanism (Enrique-Romero et al. (2022)). Indeed, in our case, CH_3 cannot extract a hydrogen atom from water to yield CH_4, neither we consider such a high abundance for CH_3 to be able to form ethane (CH_3CH_3). As far as Reaction 2 is concerned, there may be a competitive channel, i.e. H + CO → HCO, known to have a barrier of ∼5 kJ mol^{-1} and to occur through tunnelling (e.g. Rimola et al. 2014; Pantaleone et al. 2020). In our simulations, we also observe the presence of a barrier. Even though we modelled the process through an ER mechanism and we did not isolate the exact transition state of this reaction, the energy profile reaches its maximum of energy at 4.5 kJ mol^{-1}. In contrast, the formation of acetaldehyde is barrierless and therefore favoured.

The benchmark that we performed for the acetyl formation reaction on the icy surfaces stresses that the BHLYP-D3(BJ)//HF-3c computational scheme seems to underestimate the potential energy barrier of the process. Thus, a direct comparison with the gas-phase reaction (computed at full DFT level) is therefore not possible. However, if we roughly assume that the computed $\Delta E(0)_{TS}$ values on the surfaces have to be doubled to be fairly compared with the gas-phase ones (as emerged from the benchmark study), it turns out that the grain-surface reactions are less favourable than the gas-phase ones in the majority of the cases, namely, just one case out of nine is characterized by a $\Delta H(0)_{TS}$ lower than the 28.7 kJ mol^{-1} found for the gas-phase reaction. However, even in the most favourable case, the barrier is still high so that Reaction 1 is unlikely to take place in the cold molecular clouds. Additionally, in environments where the temperature can be higher (namely, with more thermal energy available to overcome the barrier), the sublimation of CO and CH_3 (above 20 K: e.g. Ferrero et al. 2020) will prevent the reaction from taking place.

Therefore, we can summarize the effect of the ice surface on the acetyl formation through the reaction of CH_3 with iced CO in two points: (i) the CO embedded in the surface is not strongly activated towards the reaction by the surrounding icy water molecules, which in fact, if possible, avoid interacting with the CO molecules by creating clathrate-like structures, as it appears during the optimization of the surfaces; and (ii) in almost all the surface reactions, the potential energy barrier is fairly larger than that in the gas-phase, meaning that there is an additional, although modest, interaction between the CH_3 radical and the surface that needs to be broken in order to allow the radical to approach the CO and form a C—C bond.

On the other hand, the second step (formation of acetaldehyde by H-addition to acetyl) is favoured by the presence of the ice, as the surface is well known to act as a reactant concentrator (e.g. Ioppolo, Cuppen & Linnartz 2011; Rimola et al. 2014; Fedoseev et al. 2015; Simons et al. 2020; Ferrero et al. 2023b) as well as third body (i.e. energy dissipator, hence stabilizing the newly formed product) (e.g. Pantaleone et al. 2020, 2021; Molpeceres et al. 2023; Ferrero et al. 2023a) in hydrogenation of atoms and small molecules. Moreover, in the event that hydrogen is approaching the acetyl with an unfavourable orientation, due to its easy diffusion, it is able to move towards the CO moiety and yield acetaldehyde.

The ER mechanism does not bring any improvement over the LH one. For the former, to be effective, the acetyl formation should not have a barrier, this way avoiding the preliminary adsorption and forming directly the product. Ruaud et al. (2015) stress the importance of this mechanism for reactions between atomic carbon and icy components. However, in our case, both mechanisms present a barrier with similar heights, so that none of the mechanisms dominate over the other (at least from an energetic standpoint). For the hydrogenation of the acetyl radical to form acetaldehyde, both mechanisms are feasible to yield the product, although the LH one is probably favoured due to the fact that at a temperature as low as 10 K the majority of atomic hydrogen would probably be adsorbed on the surface. We have seen, moreover, that the relative orientation between H and acetyl is not a hampering factor so that probably, at 10 K, H atoms have enough mobility to jump between different adsorption sites and find the orientation that would favour the formation of acetaldehyde.

Therefore, although the $CH_3 + CO_{(ice)}$ mechanism seems not to particularly enhance the formation of acetaldehyde, this result is important to constraint the active synthetic paths that drive the formation of acetaldehyde in the ISM.

Other studies have focused on acetaldehyde grain-surface formation through radical recombination between HCO and CH_3 (e.g. Enrique-Romero et al. 2016, 2019, 2021; Lamberts et al. 2019), which already highlighted the difficulty of the synthesis of this iCOM. In Enrique-Romero et al. (2016) and Enrique-Romero et al. (2019), the reactivity between CH_3 and HCO performed on H_2O ice resulted in either formation of acetaldehyde or in $CH_4 + CO$ due to a competitive H abstraction, both reactions having small or no potential energy barriers. In a subsequent work, Enrique-Romero et al. (2021) found that the efficiency of acetaldehyde formation was overall low in comparison with that of $CH_4 + CO$. In Lamberts et al. (2019), the radical pair reactivity was investigated on CO ices by means of *ab initio* molecular dynamics. By adopting a sufficient configurational sampling (namely, different trajectories based on different initial guess structures), the authors found that the reactivity results in either no reaction, formation of CH_3CHO, or $CH_4 + CO$, the last two outcomes being barrierless, while in the first case the non-formation of a product was due to the presence of a barrier. Therefore, according to these results, acetaldehyde synthesis on icy surfaces is not a favourable path. This is in agreement with the theoretical study by Simons et al. (2020), who stated that the reaction network obtained by the hydrogenation of CO may cause the production of several iCOMs (glycolaldehyde, ethylene glycol, and to a less extent methyl formate), alongside methanol and formaldehyde, but acetaldehyde is not one of them. Likewise, the experimental study by Gutiérrez-Quintanilla et al. (2021) found that acetaldehyde is not formed by the combination of radicals created by the UV illumination of methanol ice.

An alternative way of forming acetaldehyde on the grain-surfaces discussed in the literature is via the reaction of carbon atoms with the CO molecules of the ices. Fedoseev et al. (2022) experimentally studied the reaction of C + CO co-deposited with H_2O and H at 10 K, following the theoretical study of Papakondylis & Mavridis (2019). The authors observed the formation of CCO and its hydrogenated counterpart, the ketene CH_2CO. Successive hydrogenation steps result in CH_3CHO. Likewise, Ferrero et al. (2023b) carried out a theoretical study on the formation of ketene from the reaction of C with $CO_{(ice)}$ and the potential successive reactions with radicals (e.g. OH and NH_2) that could form other iCOMs and found that only hydrogenation (via H-tunneling), eventually leading to acetaldehyde could occur, because of important energy barriers. However, as Ferrero et al. (2023b) noticed, the simultaneous presence of gaseous

atomic carbon landing on the grain-surfaces and a CO-rich ice is very unlikely in the molecular ISM, except in photodissociation regions, as abundant frozen CO implies an evolved molecular cloud or pre-stellar core where atomic carbon has an extremely low abundance.

Assuming that CH_3CHO is formed on the grain-surfaces, then a thermal and/or non-thermal mechanism is needed to partially transfer it into the gas-phase, where it is observed. This is particularly problematic when considering the detection of acetaldehyde in several cold pre-stellar cores (Scibelli & Shirley 2020). The parameter establishing whether a species stays bound to the icy mantle or enriches the gas-phase is its BE. A recent computational work by Ferrero et al. (2022) highlights how the acetaldehyde BE, ranging from 3000 to 7000 K on water ice, represents an obstacle to explain its presence in the gas-phase of cold environments. The studies by Corazzi et al. (2021) and Molpeceres et al. (2022) reported a value which is close to the lower end of the distribution outlined in Ferrero et al. (2022), but it is still too large to allow desorption in cold (10 K) astronomical objects. Usually, to explain the desorption process of this and other iCOMs, non-thermal mechanisms such as photodesorption, reactive desorption, and cosmic-ray desorption are invoked (e.g. Dulieu et al. 2013; Chuang et al. 2018; Dartois et al. 2019), each of these mechanism having their drawbacks (e.g. Bertin et al. 2016; Pantaleone et al. 2020). Clearing this matter is out of the scope of this work, which aims at investigating acetaldehyde formation on icy surfaces.

In summary, all studies so far carried out, theoretical and experimental, tend to agree that acetaldehyde is unlikely to be a grain-surface product. On the contrary, several studies now seem to favour the hypothesis of acetaldehyde formed in the gas-phase. We would like to mention in particular the work by Vazart et al. (2020), who showed a very good agreement between the observed and measured abundance of acetaldehyde in hot corinos.

5 CONCLUSIONS

In this work, we studied the formation of acetaldehyde (CH_3CHO) on the grain surfaces through a two-step mechanism: (i) the reaction of a methyl (CH_3) radical with a CO molecule belonging to a periodic surface of H_2O:CO dirty ice to form acetyl (CH_3CO), and (ii) the hydrogenation of the newly formed acetyl. We characterized the process via the Langmuir–Hinshelwood and Eley–Rideal mechanisms and compared the results obtained against those simulated for the same reaction in the gas-phase. Our grain-surface benchmark on three test models stressed that the barriers computed at BHLYP-D3(BJ)//HF-3c level are fairly underestimated against CCSD(T)//BHLYP-D3(BJ).

We modelled three periodic dirty ice surfaces by cutting along the planes (001), (010), and (100) a bulk of crystalline H_2O P-ice, where one-fourth of the water molecules was substituted by CO. We obtained three amorphous-like surfaces characterized by a variable content in CO on to which we simulated several adsorption structures of CH_3, finding that dispersion interactions are crucial for the adsorption process. We computed the ZPE-corrected PES of acetyl formation in three cases for each H_2O:CO ice surface, results pointing out that in most of the cases the reaction presents high energy barriers insurmountable in the ISM. The formation of acetyl via $CH_3 + CO_{(ice)}$ on the surface is less favourable than its gas-phase counterpart in the majority of the cases.

We have elucidated that these overall unfavourable reactions are due to that (i) the CO molecule is hardly activated by the surface and the CH_3 does not present an enhanced reactivity (it does not form hemibonded systems), and (ii) the barriers for acetyl formation

2664 *J. Perrero et al.*

depend on the local environment of the CO, that is, they are high (in most of the cases) when the distance between the reactants is large or when the CO/H$_2$O interactions have to be broken for the reaction to take place. On the other hand, the hydrogenation of acetyl is barrierless, given that the electronic spin of the system is a singlet open-shell and that the H atom is so mobile that it always finds a proper orientation towards the carbonyl group of CH$_3$CO. The outcome of the reaction, specifically its barrier, does not improve when adopting the ER mechanism against the LH one.

In summary, several previous studies have challenged the hypothesis that acetaldehyde is formed on the grain-surfaces via the combination of on-surface radicals, specifically CH$_3$ and HCO (e.g. Enrique-Romero et al. 2016, 2019, 2021; Lamberts et al. 2019; Simons et al. 2020; Gutiérrez-Quintanilla et al. 2021). Leveraging on other studies showing that some iCOMs (ethanol and formamide: Rimola et al. 2018; Perrero et al. 2022a) could be formed on the grain surfaces via reactions of radicals with molecules belonging to the ice, in this work, we investigated the reaction of the CH$_3$ radical with one CO molecule of the ice. Our computations show that also this path is unfavourable to the acetaldehyde formation, reducing the possibilities that the latter is formed on the grain surfaces. Alternatively, gas-phase reactions could be at the origin of the almost ubiquitous presence of acetaldehyde in the ISM (e.g. Vazart et al. 2020).

DATA AVAILABILITY

The data underlying this article are freely available in Zenodo at https://doi.org/10.5281/zenodo.7937759.

REFERENCES

Alexander C. M. O., Cody G. D., Kebukawa Y., Bowden R., Fogel M. L., Kilcoyne A. L. D., Nittler L. R., Herd C. D. K., 2014, Meteorit. Planet. Sci., 49, 503

Bacmann A., Taquet V., Faure A., Kahane C., Ceccarelli C., 2012, A&A, 541, L12

Balucani N., Ceccarelli C., Taquet V., 2015, MNRAS, 449, L16

Becke A. D., 1988, Phys. Rev. A, 38, 3098

Becke A. D., 1993a, J. Chem. Phys., 98, 1372

Becke A. D., 1993b, J. Chem. Phys., 98, 5648

Ben Chouikha I., Kerkeni B., Ouerfelli G., Makroni L., Nyman G., 2022, RSC Adv., 12, 18994

Bennett C. J., Osamura Y., Lebar M. D., Kaiser R. I., 2005, ApJ, 634, 698

Bergner J. B., Öberg K. I., Rajappan M., 2017, ApJ, 845, 29

Bergner J. B., Öberg K. I., Rajappan M., 2019, ApJ, 874, 115

Bertin M. et al., 2016, ApJ, 817, L12

Bianchi E. et al., 2019, MNRAS, 483, 1850

Biver N. et al., 2021, A&A, 648, A49

Blake G. A., Sutton E. C., Masson C. R., Phillips T. G., 1987, ApJ, 315, 621

Boys S., Bernardi F., 1970, Mol. Phys., 19, 553

Brandenburg J. G., Alessio M., Civalleri B., Peintinger M. F., Bredow T., Grimme S., 2013, J. Phys. Chem. A, 117, 9282

Callahan M. P., Smith K. E., Cleaves H. J., Ruzicka J., Stern J. C., Glavin D. P., House C. H., Dworkin J. P., 2011, Proc. Natl. Acad. Sci., 108, 13995

Casassa S., Ugliengo P., Pisani C., 1997, J. Chem. Phys., 106, 8030

Caselli P., Ceccarelli C., 2012, A&AR, 20, 56

Cazaux S., Tielens A. G. G. M., Ceccarelli C., Castets A., Wakelam V., Caux E., Parise B., Teyssier D., 2003, ApJ, 593, L51

Ceccarelli C. et al., 2014, in Beuther H., Klessen R. S., Dullemond C. P., Henning T., eds, Protostars and Planets VI. University of Arizona Press, Tucson, AZ, p. 859

Ceccarelli C. et al., 2017, ApJ, 850, 176

Ceccarelli C. et al., 2022, Protostars and Planets VII, (arXiv:2206.13270)

Chahine L. et al., 2022, A&A, 657, A78

Chai J.-D., Head-Gordon M., 2008, J. Chem. Phys., 128, 084106

Charnley S., 2004, Adv. Space Res., 33, 23

Charnley S. B., Tielens A. G. G. M., Millar T. J., 1992, ApJ, 399, L71

Charnley S. B., Tielens A. G. G. M., Rodgers S. D., 1997, ApJ, 482, L203

Chuang K.-J., Fedoseev G., Qasim D., Ioppolo S., van Dishoeck E. F., Linnartz H., 2018, ApJ, 853, 102

Chuang K.-J., Fedoseev G., Scirè C., Baratta G. A., Jäger C., Henning T., Linnartz H., Palumbo M. E., 2021, A&A, 650, A85

Codella C. et al., 2018, A&A, 617, A10

Corazzi M. A., Brucato J. R., Poggiali G., Podio L., Fedele D., Codella C., 2021, ApJ, 913, 128

Crovisier J., Bockelée-Morvan D., Colom P., Biver N., Despois D., Lis D. C., the Team for target-of-opportunity radio observations of comets, 2004, A&A, 418, 1141

Cutini M., Civalleri B., Corno M., Orlando R., Brandenburg J. G., Maschio L., Ugliengo P., 2016, J. Chem. Theory Comput., 12, 3340

Cutini M., Corno M., Ugliengo P., 2017, J. Chem. Theory Comput., 13, 370

Cutini M., Civalleri B., Ugliengo P., 2019, ACS Omega, 4, 1838

Dapprich S., Komáromi I., Byun K., Morokuma K., Frisch M., 1999, Comput. Theor. Chem., 461–462, 1

Dartois E., Chabot M., Id Barkach T., Rothard H., Augé B., Agnihotri A. N., Domaracka A., Boduch P., 2019, A&A, 627, A55

De Simone M. et al., 2020, A&A, 640, A75

Dovesi R. et al., 2018, WIREs Comp. Mol. Sci., 8, e1360

Drozdovskaya M. N., van Dishoeck E. F., Rubin M., Jørgensen J. K., Altwegg K., 2019, MNRAS, 490, 50

Dulieu F., Congiu E., Noble J., Baouche S., Chaabouni H., Moudens A., Minissale M., Cazaux S., 2013, Sci. Rep., 3, 1338

Dunning T. H., 1989, J. Chem. Phys., 90, 1007

Eley D., Rideal E., 1940, Nature, 146, 401

Enrique-Romero J., Rimola A., Ceccarelli C., Balucani N., 2016, MNRAS, 459, L6

Enrique-Romero J., Rimola A., Ceccarelli C., Ugliengo P., Balucani N., Skouteris D., 2019, ACS Earth Space Chem., 3, 2158

Enrique-Romero J. et al., 2020, MNRAS, 493, 2523

Enrique-Romero J., Ceccarelli C., Rimola A., Skouteris D., Balucani N., Ugliengo P., 2021, A&A, 655, A9

Enrique-Romero J., Rimola A., Ceccarelli C., Ugliengo P., Balucani N., Skouteris D., 2022, ApJS, 259, 39

Fedoseev G., Cuppen H. M., Ioppolo S., Lamberts T., Linnartz H., 2015, MNRAS, 448, 1288

Fedoseev G., Qasim D., Chuang K.-J., Ioppolo S., Lamberts T., van Dishoeck E. F., Linnartz H., 2022, ApJ, 924, 110

Ferrero S., Zamirri L., Ceccarelli C., Witzel A., Rimola A., Ugliengo P., 2020, ApJ, 904, 11

Ferrero S. et al., 2022, MNRAS, 516, 2586

Ferrero S., Pantaleone S., Ceccarelli C., Ugliengo P., Sodupe M., Rimola A., 2023a, ApJ, 944, 142

Ferrero S., Ceccarelli C., Ugliengo P., Sodupe M., Rimola A., 2023b, ApJ, 951, 150

Fourikis N., Sinclair M. W., Robinson B. J., Godfrey P. D., Brown R. D., 1974, Aust. J. Phys., 27, 425

Frisch M. J. et al., 2016, Gaussian 16 Revision C.01

Garrod R. T., Herbst E., 2006, A&A, 457, 927

Garrod R. T., Weaver S. L. W., Herbst E., 2008, ApJ, 682, 283

Gilmore W., Morris M., Johnson D. R., Lovas F. J., Zuckerman B., Turner B. E., Palmer P., 1976, ApJ, 204, 43

Gottlieb C. A., 1973, in Gordon M. A., Snyder L. E., eds, Molecules in the Galactic Environment, Harvard University, Cambridge, Massachusetts, p. 181

Grimme S., Antony J., Ehrlich S., Krieg H., 2010, J. Chem. Phys., 132, 154104

Grimme S., Ehrlich S., Goerigk L., 2011, J. Comp. Chem., 32, 1456

Gutiérrez-Quintanilla A. et al., 2021, MNRAS, 506, 3734

Harris J., Kasemo B., 1981, Surf. Sci., 105, L281

Hasegawa T. I., Herbst E., 1993, MNRAS, 263, 589

Herbst E., 2017, Int. Rev. Phys. Chem., 36, 287

Herbst E., van Dishoeck E. F., 2009, ARA&A, 47, 427

Hinshelwood C., 1930, Annu. Rep. Prog. Chem., 27, 11

Ioppolo S., Cuppen H., Linnartz H., 2011, Rend. Fis. Acc. Lincei, 22, 211

Jin M., Garrod R. T., 2020, ApJS, 249, 26

Klahn B., Bingel W. A., 1977, Int. J. Quantum Chem., 11, 943

Krasnokutski S. A., Jäger C., Henning T., 2020, ApJ, 889, 67

Kruse H., Grimme S., 2012, J. Chem. Phys., 136, 154101

Lamberts T., Markmeyer M. N., Kolb F. J., Kästner J., 2019, ACS Earth Space Chem., 3, 958

Langmuir I., 1922, Trans. Faraday Soc., 17, 621

Öberg K. I., van Dishoeck E. F., Linnartz H., Andersson S., 2010, ApJ, 718, 832

Law C. J., Zhang Q., Öberg K. I., Galván-Madrid R., Keto E., Liu H. B., Ho P. T. P., 2021, ApJ, 909, 214

Lee C., Yang W., Parr R. G., 1988, Phys. Rev. B, 37, 785

Lee C.-F., Codella C., Li Z.-Y., Liu S.-Y., 2019, ApJ, 876, 63

Lefloch B., Ceccarelli C., Codella C., Favre C., Podio L., Vastel C., Viti S., Bachiller R., 2017, MNRAS Letters, 469, L73

Ligterink N. F. W. et al., 2018, A&A, 619, A28

Martín-Doménech R., Öberg K. I., Rajappan M., 2020, ApJ, 894, 98

Matthews H. E., Friberg P., Irvine W. M., 1985, ApJ, 290, 609

McClure M. K. et al., 2023, Nat. Astron., 7, 1

McElroy D., Walsh C., Markwick A. J., Cordiner M. A., Smith K., Millar T. J., 2013, A&A, 550, A36

McQuarrie D. A., 1975, Statistical Mechanics. Harper and Row, New York

Molpeceres G., Kästner J., Herrero V. J., Peláez R. J., Maté B., 2022, A&A, 664, A169

Molpeceres G., Zaverkin V., Furuya K., Aikawa Y., Kästner J., 2023, A&A, 673, A51

Moore M. H., Hudson R. L., 1998, Icarus, 135, 518

Öberg K. I., Garrod R. T., Van Dishoeck E. F., Linnartz H., 2009, A&A, 504, 891

Okoshi M., Atsumi T., Nakai H., 2015, J. Comp. Chem., 36, 1075

Paardekooper D., Bossa J.-B., Linnartz H., 2016, A&A, 592, A67

Pack J. D., Monkhorst H. J., 1977, Phys. Rev. B, 16, 1748

Pantaleone S., Enrique-Romero J., Ceccarelli C., Ugliengo P., Balucani N., Rimola A., 2020, ApJ, 897, 56

Pantaleone S., Enrique-Romero J., Ceccarelli C., Ferrero S., Balucani N., Rimola A., Ugliengo P., 2021, ApJ, 917, 49

Papakondylis A., Mavridis A., 2019, J. Phys. Chem. A, 123, 10290

Paulive A., Shingledecker C. N., Herbst E., 2020, MNRAS, 500, 3414

Peintinger M. F., Oliveira D. V., Bredow T., 2013, J. Comp. Chem., 34, 451

Perrero J., Enrique-Romero J., Martínez-Bachs B., Ceccarelli C., Balucani N., Ugliengo P., Rimola A., 2022a, ACS Earth Space Chem., 6, 496

Perrero J., Enrique-Romero J., Ferrero S., Ceccarelli C., Podio L., Codella C., Rimola A., Ugliengo P., 2022b, ApJ, 938, 158

Raghavachari K., Trucks G. W., Pople J. A., Head-Gordon M., 1989, Chem. Phys. Lett., 157, 479

Rimola A., Zicovich-Wilson C. M., Dovesi R., Ugliengo P., 2010, J. Chem. Theory Comput., 6, 1341

Rimola A., Taquet V., Ugliengo P., Balucani N., Ceccarelli C., 2014, A&A, 572, A70

Rimola A., Skouteris D., Balucani N., Ceccarelli C., Enrique-Romero J., Taquet V., Ugliengo P., 2018, ACS Earth Space Chem., 2, 720

Rotelli L., Trigo-Rodríguez J. M., Moyano-Cambero C. E., Carota E., Botta L., di Mauro E., Saladino R., 2016, Sci. Rep., 6, 38888

Ruaud M., Loison J. C., Hickson K. M., Gratier P., Hersant F., Wakelam V., 2015, MNRAS, 447, 4004

Scibelli S., Shirley Y., 2020, ApJ, 891, 73

Shingledecker C. N., Herbst E., 2018, Phys. Chem. Chem. Phys., 20, 5359

Shingledecker C. N., Tennis J., Gal R. L., Herbst E., 2018, ApJ, 861, 20

Simons M. A. J., Lamberts T., Cuppen H. M., 2020, A&A, 634, A52

Singh K. K., Tandon P., Misra A., 2019, in Singh D. K., Das S., Materny A.eds, Advances in Spectroscopy: Molecules to Materials. Springer Singapore, Singapore, p. 415

Skouteris D., Balucani N., Ceccarelli C., Vazart F., Puzzarini C., Barone V., Codella C., Lefloch B., 2018, ApJ, 854, 135

Sure R., Grimme S., 2013, J. Comp. Chem., 34, 1672

Taquet V., Wirström E. S., Charnley S. B., 2016, ApJ, 821, 46

Tatewaki H., Huzinaga S., 1980, J. Comp. Chem., 1, 205

VandeVondele J., Hutter J., 2007, J. Chem. Phys., 127, 114105

Vasyunin A. I., Caselli P., Dulieu F., Jiménez-Serra I., 2017, ApJ, 842, 33

Vazart F., Ceccarelli C., Balucani N., Bianchi E., Skouteris D., 2020, MNRAS, 499, 5547

Vilela Oliveira D., Laun J., Peintinger M. F., Bredow T., 2019, J. Comp. Chem., 40, 2364

Wakelam V. et al., 2012, ApJS, 199, 21

Yabuta H., Williams L. B., Cody G. D., Alexander C. M. O. D., Pizzarello S., 2007, Meteorit. Planet. Sci., 42, 37

Yang Y.-L. et al., 2022, ApJ, 941, L13

Zamirri L., Casassa S., Rimola A., Segado-Centellas M., Ceccarelli C., Ugliengo P., 2018, MNRAS, 480, 1427

Zhao Y., Truhlar D. G., 2004, J. Phys. Chem. A, 108, 6908

Zhao Y., Truhlar D. G., 2008, Theor. Chem. Acc., 119 525

Zhao Y., Schultz N. E., Truhlar D. G., 2006, J. Chem. Theory Comput., 2, 364

2666   *J. Perrero et al.*

APPENDIX A: BENCHMARK MODELS

APPENDIX B: H₂O ⋯ CO INTERACTION

i)

ii)

Figure B1. The interaction between CO and H₂O computed at HF-3c (black) and B3LYP-D3(BJ)/6-311G(d,p) (green) levels of theory. The H-bond established through the C-atom is energetically favoured over the one established through the O-atom of CO by only 0.3 kJ mol^{-1} at HF-3c level against 3.9 kJ mol^{-1} of B3LYP-D3(BJ).
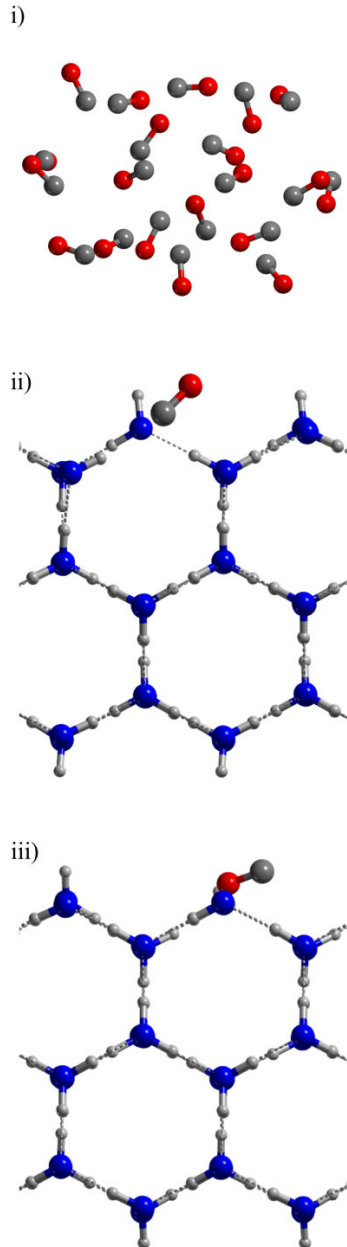
iii)

Figure A1. Ice model used for the benchmark on the surface: (i) a cluster model made of 20 CO molecules, and the 2x1 supercell of (010) P-ice surface in which (ii) a water molecule exposing a dangling oxygen atom (H₂O Ice (a)) and (iii) a water molecule exposing a dangling hydrogen atom (H₂O Ice (b)) was substituted by a CO molecule.
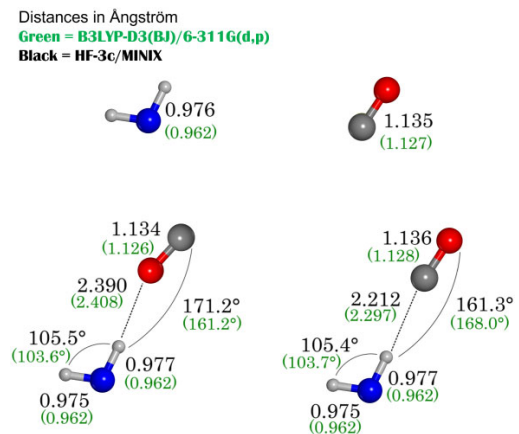
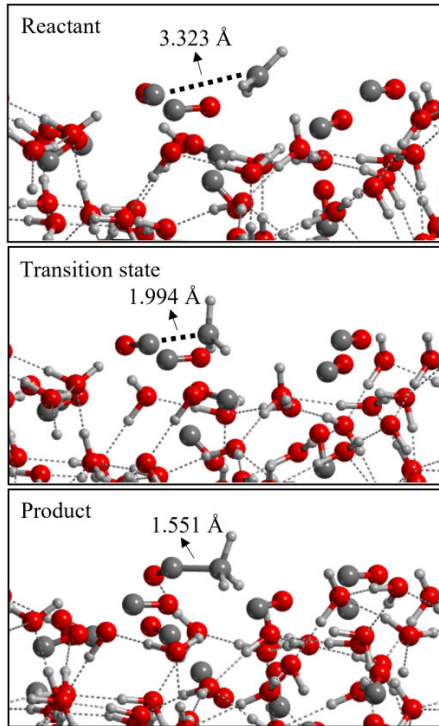**APPENDIX C: REACTION ON (100) SURFACE**

Figure C1. Reactant, transition state, and product structures of the acetyl formation reaction on (100) surface, binding site **H1**. Colour code: H, white; C, grey; O, red.
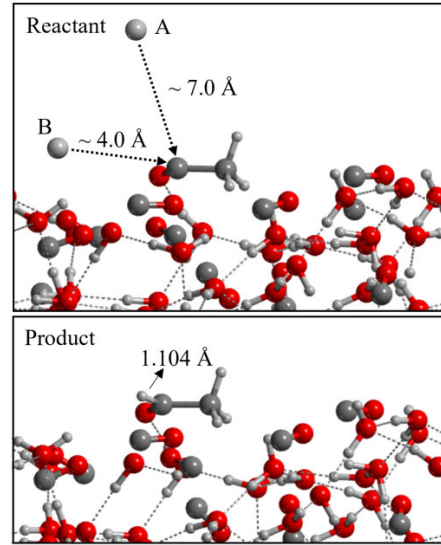

Figure C2. Reactants and product structures of the acetaldehyde formation reaction on (100) surface. The hydrogen atom approaching from the gas-phase (A) represents the Eley–Rideal mechanism, while in case of the Langmuir–Hinshelwood mechanism, the atom is adsorbed on the surface (B). Colour code: H, white; C, grey; O, red.

This paper has been typeset from a TᴇX/LᴀTᴇX file prepared by the author.

Part IV

Conclusions

Chapter 8

Conclusions

The formation of a planetary system consists of five phases during which both the physical and the chemical complexity increase together. Interstellar dust grains are thought to participate in the building up of the molecular complexity. Nevertheless, their specific roles are highly debated. This thesis is organized as a compendium of seven articles dedicated to the investigation of both adsorption and reaction processes, with the aim to provide new insights into the knowledge of grain-surface chemistry occurring in the interstellar medium (ISM). The major findings of this work are summarised in three macro-areas: i) the determination of sulphur-bearing species binding energies (BEs) and eventually spectral features; ii) the synergy between theoretical and experimental approaches in determining astrochemical parameters; iii) and the formation of a few selected complex organic molecules (COMs) on the surface of dust grains.

8.1 Advances in the sulphur depletion problem

While the abundance of sulphur in diffuse clouds is consistent with the cosmic value and mostly resides in S^+, in more dense and evolved environments sulphur progressively depletes, in accordance with the freeze-out of this element on dust grains, which should become part of the icy mantles coating the grains. However, the only species detected in the ice mantles are OCS and SO_2, but the main carriers of sulphur remain unknown. Organosulphur compounds, polysulphanes, and S_n allotropes have been proposed as candidates, and in the last years much effort has been done to synthesise and characterise the formation of these compounds.

To shed light on the mystery of sulphur depletion in the ISM, the interaction between a set of S-bearing species with the core and the mantle of dust grains has been investigated. Dust grain cores have been simulated with olivine nanoclusters, while the mantels are modelled with periodic crystalline and amorphous water ice surface structures. The first two articles presented in the compendium collect the BEs of 23 S-bearing species, classified in four groups, adsorbed on periodic crystalline and amorphous water ice surfaces. This scenario reproduces the chemistry occurring in a cold molecular cloud (T $\simeq$ 10 K).

 i) H-bond donors and H-bond acceptors: CH_3SH, H_2CS, H_2S, H_2S_2, HCS, HS, and HS_2.

 ii) Only H-bond acceptors: OCS, SO_2, NS, and SO.

 iii) Molecules with a carbene-like terminal carbon atom: CS, C_2S, C_3S, and C_4S.

 iv) Species interacting mainly through dispersive interactions: S, S_2, S_3, S_4, S_5, S_6, S_7, and S_8.

For the S_2-S_8 group, the IR and Raman spectra for the gas-phase and the adsorbed species were also simulated. The main findings of this research can be summarised in four points.

- Amorphous ice models offer a variety of binding sites characterised by a different strength, which is better represented by a distribution of BEs, therefore it would be necessary to apply these ranges rather than single values in astrochemical models.

- An accurate description of London dispersion interactions is of critical importance to properly characterise the behavior of S-bearing species, due to sulphur being more polarizable with respect to C/N/O second-period atoms.

- The observed shifts and the intensity of IR and Raman vibrational modes are insufficient to distinguish between S_5 to S_8 rings in the gas phase *versus* adsorbed on the water ice surface. In contrast, some peculiar adsorption features emerge for the chains S_2, S_3, and S_4.

- Due to their peak intensities, S_2 to S_8 species are active in Raman spectroscopy, but are not detectable in IR spectra. Therefore, their presence can be detected in the laboratory, but they cannot be directly observed in the ISM.

A smaller pool of species, comprising CS, H_2S, H_2S^+, HS, HS^+, S, S^+, SO, and SO^+, was adsorbed on olivine nanoclusters. This scenario reproduces the chemistry occurring in a diffuse cloud (T $\simeq$ 100 K). This investigation, corresponding to the third article of the compendium, highlighted that:

- S-bearing species exhibit a stronger affinity for the silicate cores of interstellar dust grains compared to the ice mantles, reinforcing the hypothesis that the majority of sulphur may be locked in a refractory form constituting part of the grain core, therefore impossible to detect in the gaseous phase.

- Charged gas-phase sulphur-bearing species or charged dust grains typically facilitate the freeze-out, driven by charge delocalisation, which plays a stabilising effect. In diffuse clouds, where both species and grain cores are positively charged, it can be assumed that electrostatic repulsion will play a significant role against the accretion of the species on the mantle.

- The freeze-out of species at the grain core could also result in a dissociative adsorption, as observed for HS^+, H_2S^+, and H_2S, the latter displaying a relatively low barrier for its dissociation into HS^- and H^+. The formation of heavier S-bearing species, such as S-chains or S-containing minerals, may be facilitated by strong adsorption interactions, which could also promote reactivity.

8.2   Synergy between theoretical and experimental chemistry

The gas-phase detection of COMs, which are known to form efficiently on the icy mantles of dust grains, requires their sublimation from the condensed phase. One possible desorption mechanism is thermal desorption, which requires a relatively low interaction energy between the species and the surface, as well as a sufficiently warm environment providing enough kinetic energy to the species, thus enabling their sublimation. The estimation of BEs serves to determine whether this mechanism is efficient or other effects, such as chemical desorption and photodesorption, have to be invoked to explain the sublimation of condensed species.

The determination of BEs can be achieved through both experimental and computational chemistry, with each technique exhibiting distinctive strengths and weaknesses. While experiments are performed under conditions of higher pressure than those of the ISM, resulting in the reproduction of grains and mantles that are significantly more dense

than those found in the ISM, simulations are performed under conditions of zero temperature and pressure, allowing for the accurate control of a limited number of chemical species. The main results of this study, which is the fourth article of the compendium, can be summarised in three points.

- Temperature programmed desorption experiments are an effective method for determining desorption energy and pre-exponential factors of species that interact weakly with water. This approach is particularly useful for elucidating the effects of different coverages.

- Computational chemistry, on the other hand, is more suitable for the description of single adsorption phenomena. Moreover, simulations are essential when the targeted species interact strongly with the ice surface and have a BE which is similar to or larger than that of water.

- Simulations typically yield large BE distributions, including a low tail due to the presence of isolated species on the ice. Conversely, experiments typically return higher values, due to the contribution of lateral interactions between the adsorbates, in addition to their interaction with the underlying surface. Both approaches are needed for a complete description of the adsorption/desorption process.

8.3   New insights in COMs formation

The two main paradigms currently adopted to explain the presence of COMs in the ISM invoke gas-phase reactions and grain-surface processes. The objective of this thesis is to gain new insights into the reactions occurring at the surface, to expand the range of investigated reactions and propose alternative mechanisms to the prevalent 'radical + radical' scheme. The main subjects of the study were the formation of acetaldehyde, ethanol and urea. While the simulations indicate that ethanol and urea are products of grain-surface chemistry, acetaldehyde is mainly identified as a product of gas-phase reactions, although some uncertainties recently arose.

In order to synthesise urea, a number of reactions involving both closed-shell and open-shell species, derived from the parent species HNCO and NH_3 have been tested. The reactions were conducted via a Langmuir-Hinshelwood mechanism, adsorbing the reactants on an amorphous cluster of 18 water molecules. From this investigation, corresponding to the fifth publication of the compendium, some interesting results emerge.

- The direct reaction between HNCO and NH_3 is favoured by the presence of a water surface, with respect to the gas-phase reaction. However, the ice surface hampers the reaction due to strongly binding the reactants.

- The formation of $NH_4^+OCN^-$ needs a strong solvation effect in order to occur spontaneously, such as that provided by the ice bulk. Conversely, the salt formation is endothermic on the surface of the ice mantle.

- The only kinetically feasible pathway is represented by a radical-radical recombination, that is $H_2NCO^\bullet + {}^\bullet NH_2$. At a temperature of 20 K, the half-life time of the reactants is only 0.03 s.

- The ice surface acts as both a reactant concentrator and eventually as an energy dissipator.

Ethanol has been synthesised through the $^\bullet$CCH + H_2O reaction, in which the water molecule belongs to the ice mantle, which is represented by an amorphous cluster of 18 water molecules. Three additional hydrogenation steps were necessary to yield the product of interest. The main findings of the sixth article are listed below.

- The 'radical + closed-shell' scheme appeared to be efficient in the context of ethanol formation, where the establishment of a hemibond was pivotal for the formation of the C$-$O bond between $^\bullet$CCH and H_2O. A successive H-transfer step along the H-bonds network of the ice yields $^\bullet$HCCHOH or $^\bullet H_2$CCOH.

- Three additional hydrogenation steps are required to yield ethanol, a process that can also occur through tunnelling effect, when in presence of an energy barrier. Indeed, the second hydrogenation involves a closed-shell species and has a barrier.

- During the hydrogenation steps, vinyl alcohol, a tautomer of acetaldehyde, is formed. Nevertheless, the computed energy barrier for the isomerization process appears to preclude the conversion of vinyl alcohol into acetaldehyde.

- In the steps that link $^\bullet$CCH to CH_3CH_2OH, it is directly observed that the ice surface serves the multiple functions of reactant supplier ($^\bullet$CCH reacts with a H_2O molecule belonging to the ice), catalyst (facilitating proton transfers through the network of H-bonds formed by the H_2O molecules), and eventually energy dissipator.

Finally, three dirty H_2O:CO ice surfaces have been modelled with the objective of investigating the formation of acetaldehyde through the reaction of the $^\bullet CH_3$ radical with a CO molecule belonging to the ice surface. The following four points outline the results of the seventh and last article of the compendium.

- The modelling of the slabs has demonstrated the propensity of the ice to reorganise into clathrate-like structures, particularly within the inner part of the surface.

- The tendency of CO molecules to separate from water is subsequently validated by the absence of activation towards the formation of a C$-$C bond, which is consistently disadvantaged with respect to the gas-phase process.

- Although the hydrogenation reaction of acetyl into acetaldehyde is favoured due to the (eventual) presence of a negligible diffusion barrier for the H atom, the overall reaction does not appear to be favoured compared to the gas-phase process.

- The warmer environments necessary to overcome the reaction barrier would hamper the reaction causing the sublimation of the $^\bullet CH_3$ radical. The most likely grain-surface formation route of acetaldehyde remains to be identified.

8.4   Final remarks

Each chapter of this thesis presents the topics that have been investigated over the past four years, with a particular emphasis on the motivations behind the development of each work, the main results that were obtained, and the future perspective opened up by such study. The nature of scientific research is such that the pursuit of a single question often gives rise to a multitude of new queries. In the field of astrochemistry, the difficulties in directly observing the phenomena that occur during the formation of stars, planets, and the other small bodies are compounded by the difficulties experienced in reproducing such conditions in order to run experiments, whether they are performed in a laboratory or on

a computer. Consequently, a dual approach is required to address both the unanswered questions and to enhance the investigative techniques employed. With the collective effort of the scientific community, we will gradually advance our understanding and provide more answers to the challenges of the Universe.

Acknowledgements

Almost everyone warned me that writing the thesis would have not been pleasant. Luckily, they were wrong (although I do not feel the same about the revision). I have always loved writing and I knew it would be hard to change my mind. I have to admit it, it was not easy. But the moments when I was alone, sipping black tea, searching for information in books and articles, when I finally had an excuse to go to the library (my favourite place on campus), and when only the soft sound of fingertips on the keyboard filled the silence... Those where the moments I enjoyed the most. Watching the sunset from the office window and noticing myself smiling. The university became my happy place, and the hallways a perfect place to sing when everyone else had left. I will definitely miss this place.

Four years ago I started my journey with a twelve-hour bus ride, breaking the curfew and crying like a fountain. There would be no great adventure without complications, but above all without amazing people, and I want to pay tribute to them. All the people who have walked with me, for a short or long time, and the effort they have made to stay by my side. It has been a wonderful journey and it would not have been possible without any of you.

First of all, I would like to thank my supervisors, who saw something good in me and decided to guide me along the path of scientific research. Piero Ugliengo, who took me on as a bachelor and master student when I knew absolutely nothing about astrochemistry, and introduced me to Albert Rimola. And Albert Rimola, who accepted me as a Ph.D. student when I was a small agglomerate of enthusiasm covered by a very thick layer of fear, and who gave me the opportunity to do a Ph.D. in cotutelle, to continue working with Piero Ugliengo. A special thanks to Prof. Asunción Fuente, thanks to whom my passion for sulphur chemistry began in 2018, when I stumbled upon a couple of her publications and found the topic of sulphur depletion too intriguing to let it slip from my hands. Four years later, we met in Madrid and we started a collaboration that I hope will last a long time. I would also like to thank Prof. François Dulieu, who hosted me for a month in his laboratory and believed in the do-it-yourself capabilities of computational chemists. I think I showed that we can do experiments too (no guarantees on the results though). A warm thank you to Prof. Cecilia Ceccarelli for her incredible ability to see the big picture and give us chemists a perspective on what we can do for the astronomical community.

Thank you to my colleagues for making the worst days worth a smile and for forcing me to take breaks when I did not want to. Thank you Nick, for always being there when I needed it the most and for teaching me to look at things from a revolutionary perspective that I had never considered before. Thank you Vitto, for the most fruitful fight that I have ever had in my life and for the friendship that came out of it. Thank you Andreha, for reminding me that I could be useful when I really did not feel like it and for being the best student and then colleague I could have ever hoped for. Thank you Panta, for listening to my silly ideas since 2020, for teaching me how to properly express my disappointment when calculations did not end the way I wanted, and for sharing your vast knowledge with me. Thank you Julie, for teaching me everything you know about lab experiments and for being a true friend since the first day we met.

And then, also a huge thank you to all the people who have always supported me, long before I could be a doctor in a suit: Gemma and Alessandro, who have always stayed by my side, even though life has taken us on very different paths; my primary school teacher,

Nerina, who has always waited for me to show up and update her on my journey. Thanks to the friends I met in Barcelona, who got to knew the moody and cosmopolitan version of me, and to my flatmate Riccardo, who listened to me carefully and shared his opinions without ever judging me. Lastly, but most importantly, thank you to my parents. I cannot understand how difficult it must be to see a daughter grow up and -literally - fly away, but I will never forget how I was able to do all this thanks to you.

Finally, as I am anything but a serious person, I would like to thank my dogs Lilli and Kira for putting up with me being abroad for so long and always bringing a smile to my face. Thank you to Thesaurus, WordReference, ChatGPT, Reverso, and DeepL for reassuring me when I felt like I had forgotten how to write in a proper English. And last but not least, thanks to the pharmacy that produces the best eye-drops in the world, allowing me to survive all those hours in front of the screen, especially the last year!

Thanks to all of you for turning a little chick into a bird that knows how to fly.